



Dedicated to the 100<sup>th</sup> Anniversary of the Founding of the Republic of Türkiye

## BOOK OF FULL TEXT

# 7<sup>th</sup> INTERNATIONAL CONFERENCE ON COMPUTATIONAL MATHEMATICS AND ENGINEERING SCIENCES

**20-21 May**  
2023, ELAZIĞ - TÜRKİYE

"CMES 2023 Symposium is supported by TUBITAK."



77733

Publish date:  
17.10.2023

# **THE SEVENTH INTERNATIONAL CONFERENCE ON COMPUTATIONAL MATHEMATICS AND ENGINEERING SCIENCES (CMES-2023), ELAZIĞ/TÜRKİYE, MAY 20-21, 2023**

The Seventh International Conference on Computational Mathematics and Engineering Sciences (CMES-2023) will be held in Firat University from 20- to 21 May 2023 in Elazığ, Türkiye. It provides an ideal academic platform for researchers and professionals to discuss recent developments in both theoretical, applied mathematics and engineering sciences. This event also aims to initiate interactions among researchers in the field of computational mathematics and their applications in science and engineering, to present recent developments in these areas, and to share the computational experiences of our invited speakers and participants.

The Organizing Committee

*©All Rights Reserved. This conference is organized by a cooperation of several international organizations including Firat University, Moulay Ismail University, Private University of Fes, Université Privée De Fés, Kırgızistan-Türkiye Manas Üniversitesi, Final International University, Harran University, Van Yüzüncü Yıl University, İnönü University, Ordu University, İstanbul Ticaret University, Azarbaycan University and Atatürk Technical University. No part of this book can be reproduced or utilized in any forms or by any means, electronic or mechanical, including photocopying, recording, or by any information storage and retrieval systems, without permission from the authors.*

© The informations provided in the papers published in this book are under the responsibility of their author(s).

## **Committee Chairs**

*Hasan Bulut, Firat University, Elazig, Türkiye*

*Zakia Hammouch, Ecole Normale Superierue de Meknes, Moulay Ismail University, Morocco*

## MESSAGE FROM THE GENERAL CHAIRS



Dear Conference Attendees,

We are honored to welcome you to the **Seventh International Conference on Computational Mathematics and Engineering Sciences (CMES-2023)** at Firat University from 20 to 21 May 2023 in Elazığ City, Türkiye.

CMES, founded in 2016 at Faculty of Science and Techniques Errachidia Moulay Ismail University Morocco is an annual international conference, which was very successful in the past years by providing opportunities to the participants in sharing their knowledge and informations and promoting excellent networking among different international universities. This year, the conference includes 200 extended abstracts, several submissions were received in response to the call for papers, selected by the Program Committee. The program features keynote talks by distinguished speakers such as: **Yusif Gasimov** from Azerbaijan University, Baku, Azerbaijan, **M. S. Osman** from Umm Al-Qura University, Makkah, Saudi Arabia, **Delfim F.M. Torres** from University of Aveiro, Portugal, **M.A. Aziz-Alaoui** from University of Le Havre, Normandy, France, **Rachid Yazami** from Nanyang Technological University Singapore, **Vatan Karakaya** from Ahi Evran University, Kırşehir, Türkiye, **Ömer Akın** from TOBB ETÜ University of Economics & Technology, Ankara, Türkiye, **Fernando León Saavedra** from University of Cádiz, Spain, **Bayram Şahin** from Ege University, Türkiye and **Zulqurnain Sabir** from United Arab Emirates University, UAE. The conference also comprises contributed sessions, posters sessions and various research highlights.

We would like to thank the Program Committee members and external reviewers for volunteering their time to review and discuss submitted abstracts. We would like to extend special thanks to the Honorary, Scientific and Organizing Committees for their efforts in making CMES-2023 a successful event. We would like to thank all the authors for presenting their research studies during our conference. We hope that you will find CMES-2023 interesting and intellectually stimulating, and that you will enjoy meeting and interacting with researchers around the world.

***Hasan Bulut,***

Firat University, Elazığ, Türkiye.

***Zakia Hammouch,***

ENS Meknes, Moulay Ismail University Morocco

Thu Dau Mot University, Binh Duong Province, Vietnam

China Medical University Hospital Taichung 40402, Taiwan.

## TOPICS

Applied Mathematics,	Information technology
Financial Mathematics,	Electrical and Electronic Engineering
Control Theory,	Ordinary, Partial, Stochastic and Delay
Game Theory	Differential Equations
Modeling of Bio-systems for Optimization	Chaos and Dynamical Systems
and Control,	Numerical methods and scientific
Linear and Nonlinear programming and	programming
Dynamics,	Fractional Calculus and Applications,
Artificial Intelligence,	Cryptography and its applications
Geometry and Its Applications,	Computational Fluids mechanics, Heat and
Analysis and Its Applications,	Mass Transfers.
Statistics and Its Applications,	Economics and Econometric Studies
Mathematics Education and Its Applications,	Topology and Its Application
Algebra and Its Applications.	Education Sciences
Engineering Sciences	Economics and Econometric Studies
Computer Science	Topology and Its Application

## COMMITTEE CHAIRS

Prof.Dr.Hasan Bulut, Firat University, Elazığ, Türkiye

Prof.Dr.Zakia Hammouch, ENS Meknes, Moulay Ismail University, Morocco

## COMMITTEE CO-CHAIRS

Prof.Dr. Carlo Cattani, Tuscia University, Viterbo, Italy

Prof.Dr. Haci Mehmet Baskonus, Harran University, Sanliurfa, Türkiye

Prof.Dr. Mohammed Ouazzani Jamil, University Privee of Fez, Morocco



## HONORARY COMMITTEE

- Prof.Dr. Fahrettin Göktaş (Rector of Fırat University, Elazığ, Türkiye)  
Prof.Dr. Alpaslan Ceylan (Rector of Kyrgyz-Turkish Manas University, Kyrgyzstan)  
Dr. Saadat Aliyeva (Rector of Azerbaijan University, Baku, Azerbaijan )  
Prof.Dr. Hamdullah Şevli (Rector of Van Yüzüncü Yıl University, Türkiye)  
Prof.Dr. Hüseyin Yaratın (Rector of Fırat International University, Girne, Cyprus)  
Prof.Dr. Ekrem Savaş (Rector of Uşak University, Türkiye)  
Prof. Dr. Mehmet Tahir Güllüoğlu (Rector of Harran University, Sanliurfa, Türkiye)  
Prof.Dr. Vatan Karakaya (Rector of Ahi Evran University, Kırşehir, Türkiye)  
Prof.Dr. Bülent Çakmak (Rector of Erzurum Technical University, Erzurum, Türkiye)  
Prof.Dr. Ali Akdoğan (Rector of Ordu University, Ordu, Türkiye)  
Prof.Dr. Yücel Oğurlu (Rector of İstanbul Ticaret University, İstanbul, Türkiye)  
Prof.Dr. Hassane Sahbi (President of Moulay Ismail University, Morocco)  
Prof.Dr. Ouazzani Jamil Mohamed (Vice President of Université Privée de Fes, Morocco)  
Prof.Dr. Mohammed Aziz Lahlou (President of Université Privée de Fes, Morocco)  
Prof.Dr. Omar Ossouaddi (Vice President of Moulay Ismail University, Morocco)  
Prof.Dr. Mohammed Amine (Director of ENS Meknes, Moulay Ismail University, Morocco)  
Prof.Dr. Etibar Penahlı (Baku State University, Baku, Azerbaijan)  
Prof.Dr. Yusif Gasimov (Azerbaijan University, Baku, Azerbaijan)  
Prof.Dr. Necdet Bildik (Retired Faculty Member)  
Prof.Dr. Mahmut Ergüt (Namık Kemal University, Tekirdağ, Türkiye)  
Prof.Dr. Rifat Colak (Fırat University, Elazığ, Türkiye)  
Prof.Dr. Doğan Kaya (İstanbul Ticaret University, İstanbul, Türkiye)  
İbrahim Taşel (Fırat International University, Girne, Cyprus)  
Şevket Ertem (Fırat International University, Girne, Cyprus)  
Veysel Demirci (Chairman of the board of Ziver Holding)  
İzzettin Toraman (Chairman of the board of Toraman Tekstil)

## SCIENTIFIC COMMITTEE

- Abdelhai Elazzouzi (Mohamed Ben Abdellah University, Morocco)  
Abdellah Rababah (University of Science and Technology Irbid, Jordan)  
Abdellah Rezzouk (Sidi Mohamed Ben Abdellah University, Morocco)  
Abdellatif Chaira (Moulay Ismail University)  
Abderhamane Ait Aadi (Ens Meknes, Moulay Ismail University, Morocco)  
Abdulhamit Subaşı (University of Turku, Finland)  
Abdulkadir Karakaş (Siirt University, Türkiye)  
Abdullah Çağman (Ağrı İbrahim Cecen University, Türkiye)  
Abdullah Kopuzlu (Atatürk University, Türkiye)  
Abdullahi Yusuf (Biruni University, İstanbul, Türkiye)  
Agamirza Bashirov (Eastern Mediterranean University, Cyprus)  
Ahmed El Khalfi (Sidi Mohamed Ben Abdellah University, Morocco)  
Ahmed Elngar (Beni Suef University Egypt.)

Ahmet Bedri Özer (Firat University, Elazığ, Türkiye)  
Ahmet Dumlu (Erzurum Technical University, Türkiye)  
Ahmet Ocak Akdemir (Ağrı İbrahim Cecen University, Türkiye)  
Ahmet Yıldız (İnönü University, Malatya, Türkiye)  
Akbar Barati Chiyaneh (Yüzüncüyıl University, Bitlis, Van)  
Ali Akgül (Siirt University, Türkiye)  
Ali Çakmak (Bitlis Eren University, Bitlis, Türkiye)  
Ali Karcı (İnönü University, Malatya)  
Ali Rostami (University of Tabriz, Tabriz, Iran)  
Ali Yousef (Kuwait College Of Science And Technology, Kuwait)  
Alireza Khalili Golmankhaneh (Department Of Physics, Faculty Of Science, Iau Urmia Branch, Iran)  
Alla Belousova (Don State Technical University, Russian Federation)  
Alper Ekinici (Bandırma 17 Eylül University, Türkiye)  
Alper Osman Öğrenmiş (Firat University, Elazığ, Türkiye)  
Alper Polat (Munzur University, Türkiye)  
Aly Ramadan Seadawy (Taibah University, Saudi Arabia )  
Amar Debbouche (Guelma University, Algeria)  
Anargül Urdaletova (Kyrgyz-Turkish Manas University, Kyrgyzstan)  
Aneta Barakoska (Faculty of Philosophy, University St. Cyril Macedonia)  
Anna Sandulyak (Université de Moscow, Russia)  
Arife Atay (Dicle University, Türkiye )  
Armando Ciancio (University of Messina, Italy)  
Arzu Akbulut (Eskişehir Osmangazi University, Türkiye)  
Arzu Denk Oguz ( Atılım University, Türkiye)  
Asan Ömüraliyev (Kyrgyz-Turkish Manas University, Kyrgyzstan)  
Asif Yokuş (Firat University, Elazığ, Türkiye)  
Avit Asanov (Kyrgyz-Turkish Manas University, Kyrgyzstan)  
Ayhan Şerbetçi (Ankara University, Ankara)  
Aynur Keskin Kaymakçı (Selçuk University, Konya)  
Aynur Yalciner (Selçuk University, Konya, Türkiye)  
Ayşe Dilek Maden (Selçuk University, Konya)  
Ayşe Metin Karakaş (Bitlis Eren University, Bitlis, Türkiye)  
Ayşegül Çetinkaya (Ahi Evran University, Türkiye)  
Bashar A.Al-Talip (University of Mosul, Iraq)  
Bayram Çekim (Gazi University, Türkiye)  
Bayram Şahin ( Ege University, İzmir, Türkiye)  
Behçet Öznacar (Near East University, Cyprus )  
Berivan Polat (Munzur University, Türkiye)  
Bilal Alatas (Firat University, Türkiye)  
Bilal Şenol (İnönü University, Malatya)  
Burcu Gürbüz (Johannes Gutenberg-University Mainz, Germany)  
Burçin Doğan (Malatya Turgut Özal University, Türkiye)  
Burhan Tiryakioğlu (Marmara University, Türkiye)  
Bülent Tavlı ( Tobb Economics And Technology University, Türkiye)  
Cameron Browne (University Of Louisiana At Lafayette ,Usa)

Carla M.A. Pinto (ISEP | Instituto Superior de Engenharia do Porto, Porto – PORTUGAL)  
Carlo Cattani (Tuscia University, Viterbo Italy)  
Cem Oguz ( Kırsehir Ahi Evran University,Türkiye)  
Cemil İnan (Mardin Artuklu University, Türkiye)  
Ceren Kına (Malatya Turgut Özal University, Türkiye)  
Ceren Sultan Elmalı (Erzurum Technical University, Türkiye)  
Cesim Temel (Yüzüncüyıl University, Türkiye)  
Chérif Ziti (Moulay Ismail University, Morocco)  
Christos Volos (Aristotle University, Greece)  
Çağrı Karaman (Atatürk University, Erzurum, Türkiye)  
Çetin Kürşat Bilir (Ahi Evran University, Türkiye)  
Çiğdem İnan (Mersin University, Türkiye)  
Damla Yılmaz (Erzurum Technical University, Türkiye)  
Danyal Soybaş (Erciyes University, Türkiye)  
Davut Hanbay (İnönü University, Malatya)  
Delfim Torres, (Aveiro University, Portugal)  
Derya Arslan (Bitlis Eren University, Bitlis, Türkiye)  
Derya Avcı (Balıkesir University, Türkiye)  
Devendra Kumar (JECRC University Jaipur, India)  
Dilek Okuyucu (Erzurum Technical University, Türkiye)  
Dumitru Baleanu (Cankaya University, Türkiye)  
Dursun İrk ( Eskişehir Osmangazi University, Eskişehir)  
Dyyak Ivan (Ivan Franko National University,Lviv,Ukraine)  
Ebru Bozkurt (Ataturk University, Türkiye)  
El Hassan Ben Ahmed (Ens Meknes, Moulay Ismail University, Morocco)  
El Houcine Lafhim (Sidi Mohamed Ben Abdellah University, Morocco)  
El Mehdi El Khattabi (Ens Meknes, Moulay Ismail University, Morocco)  
Ella Abilayeva (Kyrgyz-Turkish Manas University, Kyrgyzstan)  
Elman Hazar (İgdir University, Türkiye)  
Emel Biçer (Bingöl University, Türkiye)  
Emrah Yılmaz (Fırat University, Elazığ)  
Engin Özkan(Erzincan Binali Yıldırım University, Erzincan)  
Ennahnahi Nouredine (Sidi Mohamed Ben Abdellah University, Morocco)  
Erdal Baş (Fırat University, Elazığ, Türkiye)  
Erdal Ekici (Çanakkale Onsekiz Mart University, Çanakkale)  
Erdal Ulualan (Kutahya University, Türkiye)  
Erdal Ünlüyol (Ordu University, Türkiye)  
Erhan Deniz (Kafkas University, Türkiye)  
Erhan Güler (Bartın University, Türkiye)  
Erhan Pişkin (Dicle University,Diyarbakır,Türkiye)  
Erhan Set (Ordu University, Türkiye)  
Erol Yaşar (Mersin University, Mersin, Türkiye)  
Esin İlhan (Kırsehir Ahi Evran University / Türkiye)  
Esra Karataş Akgül (Siirt University ,Türkiye)  
Eva Kaslik (University of Timisoara, Romania)

Evrin Toklu (Ağrı İbrahim Cecen University, Türkiye)  
Ezgi Kaya (Iğdır University, Iğdır, Türkiye)  
Fahd Jarad (Cankaya University Türkiye)  
Fahrettin Muhtarov (Bakû State University Bakû, Azerbaijan)  
Fahrettin Özbey (Bitlis Eren University, Bitlis, Türkiye)  
Fatma Ayaz (Gazi University, Türkiye)  
Fatma Berna Benli (Erciyes University, Türkiye)  
Fatma Erdoğan (Fırat University, Elazığ)  
Fatma Sağsöz (Ataturk University, Türkiye)  
Fatma Taşdelen Yeşildal (Ankara University, Türkiye)  
Fethi Bin Muhammad Belgacem (Paaet, Shaamyia, Kuwait)  
Fethiye Müge Sakar (Dicle University, Türkiye)  
Feyza Esra Erdoğan (Ege University, İzmir, Türkiye)  
Fikret Aliyev (Bakû State University, Bakû, Azerbaijan)  
Filiz Taşcan (Eskişehir Osmangazi University, Eskişehir)  
Fırat Evirgen (Balıkesir University, Türkiye)  
Francesco Villecco (University Salerno, Italy)  
Fulya Şahin (Ege University, İzmir, Türkiye)  
Gonca Onargan (Final International University, Girne, Cyprus)  
Gökhan Gökdere (Fırat University, Elazığ)  
Gülşat Muhametjanov (Kyrgyz-Turkish Manas University, Kyrgyzstan)  
Gürhan İçöz (Gazi University, Türkiye)  
Güven Kaya (Bingöl University, Türkiye)  
Hacer Sengul (Harran University, Sanlıurfa, Türkiye)  
Hacı Bayram Karadağ (İnönü University, Malatya)  
Hacı Mehmet Baskonus (Harran University, Türkiye)  
Hakan Şimşek (Kırıkkale University /Türkiye)  
Halis Yılmaz (Dicle University, Türkiye)  
Halit Orhan (Ataturk University, Türkiye)  
Hamit Mirtağiloğlu (Bitlis Eren University, Bitlis, Türkiye)  
Hamza Erol (Mersin University, Mersin, Türkiye)  
Handan Öztekin (Fırat University, Elazığ, Türkiye)  
Hanlar Reşitoğlu (Iğdır University, Türkiye)  
Harun Kaya (Malatya Turgut Özal University, Türkiye)  
Hasan Bulut (Fırat University, Türkiye)  
Hasan Toğrul (Batman University, Batman, Türkiye)  
Hassan Qjidaa (Sidi Mohamed Ben Abdellah University, Morocco)  
Hatıra Günerhan (Kafkas University, Türkiye)  
Hatice Kuşak Samancı (Bitlis Eren University, Bitlis, Türkiye)  
Hatun Özlem Güney (Dicle University, Türkiye)  
Hayati Olgar (Gazi Osman Paşa University, Türkiye)  
Hayriye Esra Akyüz (Bitlis Eren University, Bitlis, Türkiye)  
Heybetkulu Mustafayev (Yüzüncüyıl University, Türkiye)  
Hıfı Altınok (Fırat University, Elazığ, Türkiye)  
Hijaz Ahmad (İstanbul Ticaret University, Türkiye)

Hikmet Kemaloğlu (Fırat University, Elazığ, Türkiye)  
Hossein Jafari (Unisa University Pretoria, South Africa)  
Hristos Anastassiu (International Hellenic University, Serres, Greece)  
Hülya Durur(Ardahan University, Ardahan, Türkiye)  
Hüseyin Demir (Ondokuz Mayıs University, Türkiye)  
Hüseyin Merdan(TOBB University of Economics and Technology, Türkiye)  
Hüseyin Yıldırım (Maraş Sütçü İmam University, K.Maraş)  
Ihor Prokodushyn (Ivan Franko National University,Lviv,Ukraine)  
Inan Ünal (Munzur University, Türkiye)  
Irina Abakumova (Don State Technical University, Russian)  
Izhar Uddin (Jamia Millia İslamia University. New Delhi, India)  
İbrahim Aktaş (Gumushane University, Türkiye)  
İbrahim Alinur Büyükaksoy (Okan University, Türkiye)  
İbrahim Karahan (Erzurum Technical University, Türkiye)  
İnci Toğrul (Batman University, Batman, Türkiye)  
İpek Abasıkeleş Turgut (İskenderun Technical University, Türkiye)  
İsa Yıldırım (Ataturk University, Türkiye)  
İsmail Onur Kıymaz (Ahi Evran University , Türkiye)  
İsmail Özgür Zembat (University of Glasgow, England)  
İsmet Altıntaş (Kyrgyz-Turkish Manas University, Kyrgyzstan)  
İsrafil Okumuş(Erzincan Binali Yıldırım University, Erzincan)  
Jagdev Singh (Jecrc University Jaipur, India))  
Jaouad Danane (University Hassan Iı, Casablanca)  
Jaouad El Makkaoui (Sidi Mohamed Ben Abdellah University, Morocco)  
Jaouad Kharbach (Sidi Mohamed Ben Abdellah University, Morocco)  
Javid Ali (Aligarh Müslim University,India)  
Juan Luis Garcia Guirao (Cartagena University, Spain)  
Kadirhan Polat (Ağrı İbrahim Cecen University, Türkiye)  
Kadriye Aydemir ( Amasya University,Türkiye)  
Kalışkan Matanova (Kyrgyz-Turkish Manas University, Kyrgyzstan)  
Karam Allali (University Hassan Iı, Casablanca)  
Kemal Aydın (Selçuk University ,Türkiye)  
Kexiang Xu (Nanjing University, China)  
Kolade Owolabi (Federal University Of Technology, Negeria)  
Kürşat Akbulut (Ataturk University, Türkiye)  
Lazar Stošić (College For Preschool Teachers, Aleksinac, Serbia)  
Luis Manuel Sánchez Ruiz (Technical University Of Valencia, Spain)  
M. Addam (Nat.School of Applied Sc.Hoceima, Morocco)  
M.A. Aziz Alaoui, (Universite De Normandie Lehavre France)  
Mahir Murat Cengiz (Ataturk University /Türkiye)  
Mahmut Isık (Harran University, Sanliurfa,Türkiye)  
Mehmet Akif Akyol (Bingöl University, Bingöl, Türkiye)  
Mehmet Atçeken (Tokat Gaziosmanpaşa University, Tokat)  
Mehmet Baki Yağbasan ( Kırşehir Ahi Evran University, Kırşehir)  
Mehmet Emir Köksal (Ondokuz Mayıs University, Türkiye)

Mehmet Karay (Final International University, Girne, Cyprus)  
Mehmet Korkmaz (Ordu University, Türkiye)  
Mehmet Küçükaslan (Mersin University, Türkiye)  
Mehmet Mendeş (Canakkale 18 Mart University, Türkiye)  
Mehmet Yavuz (Necmettin Erbakan University, Türkiye)  
Mesut Karabacak (Ataturk University, Türkiye)  
Mhamed El Omari (Sultan Moulay Slimane University, Morocco)  
Mhamed Sayyouri (Sidi Mohamed Ben Abdellah University, Morocco)  
Mohamed Addam (Nat.School Of Applied Sc.Hoceima, Morocco)  
Mohamed Lahby (University Hassan II, Casablanca)  
Mohamed Ouzahra (Mohamed Ben Abdellah University, Morocco)  
Mohamed Rhoudaf (Moulay Ismail University, Morocco)  
Mohammad Mursaleen (China Medical University, Taiwan)  
Mohammed Benslimane (Sidi Mohamed Ben Abdellah University, Morocco)  
Mohammed SEAID (Durham University United Kingdom)  
Muhammed Yiğider (Erzurum Technical University, Türkiye)  
Muhammet Kamali (Kyrgyz-Turkish Manas University, Kyrgyzstan)  
Muharrem Tuncay Gençöğlü (Fırat University, Elazığ, Türkiye)  
Murat Çağlar (Erzurum Technical University, Türkiye)  
Murat Karakaş (Bitlis Eren University, Bitlis, Türkiye)  
Murat Sat (Erzincan Binali Yıldırım University, Türkiye)  
Mustafa Açıkkar (Adana Science And Technology University, Türkiye)  
Mustafa Ali Dokuyucu (Ağrı İbrahim Cecen University, Türkiye)  
Mustafa Kemal Özdemir ( İnönü University, Malatya)  
Mustafa Mikail Özçiloğlu ( Kilis 7 Aralık University, Türkiye)  
Mustafa Yıldırım (Cumhuriyet University, Türkiye)  
Mustapha Ait Khellou (Ens Meknes, Moulay Ismail University, Morocco)  
Muzaffer Aşkın (Munzur University, Tunceli, Türkiye)  
Naci Genc (Van Yüzüncü Yıl University, Türkiye)  
Nagehan Kılinc Gecer ( Kırşehir Ahi Evran University, Türkiye)  
Najia Essbai (Sidi Mohamed Ben Abdellah University, Morocco)  
Nazlı Karaca (Atatürk Üniversitesi, Türkiye)  
Necati Ozdemir (Balıkesir University, Türkiye)  
Nejmi Cengiz (Ataturk University, Türkiye)  
Nergiz Önen Poyraz (Çukurova University, Türkiye)  
Nguyen Huy Tuan (Thu Dau Mot University, Vietnam)  
Nigar Yıldırım Aksoy (Kafkas University, Türkiye)  
Nizami Mustafa (Kafkas University, Türkiye)  
Numan Yalçın (Gumushane University, Türkiye)  
Ogün Doğru (Gazi University, Ankara, Türkiye)  
Okan Şakar (Bahçeşehir University, Türkiye)  
Olha Ivanyshyn (Izmir Institute Of Technology, Izmir, Türkiye)  
Omer Kisi (Bartın University, Türkiye)  
Onur Alp İlhan (Erciyes University, Türkiye)  
Ouadie Koubaiti (Fst, Moulay Ismail University, Morocco)

Ouazzani Jamil Mohamed (Private University Of Fez, Morocco)  
Ozen Ozer (Kırkırelı University, Türkiye)  
Ozlem Ertekin (Munzur University, Tunceli, Türkiye)  
Özge Kuran (Dicle University, Türkiye )  
Peyil Esengöl Kızı (Kyrgyz-Turkish Manas University, Kyrgyzstan)  
Praveen Agarwal (ANAND International College of Engineering Jaipur, India)  
Rajiv Aggarwal (Deshbandhu College, University Of Delhi, India)  
Ram Jiware (Indian Institute of Technology, Roorkee, India)  
Ramadhan A. Mohammed (University Of Duhok-Iraq)  
Ramin Najafi (Islamic Azad University, Iran)  
Rauf Amirov (Cumhuriyet University, Sivas, Türkiye)  
Recep Şahin (Kırıkkale University, Kırıkkale)  
Remzi Tuntas (Van Yüzüncü Yıl University, Türkiye)  
Reşat Yılmazer (Fırat University, Elazığ, Türkiye)  
Rıdvan Cem Demirkol (Muş Alparslan University, Türkiye)  
Rıdvan Şahin (Gümüşhane University, Türkiye)  
Robert Tchitnga (Dshang University, Cameroon)  
Roman Chapko ( Ivan Franko National University Lviv , Ukraine)  
Said Melliani (Sultan Moulay Slimane University, Morocco)  
Saima Rashid (Government College University Faisalabad, Pakistan)  
Sait Taş (Atatürk University, Türkiye)  
Sakthivel Rathinasamy (Bharathiar University, India)  
Salman Khodayifar (Institute For Adv.Studies In Basic Sciences,Iran)  
Sare Şengöl (Marmara University, Türkiye)  
Seçil Yalaz (Dicle University, Türkiye )  
Seda İğreti Araz (Siirt University, Siirt, Türkiye)  
Sedat İlhan (Dicle University, Türkiye )  
Seenith Sivasundaram (Université De Bethune-Cookman, Usa)  
Selahaddin Maden (Ordu University, Türkiye)  
Selçuk Baş (Muş Alparslan University, Türkiye)  
Semih Çavusoglu ( Gazi Osman Paşa University,Türkiye)  
Semra Yurttaçıkırmaz (Atatürk University, Türkiye)  
Serap Şahinkaya (Tarsus University)  
Serdal Pamuk (Kocaeli University, Türkiye)  
Serhan Eker (Ağrı İbrahim Cecen University, Türkiye)  
Sertaç Göktaş (Mersin University, Mersin, Türkiye)  
Shilpi Jain (Poornima College of Engineering, India)  
Sıdıka Şule Şener (Atatürk University, Türkiye)  
Sibel Turanlı (Erzurum Technical University, Türkiye)  
Sinan Çalık (Fırat University,Elazığ,Türkiye)  
Sizar A. Mohammed (University Of Duhok-Iraq)  
Songül Kaya Merdan (Middle East Technical University,Türkiye)  
Sonja Velickovic (College For Preschool Teachers, Serbia)  
Sunil Kumar (National Institute Of Technology Jamshedpur, India)  
Sunil Purohit (Maharana Pratap University, India)

Süleyman Şenyurt (Ordu University, Türkiye)  
Şakir İşleyen (Van Yüzüncü Yıl University, Van, Türkiye)  
Şebnem Yıldız (Ahi Evran University, Kırşehir, Türkiye)  
Şevket Gür (Sakarya University, Türkiye)  
Şükran Konca (İzmir Bakırçay University, İzmir, Türkiye)  
Talat Körpınar (Muş Alparslan University, Türkiye)  
Tamer Uğur (Ataturk University /Türkiye)  
Thabet Abdeljawad (Prince Sultan University KSA.)  
Tukur Abdulkadir Sulaiman (Biruni University, Istanbul, Türkiye)  
Ufuk Kaya (Bitlis Eren University, Bitlis, Türkiye)  
Unal İç (Firat University, Elazığ)  
Ülkü Yılmaz (Malatya Turgut Özal University, Türkiye)  
Vali Bashiry (Cyprus International University, Cyprus )  
Vehpi Yıldırım (Erzurum Technical University, Türkiye)  
Vera Stojanovska (Faculty of Philosophy, University Ss. Cyril Macedonia)  
Wei Gao (Yunnan Normal University, China.)  
Yadigar Sekerci ( Amasya University, Türkiye)  
Yarema Savula ( Ivan Franko National University Lviv , Ukraine)  
Yasin Kaya (Dicle University, Türkiye )  
Yavuz Altın (Firat University, Elazığ, Türkiye)  
Yener Altun (Van Yüzüncü Yıl University, Van, Türkiye)  
Yeşim Saraç (Ataturk University, Türkiye)  
Yıldırım Çelik (Ordu University, Türkiye)  
Youssef El Haoui (ENS Meknes, Moulay Ismail University, Morocco)  
Yury Luchko (Beuth Hochschule Für Technik Berlin, Germany)  
Yusif Gasimov (Azerbaijan University, Bakû, Azerbaijan)  
Yusuf Gurefe (Mersin University, Mersin, Türkiye)  
Yusuf Pandır (Bozok University – Türkiye)  
Zakaria Chalh (Sidi Mohamed Ben Abdellah University, Morocco)  
Zakaria El Malki (Est Moulay Ismail University, Morocco)  
Zakia Hammouch (Ens Meknes, Moulay Ismail University Morocco)  
Zanyar Anwer Ameen (University of Duhok-Iraq)  
Zeliha Körpınar (Muş Alparslan University, Türkiye)  
Zhonglong Zhao (North University of China, China)  
Zoubida Mghazli (Ibn Tofail University, Kenitra Morocco)  
Zulqurnain Sabir (Hazara University, Pakistan)

## ORGANIZING COMMITTEE

Prof. Dr. Hasan Bulut (Chair) Firat University, Türkiye  
Prof. Dr. Zakia Hammouch (Chair) ENS of Meknes, Moulay Ismail University, Morocco  
Prof. Dr. Ouazzani Jamil Mohammed (Co-Chair), Universite Privee de Fes Morocco  
Prof. Dr. Hacı Mehmet Baskonus (Co-Chair), Harran University, Türkiye  
Prof Dr. Hassan Qjidaa (Co-Chair), Sidi Mohammed Ben Abdellah University, Fes Morocco



Prof. Dr. Carlo Cattani (Co-Chair) Tuscia University, Italy  
Prof. Dr. Ercan Çelik (Co-Chair) Kyrgyz-Turkish Manas University, Kyrgyzstan  
Prof. Dr. Mikail ET, Fırat University, Türkiye  
Prof. Dr. Vedat Asil, Fırat University, Türkiye  
Prof. Dr. Mehmet Bektaş, Fırat University, Türkiye  
Prof. Dr. Fevzi Erdoğan, Yüzüncüyıl University, Türkiye  
Prof. Dr. Alaattin Esen, İnönü University, Türkiye  
Prof. Dr. Hassan Qjdaa, Sidi Mohamed Ben Abdellah University of Fes Morocco  
Assoc. Prof. Dr. Gülnur Yel, Final International University, Girne, Cyprus  
Assoc. Prof. Dr. Esin İlhan, Ahi Evran University, Türkiye  
Assoc. Prof. Dr. Tolga Aktürk, Ordu University, Türkiye  
Assoc. Prof. Dr. M. Gıyas Sakar, Yüzüncüyıl University, Türkiye  
Dr. Faculty Mem. Muhammed Yiğider, Erzurum Technic University, Türkiye

## LOCAL COMMITTEE

Özlem Orhan (Bandırma Onyedil Eylül Üniv, Balıkesir)	Dilek Günaydın (Fırat University, Elazığ, Türkiye)
Mehmet Karay (Final Int. University, Girne, Cyprus)	Hajar Farhan Ismael (University of Zakho, Iraq)
Mustafa Yeneroglu (Fırat University, Elazığ, Türkiye)	Karmina K. Ali (University of Zakho, Iraq)
Münevver Tuz (Fırat University, Elazığ, Türkiye)	Sibel Şehriban Ataş (Fırat University, Elazığ, Türkiye)
Gülden Altay Suroglu (Fırat University, Elazığ, Türkiye)	Aysenur Akkılıç (Assistant, Fırat Un.Elazığ, Türkiye)
Fatma Erdogan (Fırat University, Elazığ, Türkiye)	Sibel Tarla (Assistant, Fırat University, Elazığ, Türkiye)
Ebru Cavlak Aslan (Fırat University, Elazığ, Türkiye)	Bahar Acay (Assistant, Fırat Ün., Elazığ, Türkiye)
Şeyma T. Demiray (Osmaniye Korkut Ata Ü., Türkiye)	Aslı Alkan (Fırat University, Elazığ, Türkiye)
Tüba Gülşen (Fırat University, Elazığ, Türkiye)	Beyhan Kemaloğlu (Fırat University, Elazığ, Türkiye)
Hatice Aslan (Fırat University, Elazığ, Türkiye)	Mucahit Saydam (Fırat University, Elazığ, Türkiye)
Ahu Ercan (Fırat University, Elazığ, Türkiye)	Çağrı Yılmaz (Fırat University, Elazığ, Türkiye)
Berat Karaagac (Adıyaman University, Türkiye)	Merve Zeynep Gecmen (Ağrı İbrahim Çeçen University, Ağrı, Türkiye)
Ezgi Kaya (Iğdır University, Iğdır, Türkiye)	Necati Erdoğan (Van Yüzüncü Yıl Un., Van, Türkiye)
Mahmut İhtiyaroğlu (Van Yüzüncü Yıl Univ., Türkiye)	Arif Özkul (Fırat University, Elazığ, Türkiye)
Onur Saldır (Van Yüzüncü Yıl University, Van, Türkiye)	Sümeyye Kılbitmez (Fırat University, Elazığ, Türkiye)
Zelal Temel (Van Yüzüncü Yıl University, Van, Türkiye)	Süleyman Sarıkaya (Fırat University, Elazığ, Türkiye)
Sinan Deniz (Yüzüncü Yıl Üniversitesi, Türkiye)	Şeyma Firdevs Korkmaz (Fırat Üniv, Elazığ, Türkiye)
Beytullah Yağız (Yüzüncü Yıl Üniversitesi, Türkiye)	
Hajar Rezaei (Yüzüncü Yıl Üniversitesi, Türkiye)	
İbrahim Enam İnan (Fırat University, Elazığ, Türkiye)	

## LANGUAGE EDITORIAL COMMITTEE

Erkan Yuce (Aksaray University, Aksaray, Türkiye)  
Suheyla Demirkol Orak (Fırat University, Elazığ, Türkiye)  
Fatih Mehmet Cigerci (Harran University, Sanliurfa, Türkiye)  
Zeki Tastan (Van Yuzuncuyil University, Van, Türkiye)  
Fatma Şeyma Doğan (Harran University, Sanliurfa, Türkiye)

## International Communications Consultant

Prof. Dr. Rengin AK, Kırklareli University, Kırklareli, Türkiye  
Prof. Dr. Hikmet Kemaloğlu, Fırat University, Elazığ, Türkiye  
Prof. Dr. İlkay Açıkgöz Erkaya, Ahi evran University, Türkiye  
Assoc. Prof. Dr. M. Evren Aydın, Fırat University, Elazığ, Türkiye

## PROCEEDINGS

Full version of submitted papers will be published in Special Volumes of reputed journals. Procedure, Guidelines and Checklist for the preparation and submission of papers to the Proceedings of CMES-2023 can be found in the journals websites. The journals in which selected and peer-reviewed full papers of CMES-2023 will be published are as follows:

### 1. BOOK OF ABSTRACTS [Free of charge]

If Authors submit ABSTRACT TEXTS, then, after getting referees evaluations for these abstracts, they will be published in ABSTRACT PROCEEDING BOOK of CMES-2023. For FULL TEXT PAPERS, Authors have to submit their FULL TEXT PAPERS online via submission system of CMES-2023. These FULL TEXT PAPERS will be published in FULL TEXT PROCEEDING BOOK of CMES-2023 after getting at least two positive reports.

### 2. CONFERENCE PROCEEDINGS [Free of charge]

At the beginning, if Authors submit FULL TEXT PAPERS, then, after getting at least two positive referee reports, FULL TEXT PAPERS will be published in FULL TEXT PROCEEDING BOOK of CMES-2023 with ISBN:77733 number. Therefore, Abstracts of these FULL TEXT PAPERS will **NOT** be published in ABSTRACT PROCEEDING BOOK of CMES-2023.

### 3. FRACTAL AND FRACTIONAL JOURNAL [SCI-E],

Selected papers from CMES-2023 will be published in a special issue dedicated to the Conference entitled "**New Challenges Arising in Engineering Problems with Fractional and Integer Order-III**".

[https://www.mdpi.com/journal/fractalfract/special\\_issues/44H88MD0G9](https://www.mdpi.com/journal/fractalfract/special_issues/44H88MD0G9)

This journal is indexed by SCI-E.

### 4. PROCEEDINGS OF THE INSTITUTE OF MATHEMATICS AND MECHANICS [E-SCI]

Selected papers from CMES-2023 will be published by <https://proc.imm.az/special/>

This journal is indexed by E-SCI.

### 5. TURKISH JOURNAL OF SCIENCE, [FREE]

Participants of CMES 2023 can submit their good quality papers to Turkish Journal of Science. After the peer review process, the papers will be published at TJOS. The authors must write "CMES 2023" as comments to the editor.

(Editor in Chief: Dr. Ahmet Ocak AKDEMİR) For on-line submission: <https://dergipark.org.tr/tr/pub/tjos>

### 6. TURKISH JOURNAL OF INEQUALITIES, [FREE]

"Participants of CMES 2023 can submit their good quality papers to Turkish Journal of Inequalities. Selected papers will be published at TJI after the peer review process. The participants can send their papers to [erhanet@tjinequality.com](mailto:erhanet@tjinequality.com). The authors must write "CMES 2023" as the subject.

(Editor in Chief: Prof. Dr. Erhan SET)  
<http://tjinequality.com/>

### 7. MATHEMATICS IN NATURAL SCIENCE (MNS)

Authors can submit their full text paper directly to the journal by using the following link  
<https://www.isr-publications.com/mns>

### 8. MATHEMATICS IN ENGINEERING, SCIENCE AND AEROSPACE (MESA), [FREE, SCOPUS]

"Selected papers will be published after peer review in the Journal of Mathematics in Engineering, Science and Aerospace (MESA)"  
(Editor in Chief: Prof. Seenith Sivasundaram)  
<http://nonlinearstudies.com/index.php/mesa>

#### **9. APPLIED MATHEMATICS AND NONLINEAR SCIENCES, [E-SCI+ SCOPUS]**

Participants of CMES 2023 can submit their high quality full text papers to Applied Mathematics and Nonlinear Sciences by selecting CMES-2023 under the Select Article Type Menu.  
<https://www.editorialmanager.com/amns/default.aspx>

#### **10. MATHEMATICAL MODELLING AND NUMERICAL SIMULATION WITH APPLICATIONS (MMNSA), [TR DİZİN]**

The Special Issue on “Advanced Methods of Modelling and Numerical Computation in Science and Engineering”. Authors can submit their full text paper directly to the journal by using the information provided in the following link  
[https://mmnsa.org/index.php/mmnsa/special\\_issues/SI-CMES2023](https://mmnsa.org/index.php/mmnsa/special_issues/SI-CMES2023)

#### **11. SYMMETRY [SCI-E] ; SPECIAL ISSUE "ADVANCES IN MATRIX TRANSFORMATIONS, OPERATORS AND SYMMETRY"**

Authors can submit their full text paper directly to the journal by using the following link

[https://www.mdpi.com/journal/symmetry/special\\_issues/Advances\\_Matrix\\_Transformations\\_Operators\\_Symmetry](https://www.mdpi.com/journal/symmetry/special_issues/Advances_Matrix_Transformations_Operators_Symmetry)

#### **12. YUZUNCU YIL UNIVERSITY JOURNAL OF THE INSTITUTE OF NATURAL AND APPLIED SCIENCES (TR-Dizin)**

Authors can submit their full text paper directly to the journal by using the following link

<https://dergipark.org.tr/tr/pub/yyufbed>

#### **13. PEDAGOGICAL PERSPECTIVE (PEDPER)**

Pedagogical Perspective (**PedPer**) is an international, double blind reviewing, non-profit, professional scientific journal. PedPer is a journal that accepts manuscripts related to pedagogy and education.  
<http://pedagogicalperspective.com/>

# PLENARY & INVITED TALKS



## Applications of the Nonlinear Evolution Equations: An Efficient Analytical Technique

M. S. Osman

Department of Mathematics, Faculty of Applied Sciences, Umm Al-Qura University,  
Makkah, 21955, Saudi Arabia

[msosman@uqu.edu.sa](mailto:msosman@uqu.edu.sa); [mofatzi@cu.edu.eg](mailto:mofatzi@cu.edu.eg)

**Abstract:** Investigation of mathematical modeling and soliton concept relies mainly on the nonlinear evolution equations (NEEs) [1, 2]. Seeking exact solutions to the NEEs has emerged as one of the most intriguing and very active fields of research. The propagation of shallow-water waves, fluid dynamics, condensed matter physics, computational physics, and geophysics [3, 4] have all been extensively represented by a variety of well-known NEEs, including the nonlinear Ito integral differential equation, the nonlinear Schrödinger equation in higher dimensions, the modified KdV equation, and many others.

Our primary driving force behind this work is to look for various wave shapes for the NEEs' achieved solutions. To accomplish our objective, we use the unified method and its generalized form [5] to identify several analytical solutions, such as solitary, kink-soliton, anti-kink soliton, shock, dark-soliton, bright-soliton, elliptic wave solutions, multi-rational soliton solutions, and multi-wave solutions. Further, the diagrams of the results are additionally displayed. It's vital to note that this study is brand-new and has never been written about before, especially in relation to nonautonomous NEEs.

**Keywords:** Nonlinear Evolution Equations; Exact Solutions; The Unified Method; The Generalized Unified Method.

### References

1. Aktar, M.S., Akbar, M.A. and Osman, M.S., 2022. Spatio-temporal dynamic solitary wave solutions and diffusion effects to the nonlinear diffusive predator-prey system and the diffusion-reaction equations. *Chaos, Solitons & Fractals*, 160, p.112212.
2. Ismael, H.F., Bulut, H. and Osman, M.S., 2022. The N-soliton, fusion, rational and breather solutions of two extensions of the  $(2+1)$ -dimensional Bogoyavlenskii-Schieff equation. *Nonlinear Dynamics*, 107(4), pp.3791-3803.
3. Abdul Kayum, M., Ali Akbar, M. and Osman, M.S., 2022. Stable soliton solutions to the shallow water waves and ion-acoustic waves in a plasma. *Waves in Random and Complex Media*, 32(4), pp.1672-1693.
4. Akinyemi, L., Şenol, M. and Osman, M.S., 2022. Analytical and approximate solutions of nonlinear Schrödinger equation with higher dimension in the anomalous dispersion regime. *Journal of Ocean Engineering and Science*, 7(2), pp.143-154.
5. Osman, M.S., 2019. One-soliton shaping and inelastic collision between double solitons in the fifth-order variable-coefficient Sawada-Kotera equation. *Nonlinear Dynamics*, 96(2), pp.1491-1496.



## The speed-in-action problem for the nonlinear hyperbolic equation with a nonlocal condition

Yusif Gasimov<sup>1</sup>, Hamlet Guliyev<sup>2</sup>

<sup>1</sup>Azerbaijan University, Baku, Azerbaijan; <sup>2</sup>Baku State University, Baku, Azerbaijan  
[gasimov.yusif@gmail.com](mailto:gasimov.yusif@gmail.com)

**Abstract:** As is known, the speed-in-action problem is one of the first problems of mathematical theory of the optimal control. As a generalization of a number of practical problems of designing optimal control systems, it has become one of the intensively studied problems. In the theory of optimal control for the processes described by ordinary differential equations, the speed-in-action problems are studied rather well [1,2,3]. But for the processes described by partial differential equations, these problems are relatively less studied. Therefore, the study of speed-in-action problem for the different non-stationary partial differential equations having different applications are actual. For the systems with distributed parameters, the study of such problems relates to number of principal difficulties, while the problem statement itself can be more diverse and contain features which are not in the case of systems given by ODEs. Note that in some papers optimal control problems with an integral boundary condition are considered [4, 5].

In the present work, we study the speed-in-action problem for the non-linear second order hyperbolic equation with a non-local condition and with a control in the coefficient of the equation for the first time. The prototype of this problem is the equation rising in relativistic quantum mechanics. A theorem on the existence of an optimal control is proved and necessary optimality condition in the form of a variational inequality is derived.

**Keywords:** speed-in-action problem, nonlinear hyperbolic equation, nonlocal condition, optimality condition.

### References

1. Pontryagin L.S., Boltyansky V.G., Gomkrelidze R.V., Mishchenko E. (1969). Mathematical theory of optimal processes. Moscow, Nauka, 1969, 384 p.
2. Lee E.B, Markus L. (1972). Fundamentals of the theory of optimal control. Moscow, Nauka, 1972, 576 p.
3. Gabasov R., Kirillova F.M. (1981). Optimization Methods. Minsk, BSU, 1981, 350 p.
4. Tagiev, R.K., Habibov, V.M. (2016). On an optimal control problem for the heat equation with integral boundary condition. *J. Samara State Tech. Univ., Ser. Phys. and Math. Sci.*, 20(1), 54-64.
5. Guliyev H.F., Gasimov Y.S., Tagiev H.T., Huseynova T.M. (2017). On the inverse problem of finding the right side of the wave equation with a nonlocal condition. *Bulletin of Tomsk State University, Mathematics and Mechanics*, 49, 6-24.



## On modulated statistical and strong Cesàro convergences

Fernando León Saavedra<sup>1</sup>

<sup>1</sup>University of Cádiz, Spain

[fernando.leon@uca.es](mailto:fernando.leon@uca.es)

**Abstract:** The notions of modulated statistical convergence and modulated strong Cesàro convergences have appeared in the literature at different times and by different authors. Furthermore, there has been a great effort by different authors (for instance Et Mikail, Vinod K. Bhardwaj, Hacer Şengül,... and many others), to understand the existing structure between both notions. In lecture today we are going to see that there is a rich structure between both notions and that the concept of compatible module function is central to connect such structure. Finally, we will see that this circle of ideas continues to be efficient for double sequences, lacunary convergences, etc.

**Keywords:** Statistical convergence; Strong Cesàro convergence, modulus function, compatible modulus function.

## References

1. Bhardwaj, Vinod K. ; Dhawan, Shweta . Density by moduli and lacunary statistical convergence. Abstr. Appl. Anal. 2016, Art. ID 9365037, 11 pp.
2. Temizsu, Fatih ; Et, Mikail ; Çinar, Muhammed ; Şengül Kandemir, Hacer. On  $(\lambda, f)$ -statistical boundedness of order  $\alpha$  . Comm. Statist. Theory Methods 51 (2022), no. 19, 6766--6776.
3. León-Saavedra, Fernando ; Listán-García, María del Carmen ; Romero de la Rosa, María del Pilar . On statistical convergence and strong Cesàro convergence by moduli for double sequences. J. Inequal. Appl. 2022, Paper No. 62, 14 pp.
4. León-Saavedra, Fernando ; Listán-García, M. del Carmen ; Pérez Fernández, Francisco Javier ; Romero de la Rosa, María Pilar . On statistical convergence and strong Cesàro convergence by moduli. J. Inequal. Appl. 2019, Paper No. 298, 12 pp.
5. Romero de la Rosa, M.D.P. On Modulated Lacunary Statistical Convergence of Double Sequences(2023) Mathematics, 11 (4), art. no. 1042.





## Comparing Some Plant Communities in a Region of Turkey via Fuzzy Similarity

Ömer Akın

Honorary Chairman of Association of Mathematicians (MATDER),  
Department of Mathematics in TOBB Economics And Technology University, Türkiye  
[omerakin@etu.edu.tr](mailto:omerakin@etu.edu.tr)

**Abstract:** In this talk, firstly we explain crisp similarity, fuzzy similarity and compare them. After that, we answer the question of “why we need to use fuzzy similarity?” Furthermore, we extend the results obtained with crisp logic of “the results obtained in forest vegetation in the research project on plant sociology conducted in Black Sea Region in Turkey)” with fuzzy similarity. To do this application, it has been evaluated with the fuzzy similarity measures approach, and the similarity relations between the plant communities (plant associations) and among the relevés (sampling areas) they cover has been investigated. Finally, we compare the results by giving tables.

**Keywords:** Fuzzy similarity; crisp logic; plant communities; the relevés.

### References

- [1] Zadeh LA (1965) Fuzzy sets. Information and Control 8:338–353.
- [2] Lee-Kwang H, Yoon-Seon S, Keon-Myung L (1994) similarity measure between fuzzy sets and between elements. fuzzy sets and systems 62:291-293.
- [3] Bingöl MÜ, Geven F, Güney K (2007) “A Phytoecological and Phytosociological Research on the Sakarat Mountain (Amasya)”. Research Project. The Scientific and Technological Research Council of Turkey (TÜBİTAK). TÜBİTAK TOVAG-HD 105O018.
- [4] Akın Ö (Keynote speaker), Bingöl MÜ, Akdeniz Şafak S (2023) Fuzzy logic, fuzzy similarity and their applications on some plant communities. *International Congress on Engineering and Sciences* (Online conference), İstanbul, March 18-19, 2023, E-ISBN: 978 625-7367-93-6.

**Note:** This talk has been prepared By Bingöl M.Ü.( [mumit1111@hotmail.com](mailto:mumit1111@hotmail.com)), ŞAFAK S.A.([ssafak@ankara.edu.tr](mailto:ssafak@ankara.edu.tr), [sanem.akdeniz@hotmail.com](mailto:sanem.akdeniz@hotmail.com)) , AKIN Ö.([omerakin@etu.edu.tr](mailto:omerakin@etu.edu.tr))





**From Complex Systems & Interaction Networks to Real Life.  
Application in Neuroscience**

M. Aziz-Alaoui

LeHavre Normandie University, LMAH, FR-CNRS-3335, ISCN,  
BP. 540, 76600 Le Havre, France  
[aziz.alaoui@univ-lehavre.fr](mailto:aziz.alaoui@univ-lehavre.fr)

**Abstract:** After having situated, in a somewhat vulgarized way, the context, which is that of complex systems and networks, of self-organization and emergent properties, a concept of which we will give an example that is quite omnipresent in many fields, that of synchronization, we propose to study a fairly typical example in neuroscience. We will talk a bit about modeling and will recall the origin of the Hodgkin-Huxley (HH) PDE model and its reduction to the FitzHugh-Nagumo (FHN) model. We will then give some mathematical results on the asymptotic behavior of complex reaction-diffusion networks (graphs of  $n$  nodes). We show the existence of the global attractor for these networks, as well as the emergence of a fundamental property, that of synchronization. We determine analytically, for any network topology, the threshold of such synchronization. We finally illustrate these theoretical results by numerical simulations and present heuristic laws giving the minimum coupling strength necessary to achieve synchronization, as a function of the number of nodes and the network topology.

**Keywords:** Dynamical Systems, Complex Systems and Networks, Reaction-Diffusion Systems, Attractor, Synchronization, Neural networks.

**References:**

1. S.Das, A.A. et al (2023). Traveling pulses and its wave solution scheme in a diffusively coupled 2D Hindmarsh-Rose excitable systems, to appear in *Nonlinear Dynamics*, <https://doi.org/10.1007/s11071-022-08168-x>
2. A.Mondal, A.A. et al, (2022). The generation of diverse traveling pulses and its solution scheme in an excitable slow-fast dynamics, *Chaos: An Interdisciplinary Journal of Nonlinear Science*, Vol. 32(8), pp: 083121.
3. A. Miranville, G. Cantin & M. Aziz-Alaoui, (2021). Bifurcations and synchronization in networks of unstable reaction-diffusion systems, *Journal of Nonlinear Science*, Vol.31(2).
4. L. Naudin, N. Corson, M. Aziz-Alaoui (2021). On the modeling of the three types of non-spiking neurons of the *Caenorhabditis elegans*, *International Journal of Neural Systems (World Scientific)*, Vol. 31(2), 2050063.
5. B. Ambrosio, M. Aziz-Alaoui, A. Balti, (2021). Propagation of bursting oscillations in coupled non-homogeneous Hodgkin-Huxley Reaction-Diffusion systems, *Differential Equations and Dynamical Systems*, Vol. 29(4), pp:841-855.
6. B. Ambrosio, M. Aziz-Alaoui, V.L.E. Phan, (2019). Large Time Behavior and Synchronization of Complex Networks of Reaction-Diffusion Systems of FitzHugh-Nagumo Type, *IMA Journal of Applied Mathematics*, Vol. 84(2), Pages 416-443.



### **Spiral curves in computer aided geometric design**

Bayram Şahin

Department of Mathematics, Faculty of Science, Ege University, İzmir-Türkiye  
[bayram.sahin@ege.edu.tr](mailto:bayram.sahin@ege.edu.tr)

**Abstract:** Bezier curves and surfaces are widely used in computer-aided geometric design because they have features that will provide convenience in a design. On the other hand, spiral curves are useful in the design of highway railway and satellite orbits. The reason for this is that the spiral curves behave with respect to the its arc parameter. The most well-known of these are the Clothoids. However, since Clothoids are not easy to analyze mathematically, it creates difficulties in design. In this talk, the spiral conditions of Bezier curves and their transition curves, namely from a line to circle, from a circle to a circle with S-shaped, from a circle to circle with C-shaped, from a line to a line and circle to circle where one circle lies inside the other, to be used in the design of highway, railway and satellite orbits, are discussed. In addition, the case of spiral and transition curves of Bezier-like curves, which arise due to the deficiencies of Bezier curves in defining closed curves and the property of local variation on the curve, are discussed.

**Keywords:** CAGD, Bezier curve, Bezier surface, Spiral, transition curves;

### **References**

- [1] Ayar, A., Şahin, B., Trigonometric Bézier-like curves and transition curves. Appl. Math. (Warsaw) 48, no. 2, 125–153, 2021.
- [2] Habib, Z. and Sakai, M., On ph quintic spirals joining two circles with one circle inside the other, Computer-Aided Design, 39, 125-132, 2007.
- [3] Levent, A., Şahin, B., Beta Bézier curves. Appl. Comput. Math. 18, no. 1, 79–94, 2019.
- [4] Tong, W., Chen, M., A sufficient condition for 3D typical curves. Comput. Aided Geom. Design 8, Paper No. 101991, 14 pp, 2021.
- [5] Walton, D. J. and Meek, D.S., A Planar Cubic Bezier Spiral, Journal of Computational and Applied Mathematics 72, 85-100, 1996.
- [6] Walton, D. J. and Meek, D.S., A Pythagorean Hodograph Quintic Spiral, Computer-Aided Design, Vol 28, No 12, p. 943-950, 1996.
- [7] Walton, D. J. and Meek, D.S., 2005, A Controlled Clothoid Spline, Computers and Graphics, 29 ,353-363, 2005.
- [8] Walton, D. J. and Meek, D.S., A Further Generalisation Of The Planar cubic Bezier Spiral, J. Comput. Appl. Math. 236(11), 2869-2882, 2012.
- [9] Yeoh, W. K.; Ali, J. M. A cubic Bézier like spiral as transition curve. World Conference on 21st Century Mathematics 2004, 244–252, Sch. Math. Sci. G. C. Univ., Lahore, 2004



## Designing computational frameworks for the nonlinear singular differential models

Zulqurnain Sabir<sup>1,2</sup>

<sup>1</sup>Department of Mathematics, United Arab Emirates University, UAE

<sup>2</sup>Department of Mathematics, Hazara University, Mansehra, Pakistan

[Zulqurnain\\_maths@hu.edu.pk](mailto:Zulqurnain_maths@hu.edu.pk)

**Abstract:** The present work shows the solutions of the singular models based on the stochastic computing schemes. These investigations not only presented for the numerical results of the singular models, but the prediction, delayed, and pantograph singular models can also be handled through these stochastic paradigms. The design of the Gudermannian function is presented using the neural networks optimized with the global/local search schemes. The obtained results have been performed using the hybridization of these schemes. The exactness is approved through the comparison of the proposed and exact solutions. Moreover, the neuron analysis has been provided to authenticate the efficiency and complexity of the designed approach. For the effectiveness of the proposed approach, the absolute error performances have been performed to the singular models. For the stability of the stochastic method, the statistical performances including Theil inequality Coefficient, Variance Account For and Mean Absolute Deviation have been provided for multiple executions to solve the singular differential models. This contribution of this work is categorized in two phases as:

The Gudermannian function is designed as a neural network under the optimization of global/local search methods for the nonlinear singular differential models. In the second phase, the nonlinear higher order singular models have been solved through the global/local search techniques. The applicability and dependability of such schemes have been monitored to solve these singular models, which arises in engineering and science as well.

**Keywords:** Singular models, Gudermannian neural networks, Global and local search methods, Numerical solutions; Neurons analysis.

## References

1. Sabir, Z., 2022. Neuron analysis through the swarming procedures for the singular two-point boundary value problems arising in the theory of thermal explosion. *The European Physical Journal Plus*, 137(5), p.638.
2. Sabir, Z., Nisar, K., Raja, M.A.Z., Ibrahim, A.A.B.A., Rodrigues, J.J., Al-Basyouni, K.S., Mahmoud, S.R. and Rawat, D.B., 2021. Heuristic computational design of Morlet wavelet for solving the higher order singular nonlinear differential equations. *Alexandria Engineering Journal*, 60(6), pp.5935-5947.
3. Sabir, Z., Raja, M.A.Z. and Baleanu, D., 2021. Fractional mayer neuro-swarm heuristic solver for multi-fractional order doubly singular model based on lane–emden equation. *Fractals*, 29(05), p.2140017.
4. Sabir, Z., Baleanu, D., Shoaib, M. and Raja, M.A.Z., 2021. Design of stochastic numerical solver for the solution of singular three-point second-order boundary value problems. *Neural Computing and Applications*, 33, pp.2427-2443.

# An Algebraic Optimization Model to Conserve Water Environment by Distributing Manure for Harvesting.

Déthié Dione<sup>a</sup>

Teubé Cyrille Mbainaissem<sup>b</sup>

Bakary Koné<sup>c</sup>

Paul Python Ndeckou<sup>d</sup>

<sup>a</sup>University of Gaston Berger of Saint-Louis, Senegal.

<sup>b</sup>University of N'Djaména, N'Djaména, Chad

<sup>c</sup>University of Félix Houphouët-Boigny of Cocody

<sup>d</sup>University of Cheikh Anta Diop, Dakar, Senegal.

## Abstract

An overuse of manure on farmland creates a major environmental problem. When dumping more manure than the crops need as fertilizer, it causes an excess of manure in those fields. Rainwater drains these excessive amounts from the surface into the water reservoirs (rivers and lakes), where they pollute the water, nourish algae, and harm the fish. We develop an algebraic optimization model to formulate for the selection of the right field at the right time so that the environmental damage is limited. We gather instance data from a region of topologically connected reservoirs in northern Senegal and their adjacent farmlands. This mathematical problem then can be tackled by standard solvers for linear optimization problems. When applied in practice, this solution can improve the water quality by reducing the amount of manure and its main components, Nitrogen, Phosphorus, and Potassium.

**Keywords:** Farmland, Water Reservoirs, Manure, Mathematical Optimization Model, Linear Programming.

## 1 Introduction

In many countries over the last three decades, diffuse losses of liquid manure from agricultural land are creating significant eutrophication of surface water quantities. This is a global environmental problem. For example, the excessive use of manure as fertilizer has led to increased levels of chemicals in the soil [2, 5, 10]. The concentration of liquid manure is greater in water reservoirs next to agricultural land. In the north of Senegal, this problem is real, given the watersheds of the Guiers lake and the Senegal River, among others [9]. In these basins, intensive livestock farming and the favorable hydrological conditions present there have led to a serious problem of eutrophication. As this part of Senegal is characterized by many rivers and lakes and where agricultural activity is highly developed, an increase in the amount of freshly applied liquid manure pollutes these water reservoirs through run-off. It also creates a significant accumulation of chemicals from this manure on the soil surface [14].

Many research works have examined the contribution of liquid manure to the chemical pollution of water reservoirs. Among these works, we can cite the results of the authors [7, 11, 18]. It was reported that the chemical concentration of the soil depends strongly on that of the nutrients coming from the manure and dissolved in the water runoff. In addition, the authors' work [18] compared the relationship between the water-extractable soil chemical content and that of runoff from intensively farmed areas. However, the extraction coefficient, which is defined as the slope of the polluted water runoff, plays a

decisive role. Thus, the extraction coefficient is used to describe the relationship between the chemical content of the soil and the concentrations of the products of the runoff manure. In contrast, previous work by authors [10] was contradictory in reporting that chemical nutrients in water reservoirs were more dependent on factors such as soil type, type of runoff, soil management and topographical conditions. According to [3], excess filter runoff results in a higher mass loss of liquid manure. Therefore, several studies have showed the need to differentiate between types of liquid manure runoff when relating soil chemical content to runoff [4, 6].

The application of manure to the soil matters in controlling losses of chemicals such as phosphorus, apart from the chemical content of the soil, which is largely assessed by soil type but also by grazing history and runoff patterns. According to the authors [19], the application of manure to the soil naturally increases the chemical content available in the runoff transport and can also increase the extraction coefficients of chemical elements such as phosphorus. Increased liquid manure from agricultural land can significantly increase the chemical content of runoff [11]. Several research studies have shown that the chemical concentration of runoff decreases rapidly when the time between the application of manure and the start of runoff is high enough [17, 12]. According to the authors [16], this decrease is because of the decomposition of the chemical components from the manure applied to the soil. The application of manure to the soil can also affect the course of water runoff. Thus, according to the authors' work [1], the application of manure to agricultural land could probably increase surface runoff because of the impermeability of the soil. The authors [13] found a delay in water runoff from dry farmland because of the absorption of rainwater by manure. How manure is applied can influence the production of water runoff.

In the northern part of Senegal, the authorities have implemented no system for using banded manure application to reduce ammonia emissions. Although it was not possible to analyze the effect of banding as an additional factor in our experimental design, we used this method of manure application on all our plots as it has become common practice in Senegal. The effects of manure applied on the surface and transported in runoff in lakes next to agricultural land are the major objectives of this paper. Thus, further research to quantify rainfall volumes and runoff patterns would play an important role in achieving these objectives.

The remainder of this article is organized as follows. In Section 2 we describe the model region that consists of the lake Guiers which is connected on the surface and also in the underground to Senegal River. Particularly in connection with fishing, exact trophy predictions are necessary, because the calculation of the fishery yield value is based on the trophy forecast or the primary production, which in turn is based on the predicted of the external phosphorus production load that can be estimated. The composition of manure in nitrogen (N), phosphorus (P), and potassium (K) values of organic fertilizers is given in Section 3. We present in Section 4 the mathematical optimization model to minimize the amount of manure in the fields that is transported to the lakes of our considered model region. We use AMPL to formulate and MINOS to solve this model and computational results are presented in Section 5. Conclusions and final discussions are given in Section 6.

## 2 Description of the Model Region

Lake Guiers is in the Senegal River delta, of which it is a divalent and with which it is linked to Richard Toll by the Taouey canal. It occupies an elongated depression in the North-South axis, about 50 km long, between 15°55 and 16°16 West longitude. The lake occupies an area of nearly 300 km<sup>2</sup> and contains some 600 million cubic meters of water when the water level is at 2 m IGN. Guiers Lake is the largest freshwater reserve in



Senegal. The SONES pumping and drinking water treatment plants in Ngnith and Keur Momar Sarr provide a significant part of the drinking water needs of Dakar and the towns along the pipeline. The Figure 1 represents the model of the study region map.

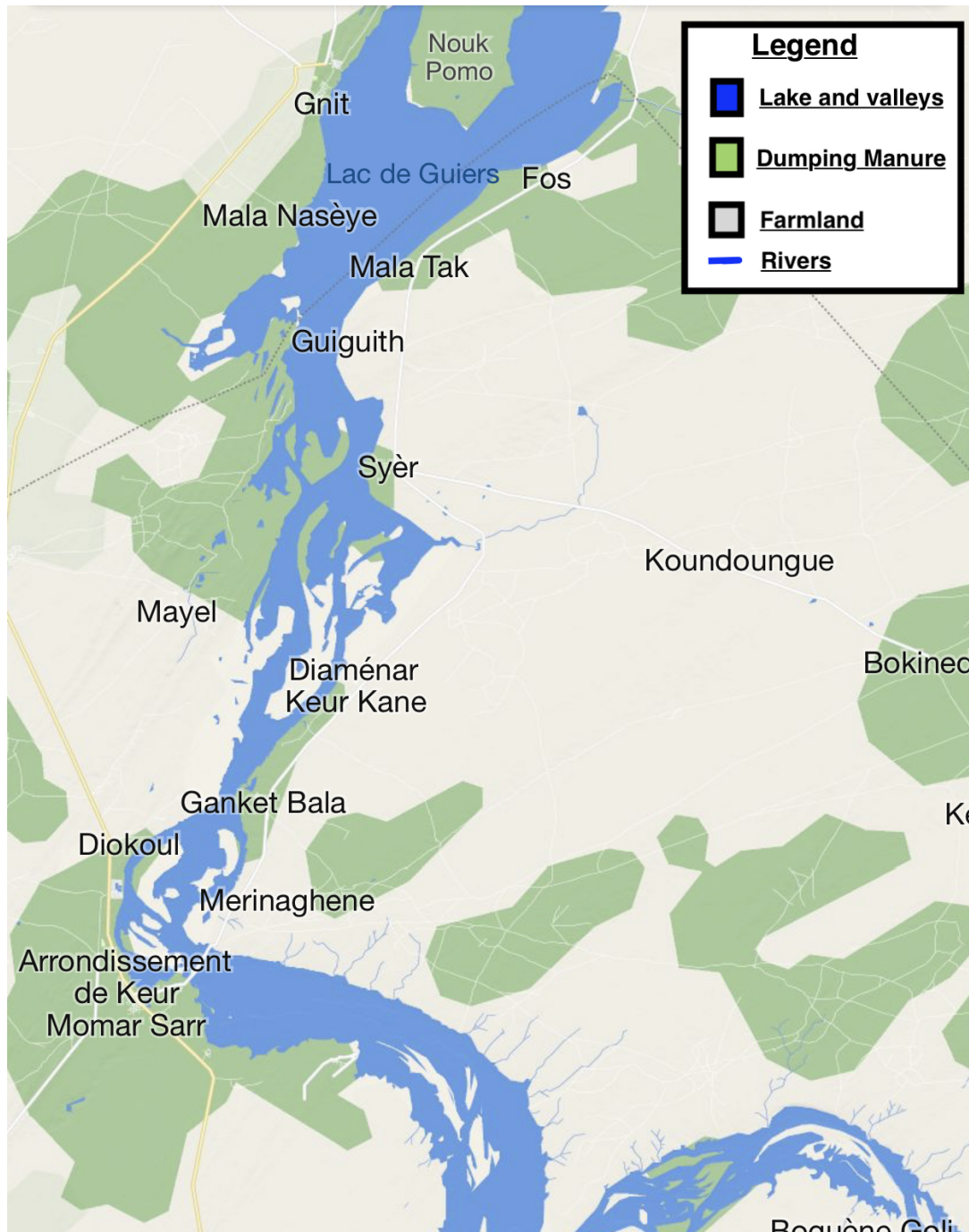


Figure 1: Map of the model region (<https://www.bing.com/maps>).

The Guiers lake allows the development of over 30,000 ha of irrigated land. The Taouey is the 17 km long canal that connects the Guiers Lake to the Senegal River. The supply of water to Lake Guiers depended on the Senegal River and the lower Ferlo valley, according to an original mechanism based on the water level in the river, the lake, and the lower Ferlo valley. The Bounoum valley, called Bas Ferlo, is connected to the Guiers Lake at Keur Momar Sarr. The Bounoum valley gradually narrows towards Yang-Yang. From this point onwards, the fossil network of the Ferlo takes shape. It is a dysfunctional network

cut transversely by the dune complex of the Ferlo plateau. The lake received water from the river during the rainy season in the north via the Taouey and in the south via the Ferlo, which ends locally in the Bounoum valley. At Keur Momar Sarr, the lake describes a bend and opens into the Bounoum valley (lower Ferlo) which has an arc shape oriented west-north-west, east-south-east in its first kilometers and then following a north-north-east, south-south-west axis between Diamet and Menguélé.

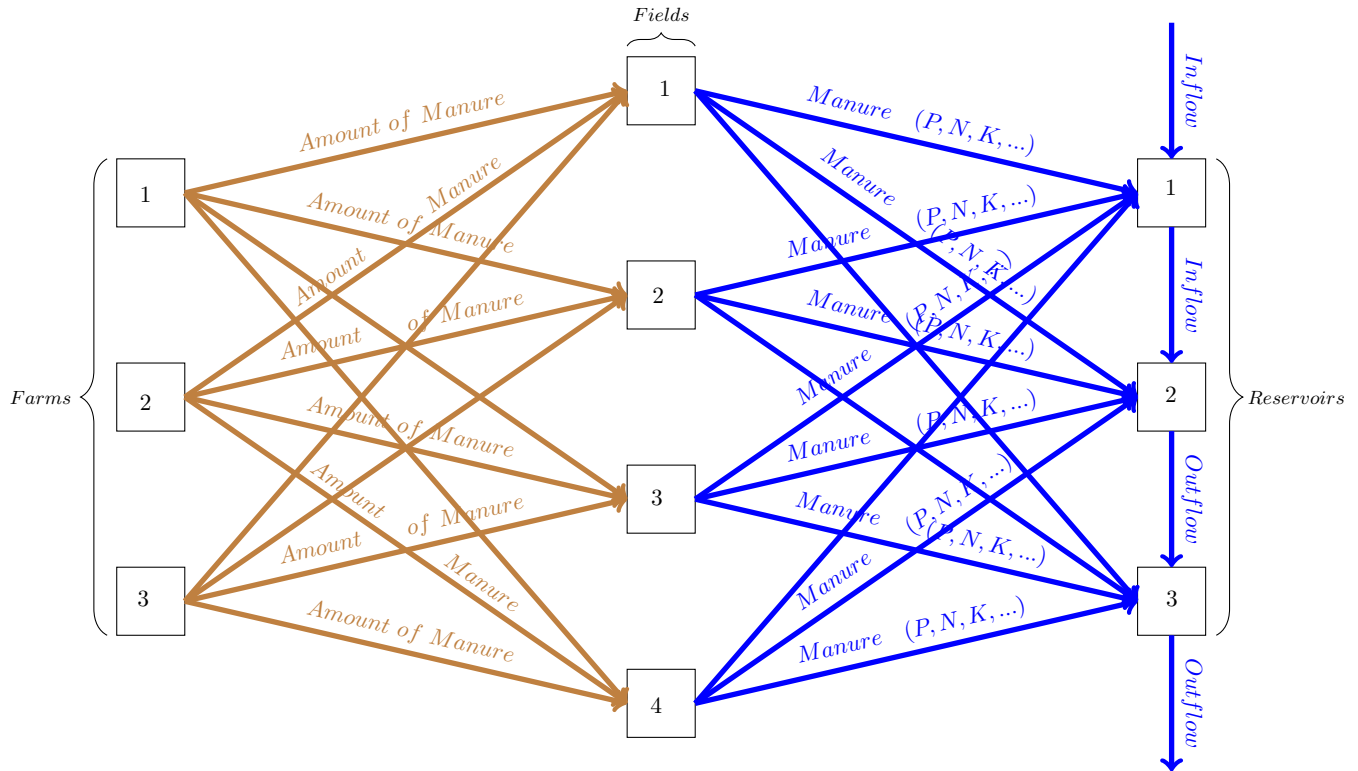


Figure 2: Diagram representing the network topology.

### 3 Percentage Values of Organic Fertilizers

Organic fertilizers are used to improve soil quality and tilth, and to provide nutrients for plant growth. They provide nitrogen, phosphorus, and potassium, as well as other elements essential for plant development and overall good health. Values for manures vary according to time of year, time in the open air, percentage of added straw, and rate of incorporation. The speed of release shown in the table indicates how quickly nutrients are made available to plants. To be considered organic, some materials must result from organic farming methods and must not be contaminated with pesticide residues. The data shown in Table 3 is taken from [8]. Nitrogen, phosphorus, and potassium are represented by N, P, and K in the table headings, to conform to standard commercial practice in labeling fertilizers.

Phosphorus is in the form  $P_2O_5$  and potassium is in the form  $K_2O$ . Ammonia can also be produced as the ammonium ion  $NH_4^+$  by the decomposition of dead organisms by saprophytic bacteria. In oxygen-rich soils, bacteria convert ammonia to nitrite  $NO_2^-$  and then to nitrate  $NO_3^-$  in a process called nitrification. Plants take up nitrate ions  $NO_3^-$  and small amounts of ammonia from the soil via their roots and incorporate them into amino acids and proteins. Plants are therefore the only source of nitrogen that animals can absorb. Potassium is taken up by plants through mass flow and diffusion as  $K^+$  ions. The mobility of  $K^+$  ions in soil is higher than that of  $PO_4^{3-}$  ions, but not so much (about

1 cm). Depending on the root system, plants have more or less the ability to extract the potassium they need from the soil. [15].

Table 1: Percentage of Nitrogen, Phosphorus and Potassium in Manure (fresh)

Manure (fresh)	%N	%P	%K	Release Speed	Effectiveness
Cattle	0.5 to 1.5	0.2 to 0.7	0.5 to 2	medium	2 years
Cattle (dairy)	0.5 to 2	0.3 to 0.5	0.4 to 1.5	medium	2 years
Duck	2.6	0.8 to 1.4	0		
Goat	4	0.6	1 to 2.8	medium	
Goose	3.3	0.4	0.6	medium	
Horse	0.7 to 1.5	0.2 to 0.7	0.6 to 0.8	medium	2 years
Pig	0.4 to 2	0.5 to 1	0.4 to 1.2		
Pigeon	6.3 to 6.5	2.5	2.5		
Poultry (75% water)	1.5	1	0.5		
Poultry (50% water)	1.5 to 2	1.8 to 2	1	medium to fast	2 years
Poultry (30% water)	3 to 4	2.5	1.5	medium to fast	2 years
Poultry (15% water)	6	4	3	medium to fast	
Rabbit	3 to 4.8	1.5 to 2.8	1 to 1.3	medium	
Sheep	2.2 to 3.6	0.3 to 0.6	0.7 to 1.7	medium	
Turkey	5	0.5	0.6 to 0.9	medium to fast	

## 4 A Mathematical Model

The problem of minimizing the amount of manure in fields and transported to the lakes is formulated as an algebraic linear programming optimization model. For simplicity, we assume linear relationships, and take into account a single containment and water transport between the reservoirs.

### 4.1 Sets and Parameters

Given are a set  $\mathcal{F} := \{1, 2, \dots, F\}$  of farms, a set  $\mathcal{S} := \{1, 2, \dots, S\}$  of fields, a set  $\mathcal{R} := \{1, 2, \dots, R\}$  of water reservoirs, and a set of animals  $\mathcal{A} := \{1, 2, \dots, A\}$ . The farms are connected to the fields, and these connections are given by the cross product  $\mathcal{F} \times \mathcal{S}$ . The connections between fields and reservoirs are given by the cross product  $\mathcal{S} \times \mathcal{R}$ . (If a particular connection is not existing in reality, the corresponding variable has to be fixed to zero before solving the optimization problem.) Each farm  $i \in \mathcal{F}$  produces a certain amount of manure  $M_i^t$  during month  $t$ . Each field  $j \in \mathcal{S}$  has an upper limit  $L_j$  it can soak. Each reservoir  $k \in \mathcal{R}$  has a certain amount  $C_k$  it can hold of the containment and capacity of water  $V_k$ . There is a transportation limit  $T_{i,j}$  for the amount of manure from farm  $i$  to field  $j$ .

The containment from  $x$  units of manure on field  $j$  traveling into reservoir  $k$  is given by a function  $f_{j,k}(x)$ , and for simplicity we assume a linear relationship, hence a constant  $\rho_{jk}$  such that  $f_{j,k}(x) := \rho_{j,k}x$  with  $0 \leq \rho_{j,k} \leq 1$ . Inflow and outflow concentrations of each chemical element (phosphorus, nitrogen, and potassium) in all reservoirs depend on several successive months. Thus, we note by  $\mathcal{T}$  this set of ordered and successive months. A month is indexed by  $t \in \mathcal{T}$ . We assume the different temperatures are normal for all parameters and variables that depend on them. The amount of water contained in reservoir  $k$  on month  $t$  is given by  $W_k \in [0, V_k]$  where  $V_k$  is the capacity of reservoir  $k$ .

We denote by  $\alpha_l, \beta_l$ , and  $\gamma_l$  the respective fraction of phosphorus, nitrogen and potassium in the manure from animal  $l$ , where  $\alpha_l, \beta_l, \gamma_l \in [0, 1]$ . By taking a mass  $m$  of manure from an animal  $l$ , then we have  $\alpha_l \cdot m$  mass of phosphorus,  $\beta_l \cdot m$  mass of nitrogen and  $\gamma_l \cdot m$  mass of potassium, so that  $\beta_l \cdot m + \gamma_l \cdot m \leq m$ .



The general flow structure around a reservoir is shown in Figure 2. A survey of the involved parameters is given in Table 2.

Table 2: Parameters of timescale.

	timescale for ...
$\tau_k^{i,t}$	filling of reservoir $k$ by inflow (precipitation and surface) during month $t$
$\tau_k^{o,t}$	outflow of reservoir $k$ water (water retention time) during month $t$
$\tau_k^{f,t}$	filling of reservoir $k$ by inflow (inflow time by filling) during month $t$
$\tau_k^{e,t}$	evaporation of reservoir $k$ (outflow time by evaporation) during month $t$

## 4.2 Variables and Bounds

Let  $x_{i,j} \in [0, T_{i,j}]$  stand for the amount of manure transported from farm  $i$  to field  $j$ . The amount of manure on field  $j$  in month is  $y_j \in [0 \leq y_j \leq L_j]$ . The amount of manure traveling from field  $j$  to reservoir  $k$  on day  $t$  is  $m_{j,k}^t \in [0, C_k]$ . The amount of manure containment in reservoir  $k$  on month  $t$  is  $z_k^t \in [0, C_k]$ .

The amount of concentration of phosphorus inflow in reservoir  $k$  during month  $t$  is  $p_k^{i,t} \in [0, +\infty)$ . The concentration of phosphorus outflow from reservoir  $k$  during month  $t$  is  $p_k^{o,t} \in [Q_k^{t,p}, +\infty)$ . The change of the amount of phosphorus in each reservoir  $k$  during month  $t$  is  $p_k^{c,t} \in (-\infty, +\infty)$ .

The concentration of nitrogen inflow in reservoir  $k$  during month  $t$  is  $n_k^{i,t} \in [0, +\infty)$ . The change of the amount of nitrogen in each reservoir  $k$  during month  $t$  is  $n_k^{c,t} \in (-\infty, +\infty)$ . The concentration of nitrogen outflow from reservoir  $k$  during month  $t$  is  $n_k^{o,t} \in [Q_k^{t,n}, +\infty)$ .

The concentration of potassium inflow in reservoir  $k$  during month  $t$  is  $k_k^{i,t} \in [0, +\infty)$ . The concentration of potassium outflow from reservoir  $k$  during month  $t$  is  $k_k^{o,t} \in [Q_k^{t,k}, +\infty)$ . The change of amount of potassium in each reservoir  $k$  during month  $t$  is  $k_k^{c,t} \in (-\infty, +\infty)$ .

The amount of water inflow into the reservoir  $k$  during month  $t$  is  $w_k^{i,t} \in [U_k^t, V_k]$ . The amount of water outflow from the reservoir  $k$  during month  $t$  is  $w_k^{o,t} \in [0, V_k]$ . The amount of water in each reservoir  $k$  during month  $t$  is  $w_k^t \in [0, V_k]$ . The change of amount of water in each reservoir  $k$  during month  $t$  is  $w_k^t \in (-\infty, +\infty)$ .

## 4.3 Objective Function and Constraints

The goal is to minimize the total amount of manure from all fields that traveling to the reservoirs:

$$\min \sum_{t \in \mathcal{T}} \sum_{i \in \mathcal{F}} \sum_{j \in \mathcal{S}} x_{i,j}^t + \sum_{t \in \mathcal{T}} \sum_{j \in \mathcal{S}} \sum_{k \in \mathcal{R}} \rho_{j,k}^t m_{j,k}^t. \quad (4.1)$$

The amount of manure transported from farm  $i$  is limited by the local production in each month  $t$ :

$$\sum_{j \in \mathcal{S}} x_{i,j}^t = M_i^t, \quad \forall i \in \mathcal{F}, t \in \mathcal{T}. \quad (4.2)$$

The amount of manure on field  $j$  during month  $t$  is computed as:

$$\sum_{i \in \mathcal{F}} x_{i,j}^t = y_j^t, \quad \forall j \in \mathcal{S}, t \in \mathcal{T}. \quad (4.3)$$

The amount of manure deposited on the fields is greater than the amount of manure traveling to reservoir  $k$  during month  $t$ :

$$\sum_{j \in \mathcal{S}} y_j^t \geq \sum_{j \in \mathcal{S}} m_{j,k}^t, \quad \forall k \in \mathcal{R}, t \in \mathcal{T}. \quad (4.4)$$

The amount of manure containment in reservoir  $k$  during month  $t$  is computed as:

$$\sum_{j \in \mathcal{S}} \rho_{jk}^t m_{jk}^t = z_k^t, \quad \forall k \in \mathcal{R}, t \in \mathcal{T}. \quad (4.5)$$

The amount of manure in the reservoir is linear to the concentrations of phosphorus, nitrogen, and potassium, respectively, in a reservoir  $k$  during month  $t$ :

$$\sum_{l \in \mathcal{A}} \alpha_l \cdot z_k^t = p_k^{i,t}, \quad \forall k \in \mathcal{R}, t \in \mathcal{T}, \quad (4.6)$$

$$\sum_{l \in \mathcal{A}} \beta_l \cdot z_k^t = n_k^{i,t}, \quad \forall k \in \mathcal{R}, t \in \mathcal{T}, \quad (4.7)$$

$$\sum_{l \in \mathcal{A}} \gamma_l \cdot z_k^t = k_k^{i,t}, \quad \forall k \in \mathcal{R}, t \in \mathcal{T}. \quad (4.8)$$

The budgets equations of phosphorus, nitrogen and potassium, respectively, in each reserve  $k$  during month  $t$  are computed as:

$$p_k^{t+1} = -\frac{1}{\tau_k^{f,t}} - \frac{1}{\tau_k^{o,t}} - \sigma_k^{ph,t}) p_k^t + \left( \frac{1}{\tau_k^{i,t}} - \sigma_k^{phi,t} r^i \right) p_k^{i,t}, \quad \forall k \in \mathcal{R}, t \in \mathcal{T}, \quad (4.9)$$

$$n_k^{t+1} = -\frac{1}{\tau_k^{f,t}} - \frac{1}{\tau_k^{o,t}} - \sigma_k^{n,t}) n_k^t + \left( \frac{1}{\tau_k^{i,t}} - \sigma_k^{ni,t} r^i \right) n_k^{i,t}, \quad \forall k \in \mathcal{R}, t \in \mathcal{T}, \quad (4.10)$$

$$k_k^{t+1} = -\frac{1}{\tau_k^{f,t}} - \frac{1}{\tau_k^{o,t}} - \sigma_k^{pot,t}) k_k^t + \left( \frac{1}{\tau_k^{i,t}} - \sigma_k^{poti,t} r^i \right) k_k^{i,t}, \quad \forall k \in \mathcal{R}, t \in \mathcal{T}. \quad (4.11)$$

The change of amount of phosphorus, nitrogen and potassium in each reservoir  $k$  per month  $t$  is calculated as:

$$p_k^{i,t} - p_k^{o,t} = p_k^{c,t}, \quad \forall k \in \mathcal{R}, t \in \mathcal{T}, \quad (4.12)$$

$$n_k^{i,t} - n_k^{o,t} = n_k^{c,t}, \quad \forall k \in \mathcal{R}, t \in \mathcal{T}, \quad (4.13)$$

$$k_k^{i,t} - k_k^{o,t} = k_k^{c,t}, \quad \forall k \in \mathcal{R}, t \in \mathcal{T}. \quad (4.14)$$

The inflow water and outflow water connections between the reservoirs  $k$  during month  $t$  are ensured by:

$$w_k^{i,t} - w_k^{o,t} = w_k^{c,t}, \quad \forall k \in \mathcal{R}, t \in \mathcal{T}, \quad (4.15)$$

The change in the amount of water in each reservoir  $k$  and each month  $t$  is computed as:

$$w_k^{c,t} = \left( \frac{1}{\tau_k^{i,t}} - \frac{1}{\tau_k^{o,t}} \right) \cdot w_k^t, \quad \forall k \in \mathcal{R}, t \in \mathcal{T}, \quad (4.16)$$

The budget equation of water in each reservoir  $k$  during month  $t$  is given by:

$$w_k^{t+1} = \left( 1 + \frac{1}{\tau_k^{i,t}} - \frac{1}{\tau_k^{o,t}} \right) \cdot w_k^t, \quad \forall k \in \mathcal{R}, t \in \mathcal{T}. \quad (4.17)$$

The amount of water inflow during month  $t$  is smaller at the water in the reservoir  $k$ , which is, in turn, smaller at the amount of water outflow in a reservoir  $k$ :

$$w_k^{o,t} \leq w_k^t, \quad \forall k \in \mathcal{R}, t \in \mathcal{T}, \quad (4.18)$$

$$w_k^{i,t} \leq w_k^t, \quad \forall k \in \mathcal{R}, t \in \mathcal{T}. \quad (4.19)$$

## 5 Computational Results

Consider the instance shown in Figure 2 with 3 farms, 4 fields, and 3 water reservoirs and connections in  $\mathcal{FS}$  and  $\mathcal{SR}$  as depicted. The Guiers lake and valleys of Ferlo and Bounoum are interconnected in a topological way where the first reservoir is poured into the second which in turn is poured into the third ( $R_1 \mapsto R_2 \mapsto R_3$ ). The minimum amount of manure used to fertilize fields 1, 2, 3, and 4, in addition to the minimum amount going into reservoirs 1, 2 and 3 is the computed result of 24835.71471 [Tons].

Table 3: Parameters of Lake and Valleys

		Reservoir 1	Reservoir 2	Reservoir 3	
Param.	Lake and Valleys	Guiers Lake	Ferlo Valley	Bounoum valley	Units
	$\tau_i$	2.19916	4.02166	50	[m/month]
	$\tau_e$	3.99848	4.06228	10.00001	[m/month]
	$\tau_f$	12.21759	402.16666	200.56145	[m/month]
	Volume	107000000	59400000	158000000	[m <sup>3</sup> ]
	Surface Area	2490000	4410000	7330000	[m <sup>2</sup> ]

Table 4: Data of amount of manure produced in each farm during month  $t$ .

T \ F				
	1	2	3	Unit
Jan	800	700	725	[tons]
Fev	300	800	725	[tons]
Mar	700	600	725	[tons]
Apr	800	750	400	[tons]
May	425	800	725	[tons]
Jun	875	600	725	[tons]
Jul	800	825	800	[tons]
Aug	775	825	825	[tons]
Sep	800	700	825	[tons]
Oct	300	600	725	[tons]
Nov	800	700	725	[tons]
Dec	400	400	825	[tons]

Table 5: Amount of manure in tons sent from farm  $i$  to field  $j$  during month  $t$ .

		Farms							
		1			2			3	
		1	2	3	2	3	4	3	4
T	S								
Jan		325	50	425	400	150	150	300	425
Fev		300	0	0	425	375	0	425	300
Mar		325	375	0	75	425	100	425	300
Apr		325	50	425	400	350	0	100	300
May		325	100	0	350	425	25	425	300
Jun		325	125	425	325	150	125	300	425
Jul		325	50	425	400	75	350	375	425
Aug		325	25	425	425	50	350	400	425
Sep		325	50	425	400	50	250	400	425
Oct		300	0	0	425	175	0	425	300
Nov		325	50	425	400	150	150	300	425
Dec		325	50	25	400	0	0	425	400

Over a period of one year, the fields 1, 2, 3 and 4 received respectively 3850 tons, 5350 tons, 9675 tons and 5950 tons of manure. The annual production of manure in farms 1, 2 and 3 is respectively 7775 tons, 8300 tons and 8750 tons. Thus, we directly deduct the following equality:  $3850 + 5350 + 9675 + 5950 = 7775 + 8300 + 8750 = 24825$  tons. These results are based on Table 4 and Table 5.

Table 6: Amount of manure in tons traveling from field  $j$  to each reservoir  $k$  during month  $t$ .

		Reservoirs								
		1		2				3		
		1	2	1	2	3	4	1	2	3
T	S									
Jan		7.511	1.91264	0.145	6.73862	0.145	0.145	0.145	0.145	1.84456
Fev		7.511	1.91264	0.491633	8.101	0.145	0.145	0.219751	5.991	5.991
Mar		0.145	3.81138	8.101	6.04598	0.145	0.145	2.42461	5.991	5.991
Apr		0.145	5.53809	0.145	0.145	0.145	3.90017	5.94244	0.145	0.145
May		7.511	3.99875	0.145	0.145	0.145	4.87492	5.991	0.145	0.700002
Jun		0.145	4.17062	0.145	0.145	0.145	3.73634	0.145	0.145	5.63234
Jul		0.145	6.32564	0.145	7.62196	0.145	0.145	0.145	2.40447	5.991
Aug		7.511	4.46995	0.145	4.49254	0.145	0.145	0.145	0.145	2.85603
Sep		7.511	4.47207	0.145	0.145	4.40164	0.145	0.145	0.145	2.23064
Oct		0.145	4.87426	0.145	0.145	0.145	2.26135	0.145	2.82653	0.145
Nov		0.145	4.76562	0.145	0.145	0.145	1.90242	0.145	2.82224	0.145
Dec		0.145	5.0096	7.17184	0.145	0.145	0.145	3.8924	0.145	0.145

Since the amount of manure dumped into the fields is a surplus, we assume that a

proportion of the remaining manure is washed away by the rains by going to the nearest reservoirs such as Guiers lakes, see Figure 4. The amount of manure traveling to the Guiers lake is equal to 81.51587 tons annually, and the amount of manure moving into the valleys of Ferlo and Bounoum are computed by 74.771413 tons and 72.352012 tons per year, respectively, and obtained by Table 6. We assume that on the farms we mainly have animals like pig and poultry which annual manure production is equal to 24,825 Tons.

Table 7: Amount of manure in tons on field  $j$  and reservoir  $k$  during month  $t$ .

T \ S	Manures						
	Fields				Reservoirs		
	1	2	3	4	1	2	3
Jan	325	450	875	575	0.132489	0.292745	0.183411
Fev	300	425	800	300	0.132489	0.354173	0.969548
Mar	325	450	850	400	0.115792	0.424159	1.07979
Apr	325	450	875	300	0.167593	0.329413	0.320322
May	325	450	850	325	0.195073	0.407393	0.3727
Jun	325	450	875	550	0.126568	0.317757	0.525761
Jul	325	450	875	775	0.191219	0.328078	0.714753
Aug	325	450	875	775	0.209209	0.202901	0.274442
Sep	325	450	875	675	0.209272	0.284399	0.218157
Oct	300	425	600	300	0.147678	0.198308	0.218157
Nov	325	450	875	575	0.144418	0.169594	0.217857
Dec	325	450	450	400	0.151738	0.169537	0.21782

Manure is mainly composed of chemical elements such as Potassium (k), Phosphorus (P) and Nitrogen (N). However, this composition in terms of percentages differs from one animal to another. If we take the animals that are on the farms we have been working on, namely pigs and poultry, the percentage compositions are as follows: For the poultry, we have 6.5% of N, 2.5% of P and 2.5% of K; for the pigs, we have the composition: 2% of N, 1% of P and 1.2% of K. Thus, knowing that all of the manure traveling to the reservoirs doesn't make it, given that there is one rate used by crops in the fields and another lost by erosion, then the actual amounts of manure in the three reservoirs are equal to 1.923538 tons, 3.478457 tons, and 5.312696 tons, respectively, and given in Table 7. The sum of all these quantities of N, P and P from the two animals must remain equal to or less than the amount of manure that arrives in each reservoir, i.e.,  $mass(N_{pig}) + mass(N_{poultry}) + mass(P_{pig}) + mass(P_{poultry}) + mass(K_{pig}) + mass(K_{poultry})$  is less than or equal to the monthly amount of manure in each reservoir.

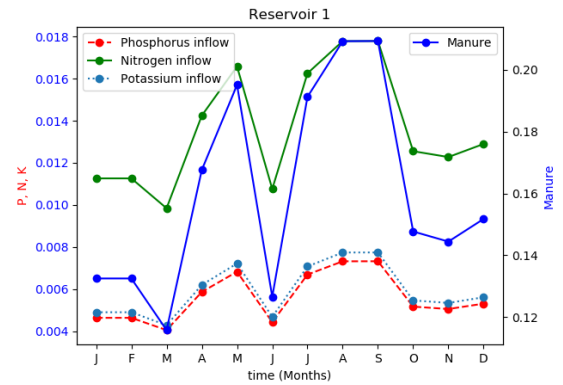
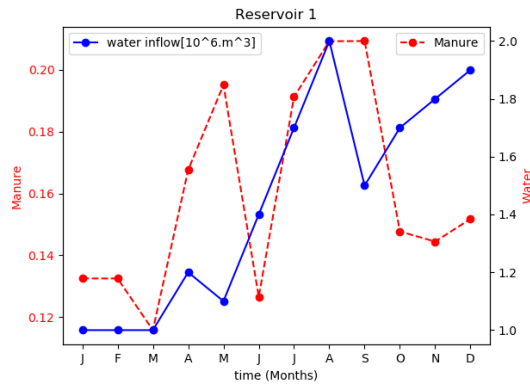


Figure 3: Temporal variation of manure as a function of inflow and outflow water, and temporal variation of Nitrogen, Phosphorus and Potassium inflow and outflow at reservoir 1.

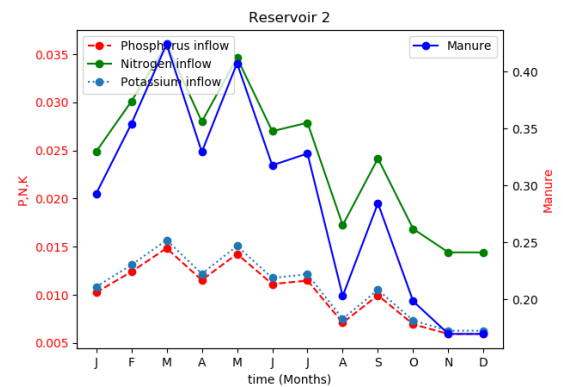
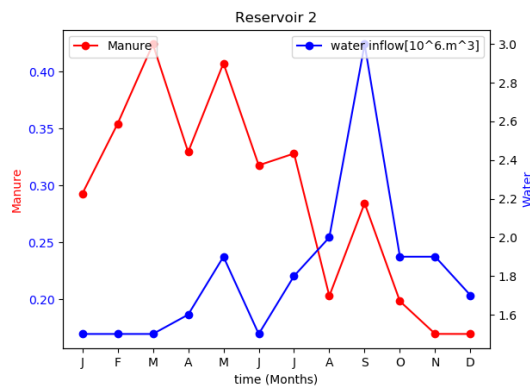


Figure 4: Temporal variation of manure as a function of inflow and outflow water, and temporal variation of nitrogen, phosphorus and potassium inflow and outflow at reservoir 2.

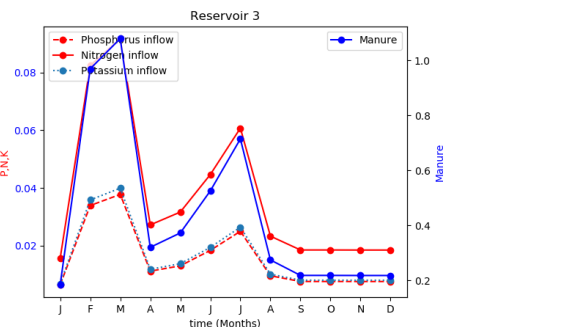
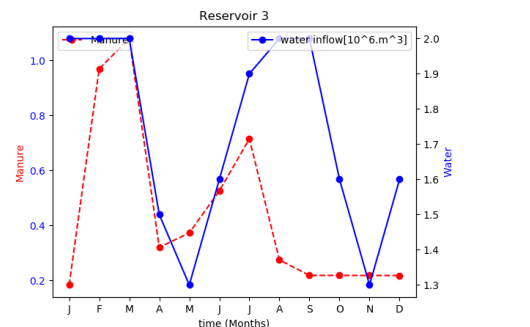


Figure 5: Temporal variation of manure as a function of inflow and outflow water, and temporal variation of Nitrogen, Phosphorus and Potassium inflow and outflow at reservoir 3.

The highest concentrations of Phosphorus, Nitrogen, and Potassium inflow are noted during August and September with average values around  $7.3223$ ,  $9.95395$  and  $7.6351 \mu\text{g/l}$  for P in the reservoirs 1, 2 and 3;  $17.881$ ,  $24.1739$  and  $23.3276 \mu\text{g/l}$  for N in reservoirs 1, 2 and 3; and  $7.74307$ ,  $10.5227$  and  $26.4459 \mu\text{g/l}$  for K in reservoirs 1, 2 and 3. We assume

that the remaining amount of these different chemical elements (N, P, K) is used by crops, sedimentation in the soil, etc. The Figures 3, 4 and 5 show the patterns of manure masses in Lake Guiers and valleys of Ferlo and Bounoum, respectively. We have water spikes in reservoir 1 in July, August, and September, which also directly implies an increase in manure inflow. Thus, in Reservoir 1, in the same months, we have a direct increase in N, P and K in this reservoir. We also noticed that the amounts of N, P, K inflow are much higher than the amounts of N, P, K outflow, therefore we have an excess of N, P, K over time in each reservoir, see 5. The annual variations of the chemical elements N, P, K are compared at 5. We find the quantities N, P, and K in an ascending order in each reservoir.

## 6 Conclusion

We have developed an algebraic model to determine the minimum amount of manure needed to fertilize fields while minimizing the amount of manure flowing into Guiers Lake and, valleys of Ferlo and Bounoum . It also allowed us to know the unit quantities (concentrations) of nitrogen, potassium, and phosphorus added each month to each of the three reservoirs. Knowing the types of animals (pig and poultry) we have on the farms and their monthly manure production, the amount of manure used by the crops in the fields and the amount of manure lost during water transport to the reservoirs, we established the amounts of manure arriving in each reservoir by deducting the monthly concentrations of N, P, and K from them. The algebraic model thus established makes it possible to predict the quantities of N, P, and K in the future for each reservoir.

As future work, we decided to model the movement of manure in the surfaces and its main components (N, P, K) in the soil and subsoil. We also plan to use other resolution methods based on a linear dynamic system to solve this important environmental problem.

## Acknowledgments

We thank all the mathematics teachers in Department of Engineering Mathematics and Optimization Numeric of Brandenburg University of Technology Cottbus - Senftenberg for the realization of these scientific works.

## References

- [1] Stamm C. Waul C. Singer H. Muller S. Burkhardt, M. Surface runoff and transport of sulfonamide antibiotics and tracers on manured grassland. 2005.
- [2] Sharpley A.N. McDowell R.W. Flaten D.N. Buda A.R. Tao L. Bergstrom L. Zhu Q. Kleinman, P.J.A. Managing agricultural phosphorus for water quality protection: principles for progress. *Plant Soil*, 349:169–182, 2011.
- [3] Srinivasan M.S. Dell C.J. Schmidt J.P. Sharpley A.N. Bryant R.B. 2006. Kleinman, P.J.A. Role of Rainfall Intensity and Hydrology in Nutrient Transport via Surface Runoff. *J. Environ. Qual.*, 35:1248–1259., 2005.
- [4] Chaubey I. Leh, M.D. GIS-Based Predictive Models of Hillslope Runoff Generation Processes(1). *J. Am. . Water Resour. Assoc.*, 45:844–856., 2009.
- [5] Turner B.L. Meissner R. Leinweber, P. Phosphorus. In: Haygarth, P. M., Jarvis, S. C. (Eds.), *Agriculture, Hydrology and Water Quality. CAB International, Wallingford, Oxon, UK*,, pages 29–55, 2002.

- [6] Ollesch G. Rode M. Lindenschmidt, K.E. Physically-based hydrological modelling for nonpoint dissolved phosphorus transport in small and medium-sized river basins. *Hydrol. Sci. J.*, 49:495–510., 2004.
- [7] Sharpley A. Brookes P. Poulton P. McDowell, R. Relationship between soil test phosphorus and phosphorus release to solution. *Soil Sci.*, 166:137 – 149., 2001.
- [8] R. Penhallegon. Nitrogen, Phosphorus and Potassium values of organic fertilizers. Technical report, OSU Extension service - Lane Country office, 2003.
- [9] Stamm C. Vollmer T. Frossard E. Oberson A. Flühler H. Sinaj S. Schärer, M. Reducing phosphorus losses from over-fertilized grassland soils proves difficult in the short term. *Soil Use Manage.*, 23:154–164., 2007.
- [10] Chapra S.C. Wedepohl R. Sims J.T. Daniel T.C. Reddy K.R. Sharpley, A.N. Managing agricultural phosphorus for protection of surface waters - issues and options. *J. Environ. Qual.*, 23:437–451, 1994.
- [11] Sharpley A. Prochnow L.I. Shigaki, F. Rainfall intensity and phosphorus source effects on phosphorus transport in surface runoff from soil trays. *Sci. Total Environ.*, 373:334–343., 2007.
- [12] Jackson D.R. Withers P.J.A. Smith, K.A. Nutrient losses by surface run-off following the application of organic manures to arable land. 2001.
- [13] McDowell R.W. Srinivasan, M.S. Hydrological approaches to the delineation of critical-source areas of runoff. 2007.
- [14] Sermet R. Leuenberger J. Wunderli H. Wyder H. Flühler H. Gehre M. Stamm, C. Multiple tracing of fast solute transport in a drained grassland soil. *Geoderma*, 109:245–268, 2002.
- [15] Unifa. Parlons fertilisation, <https://fertilisation-edu.fr/10-cycles-bio-geo-chimiques.html?start=2>, 2022.
- [16] Jokela W.E. Franklin D.H. Endale D.M. Vadas, P.A. The effect of rain and runoff when assessing timing of manure application and dissolved phosphorus loss in runoff. 2011.
- [17] Kleinman P.J.A. Sharpley A.N. Vadas, P.A. A Simple Method to Predict Dissolved Phosphorus in Runoff from Surface-Applied Manures. 2004.
- [18] Kleinman P.J.A. Sharpley A.N. Turner B.L. Vadas, P.A. Relating soil phosphorus to dissolved phosphorus in runoff: A single extraction coefficient for water quality modeling. *J. Environ. Qual.*, 34:572–580., 2005.
- [19] Ontkian G.R. Bennett D.R. Chanasyk D.S. Miller J.J. Volf, C.A. Phosphorus losses in simulated rainfall runoff from manured soils of Alberta. 2007.



# Aspect-Based Sentiment Analysis in Turkish Texts with Pre-Trained Models

<sup>1,2</sup> Melek Turan, <sup>1</sup>Metin Bilgin

<sup>1</sup>Department of Computer Engineering, Bursa Uludağ University, Bursa, Turkey

<sup>2</sup>Özdilek Ev Tekstil San. ve Tic. AŞ, Özveri Ar-Ge Merkezi, Bursa, Turkey

502131002@ogr.uludag.edu.tr, metinbilgin@uludag.edu.tr

## Abstract

Aspect-based sentiment analysis (ABSA) allows customers to evaluate service quality about multiple categories and to analyze their positive or negative comments. This study aims to perform expectation-based sentiment analysis by identifying the target term, category and sentiment class in customer comments. Token classification is used for target term identification and sequential classification model is used for sentiment analysis. As a result of the study, 91.6%, 90.9%, 90.7% and 89.9% accuracy rates were obtained for convolutional BERT (ConvBERT), efficiently learning an encoder that classifies token replacements accurately (ELECTRA), decoding-enhanced bert with disentangled attention (DeBERTa) and distilled bidirectional encoder representations from transformers (DistilBERT) models for target term extraction with token classification. In sentiment analysis with sequential classification, BERTurk and ELECTRA models were compared and analyzed. An accuracy rate of 88.8% was obtained for the BERTurk model and 86.8% for the ELECTRA model.

**Keywords:** Token Classification, Sequential Model Classification, Natural Language Processing (NLP) , Turkish NLP.

## 1.INTRODUCTION

In today's digital age, customers are constantly sharing their experiences and opinions about products and services on various online platforms. These opinions can be extremely valuable for businesses as they can provide information about customer preferences, expectations and satisfaction levels.

Aspect-based sentiment analysis aims to predict the sentiment polarity of specific targets in a given text [1]. This technique provides a more nuanced understanding of customer feedback, as it allows businesses to identify which specific aspects of their product or service are perceived most positively or negatively by customers. Unlike category classification methods, it can detect more than one category in a sentence. It determines the emotion contained in each category separately. In businesses, it ensures that customer comments are quickly analyzed and positive or negative opinions are conveyed to the relevant department. This situation benefits the business in terms of eliminating deficiencies and customer satisfaction.

Section 2 discusses previous research in the field of ABSA. Section 3 describes the methods and dataset used. Implementation, experimentation and experimental results are presented in Section 4. Conclusions are presented in Section 5.

## 2. RELATED WORKS

Cetin and Eryigit [2] focused on target category and target term extraction in their investigation. In order to identify both simultaneously, they created a tagging technique based on conditional random fields (CDF) based on word vectors and lexical analysis data. For the simultaneous identification of the target category and phrase, they received an F1 score of 46.7% [2]. To enhance BERT's performance on sensitivity analysis and appearance-based sensitivity analysis tasks, Xu et al. [3] present a post-training strategy that fine-tunes BERT on a huge corpus of inspection data. They employ a two-step procedure where they first fine-tune BERT on the target task after training it on a huge corpus of reviews using a masked language modeling job [3]. Song et al. [4] investigated sentiment bias towards targets. They proposed the Attentional Encoder Network (AEN) as a solution to the difficulties in parallelizing RNNs and remembering long-term patterns. Two different embedding layers were added to the AEN and two models, AEN-Glove and AEN-Bert, were obtained. AEN-Glove with a label smoothing regularization (LSR) achieved high accuracy while Glove without LSR achieved low accuracy [4].

## 3. GENERAL PROPERTIES OF METHOD

The methods used and information about the dataset are explained in this section. According to the Turkish language paradigm, it aims to recognize various types and emotions present in customer feedback. The restaurant dataset [5] was used for the tests, which were carried out in Python. It was carried out using an NVIDIA GeForce RTX 3070 graphics card as the hardware. For target term extraction using token classification, we utilized four different models. For sentiment analysis, we used two different sequential model.

### 3.1. Dataset

In the dataset, SemEval-2016 ABSA Restaurant Reviews-Turkish Train Data (Subtask 1) from SemEval 2016 restaurant dataset was used as training data and SemEval-2016 ABSA Restaurant Reviews-Turkish Test Data-GOLD (Subtask 1) was used as test data [5]. In this study, 1046 category labels and target term information were included in the training data and 153 category labels and target term information were included in the test data. The data count information for the categories is shown in Table 1.

Table 1. Data distribution by category

Category	Number of Training Data	Number of Test Data
FOOD#QUALITY	396	68
AMBIENCE#GENERAL	267	23
SERVICE#GENERAL	227	21
RESTAURANT#GENERAL	202	18
FOOD#STYLE_OPTIONS	111	8
RESTAURANT#PRICES	57	4
DRINKS#QUALITY	48	4
LOCATION#GENERAL	36	2
DRINKS#STYLE_OPTIONS	30	0
FOOD#PRICES	23	3
DRINKS#PRICES	8	1
RESTAURANT#MISCELLANEOUS	1	1

The dataset contains 820 positive and 586 negative emotions for training and 104 positive and 49 negative emotions for testing. In the data analysis phase, the most frequently used words were analyzed and it was observed that words such as *servis*, *mekan*, *lezzet*, *yemek*, and *manzara* were frequently used.

For token classification, sentences are first divided into words. The position of the target term in the sentence has been determined. The designated location is assigned to the label of the category it represents, as shown in Table 2.

Table 2. Example of a tag for named entity recognition(NER)

Word	NER
1	0
kere	0
denedigim	0
fiyatlarinin	RESTAURANT#PRICES
yüksek	0
yemeklerinin	FOOD#QUALITY
lezzetsiz	0
olduğu	0
bir	0
mekan	0

Target phrase, sentence, and sentiment state are organized in json format for sentiment analysis so that sequential classification models can be used.

### 3.2.Token Classification

Token classification is a common natural language processing task that involves assigning a label to each token in a text string. Tokens are discrete meaningful units in text, such as words or punctuation marks. Their labeling is used in various natural language processing applications, such as named entity recognition or sentiment analysis. Recurrent neural networks (RNNs) can be used in named entity recognition, including convolutional neural networks (CNNs) and transformers [6].

In this study, 4 different models, namely ConvBERT [7], ELECTRA [8], DeBERTa [9], and DistilBERT [10], were used for token classification.

### 3.3. Sentiment Analysis with Sequential Model Classification

Sequential model classification is a machine learning problem given a sequence or series. In this problem, a sequence is given as input and a class or label corresponding to this sequence is predicted as output. In NLP applications, it can be used to predict the nouns, verbs, adjectives, and objects of the words that make up the sentence sequence. In general, models such as RNN and LSTM are widely used [11].In this study, sentiment analysis was performed by training the target category, sentence and sentiment data with the sequential model. The success of BERTurk [12] and ELECTRA [8] models were compared. In this work, sentiment analysis was carried out by training the sequential model on the target category, text, and sentiment data. We examined the effectiveness of the BERTurk [12] and ELECTRA [8] models.

### 3.4. Method

This section describes the methods used in the study.

A diagram of the new data prediction process after the training is completed is shown in Fig.1.

The models were evaluated according to precision, recall, F1 score and accuracy metrics.

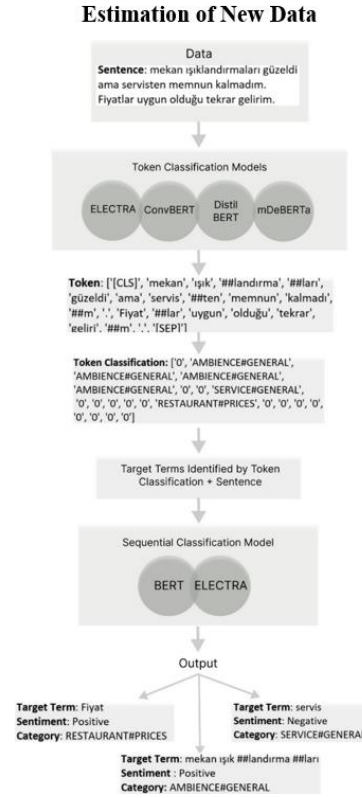


Fig. 1. Estimation of new data.

The following steps were taken in the study respectively.

1. Labeling the dataset according to the named entity recognition method, which is described in detail in Section 3.
  2. Training and testing token classification models.
  3. Organizing the dataset in json format for sequential model classification. Inclusion of target terms, sentence and sentiment labels in the training data.
  4. Performing and testing the sequential model classification.
- Comparative training results are presented in Section 4.

## 4.APPLICATIONS

In this section, the results of the experiments on target extraction with token classification and sentiment analysis with sequential model classification are evaluated.

### 4.1.Target Term Extraction - Token Classification

As a result of the token classification training, the ConvBERT model achieved the highest accuracy rate of 98.8% on the training data and 91.6% on the test data.

The results of the current study are presented in Table 3. The results of the study were evaluated with precision, recall, F1 score and accuracy metrics.

Table 3. Training and test results for marker classification models

Model	Precision	Recall	F1 Score	Accuracy	Test Accuracy
ConvBERT	0.943	0.945	0.944	0.988	0.9168
ELECTRA	0.944	0.939	0.941	0.987	0.9095
DeBERTa	0.922	0.934	0.928	0.987	0.9077
DistilBERT	0.905	0.907	0.906	0.980	0.8995

## 4.2. Sentiment Analysis

In the sentiment analysis phase, BERTurk and ELECTRA models were used as sequential classification models. The BERTurk model achieved the highest success with an accuracy rate of 88.8%. The BerTurk model achieved 87.8% F1 score, 90.2% sensitivity, 86.7% precision and 88.8% accuracy on the test data. Fig. 2. shows the test data complexity matrix.

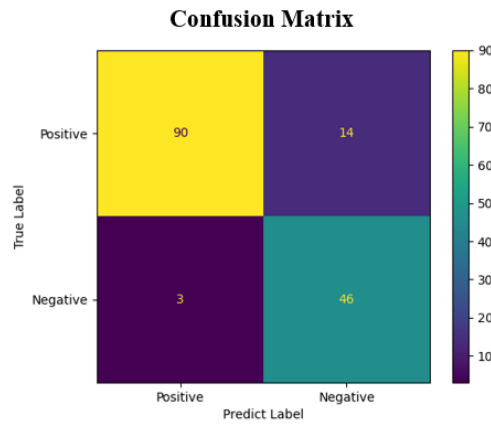


Fig. 2. BERTurk model confusion matrix for sentiment analysis

The ELECTRA model achieved an F1 score of 85.9%, sensitivity of 88.76%, precision of 86.84% and accuracy of 86.92%. Fig. 3. shows the test data complexity matrix.

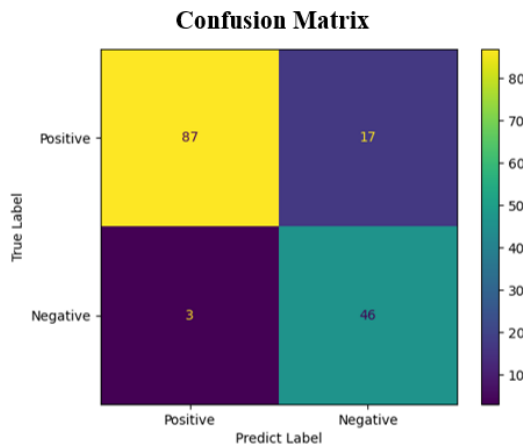


Fig. 3. ELECTRA model confusion matrix for sentiment analysis.

## 5.CONCLUSIONS

This study aims to compare the performance of BERTurk and ELECTRA models in Turkish sentiment analysis and opinion extraction tasks. In the study, first of all, the Turkish restaurant dataset [5] was revised for the problem and both models were trained on this dataset. For the sequential model, ELECTRA and BERTurk models are trained and compared on the dataset. As a result of this comparison, it was seen that the BERTurk model gave more successful results with an accuracy rate of 88.8% and an F1 score of 87.8%. In token classification, ConvBERT achieved the highest accuracy rate of 91.6% in the training conducted with ConvBERT, ELECTRA, DeBERTa, and DistilBERT models.

## REFERENCES

1. Chao Yang, Hefeng Zhang, Bin Jiang, and Keqin Li, Aspect-Based Sentiment Analysis with Alternating Coattention Networks., *Inf. Process. Manag.*, vol. 56, no. 3, pp. 463–478, 2019.
2. Fatih Samet Çetin ve Gülşen Eryiğit, Türkçe Hedef Tabanlı Duygu Analizi için Alt Görevlerin İncelenmesi – Hedef Terim, Hedef Kategori ve Duygu Sınıfı Belirleme, *Bilişim Teknol. Derg.*, 2018.
3. Hu Xu, Bing Liu, Lei Shu, Philip S. Yu BERT Post-Training For Review Reading Comprehension and Aspect-Based Sentiment Analysis, *Arxiv [Cs.CL]*, 2019.
4. Youwei Song, Jiahai Wang, Tao Jiang, Zhiyue Liu and Yanghui Rao, Attentional Encoder Network for Targeted Sentiment Classification, *arXiv [cs.CL]*, 2019.
5. Maria Pontiki et al., SemEval-2016 Task 5: Aspect Based Sentiment Analysis, in *Proceedings of the 10th International Workshop on Semantic Evaluation (SemEval-2016)*, 2016.
6. Asahi Ushio and Jose Camacho-Collados, T-NER: An All-Round Python Library for Transformer-Based Named Entity Recognition, *arXiv [cs.CL]*, 2022.
7. Zihang Jiang, Weihao Yu, Daquan Zhou, Yunpeng Chen, Jiashi Feng, Shuicheng Yan, Convbert: Improving BERT With Span-Based Dynamic Convolution, *arXiv [cs.CL]*, 2020.
8. Kevin Clark, Minh-Thang Luong, Quoc V. Le, Christopher D. Manning, ELECTRA: Pre-Training Text Encoders as Discriminators Rather Than Generators, *arXiv [cs.CL]*, 2020.
9. Pengcheng He, Xiaodong Liu, Jianfeng Gao, Weizhu Chen, Deberta: Decoding-Enhanced Bert with Disentangled Attention. *arXiv preprint arXiv:2006.03654*, 2020
10. Victor Sanh, Lysandre Debut, Julien Chaumond, Thomas Wolf, Distilbert, A Distilled Version Of BERT: Smaller, Faster, Cheaper and Lighter, *arXiv [cs.CL]*, 2019.
11. Thomas G. Dietterich , Machine learning for sequential data: A Review, in *Lecture Notes in Computer Science, Berlin, Heidelberg: Springer Berlin Heidelberg*, 2002, pp. 15–30.
12. Jacob Devlin, Ming-Wei Chang, Kenton Lee, Kristina Toutanova, BERT: Pre-training of deep bidirectional Transformers for language understanding, *arXiv [cs.CL]*, 2018.

# Optimizing SiC MOSFET Turn-Off Switching Losses with Active Gate Driver

Emin Asım Yılmaz, Ahmet Faruk Bakan<sup>1</sup>

<sup>1</sup>Department of Electrical Engineering, Yildiz Technical University, Istanbul, Turkey

[e.asimyilmaz@gmail.com](mailto:e.asimyilmaz@gmail.com),

[fbakan@yildiz.edu.tr](mailto:fbakan@yildiz.edu.tr)

## Abstract

SiC MOSFETs can provide higher current density and have the ability to work on higher switching frequencies compared to their competitors. Consequently, they have become a preferred choice for increasing power density and improving efficiency in power electronics applications. However, as the switching speed increases, the switch is subjected to oscillations and voltage spikes, which negatively impact its performance. The conventional approach to mitigate these effects is to reduce the switching speed, but this will result to increase of switching losses. To address this issue, an active gate driver that can minimize oscillations and voltage spikes on the switch with minimized increase of switching losses in SiC MOSFETs is investigated in this study. The proposed driver operates in closed loop with voltage feedback taken from the switch drain-source voltage. The studies were conducted in the SPICE simulation environment, and the CREE company's 650V discrete SiC MOSFET was tested with double pulse tests (DPT) created in the simulation environment. The results of the study showed that the active gate driver has several advantages over the conventional gate driver.

**Keywords:** Silicone Carbide (SiC); switching losses; active gate driver.

## 1.INTRODUCTION

One of the fundamental objectives in power electronics applications is to increase power density. One way to achieve this is by increasing the switching frequency in converters, which can result in smaller passive component sizes. Additionally, reducing semiconductor losses can help decrease the cooling requirements for the system. In pursuit of these objectives, wide bandgap devices, such as Silicon Carbide (SiC) and Gallium Nitride (GAN) MOSFETs, have become increasingly popular in recent years. SiC MOSFETs offer higher breakdown voltage and lower thermal resistance compared to their Si MOSFET counterparts, while also having the ability to work with higher switching frequency capabilities than Si IGBTs. By utilizing SiC MOSFETs, power electronics converters can operate at higher frequencies with lower overall losses [1]. These advantages have made SiC MOSFETs a preferred choice for renewable energy, automotive, and industrial applications [2].

The switching speed of SiC is higher compared to its competitor, Si IGBT, which results in lower switching losses [3]. However, due to high  $dv/dt$  and  $di/dt$ , voltage spikes, oscillations, and EMI problems can occur in the converter [4]. During turn-on and turn-off, the voltage across the switch



can approach its breakdown voltage because of the high  $di/dt$  caused by parasitic inductances in the converter. Moreover, the oscillations can affect the circuit and lead to EMI problems. The primary measure to reduce these parasitic elements is good PCB design, but unfortunately, it has limited effectiveness. To avoid these problems, designers can increase the gate resistance of the switch to reduce the  $di/dt$ , but this can limit the full performance of SiC MOSFETs [5]. Active gate driver circuits can separately control the  $dv/dt$  and  $di/dt$  values of the switch and mitigate the mentioned negative effects [6].

The most basic active gate driver (AGD) circuits are those made with uncontrolled open loop methods. This type of AGD works on the principle of changing the gate current after a fixed time has passed since the switch is turned on or off. This method, which is easier to implement due to its simple structure, can increase the performance of the switch. However, it can only be used in some special applications or fixed load circuits as it does not take feedback. Since the temperature effect is not considered in the circuit, the effect of AGD may decrease at different temperatures [7].

Closed loop AGD circuits, on the other hand, control the gate current by feedback taken from either the drain-source voltage, the gate-source voltage or drain current of the switch. These gate drivers mostly have multiple gate resistors and activate them at different times. The circuit complexity is higher, so the cost and design difficulty increases. High-speed comparators and control elements are required for the feedback circuit. The performance of AGD does not decrease with changes in factors such as input voltage, load, and temperature [8].

In this study, first the turn-off characteristics of SiC MOSFET were analyzed. Then, classical gate driver circuits were tested using DPT test setup in LtSpice software. The simulation results of the proposed active gate driver circuit were compared with the simulation results of the classical gate driver circuit.

### 1.1. SiC MOSFET Turn-off

In power electronic applications, MOSFETs are commonly used in conjunction with an inductor and a diode. When the MOSFET turns off, the inductor current completes its path through the diode or an equivalent switch. To test the switching behavior of the MOSFET, DPT is the most commonly used method [9]. By using this circuit, the switching characteristics of the MOSFET can be examined by turning the switch on and off at the desired current and voltage levels.

When examining the low side MOSFET turn-off behavior in this test circuit, we observe the waveforms shown in Fig. 1. Before  $t_0$ , switch is conducting and its gate voltage is  $V_{GS}$ . At time  $t_0$ , a turn-off signal is given, and there is no change in the switch current or voltage until the gate voltage reaches the Miller voltage. At time  $t_1$ , when the gate voltage reaches the Miller voltage, the switch voltage starts to rise until time  $t_2$ , when the switch voltage reaches the input voltage. During this time, there is no change in the switch current, and the gate voltage remains at the miller voltage. At time  $t_2$ , the  $C_{GD}$  capacitance becomes charged, and the current flows from the  $C_{GS}$  capacitance. As a result, the gate voltage begins to decrease again, and the switch current also starts to decrease. At time  $t_3$ , the switch current reaches zero as the gate voltage reaches the threshold value. Finally, the gate voltage drops to a low level, and the turn-off process is complete.

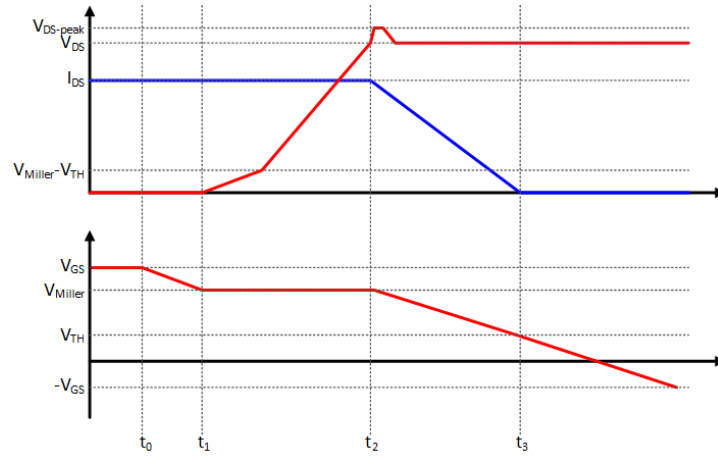


Fig. 1. MOSFET turn-off  $V_{DS}$ ,  $I_{DS}$  and  $V_{GS}$  waveforms

The most important factors that affect the switching losses of a MOSFET are the  $dv/dt$  and  $di/dt$  values. Fig. 2 shows a MOSFET model with its capacitances. When examining the effect of these capacitances during turn-off, at time  $t_0$ , the  $C_{GS}$  capacitance starts to discharge as the gate driver voltage drops. When the gate voltage reaches the miller voltage, the switch starts to increase its drain-source voltage. The miller voltage is calculated by Eq. 1, and the factor that determines the rate of increase in MOSFET voltage is the charging of the  $C_{GD}$  capacitance. The  $C_{GD}$  capacitance is discharged with a constant gate current  $I_g$ , which is calculated by Eq. 2. When charged with this current, the voltage rise time is as given in Eq. 3.

$$V_{miller} = V_{TH} + \frac{I_L}{g_{fs}} \quad (1)$$

$$I_g = \frac{V_{TH} - V_{miller}}{R_g} \quad (2)$$

$$t_{rv} = \frac{V_{TH} * V_{miller}}{C_{gd}} \quad (3)$$

After the switch voltage reaches the input voltage, the rate of decrease of the switch current is determined by the total capacitance of  $C_{GD}$  and  $C_{GS}$ , which is the  $C_{iss}$  capacitance, and the gate current. The gate current is given by Eq. 4. In this case, the current fall time can be calculated using Eq. 5 [10].

$$I_g = \frac{V_{EE} - 0.5 * (V_{th} + V_{miller})}{R_g} \quad (4)$$

$$t_{rv} = \frac{C_{iss} * (V_{miller} - V_{TH})}{I_g} \quad (5)$$

As can be seen, the rise time and fall time of voltage can be altered by changing the gate resistance. By using different resistances within these two ranges, separate control of  $dv/dt$  and  $di/dt$  can be achieved.

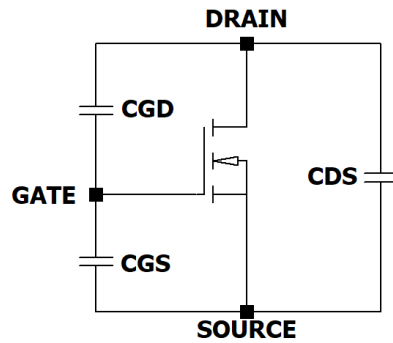


Fig. 2. MOSFET model with intrinsic capacitances

When calculating the turn-off switching energy loss, the time from the gate voltage dropping to 90% of its value to the drain current dropping to 1% of its value can be used. The switching energy loss during this time is calculated using Eq. 6.

$$P_{off} = \int_{t_1}^{t_2} V_{ds} * I_d dt$$

## 2. GENERAL PROPERTIES OF METHOD

### 2.1. Simulation Studies with Classical Gate Driver

The test circuit given in Fig.3 is set up in the LtSpice program. Parasitic inductances and capacitors were added to the simulation schematic to obtain realistic switching waveforms for the switch. Cree's C3M0015065K 650V model was selected as the SiC MOSFET for the simulation test circuit. Different resistances ranging from 5  $\Omega$  to 20  $\Omega$  were used for the gate resistance of the MOSFET. The result of the test performed with a 10  $\Omega$  resistance can be seen in Fig. 4.

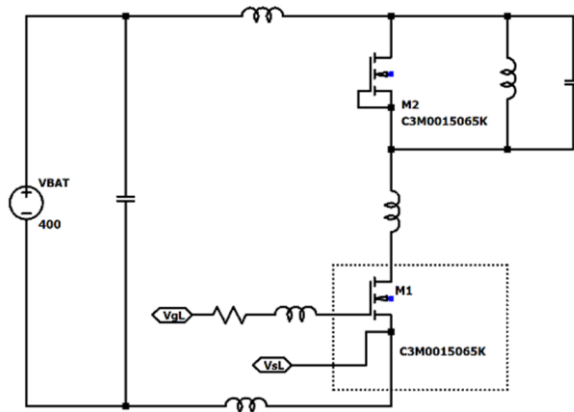


Fig. 3. Classical gate driver simulation circuit

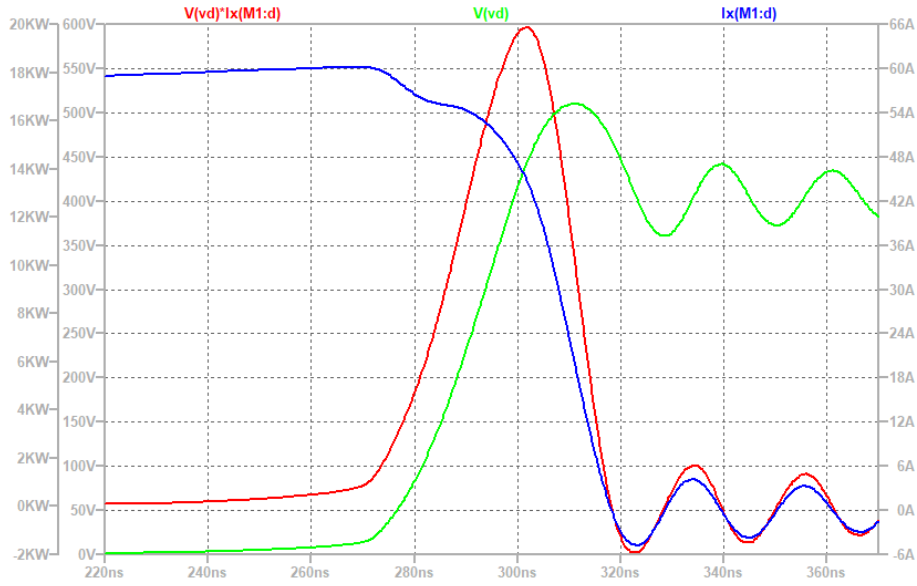


Fig. 4. Classical gate driver simulation results with 10  $\Omega$  gate resistance

Table 1 provides a comparison of the turn-off switching losses and peak drain source voltage values for different gate resistances. As expected, as the gate resistance increases, the switching loss increases and the peak voltage value decreases.

TABLE 1: Classical Gate Driver Simulation Results

$R_{goff}$	$E_{off}$	$V_{peak}$
5 $\Omega$	290.58 $\mu$ J	551 V
7.5 $\Omega$	402.22 $\mu$ J	526 V
10 $\Omega$	507.2 $\mu$ J	510 V
15 $\Omega$	708.2 $\mu$ J	491 V
20 $\Omega$	906.7 $\mu$ J	479 V

## 2.2. AGD Working Principle

SiC MOSFETs can operate with lower switching losses thanks to their switching speeds. However, the high  $dv/dt$  and  $di/dt$  values resulting from fast switching can prevent SiC MOSFET from being used at full performance due to the effect of parasitic inductances and capacitances in the circuit. Due to the parasitic inductance in the circuit, the switch peak voltage can approach the breakdown voltage. As seen in classical gate driver simulation studies, high gate resistance should be selected to protect the SiC MOSFET from overvoltage. This, in turn, increases the turn-off switching losses. The presented AGD circuit aims to reduce the peak voltage on the switch without increasing the turn-off switching losses.

The source of the voltage spike that occurs on the switch is the  $di/dt$  change on the switch and the parasitic inductance. As shown in Fig. 2. the switch current starts to decrease after the switch voltage reaches the input voltage. The proposed AGD circuit aims to reduce the current decay rate while keeping the switch voltage rise rate constant by increasing the gate resistance after the switch voltage reaches its peak value. To achieve this, an additional MOSFET is added in parallel with the

MOSFET that is active during the turn-off. Both MOSFETs are turned on with the switching signal. When an increase in resistance is desired, MOSFET M3 is turned off, thus increasing the resistance value can be achieved. The circuit diagram of the simulated AGD is shown in Fig. 5.

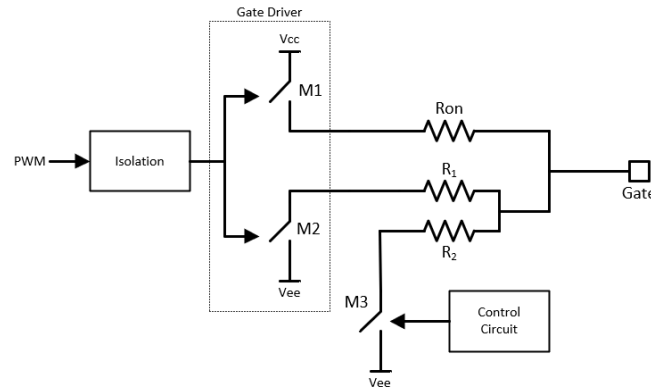


Fig. 5. Proposed AGD circuit diagram.

AGD waveforms are shown in Fig. 6.

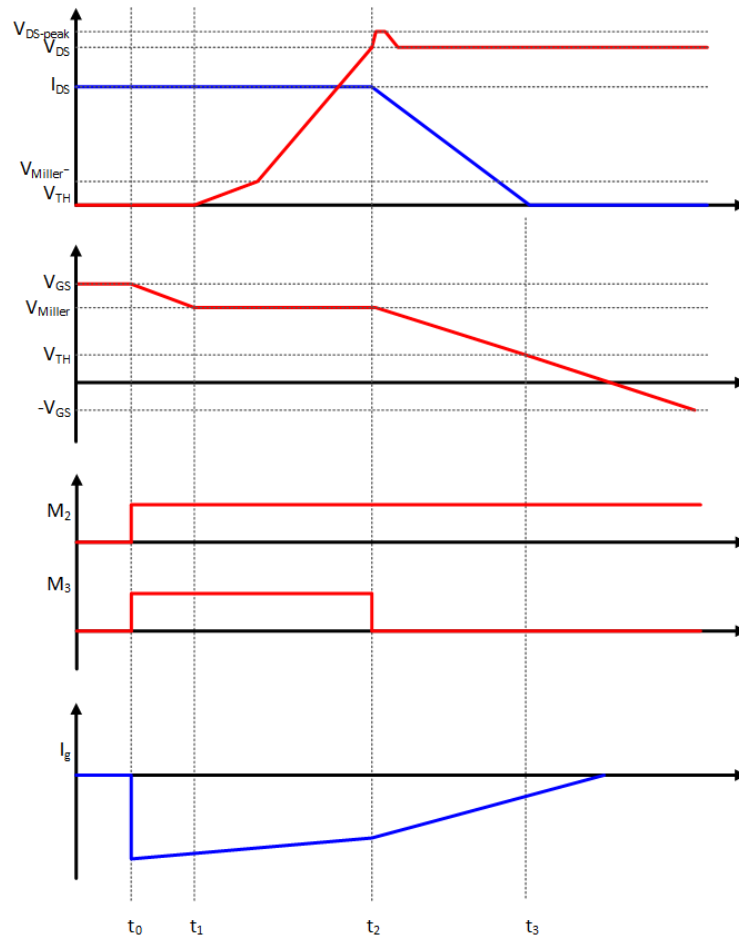


Fig. 6. Proposed AGD waveforms.

### 3.APPLICATIONS

#### 3.1. AGD Simulation Studies

During simulation studies, firstly, the open-loop control circuit was modeled with ideal components. In this way, it was aimed to observe the performance of AGD under ideal conditions. In these simulations, the parameters that were changed are R1, R2 resistors and the delay in the turn-on time of the M3 switch. For easy calculations, the equivalent resistance formed by connecting R1 and R2 resistors in parallel while M2 and M3 switches are in conduction is called  $R_{LOW}$  and the resistance formed when the M3 switch turns off is called  $R_{HIGH}$ . The simulation results obtained in this way are given in Table 2. In the simulation, the battery voltage is 400V and the switch current is 60A.

TABLE 2: Simulation results for AGD

$R_{LOW}$	$R_{HIGH}$	$T_{DELAY}$	$E_{off}$	$V_{peak}$
5 $\Omega$	20 $\Omega$	59 ns	350.8 $\mu J$	479 V
5 $\Omega$	20 $\Omega$	60 ns	331.2 $\mu J$	491 V
5 $\Omega$	20 $\Omega$	61 ns	316.6 $\mu J$	506 V
5 $\Omega$	25 $\Omega$	60 ns	343.0 $\mu J$	485 V
5 $\Omega$	25 $\Omega$	61 ns	323.4 $\mu J$	502 V
5 $\Omega$	25 $\Omega$	62 ns	310.7 $\mu J$	516 V
5 $\Omega$	30 $\Omega$	60 ns	354.4 $\mu J$	481 V
5 $\Omega$	30 $\Omega$	61 ns	329.8 $\mu J$	498 V
5 $\Omega$	30 $\Omega$	62 ns	313.8 $\mu J$	514 V

Looking at the simulation results, all values in the table are in a more advantageous situation compared to the results of the classical gate driver. When the 10  $\Omega$  turn-off resistance results of the classical gate driver are compared with the AGD results, both the switch turn-off losses and the peak voltage are lower. Fig. 7 shows the simulation waveforms when  $R_{LOW}$  is 5  $\Omega$  and  $R_{HIGH}$  is 25  $\Omega$ . The current rate has been slowed down, resulting in reduced oscillations in voltage and current.

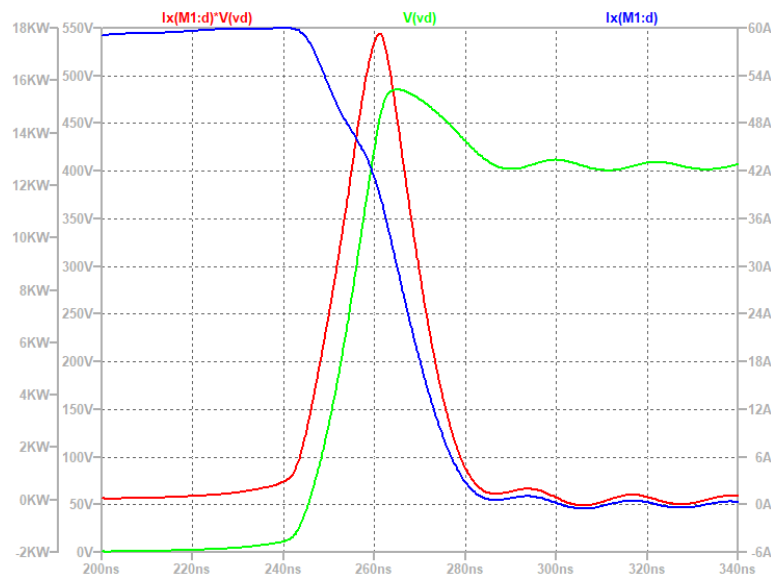


Fig. 7. Simulation results of AGD with  $R_{LOW}$  5  $\Omega$  and  $R_{HIGH}$  25  $\Omega$ .

### 3.2. Simulation Studies with Real Components

After verifying the AGD operation principle with ideal components, the circuit was implemented with real components. To simplify the implementation of AGD, the circuit was constructed by adding modifications to a standard gate driver. The UCC5350 gate driver from Texas Instruments was selected as the driver. For AGD waveform generation, feedback was taken from the switch drain-source voltage. The rise time of the drain-source voltage is in the range of 20-30 ns. To ensure proper operation of the AGD circuit, the control circuit should have very short measurement and response times.

The parasitic capacitors in the classic voltage divider circuit used for voltage measurement can affect the circuit performance and can cause an extra delay. Therefore, a compensated voltage divider circuit was used instead of the classic voltage divider when taking feedback from the switch. The compensated voltage divider circuit is obtained by placing capacitors in parallel with the voltage divider resistors and is preferred for high-frequency measurement circuits [11].

The optimum turn-off time for the M3 switch in the AGD circuit is when the switch voltage reaches the input voltage. This moment also corresponds to the end of the Miller region. A high speed comparator is used to generate the turn-off signal. The delay time of this comparator is maximum 2.9 ns. When adjusting the comparison threshold value, the total delay in the circuit should be considered. The turn-on delay time of the M3 MOSFET is 3 ns. In this case, the total delay can be considered as 6 ns. Taking this delay into account, the turn-off threshold voltage for the M3 switch is selected as 250V. The simulation results for this case are shown in Fig. 8.

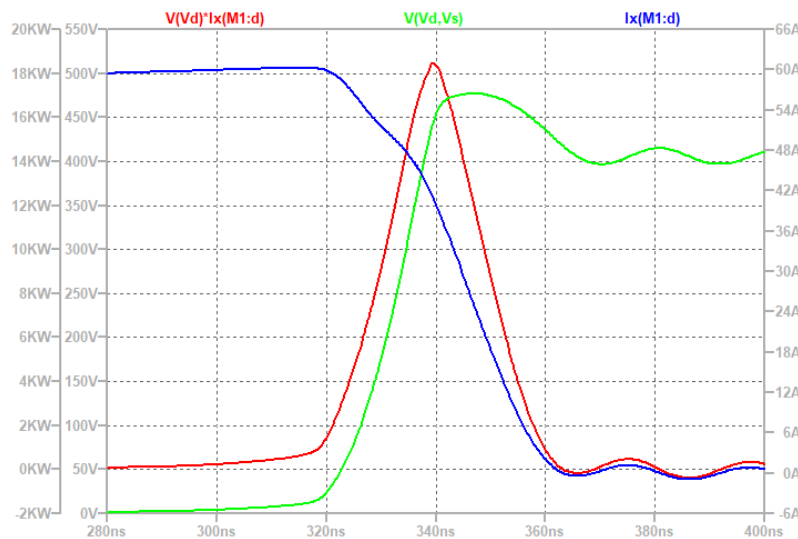


Fig. 8. Simulation waveforms of AGD with real components

The switching loss during turn-off with the closed loop AGD circuit is 383 uJ, and the peak voltage level is 480 V. These results are consistent with simulation results obtained using ideal components.

### 4.CONCLUSIONS

In this study, a closed-loop AGD circuit for SIC MOSFET has been investigated. The circuit was tested using a double-pulse test setup in the spice simulation environment. Simulation results were compared with classical gate driver simulation results. The low turn-off losses with low gate



resistance in classical gate driver achieved with having high gate resistance peak drain source voltage values. This has been achieved by separately controlling  $dv/dt$  and  $di/dt$  during turn-off. In addition to these benefits, the oscillations in the switch current and voltage have been suppressed. This suppression will result in an improvement in the EMI performance of the converter due to AGD.

## REFERENCES

1. M. M. Swamy, J.-K. Kang, and K. Shirabe, "Power loss, system efficiency, and leakage current comparison between Si IGBT VFD and SiC FET VFD with various filtering options," *IEEE Transactions on Industry Applications*, vol. 51, no. 5, pp. 3858–3866, 2015
2. X. She, A. Q. Huang, O. Lucia, and B. Ozpineci, "Review of Silicon Carbide Power Devices and Their Applications," *IEEE Transactions on Industrial Electronics*, vol. 64, no. 10, pp. 8193–8205, Oct. 2017
3. L. Zhang, X. Yuan, X. Wu, C. Shi, J. Zhang, and Y. Zhang, "Performance Evaluation of High-Power SiC MOSFET Modules in Comparison to Si IGBT Modules," *IEEE Transactions on Power Electronics*, vol. 34, no.2, pp. 1181–1196, Feb. 2019.
4. N. Oswald, P. Anthony, N. McNeill, and B. H. Stark, "An Experimental Investigation of the Tradeoff between Switching Losses and EMI Generation With Hard-Switched All-Si, Si-SiC, and All-SiC Device Combinations," *IEEE Transactions on Power Electronics*, vol. 29, no.5, pp. 2393–2407, May 2014.
5. J. Rice and J. Mookken, "SiC MOSFET gate drive design considerations," 2015 IEEE International Workshop on Integrated Power Packaging (IWIPP), May 2015.
6. Shihong Park and T. M. Jahns, "Flexible  $dv/dt$  and  $di/dt$  control method for insulated gate power switches," *IEEE Transactions on Industry Applications*, vol. 39, no. 3, pp. 657–664, May 2003.
7. N. Idir, R. Bausiere, and J. J. Franchaud, "Active gate voltage control of turn-on  $di/dt$  and turn-off  $dv/dt$  in insulated gate transistors," *IEEE Transactions on Power Electronics*, vol. 21, no. 4, pp. 849–855, Jul. 2006.
8. Y. Lobsiger and J. W. Kolar, "Closed-loop IGBT gate drive featuring highly dynamic  $di/dt$  and  $dv/dt$  control," 2012 IEEE Energy Conversion Congress and Exposition (ECCE), Sep. 2012.
9. S. S. Ahmad and G. Narayanan, "Double pulse test based switching characterization of SiC MOSFET," *IEEE Xplore*, Dec. 01, 2017.

10. A. Hu and J. Biela, "Evaluation of the  $I_{\text{max-fsw-dv/dt}}$  Trade-off of High Voltage SiC MOSFETs Based on an Analytical Switching Loss Model," 2020 22nd European Conference on Power Electronics and Applications (EPE'20 ECCE Europe), Sep. 2020.
11. M. Grubmuller, B. Schweighofer, and H. Wiegler, "Characterization of a resistive voltage divider design for wideband power measurements," IEEE SENSORS 2014 Proceedings, Nov. 2014.

# Verification of Adhesive Application in Composite Driveshafts by Using Finite Element Method

Serdar Kaan Hortooğlu<sup>1</sup>, Onur Özbek<sup>1</sup>, Sedat Tarakçı<sup>1</sup>, Efe Işık<sup>1</sup>

<sup>1</sup>Tirsan Kardan San. ve Tic. A.Ş. Manisa

[s.hortooğlu@tirsankardan.com.tr](mailto:s.hortooğlu@tirsankardan.com.tr),

## Abstract

Lightening expectations in automotive industry increases for power transmission elements. With respect to this expectation, reducing the number of unit parts in the propeller shaft design is very important. This study aimed to design a single-piece propeller shaft by using composite tube instead of a two-piece traditional propeller shaft. The removal of the center bearing group, which constitutes approximately 18% of the propeller shaft weight, and the use of aluminium and composite unit parts instead of steel unit parts were planned.

In addition to the innovations in propeller shaft design, this study determined the parameters of the adhesive used for bonding composite tubes and aluminium unit part in a numerical environment. For determining the adhesive parameters, factors such as application length, thickness and bonding surface profile of the adhesive were considered for their effects on the torque carrying capacity. The cohesive zone material (CZM) model and the finite element method (FEA) method were used for modeling the adhesive in a numerical environment. The obtained results will help to optimize the adhesive parameters to increase the efficiency of the bonding process. In addition, a lighter and more durable propeller shaft design will be obtained with the innovations in propeller shaft design.

**Keywords:** CZM, Cohesive zone material modeling, FEA

## 1.INTRODUCTION

In recent years, many industries have used composite materials that offer many advantages such as high strength, lightness, high stiffness and good wear resistance. Since two-piece propeller shafts are designed with conventional production and material selection, they can be designed as single-piece with the implementation of composite tube. This provides higher durability and lower weight. Figure 1 shows the propeller shaft and its subcomponents. [1]

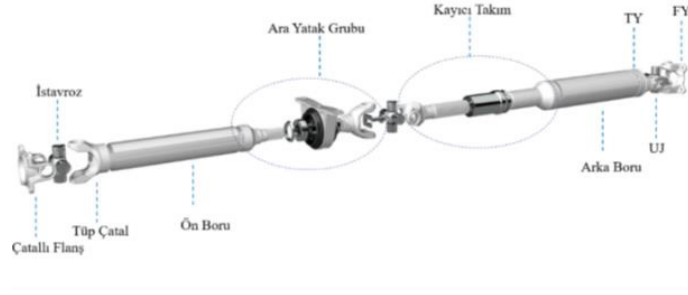


Figure 1 Traditional design cardan shaft model

The removal of the center bearing group, which constitutes approximately 18% of the propeller shaft weight, and the use of aluminum and composite unit parts instead of steel unit parts will provide approximately 35% lightening in propeller shaft weight. Figure 2 shows cardan shaft model with composite tube design.



Figure 2 Cardan shaft model with composite tube design

Pınar; compared composite and aluminum over composite composite tubes in terms of strength and natural frequency by testing and finite element method [2].

Rao have revealed that composites used in propeller shafts and generally carbon fiber and glass fibers are used in automotive industry intensively [3].

Joining of composite parts is an important issue and adhesives are often used. Bonding process is the process of joining two surfaces with adhesive and they can be exposed to various loads during this process. Therefore, the durability of bonded composite materials is an important issue in the design and production process. The types of adhesives and their maximum shear force from 3M company shown in Figure 3.



## 2.GENERAL PROPERTIES OF METHOD

This method models the behavior of adhesives and explains how stress and deformation occur on the surface of the adhesive. The CZM model is used to calculate the stress and deformation on the surface of the adhesive, which arise from the interactions between the two surfaces.

The FEA method is used to analyze the behavior of a structure or component. This method divides the structure or component into a series of small elements and calculates the behavior of each element. The FEA method calculates the stress, deformation, and other properties of a structure or component by taking into account factors such as material behavior, loads, and temperature.

In this study, CZM was used to model the behavior of the adhesive material and this model was applied by using the "LS-DYNA - Cohesive Mixed Mode Card Mat 138" material card in the LS-DYNA program. MAT 138 is a material card included in the LS-DYNA program and can be used with CZM. CZM is a technique used to model adhesion between materials. It models the stress-strain behavior that occurs when adhesion between materials is broken and the materials are separated.

In this study, tube sections and adhesive layers were created and their geometries were defined in the LS-DYNA program. The material card necessitates the parameters displayed underneath to be entered. The material card properties of mat138 are displayed in Table 1.

Table 1 Mat 138 material card properties

Ro	Mass density
Intfail	INTFAIL:=The number of integration points required for the cohesive element to be deleted. The value of INTFAIL may range from 1 to 4 with 1 the recommended value. LT.0.0: Employs a Newton - Cotes integration scheme and the element will be deleted when   INTFAIL   integration points have failed. EQ.0.0 : Employs a Newton - Cotes integration scheme and the element will not be deleted even if it satisfies the failure criterion. GT.0.0 : Employs a Gauss integration scheme and the element will be deleted when INTFAIL integration points have failed.
EN	EN:=The stiffness normal to the plane of the cohesive element.
ET	ET:=The stiffness in the plane of the cohesive element
GIC	GIC:=Energy release rate for mode I. LT.0.0: Load curve ID = (-GIC) which defines energy release rate for mode I as a function of element size.)
GIIC	GIIC:=Energy release rate for mode II LT.0.0: Load curve ID = (-GIIC) which defines energy release rate for mode II as a function of element size.)
XMU	XMU:=Exponent of the mixed mode criteria (see remarks below)
T	T:=Peak traction in normal direction
S	S:=Peak traction in tangential direction
UND	UND:=Ultimate displacement in the normal direction

UTD	UTD:=Ultimate displacement in the tangential direction
GAMMA	GAMMA:=Additional exponent for Benzeggagh-Kenane law (default = 1.0)

The parameters in the Mat 138 material card are determined based on the following tests. [5] Figure 5 shown fracture modes. The test standards necessary to determine the properties of CZM show in Figure 6

- The K and T values in the material model are determined from the tensile separation curve.

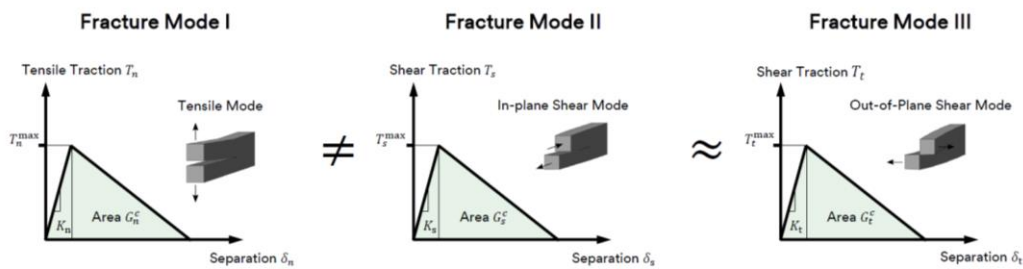


Figure 5 Fracture Modes

Physical Effect	Test Name	Test Sketch	Material Parameter	Description	Symbol	Unit
Elasticity	Uniaxial Tension Test		Young's Modulus and Poisson's Ratio	Resistance to elastic deformation and transverse contraction in tension	$E, \nu$	MPa
Damage Initiation	Thick Adherend Butt Joint Tension Test		Tensile Strength	Maximum stress in laterally constrained tension	$\sigma_{\max}$	MPa
	Thick Adherend Shear Test		Shear Strength	Maximum stress in shear	$\tau_{\max}$	MPa
Damage Evolution	Tapered Double Cantilever Beam (TDCB) Test		Mode I Fracture Energy (Critical Energy Release Rate)	Resistance to crack propagation in Mode I (opening mode)	$G_f^I$	$\frac{N}{mm}$
	(Tapered) End-Notched Flexure ((T)ENF) Test		Mode II Fracture Energy (Critical Energy Release Rate)	Resistance to crack propagation in Mode II (shear mode)	$G_f^{II} = G_f^{III}$	$\frac{N}{mm}$

Figure 6 CZM material tests

- Tensile Test: This test is described in ASTM E8/E8M-22 standard and determines the elastic modulus and Poisson ratio.
- Thick Adherend Lap Shear Test: This test is described in ASTM D5656 /DIN EN 14869-2-ASTM D3165-07(2014) standard and determines the maximum shear stress.



- Thick Adherend Butt Joint Test: This test is described in ASTM D5656 /DIN EN 14869-2-ASTM D3165-07(2014) standard and determines the maximum tensile stress.
- Tapered Double Cantilever Beam (TDCB) Test: This test is described in ASTM D3433/ ISO 25217 standard and determines the mode I energy  $G_I$ .
- Tapered End Notch Flexure (TENF) Test: This test is described in ASTM D3433/ ISO 25217 standard and determines the mode II energy  $G_{II}$  [4]

Due to the high cost and requirement of specialized equipment to determine the properties of the adhesive material, the material properties were obtained from the study conducted by Richter et al. [6].

### 3. VERIFICATION OF FEA METHOD

In this study, 3M adhesive was used for bonding Ø70 composite tubes shown Figure 7. The adhesive application was performed by using standard application methods, and the adhesive thickness was set to approximately 0.2 mm. The maximum torque that can be withstood by adhesive-bonded composite tubes is determined by applying torque from the test machine.



Figure 7 Composite Tube Static Test

Upon examination of the fracture surface, it was determined that the failure occurred through the composite tube. The adhesive was found to withstand a maximum torque of 6920 Nm. After calibration analysis with numerical simulations, the objective was to validate these experimental results by using CZM through the Ansys LS-Dyna explicit solver [7]. With this

modeling approach, possible problems such as damage and delamination in the adhesive structure can be observed. The analysis model in Figure 8 shows that the model is fixed from the blue surface and the system subjected to torque from the red surface.

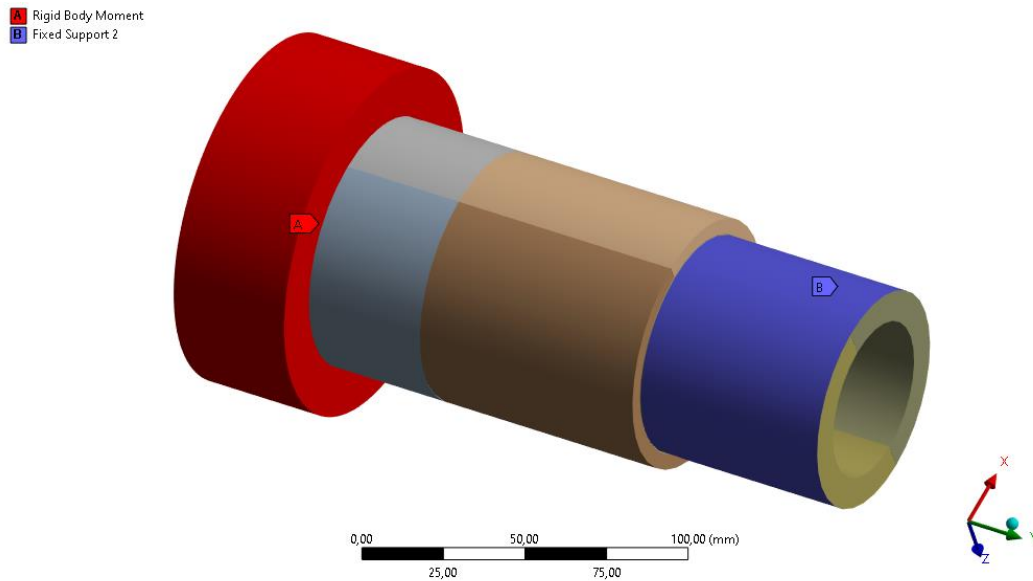


Figure 8 CZM Analysis Model

Figure 9 shows the CZM analysis model. The gray component in the Figure 9 represents the CZM element, with the material assigned as Mat 138. The analysis was terminated upon failure of the elements.

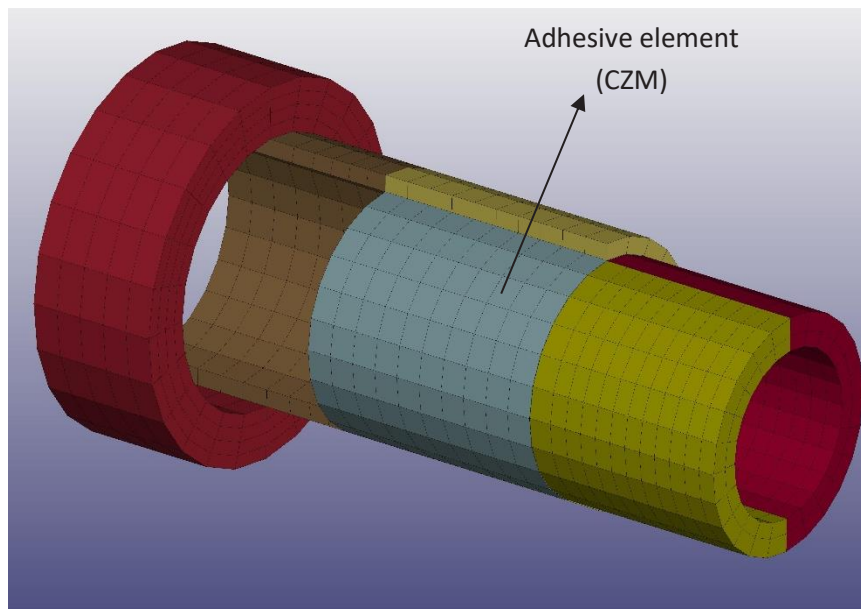


Figure 9 CZM shown on model

After the analysis performed by using the Ls-Dyna program, it was determined that the adhesive failed under 14,850 Nm torque, which was higher than the previous value of 6,920 Nm. The simulation results were highly consistent with the experimental data.

Using the CZM element parameters determined through analysis and testing verification, iterative analyses were performed for the tube with  $\varnothing 100$  outer diameter. In these analyses, the adhesive thickness was kept constant and analyses were performed based on the application surface length of the adhesive. Figure 10 shows the length of the CZM element as “L”. The thickness is shown as “t”.

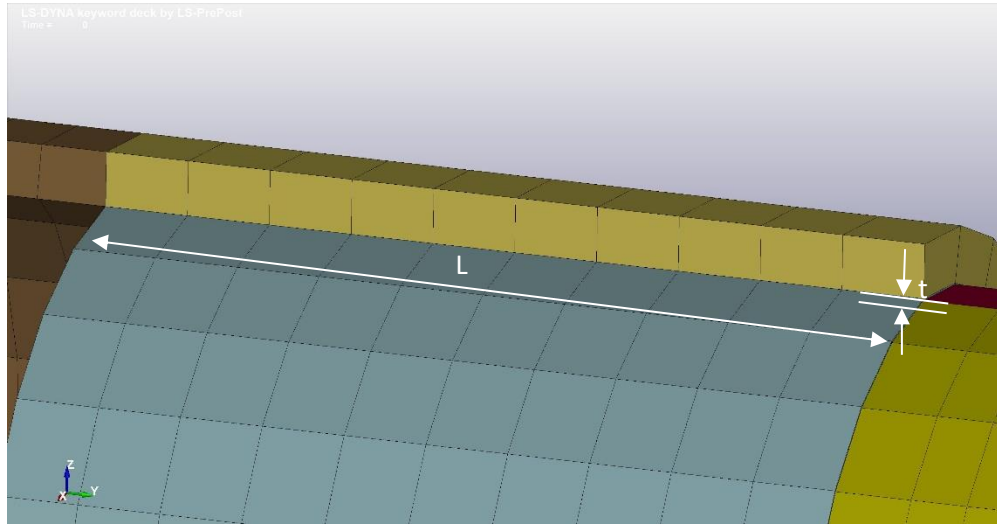


Figure 10 CZM model iterative analysis parameters

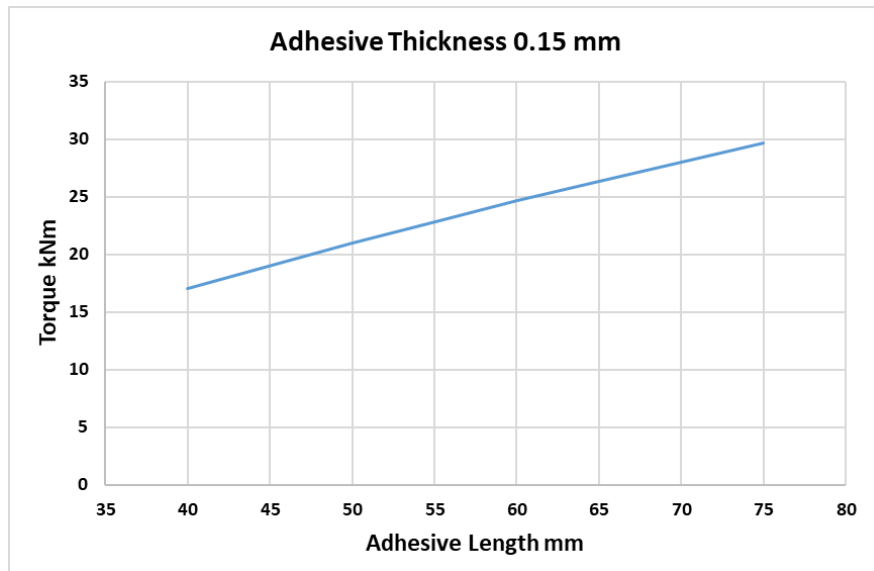


Figure 11 Iterative analysis result

According to the analysis results shown in Figure 11, increasing the length of the adhesive also increases the torque capacity that the adhesive can withstand, since it increases the bonding surface area. This study demonstrates the effects of parameters such as adhesive thickness, adhesive length, and bonding surface profile on the torque carrying capacity.

#### 4. RESULT

Analyses conducted using the CZM model and FEA method provide important information about the durability of the composite tube bonding process. These analyses determine how stresses and deformations occur on the surface of the tube adhesive and how much stress the tube is subjected during movement on the adhesive. This information is important for selecting the appropriate adhesive and performing the bonding process correctly.

Test results have shown to be consistent with numerical analysis results. Parameters such as adhesive length required for the bonding application of the Ø100 tube were determined using CZM modeling. This method enables the correct evaluation of the durability of bonded composite tubes and helps to make the bonding process more robust and reliable.

#### ACKNOWLEDGEMENTS

We would like to thank 3M R&D senior application engineer Merve Başdemir, Tirsan Kardan R&D Center, and Test Center for their support in conducting this study

#### REFERENCES

1. S.Tarakçı, S. Hortooğlu, E. Işık (2022) “Kompozit Kardan Mili Borusu Tasarım Kriterlerinin Belirlenmesine Yönelik Bir Çalışma”
2. Hasan Emrah Pınar, (2011), Hibrit Kompozit Kardan Şaftı ve Üretimi
3. B. James Prasad Raoa, D.V Srikanthb, T.Suresh Kumarc, L.Sreenivasa Roa, (2016) “Design And Analysis Of Automotive Composite Propeller Shaft Using Fea”, icmra 2016
4. 3M- Introduction to modeling 3M™ Structural Adhesives using Ansys
5. Ansys LS-DYNA Manual R13.0 Vol I
6. Richter, J.; Kuhtz, M.; Hornig, A.; Harhash, M.; Palkowski, H.; Gude, M. A Mixed (2021) “Numerical-Experimental Method to Characterize Metal-Polymer Interfaces for Crash Applications. Metals” (2021)
7. Ansys® Academic Research Mechanical, Release R21, Help System, Coupled Field Analysis Guide, ANSYS, Inc.

# THE EFFECTS OF DATA AUGMENTATION IN BRAIN TUMOR DIAGNOSIS

Gamze Ballıkaya<sup>1</sup>

Duygu Kaya<sup>2</sup>

<sup>1</sup>Department of Electrical-Elektronics Engineering, University of Bitlis Eren, Bitlis, Turkey

gballikaya@beu.edu.tr,

<sup>2</sup>Department of Electrical-Elektronics Engineering, University of Firat, Elazig, Turkey

dgur@firat.edu.tr

## Abstract

Brain tumors, which are caused by irregular proliferation of cells in the central nervous system, can be diagnosed from images obtained with Magnetic Resonance Imaging (MRI) technique. The accuracy and speed of early diagnosis can be increased with computer-aided diagnostic systems. There are systems proposed for brain tumor detection in order to accelerate and support the decision process of experts. Deep learning or machine learning based methods are proposed with MRI image data. However, large datasets cannot be created due to data privacy concerns in the medical field and the need for ethics committee approval when creating a dataset. In the present study, augmentation techniques were applied to a dataset consisting of 247 MRI images. A hybrid system is proposed for classification. A pre-trained AlexNet model is used as a deep feature extractor. The extracted features are classified by Linear Discriminant Analysis (LDA). With the AlexNet+LDA method, 83%, 89% and 92% success rates were obtained for the original dataset, 3-fold and 6-fold increase in the number of data, respectively.

**Keywords:** Brain Tumor Detection; Data Augmentation; Machine Learning; Classification; CAD.

## 1.INTRODUCTION

Brain tumors, of which there are two types, benign and malignant, are caused by irregular growth of cells in the central nervous system. Tumors are classified according to the appearance of the cells in the brain. If the cells look normal, they are called benign, and if they look abnormal, they are called malignant [1]. Different imaging techniques are used to detect brain tumors. These are Computed Tomography (CT) and Magnetic Resonance Imaging (MRI).

With early detection of the disease, irregular growth of cells can be prevented. However, personal experience comes to the fore when diagnosing the disease from the images obtained

with CT and MRI. Computer-aided diagnosis systems have been proposed in the literature for faster and more accurate detection of malignant tumors in the brain [1].

Image classification, which is current and popular in the field of computer vision, is a topic that researchers have been working on for the last 20 years and still has insurmountable challenges. There are several important factors that affect the performance of image classification problems. In order to improve the classification performance, researchers have been continuing their efforts.

In recent years, with the development of deep learning and machine learning methods, studies on early detection of diseases have also been carried out [2,3,4]. Machine learning methods and deep learning methods are frequently used in the literature in brain tumor classification for early detection of malignant brain tumors. In the study proposed by Deepa et al. [5], a hybrid machine learning method was used. Image fission is used to detect irregular cell growths from MRI images. Image segmentation was performed to estimate the boundaries of malignant tumors. An accuracy of 88.3% was achieved with the proposed method. [6] proposed a hybrid method. Classification was performed by combining convolutional neural networks (CNN) and support vector machine (SVM). The overall accuracy of the hybrid ESA-DVM was obtained as 98.49%. In the study proposed by Deepak et al. [7], the softmax layer of ESA was not used and the features obtained were classified by SVM. In the study using Figshare dataset, an accuracy of 95.82% was obtained. In another study conducted with MRI images, Machhale et al. [8] used SVM, k-Nearest Neighborhood and SVM-KEK hybrid classifier. In the study, the highest accuracy rate was obtained in the hybrid classifier with 98%.

When performing classification with deep learning methods, a large number of labeled training data is needed to train the model. There is a direct relationship between the classification performance of the model and the size of the dataset. However, it is also an important criterion that the dataset to be used during training is regularly parsed.

Deep learning methods are widely used in the medical world in many fields such as radiology, radiotherapy, pathology, ophthalmology, dermatology. However, since the data is largely protected due to privacy concerns, ethics committee approval is required for the studies to be carried out. This is an important challenge for deep learning applications planned to be realized in the field of healthcare. In cases where access to sufficient data is not provided, most classification problems cannot be solved.

In this study, a hybrid system is proposed to detect the type of brain tumor. The "Brain MRI Images for Brain Tumor Detection" dataset, which is openly available on Kaggle, is used in this study. The proposed system uses AlexNet, an ESA model trained with ImageNet dataset. Due to the high success rate obtained in the ImageNet dataset, which consists of image data, the AlexNet model was preferred for feature extraction from MRI images. After deep feature extraction, the resulting feature matrix was classified by Linear Discriminant Analysis (LDA). In order to increase the system performance, the dataset was increased by 3 and 6 times with affine transformations. The classification performance of the hybrid system is analyzed in detail for all cases.



## 2.GENERAL PROPERTIES OF METHOD

A hybrid system is proposed to classify whether a brain tumor is benign or malignant. In the study, the data set was increased by 3 and 6 times with affine transformations. Applications are performed with the original and augmented datasets and the results are analyzed comparatively. Feature matrices are obtained from the fully connected "fc8" layer of the AlexNet model and classified with LDA, one of the machine learning algorithms. The block diagram of the proposed system is presented in Figure 1.

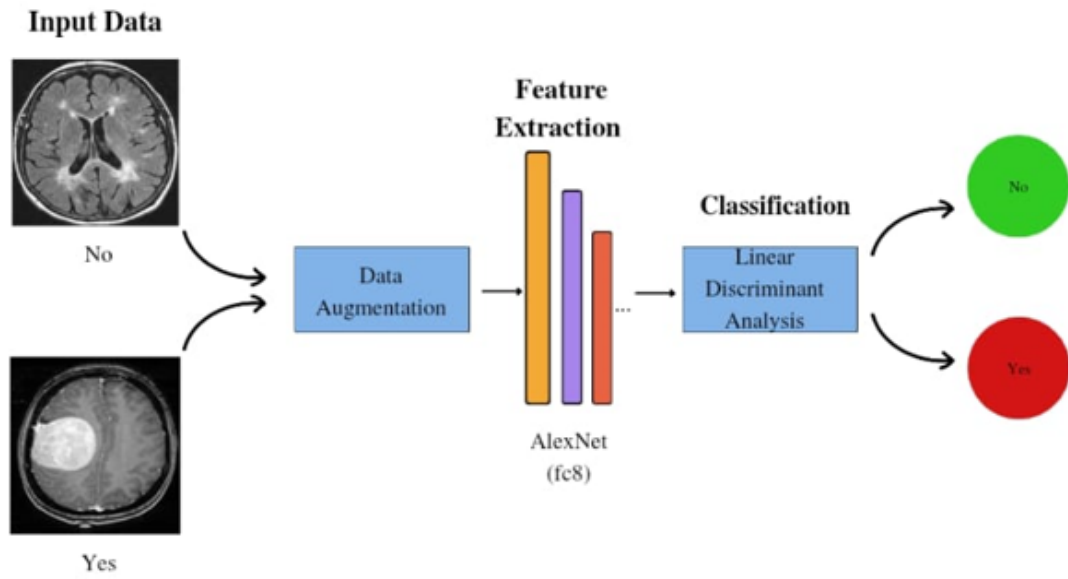


**Figure 1:** Block diagram of the proposed system.

The dataset used in the study is taken from Kaggle, which is available as open source for research and development of projects. The Kaggle dataset "Brain MRI Images for Brain Tumor Detection" is a dataset of brain MRI images that can be used for brain tumor detection. The dataset consists of healthy and tumor brain MRI images. Figure 2 shows sample images from the dataset.

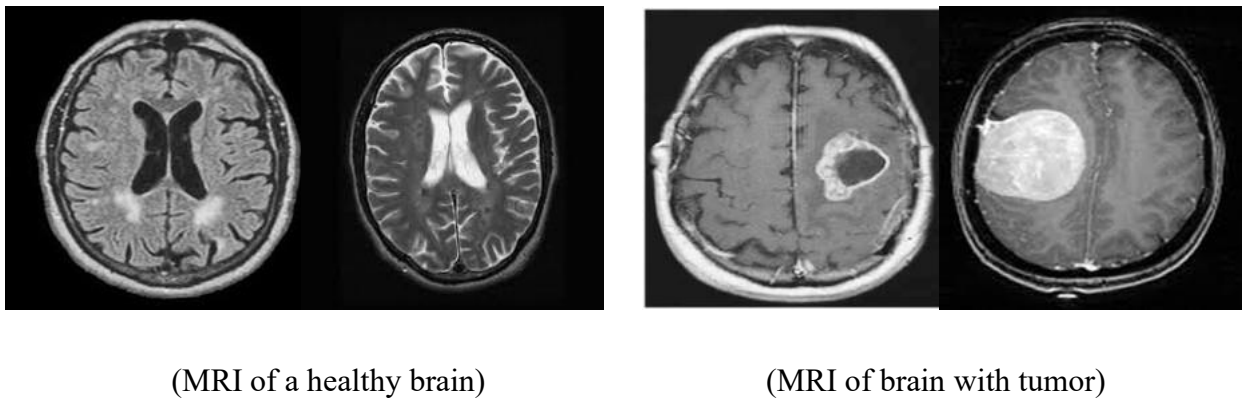


**Figure 2:** Sample images from the dataset.



The process of increasing the number of samples by multiplying the existing data in the datasets using various techniques is called Data Augmentation. By performing data augmentation on small-sized datasets that do not contain class imbalance, it is possible to increase the classification performance of the model to be used [9]. In the literature, data augmentation is performed with traditional methods or Gravity Adversarial Generating Networks (GAN).

Traditional methods applied to training data to improve performance are called affine image transformations. These include horizontal and vertical rotation, mirroring, scaling, panning, shifting, cropping and combinations thereof. They are fast, reliable and easy to integrate [9].

In 2012, the AlexNet model created by Alex Krizhevsky, Ilya Sutskever and Geoffrey Hinton won first place in an image classification competition on the ImageNet dataset. The AlexNet model is an 8-layer ESA. It consists of 5 convolution layers, 2 maximum pooling layers and 3 fully connected layers. The model uses ReLU activation function, normalization layers and dropout techniques to solve the overlearning problem [10]. By performing transfer learning, 1000-valued feature vectors were obtained from the fc8 fully connected layer of the model.

The feature vectors were classified with the LDA algorithm. In the algorithm, the mean and covariance matrix are calculated for each class in the dataset. Then the discriminant function is defined for each class and the feature vectors are evaluated. The class with the highest value is determined as the class of the feature vector [11]. With the LDA algorithm, the average difference between the data is maximized in order to achieve maximum classification accuracy.

Cross-validation technique was used to evaluate the performance of the classification model. Cross-validation is a technique that is used to prevent overlearning when the size of the dataset is small and to evaluate the performance of the model [12]. In this study, the dataset was divided into 10 parts, the model was trained with each of these parts and tested with the test data consisting of the other parts. The performance of the classification model was calculated by averaging the results obtained from the use of each part.

Performance metrics are used to evaluate the performance of the classification model and compare it with other models. True Positive (TP), True Negative (GN), False Positive (FP) and False Negative (FN) values are obtained by comparing the correct class label with the predicted class label. Different performance metrics are obtained with the TP, TN, FP and FN values that make up the complexity matrix. In this study, accuracy, precision, sensitivity, specificity and ROC curve were used as performance metrics. Table 1 shows the performance metrics used.

**Table 1.** Performance metrics

Accuracy	$\frac{TP + TN}{TP + TN + FP + FN}$
Precision	$\frac{TP}{TP + FP}$
Sensitivity	$\frac{TP}{TP + FN}$
Specificity	$\frac{TN}{TN + FP}$

### 3.APPLICATIONS

All experiments were performed in MATLAB R2019B environment with 1.5 GHz Intel Core CPU, 8 GB RAM and NVIDIA GeForce MX330 graphics card. The Classification Learner tool designed for data analysis applications in MATLAB was used. This tool allows users to create classification models. It also provides various graphs and metrics to evaluate the performance of the models.

In the study, the original data set was first increased 3 times and then 6 times and the classification performances were evaluated. Figure 3 shows some examples of images reproduced using conventional transformations, Figure 4 shows the class distributions of the datasets, and Table 2 shows the parameters and values used for the affine transformation.

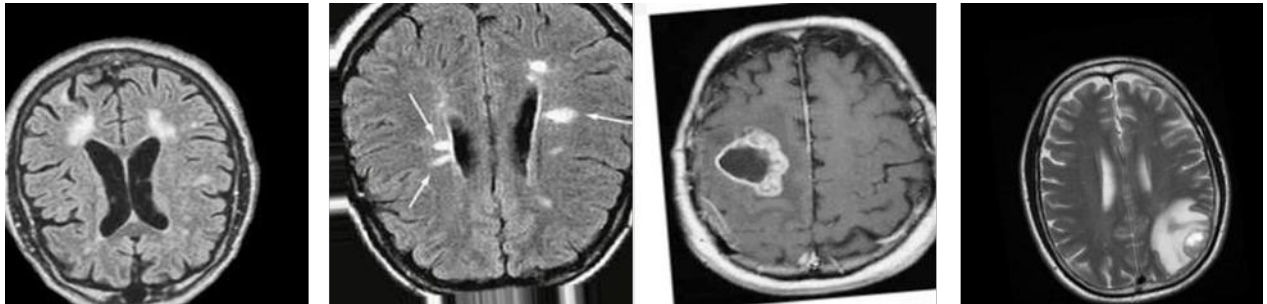


**Figure 3:** Examples of synthetic images resulting from affine transformations.

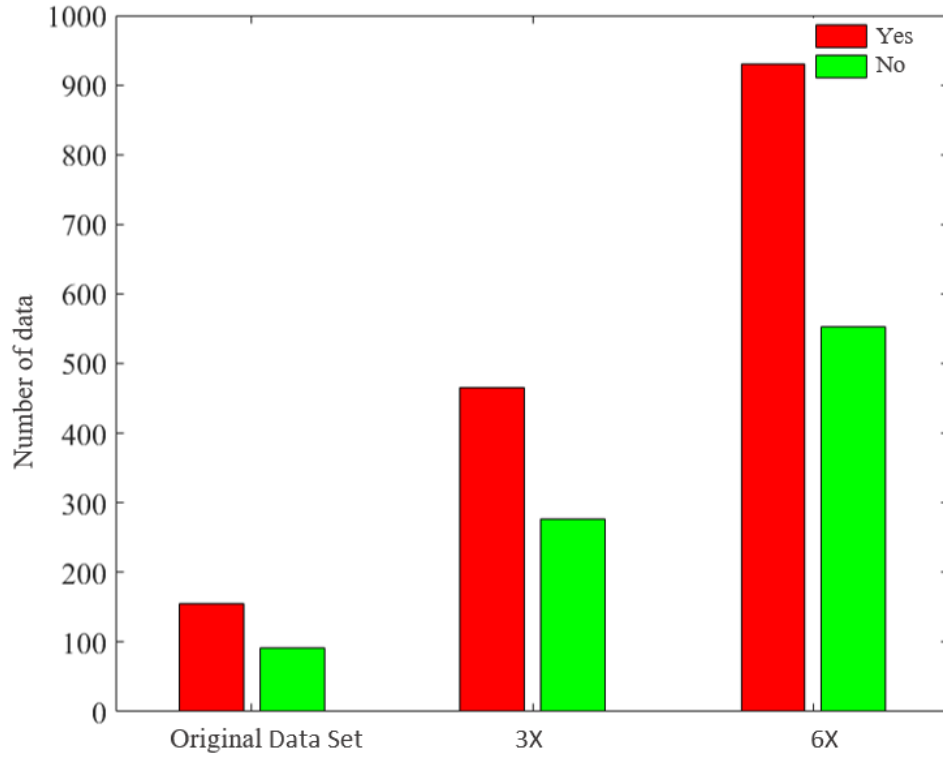


**Figure 4:** Class distributions of the data sets.

**Table 2:** Parameters used in the data augmentation method.

Parameters	Value
Rotation range	10
Width shift range	0.1
Height shift range	0.1
Shear range	0.1
Brightness range	(0.3, 1.0)
Horizontal flip	True
Vertical flip	True

AlexNet, one of the ESA models, was preferred to obtain the features of the input data. Using the weights of the pre-trained model, 1000 features were obtained for each input data from the fc8 fully connected layer.

In the classification stage, LDA, one of the machine learning algorithms, was used. Figure 5 shows the complexity matrices and ROC curves of the classification models trained with 10-fold cross validation. The accuracy, precision, sensitivity and specificity values used for performance evaluation are presented in Table 3.

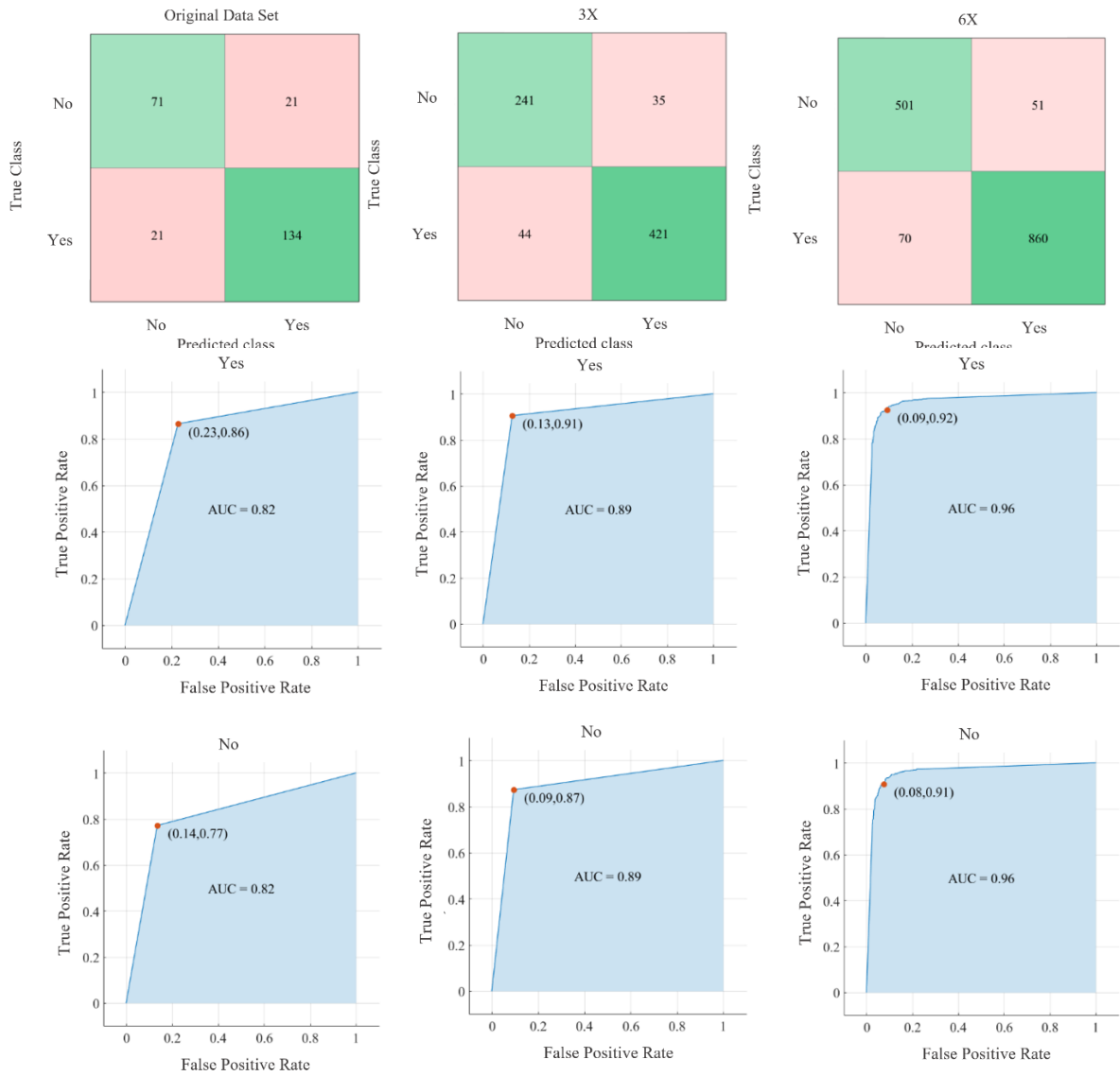


**Figure 5:** Confusion matrices and ROC curves of the classifiers.

**Table 3:** Performance metrics for the original and augmented data sets.

	TP	TN	FP	FN	Accuracy	Precision	Sensitivity	Specificity
Original Data Set	134	71	21	21	0.83	0.86	0.86	0.77
3x Increased Data Set	421	241	35	44	0.89	0.92	0.91	0.87
6x Increased Data Set	860	501	51	70	0.92	0.94	0.92	0.91

Considering the results presented in Figure 5, 83% success was achieved with the original dataset, 89% when the number of data was increased by 3 times, and 92% when the number of data was increased by 6 times. It is observed that the success of the classifier increases with the increase in the size of the dataset.

#### 4.CONCLUSIONS

In this study, a hybrid classification system is proposed to support expert opinions for brain tumor diagnosis. In classification problems, the size of the dataset is an important criterion that affects the success. However, some difficulties are encountered when creating large datasets in the health field. These are data privacy concerns and the need for ethics committee permission. In the proposed system, the size of the dataset is increased by 3 and 6 times using affine transformations in order to avoid these difficulties and increase the performance of computer-aided diagnosis systems. The features of the images in the dataset consisting of MRI images are obtained with AlexNet, one of the state-of-the-art ESA models. The weights of the pre-trained AlexNet model were used and 1000-valued feature vectors were obtained from the fully connected layer named "fc8". The features belonging to the original dataset and the datasets obtained by augmenting with basic affine transformations were classified with LDA, one of the machine learning algorithms. In the classification phase, the performance of the model was evaluated by 10-fold cross-validation. Performance metrics such as complexity matrix, ROC curve, accuracy, specificity, sensitivity and precision were obtained and the performance of the models were compared. In the results obtained, an increase in classification performance was observed with the increase in the size of the dataset. When the original dataset is used, 83% accuracy is obtained, 89% accuracy is obtained when the number of data is increased 3 times, and 92% accuracy is obtained when the number of data is increased 6 times. The performance of the proposed hybrid system increased by 9% in the best case due to the increase in the amount of data. In future studies, it is thought that the performance improvement provided by affine transformations can also be achieved by generating realistic images with adversarial generating networks.

#### REFERENCES

1. Kaplan, K. (n.d.). Kocaeli Üniversitesi Fen Bilimleri Enstitüsü Mekatronik Mühendisliği Anabilim Dalı Doktora Tezi Beyin Tümör Tiplerinin Makine Öğrenmesi Ve Derin Öğrenme Tabanlı Teknikler İle sınıflandırılması
2. Alzubaidi, M., Zubaydi, H. D., Bin-Salem, A. A., Abd-Alrazaq, A. A., Ahmed, A., & Househ, M. (2021). Role of deep learning in early detection of COVID-19: Scoping review. *Computer Methods and Programs in Biomedicine Update*, 1, 100025. <https://doi.org/10.1016/J.CMPBUP.2021.100025>
3. Liu, S., Liu, S., Cai, W., Pujol, S., Kikinis, R., & Feng, D. (2014). EARLY DIAGNOSIS OF ALZHEIMER'S DISEASE WITH DEEP LEARNING. <https://doi.org/10.1109/ISBI.2014.6868045>

4. Senturk, Z. K. (2020). Early diagnosis of Parkinson's disease using machine learning algorithms. <https://doi.org/10.1016/j.mehy.2020.109603>
5. Deepa, B., Murugappan, M., Member, S., Sumithra, M. G., Mahmud, M., & Al-rakhami, M. S. (n.d.). Pattern Descriptors Orientation and MAP Firefly Algorithm Based Brain Pathology Classification Using Hybridized Machine Learning Algorithm. <https://doi.org/10.1109/ACCESS.2021.3100549>
6. Khairandish, M. O., Sharma, M., & Jain, V. (2022). A Hybrid CNN-SVM Threshold Segmentation Approach for Tumor Detection and Classification of MRI Brain Images. *IRBM*, 43, 290–299. <https://doi.org/10.1016/j.irbm.2021.06.003>
7. Deepak, S., & Ameer, P. M. (2021). Automated Categorization of Brain Tumor from MRI Using CNN features and SVM. *Journal of Ambient Intelligence and Humanized Computing*, 12, 8357–8369. <https://doi.org/10.1007/s12652-020-02568-w>
8. Machhale, K., Nandpuru, H. B., Kapur, V., & Kosta, L. (2015). MRI brain cancer classification using hybrid classifier (SVM-KNN); MRI brain cancer classification using hybrid classifier (SVM-KNN). <https://doi.org/10.1109/IIC.2015.7150592>
9. Mikołajczyk, A., & Grochowski, M. (2018). Data augmentation for improving deep learning in image classification problem; Data augmentation for improving deep learning in image classification problem. <https://doi.org/10.1109/IIPHDW.2018.8388338>
10. Krizhevsky, A., Sutskever, I., & Hinton, G. E. (2017). ImageNet Classification with Deep Convolutional Neural Networks. *COMMUNICATIONS OF THE ACM*, 60(6). <https://doi.org/10.1145/3065386>
11. Balakrishnama, S., & Ganapathiraju, A. (n.d.). INSTITUTE FOR SIGNAL AND INFORMATION PROCESSING LINEAR DISCRIMINANT ANALYSIS-A BRIEF TUTORIAL.
12. Berrar, D. (n.d.). Cross-Validation Call for Papers for Machine Learning journal: Machine Learning for Soccer View project Cross-validation. <https://doi.org/10.1016/B978-0-12-809633-8.20349-X>

# GRAPE LEAF DETECTION AND RECOGNITION USING DATA AUGMENTATION WITH CNN-BASED MODELS

Gülay Kaya<sup>1</sup> Gökalp Çınarer<sup>2</sup>

<sup>1</sup> Faculty of Engineering and Architecture, University of Yozgat Bozok, Yozgat, Turkey,  
[kayagulay34@gmail.com](mailto:kayagulay34@gmail.com)

<sup>2</sup> Faculty of Engineering and Architecture, University of Yozgat Bozok, Yozgat, Turkey,  
[gokalp.cinarer@bozok.edu.tr](mailto:gokalp.cinarer@bozok.edu.tr)

## Abstract

Deep learning (DL) methods have become a popular approach in recent years to detect and classify complex patterns in large data sets. The use of DL techniques in the food industry is also increasing. These techniques are used in areas such as determination of food quality, production efficiency, food diversity and disease prevention. Grape leaf classification is also a very important problem in this field. Knowing the type of leaf is of great importance for vine leaf producers. Since the leaves are similar to each other, the types are mixed with each other and this causes the wrong product harvest. Accurate classification of grapevine leaves can contribute to plant taxonomy and morphology. At the same time, the correct determination of the grape species sheds light on plant phylogenetic studies. In this study, the correct classification of vine leaves has been achieved by using deep learning methods. The dataset consisting of 500 publicly available images was transformed into a dataset consisting of 2500 grape leaf images by applying different image enhancement techniques. Vine leaves were classified using convolutional neural network (CNN) based deep learning architectures and the accuracy performances of the models were evaluated. ResNet50, MobilNet, DenseNet and VGG19 architectures were each trained for 160 and 80 epochs. Results were examined based on criteria such as F1 score, accuracy, precision and recall. The highest accuracy rate was found to be 96.60% using the ResNet50 architecture. The results show that all architectures showed high performance in grape leaf classification. The application of DL in agricultural image analysis has offered a new perspective for rapid and accurate identification of grapevine species.

**Keywords:** Grape leaf diseases; Deep learning; Classification; Image augmentation; Artificial Intelligence; CNN.



## 1. INTRODUCTION

Technology and artificial intelligence (AI) are among the most rapidly developing and impressive fields of today. The increase in humanity's computing power contributes greatly to the development of these fields. Healthcare [1], finance [2], e-commerce [3] and automotive sectors [4] have undergone a major transformation thanks to AI [5]. The rapid development of technology enables the development of AI applications in these sectors.

Technology deep learning relationship is a prominent method among artificial intelligence technologies. Based on artificial neural network (ANN) structure, DL is a machine learning method that can perform complex operations on large data sets. It is especially used in areas such as image [8], natural language [9], voice [10] and game playing [11-12]. Deep learning architectures perform these classification processes very quickly with the developing technology.

The use of DL techniques in the food industry has been increasing in recent years [13]. These techniques are especially used in areas such as food quality determination, production efficiency, food safety and disease prevention [13]. For example, in food image processing applications, deep learning models can be used to perform quality control of food [14]. Another important application in the food industry is food safety and prevention of foodborne diseases [15]. Deep learning algorithms can identify potential risks in the food production process and can be used to detect and prevent foodborne diseases [15]. In recent years, deep learning techniques and artificial intelligence algorithms have emerged as an alternative method for plant disease diagnosis and classification [7].

The grapevine plant is a widely cultivated grape species worldwide [6]. However, various diseases and inaccurate identification of grapevine grape species can adversely affect the growth and productivity of grapevine leaves. Traditionally, plant species identification and classification has been carried out by visual inspection under human supervision. However, this method is slow, costly and can sometimes produce inaccurate results. At the same time, it is also important to select the right crop according to the nature of the soil and the region. Therefore, timely stacking and correct sorting of vine leaf species is important for plant health and productivity.

Studies in the literature [16-28] show that deep learning techniques are an effective method for detecting and classifying plant species and diseases in the agricultural sector. This technology helps to detect plant diseases faster and more accurately and to protect plant health.

The main contributions of this study are:

- Accurate classification of grapevine leaf species can contribute to plant taxonomy and morphology.
- Classification sheds light on plant phylogenetic studies.

- Accurate classification plays an important role in plant protection studies.

In this study, a data augmentation method is proposed for the classification of vine leaf images and the dataset is enlarged. Classification is performed using deep learning architectures with the obtained images.

The following sections of this paper are as follows. Similar works in the literature and these works are tabulated in section 2. Information about dataset, data augmentation, deep learning, transfer learning, architectures used and performance metrics are given in section 3. The results obtained from the architectures used in the study are discussed within themselves and with other studies in the literature and given in section 4. At the end, the conclusion of the study is given in section 5.

## 2. LITERATURE REVIEW

In the literature, there are studies on grapevine leaf species identification, leaf disease classification, and detection of different species. In these studies, fast and accurate diagnostic methods have been presented to limit the spread of plant diseases and reduce production losses. In the study of Nader et al. [16] on grape leaf disease classification, CNN, VGG-16, VGG-19 and Xception models are used with Plant Village (PV) dataset. Data augmentation methods such as rescale, rotation, horizontal flip, horizontal flip, zoom, etc. are used. By transfer learning to VGG and Xception and training with ImageNet weight, a 99.82% success rate is obtained.

Nagi and Tripathy [17] use vine leaf images from the PlantVillage dataset in their study. The dataset consists of 4 classes, 3 grapevine disease and 1 healthy class, and 3423 images. VGG16, VGG19, AlexNet, MobileNet and other pre-trained architectures are used in the study. Training is done with 30 epochs with Adam optimization. MobileNet model classification accuracy is achieved 98.53% with 70% training and 30% testing rate.

Balawi et al. [18] compared the accuracy of DL techniques to classify leaf images as healthy and diseased to improve the accuracy of this classification. By applying data augmentation method with data transformation like shifting, flipping, rotating, rotating, zooming methods, 5 classes and a total of 1600 leaf images are obtained. In the study, the most successful architecture is VGG16 architecture with 87% success rate.

Data augmentation methods were applied in the study of Li et al. [19] using VGG16, DenseNet, Resnet101, Resnet18 and Googlenet architectures. While there are 4200 images and 21 classes in the dataset of this study, a total of approximately 33600 images are obtained by applying data augmentation methods with transposition, rotation, translation (reflection) and Gaussian noise methods. The most successful architecture is Googlenet with a success rate of 97.4.

In the study by Köklü et al. [20], a unique dataset is created and while there are 500 images in the dataset, 2500 images are obtained by applying data augmentation methods. Support vector machine (SVM) and DL methods were used in the study and 97.60 success was achieved with SVM Cubic.

Alessandrini et al. [21] augmented 1770 images to 24,780 images using data augmentation methods in 2 classes (patient and healthy) dataset, collected for use in a research project. Images with 1280x720, 320x180 and 80x45 pixel sizes are trained and tested. The most successful test accuracy value using CNN architecture is 0.99448 at 320x180 pixel size.

Hasan et al. [22] use KNN, SVM, Decision Trees, Artificial Neural Network (ANN), Linear Decomposition (LDA) models to classify diseases in Betel vine leaves. The dataset contains 1350 images in 6 different classes (healthy leaves, black mosaic disease, spot disease, fusarium wilt disease, curly leaf disease, bacterial wilt disease) and data augmentation is applied using rotation, mirroring, cutting, brightness, contrast adjustment methods, which increases the original dataset approximately 4 times. The researchers primarily used color, shape and edge features. These features are related to the intensity of the pixels of the leaves in the RGB color spectrum, shape features (e.g., leaf length and width), edge features (e.g., the intensity of the pixels at the leaf edge). Gaussian filter and morphological operations are also used to filter and smooth the images obtained from the leaves. The highest accuracy rate of 97.5% was obtained with the KNN model.

Nasiri et al [23] covers a study using deep convolutional neural networks (CNN) to automatically classify grape varieties from leaf images. Using six different grape varieties grown in Iran, a dataset is created to automatically detect different features (e.g., color, shape, veining) on the leaves. The images were captured in different lighting conditions and from different angles, manually parsed and labeled. In the paper, data augmentation techniques are used to improve feature extraction and classification accuracy. The most successful model, VGG16, achieved 97.34% accuracy.

In the classification of plant species and diseases, there are studies on the detection of different diseases. In [24], Kukreja et al. develop a model that identifies parsley leaf spot disease and classifies it for disease severity. This model is classifying 2000 image datasets including PLS infected images and healthy. This model achieved 99.5% classification accuracy, and as a result, this study shows that DL models can be used for parsley leaf spot disease detection.

Rajiv et al. [25] work on the detection and classification of diseases in plant leaves. Their dataset consists of 14,592 leaf images from the PlantVillage database with 38 different diseases, ranging from 350 to 1,501 images in each disease class. The dataset is collected from 2 different regions in India (Andhra Pradesh and Karnataka). The data processing process consists of input image acquisition, image preprocessing, segmented region detection

and classification. SVM classifier used with GLCM features, and classification accuracy is 96.65%.

Savin and Hnatiuc [26] analyzed the color, structure and form of plant leaves using image processing techniques to identify the health benefits of plants by processing image data obtained from plant leaves. While 1009 images were used for species identification in the dataset, 7222 images for train and 1805 images used for validation in disease identification. A 95% success rate is achieved using EfficientNet. It is emphasized in the study that the data obtained from plant leaves is a valuable resource for health improvement methods and image processing techniques are an effective tool for analyzing these data.

Liu et al. [27] propose a method using deep learning and mobile devices to identify grape varieties using grape leaf images. In the study, a total of 4200 leaf images of 21 different species were obtained from the dataset, and by using various image processing techniques (adjusting the size of the dataset, rotating and resizing the images), dataset is reached 33600 and includes approximately 1600 images for every one grape leaf image classes. The GoogLeNet model outperforms the 99.91% success rate with 32 mini-batch sizes, 0.001 learning rate and 80 max epoch tuning.

Alkan et al [28] conducted a study on automatic detection of grape disease. The dataset consists of 10 classes and 100 images belonging to each class, 1000 images in total. The most successful hybrid study is AlexNet+TL with 92.5%. The general results of the literature studies and the methods used are shown in Table 1.

**Table 1.** Literature Review

	<b>Method</b>	<b>Result</b>	<b>Total Image</b>	<b>Class/Total Visual</b>	<b>Description Data augmentation (+/-)</b>
[16]	VGG and Xception	%99.82	4062	4 / -	+
[17]	CNN	%98,53	3423	4 / 3423	-
[18]	VGG	%87	-	5 / 1600	+
[19]	Googlenet	%97,4	4200	21 / ~33600	+
[20]	SVM Cubic	%97.60	500	5 / 2500	+
[21]	CNN	%99,44	1770	2 / 24.780	+
[22]	KNN	%97.5	1350	6/~5400	+
[23]	VGG16	% 99.11	300	6/1200.060	+
[24]	CNN	%99.5	2000	-	-
[25]	GLCM+SVM	%96.65	14.592	38/14.592	-
[26]	EfficientNet	%95	1009	11/10.036	+
[27]	GoogLeNet	%99.1	4200	21/33600	+
[28]	AlexNet+TL	%92.5	1000	10/1000	-

### 3. GENERAL PROPERTIES OF METHOD

#### 3.1.Dataset

The vine leaf dataset created by Köklü et al. [20] was used in this study. The dataset was placed in a special box designed to be unaffected by external factors and equipped with lighting inside to prevent shadow formation. Prosilica GT2000C RGB camera with 2.2 megapixel, 2048x2048 resolution, CMOS-type sensor with full resolution at a maximum frame rate of 53.7 fps was used in the study. The dataset contains 500 images of 512\*512 size in 5 classes, 100 images from each class. There are five classes in the dataset: "Ak, Ala\_Idris, Buzgulu, Dimnit and Nazli". Figure 1 shows the images of the vine leaf types in the dataset.

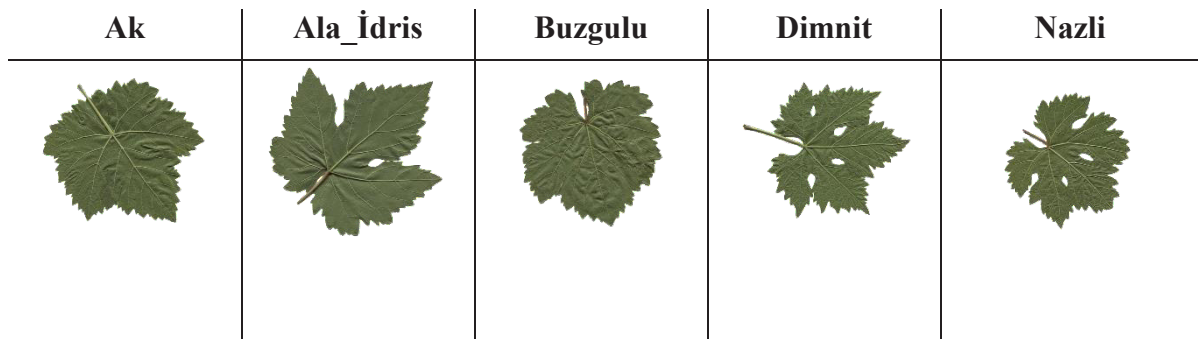


**Figure 1.** Example images of grapevine leaf classes in the dataset

#### 3.2.Data Augmentation

Data augmentation (DA) is a set of different methods used to increase the number of images. In this study, rotation, brightness, horizontal and zoom are used as data augmentation methods. The basic parameters of the methods used are given in Table 2. A total of 2500 images are obtained with the data augmentation method. Each class is divided into 70% train, 30% test, then 80% train and 20% test, the data distribution of each class is shown in Table 3.


























**Table 2.** Data Augmentation Parameters

rotation_range	45
brightness_range	0.2-1.5
zoom_range	0.3
horizontal_flip	Ture

**Table 3.** Dataset Data Distribution

Classes	Dataset	Train	Test
Ak	70-30	350	150
	80-20	400	100
Ala_İdris	70-30	350	150
	80-20	400	100
Buzgulu	70-30	350	150
	80-20	400	100
Dimnit	70-30	350	150
	80-20	400	100
Nazli	70-30	350	150
	80-20	400	100

An example of the DA methods used for each class is given in Figure 2.

	Original	Rotation	Brightness	Horizontal	Zoom
<b>Ak</b>					
<b>Ala_İdris</b>					
<b>Buzgulu</b>					
<b>Dimnit</b>					
<b>Nazli</b>					

**Figure 2.** Visuals of the data augmentation application process



### 3.3. Deep Learning

Nowadays, artificial intelligence technologies are used in many fields and one of these technologies is DL. It is a machine learning method that can perform complex operations on large data sets [29]. It is especially used in areas such as image, language process, recognition and game playing [30].

DL is based on the artificial neural network (ANN) structure. An ANN consists of layers and each layer has different types of neurons. Data input is given to the first layer of the network and then inter-layer operations are performed. These operations change the weights and thresholds used to train and calculate the outputs. The network is trained iteratively to minimize the amount of error [12].

DL is a process consisting of data extraction feature, model building and prediction. In the model building phase, the structure, weights and thresholds of the network are determined, and in the prediction phase, the model processes the data and produces its outputs [29].

The advantages of DL is the ability to automatically extract features from data instead of the classical feature extraction process. In addition, deep learning can learn from data without the need for many predetermined rules and thus can be used in different fields [30].

### 3.4. Transfer Learning

Transfer Learning (TL) refers to the use of a previously trained model in a new learning task. This technique allows the key features of a model acquired during the learning process to be used for a different task. For example, an image classification model can be used as pre-trained and retrained for a different image classification task.

Transfer Learning is particularly effective when working on large data sets. By using a pre-trained model, high accuracy rates can be achieved even on a smaller dataset, making the learning process faster and less costly [31].

As a result, Transfer Learning is a highly effective technique to optimize the learning process and achieve better results using less data [32].

### 3.5. Architectures

In the training phase, the architectures use the previously trained ImageNet weight file, while the models of the architectures are drawn from the tensorflow keras library. In the architectures used, softmax is used as the activation function and adam is used as the optimization algorithm. The reason for using softmax is that there are more than one class [30]. This algorithm changes the learning rate for each parameter like the other parameters. Adam optimization is very fast and performs subset merging very quickly [33].



### 3.5.1. DenseNet

DenseNet is a dense convolutional neural network (CNN) architecture in which dense blocks are connected together. The main idea in this architecture is that each layer has access to the outputs of previous layers as input and its own output. This allows information to flow more efficiently and also allows the network to achieve higher accuracy with fewer parameters.

The DenseNet architecture consists of two types of dense blocks: "BottleNeck" blocks and "Dense" blocks. BottleNeck blocks are used to provide a smaller number and smaller size of dense blocks with filters of smaller sizes and a predefined number of filters. Dense blocks are created with filters of larger size and a larger number of filters, where all layers are directly connected to each other, allowing the network to learn more extensive features.

DenseNet also performs dimensionality reduction by using a type of layer called "transition layers", which reduces the size of the network and thus enables a faster training process [34].

### 3.5.2. MobileNet

MobileNet is a lightweight CNN architecture designed for mobile devices. The main idea of the architecture is to create a lighter model with operations and few parameters. The MobileNet architecture uses a structure called "depthwise separable convolutions". In this structure, the "depthwise convolution" operation is first performed on the depth channels. Then, as in standard convolutions, filters are applied separately for each of these channels. In this way, a lighter architecture is achieved and at the same time, a faster model is obtained because less data needs to be processed. The MobileNet architecture has a number of variations that include models of different depths. These variations can be chosen to suit different application scenarios.

MobilNet is a popular architecture in the field of DL and is specifically designed for fast and efficient object recognition and classification on mobile devices. Unlike other deep learning architectures, MobilNet has a lightweight convolution-based architecture, which is mainly used in feature extraction functions. This architecture uses fewer parameters and performs less computation, so it works faster on mobile devices [35].

### 3.5.3. ResNet50

ResNet50 is a Convolutional Neural Network (CNN) model built in 50 layers. This model uses Convolutional (Conv) layers stacked one after the other, with a "Residual Block" between every two Conv layers. These blocks are a kind of connection that allows the learning process in each layer to work better. These connections also reduce the problem of "overfitting" in the training of deeper networks.

The ResNet50 model does not use Fully Connected (FC) layers in its final layers. Instead, the feature maps from the final Conv layer are connected to a Global Average Pooling layer, which is then combined with an FC layer used for classification [36].

### 3.5.4. VGG19

VGG19 is a CNN model with 19 layers. Most of these layers contain filters of size 3x3 and use successive Convolutional (Conv) layers and several max-pooling layers. These layers reduce the size of the input image and are then connected to several fully connected (FC) layers. The FC layers are used for the classification process.

VGG19, like previous VGG models, has an extremely simple and regularized structure. For this reason, it is frequently used, especially in TL methods [37]. In this method, the VGG19 model is loaded with a pre-trained set of weights and used to solve an image classification problem.

### 3.6. Performance Metrics

Some performance metrics are used to determine the success of the study. These metrics have their own calculation methods and are shown in Table 4.

**Table 4.** Performance Metric Formulas

<b>Precision</b>	$\frac{TP}{TP + FP}$
<b>Recall</b>	$\frac{TP}{TP + FN}$
<b>F1 Score</b>	$2 \times \frac{\text{Kesinlik} \times \text{Hassasiyet}}{\text{Kesinlik} + \text{Hassasiyet}}$
<b>Accuracy</b>	$\frac{TP + TN}{TP + TN + FP + FN}$

Another performance metric is the complexity matrix. The complexity matrix is calculated as shown in Figure 3.

		<b>Predicted</b>	
		Positive	Negative
<b>Actual</b>	Positive 1	TP	FP
	Negative 0	FN	TN

**Figure 3.** Confusion Matrix

#### 4. APPLICATIONS

Grapevine Leaves Image Dataset data was preprocessed, and the images obtained as a result of data augmentation were trained and tested on 4 different models. In order to observe the performance changes of the architectures and to obtain the best results, training and test sets divided into different ratios were used. The first split dataset was 70% training - 30% testing, the second split dataset was 80% training - 20% testing. Each architecture was run for 80 and 160 epochs. As a result of the training and testing, the success rates were compared and the split dataset with 75% success rate was taken as reference. Confusion matrices and performance metrics were obtained for each model for the training and test results according to the reference dataset. Performance evaluations of the models were made according to the metrics obtained.

The confusion matrix and accuracy-loss graphs of the training and test results at 80 and 160 epochs for the DenseNet architecture are shown in Figure 4 and Figure 5. It can be said that the DenseNet architecture is more successful in classifying the leaf images in the Nazli class at 80 epochs, while it is less successful in classifying the leaf images in the Buzgulu class. According to the classification success, Nazli > Ala\_Idris > Ak > Dimnit > Buzgulu. When 160 epochs are run, the success rate in classifying Nazli class decreases while the success rate in classifying other classes increases. While Ala\_Idris class ranks 2nd in success rate at 80 epochs, it gives the best success rate at 160 epochs.

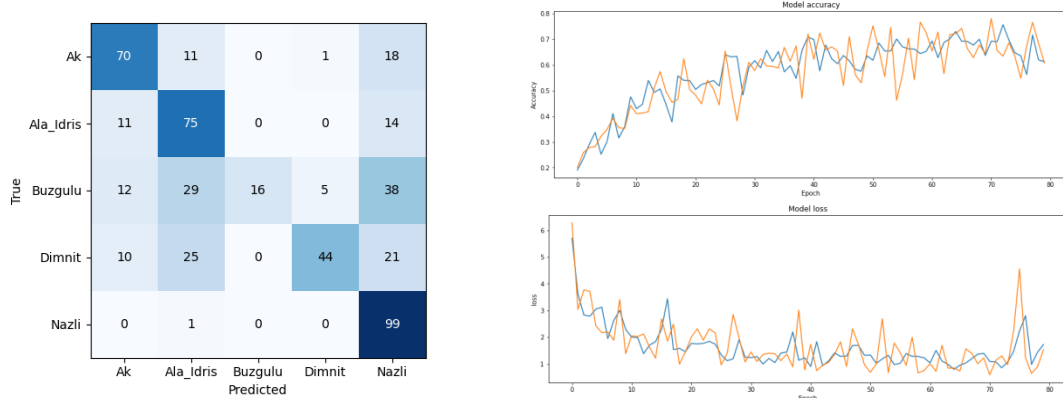


Figure 4. DenseNet 80 Epoch

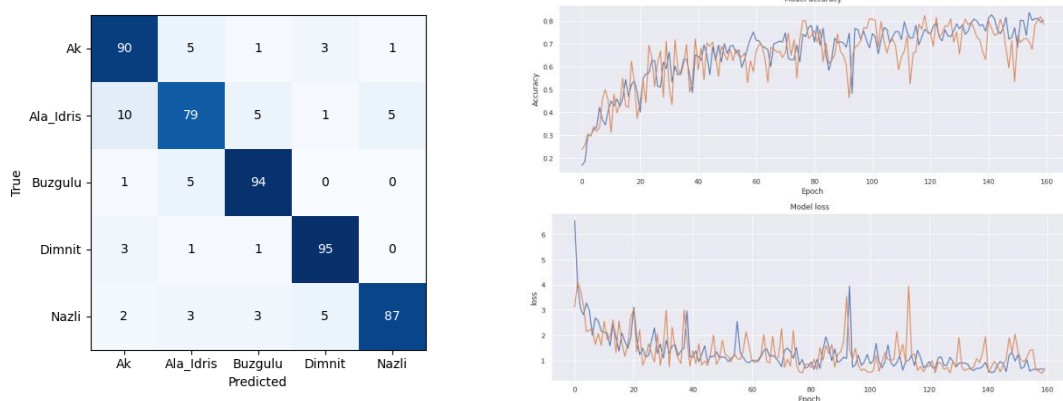
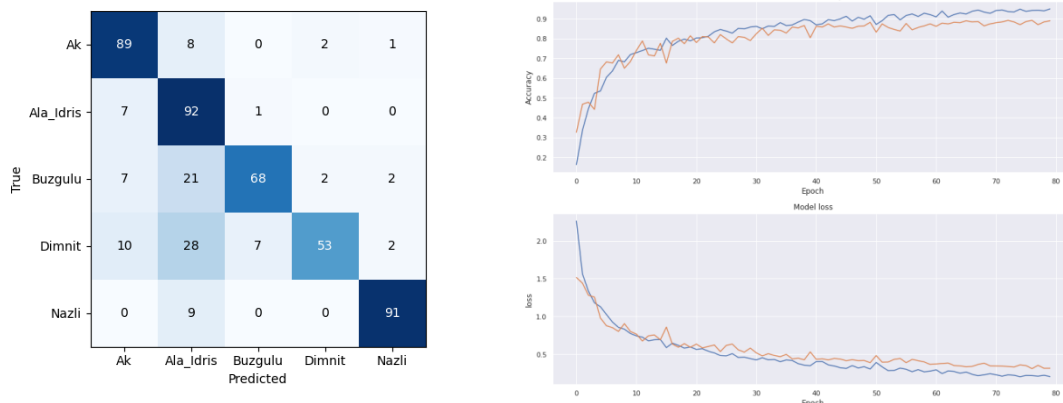
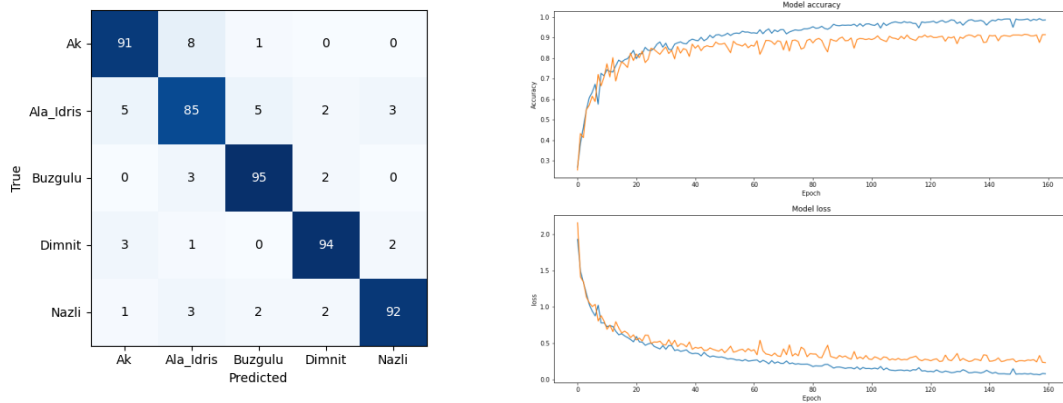


Figure 5. DenseNet 160 Epoch

The confusion matrix and ROC curves of the test results of the training at 80 and 160 epochs in the study with MobileNet architecture are shown in Figure 6 and Figure 7.



**Figure 6. MobileNet 80 Epoch**



**Figure 7. MobileNet 160 Epoch**

MobileNet gives a 91% success rate when classification is performed with 160 epochs. On a class basis, the lowest success rate is 79%, while the success rate of the majority is 90% and above. It can be said that the study with MobileNet architecture is successful. The classes with the most successful classification are Dimnit and Buzgulu.

ResNet50 architecture is the most successful classification algorithm in this study with a 97% success rate. There is no big difference between 80 and 160 epochs. While the worst classified class is Buzgulu with 92% and 94% success rates, the success rate is the same with the most successful class of MobileNet architecture. As a result of the observations, it is said that the classification of the Buzgulu class is also successful. The test results of the training with ResNet50 architecture at 80 and 160 epochs are shown in Figure 8 and Figure 9 with confusion matrix and graphs.

	Ak	Ala_idris	Buzgulu	Dimnit	Nazli
True Ak	95	0	0	3	2
Ala_idris	3	95	1	1	0
Buzgulu	0	1	92	6	1
Dimnit	3	0	2	95	0
Nazli	0	0	0	1	99
	Ak	Ala_idris	Buzgulu	Dimnit	Nazli
	Predicted				

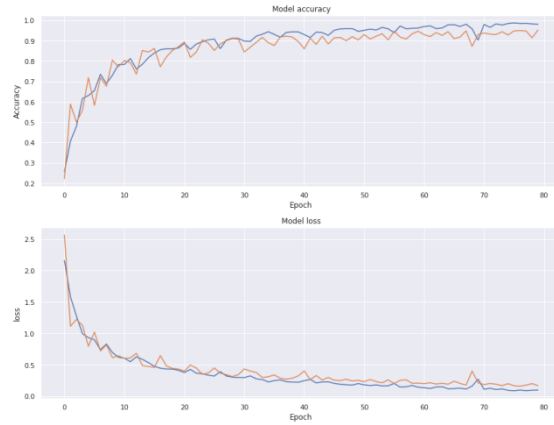


**Figure 8. ResNet50 80 Epoch**

	Ak	Ala_idris	Buzgulu	Dimnit	Nazli
True Ak	95	1	0	3	1
Ala_idris	1	99	0	0	0
Buzgulu	0	1	94	4	1
Dimnit	3	0	1	96	0
Nazli	0	0	0	1	99
	Ak	Ala_idris	Buzgulu	Dimnit	Nazli
	Predicted				

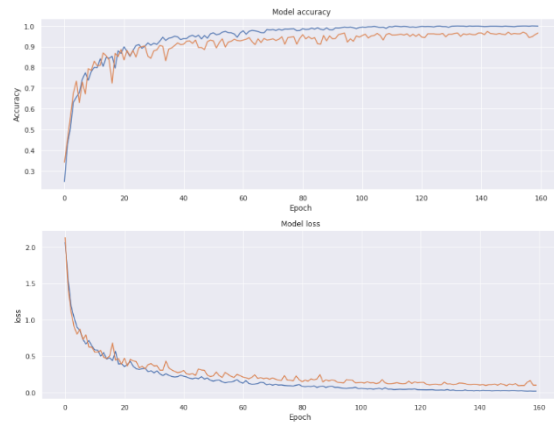


**Figure 9. ResNet50 160 Epoch**

In the study with the VGG19 architecture, the confusion matrix and ROC graphs of the test results of the training at 80 and 160 epochs are shown in Figure 10 and Figure 11.

	Ak	Ala_idris	Buzgulu	Dimnit	Nazli
True Ak	95	1	2	1	1
Ala_idris	3	90	7	0	0
Buzgulu	0	0	98	2	0
Dimnit	4	1	0	95	0
Nazli	0	0	2	1	97
	Ak	Ala_idris	Buzgulu	Dimnit	Nazli
	Predicted				

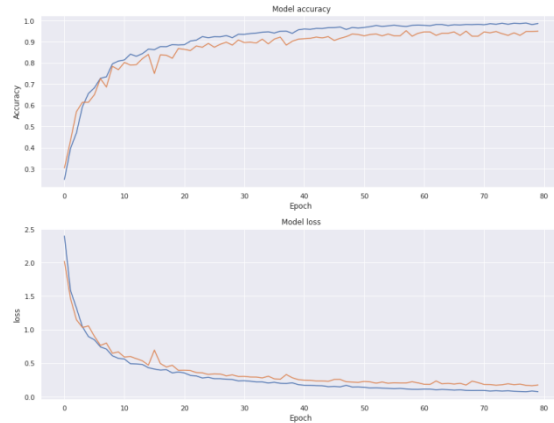


**Figure 10. VGG19 80 Epoch**

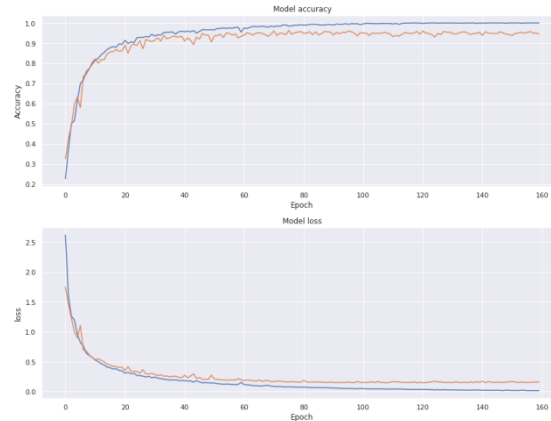
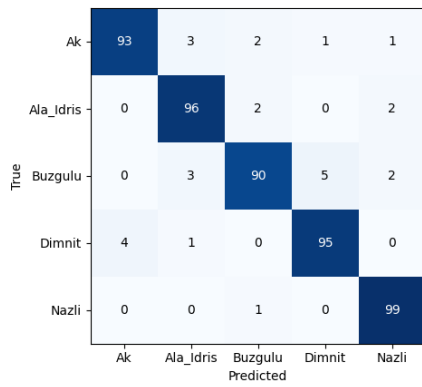


**Figure 11. VGG19 160 Epoch**

The VGG19 architecture is the 2nd most successful architecture in this study with a success rate of 95%. The Nazli class achieved the highest accuracy value with a success rate of 99%.

Table 5 shows the results of the tests with all architectures and data sets.

**Table 5. Performance Metrics**

Architecture	Dataset	Epoch	Precision	Recall	F1 Score	Accuracy
<b>DenseNet</b>	70-30	80	0,6940	0,7580	0,6500	0,6920
		160	0,6720	0,7640	0,6180	0,6720
	80-20	80	0,6040	0,7200	0,5680	0,6044
		160	0,7860	0,8280	0,7860	0,7860
<b>MobileNet</b>	70-30	80	0,8800	0,8820	0,8800	0,8813
		160	0,9040	0,9060	0,9060	0,9053
	80-20	80	0,8900	0,8900	0,8880	0,8900
		160	0,9140	0,9140	0,9140	0,9140
ResNet50	70-30	80	0,9540	0,9580	0,9540	0,9547
		160	0,9660	0,9640	0,9640	<b>0,9640</b>
	80-20	80	0,9520	0,9540	0,9520	0,9520
		160	0,9660	0,9660	0,9660	<b>0,9660</b>
<b>VGG19</b>	70-30	80	0,9180	0,9220	0,9160	0,9173
		160	0,9340	0,9340	0,9320	0,9347
	80-20	80	0,9500	0,9520	0,9500	0,9500
		160	0,9460	0,9460	0,9460	0,9460

In the results of the study, the lowest success rate belongs to DenseNet, while ResNet50 is the most successful classification architecture in the study with a success rate of 0.9640. When we look at the studies conducted with different epochs in the same dataset, it is observed that as the epoch increases, the success rate increases in MobileNet, ResNet50 in both split datasets. On the other hand, in the VGG19 architecture, it is observed that the success rate decreases when the number of epochs increases in the dataset divided into 80% training and 20% test.

Accordingly, the most successful result among the 4 different architectures is given by the Resnet50 architecture, which achieves a 96.60% success rate with 160 epochs, divided into 80% training - 20% testing.

When the study is compared with other studies in the literature, the data augmentation method is frequently used as in the study. According to the research, the same and similar methods are used with the data augmentation methods in other studies. One of the common features of the study with the dataset [20] and the current study is that the DA method uses methods such as scaling translation and rotation, while the current study uses rotation, brightness, zoom horizontal methods. In addition, different deep learning architectures were applied at different epoch rates in this study. While Köklü et al. achieved 97.60% success with SVM cubic [20], the current study achieves 96.60% success with ResNet50. As a result of the study, the training and test results of the dataset separated as 80% training and 20% test give higher results in general. While Nader et al. achieved 99% success using VGG19 in the classification of grapevine leaf diseases, maximum 95% success was achieved in this study. While training with 10 epochs, the accuracy values increased rapidly in the 2nd epoch. When we look at the classification reports on a class basis, half of them show that they are one hundred percent correct. While keeping the number of epochs of these values low, the classes gave such high success. In another study [23], VGG16 gives the most successful result 97.34%. In another study, 97.5% success is achieved with VGG19 [17], while in another study, 87% success is achieved using VGG16 [18]. In this study, the highest accuracy value of 95% was achieved with the VGG-19 algorithm. When the studies were analyzed, it was seen that data augmentation methods and the number of epochs affect the accuracy values.

## 5. CONCLUSIONS

This study aims to evaluate the performance of different deep learning architectures for grapevine leaf classification after data augmentation methods. ResNet50, MobilNet, DenseNet and VGG19 were trained for 160 and 80 epochs each. The dataset was split in two different ways: 70% training - 30% testing and 80% training - 20% testing. Each architecture was trained and tested separately for each partition. The results were evaluated based on metrics such as accuracy, precision, recall and F1 score. The results show that all architectures show high performance in the classification of vine leaves. The highest accuracy was achieved using the ResNet50 architecture for 160 epochs on a dataset divided into 80% training and 20% testing.

These results show that deep learning architectures can be successfully used to classify vine leaf types. However, future studies aim to test the results with larger datasets and more deep learning architectures to improve the accuracy.

This study shows that deep learning methods can be successfully used for grapevine leaf classification and can provide a basis for future studies.



## 6. REFERENCES

1. Shickel, B., Tighe, P. J., Bihorac, A., & Rashidi, P. (2017). Deep EHR: a survey of recent advances in deep learning techniques for electronic health record (EHR) analysis. *IEEE journal of biomedical and health informatics*, 22(5), 1589-1604.
2. Fischer, T., Krauss, C., & Trepte, T. (2018). Deep learning with long short-term memory neural networks for financial market predictions. *European Journal of Operational Research*, 270(2), 654-669. doi: 10.1016/j.ejor.2017.12.047.
3. Yang, L., Li, Y., Wang, J., & Sherratt, R. S. (2020). Sentiment analysis for E-commerce product reviews in Chinese based on sentiment lexicon and deep learning. *IEEE access*, 8, 23522-23530.
4. Qiu, R., Wu, Y., Li, L., Li, X., & Wang, X. (2019). Intelligent fault diagnosis method for electric power steering system based on machine learning. *Measurement*, 138, 425-433.
5. Gandomi, A., & Haider, M. (2015). Beyond the hype: Big data concepts, methods, and analytics. *International journal of information management*, 35(2), 137-144.
6. Liu, J., Li, B., Li, L., Li, J., Wang, C., Wang, X., & Shi, X. (2020). Identification of grape varieties based on deep learning with residual neural network. *Food Science & Nutrition*, 8(6), 2926-2935.
7. Krizhevsky, A., Sutskever, I., & Hinton, G. E. (2012). ImageNet classification with deep convolutional neural networks. *Advances in neural information processing systems*, 25, 1097-1105.
8. Krizhevsky, A., Sutskever, I., & Hinton, G. E. (2017). Imagenet classification with deep convolutional neural networks. *Communications of the ACM*, 60(6), 84-90.
9. Devlin, J., Chang, M. W., Lee, K., & Toutanova, K. (2018). Bert: Pre-training of deep bidirectional transformers for language understanding. *arXiv preprint arXiv:1810.04805*.
10. Hinton, G., Deng, L., Yu, D., Dahl, G. E., Mohamed, A. R., Jaitly, N., ... & Kingsbury, B. (2012). Deep neural networks for acoustic modeling in speech recognition: The shared views of four research groups. *IEEE Signal processing magazine*, 29(6), 82-97.
11. Mnih, V., Kavukcuoglu, K., Silver, D., Rusu, A. A., Veness, J., Bellemare, M. G., ... & Hassabis, D. (2015). Human-level control through deep reinforcement learning. *nature*, 518(7540), 529-533.
12. Schmidhuber, J. (2015). Deep learning in neural networks: An overview. *Neural networks*, 61, 85-117.
13. He, Y., Huang, J., Xie, J., & Wang, Z. (2021). Deep learning in food industry: a review. *Journal of Food Science and Technology*, 58(3), 822-834. doi: 10.1007/s13197-020-04569-4
14. Akkas, M. E., Yavuz, M. E., & Temurtas, F. (2019). Food quality control by image processing and machine learning techniques: A review. *Computers and Electronics in Agriculture*, 161, 272-282. doi: 10.1016/j.compag.2019.03.005
15. Wang, Y., Li, Z., Li, H., Li, H., Li, L., & Li, K. (2019). Application of deep learning in food safety: A review. *Trends in Food Science and Technology*, 91, 499-510. doi: 10.1016/j.tifs.2019.07.016

16. Nader, A., Khafagy, M. H., & Hussien, S. A. (2022). Grape Leaves Diseases Classification using Ensemble Learning and Transfer Learning. *International Journal of Advanced Computer Science and Applications*, 13(7).
17. Nagi, R., & Tripathy, S. S. (2021, December). Grapevine Leaf Disease Identification Using Transfer Learning. In 2021 IEEE International Women in Engineering (WIE) Conference on Electrical and Computer Engineering (WIECON-ECE) (pp. 43-46). IEEE.
18. Balawi, A., Al Zoabi, A., Junior, J. L. S., & Horváth, T. (2020). Classification of a Small Imbalanced Dataset of Vine Leaves Images using Deep Learning Techniques. In *ITAT* (pp. 108-114).
19. Liu, Y., Su, J., Xu, G., Fang, Y., Liu, F., & Su, B. (2020). Identification of grapevine (*Vitis vinifera* L.) cultivars by vine leaf image via deep learning and mobile devices.
20. Koklu, M., Unlersen, M. F., Ozkan, I. A., Aslan, M. F., & Sabanci, K. (2022). A CNN-SVM study based on selected deep features for grapevine leaves classification. *Measurement*, 188, 110425
21. Alessandrini, M., Rivera, R. C. F., Falaschetti, L., Pau, D., Tomaselli, V., & Turchetti, C. (2021). A grapevine leaves dataset for early detection and classification of esca disease in vineyards through machine learning. *Data in Brief*, 35, 106809.
22. Hasan, M. Z., Zeba, N., Malek, M. A., & Reya, S. S. (2021, January). A leaf disease classification model in betel vine using machine learning techniques. In 2021 2nd International Conference on Robotics, Electrical and Signal Processing Techniques (ICREST) (pp. 362-366). IEEE.
23. Automated Grapevine Cultivar Identification via Leaf Imaging and Deep Convolutional Neural Networks: A Proof-of-Concept Study Employing Primary Iranian Varieties
24. Kukreja, V., Sharma, R., Kaur, A., Sachdeva, R. K., & Solanki, V. (2022, April). Deep Neural Network for Multi-Classification of Parsley Leaf Spot Disease Detection. In 2022 2nd International Conference on Advance Computing and Innovative Technologies in Engineering (ICACITE) (pp. 1378-1382). IEEE.
25. Rajiv, K., Rajasekhar, N., Prasanna Lakshmi, K., Srinivasa Rao, D., & Sabitha Reddy, P. (2021, May). Accuracy evaluation of plant leaf disease detection and classification using GLCM and multiclass SVM classifier. In *Intelligent Learning for Computer Vision: Proceedings of Congress on Intelligent Systems 2020* (pp. 41-54). Singapore: Springer Singapore.
26. Savin, B. C., & Hnatiuc, M. (2021, November). Methods of Health Improving Using Leaf Image Processing. In 2021 International Conference on e-Health and Bioengineering (EHB) (pp. 1-4). IEEE.
27. Liu, Y., Su, J., Xu, G., Fang, Y., Liu, F., & Su, B. (2020). Identification of grapevine (*Vitis vinifera* L.) cultivars by vine leaf image via deep learning and mobile devices.
28. Alkan, A., Abdullah, M. U., Abdullah, H. O., Assaf, M., & Zhou, H. (2021). A smart agricultural application: automated detection of diseases in vine leaves using hybrid deep learning. *Turkish Journal of Agriculture and Forestry*, 45(6), 717-729.
29. LeCun, Y., Bengio, Y., & Hinton, G. (2015). Deep learning. *nature*, 521(7553), 436-444.
30. Goodfellow, I., Bengio, Y., & Courville, A. (2016). Deep learning (pp. 181-186). MIT press.

31. [https://en.wikipedia.org/wiki/Transfer\\_learning](https://en.wikipedia.org/wiki/Transfer_learning)
32. Pan, S. J., & Yang, Q. (2010). A survey on transfer learning. *IEEE Transactions on knowledge and data engineering*, 22(10), 1345-1359.
33. Kingma, D. P., & Ba, J. (2014). Adam: A method for stochastic optimization. *arXiv preprint arXiv:1412.6980*.
34. Huang, G., Liu, Z., van der Maaten, L., & Weinberger, K.Q. (2018). "Densely Connected Convolutional Networks." Proceedings of the IEEE Conference on Computer Vision and Pattern Recognition (CVPR), 4700-4708.
35. Howard, A.G., Zhu, M., Chen, B., Kalenichenko, D., Wang, W., Weyand, T., Andreetto, M., & Adam, H. (2017). "MobileNets: Efficient Convolutional Neural Networks for Mobile Vision Applications." arXiv preprint arXiv:1704.04861
36. He, K., Zhang, X., Ren, S., & Sun, J. (2015). Deep Residual Learning for Image Recognition. Proceedings of the IEEE Conference on Computer Vision and Pattern Recognition, 770-778. DOI: 10.1109/CVPR.2016.90
37. Simonyan, K., & Zisserman, A. (2014). Very Deep Convolutional Networks for Large-Scale Image Recognition. arXiv preprint arXiv:1409.1556.

## Geometry and Fractals

Süheyla Elmas

Ataturk University Faculty of Education ,Erzurum/Turkey

suheylaelmas@atauni.edu.tr

### Abstract

This study is on Fractal, and it is a compilation and update of some of all the studies. Our second aim is to examine the studies of Prof.Dr.Hilmi Hacısalihoğlu on Fractals.

### Key Words

Geometry, Fractals

### Introduction

The first mathematical concept of fractal was discovered in 1861. Karl Weierstrass, while investigating the changes on a curve that is continuous but not differentiable at any point, that is, consisting of corner points, was shaken by the opinion that no rate of change could be found at any point. Weierstrass used the word fractal for the first time for this kind of curves.

The first fractal studied in terms of mathematics is the Cantor Clause. Cantor (1845-1918) was a German mathematician who, while at the University of Halle, founded one of the fundamental subjects of mathematics and what is now called Sentence Theory. The first work on the Cantor sentence was published in 1883 [G. Cantor, Über Unendliche, lineare punktmannigfaltigkeiten V, Mathematische Annalen 21 (1883) 545-591] and some specific sentences are cited as examples. The Cantor sentence is an example of a perfect subordinate clause that is nowhere condensed. In the historical development of fractals, fractals created by mathematicians such as Cantor, Sierpinski, Von Koch, Peano are called mathematical monsters. In the garden of mathematical monsters or when the first fractals appear, the Cantor sentence is quite important, although less ostentatious in appearance and more naturalistic interpretation than the others. It is seen that Cantor's sentence plays an important role in many areas of mathematics, especially in Chaotic Dynamical Systems, and is a necessary model for many fractals (like Julia sentences).

We see bright, strange, beautifully shaped objects around us. These are called fractals. What are these really? There is a lot of information about fractals on the Internet, but most of this information is about either beautiful illustrations or high-level mathematical concepts. Therefore, we can say with an easily understandable expression that fractals are objects with strange pictures, mathematical objects. Most of the math we encounter in school is outdated knowledge. For example, the circles, quadrilaterals and triangles we encounter in geometry date back to BC. It was introduced by Euclid in the 300th BC. However, Fractal Geometry is rather new. Research on fractals by mathematicians has begun in the last 25 years.(7)

Fractals, the word created by Benoit Mandelbrot from the Latin word fractus means broken or uneven. The term fractal itself means a geometrical or physical structure that has an irregular and fragmented shape. Throughout history, philosophers, mathematicians, and physicists have tried to observe and explain these reoccurring patterns in nature. As a result, the definition for Fractals has been simplified and developed over the years, starting with Gottfried Leibniz in the 17<sup>th</sup> Century to Mandelbrot in the 1970s. This research will involve how fractals are defined, the history of fractals, different types of fractals, famous equation for fractals and applications in nature, life, and science research.

## **1.What is Fractal**

Fractals can be known as art, but it is a special kind of art. When observed, the image of a fractal displays self-similarity on all scales. It doesn't have to exhibit exactly the same structure at all scales but the same type of structures should appear on all scales.

All fractals can be defined by characteristics. These characteristics determine if it is a fractal or not. One, a fractal must be made on an iterative process which means to repeat again and again. Two, a fractal has to be infinitely complex, meaning it must have a set of values that have no bound. When magnified, it shows signs of self-similarity therefore proving it goes on infinitely. Three, the subsets of a fractal should be similar to the original quantity or figure. Four, the dimension of a fractal is typically a non-integer and hence, non-integer complexity. This means its dimensions are usually not defined by regular numbers such as ....-3,-2, -1, 0, 1, 2,3,.. and so forth. Five, a fractal is too

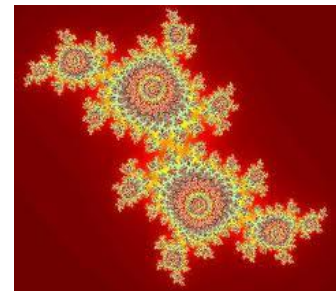
irregular to be proven by Euclidean geometric language. Finally, it has a simple and recursive definition, meaning it is characterized by recurrence or repetition. These characteristics define a fractal.

## 2. The Root and Phases of the Fractal

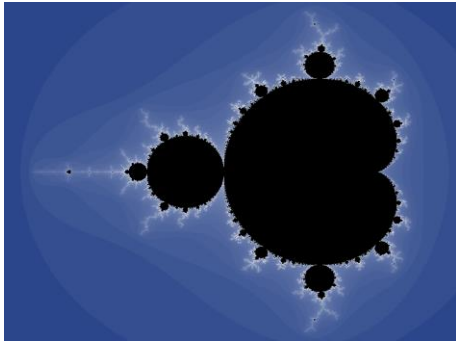
The history of fractals took many twists and turns in its progress of becoming what it is today. It grew with each individual mathematician. Leibniz did in fact research this new concept of recursive self-similarity, although he was very mistaken that a straight line was self-similar. This idea was further taken by Karl Weierstrass in 1872. He gave an example of a function such as  $f(x) = E \cdot a^n \cdot \cos(b^n \cdot \pi \cdot x)$  which could be everywhere and continuous on a graph but it is not capable of obtaining the derivative or original value, meaning that the value of  $x$  changes after the function repeats itself.

In 1904, Helga von Koch elaborated Weierstrass's abstract and analytical definition, thereof making his geometric definition of a function similar to Weierstrass's original function. His function was later called the Koch snowflake. In 1915, Waclaw Sierpinski followed the ideas of Koch and created his Triangle and Carpet. Later both designs were named after him. Paul Pierre Levy in 1938 created "space curves and surfaces consisting of parts similar to the whole" which revealed a whole different kind of fractal curve. He called it the Levy C curve.

In the late 19th Century and early 20th century, Gaston Julia studied iterated functions in the complex plane and created the Julia Sets. The set, with the equation of  $Z_{n+1} = Z^2 + c$ , defined any value that would be plugged into the equation. He set up the knowledge of modern-day fractals and created a function that revealed beautiful pictures. However, he could only visualize because they didn't have the aid of computers. The picture shown is a one of the many Julia Sets.



In the 1960s, A Yale University Professor named Benoit Mandlebrot investigated in the fields of mathematical properties that showed self-similarities too. His famous papers include "How Long Is the Coast of Britain?", and "Statistical Self-Similarity and Fractional Dimension". In 1975, Mandlebrot created the word "fractal" to describe



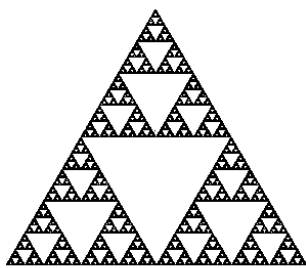
mathematical dimensions that show self-similarity in a recursion. He is also credited for discovering fractals because he clearly defined the properties and meaning of these iterating self-similar figures. The Mandlebrot Set was also named after him. The Mandlebrot Set is in fact very similar to the Julia

Sets but more simplified. The equation is  $Z=Z_{n+1}+c$ . It looks very similar to the Julia Set formula but really, it's a lot of Julia Sets combined to create the Mandlebrot Set. The picture of the Mandlebrot Set shown is the combination of a Julia Set on every point.

### 3. Some types of fractals

Sierpinski Triangle (see picture to the left), the Koch Snowflake, etc. Three, there are the Random Fractals. They are generated randomly rather than being deterministic.

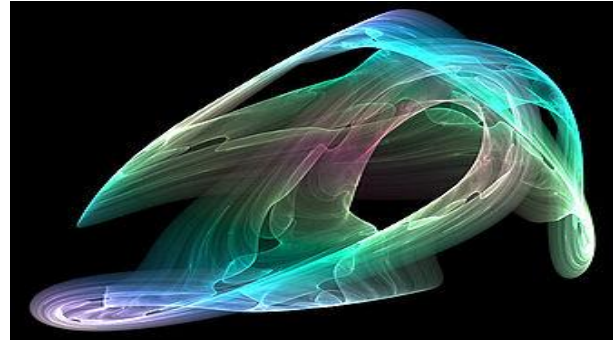
Examples of Random Fractals include the Brownian Tree, Fractal Landscapes, and Brownian Motion. Four, some fractals can be classified by the name of strange attractors (see picture bottom right). They are generated by an iteration of a map or solution of a system of initial different values that exhibit chaos. There are no famous fractals of this kind but technology today can create one. Lastly, there is L system fractals (see picture bottom left). They are generated by string rewiring and they are designed to model the branching model of plants. These are different types and layouts of the fractals. They can also be classified according to how self-similar the fractal is. They can show Exact Self-Similarity. This is the strongest type of self-similarity. For example, the Koch Snowflake and the Sierpinski Triangle show strong self-similarity. Other fractals can



classified this way.

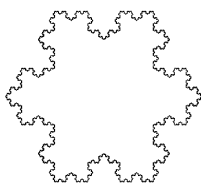
show Quasi Self-Similarity. It is a looser form of self-similarity. The recurrence show partly similarity but distorted in a way. For example, the Mandlebrot Set is Quasi Self-Similar: as the fractal is zoomed in, the tip is shifted to another direction. Lastly, there is Statistical Self-Similarity. It is the weakest type of self-similarity. Random fractals can be





## 4. Mathematical Approach to Important Fractals

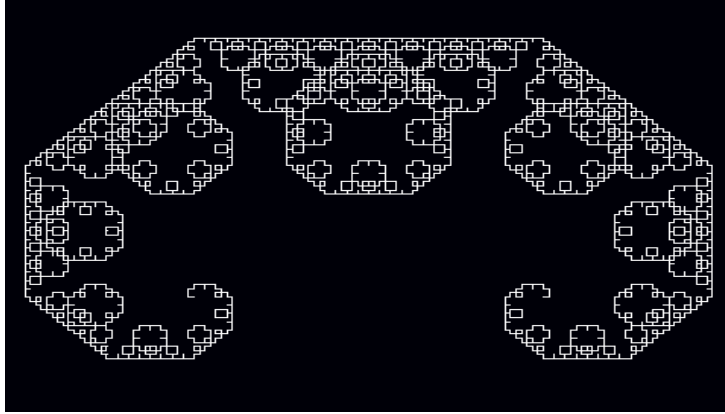
### 4.1. Helge von Koch's Fractals



Although fractals may be classified using pictures and diagrams, there are equations that help us learn what fractals are like mathematically.

Before fractals could become even more advanced and continue to be mapped on a complex plane, fractals had a definite geometric equation to solve it. However, all were recursive. For example, the Koch Snowflake has several formulas defining how it is created. To determine how many sides there are in the Koch Snowflake, you would use the equation  $n = 3 \cdot 4^a$ , of which " $n$ " is the number of sides and " $a$ " is the iteration as it goes to infinity. To find the length of a side, you would have to use the equation  $l = x \cdot 3^{-a}$ . " $x$ " is the original side length as " $a$ " would be the iteration used. To find the perimeter of the Koch Snowflake, you would use the equation  $p = (3a) \cdot (4/3)^a$ . The perimeter equation consists of both the equations of the number of sides and the length of the sides just multiplied. The perimeter increases  $(4/3)$  times each iteration and " $a$ " is again the number of iterations. The perimeter of the Koch Snowflake does go to infinity as the number of iterations reaches infinity. Many fractals that follow also become like the Koch snowflake and that the equation represents self-similarity since it is an iterated function system. Other fractals were very similar to the Koch Snowflake such as the Sierpinski Triangle.

**4.2. The Curves** Self-Similarity evolved again and Paul Levy created his own Levy C Curve. It was just another form of iteration where two separate points started to divide and go into  $45^\circ$  and  $-45^\circ$  angles.



### 4.3.The Julia Sets

It was not until the days of Gaston Julia that more complex and chaotic fractals began to take form. Gaston Julia created the beginning of the chaotic fractals. His function  $Z_{n+1}=Z^2+c$ , this function was composed of that "c" was a constant or a complex number and "Z" was the iterated number and "n+1" resembles recursive iteration. "c" is either a constant or it can be a complex number which is the sum of a real number and an imaginary number. Therefore, this fractal has a non-integer dimension and must be graphed on a complex plane. This equation is also highly sensitive to different complex numbers, which shows signs of chaotic functions. Because of these chaotic functions, many different Julia Sets can either escape to infinity or remain bounded on the complex plane. They have names. Connected Julia Sets are the iteration of a function that is always bounded and it stays in its original area. Thus, points in the bounded sets never escape to infinity. Disconnected Julia Sets are the iteration of a function but they have no space to rely on to remain within its domain and therefore, the points of the disconnected sets escape to infinity and are far apart from each other to remain near the origin.

Examples:

Connected Julia Set:  $Z_{n+1}=Z^2+c$  We first create an equation.

$Z_0=Z^2+0.25$  We now just input 0 for the value of Z.

$Z_0=0^2+0.25$  Thus, continuing with the equation...

$Z_0=0$  Then we iterate the equation.

$Z_1=(0)^2+0$  Solve it again...

$Z_1=0$  Then iterate it again...

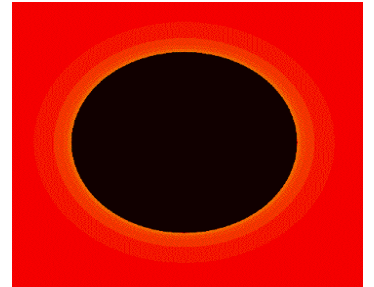
$Z_2=(0)^2+0$  Notice that "c" is always constant...

Also, notice how the constant is zero, on purpose; it is this way so it is easier to see the process and how the process works.

$$\begin{array}{ll} Z_2=0 & \text{And if the process continues...} \\ Z_3=0 & \text{.....} \\ Z_4=0 & \text{...} \\ Z_{18}=0 & \end{array}$$

The iterated number does not run off to infinity, it actually just remains bounded at the origin of the Julia Set. Since the value doesn't run off to infinity, this function is a connected Julia Set.

This function, as shown on the right, is the most basic function of all Julia Sets. The circle has its origin of the coordinate plane in the center of the circle. The circle has bounded values that gather toward the origin. This makes it a connected Julia Set.



Disconnected Julia Set :  $Z_{n+1}=Z^2+c$

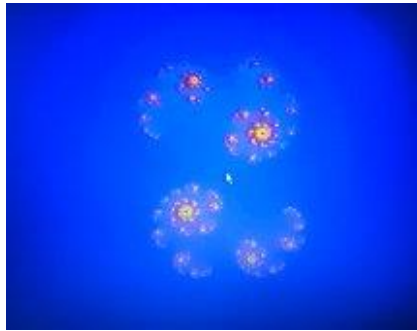
$$Z_{n+1}=Z^2+(0.4+0.1i) \quad \begin{array}{l} \text{This time our constant number} \\ \text{will be a complex number} \end{array}$$

A complex number is a combination of a real number and an imaginary number. The two values can never be combined so they are calculated separately, as shown below. This also means it must be graphed on a complex plane where the y-axis has values of imaginary number than regular real numbers.

$$\begin{array}{ll} Z_0=0^2+(0.4+0.1i) & \text{Again, replacing with zero...} \\ Z_0=0.4+0.1i & \text{That's our answer, and now we iterate.} \\ Z_1=(0.4+0.1i)^2+(0.4+0.1i) & \text{And now solve...} \\ Z_1=0.55+0.18i & \text{And we repeat this process...} \\ Z_2=0.67+0.30i & \text{...} \\ Z_3=0.76+0.50i & \text{...} \\ Z_4=0.72+0.86i & \text{It is turning around chaotically...} \\ Z_5=0.19+1.35i & \text{The distance is opened in wide gaps...} \\ Z_6=-1.39+0.62i & \text{Sharply declines into the negatives...} \\ Z_7=-36.14-19.38i & \text{The value grows very into infinity...} \end{array}$$

In summary, this equation indicates the set of values never come together to form an area to stay close to the origin of the point on the complex plane. The iterated number became "chaotic" and wildly runs into infinity. Therefore, this equation makes a disconnected Julia Set.

This set is disconnected. Look at the image on the right. The origin of this image is the



white dot in the center of a complex plane. There is no set of values that come together to form a bounded region. It's very spread out and the values go wildly into infinity.

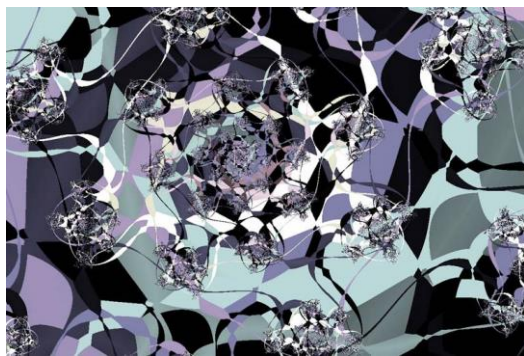
## 4.2. The Mandelbrot Set

Many years later, Benoit Mandelbrot studied this particular set and in fact simplified it to create his own set called the Mandelbrot set. This set, also with the equation  $Z_{n+1} = Z^2 + c$ , is that the value of "c" make up the Mandelbrot Set and it has to have 0 under its iteration. It's either that a complex number is in or out of the Mandelbrot Set. This set is never attracted to infinity and stays within its bounds. He thought up the idea that using zero as the base during an iteration of a function. Using a computer for a trial and error basis, he could plot dots on the complex plane that can represent the stable areas of which iterated functions can be. This shows the absolute border between finite and infinite as to determine where something is. Stating if to use a Julia Set function and to find out whether it is in or out of the Mandelbrot Set, it would have to start out as zero. Every part of the Mandelbrot Set is a different Julia Set, even the plain circle can be considered a fractal since it can be defined as a Julia Set. That is how one can determine if a Julia Set is connected or disconnected. Either a Julia Set is part of the Mandelbrot Set, or it isn't. The Mandelbrot Set and the Julia set both have infinite-zoom capability which means if a person were to zoom into the Mandelbrot Set, self-similarity appears and it goes on forever and ever.

## 5. Fractals in Nature

Digital Fractals can be a beautiful thing; however, there are fractals in life that we never realize that they exist. They're even right in your back yard, such as the simple leaf which branches out in two directions. The ferns show many signs of self-similarity. Other examples you can find in nature include river networks, fault lines, mountain ranges, craters, snowflakes, clouds, crystals, systems of blood vessels, ocean waves, DNA, and maybe even coastlines. However, unlike regular mathematical based fractals, these are classified as random fractals and show self-similarity of a large range in a finite area.

### Applications



People use fractals. They might be applying it to real life without even knowing it. For example, people can use fractals to create art like the famous American artist Jackson Pollock. His chaotic paintings have been identified as fractals. Composers use the concept of self-similarity in their creations.

For example, Johann Sebastian Bach tended to repeat melodies in his music over and over again. Although he might not make it exactly the same, it shows self-similarities in many ways. Applications can also be found in seismology. The different waves of earthquakes can represent fractals. Biologists may perhaps use fractals to help them recreate life's patterns and predict what would really happen. Meteorologists apply fractals and Chaos Theory to aid them in their studies of the weather forecast. Perhaps one of the greatest uses of fractals is in computer graphics and video game design. As mentioned earlier, ferns are very much like a fractal, therefore, computers can create digital images of ferns or leaves, mountains, hills, trees, and etc. The way fractals do these jobs is that it takes a simple picture and iterates it in different ways to create a landscape, whether it is a mountain or just a plain. Fractals can also help with digitally making graphics of dinosaur skin. Dinosaurs in the movies have very rough skin, and many creases in their skin are very much like leather. That's why they look so realistic because fractals go infinitely into detail.

In conclusion, fractals, a region of mathematics is highly useful and sensitive to little conditions, as Chaos Theory defines it. It is very important in the way we look at things in life. We can predict patterns in weather, seismology, and biological and organic life. Although we may not consider it every day, fractals are everywhere. It will continue appearing and applying to more things we do today than before.

## References

1. "2. Natural Fractals and Dimensions." Yale University. N.p., n.d. Web. 22 Nov. 2011. <classes.yale.edu/fractals/>
2. Boast, Steve. "The Characteristics of a Fractal." Wichita. N.p., n.d. Web. 22 Nov. 2011. <webs.wichita.edu/facsme/cbl/geometry/tcoaf.pdf>.
3. "Patterns of Visual Math - Fractals in Nature." welcome to MIQEL.com - Your Favorite Source of Random Information. N.p., n.d. Web. 22 Nov. 2011. <http://www.miqel.com/fractals\_math\_patterns/visual-math-natural-fractals.html.>
4. Trochet, Holly . "Fractal Geometry." MacTutor History of Mathematics. N.p., n.d. Web. 22 Nov. 2011. <http://www-history.mcs.st-andrews.ac.uk/HistTopics/fractals.html>.
5. Weisstein, Eric. "Fractal -- from Wolfram MathWorld." Wolfram MathWorld: The Web's Most Extensive Mathematics Resource. N.p., n.d. Web. 22 Nov. 2011. <http://www.mathworld.wolfram.com/Fractal.html>.
6. "Who Discovered Fractals?." Who Discovered It. N.p., n.d. Web. 22 Nov. 2011. <http://www.whodiscoveredit.com/who-discovered-fractals.html>.
- 7.H.Hacısalıhoğlu, Nobel Ölçü, Topoloji ve Fraktal Geometri ,Ankara

# NOVEL GOODNESS FUNCTIONS FOR FORWARD-FORWARD ALGORITHM

Halil EROĞLU<sup>1</sup>, Fikriye ATAMAN<sup>2\*</sup>

gelecekandroidde@gmail.com , fataman@yyu.edu.tr

(orcid: 0009-0008-8576-2771, 0000-0002-0257-7730)

<sup>1</sup>Artificial Intelligence and Robotics, Van Yüzüncü Yıl University, Van, Turkey.

<sup>2</sup> Department of Computer Engineering, Van Yüzüncü Yıl University, Van, Turkey.

## Abstract

Advances in Deep Learning Algorithms over the years have greatly changed our view of what Artificial Intelligence can do. So much so that with a new development every day, our amazement and admiration for Artificial Intelligence increases. Undoubtedly, back propagation algorithm is behind this great success. Well, "does the back propagation power of artificial intelligence, which was developed with inspiration from human intelligence, have a counterpart in human intelligence?" Is it really "does our brain back-propagate?" In this study, we explained the forward-forward algorithm, which was developed as an alternative to the back propagation algorithm, inspired by the working principle of our brain. We rearranged the goodness function in the forward-forward algorithm, tested it on the MNIST(Modified National Institute of Standards and Technology database) dataset, and compared it with the back propagation algorithm.

**Keywords:** Brain learning, Forward-forward algorithm, Goodness functions, Negative data

## 1. INTRODUCTION

Deep learning is the ability to learn representations in large data sets using computer models consisting of multiple processing layers (Lecun et al., 2015). These models transfer representations between layers using the backpropagation algorithm and thus discover complex structures (Lecun et al., 2015). It is a machine learning method that is used especially for processing complex data types such as image, sound, text and provides high performance in many application areas. The Backpropagation (BP) algorithm (Werbos, 1981; Hinton, 2022), which is the driving force behind deep learning, has long been criticized for its suitability for the functioning of our brain. (Crick, 1989; Grossberg, 1987; Lillicrap et al., 2020; Marblestone et al., 2016; Pozzi et al., 2020) The amazing power and success of backpropagation has taken deep learning, artificial intelligence and its sub-fields to serious levels. But "does our brain really update the connections between neurons by backpropagation?" This question has long attracted the attention of researchers (Lillicrap et al., 2020; Pozzi et al., 2020; Song et al., 2020;



Bellec et al., 2019; Kohan et al., 2018; Xie et al., 2003; Mazzonit et al., 1991; Song et al., 2022). There are serious challenges to how backpropagation can be accomplished in the brain.

Cortex feed-forward is a process that occurs during the forward process of information processing in the brain, that is, from input to output (Rockland, 2022). The cortex in the brain processes neural inputs from many different regions, creating the final output. Cortex feed-forward allows these inputs to be processed in the cortex and converted into output.

Cortex feed-forward occurs through a neural network formed by the combination of many different nerve cells (neurons). This neural network carries information in a specific direction (forward) and influences neural activity in the cortex (Kohan et al., 2018; Kreiman & Serre, 2020; Ravichandran, 2022; Rockland, 2022). Feedforward is the process by which inputs from sensory organs or other brain regions are transmitted to different cortex regions within the brain via nerve cells on the cortex surface (Rockland, 2022).

For example, the visual cortex is responsible for processing visual information from the eyes. Information from the eyes is processed by nerve cells in the posterior part of the visual cortex and then fed forward to the anterior cortex, where the previously processed information is. In this way, cortex feed-forward helps to perform more complex operations in higher-level cortex regions and eventually generate more sophisticated outputs (Kreiman & Serre, 2020; Rockland, 2022).

Cortex feed-forward is a process that underlies brain functions and plays an important role in performing complex cognitive functions such as learning, memory and decision making.

There is no convincing evidence that the brain clearly transmits error derivatives between real neurons or stores neural activities for backpropagation (Lillicrap et al., 2020). In particular, there are both practical and biophysical problems. Some of these problems are;

1. In backpropagation, neural activities are stored to update synaptic connections (Hinton, 1986).
2. The error calculated at the end of the neural network is propagated backwards through the entire network via a global feedback to learn the synaptic weights (Hinton, 1986).
3. This backpropagation is done backwards again, starting from the end of the path used to forward the information (Hinton, 1986).
4. In this case, inference and learning are largely sequential. First the inference is made, the error is calculated, and then the learning takes place. That is, these things do not happen in parallel (Hinton, 1986).

### **1.1. Why is Backpropagation Wrong?**

As described above, the reason deep learning is so powerful lies in the back propagation algorithm. Gradients are usually calculated using back propagation (Hinton, 1986). An

important question asked is: “Can the synaptic updates that our brain generates for learning be done in deep learning networks other than back propagation?” This question is often asked by researchers, and an alternative solution to backpropagation is being explored (Lillicrap et al., 2020; Guerguiev et al., 2017). Despite the success of backpropagation, the backpropagation algorithm remains illogical in terms of the learning process in our brain. Many studies, researches and tests have been conducted to fill this gap (Lillicrap et al., 2020; Scellier & Bengio, 2017; Richards & Lillicrap, 2019; Guerguiev et al., 2017).

Backpropagation has four basic problems:

1) While back propagation takes place, consider the same weights used in the forward pass to calculate the gradient. It is biologically impossible for the network to remember the weights used in the forward pass for the backward pass. This problem is called "weight symmetry problem" or "weight bearing problem" (Hinton, 2022).

2) During error backpropagation, neurons do not freeze neural activities while calculating their activity status. Instead, cortical feedback connections have been proven to influence the neural activity produced during the forward transition (Hinton, 2022).

3) Updating a certain weight in the neural network depends on the calculations of the neurons in the lower layers. The resulting error is transmitted back through the layers of the network, and neurons in each layer use this error to update their weights. Therefore, updating the weights depends on the calculated errors during the backward pass and plays a critical role in the learning process. But biological synapses change their strength according to local signals, that is, only to their neighboring neurons. It does not wait for the entire network to be exhausted for the weight update (Hinton, 2022).

4) In the neural network, in order to update the weights of a layer, it is necessary to complete the forward pass and wait for the backward pass to reach the relevant layer. However, the brain has the ability to process external stimuli online (Hinton, 2022).

## **2. GENERAL PROPERTIES OF METHOD**

### **2.1. Forward-Forward Algorithm**

The forward-forward algorithm is an algorithm developed by Geoffrey Hinton as an alternative to back propagation (Hinton, 2022). The back propagation algorithm described above was proposed to seek solutions to the biologically unrealistic problems (Hinton, 2022). The algorithm is expressed as: “A more promising future for artificial intelligence than current paradigms” (Hinton, 2022).

The forward-forward algorithm changes backpropagation forward-backward transitions to forward-forward. The two forward-passes have different purposes and different data sets. So two forward passes work on different data for different purposes. Their aims are opposite. In fact, the forward-forward algorithm is a kind of unsupervised learning algorithm. For example, if an image is given to the network, the goal of the forward-forward algorithm would be to

learn a useful representation of that image. The purpose of learning in the forward forward algorithm is to keep the goodness value well above the threshold for real data (positive data) and well below the threshold for negative data.

There are 3 key definitions in the forward forward algorithm:

**Goodness:** This value is very important for the learning process. The original goodness function equation explained by Hinton (Hinton, 2022) and the different favor functions proposed and implemented in this study are given below. The goodness function value to be calculated on a layer basis will be the effective value on how to make the necessary updates for the network to learn. It can be compared to the total error value in backpropagation.

**Positive Data:** It refers to the actual data that the network is trying to find patterns that it needs to learn. This dataset is the real dataset for us.

**Negative Data:** This data is fake data. In fact, it is an important issue to be studied in the forward-forward algorithm. The preparation of fake data forms the basis of some of our future studies.

The goodness function works on these two data for different purposes. It tries to increase its value on positive data and decrease its value on negative data. Figure 1 and Figure 2 below show the back propagation algorithm and the forward-forward algorithm, respectively.

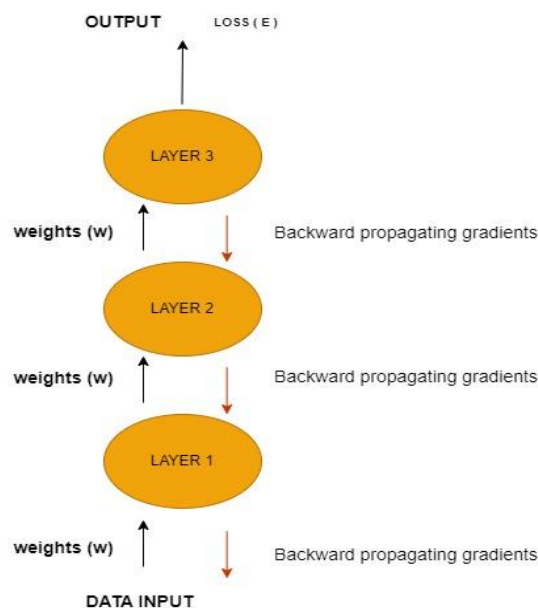
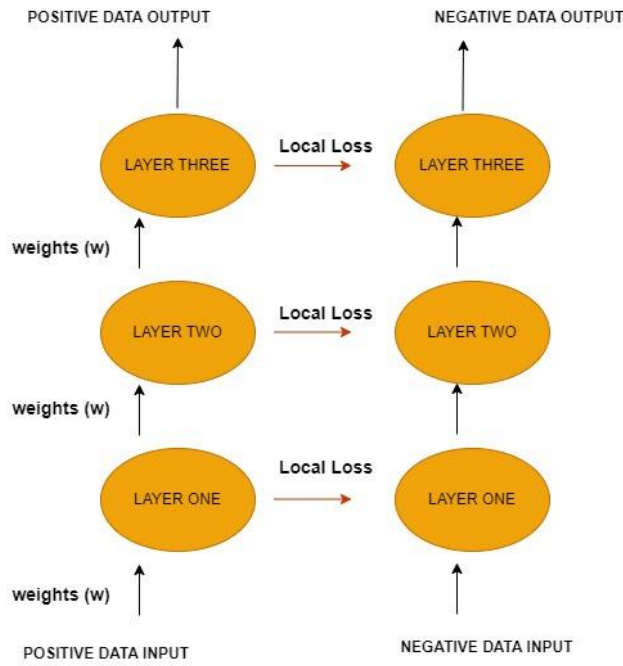


Figure 0: Backpropagation algorithm



*Figure 1: Backpropagation algorithm*

When Figure 1 is examined, an error value is calculated by comparing the input data with the output value after completing the forward pass on the network. By taking the derivative according to the error value, it is calculated how much the weights on the network will change and a backward propagation takes place over the whole network. This derivative calculation takes place according to the chain rule (Hinton, 1986).

When Figure 2 is examined, it is noted that there are two separate circuits. One is the positive circuit and the other is the negative circuit. The purposes of these two circuits are different. Calculates the total well-being of neurons in each circuit layer. The positive circuit tries to increase this goodness, while the negative circuit tries to reduce it as much as possible. The loss function is calculated locally on a layer-by-layer basis, not after the network has traveled forward through all layers, as in back propagation.

Positive data is real data. It can be a picture of a cat, dog, etc. Negative data will be data that is not from our positive dataset. One of the unsolved problems in the forward-forward algorithm study by Hinton (Hinton, 2022) is what the negative data will be. It is not fully specified in the study. Probably the answer to this question will depend on the situation. Negative data can also be completely noisy data.

### 2.1.1 Goodness Function

In this study, tests are carried out on the MNIST data set by making changes on the Goodness function. There are many ways in which the Goodness function can be defined. However, in the original study, the goodness function is defined by Equation 1 (Hinton, 2022). In this equation,  $\sigma$  is activation function,  $j$  is the neuron index by layer,  $y$  is activity of the neuron before normalization, and  $\theta$  is the threshold value.

$$p(\text{positive}) = \sigma(\sum_j y_j^2 - \theta) \quad \text{Equation 1}$$

Let there be a neural network with an input layer and a hidden layer. Completely unsupervised learning is accomplished without putting in an output layer.

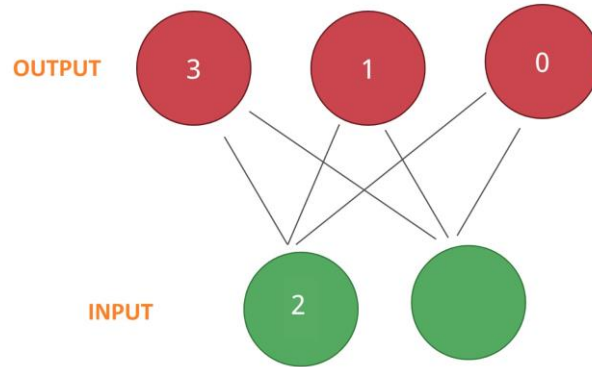


*Figure 3: Representative circuit with a hidden layer*

The goodness function used by Hinton in his study (Hinton, 2022) is the first goodness function. In this study, we will be tested using different goodness measures. According to Hinton's goodness function, we should square the activations on a layer basis. In this case, we calculate the goodness of 2 input data as  $3*3 + 1*1 + 0*0 = 10$ . There is also a value of  $\theta$  in the original equation. This value is called the threshold value. Let's consider our threshold value as  $\theta=2$ . Here the threshold value is the hyper parameter. Our goal is to achieve a value above the threshold. We get the value  $10-2 = 8$ .

In this case, our goodness value would be above the threshold value. So we got a positive value. Then we can reduce this 8 value to a probabilistic value between 0-1 by passing it through the sigmoid function. This will give us a probability value. Therefore, we increase the probability of positive data.

This is also true for negative data. We will have a goodness value below the threshold value of  $\theta=2$ . Substitute in the goodness function, we will get a negative number. Therefore, after passing it in the sigmoid function, we will have obtained a value close to 0. If we are not going to use back propagation, we will update the network parameters to get the goodness as high as possible for positive data (Hinton, 2022) and as low as possible for negative data (Hinton, 2022). So, how is this done in a multi-layer network?

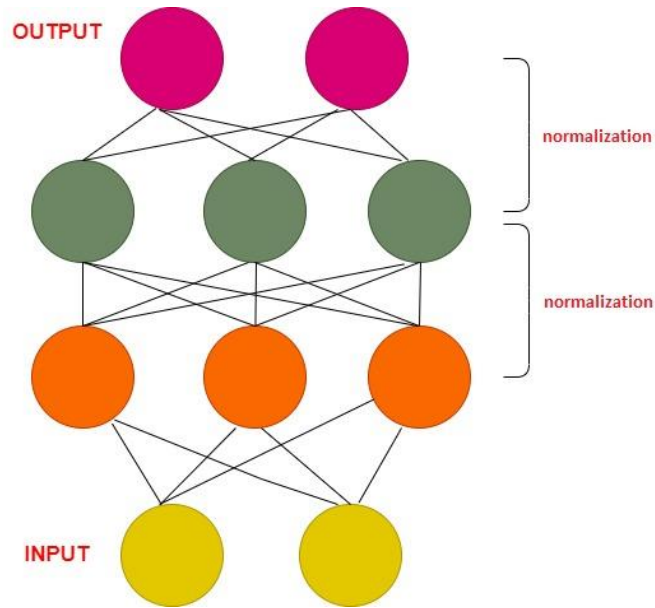


*Figure 4: A multi-layer neural network in a forward-forward algorithm*

When Figure 4 is examined; The data entering from the input reaches the output layer after passing through the hidden layers. Once we hit the target in the last layer, won't we need backpropagation to get it all the way to the first layer? The forward-forward algorithm has found a solution to the third problem of back propagation problems. Each different layer should have a goal. In other words, our goodness function is calculated in each layer. Then gradient descent is used and the weights are updated. Then it comes to the second hidden layer, now the new input is the values activated after the first layer. Goodness is calculated within this layer. We continue by doing this for each layer. Because each layer has its own active object. So there are no global updates regarding the previous layer. There is no transition from the top layer to the bottom layer as we do with backpropagation. All updates are done locally. So it's local. This update is potentially similar to the structure of the brain.

However, there is a problem with this structure. It is known that the activities to be moved to the upper layer after the goodness function is calculated in a lower layer already come from the positive data source. Because the processing layer has decided this. So if the processing layer doesn't change anything, if the values have a high magnitude, the next layer knows that the data is positive. The opposite is also true. If there is a low value, it is known that the data is negative. In this case, our network may not fully learn the representations. This is not a preferred situation and the solution is normalization at the layer level. Before using feedforward, the length of the hidden vector can be normalized and used as input to the next layer. As a result, they remove all size-related data. This length is defined as the goodness value for the layer in which it is located. The operation is directed by transferring it to the next layer.

### 3. APPLICATIONS

#### 3.1. Dataset

In this section, some experiments are performed using the MNIST dataset. MNIST is a dataset for handwritten numerals recognition. This dataset is a frequently used dataset in the fields of machine learning and artificial intelligence. The MNIST dataset contains 60,000 training samples and 10,000 test samples. Each example is a 28x28 pixel image and each of these images contains a handwritten number (0 to 9). The dataset was prepared by the American National Institute of Standards and Technology and was used for recognition of handwritten digits by optical character recognition (OCR) algorithms. It is a popular dataset for training deep learning models, especially in the field of machine learning. This dataset is frequently used to evaluate the learning performance of neural networks and is offered as a sample dataset by many machine learning libraries.

There are two important questions that we focus on in this study. These:

1. Where does negative data come from or how should it be provided?
2. If we have a good source of negative data, does the forward-forward algorithm effectively learn a multilayer representation with the proposed new goodness function?

#### 3.2. Creating Negative Data

A good negative data source prepared for the forward-forward algorithm can enable the algorithm to learn much better a multi-layered representation that can capture the structure of the data. For the MNIST dataset, we wrote a hard-coded masking function and applied it to 2 different images and got specific parts of each image. As a result, we got a fake image.

We did not use random images and just noise. Because using random images or only noise makes the learned information dependent or positive. This causes the algorithm to learn patterns very easily, and therefore the algorithm cannot learn complex information and patterns.

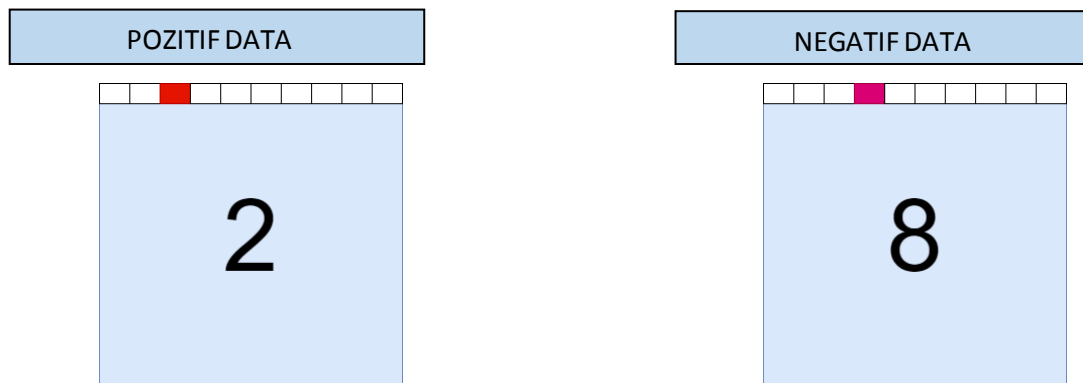


*Figure 5: Positive data (left), Negative data (right)*



In Figure 5, the specific structure of the MNIST dataset is given. In the MNIST dataset, the first row consists of all zeros. For positive data, the label of the input data is encoded in the first line and the label information is given to the network over the input data. For example, the data is the image of the number 2, and the label is index 2. For negative data, it is the data generated from the negative data generation method mentioned above, and its labels are also incorrectly processed and given to the network. Let the generated synthetic data be a number similar to 8. It is mislabeled by giving the label a 3. In this way, negative data is obtained.

### 3.3. Experimental Environment and Results

#### 3.3.1. Original Goodness Function:

In the experiment in the original study, the network was trained with four hidden layers, each model containing 2000 ReLU (Rectified Linear Unit) for 100 epochs. The normalized activity vectors of the last three hidden layers were used by softmax to determine the predictive label, resulting in an error rate of 1.37% (Hinton, 2022).

#### 3.3.2. Experiment 1: Proposed Goodness Function 1 (PGF1)

The first proposed goodness function is represented by equation 2 and equation 3 for positive and negative data, respectively.

$$\frac{1}{n} \sum_{i=1}^n \left( f(x_{pos,i})^2 - \left( \frac{1}{n} \sum_{j=1}^n f(x_{pos,j}) \right)^2 \right) \quad \text{Equation 2}$$

$$\frac{1}{n} \sum_{i=1}^n \left( f(x_{neg,i})^2 - \left( \frac{1}{n} \sum_{j=1}^n f(x_{neg,j}) \right)^2 \right) \quad \text{Equation 3}$$

- $x_{pos/neg,i}$  : is the input data for i.
- $f(x_{pos/neg,i})^2$  : It refers to the output produced for the input data.
- N: represents the total number of input data.
- $f(x_{pos,j})$  : It is the average of the outputs obtained as a result of passing all inputs through the model.
- The difference in the two parentheses is a measure calculated for each input data. This measure determines how the outputs are homogeneous.

Both equations use the squares of the summed values. However, the second and third equations also contain the expression  $\frac{1}{n} \sum_{j=1}^n f(x_{pos,j})$  and  $\frac{1}{n} \sum_{j=1}^n f(x_{neg,j})$ . This expression means calculating the efficiency in a layer of the network, averaging all the input values in this layer and subtracting each input value from this average. Each input value is differentiated according to its mean.

This extra expression in the second equation can highlight the deviation of the input values from the overall mean by differentiating according to the mean of the input values and help reveal more specific features. Then the values obtained from these equations were subtracted from the fixed threshold value and subjected to softmax activation. The final efficiency was calculated on a layer basis.

Activations in the neural network layer are the outputs of neurons. When a neural network processes inputs in a dataset, the variance of neurons' output measures how neurons respond and how much variation they show. The variance of the activations indicates how active the neurons are. The higher the variance, the more different the neurons' outputs, and the lower they are, the more similar the neurons' outputs. The variance of the activations is an important metric to measure the performance of the neural network and to understand whether the model is working properly. It can also affect the learning rate of the neural network, so the variance of the activations may need to be controlled.

With the Equations 2 and 3, we calculated the variance of the activations in the neural network layer using the forward-forward algorithm. Here,  $(x_{pos,i})$  denotes the activation value in the  $i$  sample of the function. The first part of the equation calculates the variability between samples. The second part is used to correct the variance. The  $1/n$  in this equation is the number of samples. Therefore, the proposed equation is a suitable method for calculating the variance of the activations in the neural network layer. We have verified this with the tests.

In general, determining which equation is ideal for calculating efficiency in a layer depends on the specific characteristics of the model used and the problem under consideration. Both equations involve different approaches, and which equation is more appropriate is based on the results to be obtained through experiments and analyzes on a specific scenario and problem. Both equations can be used to evaluate the problem from different angles, and determining which equation is more ideal will depend on the requirements of the problem space, the characteristics of the dataset, and the goal of the model.

With the goodness functions suggested in Equation 2 and Equation 3, our model (Hinton, 2022) was trained for 100 epochs and the final loss was calculated as 0.3719. This result proves that the favor function we proposed works.

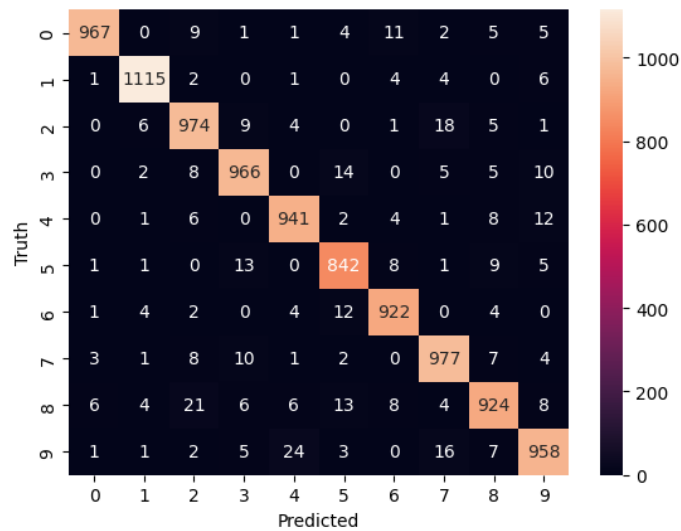


Figure 6: Confusion Matrix

There is the confusion matrix of the forward-forward algorithm that is tested with proposed goodness functions in Figure 6.

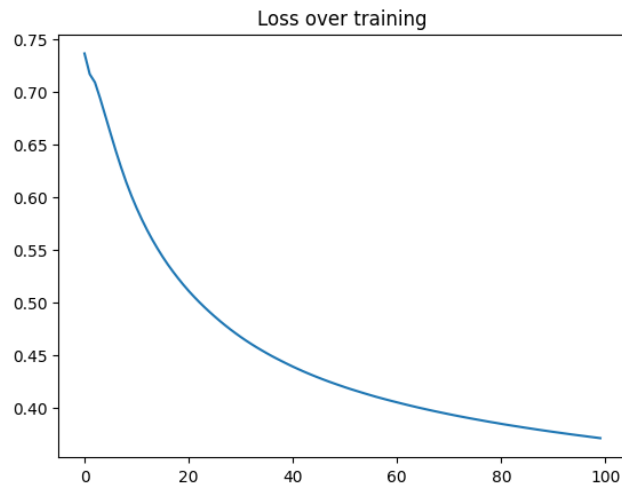


Figure 7: Loss on training data

In Figure 7, the loss on the training data of the forward-forward algorithm modeled with the proposed goodness functions is shown. As shown in Figures 6 and 7, the model is improved with the proposed goodness functions.

### 3.3.3. Experiment 2: Proposed Goodnes Function 2 (PGF2)

The goodness function in the original study was given in Equation 1. Hinton stated that one of the important issues to be investigated is the goodness function (Hinton, 2022). In this

experimental environment, we re-run the experimental environment without squaring the activities in the goodness function. PGF2 is shown in the equation 4. The model was trained for 100 epochs and a final loss of 0.6749 was calculated.

$$p(\text{positive}) = \sigma(\sum_j y_j - \theta) \quad \text{Equation 4}$$

Parameters	Goodness Function Loss			
	Original	PGF1	PGF2	BP
2000 ReLU 100 epoch softmax activation	1,37	0.3719	0.6749	0.004

Table 1: Comparison of experimental results

When the results given in Table 1 are examined, the proposed goodness functions give better results. However, the success of the back propagation algorithm could not be achieved. It may be possible to catch improvements in future studies with different goodness functions and architectural changes.

#### 4. CONCLUSIONS

In this study, the proposed new goodness functions for the forward-forward algorithm are tested. The better results than the original study were obtained. This study may pave the way for the investigation of different goodness functions for the algorithm. In the next study, the negative data source will be changed by combining the forward-forward algorithm with the predictive coding logic with the arranged goodness function. The resulting model is planned to be generalized on computational graphs and tested on large deep learning architectures. Just the forward-forward algorithm will not lead to human-like intelligence. It is necessary to combine and develop the algorithm according to different views and learning rules in the brain. Because our brain is full of repetitive and parallel connections.

#### REFERENCES

- Bellec, G., Scherr, F., Hajek, E., Salaj, D., Legenstein, R., & Maass, W. (2019). *Biologically Inspired Alternatives To Backpropagation Through Time For Learning in Recurrent Neural Networks*. <http://arxiv.org/abs/1901.09049>
- Crick, F. (1989). *The Recent Excitement About Neural Networks*. <https://www.nature.com/articles/337129a0>
- Grossberg, S. (1987). *Competitive Learning: From Interactive Activation to Adaptive Resonance*. <https://www.sciencedirect.com/science/article/abs/pii/S0364021387800253>
- Guerguiev, J., Lillicrap, T. P., & Richards, B. A. (2017). *Towards Deep Learning with Segregated Dendrites*. <https://doi.org/10.7554/eLife.22901.001>

Hinton, G. (1986). *Learning Representations by Back-Propagating Errors in a Layered Network*. <https://www.nature.com/articles/323533a0>

Hinton, G. (2022). *The Forward-Forward Algorithm: Some Preliminary Investigations*. <http://arxiv.org/abs/2212.13345>

Kohan, A. A., Rietman, E. A., & Siegelmann, H. T. (2018a). *Error Forward-Propagation: Reusing Feedforward Connections to Propagate Errors in Deep Learning*. <http://arxiv.org/abs/1808.03357>

Kohan, A. A., Rietman, E. A., & Siegelmann, H. T. (2018b). *Error Forward-Propagation: Reusing Feedforward Connections to Propagate Errors in Deep Learning*. <http://arxiv.org/abs/1808.03357>

Kreiman, G., & Serre, T. (2020). *Beyond the feedforward sweep: feedback computations in the visual cortex*. In *Annals of the New York Academy of Sciences* (Vol. 1464, Issue 1, pp. 222–241). Blackwell Publishing Inc. <https://doi.org/10.1111/nyas.14320>

Lecun, Y., Bengio, Y., & Hinton, G. (2015). *Deep learning*. In *Nature* (Vol. 521, Issue 7553, pp. 436–444). Nature Publishing Group. <https://doi.org/10.1038/nature14539>

Lillicrap, T. P., Santoro, A., Marris, L., Akerman, C. J., & Hinton, G. (2020). *Backpropagation and The Brain*. *Nature Reviews Neuroscience*, 21(6), 335–346. <https://doi.org/10.1038/s41583-020-0277-3>

Marblestone, A. H., Wayne, G., & Kording, K. P. (2016). *Toward an Integration of Deep Learning and Neuroscience*. *Frontiers in Computational Neuroscience*, 10(SEP). <https://doi.org/10.3389/fncom.2016.00094>

Mazzoni, P., Andersen, R. A., & Jordan, M. I. (1991). *A more biologically plausible learning rule for neural networks (reinforcement learning/coordinate transformation/posterior parietal cortex/sensorimotor integration/Hebbian synapses)*. In *Proc. Natl. Acad. Sci. USA* (Vol. 88). <https://www.jstor.org/stable/2357059>

Pozzi, I., Bohté, S. M., & Roelfsema, P. R. (2020). *Attention-Gated Brain Propagation: How The Brain Can Implement Reward-Based Error Backpropagation*. <https://proceedings.neurips.cc/paper/2020/hash/1abb1e1ea5f481b589da52303b091cbb-Abstract.html>

Ravichandran, N. B. (2022). *Brain-like combination of feedforward and recurrent network components achieves prototype extraction and robust pattern recognition*. <https://arxiv.org/abs/2206.15036>

Richards, B. A., & Lillicrap, T. P. (2019). *Dendritic Solutions To The Credit Assignment Problem*. In *Current Opinion in Neurobiology* (Vol. 54, pp. 28–36). Elsevier Ltd. <https://doi.org/10.1016/j.conb.2018.08.003>

Rockland, K. S. (2022). *Notes on Visual Cortical Feedback and Feedforward Connections*. *Frontiers in Systems Neuroscience*, 16.  
<https://doi.org/10.3389/fnsys.2022.784310>

Scellier, B., & Bengio, Y. (2017). *Equilibrium propagation: Bridging The Gap Between Energy-Based Models and Backpropagation*. *Frontiers in Computational Neuroscience*, 11. <https://doi.org/10.3389/fncom.2017.00024>

Song, Y., Lukasiewicz, T., Xu, Z., & Bogacz, R. (2020). *Can the Brain Do Backpropagation?-Exact Implementation of Backpropagation in Predictive Coding Networks*.  
<https://proceedings.neurips.cc/paper/2020/hash/fec87a37cdeec1c6ecf8181c0aa2d3bf-Abstract.html>

Song, Y., Millidge, B., Salvatori, T., Lukasiewicz, T., Xu, Z., & Bogacz, R. (2022). *Inferring Neural Activity Before Plasticity: A Foundation for Learning Beyond Backpropagation*. <https://doi.org/10.1101/2022.05.17.492325>

Werbos, P. J. (1981). *Applications of Advances in Nonlinear Sensitivity Analysis*.  
<https://link.springer.com/chapter/10.1007/BFb0006203>

Xie, X., Seung, H. S., & Hughes, H. (2003). *Equivalence of Backpropagation and Contrastive Hebbian Learning in a Layered Network*.  
<https://pubmed.ncbi.nlm.nih.gov/12590814/>

# A NEW LIGHTWEIGHT CONVOLUTIONAL NEURAL NETWORK SENGULNET: PERFORMANCE INVESTIGATION FOR THE SKIN CANCER DETECTION

Sengul Dogan<sup>1\*</sup>, Turker Tuncer<sup>1</sup>

<sup>1</sup>Department of Digital Forensics Engineering, College of Technology, Firat University, 23119, Elazig, Turkey

\*sdogan@firat.edu.tr; turkertuncer@firat.edu.tr

## Abstract

In this work, we introduce a novel deep-learning model called SengulNet and investigate its efficacy on a publicly available skin tumor image dataset. Our approach involves using this dataset to obtain comparative results, which we leverage to demonstrate the superior performance of SengulNet. SengulNet comprises an inception block as the initial block, followed by four bottleneck blocks, and incorporates a depth concatenation block to address the vanishing gradient problem. Through experiments on the skin cancer dataset comprising two classes (malignant and benign), SengulNet achieves a remarkable testing accuracy of 87.12%. Moreover, we present a novel deep feature engineering model, which utilizes the pretrained SengulNet to extract features. This model utilizes neighborhood component analysis (NCA) for feature selection and support vector machine (SVM) for classification and achieves a classification accuracy of 88.33% on the same dataset. Our findings conclusively demonstrate the effectiveness of SengulNet as a deep learning model for skin tumor image classification and highlight the potential of our proposed deep feature engineering model for improving performance in related tasks.

**Keywords:** SengulNet; CNN; skin cancer classification; deep feature engineering.

## 1. INTRODUCTION

The skin, being the largest organ in the human body, has a multitude of functions, which include safeguarding the internal organs, shielding the body against potential harm, minimizing fluid loss,



defending against microbes, shielding against hazardous ultraviolet rays, and regulating body temperature [1, 2].

Skin cancer is a complex disease that arises from the uncontrolled proliferation of skin cells, ultimately leading to the formation of malignant tumors [3, 4]. The scientific literature has identified several types of skin cancer, including melanoma, intraepithelial carcinoma, squamous cell carcinoma and basal cell carcinoma [5]. Basal cell carcinoma is the most common type, whereas melanoma is the most deadly [6]. While exposure to ultraviolet radiation from sunlight is a well-established risk factor for skin cancer, the disease can also manifest in areas of the skin that are not directly exposed to sunlight [7]. Skin cancer remains a significant public health concern and a challenging problem for medical research [8, 9].

Machine learning techniques are an important field that can automatically analyze medical images and help diagnose [10-12]. Machine learning-based automated systems have been developed in the literature to diagnose many diseases. Some recent studies related to skin cancer among these methods are given as follows. Karthik and Muthupandi [13] used convolutional neural networks (CNN) and SVM methods for skin tumor detection. They selected the International Skin Imaging Collaboration (ISIC) dataset for experiments. They attained an accuracy of 98.50%. Ali and Al-Marzouqi [14] proposed a melanoma detection method for regular CNN. They achieved an accuracy of 81.60% using the ISIC dataset. Alagu and Bagan [15] presented a skin cancer classification approach using the DenseNet method. They collected 500 skin cancer images. They obtained an accuracy of 95.00%. Gilani et al. [16] utilized spiking VGG-13 for skin cancer classification. They used 740 melanoma and 660 non-melanoma images and attained an accuracy of 89.57%. Tahir et al. [17] classified dermoscopic images for skin cancer detection. They used CNN and calculated a 94.17% accuracy value using three public datasets (containing 721 images). Huang et al. [18] a skin cancer diagnosis method using YOLO5. They used 1854 skin cancer images. They attained an accuracy of 79.20%. Dandu et al. [19] developed a method for melanoma skin cancer detection. They used ISIC 2018 dataset for this aim. They obtained an accuracy of 90.96 % using image feature extraction techniques.

### **1.1. Motivation and our model**

Computer vision is an increasingly popular research area in machine learning and deep learning [20, 21]. Numerous models have been proposed to classify images, with vision transformers and

convolutional neural networks being the most prominent [22, 23]. Our primary objective is to introduce a new and highly competitive CNN model named SengulNet.

To design SengulNet, we draw inspiration from inception networks [24] and MobileNetV2 [25] and employ depth concatenation similar to dense networks in place of addition blocks. We integrate components from inception, mobile, and dense networks to create a model that outperforms existing approaches.

Our secondary objective is to make contributions to the field of deep feature engineering. Thus, we present a novel SengulNet-based deep feature engineering model that utilizes pretrained SengulNet to extract deep features from test images. Neighborhood component analysis (NCA) [26] is then used to select the most informative features from the generated features.

Overall, our proposed SengulNet model and SengulNet-based deep feature engineering approach demonstrate the potential for further advancements in computer vision and image classification.

## **1.2. Contribution**

This paper proposes a new deep CNN model, SengulNet, and evaluates its performance on a public skin cancer image dataset. Our research presents several innovations and contributions to the field of computer vision.

Innovations:

- A novel CNN architecture, SengulNet, has been proposed.
- A new deep feature engineering model has been introduced.

Contributions:

- Existing CNNs are often used or modified to ensure high classification performance, particularly those based on the VGG architecture. Our research proposes a competitive CNN, SengulNet, as an alternative to existing models.
- We evaluate the performance of SengulNet on a public skin cancer image dataset, achieving a testing accuracy of 87.12%.
- To further contribute to the field of deep feature engineering, we present a novel model that extracts deep features from pretrained SengulNet and applies neighborhood component analysis (NCA) and support vector machines (SVM) [27] for classification. This approach achieved a classification accuracy of 88.33% on the test images.

Our proposed SengulNet model and deep feature engineering approach demonstrate promising results and hold potential for future advancements in image classification and computer vision.

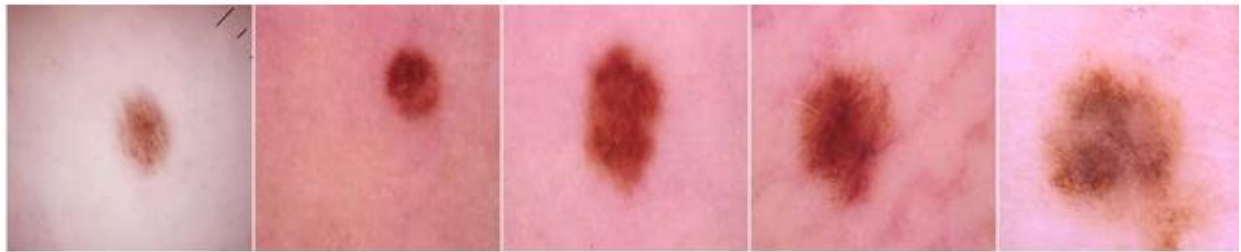
## 2. DATASET

In this section, we have utilized a publicly available image dataset that can be accessed on Kaggle [28]. The dataset comprises 3297 images categorized into two classes: (i) benign and (ii) malignant. The dataset contains 1800 benign and 1497 malignant tumor images, and all the images are in JPG format with a size of  $224 \times 224$ . The distribution of the dataset is shown in Table 1.

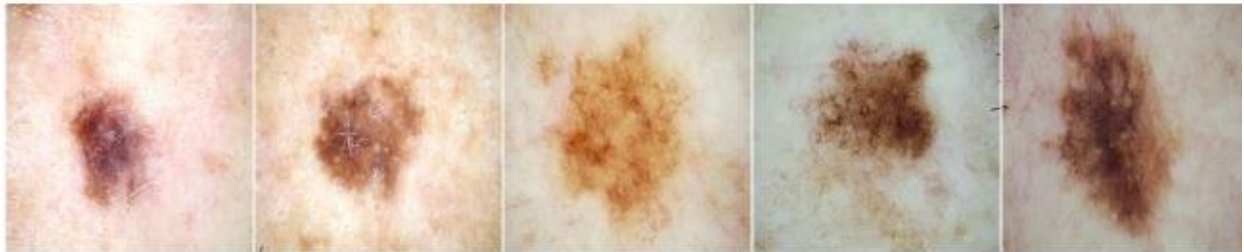
Table 1. Characteristic of the used skin tumor image dataset.

Category	Train	Test
Benign	1440	360
Malign	1197	300
Total	2637	660

The sample images of this dataset are also depicted in Figure 1.



(a) Benign



(b) Malignant

Fig. 1. Samples of the used dataset per the class.

## 3. SENGULNET

The primary objective of this section is to provide a detailed exposition of our newly introduced SengulNet model. Our proposal is centered around a lightweight convolutional neural network (CNN) with only 3.9 million learnable parameters. This network architecture constitutes a highly efficient solution in this domain. A general block diagram of the SengulNet is presented in Figure 2, facilitating a comprehensive understanding of our proposed architecture.

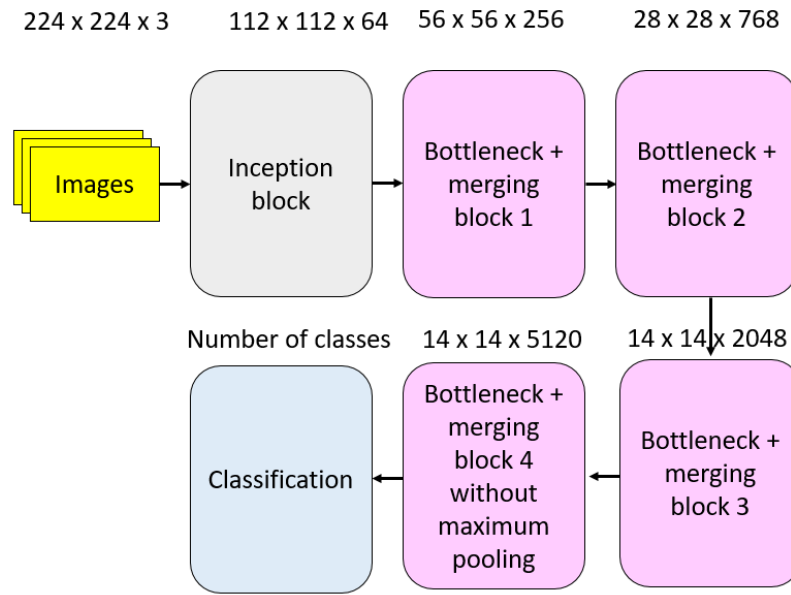


Fig. 2. The sketch of the proposed SengulNet

As depicted in Figure 2, the proposed SengulNet consists of three different types of blocks, namely, inception, bottleneck + merging, and classification blocks. In this section, we provide a detailed explanation of each block.

### 3.1. Inception block

The proposed model's initial block is the inception block, which uses two types of convolution to extract diverse features. Figure 3 illustrates the block diagram of this block.

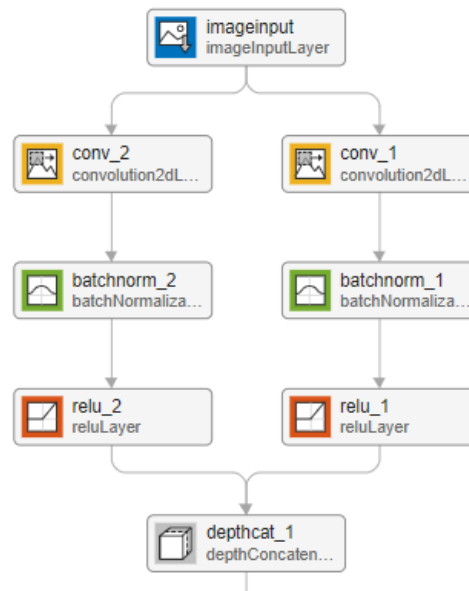


Fig. 3. Initial inception block.

The transition of this block is listed in Table 2.

Table 2. Parameters of the inception block.

No	Input	Operation	Filter	Stride	Output
1	224×224×3	Convolution	3×3×3×32	2× 2	112×112×32
2	112×112×32	Batch normalization	-	-	112×112×32
3	112×112×32	ReLu	-	-	112×112×32
4	224×224×3	Convolution	1×1×3×32	2× 2	112×112×32
5	112×112×32	Batch normalization	-	-	112×112×32
6	112×112×32	ReLu	-	-	112×112×32
7	112×112×32×2	Depth concatenation	-	-	112×112×64

### 3.2. Bottleneck + merging block

In our proposed SengulNet, we have incorporated a bottleneck + merging block, which is inspired by the MobileNet architecture. This block is designed to generate compact features while minimizing the computational cost. To address the issue of vanishing gradients, we have employed a depth concatenation block, which concatenates the input with the output of the block. Additionally, we have used maximum pooling to reduce the size of the features/activations. However, in the last block, we have avoided using maximum pooling as it can cause the routing problem by routing the peak values to the next layer. Instead, we have used 3×3 sized convolutions in the first and third convolution layers. In the bottleneck, we have used pixel-wise convolution. The detailed architecture of this block has been illustrated in Figure 4.

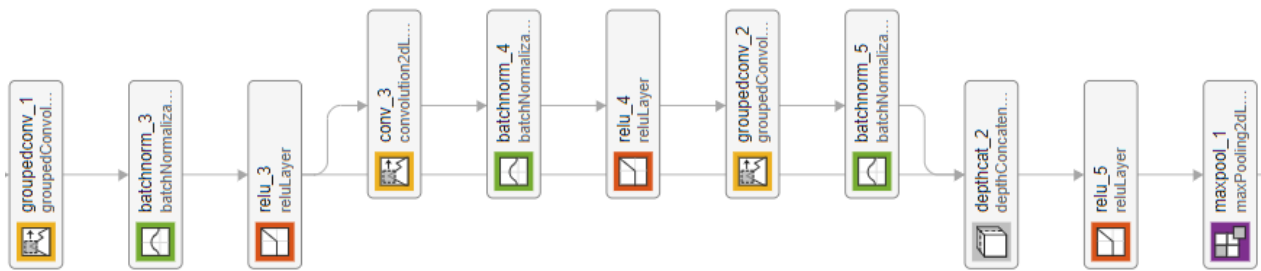


Fig. 4. Sketch of the proposed bottleneck + merging.

In this work, we have employed grouped convolutions with 3×3 sized filters, which have been shown to be effective in increasing the number of filters while keeping the computational cost

under control. Additionally, we have utilized  $1 \times 1$  sized filters in the convolution layer, reducing the number of filters by half compared to the previous layer.

### 3.3. Classification

In the final stage of the SengulNet architecture, we employ the classification block for the purpose of image classification. The illustration of this block can be observed in Figure 5.



Fig. 5. Block diagram of the classification block.

In order to present deep feature engineering models, our presented SengulNet utilizes global average pooling (gapool), fc\_1, and batchnorm\_16 layers to obtain features from the pretrained network. The model includes two fully connected layers, with the first fully connected layer having a size of 256 and the second fully connected layer having a size equal to the number of classes. The architecture of our model is designed to enable effective deep-feature engineering.

## 4. PRETRAINED SENGULNET-BASED DEEP FEATURE ENGINEERING MODEL

This section presents a deep feature engineering model utilizing our proposed SengulNet. Specifically, we trained the SengulNet using the training images and extracted features from the gapool, fc\_1, and batchnorm\_16 layers. From these layers, 5120, 256, and 256 features were extracted, respectively, resulting in a total of 5632 features per image. We employed the NCA feature selector and selected the top 512 features to reduce the dimensionality and select the most informative features. Finally, we fed the selected features into an SVM classifier. The block diagram of this deep feature engineering model is shown in Figure 6.

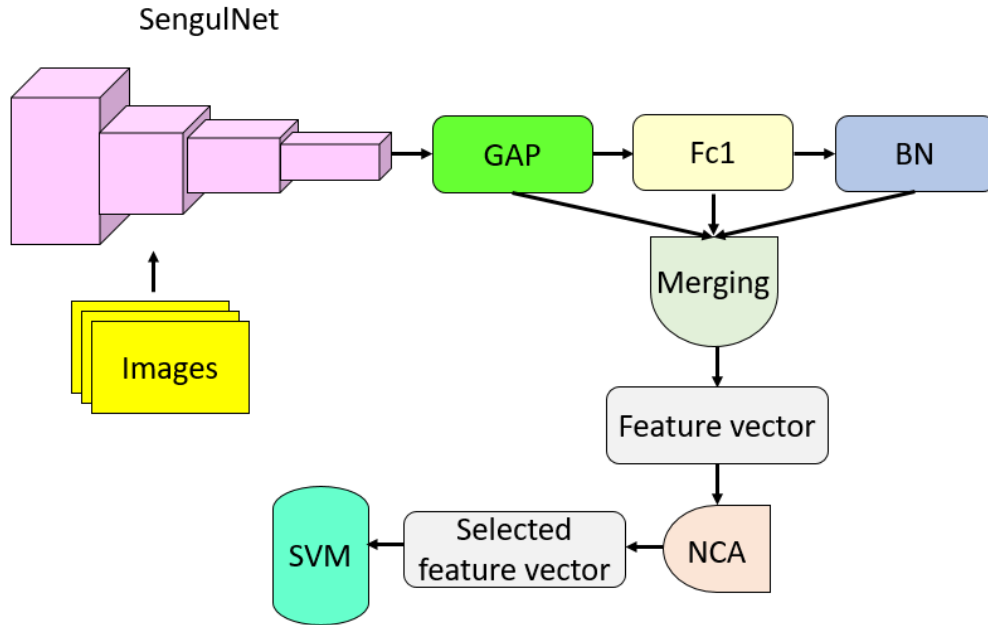


Fig. 6. The proposed SengulNet-based deep feature extraction model.

Steps of this deep feature extraction model are given below.

**Step 1:** Read each image from the test image dataset.

**Step 2:** Load the pretrained SengulNet.

**Step 3:** Extract features from the GAP (global average pooling), Fc1 (fully connected), and BN (batch normalization).

**Step 4:** Merge these features and obtain the final feature vector.

**Step 5:** Select the most informative 512 features from the generated 5632 features by deploying NCA.

**Step 6:** Classify the selected features by applying linear SVM with 10-fold cross-validation.

## 5. PERFORMANCE ANALYSIS

In this section, we present a performance analysis of the proposed models. The dataset used in this study was downloaded from the Kaggle website and consisted of training and test folders. We used only the original images without any augmentation or modification. The test results of our models were calculated using two methods: (i) SengulNet and (ii) deep feature engineering model. These models were implemented on a computer with a simple configuration and an Nvidia 2070 GPU. We used MATLAB as the programming environment, and the computer had 64 GB memory, a 3.6 GHz processor, and Windows 11 operating system.



We first created the proposed SengulNet using the deep network designer of MATLAB and trained it on the training images. The training options for this CNN are as follows: learning rate = 0.005, number of epochs = 30, mini-batch size = 32, and optimizer = stochastic gradient descent. In the second (deep feature engineering model) model, we used three layers (gapool/GAP, fc\_1, and batchnorm\_16) to generate features. NCA with default settings was used to select the most informative features. In the classification phase, linear SVM was used, and 10-fold cross-validation was utilized as the validation technique.

We trained the proposed SengulNet with a 75:25 training and validation ratio. The training and validation accuracy curves are depicted in Figure 7.

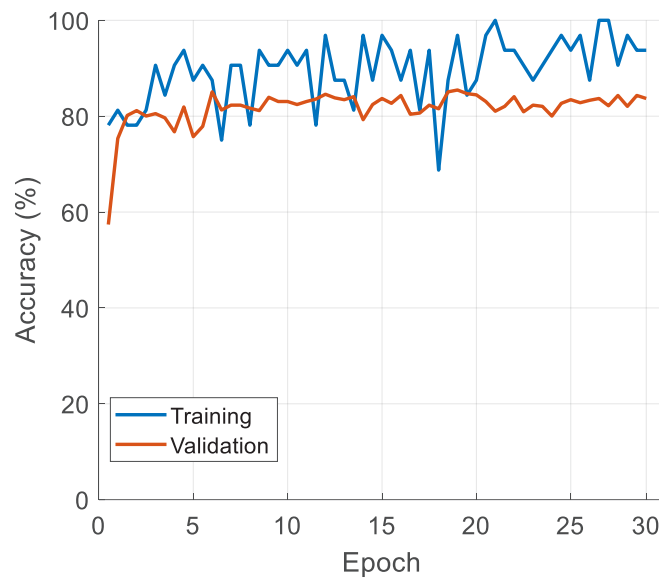


Fig. 7. Training and validation curve of the proposed SengulNet on the used skin tumor image dataset.

As seen in Figure 7, our proposed model achieved a validation accuracy of 84.58% and an average training accuracy of 89.87% for the skin tumor image dataset. Moreover, we applied this trained SengulNet to the test images, and the calculated test results are reported in Table 3.

Table 3. Confusion matrix of the presented SengulNet for test images.

Actual	Predicted		Recall (%)
	Benign	Malignant	
Benign	331	29	97.94
Malignant	56	244	81.33
Precision (%)	85.33	89.38	Accuracy (%):87.12

Table 3 demonstrated that our presented SengulNet attained 87.12% testing accuracy. Moreover, the confusion matrix of the proposed deep feature engineering model is depicted in Table 4. Table 4. Confusion matrix of the presented SengulNet-based deep feature engineering model for test images.

Actual	Predicted		Recall (%)
	Benign	Malignant	
Benign	317	43	88.06
Malignant	34	266	88.67
Precision (%)	90.31	86.08	Accuracy (%):88.33

The test results of the proposed SengulNet-based deep feature engineering model achieved 88.33% classification accuracy.

In order to show the superiority of our model, we have compared our model to MobileNetV2 and the calculated comparative results have been depicted in Figure 8.

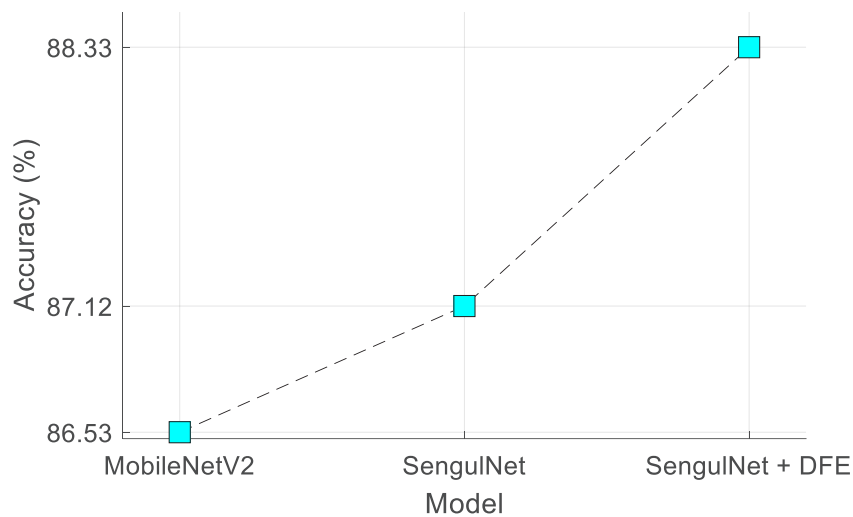


Fig. 8. Comparative results.

As depicted in Figure 8, our proposed SengulNet-based model outperformed the MobileNetV2 model. It is worth noting that the MobileNetV2-based model is a deep feature engineering (DFE) model that uses 1000 features and an SVM classifier for classification [29]. On the other hand, our proposed SengulNet-based DFE model uses only 512 features (which is fewer than the other model) and achieved over 1.80% classification performance than the MobileNetV2-based model.

## 6. CONCLUSIONS

We presented a new competitive CNN in this work named SengulNet. The proposed SengulNet model achieved promising results in accuracy, with a validation accuracy of 84.58% and an average

training accuracy of 89.87%. Moreover, when compared to the MobileNetV2-based model used in a previous study, our SengulNet-based DFE model showed significantly better performance, achieving over 1.80% classification performance than the MobileNetV2-based model.

The proposed SengulNet model utilizes two grouped convolution layers with  $3 \times 3$  sized filters and one convolution layer with  $1 \times 1$  sized filters. Additionally, the model utilizes two fully connected layers with sizes of 256 and the number of classes, and global average pooling, fc\_1, and batchnorm\_16 layers are used to extract features. These features are then fed to an NCA feature selector to select the most informative 512 features, which are then classified using a linear SVM with 10-fold cross-validation.

In conclusion, the presented SengulNet model and the associated deep feature engineering model offer a promising approach for skin tumor classification. The model's superior performance when compared to the MobileNetV2 shows its potential to be used as an effective tool for skin cancer diagnosis.

**Author contributions:** All authors contributed equally to the study.

**Funding:** The authors state that this work has not received any funding.

**Conflict of interest** The authors declare that they have no conflict of interest.

**Ethical approval** Ethics approval was not required for this research.

## References

- [1] N. Neagu, C. Dinzani, A. Venuti, S. Bonin, S. Voidăzan, I. Zalaudek, C. Conforti, The role of HPV in keratinocyte skin cancer development: A systematic review, *Journal of the European Academy of Dermatology and Venereology*, 37 (2023) 40-46.
- [2] A. Srivastava, T. Bencomo, I. Das, C.S. Lee, Unravelling the landscape of skin cancer through single-cell transcriptomics, *Translational Oncology*, 27 (2023) 101557.
- [3] R. Venzel, M.C.P. Campos, L.P. de Oliveira, R.V.D. Lins, Á.D.D. Siena, K.T. Mesquita, T.P.M. Dos Santos, N. Nohata, L.C.M. Arruda, H. Sales-Campos, Clinical and molecular overview of immunotherapeutic approaches for malignant skin melanoma: Past, present and future, *Critical Reviews in Oncology/Hematology*, (2023) 103988.
- [4] J. Choudhari, R. Nimma, S.K. Nimal, S.K.T. Venkata, G.C. Kundu, R.N. Gacche, *Prosopis juliflora* (Sw.) DC phytochemicals induce apoptosis and inhibit cell proliferation signaling

pathways, EMT, migration, invasion, angiogenesis and stem cell markers in melanoma cell lines, *Journal of Ethnopharmacology*, (2023) 116472.

[5] A. Mankawade, A. Bodhankar, A. Mahajan, D. Prasad, S. Mahajan, R. Dhakalkar, Skin Cancer Detection and Intensity Calculator using Deep Learning, 2023 International Conference for Advancement in Technology (ICONAT), IEEE, 2023, pp. 1-4.

[6] A. Lin, C.E. Schmalbach, Surgery in the Era of Immunotherapy for Advanced Head and Neck Non-melanoma Skin Cancer, *Current Oncology Reports*, (2023) 1-8.

[7] R. Neale, R. Lucas, S. Byrne, L. Hollestein, L. Rhodes, S. Yazar, A. Young, M. Berwick, R. Ireland, C. Olsen, The effects of exposure to solar radiation on human health, *Photochemical & Photobiological Sciences*, (2023) 1-37.

[8] M.M. Asgari, L.A. Crane, Skin Cancer Screening: The Importance of Identifying High-risk Subgroups and the Need for US-Based Population Research, *JAMA*, 329 (2023) 1259-1260.

[9] N. Melarkode, K. Srinivasan, S.M. Qaisar, P. Plawiak, AI-Powered Diagnosis of Skin Cancer: A Contemporary Review, Open Challenges and Future Research Directions, *Cancers*, 15 (2023) 1183.

[10] E. Kaplan, M. Baygin, P.D. Barua, S. Dogan, T. Tuncer, E. Altunisik, E.E. Palmer, U.R. Acharya, ExHiF: Alzheimer's disease detection using exemplar histogram-based features with CT and MR images, *Medical Engineering & Physics*, 115 (2023) 103971.

[11] Y. Gul, T. Muezzinoglu, G. Kilicarslan, S. Dogan, T. Tuncer, Application of the deep transfer learning framework for hydatid cyst classification using CT images, *Soft Computing*, (2023) 1-11.

[12] T. Muezzinoglu, N. Baygin, I. Tuncer, P.D. Barua, M. Baygin, S. Dogan, T. Tuncer, E.E. Palmer, K.H. Cheong, U.R. Acharya, PatchResNet: Multiple Patch Division-Based Deep Feature Fusion Framework for Brain Tumor Classification Using MRI Images, *Journal of Digital Imaging*, (2023) 1-15.

[13] B. Karthik, G. Muthupandi, SVM and CNN based skin tumour classification using WLS smoothing filter, *Optik*, 272 (2023) 170337.

[14] A.A. Ali, H. Al-Marzouqi, Melanoma detection using regular convolutional neural networks, 2017 International Conference on Electrical and Computing Technologies and Applications (ICECTA), IEEE, 2017, pp. 1-5.

[15] S. Alagu, K.B. Bagan, Skin cancer classification in dermoscopy images using convolutional neural network, *AIP Conference Proceedings*, AIP Publishing LLC, 2021, pp. 040013.

- [16] S. Qasim Gilani, T. Syed, M. Umair, O. Marques, Skin Cancer Classification Using Deep Spiking Neural Network, *Journal of Digital Imaging*, (2023) 1-11.
- [17] M. Tahir, A. Naeem, H. Malik, J. Tanveer, R.A. Naqvi, S.-W. Lee, DSCC\_Net: Multi-Classification Deep Learning Models for Diagnosing of Skin Cancer Using Dermoscopic Images, *Cancers*, 15 (2023) 2179.
- [18] H.-Y. Huang, Y.-P. Hsiao, A. Mukundan, Y.-M. Tsao, W.-Y. Chang, H.-C. Wang, Classification of Skin Cancer Using Novel Hyperspectral Imaging Engineering via YOLOv5, *Journal of Clinical Medicine*, 12 (2023) 1134.
- [19] R. Dandu, M.V. Murthy, Y.R. Kumar, Transfer learning for segmentation with hybrid classification to detect Melanoma Skin Cancer, *Heliyon*, (2023).
- [20] M. Rafiei, J. Raitoharju, A. Iosifidis, Computer Vision on X-Ray Data in Industrial Production and Security Applications: A Comprehensive Survey, *IEEE Access*, 11 (2023) 2445-2477.
- [21] J. Liu, Z. Xiao, S. Lu, D. Che, M. Dong, C. Bai, Infrastructure-level Support for GPU-Enabled Deep Learning in DATAVIEW, *Future Generation Computer Systems*, 141 (2023) 723-737.
- [22] S.I. Nafisah, G. Muhammad, M.S. Hossain, S.A. AlQahtani, A Comparative Evaluation between Convolutional Neural Networks and Vision Transformers for COVID-19 Detection, *Mathematics*, 11 (2023) 1489.
- [23] K. Wang, C. Xu, G. Li, Y. Zhang, Y. Zheng, C. Sun, Combining convolutional neural networks and self-attention for fundus diseases identification, *Scientific Reports*, 13 (2023) 76.
- [24] C. Szegedy, V. Vanhoucke, S. Ioffe, J. Shlens, Z. Wojna, Rethinking the inception architecture for computer vision, *Proceedings of the IEEE conference on computer vision and pattern recognition*, 2016, pp. 2818-2826.
- [25] M. Sandler, A. Howard, M. Zhu, A. Zhmoginov, L.-C. Chen, Mobilenetv2: Inverted residuals and linear bottlenecks, *Proceedings of the IEEE conference on computer vision and pattern recognition*, 2018, pp. 4510-4520.
- [26] J. Goldberger, G.E. Hinton, S. Roweis, R.R. Salakhutdinov, Neighbourhood components analysis, *Advances in neural information processing systems*, 17 (2004) 513-520.
- [27] V. Vapnik, The support vector method of function estimation, *Nonlinear Modeling*, Springer 1998, pp. 55-85.

[28] C. Fanconi, Skin Cancer: Malignant vs. Benign, <https://www.kaggle.com/datasets/fanconic/skin-cancer-malignant-vs-benign>, accessed on April 29, 2023, 2019.

[29] M. Toğaçar, Z. Cömert, B. Ergen, Intelligent skin cancer detection applying autoencoder, MobileNetV2 and spiking neural networks, Chaos, Solitons & Fractals, 144 (2021) 110714.

## Appendix

The real code of the proposed SengulNet is demonstrated below.

```
tempLayers = imageInputLayer([224 224 3], "Name", "imageinput");
lgraph = addLayers(lgraph, tempLayers);

tempLayers = [
    convolution2dLayer([1 1], 32, "Name", "conv_2", "Padding", "same", "Stride", [2 2])
    batchNormalizationLayer("Name", "batchnorm_2")
    reluLayer("Name", "relu_2")];
lgraph = addLayers(lgraph, tempLayers);

tempLayers = [
    convolution2dLayer([3 3], 32, "Name", "conv_1", "Padding", "same", "Stride", [2 2])
    batchNormalizationLayer("Name", "batchnorm_1")
    reluLayer("Name", "relu_1")];
lgraph = addLayers(lgraph, tempLayers);

tempLayers = [
    depthConcatenationLayer(2, "Name", "depthcat_1")
    groupedConvolution2dLayer([3 3], 2, "channel-
wise", "Name", "groupedconv_1", "Padding", "same")
    batchNormalizationLayer("Name", "batchnorm_3")
    reluLayer("Name", "relu_3")];
lgraph = addLayers(lgraph, tempLayers);

tempLayers = [
    convolution2dLayer([1 1], 64, "Name", "conv_3", "Padding", "same")
```

```

        batchNormalizationLayer("Name", "batchnorm_4")
        reluLayer("Name", "relu_4")
        groupedConvolution2dLayer([3 3], 2, "channel-
wise", "Name", "groupedconv_2", "Padding", "same")
        batchNormalizationLayer("Name", "batchnorm_5"]];
lgraph = addLayers(lgraph, tempLayers);

tempLayers = [
    depthConcatenationLayer(2, "Name", "depthcat_2")
    reluLayer("Name", "relu_5")
    maxPooling2dLayer([3 3], "Name", "maxpool_1", "Padding", "same", "Stride", [2 2])
    groupedConvolution2dLayer([3 3], 2, "channel-
wise", "Name", "groupedconv_3", "Padding", "same")
    batchNormalizationLayer("Name", "batchnorm_6")
    reluLayer("Name", "relu_6"]];
lgraph = addLayers(lgraph, tempLayers);

tempLayers = [
    convolution2dLayer([1 1], 128, "Name", "conv_4", "Padding", "same")
    batchNormalizationLayer("Name", "batchnorm_7")
    reluLayer("Name", "relu_7")
    groupedConvolution2dLayer([3 3], 2, "channel-
wise", "Name", "groupedconv_4", "Padding", "same")
    batchNormalizationLayer("Name", "batchnorm_8"]];
lgraph = addLayers(lgraph, tempLayers);

tempLayers = [
    depthConcatenationLayer(2, "Name", "depthcat_3")
    reluLayer("Name", "relu_8")
    maxPooling2dLayer([3 3], "Name", "maxpool_2", "Padding", "same", "Stride", [2 2])
    groupedConvolution2dLayer([3 3], 2, "channel-
wise", "Name", "groupedconv_5", "Padding", "same")
    batchNormalizationLayer("Name", "batchnorm_9")
    reluLayer("Name", "relu_9"]];
lgraph = addLayers(lgraph, tempLayers);

```



```

tempLayers = [
    convolution2dLayer([1 1],256,"Name","conv_5","Padding","same")
    batchNormalizationLayer("Name","batchnorm_10")
    reluLayer("Name","relu_10")
    groupedConvolution2dLayer([3 3],2,"channel-
wise","Name","groupedconv_6","Padding","same")
    batchNormalizationLayer("Name","batchnorm_11")];
lgraph = addLayers(lgraph,tempLayers);

tempLayers = [
    depthConcatenationLayer(2,"Name","depthcat_4")
    reluLayer("Name","relu_11")
    maxPooling2dLayer([3 3],"Name","maxpool_3","Padding","same","Stride",[2 2])
    groupedConvolution2dLayer([3 3],2,"channel-
wise","Name","groupedconv_7","Padding","same")
    batchNormalizationLayer("Name","batchnorm_12")
    reluLayer("Name","relu_12")];
lgraph = addLayers(lgraph,tempLayers);

tempLayers = [
    convolution2dLayer([1 1],512,"Name","conv_6","Padding","same")
    batchNormalizationLayer("Name","batchnorm_13")
    reluLayer("Name","relu_13")
    groupedConvolution2dLayer([3 3],2,"channel-
wise","Name","groupedconv_8","Padding","same")
    batchNormalizationLayer("Name","batchnorm_14")];
lgraph = addLayers(lgraph,tempLayers);

tempLayers = [
    depthConcatenationLayer(2,"Name","depthcat_5")
    reluLayer("Name","relu_14")
    batchNormalizationLayer("Name","batchnorm_15")
    globalAveragePooling2dLayer("Name","gapool")
    fullyConnectedLayer(256,"Name","fc_1")

```

```
    batchNormalizationLayer("Name","batchnorm_16")
    fullyConnectedLayer(2,"Name","fc_2")
    softmaxLayer("Name","softmax")
    classificationLayer("Name","classoutput")];
lgraph = addLayers(lgraph,tempLayers);

% clean up helper variable
clear tempLayers;
```

# Ensuring Data Security in The Blockchain Based Smart Home Network

Kadriye Nur ERMAN<sup>1\*</sup>

Ahmet Cevahir CINAR<sup>2</sup>

<sup>1</sup>Department of Computer Engineering, Kirikkale University, Kirikkale, Turkey

kadriyenurerman@kku.edu.tr,

<sup>2</sup>Department of Computer Engineering, Selcuk University, Konya, Turkey

accinar@selcuk.edu.tr

## Abstract

Smart home systems are frequently preferred today because they bring the standard of living to higher levels. The variety of Internet of Things (IoT) devices used in smart homes is also increasing. With this increased demand and variety, there has been an increase in processing power and amount of storage, thus raising several security concerns. The heterogeneous use of blockchain technology is proposed to ensure transparency, privacy, and security of user data. Since blockchain technology is a distributed database in the network, it provides a homogeneous network structure to the IoT technology. Thanks to the immutability, transparency, authorization, authentication, and decentralization features of blockchain technology, data obtained from smart home devices and added to the chain become securely stored. In this study, an exemplary application has been carried out to ensure security, transparency, and privacy in the smart home network using blockchain technology. In this application, 1 gateway, 1 DHT11 temperature and humidity sensor, 1 MQ2 gas sensor, and 3 NodemCU ESP8266 cards are used. NodemCU ESP8266 card is preferred as the gateway. The gateway was used to transmit the data received from the sensors to the blockchain. Local storage and cloud storage were used for storage in the blockchain.

**Keywords:** Blockchain; Privacy; Security; Smart home; Transparency.

## 1.INTRODUCTION

In the near future, the use of smart home technology will become widespread in many homes [1]. Smart homes are residences that provide automated and intelligent services with a variety of devices, sensors, monitors, and interfaces connected to a network that provides security, comfort, and increased quality of life to people [2-4]. Smart homes are a network where various smart devices like smartphones and smart wall sockets are interconnected, and IoT is the basic platform of this network. Smart homes send and receive data in real-time. Users

---

\* This paper produces from the Master of Science thesis of Kadriye Nur Erman.

use multiple smart home products to control and monitor various functions depending on the home's network arrangement and user settings. The network structure of the smart home consists of devices communicating over the internet and embedded computers. This network structure is transitioning from conventional wired systems to wireless technologies [5]. The demand for the smart home market is increasing. Leading IT companies such as Google, Samsung, and Amazon have moved quickly to expand their smart home services and products by entering the nascent competitive market in response to this increasing demand [6-8]. According to predictions, the worldwide adoption rate of smart home appliances is expected to double from 10.62% in 2020 to 21.09% by 2025 [9]. Many IoT devices used in smart homes generate large amounts of data. For example, storing video information on the camera requires a large amount of memory area. Today, traditional information systems face different problems in managing and maintaining this produced smart home data. Data storage has been significantly impacted by the emergence of cloud storage technology. [10, 11]. It has reduced the storage cost and solved the storage capacity issue [12]. Smart home applications extensively utilize cloud technology. Despite all these comforts and while providing many benefits to smart homeowners, it poses risks for malicious cyber-attacks. Attackers can gain unauthorized access to smart homes, and access and modify user data. For example, it can access the temperature data and endanger the life and property of the user. This poses a risk to privacy and security. Centralized and traditional approaches to addressing these risks are susceptible to malicious attacks. The increasing prevalence of blockchain technology as a transparent and reliable technology in data storage opens new potentials for solving the serious problems of data integrity, security, and privacy in smart homes. Recently, blockchain technology is preferred to provide security in most new-generation IoT applications [13].

In this study, the MQ2 gas sensor, and a DHT11 temperature and humidity sensor were used in the smart home. To establish healthy communication in terms of communication, each sensor is connected to 1 NodemCU ESP8266 card. NodemCU ESP8266 card, which is used alone as a gateway, is preferred. The data received from the sensors is transferred to the gateway. After the gateway, it is stored on the blockchain.

The rest of the paper is organized as follows: In Section 2, the smart home is described. The recommended network configuration is given in Section 3. Finally, the paper is concluded in Section 4.

## 2.WHAT IS A SMART HOME?

In order to comprehend the operations of smart homes, it is necessary to know that there are various devices that make up the smart home and that these devices can be used, controlled, and regulated remotely. Smart homes are communicative networks, and these communicative networks help establish a personalized environment that fits the lifestyles of individuals in the smart home network and is involved in sending and receiving data between devices.

Gram-Hanssen and Darby define a smart home as “a home located in the context of frequent and regular communication services, allowing household members to monitor and remotely control sensors and devices in the communication network” [14].

As seen in Figure 1, the main technical feature of smart home systems is that a central control center acts as an intermediary between devices and sensors and smart home individuals. This central control is called the “home gateway”. It uses a set of communication protocols that connect the external network to the home network [15].

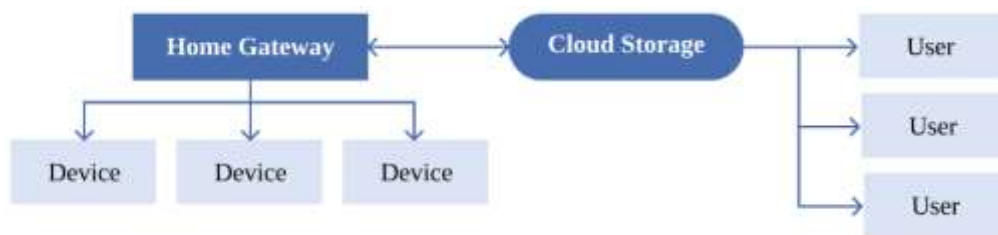


Figure 1. Structure of the smart home system

### 2.1. Necessary Elements for Executing a Blockchain-Powered Smart Home

Since the mining nodes in the blockchain network copy the entire blockchain, the prerequisites for the use of blockchain in smart homes will be made from the standpoint of a single mining node. The requirements are addressed through 4 implementation steps.

- Determining the smart home usage scenario: It is the stage where the system of the smart home is determined according to the user's request. It is one of the essential steps required before a smart home network adopts blockchain technology. It involves the identification, interpretation, and synthesis of needs.
- Solution creation and testing: Creating a blockchain-based smart home solution involves the consideration of numerous hardware and software parameters by developers. The key part of these parameters for the software is the selection of the blockchain platform and the platform's consensus algorithm. The factors that determine the selection criteria may vary, including the number of miners participating in the

network, the frequency of transactions taking place, and the rate at which new blocks are added. Hardware requirements depend on software architecture and system efficiency. It is the application of the realized prototype to the real smart home environment after proper determination of the software and hardware prerequisites.

- Integration and rollout: After the development and testing of the smart home blockchain solution is finished potential complexities can be triggered in traditional systems because the new platform poses unique advantages and constraints for each application to conform to. Consequently, it is advisable to migrate entirely from outdated legacy systems to newly established blockchain systems.
- Usability: At this stage, it is to create UX/UI (User experience/User Interface) for usability. This step plays an important role because this is the interface where the user's requests are received. Realizing a mobile or web-based interface can provide healthy communication between the user and the developer.

### 3. RECOMMENDED NETWORK CONFIGURATION

Integrating blockchain technology into smart home gateway storage is crucial for ensuring the secure and confidential transfer of data between sensors, IoT devices, and other environments. Although each smart home operates on a centralized network, implementing blockchain at the storage layer can transform the smart home network into a distributed network. The blockchain-based smart home framework comprises three layers: the "detection layer," "gateway layer," and "storage layer." The sensing layer, which is the first layer, includes the IoT devices and sensors found in a smart home. The gateway layer, the second layer, stores the data generated by the sensing layer and provides it to users as needed. Finally, the storage layer, the third layer, records the gateway ID and data processed by each gateway in the blockchain. The blocks are distributed to ensure that information is accessible to users at any time and from anywhere. This can be expressed as shown in Figure 2.

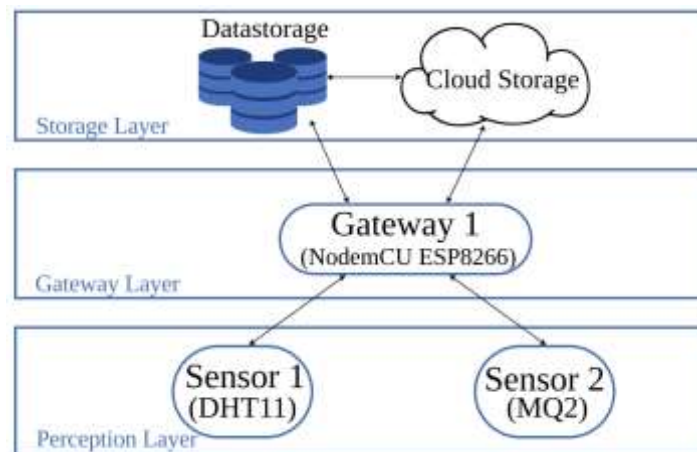


**Figure 2.** Overview of the proposed network design

In the study, there are MQ2 gas, DHT11 temperature and humidity sensors in the first layer. These sensors are used with NodemCU ESP8266 card to communicate. The second layer contains the NodemCU ESP8266 board used as the gateway. In the third layer, there are areas used for storage. In the study, local and cloud storage was used to provide distributed storage.

Figure 3 shows the methodological flowchart of the architecture that allows data to be collected from devices and sensors at the edge, stored in the blockchain, and presented to users appropriately. The collected data goes through the hash generation and formatting process. Regular data analysis and maintenance are imperative to deliver users with relevant and essential information.

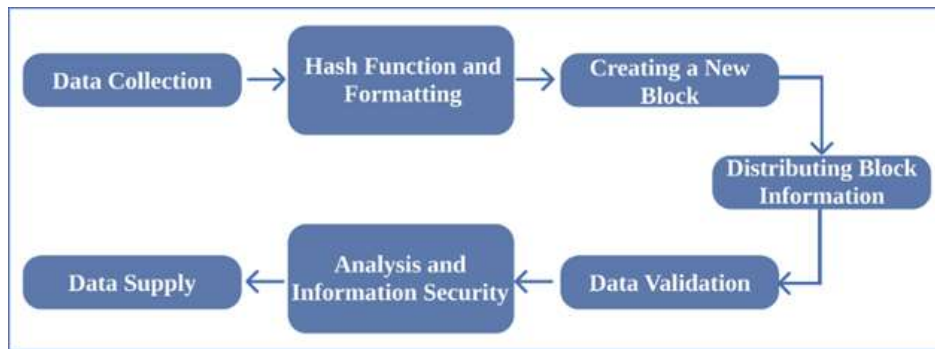


**Figure 3.** Flowchart of blockchain based cloud enabled architecture for smart home gateway

### 3.1. Recognizing Gateway Devices and Collecting Data

In this study, MAC addresses are used while transferring data. Each IoT device or sensor integrated into a smart home is linked to a gateway, with each component possessing a distinct MAC (Media Access Control Address) address. The MAC address is the identity used to identify every hardware device on a network. Gateways and devices are assigned static MAC addresses. The interconnection protocols and data storage process steps between devices and gateways are shown in Figure 4.

In this study, data is transferred between sensors, gateway, and storage layer according to certain rules. Transfer sequence and transfer rules are given in Figure 4.

**1-2-3.** Sensors identified by MAC addresses to a gateway must be verified on every transaction. The sensors in the detection layer are registered directly to the gateway and automatically connected to the gateway. The gateway can get an ID from the sensor it connects to or get the relevant details from the connected sensor.



4. Gateways identified by MAC addresses to a sensor must be verified on each transaction. Since the Gateway information is registered to the sensor and the sensor information is registered to the Gateway, there is no problem in communication.
- 5-6. The gateway decrypts to ensure that the correct and registered sensors are connected.
7. The gateway generates a request message to obtain the data generated by the sensors and forwards it to the sensor.
8. Data request messages are sent to the sensor in encrypted form.
- 9-10. Encrypted data request messages are decoded in the sensor, the request is fulfilled, and the information is sent encrypted to the gateway.
- 11-12. The gateway decrypts the received raw data and forwards it to the storage units and the cloud or clouds located in the storage layer.
13. In the data warehouse, the information received from the sensors is stored encrypted.

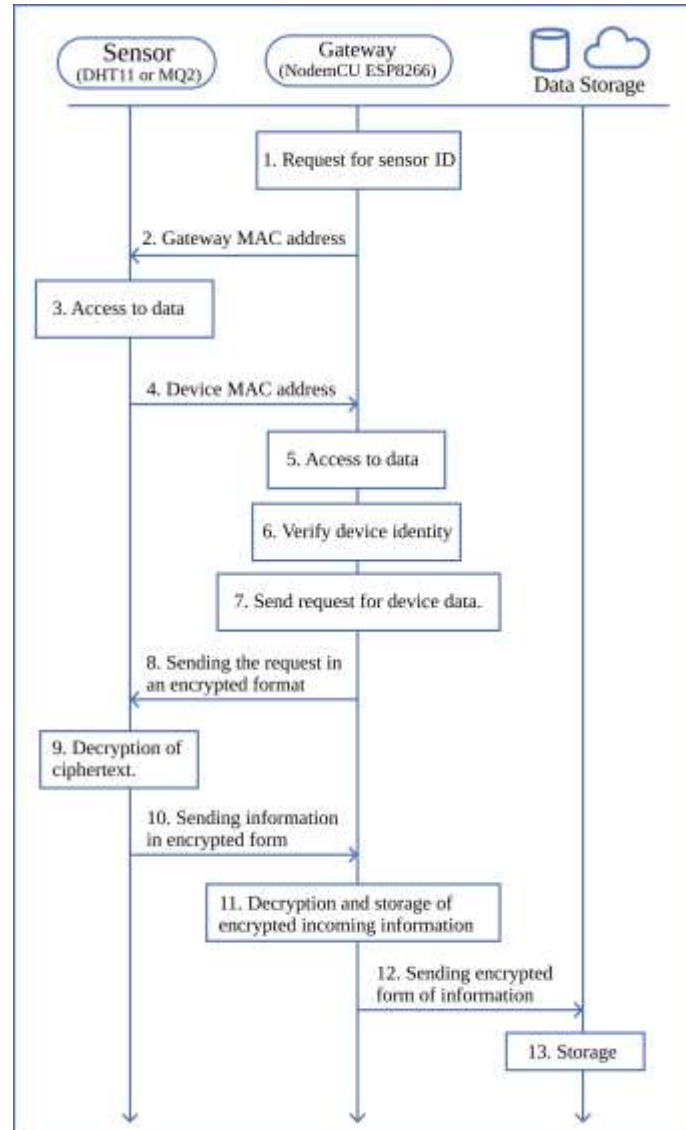


**Figure 4.** Gateway devices recognition and data collection scheme

#### 4.CONCLUSIONS

The growth of the Internet of Things (IoT) has been remarkable in both research and industry. However, security and privacy vulnerabilities have emerged as significant challenges in IoT. Blockchain technology, originally developed for the Bitcoin cryptocurrency, has shown potential in addressing the security and privacy concerns of peer-to-peer networks with similar topologies to IoT.

Only gateways registered to the blockchain should be able to send data, and only sensors or devices registered to gateways should be able to send data. It must be reliable, the data cannot be changed. Blockchain technology is a decentralized distributed database. So it is not centrally managed, data is stored in multiple databases. In the blockchain, blocks are created by holding the hash value of the previous block header. This ensures that no data in the blockchain can be changed when a new block is added. In any change to be made, the chain is broken and is not accepted by the miner or miners. The slightest change to be made in each data that passes through the summary function causes a major change in the summary of the data. This causes a change in the chain structure and an unacceptable situation arises.

All data is recorded anonymously. According to the users who request the data, they are registered in the blockchain.

The smart home gateway should be designed to be resilient against potential attacks. Given that the media network and IoT are continually evolving, the attack methods targeting existing smart home gateways are constantly evolving as well. Moreover, IoT devices are usually resource-constrained, which means they have limited computing power and battery capacity. Under these conditions, an attacker can identify various attack scenarios depending on the target device.

In this study, a blockchain-based smart home application was implemented. According to the results obtained, a safer and more efficient smart home storage system in terms of privacy has been obtained.

The way data is stored in the cloud is often unstructured, which can make it difficult to manage and track. In contrast, blockchain technology offers a structured way of storing data that can be easily tracked using a unique hash key for each block. The blocks are linked together in a chain with the hash key of the previous block, providing a transparent record of all data transactions on the network. This data is validated and can be accessed by nodes on the network while ensuring the anonymity of the user. Additionally, users can be securely removed from the system to prevent third-party access to their information. By integrating the cloud with

blockchain, businesses can increase their trust and offer on-demand services. Blockchain offers several key advantages over cloud computing, such as data transparency and authorization, and can provide cost-effective solutions. Therefore, adopting blockchain can enhance the security of data in the cloud.

## REFERENCES

1. Stojkoska, B.L.R. and K.V. Trivodaliev, *A review of Internet of Things for smart home: Challenges and solutions*. Journal of cleaner production, 2017. 140: p. 1454-1464.
2. Kim, Y., Y. Park, and J. Choi, *A study on the adoption of IoT smart home service: using Value-based Adoption Model*. Total Quality Management & Business Excellence, 2017. 28(9-10): p. 1149-1165.
3. Fisk, M.J., *The implications of smart home technologies*, in *Inclusive housing in an ageing society*. 2001, Policy Press. p. 101-124.
4. Wilson, C., T. Hargreaves, and R. Hauxwell-Baldwin, *Benefits and risks of smart home technologies*. Energy Policy, 2017. 103: p. 72-83.
5. Wang, J., et al., *Energy efficient routing algorithm with mobile sink support for wireless sensor networks*. Sensors, 2019. 19(7): p. 1494.
6. Pal, D., et al., *Analyzing the elderly users' adoption of smart-home services*. IEEE access, 2018. 6: p. 51238-51252.
7. Shin, J., Y. Park, and D. Lee, *Who will be smart home users? An analysis of adoption and diffusion of smart homes*. Technological Forecasting and Social Change, 2018. 134: p. 246-253.
8. Sanguinetti, A., et al., *What's energy management got to do with it? Exploring the role of energy management in the smart home adoption process*. Energy efficiency, 2018. 11(7): p. 1897-1911.
9. Statista. *Smart Home penetration rate forecast in the world from 2017 to 2025*. 2022 [cited 2022; Available from: <https://www.statista.com/forecasts/887636/penetration-rate-of-smart-homes-in-the-world>]
10. Zhao, W., et al., *ETC-IoT: Edge-node-assisted transmitting for the cloud-centric internet of things*. IEEE Network, 2018. 32(3): p. 101-107.
11. Han, D.-M. and J.-H. Lim, *Design and implementation of smart home energy management systems based on zigbee*. IEEE Transactions on Consumer Electronics, 2010. 56(3): p. 1417-1425.

12. Alam, M.R., M. St-Hilaire, and T. Kunz, *Peer-to-peer energy trading among smart homes*. Applied energy, 2019. 238: p. 1434-1443.
13. Sharma, P.K., S. Rathore, and J.H. Park, *DistArch-SCNet: blockchain-based distributed architecture with li-fi communication for a scalable smart city network*. IEEE Consumer Electronics Magazine, 2018. 7(4): p. 55-64.
14. Gram-Hanssen, K. and S.J. Darby, "Home is where the smart is"? *Evaluating smart home research and approaches against the concept of home*. Energy Research & Social Science, 2018. 37: p. 94-101.
15. Li, M., et al., *Smart home: architecture, technologies and systems*. Procedia computer science, 2018. 131: p. 393-400.

# INVESTIGATION OF THE CHARACTERISTICS OF AA6060 ALLOY UNDER THREE-POINT BENDING USING EXPERIMENTAL AND NUMERICAL METHODOLOGIES

Devran Demir<sup>1</sup>, Bora Şener<sup>2</sup>, Emre Esener<sup>\*1</sup>

<sup>\*1</sup> Department of Mechanical Engineering, Bilecik Şeyh Edebali University, Bilecik, Turkey

<sup>2</sup> Department of Mechanical Engineering, Yildiz Technical University, İstanbul, Turkey

devran.dmr41@gmail.com, borasen@yildiz.edu.tr, emre.esener@bilecik.edu.tr

## Abstract

In this study, the deformation behavior of 6060 aluminum alloy profile structure under three-point bending load was investigated experimentally and numerically. In this purpose, the use of crash-critical profile structures, which are used to increase safety against collisions, especially in automobiles, are examined. Within the scope of the paper, three-point bending tests were carried out using aluminum 6060 alloy, which has elliptical cross-section geometry with 100 mm and 200 mm span distances and 5 mm punch radius has been obtained experimentally. As a result of the experimental studies, it has been determined that the force required for bending of the material is decreases when the distances beetwen the spans increase. In the second step of the study, finite element analyses were performed using  $\sigma$ -based Hill-48 (S) and  $r$ -based Hill-48 (r) plasticity models, and forming force-punch stroke curves and shaped product forms were compared with the experimental results. As a result of the comparisons, it was determined that the forming force-punch storke curves and product forms obtained from finite element analyses were compatible with the experimental results.

**Keywords:** Profiles; Three-point bending; Aluminum alloy, Finite element analyses.

## 1.INTRODUCTION

In recent years, the trend of the world has turned towards vehicles that are more resistant to collisions, lighter and more fuel efficient [1]. For this purpose, automobile manufacturers are working on features such as lightening vehicle parts by preserving their high strength properties at the time of collision and reducing carbon dioxide emissions [2]. On the other hand, automobile accidents such as front and side crashes occur frequently around the world, many reports of car crashes show that side crash has a secondary major accident rate after frontal crash [3]. For this reason, automobile manufacturers have produced components that increase safety in the event of a collision, such as airbags, energy-absorbing steering columns and side door impact beams [4]. In the early 1960s, a beam was placed inside the side door for the first

time by General Motors, in order to prevent the instability of side collisions due to the minimum gap between the car side door and the passenger compartment [4]. The design of the side body elements such as the side door impact beam is rather complicated to arrange the side body elements, which can maintain their rigidity while absorbing the energy during a side impact compared to front and rear impacts [5, 6]. Damage to the side door impact beam during an accident can be simplified to a three-point bending mechanism. Fig. 1 shows a simulative of the three-point bending arrangement.

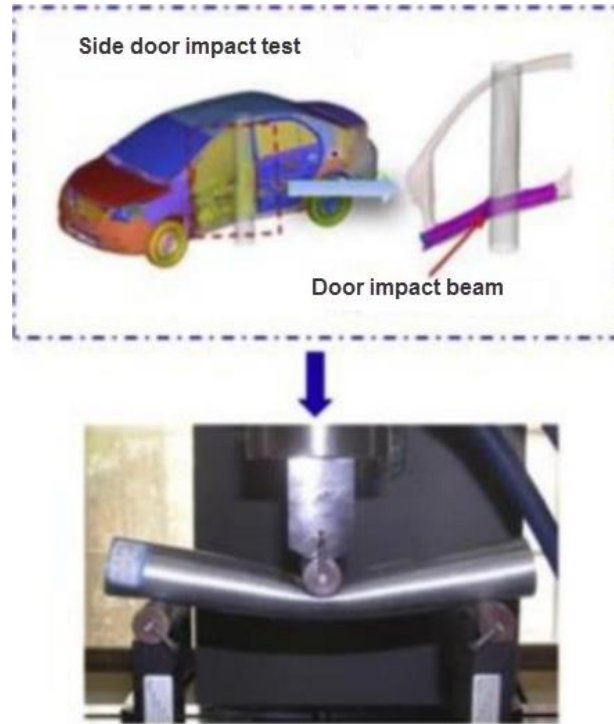


**Fig. 1.** Three point bending test of side door impact beam [7]

These elements are used both to provide safety during a side collision and to distribute the energy distribution more smoothly and effectively in front and rear collision situations [8, 9]. Impact beams are used to reduce the damage to the passengers in the passenger compartment by absorbing the kinetic energy that occurs with the deformation that will occur in the side door during the collision [10, 11].

In the light of the above, it is seen that the cause of death and injury in vehicle accidents today is a side collision with a rate of 25% after the frontal collision. Therefore, the side door impact beams have become a special and important element in vehicles due to important reasons such as the low contact distance with the passenger during a side collision and the change in the energy distribution on the vehicle during the collision. In this context, for an important element to be used for this purpose, a design that includes high energy absorption ability and formability features should be realized. Within the scope of the paper, three-point bending tests were carried out using AA6060 alloy, which has elliptical cross-section geometry with 100 mm and 200 mm span distances and 5 mm punch radius has been obtained experimentally. In the second step of the study, finite element analyzes were performed using  $\sigma$ -based Hill-48 (S) and  $r$ -based Hill-

48 (r) plasticity models, and force-elongation curves, thickness values and shaped product forms were compared with the experimental results.

## 2.GENERAL PROPERTIES OF METHOD

In this study, the behavior of aluminum 6060 material under three-point bending loading was investigated with different process parameters. In the first step of the study, three point bending tests were carried out to determine the bending behavior of the material. The test setup for the three-point bending test is given in Fig. 2.

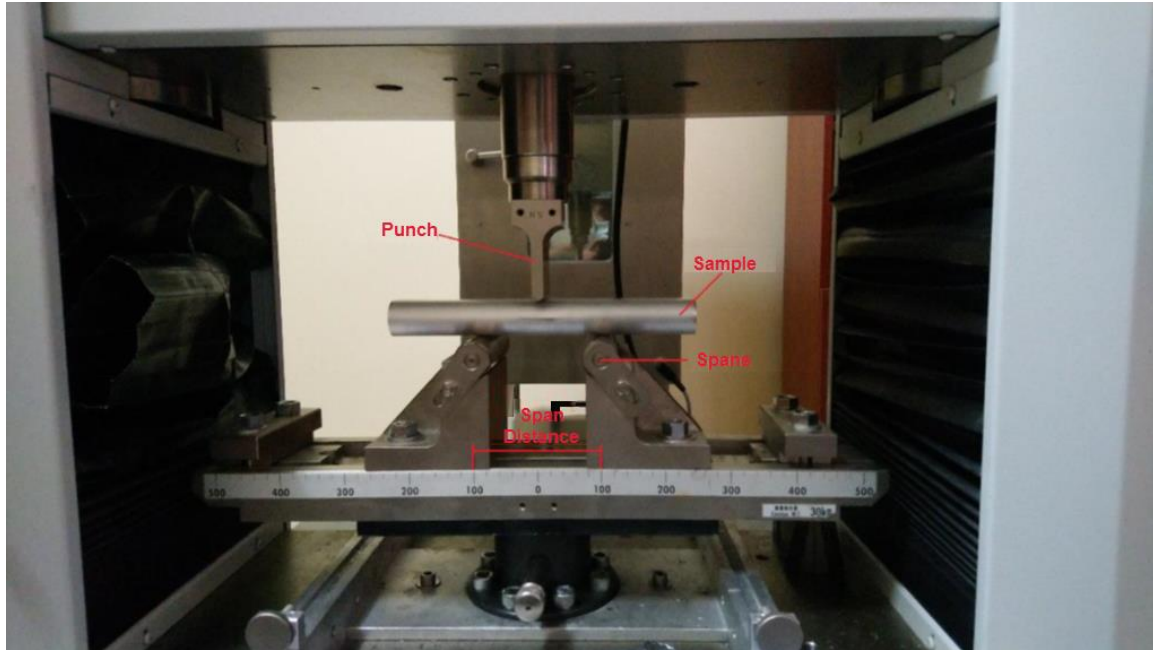


**Fig. 2.** The test setup for the three-point bending test

The radius of the supports used in the experiments is 15 mm. The experiments were carried out using a constant speed of 20 mm/min and a constant forming distance of 40 mm. Experimental studies were carried out using 250 mm long extrusion products with elliptical cross-section geometry, the dimensions of which are indicated in Figure 3.

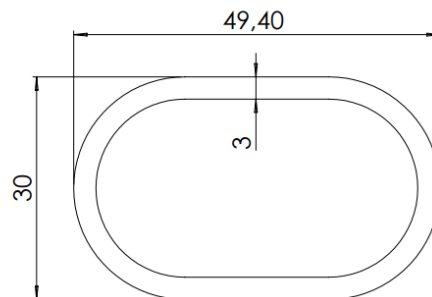


**Fig. 3.** Section geometry of the test sample (All dimension are in mm)



### 3.APPLICATIONS

Comparative images of profiles with different cross-section geometries deformed at different support intervals for 5 mm punch radius after the three-point bending test are given in Figure 4. The forming force vs punch stroke graph obtained during the experiments is shown in Figure 5.

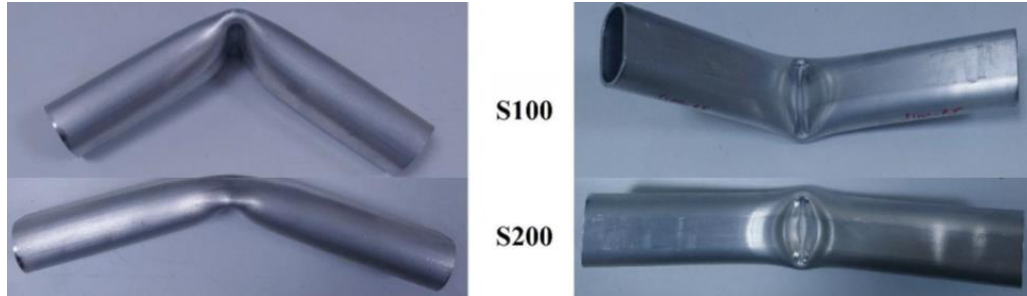


**Fig 4.** Deformed forms of ellipse section geometry at different support distances for 5 mm punch radius

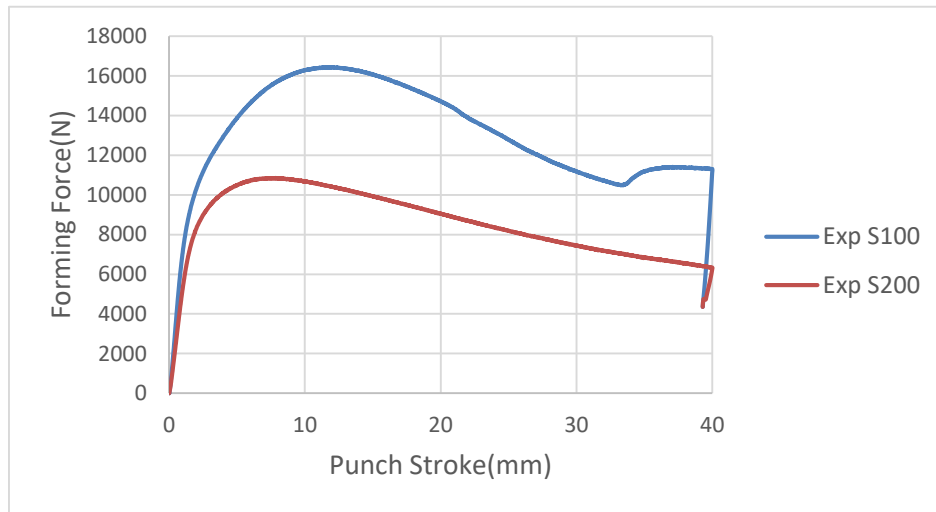


**Fig. 5.** Forming force vs Punch stroke curves of three-point bending samples

It has been observed that there is a decrease in the forming force with increasing span distances, and this effect is thought to be caused by the moment.

In the second stage of the study, the experimental processes were simulated using the finite element method. Dynaform commercial software was used to create the finite element model. Since all calculations are made on the profile and the die tool elements are considered as rigid, the mesh structure of the profile is generated more precisely than the die tool elements. The finite element model of profiles with elliptical section geometry is given in Fig. 6 and the calculation parameters of the finite element model are given in Table 1. The mechanical properties of 6060 aluminum alloy, which are given as input to the material models used in the finite element analysis, are shown in Table 2.

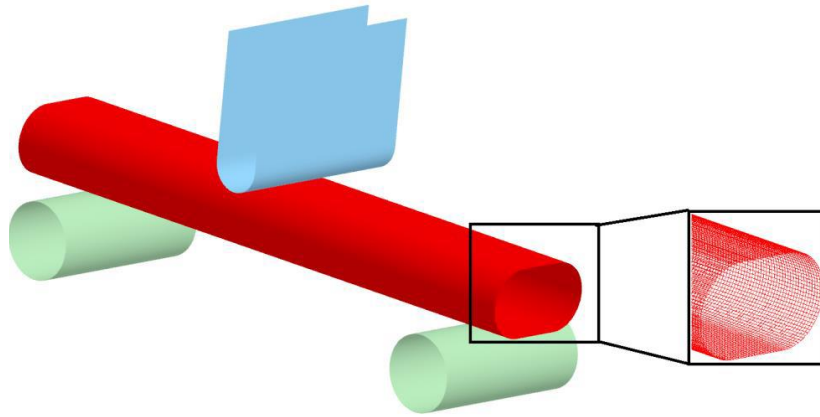


**Fig. 6.** Finite element model of the three-point bending process

**Table 1.** Finite element parameters of three-point bending process

Parameter	Value
Blank element size	1 mm
Number of blank elements	30500
Element formulation	Fully Integrated Shell Element
Number of integration point	7

**Table 2.** Mechanical properties of 6060 Aluminum alloy [12]

Parameter	Value
Modulus of elasticity (GPa)	51
Poisson ratio	0.33
Yield Strength (MPa)	111.8
Strength Coefficient	128.61
$r_0$	0.492
$r_{45}$	0.367
$r_{90}$	1.277

The Hill-48 model, which is the first anisotropic yield criterion, was used in two different versions as the material model in finite element analysis. In the first version, the plasticity parameters were calculated based on the yield stresses and this version was named Hill-48 (S). In the second version, the plasticity parameters were obtained depending on the anisotropy coefficients, and this version was named Hill-48 (r). The finite element analysis results are compared with the experimental forming force-punch stroke curves and are given in Fig. 7 and Fig. 8.

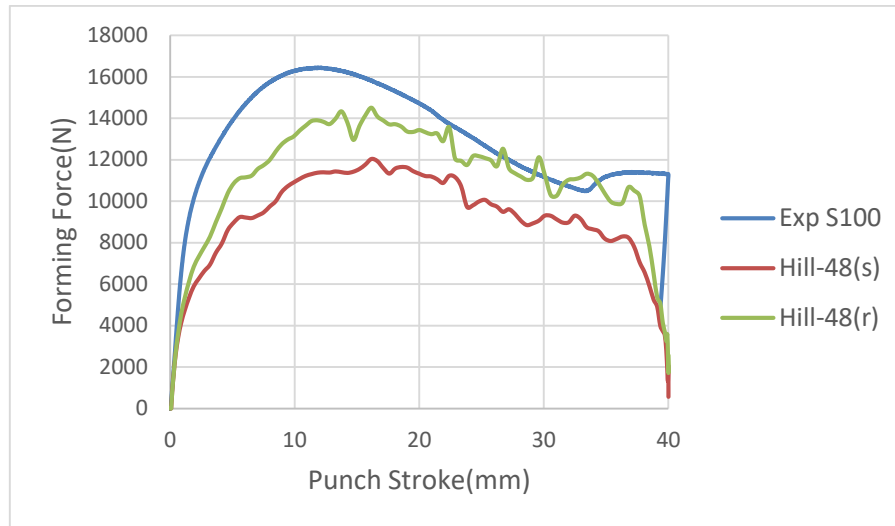


**Fig. 7.** Comparison of finite element analysis results with test results for 100 mm span distance

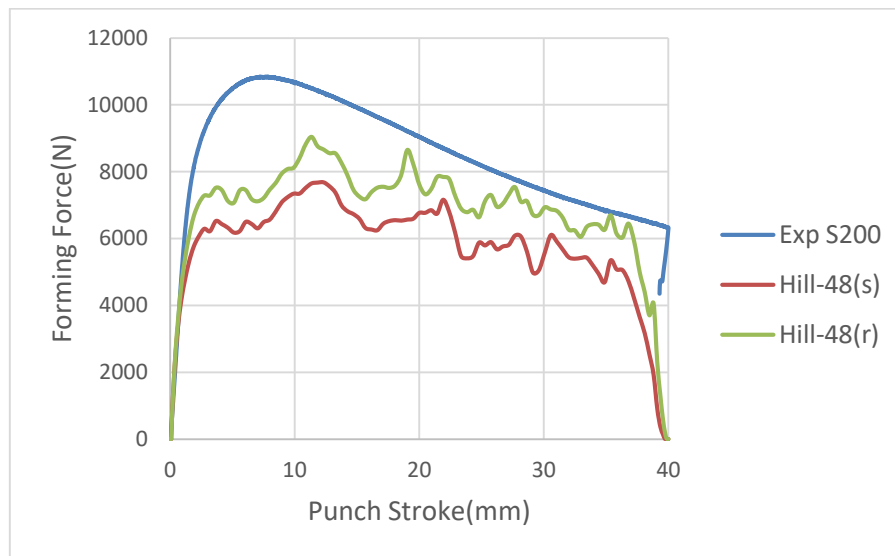


**Fig. 8.** Comparison of finite element analysis results with test results for 200 mm span distance

Finite element analysis results were evaluated on shaped geometries as well as forming force-punch stroke graphs. The deformed form of the profile with elliptical section geometry as a result of the finite element analysis and the experimentally obtained material forms are given in Fig. 9 and Fig. 10 with different span distances for 5 mm punch radius.

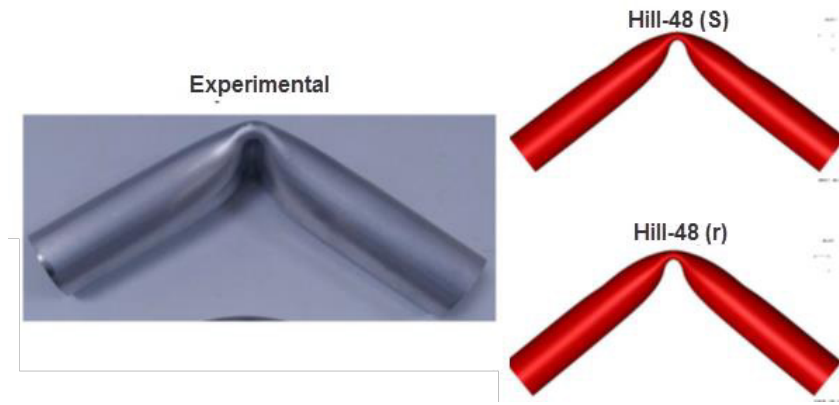


**Fig. 9.** Comparison of experimental and finite element analyzes of profile with elliptical section geometry with 100 mm span distance and 5 mm punch radius



**Fig. 10.** Comparison of experimental and finite element analyzes of profile with elliptical section geometry with 200 mm span distance and 5 mm punch radius

#### 4.CONCLUSIONS

In this study, profiles with elliptical cross-section geometry produced by extrusion method were investigated in experimental and finite element environments. Due to its low weight and high energy absorption capabilities, aluminum 6060 series alloy was used within the scope of the study and it was aimed to examine its usability as a side door impact beam and to examine the performance of plasticity models representing the plastic behavior of the material in the finite element environment. Side door impact beams have generally been subjected to three-point bending in research and testing. Therefore, within the scope of the study, three point bending tests were carried out using 100 mm and 200 mm support distances, 5 mm punch radius, constant speed and constant forming distance. As a result of the experiments carried out, forming force – punch stroke data, material forms after forming were obtained. Ls-Dyna/Dynaform commercial software was used to simulate the experiments performed in the next stage of the study with the finite element method. Stress-based Hill-48 (S) and anisotropy coefficient-based Hill-48 (r) plasticity models were used to determine the plastic behavior of materials in finite element analysis.

As a result of the experiments, it was determined that as the distance between the spans increases, the forming force decreases, and it is thought that this is due to the effect of the

bending moment. When examined as forms after three-point bending, the angle between the two arms of the profiles exposed to bending increases as the distance between the spans increases. According to the results obtained as a result of the finite element analysis, it was determined that the Hill-48 (r) material model based on the anisotropy coefficient gave the accurate results to the experiments. When the results are summarized; It has been observed that the increase in the support distance has a dominant effect on the forming force.

## REFERENCES

1. Nemani K. R. & Arakerimath R, Taguchi Based Design Optimization of Side Impact Beam for Energy Absorption, International Journal for Advance Research in Engineering and Technology, Vol:3, No: 9, 100-104, 2015.
2. Li M. F., Chiang T. S., Tseng J. H., Tsai C. N., Hot stamping of door impact beam, Procedia Engineering, 11th International Conference on Technology of Plasticity, 19-24 October 2014, Nagoya Congress Center, Nagoya, Japan, pp. 1786-1791, 2014.
3. Sookchanchai K. & Hlaih S.S & Uthaisangsuk V., A Geometrical Parametric Study of Side Door Reinforced Beams Under Lateral Impact Load, International Journal of Crashworthiness, Vol.:27, No: 6, 1662-1677, 2022.
4. Shaharuzaman M. A., Sapuan S. M., Mansor M. R., Zuhri M. Y. M., Passenger Car's Side Door Impact Beam: A Review, Journal of Engineering and Technology, Vol.:9, No:1,2180-3811, 2018.
5. Xu H., Zhang M., Gu Z., Li X., Investigation on Hot Stamping Process for Door Beam of Ultra-High Strength Steel, International Journal of Engineering Science and Innovative Technology, Vol.:3, No:1, 384-392, 2014.
6. Lim T.S., Lee D.G, Mechanically Fastened Composite Side-door Impact Beams for Passenger Cars Designed for Shear-out Failure Modes, Composite Structures, Vol.:56, 211-221, 2002.
7. Sun G., Pang T., Zheng G., Song J., Li Q., On Energy Absorption of Functionally Graded Tubes Under Transverse Loading, International Journal of Mechanical Sciences, Vol.:115, 465-480, 2016.
8. Cerniauskas E., Kersys A., Lukosevicius V., Saproganas J., Investigation of Anti intrusion Beams in Vehicle Side Door. Mechanika, Vol.:6, No:86, 11-16, 2010.
9. Sonawane C.R & Shelar L.A., Strength Enhancement of Car Front Bumper for Slow Speed Impact by FEA Method as per IIHS Regulation, Journal of The Institution of Engineers, Vol.:99, No:5, 599-606, 2018.

10. Abdollah M., F., Hassan R., Preliminary Design of Side Door Impact Beam for Passenger Cars Using Aluminium Alloy, Center of Advanced Research on Energy, Vol.:5, No:1, 11-18, 2013.
11. Tanabe H., Yamazaki K., Akada H., Miyasaka A., Iwasaki T., High-Strength Steel Tubes for Automobile Door Impact Beams, Nippon Steel Technical Report., 55-60, 1995.
12. Liao J., Xue X., Barlat F. & Gracio J., Material Modelling and Springback Analysis for Multi-stage Rotary Draw Bending of Thin-walled Tube Using Homogeneous Anisotropic Hardening Model, International Conference on Technology of Plasticity, 1228-1233, 2014.

# Development of Ontologies Through Maintenance

Halil Arslan<sup>\*1</sup> İhsan Tolga Medeni<sup>1</sup> Tunç Durmuş Medeni<sup>1</sup>

<sup>1</sup> Department of Management Information Systems, Faculty of Business Administration,  
Ankara Yıldırım Beyazıt University, 06970, Esenboğa Çubuk/Ankara/Turkey

halilarslan5006@gmail.com, ihsantolgamedeni@aybu.edu.tr, tdmedeni@aybu.edu.tr

## ABSTRACT

In computing and information sciences, complex representational relationships in concepts make the process challenging for scientists and engineers. Conceptual knowledge provides solutions to systems that require interaction between teams, thanks to its ability to successfully discover relationships between concepts. Conceptual knowledge, whose discovery continues manually, is often inadequate because it involves subjective interpretations and judgments, is time-consuming, and has scalability problems. With the transition to automated systems, it can contribute to accelerating processes and minimizing conceptual complexity. Ontologies have an important role in managing and modeling conceptual relationships. Ontology systems realize digital reflections of physical entities, domains and relationships. Artificial intelligence technologies (machine learning methods) contribute to the automatization of these reflections. Systems need maintenance and renewal for their sustainability. The idea of ontology maintenance has emerged due to the fact that institutions and organizations are affected by environmental changes. In this study, the requirements of maintenance are examined through the BIHAP ontology of the Turkish Ministry. In the study, the process of determining the ontology tasks and requirements in a collective working environment by collaborating with participants such as software developers, system analysts, system developers, end-users, government officials was carried out through academic reviews and technical approaches. The study is measured by qualitative study. As a result of the approaches, the basic requirements of the ontology maintenance phase were revealed. The results emphasize the importance of ontology maintenance in ontology tasks.

**Keywords:** Ontology Maintenance, Artificial Intelligence, Machine Learning



## 1.INTRODUCTION

Knowledge/Information Systems is an academic and engineering field that provides software and technology-supported management of interdisciplinary information. It enables the presentation, processing and reusable resource formation of many subsystem components with the information used according to the subject of the research. Scientists, engineers and users will be able to keep their data systematically thanks to information systems [1]. The constant renewal of the world of information and informatics shows that systems always need control processes. Control processes basically evaluate situations such as updating information, eliminating errors and not including information that is contrary to the system [2]. Today, systems ensure the existence of the results obtained by subjecting the inputs suitable for their purposes to certain processes. In this context, a system cycle is created. Control processes are needed at every stage of the system cycles. System control processes are built on system maintenance practices. System maintenance ensures the continuity of a system's life cycle and is extremely important for optimization [3]. Through system maintenance, the consistency in inputs increases and complexities and errors in the system are eliminated. With the advancement of technology, the use of information/information systems in human life has increased [4]. As a result of this situation, big data has emerged. The management of the use and modeling of this data in the developed systems causes difficulties such as classification, scaling and control. Artificial intelligence technologies, which are used interdisciplinary by system developers, are preferred because they have the ability to produce optimal solutions to problem formations with approaches such as analyzing, understanding, interpreting, inferring, scaling, controlling, data generation against these difficulties. Artificial intelligence technologies aim to minimize optimization problems with supervised / unsupervised learning techniques. The use of artificial intelligence technologies for an optimal information/information system contributes to the reduction in the error rates of operational processes and the prolongation of the life cycle in maintenance and repair. Considering these situations, system developers prefer network technologies that offer fast and widespread development opportunities. Network technologies are also the most convenient resource in terms of accessibility for users. These technologies started in the early 1960s using the Internet Protocol (IP). There are many network technologies developed today. Among the network technologies, Semantic Web technology provides an understandable description, interpretation, use and search of data in accordance with the natural language structure for the search of information. Semantic Web technology has been developed in a structure suitable for software to easily find, access and process data. In these structures, ontologies are used in the data modeling phase. Ontologies contain a representation, formal name and definition of properties and relationships between concepts, data and entities in the data modeling process. They are also a practical tool for conceptualizing what is expressed in computer format (Brodie et al. 1984; Guarino 2009). Accordingly, ontologies tend to be ubiquitous. They are seen as a magic wand for many applications such as database integration, peer-to-peer systems, e-commerce, application programming interfaces (APIs), semantic web services, social networks (Fensel 2004). Ontologies, which offer development opportunities suitable for many fields, should be developed with specific task definitions in order to be developed for the part or the whole of the system [5]. In the life cycle of ontology-based systems, mapping, matching and alignment,

translation, versioning, integration, debugging definitions are determined. In the maintenance implementation phase of ontology-based systems, the suitability of the tasks defined in line with the identified needs is examined and it is seen that the tasks are the most appropriate approaches in terms of maintenance.

## 2.GENERAL PROPERTIES OF METHOD

### 2.1 Maintenance and Ontology Tasks

Maintenance is defined as corrective maintenance methodologies to eliminate detected faults, adaptive maintenance methodologies to adapt to system changes and remedial maintenance methodologies to improve performance by adding new features and functionality to the system. Separate methodologies are developed for the needs of the system in maintenance life cycles. This situation creates the need for system developers to create a standard method for common maintenance methodology and for researchers to create a documentation that can be applied to all kinds of software-based systems. In this context, a common standard for software maintenance [6] and the maintenance requirements of ontologies, which are the knowledge bases of applications and systems, can contribute to the creation of a methodology. However, the semantic part of maintenance and its relationship with software systems is a problem that has not been clarified. In general, a standard that does not include semantic relationship definitions may not be sufficient to meet the requirements. In the literature, a maintenance framework can be created by looking at separate tasks for ontology maintenance purposes. The maintenance approach is found under different headings and in different studies. Ontology maintenance is proposed to focus on the management of ontology changes defined to unify non-static domains [7]. By analyzing ontology changes, key tasks such as mapping, matching and alignment, translation, versioning, integrations and debugging are identified (Figure 1).

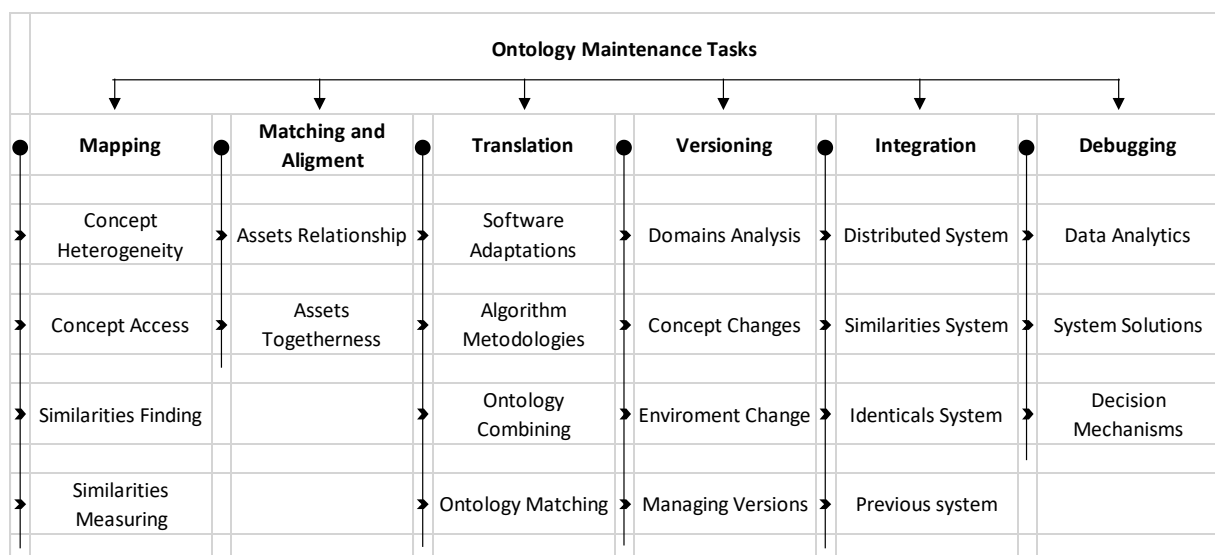


Figure 1: Ontology Maintenance Tasks

**2.1.1 Ontology Mapping**, the ontology task is defined as the task of identifying and measuring the similarity of concepts in terms of meaning [8]. In the study, the aim of the task is to solve the heterogeneity problem that arises as a problem in the ontology [9]. In cases where the

ontology is insufficient to meet the system requirement, ontology mapping is required to support and access the ontologies required for use [10]. Here, this task provides a common layer for ontologies that can respond to new needs in cases where they are insufficient. Mapping also enables different ontologies to be used together and thus helps to support maintenance [11]. Similarity-based approaches have been mostly applied for ontology mapping [8].

**2.1.2 Ontology Matching and Alignment**, it defines the relationships between the entities in the ontology infrastructure and each other in the ontology to be used or with the entities of other ontologies accessed [12]. As applied in the ontology mapping task, it aims to find a solution to the problem of heterogeneity and interoperability of ontologies [11]. The goal of the task is defined as finding the relationships between ontology entities used in systems [13].

**2.1.3 Ontology Translation**, the task definition is the realization of transformations suitable for the software language and system infrastructure used to ensure ontology-based development in newly developed systems [14]. Translation of the ontologies to be used together in the system into the system software language and mapping applications of ontology entities are included in the definition [9]. The approach of implementing part or all of the ontology into the system using an auxiliary tool module is defined as translation [15]. In addition, merging the ontologies adapted to the software after translation is the definition of the task [17]. In order to transform ontologies, which are symbolic representations of knowledge, into one another, we looked at the translation task. This task is identified as an important task for the sustainability of the system and the understandable implementation of the ontology. In these perspectives, the translation of the ontology language into another ontology is the main goal [18].

**2.1.4 Ontology Versioning**, Managing the versions of ontologies during the development stages is the definition of the task (Klein and Fensel, 2013). Changes in the area where the application is used, updating of assets, and applications for system adaptations trigger versioning (Kohantorabi, 2016). Versioning management is a requirement for systems developed in distributed environments as an infrastructure. If there is an ontology-based document management system, changes and innovations in documents can also be supported by versioning (Helfin et al, 2004).

**2.1.5 Ontology Integration**, it is the task of integrating a whole or part of an ontology from one or more ontologies into another ontology other than the ontology used [20]. In this definition, the creation of a new ontology using old ontologies or the development and merging of a single ontology from several separate ontologies is defined as integration [9]. For the integration of different ontologies, integration for change management was used as a process step in managing the ontology change task in distributed system infrastructures [21].

**2.1.6 Ontology Debugging**, the task of identifying and removing outlier and inconsistent data from the ontology as a result of data analysis is defined as debugging [9]. In addition, debugging can be applied when the ontology is completely retired. However, in this research, the debugging task is not defined due to the lack of change in the system infrastructure in ontologies that are not merged. Debugging has been applied to repair unwanted concepts in the OWL ontology file [18]. The concept of debugging has been applied to correct semantic errors in any changes reflected through ontology debugging, including translation [19].

### 3.APPLICATIONS

#### 3.1 Ontology-based BIHAP System Tasks

The Ministry of Development of the Republic of Turkey launched the BIHAP (Information Map Research and Development Project) project in April 2013 to keep public data in the E-Government System infrastructure and to visualize the information. The project was developed and completed until October 2014. The developed project system is built on an ontology. Instead of developing the system through a database, the system developers preferred the ontology structure that is suitable for the knowledge base. The information of all departments within the Ministry was included as a single knowledge node. All of this information corresponds to more than 60,000 ontology entities. The BIHAP Project aims to expand the scope of the system to include other government agencies. Therefore, the project was chosen as a suitable model for the development of the ontology through maintenance. After the development of the system, a review was conducted to see the necessity of the maintenance process of the ontology maintenance implementation. The review was conducted with the ministry staff and the project system developer team. To increase the validity of the results, face-to-face interviews with open-ended questions were conducted with volunteers from the review team. Twenty-six participants participated in the review. Participant responses were received by email. These participants were divided into three groups: system developers, end users, and both developers and users. Developers are the participants who ensure the ontology-based development of the system and its compatibility with other systems. End-users are the participants who define the official and internal information within the ministry and create the information/concept maps that should be included in the system. Participants specified as "both" are defined as participants who have both developer and end-user participant group competencies. "Both" can be defined as managers or semantic relationship developers experienced in information/information systems. In these reviews, nine participants were identified as system developers, eleven as system end-users, and the remaining six as "both". Two data collection activities, system reviews and open-ended interview questions, were included, resulting in the table below.

#### 3.2 BIHAP Project System Structure Questionnaire, Ontology Approach (Questionnaire, Ontology)

The review includes participants' approaches to ontology. Approaches are categorized as whether the participant has knowledge about ontology or not. Participants with knowledge are categorized as low, medium and high level. As a result of this grouping, only two users did not have any ontology knowledge, while twenty-four participants were determined to have knowledge. Among the participants with knowledge, nineteen participants had a medium level of ontology knowledge and five participants had a high level of ontology knowledge. In addition to the existing answers, information about the ontology requirement of the participants, the ontology awareness of the participants after using the system, and the current system status in meeting the information requirements were obtained. Table 1 shows the ontology need, ontology awareness and approaches to responding to the knowledge requirements of all users.

**Table 1. Ontology Approach of All Participants**

	Before System		After System
	Ontology Need	Ontology Awareness	Response to Information Needs
Yes	9	5	16
No	17	21	10

The distribution of the answers according to the respondent groups is presented in Table 2. This distribution sub-grouping ontology need and ontology awareness shows the approaches before and after the implementation of the system. The need for ontology is not seen as a need by the majority of developers. Only two developers indicated the need for an ontology. However, five of the eleven end-users felt this need before the system. Two of the participants in each of the two groups stated this need. As for the awareness of the ontology approach, as indicated in Table 2, the developers did not know the concept of the ontology existed. Four of the end-user participants were aware of the existence of the ontology. Among the remaining two participants, only one participant knew about it. While the awareness of the ontology in general was very low, the "yes" answers increased after the implementation of the system. Among the developers and end-users, six respondents answered yes and four of the both respondents answered yes. This result shows that maintenance of the developed system is necessary to support the sustainability of the system. In order to see which system is currently required, it should first be determined which tasks should be implemented in the ontology.

**Table 2. Distribution of responses according to groups**

Participants	Responses	Before System		After System
		Ontology Need	Ontology Awareness	Response to Information Needs
Developers	Yes	2	0	6
	No	7	9	3
End Users	Yes	5	4	6
	No	6	7	5
Both	Yes	2	1	4
	No	4	5	2
Total	Yes	9	5	16
	No	17	21	10

### 3.3 System Questionnaire, Ontology Maintenance Tasks

In this part of the system review, users' expectations of the system are measured based on ontology maintenance tasks. Each ontology task is coded as shown in Table 3.

**Table 3. Ontology tasks and given abbreviation**

Ontology Maintenance Tasks	Abbreviation
Mapping for Ontology	OM
Matching and Alignment for Ontology	OMA
Translation for Ontology	OT
Integration for Ontology	OI
Versioning for Ontology	OV
Debugging for Ontology	OD

Task groups to be implemented according to the user group were investigated. Table 4 shows the results of the research for the participant groups of nine developers, eleven end users and six both. Among the participant groups, the majority of the developers responded ontology mapping, ontology translation and ontology debugging. Two of the developers responded that these tasks should be used together. In addition, two of the developers stated that integration and versioning tasks should be included. There is only one developer who stated that all of them should be included in this task grouping. The other group of respondents, the majority of end users, indicated that translation and debugging tasks should be implemented. In this group, two participants responded that both tasks should be used together. They also mentioned the inclusion of mapping in these tasks. Three end-user participants answered that only the debugging task would be sufficient. No one in the end-user group answered that all of them should be implemented. The last of the participant groups, the both group, mostly mentioned versioning and debugging tasks together as a response. There were four participants who included the mapping task in these tasks. Two of these four participants did not specify any other task, while the other two included the matching and alignment task and the translation task. In addition, one participant in this group responded to all tasks. When all of the individual responses are analyzed, only two out of twenty-six participants indicated all tasks as responses. When analyzed according to the task descriptions, nineteen participants responded to the debugging task, fifteen to the translation task, fourteen to the mapping task, eleven to the versioning task, eight to the matching and alignment task, and eight to the integration task. In the details of their groupings, ten participants mentioned integration and debugging tasks together. Eight participants mentioned mapping and translation together. Seven participants combined the mapping and alignment task with the translation task. Six participants mentioned mapping, translation and debugging tasks together.

**Table 4. Ontology Task Grouping by Participants**

Task / Participants	OM	OMA	OT	OI	OV	OD
Developer	X	X	X			
Developer	X	X	X	X	X	X
Developer	X		X	X	X	X
Developer	X			X	X	
Developer	X					X
Developer	X					X
Developer			X		X	X
Developer		X	X		X	X
Developer			X			X
End User	X	X		X		
End User	X		X			
End User	X		X			X
End User	X		X			X
End User			X	X		
End User		X	X			
End User				X		X
End User					X	X
End User						X
End User						X
End User						X
Both	X	X	X	X	X	X
Both	X	X	X		X	X
Both	X			X	X	X
Both	X				X	X
Both		X	X			
Both			X		X	X
Total (26)	OM (14)	OMA (8)	OT (15)	OI (8)	OV (11)	OD (19)

### 3.4 Interview

In order to identify the relationship between maintenance and ontology tasks, a detailed investigation was carried out with the participants in the process of defining the tasks who accepted the interview request. In particular, participants from the BIHAP project were invited. The interview request was sent to seventeen participants in the system development team. Six of the developers were identified as both, as they were separate end users, and eleven were identified as developers, as they were only system developers. Only six participants accepted the invitation. With the participants who accepted, different interview meetings were organized for each participant at specified times and dates. The results are described as expert



perspectives. The questions asked during the interview were designed to capture the ontology tasks and maintenance. Four open-ended questions were asked during the interviews. These questions were designed to measure participant experience, the relationship between ontology tasks and ontology maintenance requirements from the participant's perspective, suggestions for maintenance requirements other than existing ontology tasks, and sustainable system expectations with the implementation of the given ontology tasks. Each ontology task in the system was explained before the interview. In addition, the purpose of each question was explained to the participants. The answers were organized and tabulated for this study. The answers obtained in line with the participant responses are shown in a table after each question. As a result of the answers received from the participants, the following data were obtained:

### **3.4.1 Question 1: Prior to the ontology-based BIHAP project, do you have any professional or academic experience associated with knowledge/information systems projects?**

This question was asked to measure the participants' experience with the concept of ontology development in information/information systems from an academic or professional perspective. According to the academic title of the participants, it is known that Participant 1, Participant 5 and Participant 6 have PhD degree experience, while Participant 2, Participant 3 and Participant 4 have master's degree experience. Project development and maintenance requirements are categorized into two different categories: academic or professional information/information system project experience. In terms of academic project experience, Participants 1, 3, 4 and 6 have an academic background in ontology systems and information/information systems management. Participants 2, 5 and 6 have project experience in information/information systems. Participant 1 has no project experience in information/information systems. However, his experience with document management systems was evaluated in terms of other project experiences. Among the participants who accepted the invitation, participant 2 is the most important participant in terms of information/information systems project experience. Participant 2 is a member of another ministry project team apart from the BIHAP project. He also contributed to the development of the ontology infrastructure from the first stage of the ontology-based system development process until its finalization. Participant 3 does not have computer programming / software development skills. He also does not have an academic project development background. Only in his doctoral thesis, he conducted research based on web service compositions through ontologies in the decision-making phase of information systems. Participant 4 has no experience in developing ontology-based systems professionally. From an academic point of view, Participant 4 is currently working on ontology learning as a thesis topic in her PhD study. Participant 5 has the highest level of knowledge and experience among the participants in terms of academic and professional project development experience. As a project leader, Participant 5 applies his experience in different Governmental organizations projects. Participant 6 is a professional in terms of both experiences. Participant 6 holds a PhD degree in Information/Information Management research. He also received project support from the Ministry of Industry in 2009 from the Techo-Enterprise program related to information/information visualization systems. As a result of the answers given, all of the participants have some basic knowledge about ontology tasks in the BIHAP project and their contribution to the maintenance application.

**Table 5. Participants' Academic and Project Experience to Question 1**

Participants	Academic Experiences		Project Experiences	
	Master's Degree	PhD	Academic	Professional
P1		x	x	
P2	x			x
P3	x		x	
P4	x		x	
P5		x		x
P6		x	x	x

### 3.4.2 Question 2: Are the ontology tasks specified in this research sufficient to support ontology maintenance requirements?

This question explores participants' perspectives on the ontology tasks implemented in the BIHAP system to support ontology maintenance. The collection of system process descriptions, ontology task descriptions and 5W1K (What, Where, How, When, Why and Who questions) data from the Ministry's system employees provided important information for the formation of the basic ontology structure. The structure formed in line with the information obtained contributed to the realization of maintenance. As a result of the answers given, it was determined that ontology translation was necessary in the transformation from the basic document to the ontology. In the participant group, Participants 1, 2, 3, 5 and 6 therefore defined ontology translation as the main task of ontology maintenance. From Participant 1's point of view, mapping, mapping and alignment and versioning tasks are not currently implemented. On the other hand, ontology debugging has been implemented for the creation of ontology entities and the maintenance of ontologies. When the conversion of the developed ontology entities into different document formats after their control and integration into the ontology were examined, these two activities made translation and integration tasks mandatory in the ontology maintenance process. Participant 2 states that the transformation of the documents to be used in the system into ontology and their inclusion in the existing ontology is a versioning task. It shows that the process of adapting the document to the system is a natural part of ontology maintenance with the ontology versioning task definition. Participant 3 states that all these tasks, except ontology integration, are implemented in maintenance activities. This participant emphasizes the existence of ontology maintenance by specifying the system interfaces related to each ontology task. Another important point to be noted is that from Participant 3's point of view, the integration task in ontology systems can be applied in order to be able to associate knowledge bases and use systems between government agencies. Participant 4 states ontology matching and alignment and debugging tasks to correct semantic errors and conceptual disorders in ontologies. From Participant 4's point of view, these tasks are sufficient to support future maintenance requirements. Participant 5 responded that ontology debugging and ontology translation are necessary. He also mentioned that there is versioning support available in the system, but it is not in active use. Among the participants, the integration task was mentioned only by participant 6. Mapping, integration, matching and

alignment tasks were mentioned together in collecting terms that meet the structural characteristics of institutions and associating them with the system. The answers are summarized in Table 6. As a result, it is seen that the ontology debugging task was mentioned by all participants. Five respondents mentioned the translation task, three mentioned the matching and alignment task, and two mentioned the ontology mapping task.

**Table 6. Ontology tasks mentioned by the participants**

Participants	OM	OMA	OT	OI	OV	OD
P1			x			x
P2			x		x	x
P3	x	x	x		x	x
P4		x				x
P5			x			x
P6	x	x	x	x	x	x

### 3.4.3 Question 3: Are there any tasks you can suggest to meet the maintenance requirements of ontologies?

The scope of the problem is to collect appropriate job descriptions that are recommended to be included in order to identify the issues where ontology maintenance is insufficient [Table 7]. With their analysis in this direction, the participants stated that there should be different tasks in ontology maintenance. Participants 1 and 6 stated that search/scan maintenance tasks should be included in the process in order to obtain fast maintenance results in response to the increase in the number of users caused by the widespread use of information/information systems. Participant 1 suggests a gap analysis task for knowledge/asset management in ontologies and knowledge/asset structures that need to be integrated for adaptation to future developments. Participants 2, 5 and 6 suggested feasibility and gap analysis by including the feasibility task to determine the necessary preliminary preparation and possible situations. Participant 3 suggested meta transformations in the ontology as a maintenance task to adapt the ontology to the developing technology. It can also facilitate the alignment of ontology structures in the BIHAP project structure to be included for integration purposes. Participant 4 suggested ontology learning as a maintenance task to support the dynamic, non-autonomous matching and alignment of entities in the ontology using artificial intelligence systems models. Participant 5 suggested that the task of quality and measurement in maintenance should be included to standardize ontology systems. Participants 1, 5 and 6 stated that human aspects are needed in administrative management control in response to the problems in controlling ontology maintenance on the system side. However, no specific ontology task was given to support the suggestion.

**Table 7. Suggestion ontology tasks for maintenance by participants**

Participants	Feasibility and Gap Analysis	Ontology Search and Crawl Development	Administratively Supported Users Aspect	Management Services	Ontology Based Meta Transformations	Ontology Learning	Quality and Standardization
P1	x	x	x	x			
P2	x						
P3					x		
P4							
P5	x		x			x	
P6	x	x	x	x			x

#### 3.4.4 Question 4: Is it a sustainable system model in line with the ontology maintenance task responses for the ontology-based BIHAP project?

As a result of the answers given to the question, it measures whether the system is sustainable with the implementation of the existing ontology tasks and the ontology tasks proposed by the participants [Table 8]. Participants 1, 2, 3, 4 and 6 stated that it would be sustainable with the implementation of maintenance tasks. However, Participants 1 and 6 re-state the needs for the requirements of information management and the situations that may occur on the user side. Participant 5 stated that it would not be sustainable.

**Table 8. Participants' approach to sustainability of the Ontology-based BIHAP system**

Participants	Trust in Sustainability		No Trust in Sustainability
	Without New Tasks	With New Challenges	
P1		x	
P2	x		
P3	x		
P4	x		
P5			x
P6		x	

## 4.CONCLUSIONS

As a result of the study, ontology maintenance, ontology tasks and sustainability, sustainability definition and improvement indicators give the results.

## 4.1 Ontology Maintenance

BIHAP is the appropriate project for the inclusion of approaches to ontology maintenance by users. Therefore, the link between ontology maintenance requirements and ontology tasks in the BIHAP system was analyzed at the user level. Out of the six participants, all participants translated ontologies, while five participants translated ontologies (Table 6). Question 3 asked the participants to suggest ontology tasks that might be needed in maintenance requirements. The feasibility/gap analysis ontology task suggested by participants 1, 2, 5 and 6 is realized with the ontology mapping application from existing tasks. The search and crawl improvements ontology tasks proposed by Participants 1 and 6 can be implemented in ontology translation operations from existing tasks. The meta translation proposed by participant 3 can be applied in debugging and translation tasks. The ontology learning task proposed by Participant 4 requires more than one possibility to be applied to all ontology tasks. The suggestion for a user-scale approach by participants 1, 5, and 6, the suggestion for administrative factors in knowledge management by participants 1 and 6, and the suggestion for quality and standardization in ontology maintenance by participant 5 can be taken as supporting ontology tasks in terms of maintenance requirements.

## 4.2 Defining Ontology Tasks and Maintenance

For BIHAP, the results of the ontology maintenance tasks section were considered to determine which ontology tasks should be implemented in the system review (Table 4). Two groupings are important in these results. The first grouping was based on whether the existing task descriptions met the requirement and the second grouping was based on the perspective of improving and correcting the maintenance requirements by using them together. Participants stated that all existing job descriptions should be used. Participants in the developer role pay attention to task alignment in determining task groups since they have system development knowledge. The approach taken by these participants was to include the ontology mapping task and the translation task while also including the debugging task for maintenance due to the changes in the process. For this reason, seven out of the nine developer participants definitely mentioned the debugging task together with tasks other than the debugging task. However, the end-users and the participants in both roles mentioned the debugging task with the same approach. In the overall results, nineteen out of twenty-six participants expressed this view. In the same direction, when we look at the approaches to ontology task definitions, mapping and translation tasks stand out. The majority of the participants stated that these two tasks are important maintenance tasks like debugging tasks. In addition, all of the participants who accepted the interview invitation mentioned the debugging task in performing ontology maintenance. On mapping, these participants were not in the majority. However, in the case of translation, except for one participant, the majority of them mentioned the ontology translation task (Table 6). As a result of all these results, it is seen that in terms of the maintenance approach, application responses were mostly given for correction and improvement reasons. In maintenance requirements, the need for correction indicates corrective maintenance and the need for improvement indicates perfecting maintenance. These situations are effective in determining the requirements depending on the length of time the system is active. In case of obsolescence of systems, corrective maintenance is seen as a need. These types of approaches

were observed to affect the approaches both in the review studies and in the interviews. The ontology-based BIHAP project, which was examined in terms of maintenance, tends to be a high-level system with the realization of the necessary maintenance. In order to achieve this, sustainability will be mostly thanks to the answers given.

### **4.3 Sustainability Definition and Improvement**

Ontology plays an important role for BIHAP to be a sustainable system. All information visualization functions of BIHAP work through the ontology. Therefore, the sustainability of BIHAP depends on the sustainability of its ontology. In the interviews, except for participant 5, the other participants were of the opinion that BIHAP will be a sustainable system with the implemented tasks. Participant 5 has academic and project experience in terms of experience. This has given this participant an important technical and administrative perspective. In Question 3, where approaches to sustainability were examined, this participant suggested the task of maintenance quality and standardization, user factor and feasibility and gap analysis tasks together. This participant states that sustainability will not occur if the improvement suggestion of this participant is not applied to the system. On the other hand, for Participants 2, 3 and 4, the existing ontology tasks are sufficient for a sustainable system. Participants 1 and 6 state that new tasks should be included. The proposed tasks are important to support maintenance and sustainability in terms of improvements and fixes. In addition, ontology search/scanning, complex versioning, meta transformation approach and ontology learning task that provides supervised/unsupervised learning from the autonomous system, which will benefit from the ontology task suggestions given in the interviews, are included in the standard system functions. However, the parts related to ontology gap/feasibility analysis and human factors can be defined as pre-processing step tasks before the ontology tasks. These distinctions help in the appropriate ontology maintenance structure. Furthermore, ontology-based system implementations can be limited to support user needs. As system technological structures mentioned by participant 6, database and XML infrastructures offer the possibility to work faster in visualizing and mapping information/information systems data. The ontology structure may or may not be developed. In case it is not developed, the ontology can be translated into a database or XML structure for sustainability purposes. In addition, ontology-based systems can be ontomatized with artificial intelligence structures and supervised learning methods, and measures and precautions can be taken early. Thanks to the measures and precautions taken, adaptation to developing systems in line with sustainability can be ensured and data uncertainties can be prevented.

### **4.4 Further Work**

The applied academic review should be transformed from a manual to an automated structure for the adaptation of ontology tasks in line with ontology maintenance requirements. Time/resource advantage should be gained through this transformation. By reflecting the requirement demands with artificial intelligence models to information/information management systems, changing trends can increase ontology knowledge base management in BIHAP system structure. In this direction, as part of the ontology knowledge base system, artificial intelligence deep learning techniques applications should be used to transform the



system. A knowledge management model is required for the ontology tasks, development and maintenance processes studied. For future research, this is an important area of study that is open for further study opportunities. However, a structure suitable for an AI-based supervised learning model can be developed to respond to the requirements of different systems. As a result of academic research, ontology structures should be supported by meta-transformation and dynamic/autonomous learning tasks in ontologies built with ontology tasks. With the changes in information/information technologies in the system infrastructures of organizations, ontology-related approaches can be expected to be applied more and more, so ontology maintenance is an open field that awaits more researchers today.

## REFERENCES

1. Kırıl A., Yazılımların Bakım Kolaylığı Ölçümü İçin Yazılım Ölçütleri Önerisi, Yüksek Lisans Tezi, Başkent Üniversitesi, Fen Bilimleri Enstitüsü, Ankara, 2019.
2. Torunoğlu-Selamet D., Eryiğit G., Veri Artırımı için Yarı-Denetimli Bağlamsal Anlam Belirsizliği Giderme, Türkiye Bilişim Vakfı Bilgisayar Bilimleri ve Mühendisliği Dergisi, 14(1), 1-13 2021.
3. Timur M., Kılıç H., İşletmelerde Bakım Onarım Süreci İçin Yenilikçi Bakım Modülü, JOSS Akıllı Sistemler Dergisi, 1(1), 1-13, 2022.
4. Scheneberger S.L., McLean E., Distributed Computing Environment Software Maintenance: Problems of Measurement and Research, Datamation, 15,227-35, 1969.
5. Khalid Abd Alrahman Al-Bakoa A., Software Maintenance Adaptation In Software Companies: A Case Study For Turkey, Atılım University, The Graduate School Of Natural and Applied Sciences, 2021.
6. International Organization for Standardization and the International Electrotechnical Commission, ISO/IEC 14764:2006:Standard for Software Maintenance, [https://mireilleblayfornarino.i3s.unice.fr/lib/exe/fetch.php?media=teaching:reverse:10.1109\\_eeestd.2006.235774.pdf](https://mireilleblayfornarino.i3s.unice.fr/lib/exe/fetch.php?media=teaching:reverse:10.1109_eeestd.2006.235774.pdf), Eylül 1,2006. Erişim Tarihi Aralık 12, 2022.
7. Shaban-Nejad A., A Framework For Analyzing Changes In Health Care Lexicons And Nomenclatures, Master Thesis, Concordia University, Computer Science and Software Engineering, Canada, 2010
8. Couto, F. M., Silva, M. J., & Coutinho, P. M., Measuring Semantic Similarity Between Gene Ontology Terms, Elsevier Science, Data & Knowledge Engineering, France, 2007
9. Flouris, G., Manakanatas, D., Kondylakis, H., Plexousakis D., Antoniou G., Ontology Change: Classification and Survery, Master Thesis, Cambridge University, Foundation for Research and Technology, England, 2007
10. Kalfoglou, Y., Schorlemmer, M., Ontology Mapping: The State of The Art, Master Thesis, University of Southampton, Advanced Knowledge Technologies, Southampton, 2003



11. Ehrig, M., Sure, Y., *Ontology Mapping an Integrated Approach*, University of Karlsruhe, Karlsruhe Institute of Technology, Karlsruhe, 2004
12. Euzenat, J., & Shvaiko, P., *Methodology, Ontology Matching*, Second Edition, Editör: Pavel Shvaiko, Informatica Trentina SpA, Department of Engineering and Computer Science (DISI), Trento, Italy 55-68, 2007
13. Ziembicki, J. I., *Distributed Search in Semantic Web Service Discovery*, Master Thesis, University of Waterloo, Computer Science, Ontario, Canada, 2006
14. Corcho, O., *A Layered Declarative Approach to Ontology Translation with Knowledge Preservation*, PhD Thesis, University of Manchester, United Kingdom, 2005
15. Corcho, O., *A Declarative Approach to Ontology Translation with Knowledge Preservation*, Master Thesis, Universidad Politécnica De, Facultad De Informática, Madrid, 2004
16. Klein, M., *Combining and Relating Ontologies: An Analysis of Problem and Solutions*, Master Thesis, Vrije Universiteit, Amsterdam, 2001
17. Chalupsky, H., *OntoMorph: A Translation System for Symbolic Knowledge*, Master Thesis, USC, Information Sciences Institute, U.S.A., 2000
18. Kalyanpur, A., Parsia, B., Sirin E., and Cuenca-Grau, B., *Repairing Unsatisfiable Concepts in Owl Ontologies*, Master Thesis, University of Maryland, U.S.A., 2006
19. Purohit N., Joshi A., *Pellet: a Practical OWL-DL Reasoner*, Georgia State University, Department of Computer Science, Atlanta, Georgia, 2007
20. Pinto, H.S., Gomez-Perez A. & Martins, J.P., *Some Issues on Ontology Integration*, Master Thesis, Instituto Superior Tecnico Departamento de Eng. Informatica, Grupo de Inteligencia, Artificial, 1999
21. Klein, M.C.A., *Change Management for Distributed Ontologies*, Vrije Universiteit, van de faculteit der Exacte Wetenschappen, Amsterdam, 2004

# TIME SERIES BASED REVENUE FORECAST MODELS

Gökhan Burtul<sup>1</sup>, Hüseyin Temür<sup>1</sup>, Engin Durmaz<sup>1</sup>, Tarık Güneş<sup>1</sup>, M. Fatih Akay<sup>2</sup>

<sup>1</sup> Hugin Retail Solutions, İstanbul, Turkey

<sup>2</sup> Çukurova University, Department of Computer Engineering, Adana, Turkey

[gokhan.burtul@hugin.com.tr](mailto:gokhan.burtul@hugin.com.tr), [huseyin.temur@hugin.com.tr](mailto:huseyin.temur@hugin.com.tr), [engin.durmaz@hugin.com.tr](mailto:engin.durmaz@hugin.com.tr),  
[tarik.gunes@hugin.com.tr](mailto:tarik.gunes@hugin.com.tr), [mfakay@cu.edu.tr](mailto:mfakay@cu.edu.tr)

## Abstract

Financial planning is the process of developing a strategy to help organizations manage their financial resources as effectively as possible. It involves analyzing an organization's current financial situation, setting its financial goals and developing a plan to achieve those goals. This study aims to develop revenue forecasting models using univariate time series methods. For this purpose, deep learning based Long Short-Term Memory (LSTM), Gated Recurrent Unit (GRU) and Convolutional Long Short-Term Memory (ConvLSTM) have been used. The performance of the developed models has been evaluated using Mean Absolute Percentage Error (MAPE). The dataset includes 113 rows of total revenue data in weekly format from June 1<sup>st</sup>, 2020 to July 31<sup>st</sup>, 2022. Forecast models have been developed for two different weeks and months randomly selected from the dataset. The MAPE's obtained with LSTM, GRU and ConvLSTM varied from 1.23% to 4.67% for different weeks and from 9.9% to 13.86% for different months. The results show that LSTM based models yield superior performance for both weekly and monthly revenue forecasting.

**Keywords:** Time Series, Machine Learning, Financial Planning, Revenue Forecasting

## 1. INTRODUCTION

Financial planning and budgeting ensure that the company has sufficient liquidity. A company that carries out financial planning can organize its financial roadmap and evaluate the reasons for deviations from the target data. Financial planning identifies financial weaknesses and strengths as well as needs based on income and expense statements. Financial planning provides the most ideal solutions for companies to achieve their desired goals. With financial planning, companies get the privilege to expand their range of products or services and take advantage of new opportunities for methods that increase their productivity and profitability.

The status of income and expenses, assets, risks, liabilities, costs and time are elements of financial planning. For a good financial planning, it is necessary to know the future values of some financial components and manage the related processes. It is very important to make accurate forecasts for the relevant components.

This study aims to develop revenue forecasting models using univariate time series methods. For this purpose, deep learning based LSTM, GRU and ConvLSTM have been used. The performance of the developed models has been evaluated using MAPE.

This paper is organized as follows: Section 2 presents related literature. The materials, methodology and details of the forecast models are presented in Section 3. Results and discussion are presented in Section 4. Section 5 concludes the paper.

## 2. LITERATURE REVIEW

In recent years, various methods have been used for revenue forecasting. [1] presented the data sources, techniques, features and evaluation criteria used in movie revenue forecasting. 36 related articles were selected and examined. It was observed that regression and classification approaches were mostly used in the articles that examined movie revenue estimation. In addition, it was determined that the MAPE, Root Mean Square Error (RMSE) and Mean Percent Hit Rate (MPHR) were the most used evaluation metrics. [2] used machine learning methods and high-dimensional financial data to predict the direction of one-year-ahead earnings changes. The outperformed models used Logistic Regression (LR) and small sets of accounting variables and professional analyst's estimates. [3] explored how different machine learning models performed in revenue estimation for local methods and compared revenue estimation performance by various machine learning algorithms. The results showed that traditional statistical methods were better than machine learning algorithms and more effective at predicting the property tax revenue of K-Nearest Neighbors (KNN). [4] proposed an enterprise economic forecasting method based on the Auto-Regressive Integrated Moving Average – LSTM (ARIMA-LSTM). ARIMA was used to estimate the linear data of the time series and the LSTM was used to estimate the nonlinear relationship. The ARIMA-LSTM was used to predict the future economic development of enterprises. The results show that the model can effectively predict the economic situation of enterprises. [5] presented the market revenue forecast result and error analysis result of the products based on fuzzy logic and artificial intelligence algorithms. In the results, it was observed that the Neural Network (NN) algorithm had high accuracy in predicting the future sales of the product. [6] studied and analyzed prediction models developed with machine learning algorithms using publicly available information. It was concluded that machine learning algorithms provided more accurate revenue forecasts compared to financial analysts. [7] proposed a model to predict business revenue data based on controllable model complexity. They used multiple models such as Support Vector Machine (SVM). In addition, the ability of the predictive models was evaluated using three indices: MAE, RMSE and MAPE. [8] proposed machine learning to develop movie revenue forecast models. Then, they used basic theories to prove the validity of each model and compare their performance. [9] presented the Generalized Additive Models (GAMs) and machine learning models developed based on Artificial Neural Networks (ANNs) to predict the optimum revenues of an integrated power generation and storage system. Predictive equations and models were created based on optimized solutions from the Conventional Hydroelectric

Power and Environmental Resource System (CHEERS) model. Model validation prediction errors of GAMs and machine learning models were less than 5%; better performance was obtained from the regression equations in the machine learning models. [10] proposed using earnings per share as a performance measure to predict corporate financial performance and used three supervised machine learning methods: Linear Discriminant Analysis (LDA), Quadratic Discriminant Analysis (QDA) and Random Forest (RF). They also used a sample of 63 banks listed from 8 emerging markets between 2008 and 2017. In the study, it was concluded that the best prediction model was created with the RF and evidence was found about the accuracy and performance of the presented models.

### **3. MATERIAL AND METHOD**

The dataset includes 113 rows of total revenue data in weekly format from June 1<sup>st</sup>, 2020 to July 31<sup>st</sup>, 2022. Forecast models have been developed for two different weeks (23.05.2022 - 29.05.2022, 18.07.2022 - 24.07.2022) and two different months (May 2022 and June 2022) randomly selected from the data set. Forecast models have been developed using LSTM, GRU and ConvLSTM on historical total revenue data.

#### **3.1. Long Short Term Memory**

LSTM is recursive and is used in deep learning methods. LSTM has a similar control flow to a Recursive Neural Network (RNN). It processes data propagating forward and transmits information. Unlike standard recursive networks, the LSTM network has a feedback loop that allows it to process not only individual data points but also entire sequences. Therefore, these networks are used for the classification, processing, and prediction of time series data [11].

#### **3.2. Gated Recurrent Unit**

GRU, like LSTM, is a variant of RNN. However, unlike LSTM, GRUs are not in a cell state and use hidden layers to transmit information. Also unlike LSTM, it has reset and updated gates. LSTM module has a large number of parameters and a complex structure; therefore, it is inclined to overfitting. To solve this problem, the GRU structure was proposed in 2014 as a variant of LSTM. GRU architecture has a simpler structure. Each of these RNN variants has a structure that consists of replicated instances of a particular module; however, the structure of the replicated module in a GRU network is somewhat simpler than in an LSTM network. Since the GRU architecture has only two types of control gates, the calculation speed of a GRU model is much faster than that of an LSTM model [12].

#### **3.3. Convolutional Long Short-Term Memory (ConvLSTM)**

The convolutional LSTM model is a variation of LSTM that replaces FC layer operators with convolutional operators. It uses convolution operators for input-to-private and confidential connections. By replacing the convolution operators with an LSTM memory cell, ConvLSTM

can know what information to remember or forget from the previous cell state using the forget gate. Similarly, ConvLSTM also decides what information to store in the current cell state. In ConvLSTM, the transition between states is similar to the movement between frames [13].

#### 4. RESULTS AND DISCUSSION

The performance of the developed models has been evaluated using MAPE. Table 1 and Table 2 show MAPE's of weekly and monthly forecast models, respectively.

*Table 1. MAPE's of the weekly forecast models*

Week	LSTM	GRU	ConvLSTM
23.05.2022 - 29.05.2022	1.82	1.95	4.05
18.07.2022 - 24.07.2022	1.23	2.14	4.67

*Table 2. MAPE's of the monthly forecast models*

Month	LSTM	GRU	ConvLSTM
May 2022	10.83	13.86	12.09
June 2022	9.90	12.30	10.80

For weekly forecast models;

- For 23.05.2022 - 29.05.2022; LSTM model yields 0.13% and 2.23% lower MAPE's than that of GRU model and ConvLSTM model, respectively.
- For 18.07.2022 - 24.07.2022; LSTM model yields 0.91% and 3.44% lower lower MAPE's than that of GRU model and ConvLSTM model, respectively.

For monthly forecast models;

- For May 2022; LSTM model yields 3.03% and 1.26% lower MAPE's than that of GRU model and ConvLSTM model, respectively.
- For June 2022; LSTM model yields 2.40% and 0.90% lower MAPE's than that of GRU model and ConvLSTM model, respectively.

#### 5. CONCLUSION

In this study, revenue forecast models have been developed for two different weeks and two different months by time series-based methods. The MAPE's obtained with LSTM, GRU and ConvLSTM varied from 1.23% to 4.67% on different weeks, 9.9% to 13.86% on different months. As a result of this study, LSTM-based models yield superior performance for both weekly and monthly revenue forecasting.

## REFERENCES

1. Ibrahim Said Ahmad, Azuraliza Abu Bakar, Mohd Ridzwan Yaakub, Shamsuddeen Hassan Muhammad, A survey on machine learning techniques in movie revenue prediction, *SN Computer Science*, Vol: 1, No: 4, 1-14, 2020.
2. Xi Chen, Yang Ha (Tony) Cho, Yiwei Dou, Baruch Lev, Predicting Future Earnings Changes Using Machine Learning and Detailed Financial Data, *Journal of Accounting Research*, Vol: 60, No: 2, 467-515, 2022.
3. Chung, Il Hwan, Daniel W. Williams, Myung Rok Do, For Better or Worse? Revenue Forecasting with Machine Learning Approaches, *Public Performance & Management Review*, Vol: 45, No: 5, 1-21, 2022.
4. Xiaofei Dong, Xuesen Zong, Peng Li, Jinlong Wang, Enterprise Economic Forecasting Method Based on ARIMA-LSTM Model, *International Conference on Intelligent Technologies for Interactive Entertainment*, Vol: 429, 36-57, 2021.
5. Jian, Zhao, Zhang Qingyuan, Tian Liying, Market revenue prediction and error analysis of products based on fuzzy logic and artificial intelligence algorithms, *Journal of Ambient Intelligence and Humanized Computing*, Vol: 11, No: 10, 4011-4018, 2020.
6. Kureljusic, Marko, Lucas Reisch, Revenue forecasting for European capital market-oriented firms: A comparative prediction study between financial analysts and machine learning models, *Corporate Ownership & Control*, Vol: 19, No: 2, 159-178, 2022.
7. Lei, Huang, Huang Cailan, Comparison of multiple machine learning models based on enterprise revenue forecasting, *2021 Asia-Pacific Conference on Communications Technology and Computer Science (ACCTCS)*, 354-359, 2021.
8. Li, Haibo, Using machine learning forecasts movie revenue, *2021 2nd International Conference on Artificial Intelligence and Computer Engineering (ICAICE)*, 455-460, 2021.
9. Yingqian Lin, Binghui Li, Thomas M. Moiser, L. Michael Griffel, Matthew R. Mahalik, Jonghwan Kwon, S. M. Shafiul Alam, Revenue prediction for integrated renewable energy and energy storage system using machine learning techniques, *Journal of Energy Storage*, Vol: 50, 104123, 2022.
10. Gehan A. Mousa, Elsayed A. H. Elamir, Khaled Hussainey, Using machine learning methods to predict financial performance: Does disclosure tone matter?, *International Journal of Disclosure and Governance*, Vol: 19, No: 1, 93-112, 2022.
11. Manowska, Anna, Using the LSTM network to forecast the demand for electricity in Poland, *Applied Sciences*, Vol:10, No: 23, 8455, 2020.

12. Pengtao Jia, Hangduo Liu, Sujian Wang, Peng Wang, Research on a mine gas concentration forecasting model based on a GRU network, IEEE Access, Vol: 8, 38023-38031, 2020.
13. Essien, Aniekan, Cinzia Giannetti, A deep learning model for smart manufacturing using convolutional LSTM neural network autoencoders, IEEE Transactions on Industrial Informatics, Vol:16, No: 9, 6069-6078, 2020.



# MACHINE LEARNING MODELS FOR DETERMINING THE PRICE ELASTICITY OF FLASH SALE PRODUCTS ON AN E-COMMERCE MARKETPLACE

Melisa Bal<sup>1</sup>, Öztürk Saraçoğlu<sup>1</sup>, Mustafa Yahşi<sup>1</sup>, H. Şebnem Arlı<sup>2</sup>, M. Fatih Akay<sup>2</sup>

<sup>1</sup>Data Science, Trendyol, Istanbul, Turkey

<sup>2</sup>Department of Computer Engineering, Çukurova University, Adana, Turkey

[melisa.bal@trendyol.com](mailto:melisa.bal@trendyol.com), [ozturk.saracoglu@trendyol.com](mailto:ozturk.saracoglu@trendyol.com), [mustafa.yahsi@trendyol.com](mailto:mustafa.yahsi@trendyol.com),  
[ssebnemarlii@gmail.com](mailto:ssebnemarlii@gmail.com), [mfakay@cu.edu.tr](mailto:mfakay@cu.edu.tr)

## Abstract

E-commerce companies use promotional pricing to attract the attention of online consumers by applying a flash sale program. The flash sale aims to increase demand through a pricing strategy for a company's products. Price elasticity is a type of pricing strategy in which the company uses flexible prices that change according to market demand. Price elasticity shows the relationship between price and quantity demanded and allows an estimation of the impact of a price change on quantity demanded. In other words, it measures the response of consumers to changes in the price of a product. If a product has price elasticity, a slight change in price will result in a large change in demand for that product. This study aims determining the price elasticity of flash sale products on Trendyol.com. The main purpose is to generate price-based sales forecasts for products in order to highlight discounted products and increase sales. In this context, forecast models have been developed using Generalized Additive Models (GAM) and Linear Regression (LR). The performance of the developed models has been evaluated using Mean Squared Error (MSE) for 50 different products. Results show that the average MSE's of LR-based model and GAM-based model are 21.41 and 29.33, respectively.

**Keywords:** Price Elasticity, Generalized Additive Models, Linear Regression

## 1. INTRODUCTION

Over the past decade, e-commerce has become an increasingly popular way for consumers to purchase products online. The convenience, accessibility, and variety of online shopping have made it an attractive alternative to traditional brick-and-mortar stores. With the rise of e-

commerce, companies have started using various advertising strategies to attract the attention of online customers. One of these strategies is the use of flash sales, which are short-term sales promotions that offer products at reduced prices for a limited time.

Flash sales are a popular method for e-commerce companies to drive demand for their products and increase sales. They create a sense of urgency among consumers and prompt them to make a quick purchase decision before the sale ends. Flash sales also provide e-commerce companies with an opportunity to showcase their products and promote their brand. They can be used to reduce inventory, introduce new products, or simply to promote the company.

However, pricing strategies such as flash sales can have a significant impact on consumer behavior, especially in terms of price elasticity. E-commerce brands monitor a product's sales and dynamically change the price to maximize expected revenue. This is referred to as price elasticity. Price elasticity refers to the extent to which price changes affect demand for a product. It is an important concept for e-commerce businesses to understand in order to make informed pricing decisions. By understanding the price elasticity of their products, e-commerce companies can optimize their pricing strategies to maximize sales and profitability.

The aim of this study is to determine the price elasticity of products offered at instant discounts on Trendyol.com, a popular e-commerce platform in Turkey. Therefore, price elasticity models have been developed using GAM and LR to predict the impact of price changes on consumer behavior and generate price-based sales forecasts for discount products. The performance of the developed models has been evaluated using Mean Squared Error (MSE).

This paper is organized as follows: Section 2 presents related literature. The methodology and details of the prediction models are given in Section 3. Results and discussions are presented in Section 4. Section 5 concludes the paper.

## 2. LITERATURE REVIEW

In recent years, many methods have been used for price elasticity. [1] presented a prescriptive analysis approach to optimize pricing for an e-commerce retailer, allowing price differentiation based on customer demand elasticity. The model aimed to maximize gross profit by predicting customer demand as a function of price using historical data and formulating optimization using nonlinear objective functions and constraints. A randomized decomposition approach was used to find a near-optimal solution. The results of the computational experiments were also discussed. [2] proposed a novel elastic demand function for hotel occupancy prediction, incorporating a price elasticity prediction model (PEM) with competitive representation and multi-sequence fusion. A multi-task framework mitigated data sparsity. Experiments

demonstrated superior performance of PEM for occupancy prediction and dynamic pricing, with successful deployment at Fliggy for online hotel bookings. [4] proposed a data-driven and interpretable discount pricing approach using transaction data. The approach included counterfactual forecasting and multi-period price optimization. A semiparametric structural model was developed to learn price elasticity and predict demand, combining the predictability of machine learning with the interpretability of economic models. A dynamic multi-period pricing algorithm was proposed to maximize profit over the sales horizon, with a sequential pricing strategy derived from a Markov decision process. [5] introduced a price optimization technique in retail, considering substitution effects. An algorithm was developed for demand prediction and price optimization, reducing execution time and price combinations significantly. [7] demonstrated that incorporating cross effects in models enhanced forecasting accuracy by 39% compared to naïve models and 14% compared to models without cross effects. Optimized pricing based on these models led to a 30% revenue increase. [8] proposed prescriptive price optimization using machine learning. The problem was formulated as binary quadratic programming, achieving significant profit improvement (approx. 30%) for multiple products. [9] introduced an improved Convolutional Long-Short Term Memory (ConvLSTM) model for pricing strategy, incorporating it into the field previously dominated by the LSTM model. The results showed that the proposed ConvLSTM-based pricing strategy model demonstrated superiority in comparison experiments. [10] proposed a method using historical data to optimize a retailer's price discount system. First, initial estimates of discounted prices were obtained for each product. Then, machine learning and deep learning algorithms were used to generate sales forecasts, calculate price elasticities, and develop a nonlinear price optimization system to recommend optimal prices. The results were presented in detail for the textiles category, and backtesting was performed. [11] proposed a dynamic pricing system including competitor analysis for base price determination, a novel occupancy prediction model (Deep Factorization Machine (DeepFM) + seq2seq), and a DNN for rational price adjustments. Compared to rule-based strategies, the proposed system improved revenue management efficiency. [12] presented a decision-support system for retail pricing and revenue optimization. It used regression tree/random forest-based algorithms to predict demand and an integer linear programming model for optimal price allocation. The methodology was applied to offline retailing of expensive products, optimizing revenue through branch & bound and heuristic methods.

### 3. METHODOLOGY

In order to achieve the research aims, a systematic and well-structured methodology consisting of nine key steps was implemented. By adhering to this methodological framework, the study aims to provide valuable insights and actionable recommendations for the pricing and selection of Flash Sale Products (FSP). Each step was thoughtfully crafted to contribute to the overall analysis and decision-making process, resulting in a robust methodology that facilitated accurate predictions and informed pricing strategies. The summarized steps of the methodology are as follows:

**Step 1:** A rule-based filtering is applied to products to identify the ones that meet the following criteria:

1. The order count in the last 90 days should be greater than 38 and greater than the 75th percentile overall,
2. The visit count in the last 90 days should be greater than 500,
3. The category name should not be Supermarket or Digital Goods,
4. The product should have at least 3 distinct prices in the last 90 days.

**Step 2:** In the second step, feature preparation is started within the retained products from step 1. The last 90 days' impression and price data are collected as features.

**Step 3:** After the data collection, exploratory data analysis is implemented. Applied logarithmic transformation for both impression and price data.

**Step 4:** LR model and GAM model are trained with -91 days of data and validation is made by -1 days order count.

**Step 5:** Order count predictions are found with GAM model and LR for the current price, the last 2 weeks' median price and FSP price.

**Step 6:** FSP price is calculated by the following formula:  $\text{current price} * 0.8$ .

**Step 7:** Based on a set of rules, which model is going to be chosen for order count prediction is selected.

**Step 8:** Incremental order FSP is calculated as follows:  $\text{FSP price model sales prediction results} - \text{current price model sales prediction results}$ .

**Step 9:** Whether incremental order FSP formula accepts the  $<0$  rules, then the product is selected as Flash Product.

The summary of the methods used for developing the forecast models are given below.

### 3.1. Generalized Additive Model

GAM is an extension of the classical general linear model that allows for the inclusion of non-linear functions of variables. It provides a flexible way to specify the response variable by using smooth functions rather than detailed parametric relationships with the covariates.

GAM uses link functions to connect the dependent variable with unspecified functions, which helps to limit the error in predicting the dependent variable from various distributions. However, this flexibility comes at the cost of needing to represent the smooth functions in a similar pattern and selecting the appropriate level of smoothness [6].

### 3.2. Linear Regression

LR is a simple approach for supervised learning, which is particularly useful for predicting a quantitative response. Although it may seem less exciting than some of the newer statistical learning approaches, LR remains a widely used and important method. In fact, many modern approaches are generalizations or extensions of LR [3].

## 4. RESULTS AND DISCUSSION

The performance of the models was evaluated using MSE. Table 2 and Table 3 show the MSE's of the models using LR and GAM.

**Table 2.** MSE's of the models

Product ID	LR	GAM	Product ID	LR	GAM
0	2.63	6.64	14	6.57	7.13
1	27.53	1.99	15	16.61	105.05
2	2.25	0.21	16	0.21	0.21
3	3.54	14.54	17	2.30	10.56
4	1.36	4.77	18	7.83	29.89
5	0.00	0.36	19	4.64	4.26
6	3.47	3.46	20	1.01	1.45
7	0.09	0.08	21	17.16	0.75
8	21.85	14.80	22	439.04	133.49
9	167.55	132.99	23	2.76	1.46
10	0.68	0.99	24	25.12	115.59
11	0.73	0.24	25	3.28	2.48
12	2.85	4.69	26	0.74	1.38
13	127.87	175.37	27	33.52	45.79

**Table 3.** MSE's of the models (continued)

Product ID	LR	GAM	Product ID	LR	GAM
28	80.59	58.77	39	0.20	0.00
29	24.99	9.82	40	3.09	1.41
30	3.80	29.40	41	0.41	1.01
31	0.96	14.16	42	20.79	13.18
32	1.54	0.23	43	1.32	1.10
33	1.28	1.22	44	0.65	0.67
34	2.96	254.87	45	1.04	4.49
35	0.46	86.11	46	0.25	4.83
36	0.26	0.42	47	0.05	103.91
37	0.41	0.27	48	1.81	59.74
38	0.02	0.03	49	0.39	0.05

- The lowest MSE has been observed with LR-based model for the 5<sup>th</sup> product, while the lowest MSE was observed with GAM-based model for the 39<sup>th</sup> product.
- The highest MSE (439.04) has been observed with LR-based model for the 22<sup>th</sup> product.
- The average MSEs' of LR-based and GAM-based models are 21.41 and 29.33, respectively.
- In terms of individual product performance, LR-based model has lower MSE for 28 out of the 50 products tested, while GAM-based model has a lower MSE for 22 products.

## 5. CONCLUSION

Price elasticity analysis plays a crucial role in understanding consumer behavior and optimizing pricing strategies in various industries. In the field of e-commerce, determining the price elasticity of products, especially in flash sales, is of paramount importance. In this study, the price elasticity of products that are instantly discounted on an e-commerce platform like Trendyol.com has been determined. Using GAM and LR, the impact of price changes on consumer behavior has been predicted and price-based sales forecasts for discounted products have been generated. The study results show that the LR-based model outperforms the GAM-based model. This study provides a guide for e-commerce businesses to optimize their pricing strategies and demonstrates the potential of flash sales.

## REFERENCES

1. Andrew Vakhutinsky, Kresimir Mihic, Su-Min Wu, A prescriptive analytics approach to markdown pricing for an e-commerce retailer. *Journal of Pattern Recognition Research*, Vol: 14, No:1, 1-20, 2019.
2. Fanwei Zhu, Wendong Xiao, Yao Yu, Ziyi Wang, Zulong Chen, Quan Lu, Zemin Liu, Minghui Wu, Shenghua Ni, Modeling Price Elasticity for Occupancy Prediction in Hotel Dynamic Pricing. In *Proceedings of the 31st ACM International Conference on Information & Knowledge Management*, 4742-4746, 2022.
3. Gareth James, Daniela Witten, Trevor Hastie, Robert Tibshirani, Linear regression. *An introduction to statistical learning: with applications in R*, 59-128, 2021.
4. Junhao Hua, Ling Yan, Huan Xu, Cheng Yang, Markdowns in e-commerce fresh retail: a counterfactual prediction and multi-period optimization approach. In *Proceedings of the 27th ACM SIGKDD Conference on Knowledge Discovery & Data Mining*, 3022-3031, 2021.
5. Keun Hee Lee, Malihe Akhavan-Abdollahian, Sergei Schreider, Utilising Machine Learning Approaches to Develop Price Optimisation and Demand Prediction Model for Multiple Products with Demand Correlation, 2022.
6. Khaiwal Ravindra, Preety Rattan, Suman Mor, Ashustosh Nath Aggarwal, Generalized additive models: Building evidence of air pollution, climate change and human health. *Environment international*, 2019.
7. Nikhil Gupta, Massimiliano Moro, Kailey A. Ayala, Bivin Sadler, Price Optimization for Revenue Maximization at Scale. *SMU Data Science Review*, Vol:3, No:3, 2020.
8. Shinji Ito, Ryohei Fujimaki, Optimization beyond prediction: Prescriptive price optimization. In *Proceedings of the 23rd ACM SIGKDD international conference on knowledge discovery and data mining*, 1833-1841, 2017.
9. Shusong Yu, Zhicheng Wang, Xiangqian Ding, Research on the model of manufacturing product pricing strategy based on ConvLSTM. In *International Conference on Computer Application and Information Security (ICCAIS 2021)*, Vol. 12260, 212-219, 2022.
10. Vibhati Burman, Rajesh Kumar Vashishtha, Sricidhya Sethuraman, Ganesh Radhakrishnan, Prashanth Ganesan, Suresh Kumar V, Sharadha Ramanan, Markdown Pricing For a Large Scale Retailer. In *2021 IEEE International Conference on Big Data (Big Data)*, 1817-1826, 2021.



11. Qing Zhang, Liyuan Qiu, Huaiwen Wu, Jinshan Wang, Hengliang Luo, Deep learning based dynamic pricing model for hotel revenue management. In 2019 International Conference on Data Mining Workshops (ICDMW), 370-375, 2019.
12. Woo-yong Park, Manoj Kumar Tiwari, R S Srivastava, Felix Tung Sun Chan, Jianhua Zhang, Ting Qu, Demand prediction and price optimization for semi-luxury supermarket segment. Computers & industrial engineering, 91-102, 2017.

# CUSTOMER CHURN PREDICTION USING SUPERVISED LEARNING FOR E-COMMERCE

Miray Endican<sup>1</sup>, Gökay Dağdaş<sup>1</sup>, Fatih Cudi Ünal<sup>1</sup>, Z. Sude Sarı<sup>2</sup>, M. Fatih Akay<sup>2</sup>

<sup>1</sup> Research and Development Department, Inveon, Istanbul, Turkey

<sup>2</sup> Department of Computer Engineering, Çukurova University, Adana, Turkey

[miray.endican@inveon.com](mailto:miray.endican@inveon.com), [gokay.dagdas@inveon.com](mailto:gokay.dagdas@inveon.com), [cudi.unal@inveon.com](mailto:cudi.unal@inveon.com),  
[zsudesarii@gmail.com](mailto:zsudesarii@gmail.com), [mfakay@cu.edu.tr](mailto:mfakay@cu.edu.tr)

## Abstract

With the developments in artificial intelligence, better insights about customers can be gained by using machine learning techniques. In order to develop efficient and effective customer retention strategies, it is necessary to create a data-driven model to predict customer churn. The aim of this study is to develop customer churn prediction models based on supervised machine learning algorithms for the e-commerce sector. The prediction models have been developed using Support Vector Machine (SVM), Extreme Gradient Boosting (XGBoost), Random Forest (RF) and Deep Neural Network (DNN). Minimum Redundancy Maximum Relevance (mRMR) has been used to correctly select the attributes that affect the quality of customer churn models. The data has been collected from Inveon's customers for 2 brands, encoded as A and S for privacy reasons. The performance of the developed models has been evaluated using accuracy and F-Score by utilizing 5-fold cross-validation on the dataset. For brand A, the Accuracies and F-Scores of the models varied from 0.70 to 0.86 without feature selection and 0.73 to 0.87 with feature selection. For brand S, the Accuracies and F-Scores of the models varied from 0.58 to 0.83 without feature selection and 0.80 to 0.83 with feature selection. Results show that the mRMR feature selection algorithm improves the performance of the models.

**Keywords:** Customer Churn, Supervised Learning, Machine Learning, E-commerce

## 1. INTRODUCTION

E-commerce, also known as electronic commerce, is a concept that entered our lives after 1995 when the use of the Internet began to increase. The interest in e-commerce, which is one of the fastest-growing sectors in the world, is increasing day by day. The main reason why users choose e-commerce is that they can shop effortlessly, around the clock, from any location, with only an Internet connection and with a variety of options.

Businesses on e-commerce platforms are constantly striving to attract new customers and increase sales on the platform to ensure their continued existence. However, research has shown that acquiring a new customer is more expensive than retaining an existing one. For this reason, companies spend most of their efforts on customer retention. However, the cost of wrong strategy can lead to negative consequences for the company. Assessing the risk of churn is an important task in customer retention.

In this digital age, companies have begun to rely heavily on data analytics to predict customer churn. With developments in the field of artificial intelligence, better insights into the customer base can be gained through the use of advanced techniques supported by business intelligence applications and machine learning methods. A data-driven customer churn prediction model is essential for developing efficient and effective customer retention strategies in the e-commerce industry.

This study aims to develop customer churn prediction models based on supervised machine learning algorithms for the e-commerce sector. The prediction models have been developed using SVM, XGBoost, RF and DNN. The performance of the developed models has been evaluated using accuracy and F-score.

This paper is organized as follows: Section 2 presents related literature. Section 3 provides details on dataset generation. Methodology and details of the prediction models are given in Section 4. Results and discussion are presented in Section 5. Section 6 concludes the paper.

## 2. LITERATURE REVIEW

In recent years, various methods have been used for customer churn prediction. [1] presented a comprehensive assessment of the capacity of Recurrent Neural Networks (RNN) and transducers for Customer Attrition Prediction (CCP) using behavioral characteristics that change over time in the form of novelty, frequency, and monetary value. In this context, hybrid approaches combining DNN outputs from traditional CCP models were also evaluated. The obtained results highlighted that DNNs and especially RNN were suitable for CCP using time-varying recency, frequency, and monetary measurements. [2] proposed an adaptive learning approach for loss estimation using a Naive Bayes (NB) classifier with a Genetic Algorithm (GA) based feature weighting approach. They also evaluated the performance of the proposed approach in public datasets compared to the classifier, with mean precision of 0.97, 0.97, 0.98, and sensitivity rates of 0.84, 0.94, 0.97. The suggested approach provided 0.89, 0.96, 0.97 F scores, 0.89, 0.96, 0.97 Matthews Correlation Coefficient and 0.95, 0.97, 0.98 Accuracies. [3], presented a hybrid recommendation strategy with targeted retention attempts for an e-commerce loss forecast based on SVM. Experimental findings showed a significant increase in coverage rate, hit rate, removal rate, precision rate, and other metrics when the integrated forecasting model was used. [4] explained how the organization could build a customer churn model based on mathematical and statistical approaches using customer acquisition, usage, interaction and customer call center data and focused on minimizing customer churn. This work assisted many organizations and data scientists in the process of developing a customer churn model. [5] presented current approaches for loss prediction models and identified Graph Neural Network (GNN) as a promising end-to-end solution. [6] proposed the theoretical basis of customer churn and customer segmentation and suggested the use of supervised machine learning techniques for churn prediction. They used K-Means, K-Nearest Neighbors (KNN), Logistic Regression (LR), Decision Tree (DT), and RF to segment customers. They used the SVM to predict customer churn. As a result, it was determined that the data set achieved an Accuracy of about 97% with the RF model, and the average Accuracy of each model performed well after customer segmentation, while LR had the lowest Accuracy (87.27%). [7] proposed a

RF-Multilayer Perceptron (RF-MLP) algorithm for customer churn prediction. RF combined with an Artificial Neural Networks (ANN) to capture nonlinear feature variables and obtain a more powerful model. The applicability of the algorithm model verified with a real and effective churn dataset. According to the experimental results, the Area Under the Curve (AUC) score of RF-MLP in the test set was 84.9%, which was 9.1% and 21.7% higher than the RF and MLP algorithm. [8] presented a classifier associated with the Apriori Algorithm as a reinforcer that combined classification and association rule mining to create a robust classification model from which frequent items were obtained. They also provided an accurate prediction by testing misclassified samples from the bagging stage using rules created in a relational classifier. The proposed models were simulated and the results achieved high Accuracy, Receiver Operator Characteristic score, precision, specificity, F-measure and recall. [9] used a data mining algorithm to predict customer churn. They used LR and Gradient Boosting (GB) as one of the data mining techniques to perform customer churn predictions. The GB model was found to perform better in predicting churn compared to the LR model, which achieved 87% Accuracy in training and 88% in testing, respectively. The results showed that the GB model performed the training and testing process with 93% training Accuracy and 91% testing Accuracy. [10] provided a depth comparison between Neural Network, SVM, NB and, RF to predict customer churn in e-commerce. They used a balanced dataset of 11,224 samples. The performance of the developed models was evaluated with Accuracy, sensitivity, specificity, true positive value and true negative value. They found that the RF classifier for selected features using the Neighbor Component Analysis (NCA) technique gave the highest prediction Accuracy of 99.35% compared to the classifiers used in this study and those used by previous researchers.

### 3. DATASET GENERATION

The data has been collected from Inveon's customers for 2 brands, encoded as A and S for privacy reasons. The dataset for brand A consists of 77766 lines of data and includes 70855 churned customer whereas the dataset for brand S consists of 7510 lines of data and includes churned customer. Attributes in the dataset and their explanations are given in Table 1.

## 4. METHODOLOGY

### 4.1. Undersampling

Undersampling is a technique to balance imbalanced datasets by keeping all of the data in the minority class and decreasing the size of the majority class. It is one of several techniques data scientists can use to extract more accurate information from originally imbalanced datasets. Though it has disadvantages, such as the loss of potentially important information, it remains a common and important skill for data scientists [11].

### 4.2. Support Vector Machine

SVM is an analytical technique for examining the relationship between one or more predictor variables and a real-valued (continuous) dependent variable. Unlike traditional regression methods that depend on assumptions of the model that may not be true (e.g., linear data distribution), SVM is a machine learning technique in which a model has learned the importance of a variable in characterizing the relationship between input and output [12]

**Table 1.** Attributes and Explanations in Product Tables of A and S Brands

Attribute	Description
<b>Id</b>	Unique identifier of the order
<b>CustomerId</b>	Customer unique identifier
<b>OrderStatusId</b>	Order status code
<b>ShippingStatusId</b>	Delivery status code
<b>PaymentStatusId</b>	Payment status code
<b>OrderDiscount</b>	Total discount for order
<b>OrderTotal</b>	Order total amount
<b>CreatedOnUtc</b>	Order date information
<b>OrderNumber</b>	Order count
<b>OrderId</b>	Unique identifier of the order
<b>ProductId</b>	Unique number information of the relevant product
<b>Sku</b>	Stock keeping unit
<b>PriceInclTax</b>	Price including taxes
<b>DiscountAmountInclTax</b>	Discount including taxes
<b>ProductName</b>	Product name
<b>OrderItemStatusId</b>	Order detail status code
<b>Barcode</b>	Barcode information
<b>InvoiceDate</b>	Invoice date
<b>MarketplaceId</b>	Order number in the marketplace sale
<b>Active</b>	Activity in terms of database
<b>CreatedOnUtc</b>	Creation date of customer record
<b>LastLoginDateUtc</b>	The date the customer last logged into the site
<b>LastActivityDateUtc</b>	The date the customer last did any activity on the site (page click, etc.)
<b>OrderCount</b>	The total number of orders from the date the customer created the record to the current date of data extraction
<b>AllowEmailCommunication</b>	Email permission information
<b>AllowSmsCommunication</b>	SMS permission information

### 4.3. Extreme Gradient Boosting

XGBoost is a machine-learning classification method. It features high information processing speed and improved performance characteristics. The method is created by increasing the size of tree models. In this process, existing models are developed by repeatedly adding new models. In this method, gradient descent algorithm is used for reduction when a new model is added [13].

### 4.4. Random Forest

RF is a learning method used in random decision forest, classification, and regression, among others. In this method, a cluster of DTs is first created. Then the data is classified based on the

randomly generated DTs. In this method, there is a directly proportional relationship between the number of trees in the forest and the Accuracy rate [14].

#### 4.5. Deep Neural Network

Typically, a DNN is a machine learning algorithm based on an ANN that mimics the principles and structure of a human neural network. An ANN is composed of an input layer, a hidden layer, and an outer layer. If the number of hidden layers is greater than or equal to three, the system is denoted as a DNN [15].

The prediction models have been developed using SVM, XGBoost, RF and DNN. Undersampling has been performed to balance the dataset. The performance of the developed models has been evaluated using accuracy and F-Score by utilizing 5-fold cross-validation on the dataset. mRMR has been used to correctly select the attributes that affect the quality of customer churn models.

### 5. RESULTS AND DISCUSSION

The performance of the developed models has been evaluated using accuracy and F-score. Table 2 and Table 3 show the accuracies and F-Score for brand A and brand S, respectively.

**Table 2.** Accuracies and F-Score's of the models for brand A

Method	Accuracy	F-Score
SVM	0.75	0.76
mRMR + SVM	0.77	0.78
XGBoost	0.86	0.86
mRMR + XGBoost	0.86	0.87
RF	0.83	0.83
mRMR + RF	0.83	0.83
DNN	0.70	0.70
mRMR + DNN	0.73	0.76

**Table 3.** Accuracies and F-Score's of the models for brand S

Method	Accuracy	F-Score
SVM	0.64	0.58
mRMR + SVM	0.82	0.80
XGBoost	0.83	0.81
mRMR + XGBoost	0.83	0.81
RF	0.80	0.80
mRMR + RF	0.82	0.81
DNN	0.65	0.58
mRMR + DNN	0.83	0.81

For brand A,

- the lowest accuracy has been obtained with DNN model. The highest accuracy has been obtained with XGBoost models.
- the lowest F-Score has been obtained with the DNN model. The highest F-Score has been obtained with mRMR + XGBoost model.

For brand S,

- the lowest accuracy has been obtained with SVM model. The highest accuracy has been obtained with mRMR + XGBoost model and mRMR + DNN model.
- the lowest F-Score has been obtained with SVM and DNN model. The highest F-Score has been obtained with mRMR + XGBoost model.
- XGBoost and mRMR + XGBoost models have showed the highest performance for both brands. On the other hand, DNN model has showed the lowest performance for both brands.
- While mRMR feature selection algorithm has not improved the performance of the models for brand A, it has improved the performance of SVM and DNN models for brand S.

## 5. CONCLUSION

The use of artificial intelligence technologies helps companies learn more about their customers and develop effective customer retention strategies. Therefore, data-driven prediction models have become an important tool for predicting customer churn and retaining potential customers. This study investigates the usability of various supervised machine learning algorithms in predicting customer churn in the e-commerce industry. In this context, customer churn prediction models have been developed using SVM, XGBoost, RF and DNN. In addition, the mRMR feature selection algorithm has been used to select the features that affect the quality of the churn prediction model. The performance of the developed models has been evaluated using Accuracy and F-Score by utilizing 5-fold cross-validation on the dataset. For brand A, the Accuracies and F-Score's of the models varied from 0.70 to 0.86 without feature selection and 0.73 to 0.87 with feature selection. For brand S, the Accuracies and F-Score's of the models varied from 0.58 to 0.83 without feature selection and 0.80 to 0.83 with feature selection.

## REFERENCES

1. Gary Mena, Kristof Coussement, Koen W. De Bock, Arno De Caigny, Stefan Lessmann, Exploiting time-varying RFM measures for customer churn prediction with deep neural networks, *Annals of Operations Research*, Vol:1, No:23, 2023.
2. Amin Adnan, Awais Adnan, and Sajid Anwar, An adaptive learning approach for customer churn prediction in the telecommunication industry using evolutionary computation and Naïve Bayes, *Applied Soft Computing*, Vol:137, No: 110103, 2023.
3. Shobana J., Ch. Gangadhar, Rakesh Kumar Arora, P.N. Renjith, J. Bamini, Yugendra devidas Chincholkar, E-commerce customer churn prevention using machine learning-based business intelligence strategy, *Measurement: Sensors*, Vol:27, No:100728, 2023.



4. Sharma, Alok, Predictive Modelling (Customer Churn) Measurement and Prevention, 2023.
5. Ljubičić, Karmela, Andro Merćep, and Zvonko Kostanjčar, Churn prediction methods based on mutual customer interdependence, *Journal of Computational Science*, Vol: 67, No:101940, 2023.
6. Tran, Hoang, Ngoc Le, and Van-Ho Nguyen. Customer Churn Prediction in the Banking Sector Using Machine Learning-Based Classification Models, *Interdisciplinary Journal of Information, Knowledge & Management*, Vol:18, 87-105, 2023.
7. Zhang, Jiaqi, Customer churn prediction based on a novelty hybrid random forest algorithm, *Third International Conference on Computer Vision and Data Mining (ICCVDM 2022)*, SPIE, Vol: 12511, 2023.
8. Anitha M. A, and Sherly K K, An Efficient Hybrid Classifier Model for Customer Churn Prediction." *International Journal of Electronics and Telecommunications*, Vol:11, No:18, 2023.
9. Arif Ridho Lubis; Santi Prayudani; Julham; Okvi Nugroho; Yuyun Yusnida Lase, Muharman Lubis, Comparison of Model in Predicting Customer Churn Based on Users' habits on E-Commerce, In *2022 5th International Seminar on Research of Information Technology and Intelligent Systems (ISRITI)*, IEEE, 300-305, 2022.
10. Baghla, Seema, and Gaurav Gupta, Performance Evaluation of Various Classification Techniques for Customer Churn Prediction in E-commerce, *Microprocessors and Microsystems* Vol: 94, No:104680, 2022.
11. Ashish Anand, Ganesan Pugalenthi, Gary B. Fogel, P. N. Suganthan, An approach for classification of highly imbalanced data using weighting and undersampling, *Amino acids* Vol: 39, 1385-1391, 2010.
12. Fan Zhang, Lauren J. O'Donnell, Support vector regression, *Machine learning*. Academic Press, 123-140, 2020.
13. Anju Prabha, Jyoti Yadav, Asha Rani, Vijander Singh, Design of intelligent diabetes mellitus detection system using hybrid feature selection based XGBoost classifier, *Computers in Biology and Medicine* Vol:136, No: 104664, 2021.
14. Zainib Noshad, Nadeem Javaid, Tanzila Saba, Zahid Wadud, Muhammad Qaiser Saleem, Mohammad Eid Alzahrani, Osama E. Sheta, Fault detection in wireless sensor networks through the random forest classifier, *Sensors*, Vol:19, No:7,1568, 2019.
15. Jonghun Lim, Soohwan Jeong, Sungsu Lim, Hyungtae Cho, Jae Yun Shim, Seok Il Hong, Soon Chul Kwon, Heedong Lee, Il Moon, Junghwan Kim, Development of dye exhaustion behavior prediction model using deep neural network, *Computer aided chemical engineering*. Elsevier, Vol: 49, 1825-1830, 2022.

# Approximate Solution of Coupled System of Fractional Order Partial Differential Equations with Variable Coefficients

Murad Khalil<sup>1,\*</sup>, Hammad Khalil<sup>2</sup>

<sup>1</sup>Department of Basic Sciences, University of Engineering and Technology Peshawar, Pakistan.

<sup>2</sup>Department of Mathematics, University of Education, Lahore Attock Campus, Pakistan.

\*Correspondence: murad.khalil@uetpeshawar.edu.pk

## Abstract

This paper describes a method for approximating smooth solutions to a system of coupled fractional order partial differential equations (FPDEs) with variable coefficients. The proposed approach involves using operational matrices of shifted Legendre polynomials to replace the product of fractional derivatives and variable coefficients. This conversion allows for the FPDEs with variable coefficients to be expressed as easily solvable algebraic equations. We utilized the Matlab platform to solve the algebraic system of equations and present numerical results in the form of tables and graphs to validate the effectiveness of the proposed method. Additionally, the paper provides a detailed discussion of the application of this method for approximating smooth solutions subject to initial and Dirichlet boundary condition

**Keywords.** Orthogonal Polynomials; Approximation theory; Computational Scheme; Fractional Calculus.

## Introduction

Fractional calculus continues to captivate scientists worldwide due to its wide range of applications in various fields. One of the main reasons for its popularity is its significant contributions to economics [1–4], biophysics [5, 6], engineering, and biotechnology [7–9]. The use of fractional order derivatives and integrals also plays a crucial role in the theory of controlled dynamical systems [10–12], where the dynamics of the entire system are fully described by fractional order differential equations. For a comprehensive understanding of the importance of fractional calculus and its mathematical theory, we recommend the readers to refer to [13–16]. Furthermore, for exploring the applications of fractional calculus in various scientific disciplines, we suggest the readers to refer to [17–22]

A coupled system of fractional order partial differential equations play important role in the field of modeling various engineering phenomena like compartment analysis, microorganism culturing, pond pollution, home heating, chemostats, cascades, biomass transfer, nutrient flow in an aquarium, forecasting prices, earthquake effects on buildings, electrical network, and so on (see, for examples [23–26]).

Recently researchers discovered that in a wide variety of physical problems, fractional-order derivatives provide more accurate results as compared to ordinary derivatives. But due to the computational complexities of fractional-order derivatives, obtaining the exact analytical solution is some time difficult or even not possible, therefore it is important to find an approximate solution

for these systems. The establishment of numerical scheme for these physical problems remains an important task in current field of fractional calculus.

Compartment analysis, microorganism culturing, pond pollution, home heating, chemostats, cascades, biomass transfer, nutrient flow in an aquarium, forecasting prices, earthquake effects on buildings, electrical networks, and many other physical problems have been investigated (see, for example, [23–26]).

In recent years, researchers have discovered that fractional-order derivatives yield more accurate results than ordinary derivatives in a wide range of physical problems. However, the computational complexities associated with fractional-order derivatives often make it challenging or even impossible to obtain exact analytical solutions. Therefore, finding approximate solutions for these systems becomes crucial. Developing numerical schemes for solving these physical problems remains an important task in the field of fractional calculus.

Over the past century, various methods have been employed to solve fractional-order differential equations, fractional-order partial differential equations, fractional-order integro-differential equations, and dynamic systems with fractional-order integro-differential equations. Among these methods, some useful approaches include He's variational iteration method [27–31], Adomian's decomposition method [32, 33], collocation method [34], homotopy perturbation method [35], Galerkin method [36], homotopy analysis method [37], spectral method [38], and various analytical strategies [39–42].

Orthogonal functions have gained significant attention in dealing with different types of fractional-order differential equations. One notable characteristic of approaches based on orthogonal polynomials is their ability to transform problems into easily solvable algebraic structures. In [43], the authors combine shifted Legendre polynomials with an operational matrix approach to solve fractional-order derivatives. Additionally, shifted Jacobi polynomials and shifted Chebyshev polynomials are applied together with tau and collocation spectral methods to solve multiterm linear and nonlinear fractional-order differential equations [44, 45]. For further exploration and applications of these polynomials, we recommend studying [46–52]. The main goal of the proposed paper is recommended to derive a suitable way to approximate the coupled system of fractional order partial differential equations of the form

$$\mathcal{D}_y^\alpha U = \lambda \mathcal{D}_x^\beta U + \theta(x, y) \mathcal{D}_x U + \Theta(x, y) U + f(x, y), \quad (1)$$

the coupled system is

$$\begin{aligned} \mathcal{D}_y^\alpha U &= \lambda_1 \mathcal{D}_x^\beta U + \lambda_2 \mathcal{D}_x^\beta V + \theta_1(x, y) \mathcal{D}_x U + \theta_2(x, y) \mathcal{D}_x V + \Theta_1(x, y) U + \Theta_2(x, y) V + f(x, y), \\ \mathcal{D}_y^\alpha V &= \lambda_3 \mathcal{D}_x^\beta U + \lambda_4 \mathcal{D}_x^\beta V + \theta_3(x, y) \mathcal{D}_x U + \theta_4(x, y) \mathcal{D}_x V + \Theta_3(x, y) U + \Theta_4(x, y) V + g(x, y). \end{aligned} \quad (2)$$

The equation's analytical solution is known to be limited to the domain  $[0, 1] \times [0, 1]$ , where  $0 < \beta \leq 2$  and  $1 < \alpha \leq 2$ . The operators represent certain constants, and  $\mathcal{D}_x^\beta$  and  $\mathcal{D}_y^\alpha$  denote the Caputo fractional derivatives with respect to  $x$  and  $y$ . The coefficients  $\lambda_i$  are also constants, while  $\phi_i(x, y)$  and  $\Theta_i(x, y)$  are known functions.  $U(x, y)$  and  $V(x, y)$  are the unknown scalar functions that need to be determined as the solution to the problem. We discuss our approach for finding an approximate solution to this type of equation, taking into account the given initial and boundary conditions

## 1 Preliminaries

In this section, we will provide an overview of some fundamental definitions and established results from the field of fractional calculus. This will include a brief introduction to the concepts

and notation used in fractional calculus, as well as a summary of some of the key results and theorems that have been widely accepted and utilized in this field. Additionally, we will also present some of the most common methods and techniques used in fractional calculus, and how they are used to solve various types of problems and applications.

## 2 Shifted Legendre polynomials

The Legendre polynomials can be defined using a recurrence relation, as outlined in [53]

$$Q_{k+1}(y) = \frac{2k+1}{1+k}y Q_k(y) - \frac{k}{1+k}Q_{k-1}(y), \quad (3)$$

where  $Q_0(y) = 1$ ,  $Q_1(y) = 2y - 1$ ,  $k = 1, 2, 3, \dots$

The transformation  $x = \frac{(y+1)\bar{\tau}}{2}$  effects a change of interval from  $[-1, 1]$  to  $[0, \bar{\tau}]$ . The shifted Legendre polynomials can be expressed as

$$Q_k(x) = \sum_{j=0}^k \zeta_{(k,j)} x^j \quad k = 0, 1, 2, 3, \dots \quad (4)$$

where

$$\zeta_{(k,j)} = (-1)^{j+k} \frac{(j+k)!}{(k-j)!(j!)^2}, \quad (5)$$

The orthogonality condition satisfy as

$$\int_0^1 Q_l(x) Q_m(x) dx = \begin{cases} 0, & \text{if } l \neq m, \\ \frac{\bar{\tau}}{2l+1}, & \text{if } l = m. \end{cases}$$

The S-term Legendre approximation of a function  $h(x) \in C[0, \bar{\tau}]$ , as

$$h(x) = \sum_{k=0}^S C_k Q_k(x), \quad (6)$$

where

$$C_k = \frac{2k+1}{\bar{\tau}} \int_0^1 h(x) Q_k(x) dx.$$

In vector notation, we can write as

$$h(x) \approx K_S^T \Omega_S(x), \quad (7)$$

$$\Omega(x) = [ Q_0(x), Q_1(x), \dots, Q_S(x) ],$$

and

$$K_S^T = [ k_0, k_1, \dots, k_S ],^T$$

where the scale level of approximation is  $S = s + 1$ . In case of two variables function  $h(x, y) \in C([0, 1] \times [0, 1])$

$$g(x, y) \approx \sum_{k=0}^{S^2} C_k \Omega_k(x, y).$$

where

$$\Omega_k(x, y) = Q_i(x) Q_j(y), \quad \text{for } k = Si + j + 1.$$

The orthogonality condition is hold as

$$\begin{aligned} \int_0^1 \int_0^1 \Omega_l(x, y) \Omega_m(x, y) dx dy &= \int_0^1 \int_0^1 Q_i(x) Q_j(y) Q_a(x) Q_b(y) dx dy, \\ &= \frac{\zeta_{(j,b)} \zeta_{(i,a)}}{(2i+1)(2j+1)} \quad l = Si + j + 1, \quad m = Sa + b + 1. \end{aligned}$$

where  $C_k$  can be written as

$$C_k = (2i+1)(2j+1) \int_0^1 \int_0^1 g(x, y) Q_i(x) Q_j(y) dx dy.$$

In vector notation

$$g(x, y) \approx K_{S^2}^T \varphi_{S^2}(x, y).$$

where  $\varphi_{S^2}$  is a  $(S^2 \times 1)$  column vector and  $K_{S^2}^T$  is a  $(1 \times S^2)$  coefficient row vector and is defined by

$$K_{S^2}^T = [k_{11}, \dots, k_{1S}, k_{21}, \dots, k_{2S}, \dots, k_{SS}]^T.$$

### 3 Operational matrix development and its application

**Lemma 3.1.** *The integral of three Legendre polynomials on  $[0, 1]$  is defined as*

$$\int_0^1 Q_k(x) Q_j(x) Q_l(x) dx = \beth^{(k,j,l)}, \quad (8)$$

where

$$\beth^{(k,j,l)} = \sum_{a=0}^k \sum_{b=0}^j \sum_{c=0}^l \zeta_{(k,a)} \zeta_{(j,b)} \zeta_{(l,c)} Z_{(a,b,c)}. \quad (9)$$

Where  $\zeta_{(.,.)}$  is define in Eq. 5 and

$$Z_{(a,b,c)} = \frac{1}{(a, b, c + 1)}.$$

The lemma's proof can be found in [54].

**Theorem 3.1.** *For function vector  $\varphi_{S^2}(x, y)$ , then the  $\alpha$  order integration of  $\varphi_{S^2}(x, y)$  with respect to  $x$  is*

$${}_x J^\alpha \varphi_{S^2}(x, y) = {}_x J_{(S^2 \times S^2)} \varphi_{S^2}(x, y),$$

where  ${}_x J_{(S^2 \times S^2)}$  is

$${}_x J_{(S^2 \times S^2)} = \begin{pmatrix} \Omega_{(0,0)} & \Omega_{(0,1)} & \cdots & \Omega_{(0,s)} & \cdots & \Omega_{(0,S^2)} \\ \Omega_{(1,0)} & \Omega_{(1,1)} & \cdots & \Omega_{(1,s)} & \cdots & \Omega_{(1,S^2)} \\ \vdots & \vdots & \ddots & \vdots & \vdots & \vdots \\ \Omega_{(r,0)} & \Omega_{(r,1)} & \cdots & \Omega_{(r,s)} & \cdots & \Omega_{(r,S^2)} \\ \vdots & \vdots & \vdots & \vdots & \ddots & \vdots \\ \Omega_{(S^2,0)} & \Omega_{(S^2,1)} & \cdots & \Omega_{(S^2,s)} & \cdots & \Omega_{(S^2,S^2)} \end{pmatrix} \quad (10)$$

where

$$\Omega_{(r,s)} = \sum_{k=0}^i \frac{(-1)^{i+k}(i+k)!}{(k!)^2(i-k)!} \frac{\Gamma(1+k)}{\Gamma(1+k+\alpha)} \sum_{a=0}^{S^2} C_a.$$

*Proof.* For a function vector  $\varphi_{S^2}(x, y)$ , then the integration of order  $\alpha$  of  $\varphi_{S^2}(x, y)$  with respect to  $x$

$$x J^\alpha \varphi_{S^2}(x, y) = J_x^\alpha Q_i(x) Q_j(y).$$

$$x J^\alpha Q_i(x) Q_j(y) = \sum_{k=0}^i (-1)^{i+k} \frac{\Gamma(1+k)}{\Gamma(1+k+\alpha)} \frac{(i+k)!}{(k!)^2(i-k)!} Q_j(y) x^{k+\alpha}.$$

Legendre approximating of  $Q_j(y) x^{k+\alpha}$  in two variables are

$$x^{k+\alpha} Q_j(y) = \sum_{c=0}^S \sum_{d=0}^S C_{cd} Q_c(x) Q_d(y) = \sum_{a=0}^{S^2} C_a Q_c(x) Q_d(y),$$

where

$$C_{(a)} = (2c+1)(2d+1) \int_0^1 \int_0^1 Q_j(y) Q_d(y) Q_c(x)^{k+\alpha} (x) dx dy.$$

Due to the orthogonality condition of Legendre polynomials we can write as

$$C_{(a)} = (2c+1) \delta_{(j,d)} \int_0^1 Q_c(x) x^{k+\alpha} dx,$$

by definition

$$\delta_{(a,b)} = \begin{cases} 1, & \text{if } a = b, \\ 0, & \text{if } a \neq b. \end{cases}$$

$$C_{(a)} = \delta_{(j,d)} (2c+1) \sum_{c=0}^j \frac{(-1)^{j+c}(j+c)!}{(k+\alpha+c+1)(j-c)!(c!)^2},$$

$$x J^\alpha \varphi_{S^2}^T(x, y) = \sum_{k=0}^i (-1)^{i+k} \frac{\Gamma(1+k)}{\Gamma(1+k+\alpha)} \frac{(i+k)!}{(k!)^2(i-k)!} \sum_{a=0}^{S^2} C_a \varphi_a(x, y).$$

Similarly the integration of order  $\beta$  of  $\varphi_{S^2}(x, y)$  with respect to  $y$  is

$$J_y^\beta \varphi_{S^2}(x, y) = {}^y J_{(S^2 \times S^2)} \varphi_{S^2}(x, y).$$

□

**Theorem 3.2.** For a function vector  $\varphi_{S^2}(x, y)$ , then the derivative of order  $\alpha$  of  $\varphi_{S^2}(x, y)$  with respect to  $x$  is

$$x D^\alpha \varphi_{S^2}(x, y) = {}^x D_{(S^2 \times S^2)} \varphi_{S^2}(x, y).$$

where  ${}^x D_{(S^2 \times S^2)}$  is

$${}^x D_{(S^2 \times S^2)} = \begin{pmatrix} \mathfrak{J}_{(0,0)} & \mathfrak{J}_{(0,1)} & \cdots & \mathfrak{J}_{0,s} & \cdots & \mathfrak{J}_{0,S^2} \\ \mathfrak{J}_{(1,0)} & \mathfrak{J}_{(1,1)} & \cdots & \mathfrak{J}_{(1,s)} & \cdots & \mathfrak{J}_{(1,S^2)} \\ \vdots & \vdots & \ddots & \vdots & \vdots & \vdots \\ \mathfrak{J}_{(r,0)} & \mathfrak{J}_{(r,1)} & \cdots & \mathfrak{J}_{(r,s)} & \cdots & \mathfrak{J}_{(r,S^2)} \\ \vdots & \vdots & \vdots & \vdots & \ddots & \vdots \\ \mathfrak{J}_{(S^2,0)} & \mathfrak{J}_{(S^2,1)} & \cdots & \mathfrak{J}_{(S^2,s)} & \cdots & \mathfrak{J}_{(S^2,S^2)} \end{pmatrix} \quad (11)$$

where

$$\mathfrak{J}_{(r,s)} = \sum_{k=0}^i \sum_{a=0}^{S^2} (-1)^{k+i} \frac{\Gamma(1+k)(k+i)!}{\Gamma(1+k-\alpha)(i!)^2(k-i)!} C_a.$$

*Proof.* Let the derivative of order of  $\alpha$  of  $\varphi_{S^2}(x, y)$  with respect to  $x$  is

$${}_x D^\alpha \varphi_{S^2}(x, y) = {}_x D^\alpha Q_i(x) Q_j(y).$$

$$D_x^\alpha Q_i(x) Q_j(y) = \sum_{k=0}^i (-1)^{i+k} \frac{\Gamma(1+k)(i+k)!}{\Gamma(1+k-\alpha)(k!)^2(i-k)!} x^{k-\alpha} Q_j(y).$$

The Lagendre approximating of  $x^{k-\alpha} Q_j(y)$  in two variables

$$x^{k-\alpha} Q_j(y) = \sum_{c=0}^S \sum_{d=0}^S C_{(cd)} Q_c(x) Q_d(y) = \sum_{a=0}^{S^2} C_a Q_c(x) Q_d(y),$$

the term  $C_{(a)}$  is defined as

$$C_{(a)} = (2c+1)(2d+1) \int_0^1 \int_0^1 x^{k-\alpha} Q_c(x) Q_j(y) Q_d(y) dx dy.$$

$$C_{(a)} = (2c+1) \delta_{(j,d)} \sum_{c=0}^j (-1)^{j+c} \frac{(j+c)!}{(k+\alpha-c+1)(j-c)!(c!)^2},$$

$${}_x D^\alpha \Omega_{S^2}^T(x, y) = \sum_{k=0}^i \sum_{a=0}^{S^2} (-1)^{i+k} \frac{\Gamma(1+k)(i+k)!}{\Gamma(1+k-\alpha)(i-k)!(k!)^2} C_a \Omega_a(x, y).$$

Similarly the  $\beta$  order derivative of  $\varphi_{S^2}(x, y)$  with respect to  $y$  is

$${}_y D^\beta \varphi_{S^2}(x, y) = {}_y D_{(S^2 \times S^2)} \varphi_{S^2}(x, y).$$

□

**Theorem 3.3.** Let  $f(x, y)$  be any function of the space  $C([0, 1] \times [0, 1])$  and  $U(x, y)$  be the unknown solution. Then

$$f(x, y) U(x, y) = K_{S^2}^T G_{(S^2 \times S^2)}^f \varphi_{S^2}(x, y).$$



where  $K_{S^2}^T$  is the coefficients vector of  $u(x, y)$

$$G_{(S^2 \times S^2)}^f = \begin{pmatrix} \Lambda_{(0,0)} & \Lambda_{(0,1)} & \cdots & \Lambda_{0,s} & \cdots & \Lambda_{0,S^2} \\ \Lambda_{(1,0)} & \Lambda_{(1,1)} & \cdots & \Lambda_{(1,s)} & \cdots & \Lambda_{(1,S^2)} \\ \vdots & \vdots & \ddots & \vdots & \vdots & \vdots \\ \Lambda_{(r,0)} & \Lambda_{(r,1)} & \cdots & \Lambda_{(r,s)} & \cdots & \Lambda_{(r,S^2)} \\ \vdots & \vdots & \vdots & \vdots & \ddots & \vdots \\ \Lambda_{(S^2,0)} & \Lambda_{(S^2,1)} & \cdots & \Lambda_{(S^2,s)} & \cdots & \Lambda_{(S^2,S^2)} \end{pmatrix} \quad (12)$$

where

$$\Lambda_{(r,rr)} = (2p+1)(2q+1) \sum_{i=0}^{S^2} c_i \mathfrak{I}_{(l,m,n)}^{(a,i,p)} \mathfrak{I}_{(u,v,w)}^{(b,j,q)}.$$

where the value of  $\mathfrak{I}_{(l,m,n)}^{(a,i,p)}$  and  $\mathfrak{I}_{(u,v,w)}^{(b,j,q)}$ , is defined in Eq. (9).

*Proof.* Let the vector form of  $V(x, y) \simeq C_{S^2} \varphi_{S^2}(x, y)^T$ , then we can write

$$g(x, y)V(x, y) = C_{S^2} \overbrace{\varphi_{M^2}^T(x, y)}.$$

Where

$$\overbrace{\varphi_{S^2}^T} = [ X_0(x, y) \quad X_1(x, y) \quad \dots \quad X_r(x, y) \quad \dots \quad X_{S^2}(x, y) ]^T$$

and

$$X_r(x, y) = g(x, y)\phi_r(x, y),$$

S-terms Legendre approximation of  $g(x, y)$  is

$$g(x, y) = \sum_{i=0}^{S^2} c_i \phi_i(x, y),$$

implies that

$$X_r(x, y) = \sum_{i=0}^{S^2} c_i \phi_i(x, y)\phi_r(x, y).$$

S-terms Legendre approximations of  $X_r(x, y)$  are

$$X_r(x, y) = \sum_{rr=0}^{S^2} h_{(r,rr)} \phi_{rr}(x, y),$$

where

$$h_{(r,rr)} = \sum_{i=0}^{S^2} c_i (2p+1)(2q+1) \int_0^1 \int_0^1 \phi_i(x, y) \phi_r(x, y) \phi_{rr}(x, y) dx dy.$$

Using the above results, it can be written as

$$\begin{aligned} \phi_i(x, y) &= Q_a(x) Q_b(y), & \text{where } i &= aS + b + 1, \quad a, b = 0, 1, 2 \dots S, \\ \phi_r(x, y) &= Q_i(x) Q_j(y), & \text{where } r &= iS + j + 1, \quad i, j = 0, 1, 2 \dots S, \\ \phi_{rr}(x, y) &= Q_p(x) Q_q(y), & \text{where } rr &= pS + q + 1, \quad p, q = 0, 1, 2 \dots S. \end{aligned}$$

$$h_{(r,rr)} = \sum_{i=0}^{S^2} c_i(2p+1)(2q+1) \int_0^1 \int_0^1 Q_a(x) Q_i(x) Q_p(x) Q_b(y) Q_j(y) Q_q(y) dx dy,$$

$$h_{(r,rr)} = \sum_{i=0}^{S^2} c_i(2p+1)(2q+1) \beth^{(a,i,p)} \beth^{(b,j,q)}.$$

Using  $h_{(r,rr)} = \Lambda_{r,rr}$  and simulating the procedure for  $r = 0, 1 \dots S^2$  and  $rr = 0, 1 \dots S^2$  we get

$$\begin{pmatrix} X_0(x, y) \\ X_1(x, y) \\ \vdots \\ X_r(x, y) \\ \vdots \\ X_{S^2}(x, y) \end{pmatrix} = \begin{pmatrix} \Lambda_{(0,0)} & \Lambda_{(0,1)} & \cdots & \Lambda_{(0,s)} & \cdots & \Lambda_{(0,S^2)} \\ \Lambda_{(1,0)} & \Lambda_{(1,1)} & \cdots & \Lambda_{(1,s)} & \cdots & \Lambda_{(1,S^2)} \\ \vdots & \vdots & \ddots & \vdots & \vdots & \vdots \\ \Lambda_{(r,0)} & \Lambda_{(r,1)} & \cdots & \Lambda_{(r,s)} & \cdots & \Lambda_{(r,S^2)} \\ \vdots & \vdots & \vdots & \vdots & \ddots & \vdots \\ \Lambda_{(S^2,0)} & \Lambda_{(S^2,1)} & \cdots & \Lambda_{(S^2,s)} & \cdots & \Lambda_{(S^2,S^2)} \end{pmatrix} \begin{pmatrix} Q_0(x, y) \\ Q_1(x, y) \\ \vdots \\ Q_r(x, y) \\ \vdots \\ Q_{S^2}(x, y) \end{pmatrix}$$

we can write as

$$\overbrace{\varphi_S^2(x, y)} = G_{(S^2 \times S^2)}^f \varphi_S^2(x, y).$$

□

**Theorem 3.4.** Let  $U(x, y)$  and  $f(x, y)$  are arbitrary elements in the space  $C([0, 1] \times [0, 1])$ . Then

$$f(x, t) \frac{\partial^\alpha U(x, y)}{\partial x^\alpha} = K_{S^2}^{T^x} H_{(S^2 \times S^2)}^f \varphi_{S^2}(x, y),$$

where  $K_{S^2}^T$  is the coefficients vector of  $U(x, y)$ , and

$${}^x H_{(S^2 \times S^2)}^f = {}^x D_{(S^2 \times S^2)} G_{(S^2 \times S^2)}^f$$

$${}^x H_{(S^2 \times S^2)}^f = \begin{pmatrix} \beth_{(0,0)} & \beth_{(0,1)} & \cdots & \beth_{(0,s)} & \cdots & \beth_{(0,S^2)} \\ \beth_{(1,0)} & \beth_{(1,1)} & \cdots & \beth_{(1,s)} & \cdots & \beth_{(1,S^2)} \\ \vdots & \vdots & \ddots & \vdots & \vdots & \vdots \\ \beth_{(r,0)} & \beth_{(r,1)} & \cdots & \beth_{(r,s)} & \cdots & \beth_{(r,S^2)} \\ \vdots & \vdots & \vdots & \vdots & \ddots & \vdots \\ \beth_{(S^2,0)} & \beth_{(S^2,1)} & \cdots & \beth_{(S^2,s)} & \cdots & \beth_{(S^2,S^2)} \end{pmatrix}, \quad (13)$$

where

$$\beth_{(r,s)} = \sum_{i=0}^{S^2} \mathfrak{U}_{(r,i)} \Lambda_{(i,s)}.$$

*Proof.* Considered the vector form of  $U(x, y) \simeq K_{S^2}^T \varphi_{S^2}(x, y)$ , using the theorem (3.2)

$$\frac{\partial^\alpha U(x, y)}{\partial x^\alpha} = K_{S^2}^{T^x} D_{(S^2 \times S^2)} \varphi_{S^2}(x, y).$$

the entries of  ${}^x D_{(S^2 \times S^2)}$  is associated with  $\mathfrak{U}_{(r,s)}$  and define is

$$\mathfrak{U}_{(r,s)} = \sum_{k=0}^i \sum_{a=0}^{S^2} \frac{(-1)^{i+k} (i+k)!}{(i-k)! (k!)^2} \frac{\Gamma(1+k)}{\Gamma(1+k-\alpha)} C_a,$$

$$f(x, t) \frac{\partial^\alpha U(x, y)}{\partial x^\alpha} = K_{S^2}^T x D_{(S^2 \times S^2)} \overbrace{\varphi_{S^2}(x, y)},$$

where

$$\overbrace{\varphi_{S^2}(x, y)} = [ A_0(x, y) \quad A_1(x, y) \quad \dots \quad A_r(x, y) \quad \dots \quad A_{S^2}(x, y) ]^T$$

and

$$A_r(x, y) = f(x, y) \phi_r(x, y).$$

Then by theorem (3.3)

$$\overbrace{\varphi_{S^2}(x, y)} = f(x, t) G_{(S^2 \times S^2)} \varphi_{S^2}(x, y),$$

where the entries of  $G_{(S^2 \times S^2)}^f$  is associated with  $\Lambda_{(r, rr)}$  and is defined as

$$\Lambda_{(r, rr)} = (2p+1)(2q+1) \sum_{i=0}^{S^2} c_i \mathfrak{I}_{(l, m, n)}^{(a, i, p)} \mathfrak{I}_{(u, v, w)}^{(b, j, q)}.$$

where the value of  $\mathfrak{I}_{(l, m, n)}^{(a, i, p)}$  and  $\mathfrak{I}_{(u, v, w)}^{(b, j, q)}$ , is defined in Eq. (9).

$$f(x, y) \frac{\partial^\alpha U(x, y)}{\partial x^\alpha} = K_{S^2}^T x D_{(S^2 \times S^2)} G_{(S^2 \times S^2)}^f \varphi_{S^2}(x, y).$$

$$f(x, y) \frac{\partial^\alpha U(x, y)}{\partial x^\alpha} = \begin{pmatrix} K_0 \\ K_1 \\ \vdots \\ K_r \\ \vdots \\ K_{S^2} \end{pmatrix}^T \begin{pmatrix} \mathfrak{I}_{(0,0)} & \mathfrak{I}_{(0,1)} & \cdots & \mathfrak{I}_{0,s} & \cdots & \mathfrak{I}_{0,S^2} \\ \mathfrak{I}_{(1,0)} & \mathfrak{I}_{(1,1)} & \cdots & \mathfrak{I}_{(1,s)} & \cdots & \mathfrak{I}_{(1,S^2)} \\ \vdots & \vdots & \ddots & \vdots & \ddots & \vdots \\ \mathfrak{I}_{(r,0)} & \mathfrak{I}_{(r,1)} & \cdots & \mathfrak{I}_{(r,s)} & \cdots & \mathfrak{I}_{(r,S^2)} \\ \vdots & \vdots & \ddots & \vdots & \ddots & \vdots \\ \mathfrak{I}_{(S^2,0)} & \mathfrak{I}_{(S^2,1)} & \cdots & \mathfrak{I}_{(S^2,s)} & \cdots & \mathfrak{I}_{(S^2,S^2)} \end{pmatrix} \begin{pmatrix} \Lambda_{(0,0)} & \Lambda_{(0,1)} & \cdots & \Lambda_{(0,s)} & \cdots & \Lambda_{(0,S^2)} \\ \Lambda_{(1,0)} & \Lambda_{(1,1)} & \cdots & \Lambda_{(1,s)} & \cdots & \Lambda_{(1,S^2)} \\ \vdots & \vdots & \ddots & \vdots & \ddots & \vdots \\ \Lambda_{(r,0)} & \Lambda_{(r,1)} & \cdots & \Lambda_{(r,s)} & \cdots & \Lambda_{(r,S^2)} \\ \vdots & \vdots & \ddots & \vdots & \ddots & \vdots \\ \Lambda_{(S^2,0)} & \Lambda_{(S^2,1)} & \cdots & \Lambda_{(S^2,s)} & \cdots & \Lambda_{(S^2,S^2)} \end{pmatrix} \begin{pmatrix} \varphi_0(x, y) \\ \varphi_1(x, y) \\ \vdots \\ \varphi_r(x, y) \\ \vdots \\ \varphi_{S^2}(x, y) \end{pmatrix} \quad (14)$$

$${}^x H_{(S^2 \times S^2)}^f = \begin{pmatrix} \sum_{i=0}^{S^2} \mathfrak{I}_{(0,i)} \Lambda_{(i,0)} & \sum_{i=0}^{S^2} \mathfrak{I}_{(0,i)} \Lambda_{(i,1)} & \cdots & \sum_{i=0}^{S^2} \mathfrak{I}_{(0,i)} \Lambda_{(i,s)} & \cdots & \sum_{i=0}^{S^2} \mathfrak{I}_{(0,i)} \Lambda_{(i,S^2)} \\ \sum_{i=0}^{S^2} \mathfrak{I}_{(1,i)} \Lambda_{(i,0)} & \sum_{i=0}^{S^2} \mathfrak{I}_{(1,i)} \Lambda_{(i,1)} & \cdots & \sum_{i=0}^{S^2} \mathfrak{I}_{(1,i)} \Lambda_{(i,s)} & \cdots & \sum_{i=0}^{S^2} \mathfrak{I}_{(1,i)} \Lambda_{(i,S^2)} \\ \vdots & \vdots & \ddots & \vdots & \ddots & \vdots \\ \sum_{i=0}^{S^2} \mathfrak{I}_{(r,i)} \Lambda_{(i,0)} & \sum_{i=0}^{S^2} \mathfrak{I}_{(r,i)} \Lambda_{(i,1)} & \cdots & \sum_{i=0}^{S^2} \mathfrak{I}_{(r,i)} \Lambda_{(i,s)} & \cdots & \sum_{i=0}^{S^2} \mathfrak{I}_{(r,i)} \Lambda_{(i,S^2)} \\ \vdots & \vdots & \ddots & \vdots & \ddots & \vdots \\ \sum_{i=0}^{S^2} \mathfrak{I}_{(S^2,i)} \Lambda_{(i,0)} & \sum_{i=0}^{S^2} \mathfrak{I}_{(S^2,i)} \Lambda_{(i,1)} & \cdots & \sum_{i=0}^{S^2} \mathfrak{I}_{(S^2,i)} \Lambda_{(i,s)} & \cdots & \sum_{i=0}^{S^2} \mathfrak{I}_{(S^2,i)} \Lambda_{(i,S^2)} \end{pmatrix},$$

where  $\mathfrak{I}_{(r,s)}$  is defined as

$$\mathfrak{I}_{(r,s)} = \sum_{i=0}^{S^2} \mathfrak{I}_{(r,i)} \Lambda_{(i,s)}.$$

Which is the required proof of the theorem.  $\square$

**Lemma 3.2.** Let  ${}_c \Phi^n(x) = cx^n$  be a polynomial,  $\varphi_{S^2}(x, y)$  be a function vector and  $\zeta \in R$ , then

$$cx^n \Phi_{S^2}(\zeta, y) = {}^x A^{(c,n,\zeta)} \varphi_{S^2}(x, y).$$

The matrix  ${}^x A^{(c,n,\zeta)}$  is defined as

$${}^x A^{(c,n,\zeta)} = \begin{pmatrix} \Delta_{(0,0)} & \Delta_{(0,1)} & \cdots & \Delta_{(0,S^2)} \\ \Delta_{(1,0)} & \Delta_{(1,1)} & \cdots & \Delta_{(1,S^2)} \\ \vdots & \vdots & \ddots & \vdots \\ \Delta_{(S^2,0)} & \Delta_{(S^2,1)} & \cdots & \Delta_{(S^2,S^2)} \end{pmatrix},$$

The term  $\Delta_{(r,s)}$  is associated with  $A_{(i,j,k,l)}$  and  $s = Sl+k+1$ ,  $r = Si+j+1$ , for  $i,j,k,l = 0,1,2,3,\dots,S$ ,

$$A_{(i,j,k,l)} = \sum_{b=0}^i \frac{(i+b)!(-1)^{i+b}}{(b!)^2(i-b)!} c\zeta^b \sum_{k=0}^S \sum_{l=0}^S \mathfrak{S}_{(k,l)}.$$

*Proof.* The general term of equality can be written as

$$\phi_c^n(x) Q_i(\zeta) Q_j(y) = c \sum_{b=0}^i \mathfrak{I}_{(i,b)} \zeta^b x^n Q_j(y).$$

and S-terms Legendre approximation of  $Q_j(y)x^n$  is

$$Q_j(y)x^n = \sum_{k=0}^S \sum_{l=0}^S \mathfrak{S}_{(k,l)} Q_k(x) Q_l(y),$$

where

$$\mathfrak{S}_{(k,l)} = (2k+1)(2l+1) \int_0^1 \int_0^1 x^n Q_k(x) Q_l(y) Q_j(y) dx dy.$$

$$\mathfrak{S}_{(k,l)} = (2k+1)\delta_{(j,l)} \int_0^1 \sum_{c=0}^k \frac{(-1)^{k+c}(k+c)!}{(k-c)!(c!)^2} x^{n+c} dx,$$

$$\mathfrak{S}_{(k,l)} = (2k+1)\delta_{(j,l)} \sum_{c=0}^k \frac{(-1)^{k+c}(k+c)!}{(n+c+1)(k-c)!(c!)^2},$$

$$cx^n \varphi_{S^2}(\zeta, t) = \sum_{b=0}^i \sum_{l=0}^S \sum_{k=0}^S \frac{(-1)^{i+b}(i+b)! c\zeta^b \mathfrak{S}_{(k,l)} Q_k(x) Q_l(y)}{(i-b)!(b!)^2}.$$

□

## 4 Solution Methodology for Fractional Order Partial Differential Equations

This section presents a methodology for obtaining solutions to fractional partial differential equations (FPDEs) subject to initial and boundary conditions.

### 4.1 Initial Conditions

Considered the problem in Eq. (1) with the following initial conditions

$$U(x, 0) = f_1(x) \quad U'(x, 0) = f_2(x).$$

We assume that the solution can be expressed in terms of Legendre polynomials, such that

$$\frac{\partial^\alpha U(x, y)}{\partial y^\alpha} = K_{S^2}^T \varphi_{S^2}(x, y),$$

By integrating of order  $\alpha$  with respect to  $y$  and utilizing Theorem 3.1, we obtain the following relationship

$$U(x, y) = K_{S^2}^T J_{(S^2 \times S^2)} \varphi_{S^2}(x, y) + yc_0 + c_1, \quad (15)$$

Upon utilizing the initial conditions, we can determine the values of  $c_0 = f_1(x)$ . By substituting these values of  $c_0$  and  $c_1$  into Equation 15, we obtain

$$U(x, y) = K_{S^2}^T y J_{(S^2 \times S^2)} \varphi_{S^2}(x, y) + y f_2(x) + f_1(x),$$

Let approximate the function in S-terms Legendre polynomials as

$$f_1(x) + y f_2(x) = F_1^T S^2 \varphi_{S^2}(x, y) \text{ and } f(x, y) = S_{S^2}^T \varphi_{S^2}(x, y),$$

$$U(x, y) = K_{S^2}^T y J_{(S^2 \times S^2)} \varphi_{S^2}(x, y) + F_1^T S^2 \varphi_{S^2}(x, y).$$

Let suppose

$$X' = K_{S^2}^T y J_{(S^2 \times S^2)} + F_1^T S^2,$$

then

$$U(x, y) = X' \varphi_{S^2}(x, y).$$

In the view of Theorems 3.2, 3.3, and 3.4, we can write as

$$\begin{aligned} \mathcal{D}_x^\beta U &= X'^x D_{(S^2 \times S^2)} \varphi_{S^2}(x, y), \\ \Theta(x, y) U &= X' G_{(S^2 \times S^2)}^\Theta \varphi_{S^2}(x, y), \\ \theta(x, y) \mathcal{D}_x U &= X'^x H_{(S^2 \times S^2)}^\theta \varphi_{S^2}(x, y). \end{aligned}$$

Substituting these estimates into Eq. (1) yields the following results

$$K_{S^2}^T \varphi_{S^2}(x, y) = [\lambda X'^x D_{(S^2 \times S^2)} + X'^x H_{(S^2 \times S^2)}^\theta + X' G_{(S^2 \times S^2)}^\Theta + S_{S^2}^T] \varphi_{S^2}(x, y),$$

After canceling  $\varphi_{S^2}(x, y)$  from both sides and substituting the value of  $X'$ , we can then

$$\begin{aligned} K_{S^2}^T &= \lambda K_{S^2}^T y J_{(S^2 \times S^2)}^x D_{(S^2 \times S^2)} + \lambda F_1^T S^2 x D_{(S^2 \times S^2)} + K_{S^2}^T y J_{(S^2 \times S^2)}^x H_{(S^2 \times S^2)}^\theta + F_1^T S^2 x H_{(S^2 \times S^2)}^\theta \\ &+ K_{S^2}^T y J_{(S^2 \times S^2)} G_{(S^2 \times S^2)}^\Theta + F_1^T S^2 G_{(S^2 \times S^2)}^\Theta + S_{S^2}^T, \end{aligned}$$

further simplification, we can write as

$$\begin{aligned} K_{S^2}^T &= K_{S^2}^T y J_{(S^2 \times S^2)} [\lambda^x D_{(S^2 \times S^2)} +^x H_{(S^2 \times S^2)}^\theta + G_{(S^2 \times S^2)}^\Theta] \\ &+ F_1^T S^2 [\lambda^x D_{(S^2 \times S^2)} +^x H_{(S^2 \times S^2)}^\theta + G_{(S^2 \times S^2)}^\Theta] + S_{S^2}^T. \end{aligned} \quad (16)$$

Which is the algebraic structure of the FPDEs in the form of Sylvester equation.

## 4.2 Dirichlet boundary conditions

Considered the problem in Eq. (1) with the following initial and boundary conditions

$$\begin{aligned} U(x, 0) &= f_1(x) & U'(x, 0) &= f_2(x), \\ U(0, y) &= g_1(y), & U(1, y) &= g_2(y). \end{aligned} \quad (17)$$

We suppose the solution of the problem in the term of the Legendre polynomials, such that the following holds

$$\frac{\partial^\alpha U(x, y)}{\partial y^\alpha} = K_{S^2}^T \varphi_{S^2}(x, y),$$

Using the initial conditions and applying Theorems (3.3) and (3.4), we can obtain estimates for the solution. Substituting these estimates into Eq. (1) and rearranging the terms, we obtain the following expression

$$\begin{aligned} \frac{\partial^\beta U(x, y)}{\partial x^\beta} &= \frac{1}{\lambda} [K_{S^2}^T (\mathbb{I} - {}^y J_{(S^2 \times S^2)} {}^x H_{(S^2 \times S^2)}^\theta - {}^y J_{(S^2 \times S^2)} G_{(S^2 \times S^2)}^\Theta) \\ &\quad + F_{1S^2}^T (-{}^x H_{(S^2 \times S^2)}^\theta - G_{(S^2 \times S^2)}^\Theta - S_{S^2}^T) \varphi_{S^2}(x, y), \end{aligned}$$

For the sake simplicity, let suppose

$$\begin{aligned} W_{(S^2 \times S^2)} &= \frac{1}{\lambda} [K_{S^2}^T (\mathbb{I} - {}^y J_{(S^2 \times S^2)} {}^x H_{(S^2 \times S^2)}^\theta - {}^y J_{(S^2 \times S^2)} G_{(S^2 \times S^2)}^\Theta) \\ &\quad + F_{1S^2}^T (-{}^x H_{(S^2 \times S^2)}^\theta - G_{(S^2 \times S^2)}^\Theta - S_{S^2}^T)], \\ \frac{\partial^\beta U(x, y)}{\partial x^\beta} &= [W_{(S^2 \times S^2)}] \varphi_{S^2}(x, y), \end{aligned}$$

Taking integration on both sides of the equation with respect to  $x$  of order of  $\beta$

$$U(x, y) = [W_{(S^2 \times S^2)}]^x J_{(S^2 \times S^2)} \varphi_{S^2}(x, y) + d_0 + x d_1, \quad (18)$$

Substituting the boundary condition  $U(0, y) = g_1(y)$  and  $U(1, y) = g_2(y)$  into the solution, we get  $d_0 = g_1(y)$ , and

$$u(1, t) = [W_{(S^2 \times S^2)}]^x J_{(S^2 \times S^2)} \Phi(1, t) + g_1(t) + d_1,$$

By substituting the values of  $d_0$  and  $d_1$  in Eq. (18)

$$U(x, y) = [W_{(S^2 \times S^2)}]^x J_{(S^2 \times S^2)} \varphi_{S^2}(x, y) + x g_2(y) + g_1(y) - [W_{(S^2 \times S^2)}]^x J_{(S^2 \times S^2)} x \Phi(1, y) - x g_1(y)$$

let S-term approximation in the term of Legendre polynomials as

$$\begin{aligned} x g_2 + (1 - x) g_1(y) &= F_{2S^2}^T \varphi_{S^2}(x, y) \text{ and } c x^n \Phi(\xi, y) = {}^x \mathbb{A}^{(c, n, \xi)} \varphi_{S^2}(x, y), \\ U(x, y) &= [W_{(S^2 \times S^2)}]^x J_{(S^2 \times S^2)} \varphi_{S^2}(x, y) - [W_{(S^2 \times S^2)}]^x J_{(S^2 \times S^2)} {}^x \mathbb{A}^{(1, 1, 1)} \varphi_{S^2}(x, y) \\ &\quad + F_{2S^2}^T \varphi_{S^2}(x, y), \end{aligned}$$

combining the equations and canceling  $\varphi_{S^2}(x, y)$  from both sides

$$K_{S^2}^T {}^y J_{(S^2 \times S^2)} + F_{1S^2}^T = [W_{(S^2 \times S^2)}] \left( {}^x J_{(S^2 \times S^2)} - {}^x J_{(S^2 \times S^2)} {}^x \mathbb{A}^{(1, 1, 1)} \right) + F_{2S^2}^T \quad (19)$$

putting the value of  $W_{(S^2 \times S^2)}$  as,

$$\begin{aligned} K_{S^2}^T {}^y J_{(S^2 \times S^2)} &= \frac{1}{\lambda} [K_{S^2}^T (\mathbb{I} - {}^y J_{(S^2 \times S^2)} {}^x H_{(S^2 \times S^2)}^\theta - {}^y J_{(S^2 \times S^2)} G_{(S^2 \times S^2)}^\Theta) \\ &\quad + F_{1S^2}^T (-{}^x H_{(S^2 \times S^2)}^\theta - G_{(S^2 \times S^2)}^\Theta - S_{S^2}^T) \\ &\quad \left( {}^x J_{(S^2 \times S^2)} - {}^x J_{(S^2 \times S^2)} {}^x \mathbb{A}^{(1, 1, 1)} \right) + F_{2S^2}^T - F_{1S^2}^T. \end{aligned} \quad (20)$$

Which is the algebraic structure of the equations.

### 4.3 Generalized Coupled System

Considered the Coupled system in Eq. (2) with the following initial and boundary conditions

$$\begin{aligned} U(x, 0) &= f_1(x), & U'(x, 0) &= f_2(x), \\ U(0, y) &= g_1(y), & U(1, y) &= g_2(x), \\ V(x, 0) &= f_3(x), & V'(x, 0) &= f_4(x), \\ V(0, y) &= g_3(y), & V(1, y) &= g_4(x). \end{aligned}$$

We suppose the solution of the problem in the term of the legendre polynomials, such that the following holds.

$$\begin{aligned} \frac{\partial^\alpha U(x, y)}{\partial y^\alpha} &= K_{S^2}^T \varphi_{S^2}(x, y), \\ \frac{\partial^\alpha V(x, y)}{\partial y^\alpha} &= L_{S^2}^T \varphi_{S^2}(x, y), \end{aligned}$$

by application of fractional integral of order  $\alpha$  with respect to  $y$  and making the use of Theorem (3.1), we get the following relation

In the view of Theorems (3.3) and (3.4), we can write as putting these estimates in Eq. (2) and re-arranging the terms, we get

$$\begin{aligned} \frac{\partial^\beta U(x, y)}{\partial x^\beta} &= \frac{1}{\lambda_1} [K(II - {}^y J_{(S^2 \times S^2)} G^{\theta_1} - {}^y J_{(S^2 \times S^2)} G^{\Theta_1}) + L(-\lambda_2 {}^y J_{(S^2 \times S^2)} {}^x D_\beta - {}^y J_{(S^2 \times S^2)} G^{\theta_2} - {}^y J_{(S^2 \times S^2)} G^{\Theta_2}) \\ &\quad + F_1(-G^{\theta_1} - G^{\Theta_1}) + F_2(-\lambda_2 {}^x D_\beta - G^{\theta_2} - G^{\Theta_2}) - S_1] \varphi_{S^2}(x, y), \\ \frac{\partial^\beta V(x, y)}{\partial x^\beta} &= \frac{1}{\lambda_4} [L(II - {}^y J_{(S^2 \times S^2)} G^{\theta_4} - {}^y J_{(S^2 \times S^2)} G^{\Theta_4}) + K(-\lambda_3 {}^y J_{(S^2 \times S^2)} {}^x D_\beta - {}^y J_{(S^2 \times S^2)} G^{\theta_3} - {}^y J_{(S^2 \times S^2)} G^{\Theta_3}) \\ &\quad + F_2(-G^{\theta_4} - G^{\Theta_4}) + F_1(-\lambda_3 {}^x D_\beta - G^{\theta_3} - G^{\Theta_3}) - S_2] \varphi_{S^2}(x, y), \end{aligned}$$

let suppose

$$\begin{aligned} M_{(S^2 \times S^2)} &= \frac{1}{\lambda_1} [K(II - {}^y J_{(S^2 \times S^2)} G^{\theta_1} - {}^y J_{(S^2 \times S^2)} G^{\Theta_1}) + L(-\lambda_2 {}^y J_{(S^2 \times S^2)} {}^x D_\beta - {}^y J_{(S^2 \times S^2)} G^{\theta_2} - {}^y J_{(S^2 \times S^2)} G^{\Theta_2}) \\ &\quad + F_1(-G^{\theta_1} - G^{\Theta_1}) + F_2(-\lambda_2 {}^x D_\beta - G^{\theta_2} - G^{\Theta_2}) - S_1], \\ N_{(S^2 \times S^2)} &= \frac{1}{\lambda_4} [L(II - {}^y J_{(S^2 \times S^2)} G^{\theta_4} - {}^y J_{(S^2 \times S^2)} G^{\Theta_4}) + K(-\lambda_3 {}^y J_{(S^2 \times S^2)} {}^x D_\beta - {}^y J_{(S^2 \times S^2)} G^{\theta_3} - {}^y J_{(S^2 \times S^2)} G^{\Theta_3}) \\ &\quad + F_2(-G^{\theta_4} - G^{\Theta_4}) + F_1(-\lambda_3 {}^x D_\beta - G^{\theta_3} - G^{\Theta_3}) - S_2]. \end{aligned}$$

Now taking the integration with respect to  $x$  of order  $\beta$

$$\begin{aligned} U(x, y) &= M_{(S^2 \times S^2)} \varphi_{S^2}(x, y) + d_0 + x d_1, \\ V(x, y) &= N_{(S^2 \times S^2)} \varphi_{S^2}(x, y) + e_0 + x e_1, \end{aligned} \tag{21}$$

by putting the BCs and solving for  $d_1$  and  $e_1$

$$\begin{aligned} d_1 &= g_2(y) - [M_{(S^2 \times S^2)}]^{(x, \beta)} I_{(S^2 \times S^2)} \Phi(1, y) - g_1(y), \\ e_1 &= g_4(y) - [N_{(S^2 \times S^2)}]^{(x, \beta)} I_{(S^2 \times S^2)} \Phi(1, y) - g_3(y), \end{aligned}$$

putting the values of  $e_1$  and  $d_1$  in Eq. (21), we will get

$$\begin{aligned} U(x, y) &= [M_{(S^2 \times S^2)}]^x J_{(S^2 \times S^2)} \varphi_{S^2}(x, y) + g_1(y) + x g_2(y) - [M_{(S^2 \times S^2)}]^x J_{(S^2 \times S^2)} x \Phi(1, y) - x g_1(y), \\ V(x, y) &= [N_{(S^2 \times S^2)}]^x J_{(S^2 \times S^2)} \varphi_{S^2}(x, y) + g_3(y) + x g_4(y) - [N_{(S^2 \times S^2)}]^x J_{(S^2 \times S^2)} x \Phi(1, y) - x g_3(y). \end{aligned}$$



let M term legender approximation of

$$(1-x)g_1(y) + xg_2 = F_3^T \varphi_{S^2}(x, y) \text{ and } (1-x)g_3(y) + xg_4 = F_4^T \varphi_{S^2}(x, y),$$

using the result of Lemma (3.2), then

$$\begin{aligned} U(x, y) &= [M_{(S^2 \times S^2)}]^x J_{(S^2 \times S^2)} - [M_{(S^2 \times S^2)}]^x J_{(S^2 \times S^2)}^x \mathbb{A}^{(1,1,1)} + F_3, \\ V(x, y) &= [N_{(S^2 \times S^2)}]^x J_{(S^2 \times S^2)} - [N_{(S^2 \times S^2)}]^x J_{(S^2 \times S^2)}^x \mathbb{A}^{(1,1,1)} + F_4, \end{aligned} \quad (22)$$

let  $\mathbb{B} = \left( {}^x J_{(S^2 \times S^2)} - {}^x J_{(S^2 \times S^2)}^x \mathbb{A}^{(1,1,1)} \right)$ , then Eq. (22) implies that

$$\begin{aligned} [K^y J_{(S^2 \times S^2)} + F_1] &= [M_{(S^2 \times S^2)}] \mathbb{B} + F_3, \\ [L^y J_{(S^2 \times S^2)} + F_2] &= [N_{(S^2 \times S^2)}] \mathbb{B} + F_4, \end{aligned} \quad (23)$$

putting the value of  $M_{(S^2 \times S^2)}$  and  $N_{(S^2 \times S^2)}$  as

$$\begin{aligned} [K^y J_{(S^2 \times S^2)} + F_1] &= \left[ \frac{1}{\lambda_1} [K(II - {}^y J_{(S^2 \times S^2)} G^{\theta_1} - {}^y J_{(S^2 \times S^2)} G^{\Theta_1}) + L(-\lambda_2 {}^y J_{(S^2 \times S^2)}^x D_\beta - {}^y J_{(S^2 \times S^2)} G^{\theta_2} \right. \\ &\quad \left. - {}^y J_{(S^2 \times S^2)} G^{\Theta_2}) + F_1(-G^{\theta_1} - G^{\Theta_1}) + F_2(-\lambda_2 {}^x D_\beta - G^{\theta_2} - G^{\Theta_2}) - S_1] \right] \mathbb{B} + F_3, \\ [L^y J_{(S^2 \times S^2)} + F_2] &= \left[ \frac{1}{\lambda_4} [L(II - {}^y J_{(S^2 \times S^2)} G^{\theta_4} - {}^y J_{(S^2 \times S^2)} G^{\Theta_4}) + K(-\lambda_3 {}^y J_{(S^2 \times S^2)}^x D_\beta - {}^y J_{(S^2 \times S^2)} G^{\theta_3} \right. \\ &\quad \left. - {}^y J_{(S^2 \times S^2)} G^{\Theta_3}) + F_2(-G^{\theta_4} - G^{\Theta_4}) + F_1(-\lambda_3 {}^x D_\beta - G^{\theta_3} - G^{\Theta_3}) - S_2] \right] \mathbb{B} + F_4. \end{aligned} \quad (24)$$

Writing the system in matrix form we get

$$\begin{aligned} \begin{bmatrix} K^y J_{(S^2 \times S^2)} + F_1 \\ L^y J_{(S^2 \times S^2)} + F_2 \end{bmatrix} &= \begin{bmatrix} \frac{1}{\lambda_1} [K(II - {}^y J_{(S^2 \times S^2)} G^{\theta_1} - {}^y J_{(S^2 \times S^2)} G^{\Theta_1}) \mathbb{B}] \\ \frac{1}{\lambda_4} [L(II - {}^y J_{(S^2 \times S^2)} G^{\theta_4} - {}^y J_{(S^2 \times S^2)} G^{\Theta_4}) \mathbb{B}] \end{bmatrix} + \begin{bmatrix} \frac{1}{\lambda_1} F_2(-\lambda_2 {}^x D_\beta - G^{\theta_2} - G^{\Theta_2}) \mathbb{B} \\ \frac{1}{\lambda_4} F_1(-\lambda_3 {}^x D_\beta - G^{\theta_3} - G^{\Theta_3}) \mathbb{B} \end{bmatrix} \\ &\quad + \begin{bmatrix} \frac{1}{\lambda_1} F_1(-G^{\theta_1} - G^{\Theta_1}) \mathbb{B} \\ \frac{1}{\lambda_4} F_2(-G^{\theta_4} - G^{\Theta_4}) \mathbb{B} \end{bmatrix} + \begin{bmatrix} \frac{1}{\lambda_1} L(-\lambda_2 {}^y J_{(S^2 \times S^2)}^x D_\beta - {}^y J_{(S^2 \times S^2)} G^{\theta_2} - {}^y J_{(S^2 \times S^2)} G^{\Theta_2}) \mathbb{B} \\ \frac{1}{\lambda_4} K(-\lambda_3 {}^y J_{(S^2 \times S^2)}^x D_\beta - {}^y J_{(S^2 \times S^2)} G^{\theta_3} - {}^y J_{(S^2 \times S^2)} G^{\Theta_3}) \mathbb{B} \end{bmatrix} \\ &\quad + \begin{bmatrix} -\frac{1}{\lambda_1} S_1 \mathbb{B} \\ -\frac{1}{\lambda_4} S_2 \mathbb{B} \end{bmatrix} + \begin{bmatrix} F_3 \\ F_4 \end{bmatrix}. \\ \begin{bmatrix} K & L \end{bmatrix} \begin{bmatrix} {}^y J_{(S^2 \times S^2)} & O \\ O & {}^y J_{(S^2 \times S^2)} \end{bmatrix} &= \begin{bmatrix} K & L \end{bmatrix} \begin{bmatrix} \frac{1}{\lambda_1} [(II - {}^y J_{(S^2 \times S^2)} G^{\theta_1} - {}^y J_{(S^2 \times S^2)} G^{\Theta_1}) \mathbb{B}] & O \\ O & \frac{1}{\lambda_4} [(II - {}^y J_{(S^2 \times S^2)} G^{\theta_4} - {}^y J_{(S^2 \times S^2)} G^{\Theta_4}) \mathbb{B}] \end{bmatrix} \\ &\quad + \begin{bmatrix} K & L \end{bmatrix} \begin{bmatrix} O & \frac{1}{\lambda_4} (-\lambda_3 {}^y J_{(S^2 \times S^2)}^x D_\beta - {}^y J_{(S^2 \times S^2)} G^{\theta_3} - {}^y J_{(S^2 \times S^2)} G^{\Theta_3}) \mathbb{B} \\ \frac{1}{\lambda_1} (-\lambda_2 {}^y J_{(S^2 \times S^2)}^x D_\beta - {}^y J_{(S^2 \times S^2)} G^{\theta_2} - {}^y J_{(S^2 \times S^2)} G^{\Theta_2}) \mathbb{B} & O \end{bmatrix} \\ &\quad + \begin{bmatrix} F_1 & F_2 \end{bmatrix} \begin{bmatrix} \frac{1}{\lambda_1} (-G^{\theta_1} - G^{\Theta_1}) \mathbb{B} & O \\ O & \frac{1}{\lambda_4} (-G^{\theta_4} - G^{\Theta_4}) \mathbb{B} \end{bmatrix} \\ &\quad + \begin{bmatrix} F_1 & F_2 \end{bmatrix} \begin{bmatrix} O & \frac{1}{\lambda_4} (-\lambda_3 {}^x D_\beta - G^{\theta_3} - G^{\Theta_3}) \mathbb{B} \\ \frac{1}{\lambda_1} (-\lambda_2 {}^x D_\beta - G^{\theta_2} - G^{\Theta_2}) \mathbb{B} & O \end{bmatrix} \\ &\quad + \begin{bmatrix} -\frac{1}{\lambda_1} S_1 \mathbb{B} \\ -\frac{1}{\lambda_4} S_2 \mathbb{B} \end{bmatrix} + \begin{bmatrix} F_3 & F_4 \end{bmatrix} - \begin{bmatrix} F_1 & F_2 \end{bmatrix}, \\ \begin{bmatrix} K & L \end{bmatrix} \begin{bmatrix} {}^y J_{(S^2 \times S^2)} & O \\ O & {}^y J_{(S^2 \times S^2)} \end{bmatrix} &= \begin{bmatrix} -\frac{1}{\lambda_1} S_1 \mathbb{B} \\ -\frac{1}{\lambda_4} S_2 \mathbb{B} \end{bmatrix} + \begin{bmatrix} F_3 & F_4 \end{bmatrix} - \begin{bmatrix} F_1 & F_2 \end{bmatrix} \\ &\quad + \begin{bmatrix} K & L \end{bmatrix} \begin{bmatrix} \frac{1}{\lambda_1} [(II - {}^y J_{(S^2 \times S^2)} G^{\theta_1} - {}^y J_{(S^2 \times S^2)} G^{\Theta_1}) \mathbb{B}] & \frac{1}{\lambda_4} (-\lambda_3 {}^y J_{(S^2 \times S^2)}^x D_\beta - {}^y J_{(S^2 \times S^2)} G^{\theta_3} - {}^y J_{(S^2 \times S^2)} G^{\Theta_3}) \mathbb{B} \\ \frac{1}{\lambda_1} (-\lambda_2 {}^y J_{(S^2 \times S^2)}^x D_\beta - {}^y J_{(S^2 \times S^2)} G^{\theta_2} - {}^y J_{(S^2 \times S^2)} G^{\Theta_2}) \mathbb{B} & \frac{1}{\lambda_4} [(II - {}^y J_{(S^2 \times S^2)} G^{\theta_4} - {}^y J_{(S^2 \times S^2)} G^{\Theta_4}) \mathbb{B}] \end{bmatrix} \\ &\quad + \begin{bmatrix} F_1 & F_2 \end{bmatrix} \begin{bmatrix} \frac{1}{\lambda_1} (-G^{\theta_1} - G^{\Theta_1}) \mathbb{B} & \frac{1}{\lambda_4} (-\lambda_3 {}^y J_{(S^2 \times S^2)}^x D_\beta - {}^y J_{(S^2 \times S^2)} G^{\theta_3} - {}^y J_{(S^2 \times S^2)} G^{\Theta_3}) \mathbb{B} \\ \frac{1}{\lambda_1} (-\lambda_2 {}^x D_\beta - G^{\theta_2} - G^{\Theta_2}) \mathbb{B} & \frac{1}{\lambda_4} (-G^{\theta_4} - G^{\Theta_4}) \mathbb{B} \end{bmatrix}. \end{aligned}$$

Which is the algebraic structure of the fractional order partial differential equations.

## 5 Test Experiments

### Test problem 1.

$$\mathcal{D}_y U = 5\mathcal{D}_x^2 U + \frac{(y+x)^3}{3}\mathcal{D}_x U + 5(x-y)U + f(x,y), \quad (25)$$

with the ICs

$$U(x,0) = \sin(x) + 1, \quad U'(x,0) = x + \cos(x),$$

where the source function is

$$f(x,y) = (5y - 5x)(e^{yx} + \sin(y+x)) - \sin(y+x) - 5\cos(y+x) - 5ye^{yx} - \frac{(y+x)^3(\cos(y+x) + ye^{yx})}{3} + x^2 e^{yx}$$

The exact solution of the problem is

$$U(x,y) = e^{xy} + \sin(y+x).$$

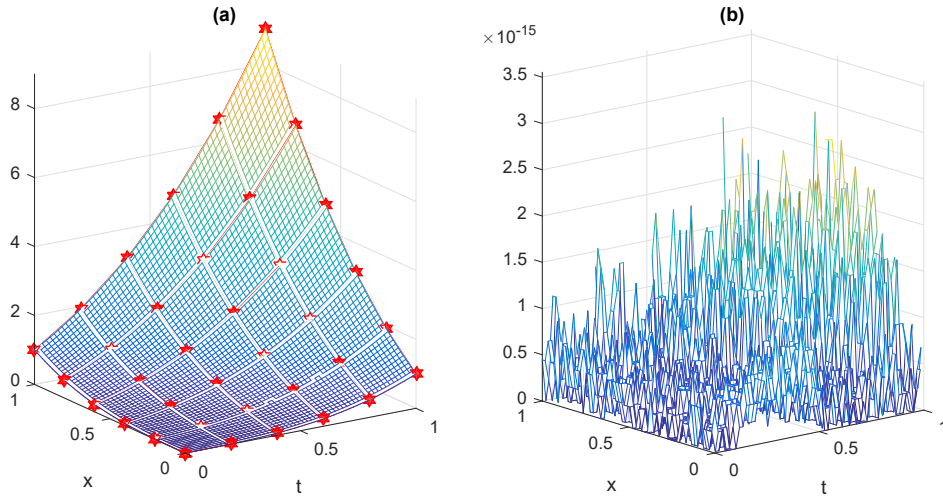


Figure 1: (a) The comparison of exact and approximate solutions, and (b) the absolute error of test problem 1 at scale level  $S = 5$ .

### Test problem 2.

$$\mathcal{D}_y^2 U = 6\mathcal{D}_x^2 U + 2(y+x)\mathcal{D}_x U + (y-x)^2 U + f(x,y) \quad (26)$$

with the ICs and the BCs

$$\begin{aligned} U(x,0) &= \frac{9(x - \frac{1}{2})^2}{25}, & U'(x,0) &= -\frac{6(x - \frac{1}{2})^2}{5}, \\ U(0,y) &= \frac{(t - \frac{3}{5})^2}{4}, & U(1,y) &= \frac{(t - \frac{3}{5})^2}{4}. \end{aligned}$$

with the exact solution is

$$U(x, y) = \left(y - \frac{3}{5}\right)^2 \times \left(x - \frac{1}{2}\right)^2$$

The source function is

$$f(x, y) = 2 \left(x - \frac{1}{2}\right)^2 - 12 \left(t - \frac{3}{5}\right)^2 - (2y + 2x)(2x - 1) \left(y - \frac{3}{5}\right)^2 - (y - x)^2 \left(y - \frac{3}{5}\right)^2 \left(x - \frac{1}{2}\right)^2.$$

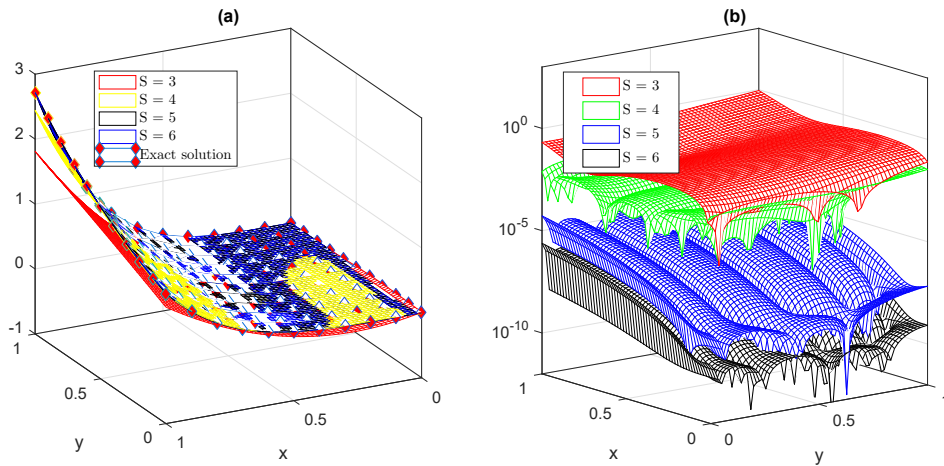


Figure 2: Comparison and Absolute error of  $U(x,y)$  of test problem 2 for  $S = 3, 4, 5, 6$ .

Table 1: Absolute error of  $U(x,t)$  of the test problem 2 on different points of the plane at different scale level.

(x,y)	S = 3	S = 4	S = 5	S = 6
(0.1, 0.1)	6.0492e-02	3.6283e-03	9.9356e-09	4.6506e-10
(0.2, 0.2)	1.1495e-01	6.3315e-03	2.7994e-08	4.6154e-10
(0.3, 0.3)	1.4364e-01	1.2180e-03	1.0812e-07	6.1502e-09
(0.4, 0.4)	1.4390e-01	6.6235e-03	4.4193e-07	4.0330e-09
(0.5, 0.5)	1.2074e-01	1.1812e-02	5.8576e-08	4.8434e-08
(0.6, 0.6)	9.0002e-02	1.0483e-02	2.1593e-06	2.9797e-08
(0.7, 0.7)	8.6065e-02	5.1895e-03	3.7478e-06	1.7442e-07
(0.8, 0.8)	1.6198e-01	1.2921e-02	3.2539e-06	1.8825e-07
(0.9, 0.9)	3.9689e-01	7.5419e-02	1.5098e-05	6.5678e-07

### Test problem 3.

$$\begin{aligned} \mathcal{D}_y^\alpha U &= 0.6 \mathcal{D}_x^\beta U + 0.5 \mathcal{D}_x^\beta V + \theta_1(x, y) \mathcal{D}_x U + \theta_2(x, y) \mathcal{D}_x V + \Theta_1(x, y) U + \Theta_2(x, y) V + f(x, y), \\ \mathcal{D}_y^\alpha V &= 0.2 \mathcal{D}_x^\beta U + 0.3 \mathcal{D}_x^\beta V + \theta_3(x, y) \mathcal{D}_x U + \theta_4(x, y) \mathcal{D}_x V + \Theta_3(x, y) U + \Theta_4(x, y) V + g(x, y), \end{aligned} \quad (27)$$

with the ICs and the BCs

$$U(x, 0) = x + \sin(x),$$

$$U(0, y) = -\sin(y),$$

$$V(x, 0) = \cos(x),$$

$$V(0, t) = y + \cos(y),$$

$$U'(x, 0) = -\cos(x),$$

$$U(1, y) = 1 - \sin(y - 1),$$

$$V'(x, 0) = \sin(x) + 1,$$

$$V(1, y) = y + \cos(y - 1).$$

with the exact solutions

$$U(x, y) = x + \sin(x - y),$$

$$V(x, y) = y + \cos(x - y),$$

the source functions is

$$f(x, y) = \frac{\cos(x - y)}{2} - \frac{2 \sin(x - y)}{5} + \sin(x - y) (x + y)^2 - (2x + 2y) (x + \sin(x - y)) \\ - \sin(x + y) (\cos(x - y) + 1) - 2xy (y + \cos(x - y)),$$

$$g(x, y) = \frac{\sin(x - y)}{5} - \frac{7 \cos(x - y)}{10} - (x + y)^2 (x + \sin(x - y)) + \sin(x - y) e^{x+y} \\ - \cos(x + y) (\cos(x - y) + 1) - (y^2 + x) (y + \cos(x - y)).$$

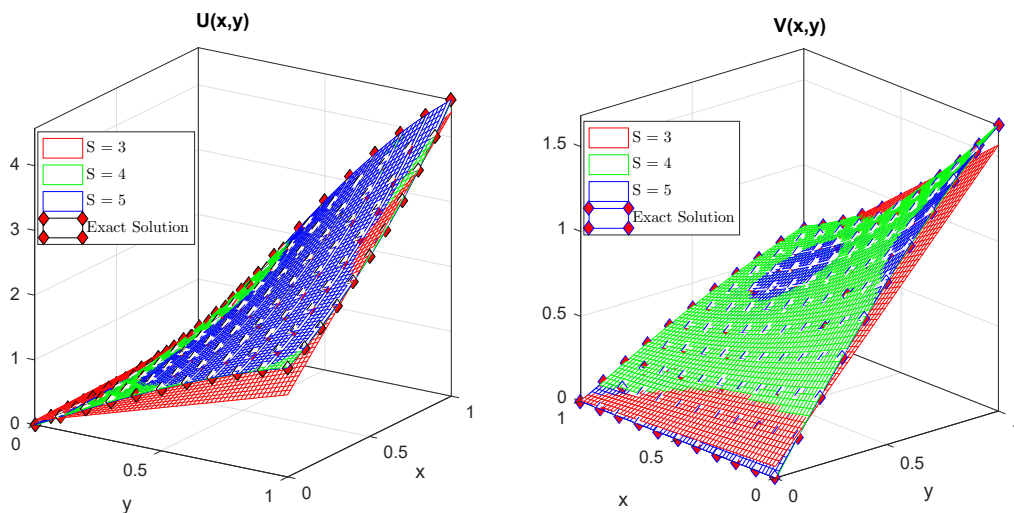


Figure 3: Comparison of exact solution and approximate solution of  $U(x, y)$  and  $V(x, y)$  for  $S = 3, 4, 5$ .

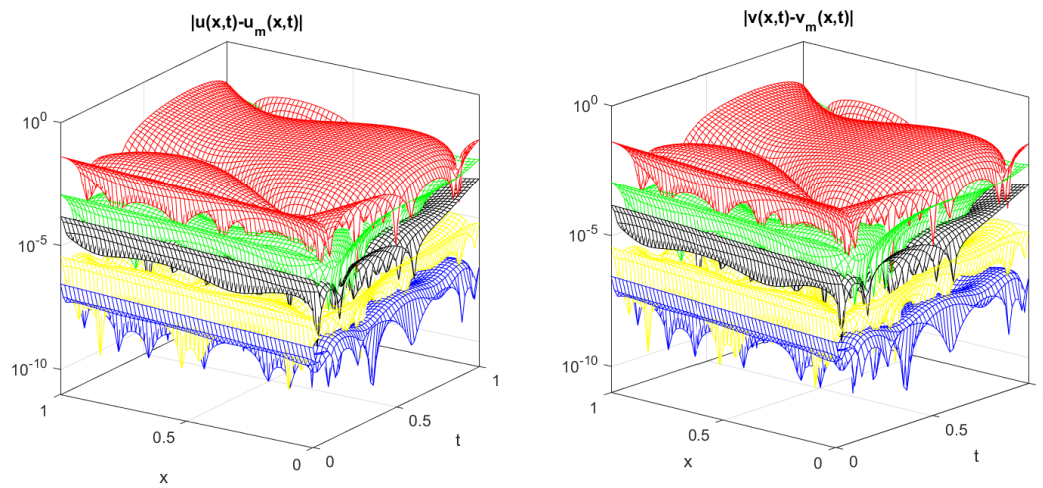


Figure 4: Absolute error of the approximate solution of  $U(x, y)$  and  $V(x, y)$  for  $S = 3, 4, 5..$

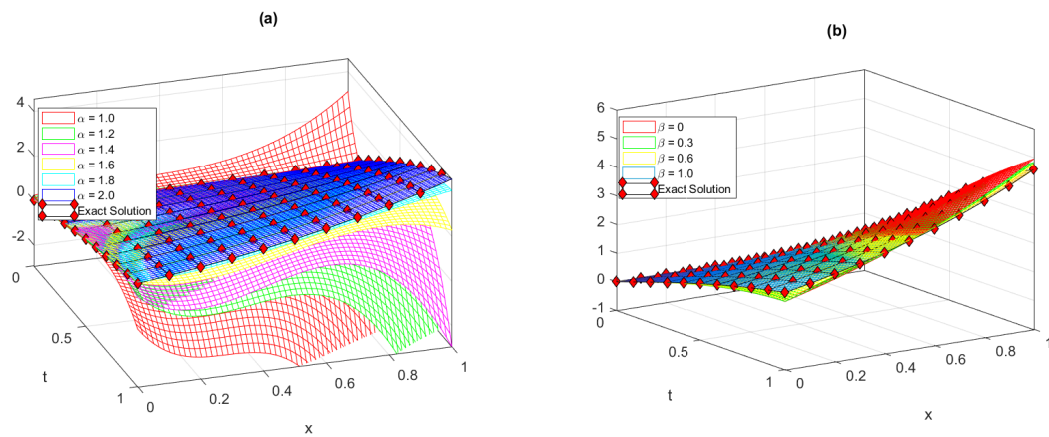


Figure 5: Variation in  $\alpha$  and  $\beta$  in test problem 3 of  $U(x,y)$  for  $S = 5$ .

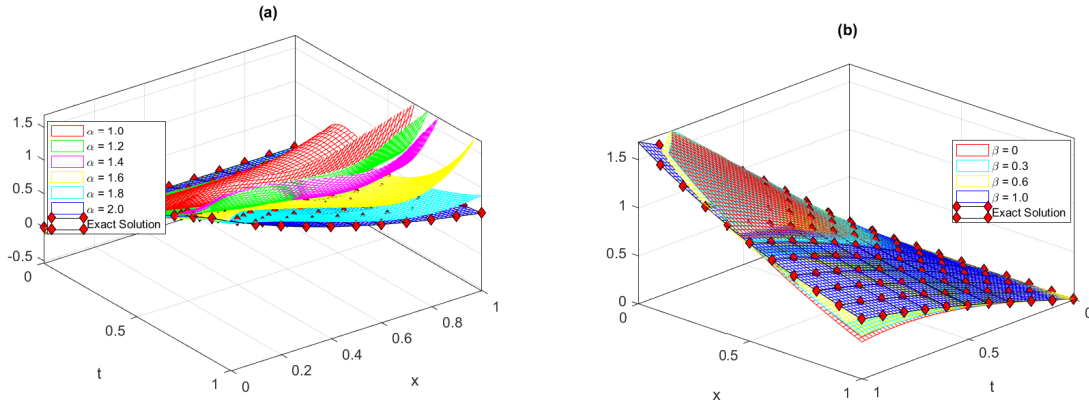


Figure 6: Variation in  $\alpha$  and  $\beta$  in  $V(x,y)$  in test problem 3 of for  $S = 5$ .

Table 2: Absolute error of the test problem 3 on different points of the plane at different scale level.

(x,y)	S = 3	S = 4	S = 5	S = 6
	$U_{(abs)}, V_{(abs)}$	$U_{(abs)}, V_{(abs)}$	$U_{(abs)}, V_{(abs)}$	$U_{(abs)}, V_{(abs)}$
(0.1, 0.1)	8.4140e-3, 1.6655e-3	5.6221e-4, 9.2345e-4	3.3871e-6, 1.6078e-6	2.0992e-6, 3.7928e-6
(0.2, 0.2)	4.6137e-3, 7.3710e-3	2.4581e-3, 3.7705e-3	3.2549e-7, 1.5342e-5	3.2768e-6, 2.4282e-7
(0.3, 0.3)	2.1116e-3, 9.7669e-3	1.6189e-3, 2.6813e-3	2.1144e-5, 1.2249e-5	1.8192e-6, 2.8551e-5
(0.4, 0.4)	1.1155e-3, 8.0720e-3	1.1933e-4, 3.8112e-4	1.5882e-5, 9.8144e-7	5.3284e-7, 3.0007e-7
(0.5, 0.5)	1.7071e-3, 2.6059e-3	9.1833e-5, 1.7020e-4	2.8232e-5, 1.4792e-5	2.7891e-6, 5.1395e-6
(0.6, 0.6)	3.7728e-3, 5.2476e-3	3.3831e-3, 4.2104e-3	8.1663e-5, 7.4887e-5	4.6880e-6, 8.8008e-6
(0.7, 0.7)	6.9186e-3, 1.3074e-2	1.2157e-2, 1.5226e-2	5.9210e-5, 2.6880e-4	1.0005e-6, 1.8289e-5
(0.8, 0.8)	1.0376e-2, 1.7457e-2	2.4071e-2, 2.9706e-2	1.3684e-4, 6.2126e-4	3.3435e-5, 5.7972e-5
(0.9, 0.9)	1.2890e-2, 1.4014e-2	2.8369e-2, 3.4522e-2	4.1028e-4, 8.4497e-4	8.6757e-5, 1.4158e-5

## 6 Results and discussion

The absolute error is defined as the norm of the difference between the exact solution  $U(x,y)$  and the approximate solution  $U_S(x,y)$ , denoted as  $U_{(abs)} = ||U(x,y) - U_S(x,y)||$ . Similarly, the absolute error between the exact solution  $V(x,y)$  and the approximate solution  $V_S(x,y)$  is defined as  $V_{(abs)} = ||V(x,y) - V_S(x,y)||$ .

In test problem 1, we employ the proposed technique to solve the problem. Initially, we set  $\alpha = 2$  and  $\beta = 1$ . The exact solution is given by  $U(x,y) = e^{x,y} + \sin(y+x)$ . Figure 1 displays the comparison between the exact and approximate solutions for a scale level of  $S = 5$ , with (a) and (b) illustrating the absolute error. As the scale level increases, the approximate solution progressively aligns with the exact solution. For the test problem 2, Figure 2 exhibits the comparison between the exact and approximate solutions, along with the absolute error. Notably, at  $S = 5$ , the error of approximation is below  $10^{-10}$ . Similarly, Figure 3 illustrates the

comparison between the approximate and exact solutions at a scale level of  $S = 5$  for the problem 3. Additionally, Figure 4 presents the absolute error at different scale levels for the same test problem. Table 1 provides a comparison of the exact and approximate solutions at various points in the plane and different scale levels. We approximate the solution of the scheme using specific fractional values of  $\alpha$  and  $\beta$ , while fixing the scale level at  $S = 5$ . The results demonstrate that as  $\alpha$  approaches 2, the approximate solution closely matches the exact solution, as shown in Figure 5. Similarly, the same observation applies to  $\beta$  approaching 1, as depicted in Figure 6. By solving the test problem 3 with  $\alpha = 2$  and  $\beta = 1$ , the exact solution is given by  $U(x, y) = x + \sin(x - y)$  and  $V(x, y) = y + \cos(x - y)$ . We approximate the solution at different scale levels and observe that the method is highly efficient and yields highly accurate solutions. Even for small scale levels, the results are remarkably accurate. Furthermore, through numerical error analysis, we find that the error falls below  $10^{-3}$ , which is an acceptable level of accuracy for a choice of  $S \leq 5$ . Table 2 presents the results showcasing further error reduction as the scale level increases.

## 7 Conclusion and future work

Our analysis and experimental work have led us to the conclusion that the proposed method is highly effective in approximating solutions for a system of coupled fractional order partial differential equations with variable coefficients. The derivatives are defined in the Caputo-Fabrizio sense. The results obtained from our study are deemed satisfactory. Furthermore, we anticipate that the method can produce even more accurate solutions by incorporating other orthogonal polynomials or wavelets. In this study, we have applied the method to solve linear multi-term coupled fractional order partial differential equations, considering initial and Dirichlet type boundary conditions. It is worth noting that the method can be easily extended to address systems with different types of non-local boundary conditions. As part of our future work, we aim to generalize the method to tackle similar problems involving nonlinear boundary conditions.

### Availability of data and material

All the data used in this research are available in the document.

### Competing interests

We declare that there is no competing interest.

### Funding

NA

### Authors contributions

### Acknowledgements

NA



## Acknowledgment

## References

- [1] Luo, D., Wang, J. R., and Feckan, M. 2018. Applying fractional calculus to analyze economic growth modelling. *Journal of Applied Mathematics, Statistics and Informatics*, 14(1): 25-36.
- [2] Tejado, I., Valrio, D., Prez, E., and Valrio, N. 2017. Fractional calculus in economic growth modelling: the Spanish and Portuguese cases. *International Journal of Dynamics and Control*, 5(1): 208-222.
- [3] Tarasov, and Vasily E., 2019. On history of mathematical economics: Application of fractional calculus. *Mathematics*, 7(6) : 509.
- [4] Gnerhan, H., and elik, E. 2020. Analytical and approximate solutions of fractional partial differential-algebraic equations. *Applied Mathematics and Nonlinear Sciences*, 5(1): 109-120.
- [5] Hilfer, R. (Ed.). 2000. *Applications of fractional calculus in physics*. World scientific.
- [6] Modanli, M., and Akgı, A. 2020. On Solutions of Fractional order Telegraph partial differential equation by Crank-Nicholson finite difference method. *Applied Mathematics and Nonlinear Sciences*, 5(1): 163-170.
- [7] Marques, F. C. F., Saraiva, A. A., Sousa, J. V. M., Ferreira, N. F., and Valente, A. 2018. Manipulation of bio-inspired robot with gesture recognition through fractional calculus. In *2018 Latin American Robotic Symposium, 2018 Brazilian Symposium on Robotics (SBR) and 2018 Workshop on Robotics in Education (WRE)* 230-235. IEEE.
- [8] Debnath, L. 2003. Recent applications of fractional calculus to science and engineering. *International Journal of Mathematics and Mathematical R Sciences*, 2(54): 3413-3442.
- [9] Kabra, S., Nagar, H., Nisar, K. S., and Suthar, D. L. 2020. The Marichev-Saigo-Maeda Fractional Calculus Operators Pertaining to the Generalized-Struve Function. *Applied Mathematics and Nonlinear Sciences*, 5(2): 593-602.
- [10] Machado, J. T., Kiryakova, V., and Mainardi, F. 2011. Recent history of fractional calculus. *Communications in nonlinear science and numerical simulation*, 16(3): 1140-1153.
- [11] Sun, H., Zhang, Y., Baleanu, D., Chen, W., and Chen, Y. 2018. A new collection of real world applications of fractional calculus in science and engineering. *Communications in Nonlinear Science and Numerical Simulation*, 64(2): 213-231.
- [12] Kaur, D., Agarwal, P., Rakshit, M., and Chand, M. 2020. Fractional Calculus involving  $(.)$ -Mathieu Type Series. *Applied Mathematics and Nonlinear Sciences*, 5(2): 15-34.
- [13] Yang, A., and Ge, W. 2009. Positive solutions of multi-point boundary value problems of nonlinear fractional differential equation at resonance. *The Pure and Applied Mathematics*, 16(2): 213-225..
- [14] Podlubny, I., Chechkin, A., Skovranek, T., Chen, Y., and Jara, B. M. V. 2009. Matrix approach to discrete fractional calculus II: partial fractional differential equations. *Journal of Computational Physics*, 228(8): 3137-3153.



- [15] Kilbas, A. A., Srivastava, H. M., and Trujillo, J. J. 2006. Theory and applications of fractional differential equations (Vol. 204). elsevier.
- [16] Modanli, M., and Akgl, A. (2020). On Solutions of Fractional order Telegraph partial differential equation by Crank-Nicholson finite difference method. *Applied Mathematics and Nonlinear Sciences*, 5(1): 163-170.
- [17] Diethelm, K., and Ford, N. J. 2002. Analysis of fractional differential equations. *Journal of Mathematical Analysis and Applications*, 265(2): 229-248.
- [18] Herzallah, M. A., El-Sayed, A. M., and Baleanu, D. 2010. On the fractional-order diffusion-wave process. *Rom. J. Phys*, 55(3-4): 274-284.
- [19] Tarasov, V. E. 2011. Fractional dynamics: applications of fractional calculus to dynamics of particles, fields and media. Springer Science and Business Media, 2(1): 193-204.
- [20] Saqib, M., Khan, I., and Shafie, S. 2019. Application of fractional differential equations to heat transfer in hybrid nanofluid: modeling and solution via integral transforms. *Advances in Difference Equations*, 2(1): 1-18.
- [21] Ilhan, E., and Kiymaz, I. O. 2020. A generalization of truncated M-fractional derivative and applications to fractional differential equations. *Applied Mathematics and Nonlinear Sciences*, 5(1): 171-188.
- [22] Koca, I., and Yaprakdal, P. 2020. A new approach for nuclear family model with fractional order Caputo derivative. *Applied Mathematics and Nonlinear Sciences*, 5(1): 393-404.
- [23] Oldham, K., and Spanier, J. 1974. The fractional calculus theory and applications of differentiation and integration to arbitrary order. Elsevier, 3(1): 93-103.
- [24] Podlubny, I., Chechkin, A., Skovranek, T., Chen, Y., and Jara, B. M. V. 2009. Matrix approach to discrete fractional calculus II: partial fractional differential equations. *Journal of Computational Physics*, 228(8): 3137-3153.
- [25] Sahin, R., and Yagci, O. 2020. Fractional calculus of the extended hypergeometric function. *Applied Mathematics and Nonlinear Sciences*, 5(1): 369-384.
- [26] Ilhan, E., and Kiymaz, I. O. 2020. A generalization of truncated M-fractional derivative and applications to fractional differential equations. *Applied Mathematics and Nonlinear Sciences*, 5(1): 171-188.
- [27] Yang, Aijun, and Weigao Ge. 2019. Positive solutions of multi-point boundary value problems of nonlinear fractional differential equation at resonance, 16(2): 213-225.
- [28] Krpinar, Z. S. 2013. Legendre Seudospectral Method For The Approximate Solutions Some Of The Fractional-Order Differential Equations. *i-Manager's Journal on Mathematics*, 2(2): 22.
- [29] Momani, S., and Odibat, Z. 2006. Analytical approach to linear fractional partial differential equations arising in fluid mechanics. *Physics Letters A*, 355(5): 271-279.
- [30] Momani, S., and Odibat, Z. 2006. Analytical solution of a time-fractional NavierStokes equation by Adomian decomposition method. *Applied Mathematics and Computation*, 177(2): 488-494.

- [31] Mohyud-Din, S. T., and Noor, M. A. 2008. Solving Schrödinger equations by modified variational iteration method. *World Applied Sciences Journal*, 5(3): 352-357.
- [32] Heo, S. C., Seo, Y. H., Ku, T. W., Kim, J., and Kang, B. S. 2009. Study on application of flexible die to sheet metal forming process. *Transactions of Materials Processing*, 18(7): 556-564.
- [33] Ray, S. S., and Bera, R. K. 2006. Analytical solution of a fractional diffusion equation by Adomian decomposition method. *Applied Mathematics and Computation*, 174(1): 329-336.
- [34] Krpinar, Z. S. 2013. Legendre Seudospectral Method For The Approximate Solutions Some Of The Fractional-Order Differential Equations. *i-Manager's Journal on Mathematics*, 2(2): 22.
- [35] Vanani, S. K., and Aminataei, A. 2012. A numerical algorithm for the space and time fractional Fokker-Planck equation. *International Journal of Numerical Methods for Heat and Fluid Flow*, 22(8): 1037-1052.
- [36] Xu, Q., and Hesthaven, J. S. 2014. Discontinuous Galerkin method for fractional convection-diffusion equations. *SIAM Journal on Numerical Analysis*, 52(1): 405-423.
- [37] Hashim, I., Abdulaziz, O., and Momani, S. 2009. Homotopy analysis method for fractional IVPs. *Communications in Nonlinear Science and Numerical Simulation*, 14(3): 674-684.
- [38] Krpinar, Z. S. 2013. Legendre Seudospectral Method For The Approximate Solutions Some Of The Fractional-Order Differential Equations. *i-Manager's Journal on Mathematics*, 2(2): 22.
- [39] Alshabanat, A., Jleli, M., Kumar, S., and Samet, B. 2020. Generalization of Caputo-Fabrizio fractional derivative and applications to electrical circuits. *Frontiers in Physics*, 80(2): 64.
- [40] Oldham, K., and Spanier, J. 1974. *The fractional calculus theory and applications of differentiation and integration to arbitrary order*. Elsevier.
- [41] Podlubny, I., Chechkin, A., Skovranek, T., Chen, Y., and Jara, B. M. V. 2009. Matrix approach to discrete fractional calculus II: partial fractional differential equations. *Journal of Computational Physics*, 228(8): 3137-3153.
- [42] Balci, M. A. 2020. Fractional interaction of financial agents in a stock market network. *Applied Mathematics and Nonlinear Sciences*, 5(1): 317-336.
- [43] Saadatmandi, A., and Dehghan, M. 2010. A new operational matrix for solving fractional-order differential equations. *Computers and mathematics with applications*, 59(3): 1326-1336.
- [44] Doha, E. H., Bhrawy, A. H., and Ezz-Eldien, S. S. 2011. Efficient Chebyshev spectral methods for solving multi-term fractional orders differential equations. *Applied Mathematical Modelling*, 35(12): 5662-5672.
- [45] Kossoy, A., Oppermann, K., Reddy, R. C., Bosi, M., Boukerche, S., Hhne, N., and Warnecke, C. 2013. *Mapping Carbon Pricing Initiatives: Developments and Prospects 2013*.

- [46] Abd-Elhameed, W. M., and Youssri, Y. 2019. Sixth-kind Chebyshev spectral approach for solving fractional differential equations. *International Journal of Nonlinear Sciences and Numerical Simulation*, 20(2): 191-203.
- [47] Moradi, L., Mohammadi, F., and Conte, D. 2019. A discrete orthogonal polynomials approach for coupled systems of nonlinear fractional order integro-differential equations. *Tbilisi Mathematical Journal*, 12(3): 21-38.
- [48] Erfani, S., Babolian, E., Javadi, S., and Shamsi, M. 2019. Stable evaluations of fractional derivative of the MntzLegendre polynomials and application to fractional differential equations. *Journal of Computational and Applied Mathematics*, 348(4): 70-88.
- [49] Behroozifar, M., and Ahmadpour, F. 2019. A study on spectral methods for linear and nonlinear fractional differential equations. *International Journal of Computing Science and Mathematics*, 10(6): 545-556.
- [50] Qu, H., Yang, X., and She, Z. 2020. Left-and Right-Shifted Fractional Legendre Functions with an Application for Fractional Differential Equations. *Advances in Mathematical Physics*, 2020.
- [51] Rani, D., and Mishra, V. 2019. Solving linear fractional order differential equations by Chebyshev polynomials based numerical inverse Laplace transform. *Mathematics in Engineering, Science and Aerospace (MESA)*, 10(4): 234-246.
- [52] Mohammadi, F., Moradi, L., and Tenreiro Machado, J. A. 2022. A discrete polynomials approach for optimal control of fractional Volterra integro-differential equations. *Journal of Vibration and Control*, 28(2): 72-82.
- [53] Bhrawy, A. H., Doha, E. H., Ezz-Eldien, S. S., and Abdelkawy, M. A. 2016. A numerical technique based on the shifted Legendre polynomials for solving the time-fractional coupled KdV equations. *Calcolo*, 53(1): 1-17.
- [54] Khalil, H., Ali Khan, R., H Al-Smadi, M., A Freihat, A., and Shawagfeh, N. 2020. New operational matrix for shifted Legendre polynomials and fractional differential equations with variable coefficients. *Punjab University Journal of Mathematics*, 47(1): 32-44.
- [55] Khalil, H., Ali Khan, R., H Al-Smadi, M., A Freihat, A., and Shawagfeh, N. 2020. New operational matrix for shifted Legendre polynomials and fractional differential equations with variable coefficients. *Punjab University Journal of Mathematics*, 47(1): 45-54.
- [56] Khalil, H., and Khan, R. A. 2015. The use of Jacobi polynomials in the numerical solution of coupled system of fractional differential equations. *International Journal of Computer Mathematics*, 92(7): 1452-1472.
- [57] Khalil, H., and Khan, R. A. 2014. A new method based on Legendre polynomials for solutions of the fractional two-dimensional heat conduction equation. *Computers and Mathematics with Applications*, 67(10): 1938-1953.
- [58] Ma, R. 2007. A survey on nonlocal boundary value problems. *Appl. Math. E-Notes*, 7(3): 257-279.

# EXPERIMENTAL AND NUMERICAL ANALYSIS OF PLATE FIN HEAT SINKS IN A SQUARE CHANNEL UNDER FORCED CONVECTION

Muhammet Nasif KURU<sup>1</sup>

<sup>1</sup> Vocational School of Technical Sciences at Mersin Tarsus Organized Industrial Zone, Machinery Program, Tarsus University, Tarsus, Mersin, Turkey

[mnasifkuru@tarsus.edu.tr](mailto:mnasifkuru@tarsus.edu.tr)

## Abstract

Plate Fin Heat Sinks (PFHSs) are the most used equipment to remove heat from a surface to surrounding fluid. So, it is important to analyze PFHSs detailly in order to reduce operating temperature, pumping power, sound of fan, volume and weight of the device. In this study, a PFHS is placed in the direction of the flow and perpendicular to the flow in a square channel where the width and length of the PFHS is 100 mm, the fin height ( $H_{fin}$ ) is 15 mm, number of fins ( $N$ ) are 10 and 20, thickness of the fin ( $t_{fin}$ ) is 1.5 mm and Reynolds number based on the channel's hydraulic diameter varies between 10268 and 97550. Full-scale models are investigated numerically using Computational Fluid Dynamics (CFD) method. Furthermore, experimental system of square channel having 150 mm x 150 mm cross-section and length of 3.9 m is designed and constructed where the two type of heat sinks are tested. Base plate temperature, pressure drop, velocity/pressure/temperature contours of PFHSs are investigated using numerical methods, pressure drop values are also obtained experimentally. It is shown that PFHS located in the flow direction has lower base plate temperature and lower pressure drop values as compared to perpendicular to flow replacement.

**Keywords:** plate fin heat sink, experimental, CFD, base plate temperature, pressure drop.

## 1.INTRODUCTION

Plate fin heat sinks are preferred in thermal design systems for effective cooling i.e. electric vehicle battery, electronic devices. Moreover, the use of plate fins in heat sinks is used in many engineering applications because it is simple in structure and easy to manufacture. It is essential to investigate the operating temperature of cooled equipment, pumping power, fan sound, volume and weight must be controlled.

Inci and Bayer [1] carried out a geometric optimization study to increase the heat transfer in the heat sinks in the case of using plate fin and square/circular pin fins. As a result, base temperature of heat sink was reduced by 4.5% in the case of using circular pin fins. Gupta et al. [2] experimentally investigated the heat transfer and flow characteristics of the plate fin heat sink in the horizontal rectangular channel by creating a dimple on the fin surface for in-line and staggered arrays. The Reynolds number ranges from 6800 to 15200. As a result, they found that dimple formation on plate fin surfaces led to higher heat transfer, friction factor and fin efficiency than flat plate fin surface. In addition, they stated that the staggered arrangement is more effective than the in-line one. Ayli et al. [3] carried out numerical and experimental studies in the case of using flat rectangular plate fins in heat sinks perpendicular to flow in square section duct. The fin spacing ratio ( $d/w$ ) ranges from 0.089 to 0.0625, the fin width to fin length ratio ( $t/L$ ) ranges from 0.24875 to 0.729, and the Reynolds number ranges from  $17 \times 10^7 < Re < 2.47 \times 10^8$ . They found that the average Nusselt number increased with the increase in the inter-fin distance ( $d/t$ ) and the decrease in clearance ratio ( $C/L$ ), and the highest local heat transfer coefficient was obtained at the smallest value of the clearance ratio ( $C/L$ ).

Yuan et al. [4] investigated numerically the thermal and hydraulic performances of the plate pin fin heat sinks which were constructed mounting pin fins between plate fins. Increasing the diameter of pin, pressure drop increased and thermal resistance decreased. It was shown that base plate temperature of CPU was less than 358 K for inlet velocity of 6.5 m/s and a heat flux value of  $2.20 \text{ W/cm}^2$ . Zhou and Catton [5] studied plate-pin fin heat sinks where circular, square, elliptic, NACA profile and dropform were the shape of pin cross-sections. Pin width to plate fin spacings ranged between 0.3 to 0.6. It was observed that plate pin fin heat sinks have higher Nusselt numbers, pressure drops as compared to plate fin heat sinks and pin fin heat sinks. The performance of elliptic and NACA form was superior to other shapes. Sara [6] experimentally investigated the effect of using square pin fins on heat transfer and pressure loss in heat sinks in terms of average Nusselt number and friction factor. As a

result of examining the cases where the aspect ratio ( $C/H$ ) is between 0 and 1, the Reynolds number is between 10000 and 34000, and the ratio of the distance between the pin fins in the flow direction is 1.58, 4.17, 9.33, the average Nusselt number and friction factor are decreased with the decrease in the aspect ratio and the distance between the pin fins. Sparrow and Grannis [7] investigated diamond pin fins, Jin et al. [8] studied circular, elliptical, drop, NACA pin fins.

Kotcioglu et al. [9] experimentally investigated the effects of using hexagonal, square and cylindrical pin fins on thermal efficiency and pressure drop in heat sinks for fixed dimensionless transverse ( $s_T / D = 2$ ) and longitudinal ( $s_L / D = 2$ ) pitches. As a result, they found that the use of cylindrical pin fins had a lower pressure drop than square and hexagonal pin fins. Zhao et al. [10] experimentally investigated the pressure drop and friction factor in mini pin fin type heat sinks where different geometric cross sections (circular, elliptical, square, diamond, triangular) are used and the pin fins are arranged in a staggered manner in the same height and transverse pitch range. As a result, they stated that the elliptic cross-section has the lowest flow resistance since it most resembles the streamline form, and the triangle section has the highest flow resistance because it least resembles the streamline form. Choudhary et al. [11] investigated pin-fin heat sinks in terms of heat transfer and pressure drop with and without wings. They defined the Reynolds number according to the hydraulic diameter of the channel and Reynolds number was ranged from 6800 to 15100. They stated that the heat transfer gets better and frictional losses increase a little with the addition of wings.

In this study, a PFHS is placed in the direction of the flow and perpendicular to the flow in a square channel where the width and length of the PFHS is 100 mm, the fin height ( $H_{fin}$ ) is 15 mm, number of fins ( $N$ ) are 10 and 20, thickness of the fin ( $t_{fin}$ ) is 1.5 mm and Reynolds number based on the channel hydraulic diameter ranges between 10268 and 97550. Full-scale models are studied numerically using Ansys Fluent commercial program. Moreover, experimental system of square channel having 150 mm x 150 mm cross-section and length of 3.9 m is designed and constructed where the two type of heat sinks are tested.

## 2.EXPERIMENTAL SETUP

Experiments were carried out in a 3.9 m long square channel (150 mm x 150 mm) as illustrated in Figure 1.

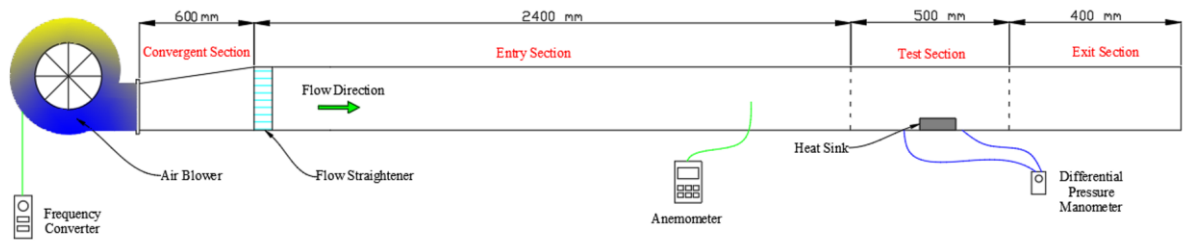


**Figure 1.** Experimental setup

Air is forced with a blower which passes through the square channel, exits from channel to the atmosphere. Frequency converter is used to set the inlet velocity  $V_{in}$ . The inlet velocity is determined with anemometer and differential pressure manometer is used to measure pressure drop value. The square channel consists of three sections: (1) entry (2) test and (3) exit where the lengths of these sections are 2400 mm, 500 mm and 400 mm, respectively. These dimensions are determined after the numerical simulations that provides fully developed flow in front of the test section. Flow straightener is used after the convergent section to minimize turbulence. Heat sink is manufactured from a three-dimensional printer and mounted in the middle of the test section as shown in Figure 2. The replacement of heat sink is done with an opened window in the top of the test section. Moreover, experimental setup system and manufactured plate fin heat sink are shown in Figure 3. Locations of anemometer and pressure taps in the test section is presented in Figure 4.

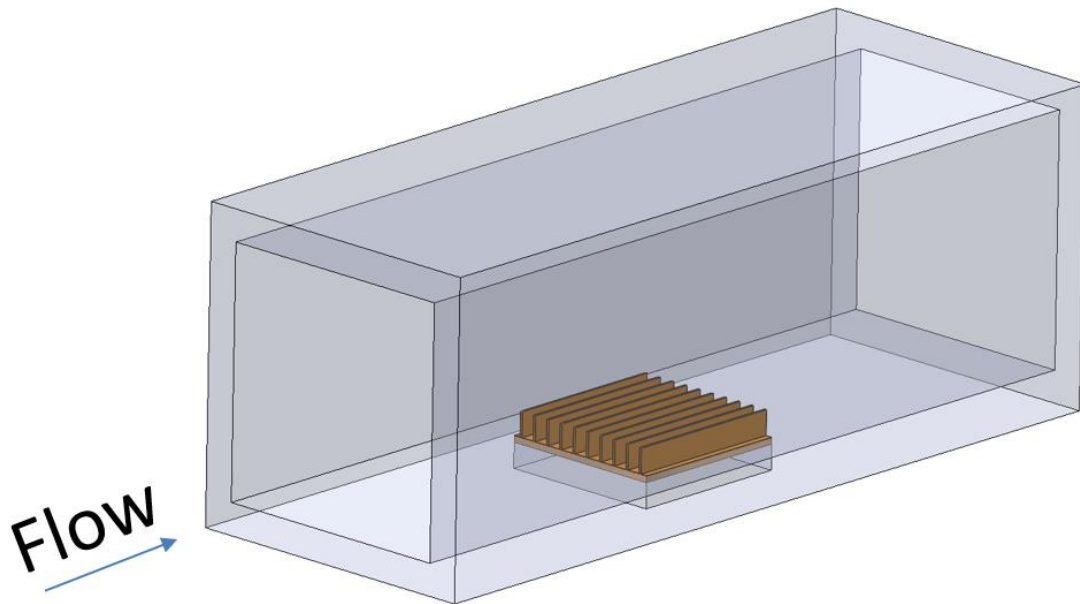


**Figure 2.** Test section





**Figure 3. (a) Experimental setup system (b) manufactured plate fin heat sink**

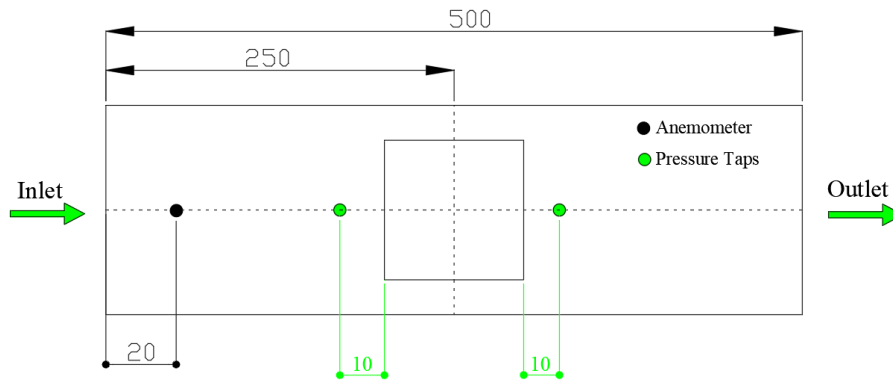


**Figure 4. Measurement points**

### 3. PHYSICAL MODEL AND SOLUTION PROCEDURE

Three-dimensional view and dimensions of PFHS are presented in Figure 5. Parameters and data of present study are given in Table 1. Replacements of PFHSs in the direction of the flow and perpendicular to the flow in the square channel are shown in Figures 6a and 6b, respectively.



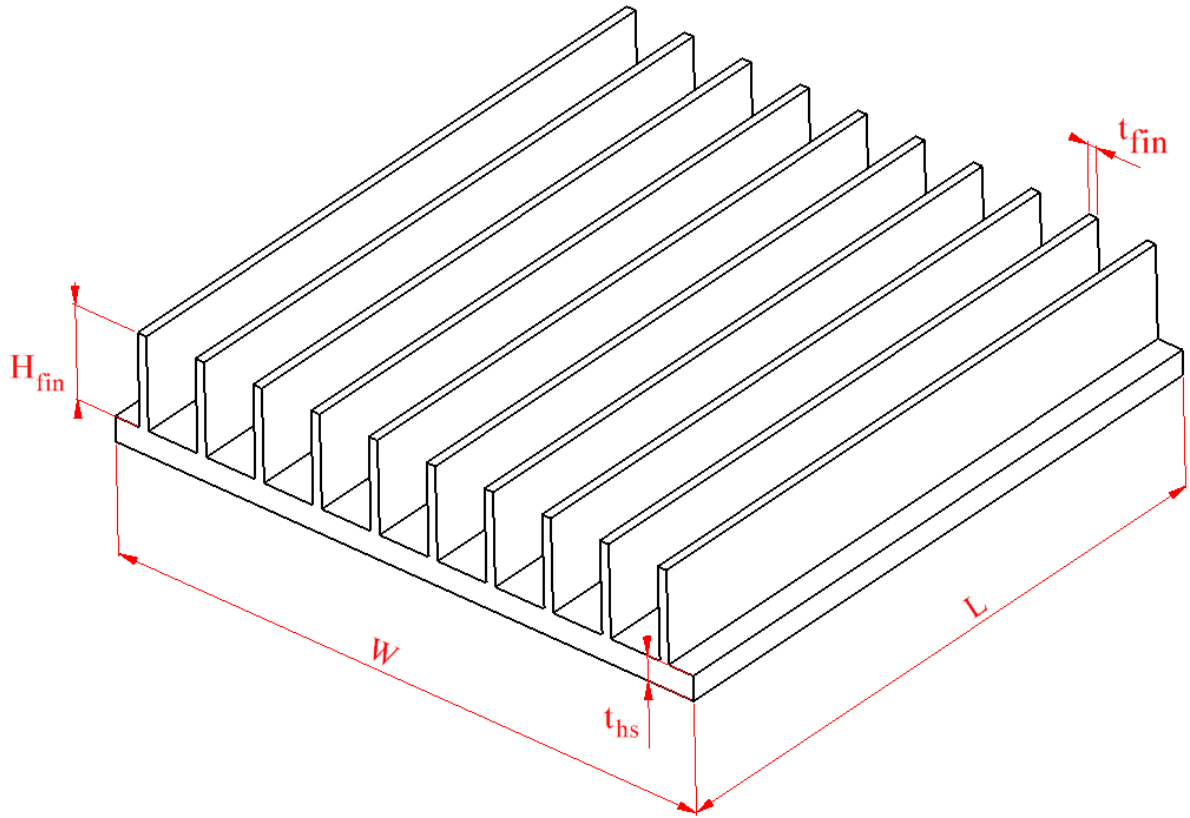
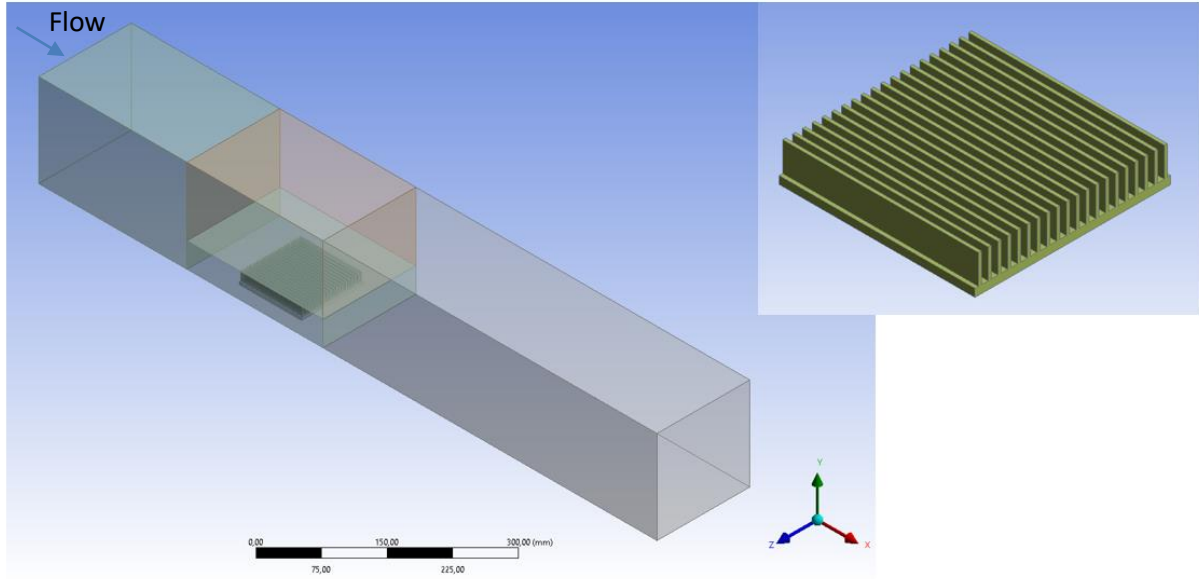


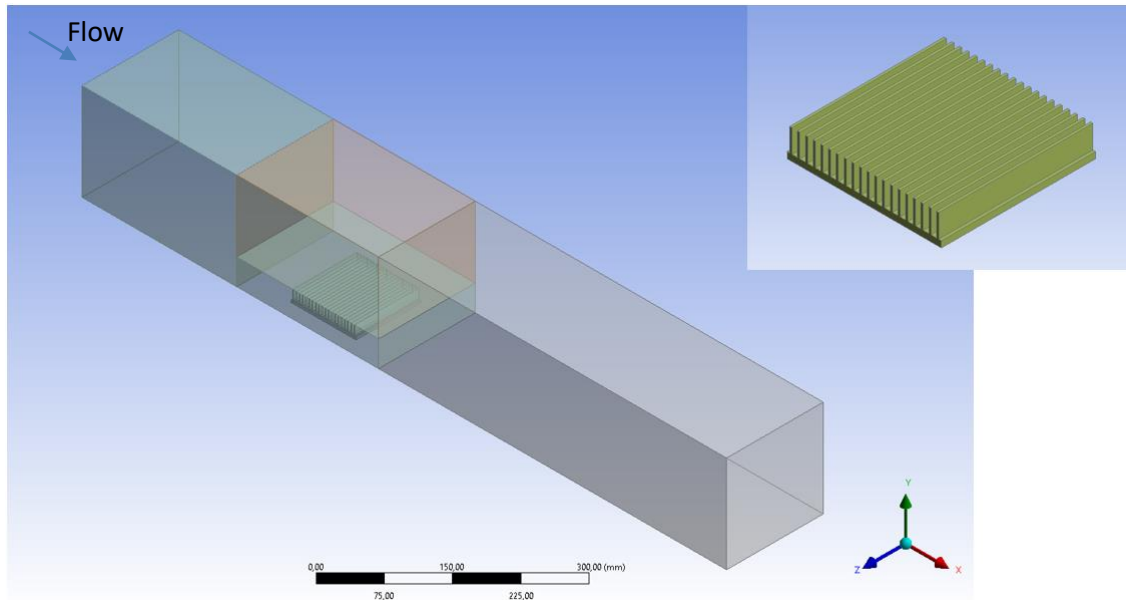
**Figure 5.** Three-dimensional view and dimensions of PFHS

**Table 1.** Parameters and data of present study

Parameter	Value
Fin length, $L$	100 mm
Fin height, $H_{fin}$	15 mm
Fin width, $W$	100 mm
Thickness of base plate, $t_{base}$	4 mm
Thickness of fin, $t_{fin}$	1.5 mm
Number of fins, $N$	10 and 20
Channel Height, $H_{channel}$	150 mm
Channel Width, $W_{channel}$	150 mm
Heat load, $Q$	50 W
Inlet velocity, $V_{in}$	1, 2, 3.5, 4.23, 5, 6.3, 7.2, 7.8, 8.5, 9.5
Inlet temperature, $T_{in}$	300 K



(a)



(b)

**Figure 6.** PFHS in the square channel (a) in the direction of the flow (b) perpendicular to the flow

### Conservation Equations

Conservation equations of continuity, momentum, energy and turbulence equations are used for numerical computations. The heat sink and flow domain are modeled as three-dimensional, the flow is incompressible and turbulent. The heat transfer is modeled as conjugate heat transfer which considers conductive and convective heat transfer. The conservation equations are given as follows ([12],[13]):

Conservation of Continuity:

$$\frac{\partial}{\partial x_i}(u_i) = 0 \quad (1)$$

Conservation of Momentum:

$$\rho_{air} u_j \frac{\partial u_i}{\partial x_j} = -\frac{\partial p}{\partial x_i} + \frac{\partial}{\partial x_j} \left[ (\mu + \mu_t) \frac{\partial u_i}{\partial x_j} \right] \quad (2)$$

Conservation of Energy:

$$\rho_{air} u_j \frac{\partial T}{\partial x_j} = \frac{\partial}{\partial x_j} \left[ \left( \frac{\mu}{Pr} + \frac{\mu_t}{Pr_t} \right) \frac{\partial T}{\partial x_j} \right] \quad (3)$$

Renormalization Group (RNG) k-ε turbulence model with enhanced wall treatment is preferred in this work, turbulence equations can be found in [14].

### Data Analysis

Reynolds number is defined as

$$Re_{D_h} = \frac{V_{in} D_h}{\nu} \quad (4)$$

$\nu$  is the air kinematic viscosity.  $D_h$  is the hydraulic diameter of channel,

$$D_h = \frac{2 H_{channel} W_{channel}}{H_{channel} + W_{channel}} \quad (5)$$

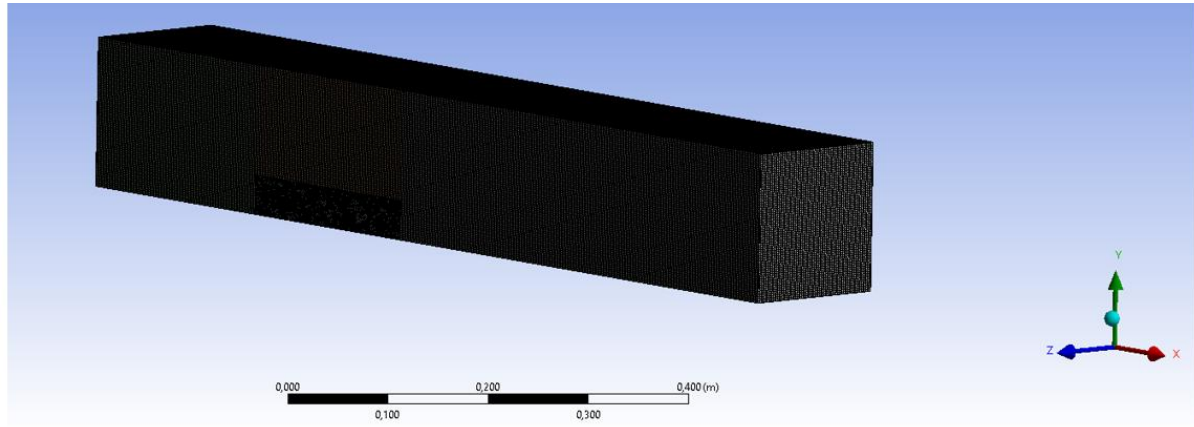
$\Delta P$  is the difference of pressure values in the pressure taps.

$$\Delta P = P_{in} - P_{out} \quad (6)$$

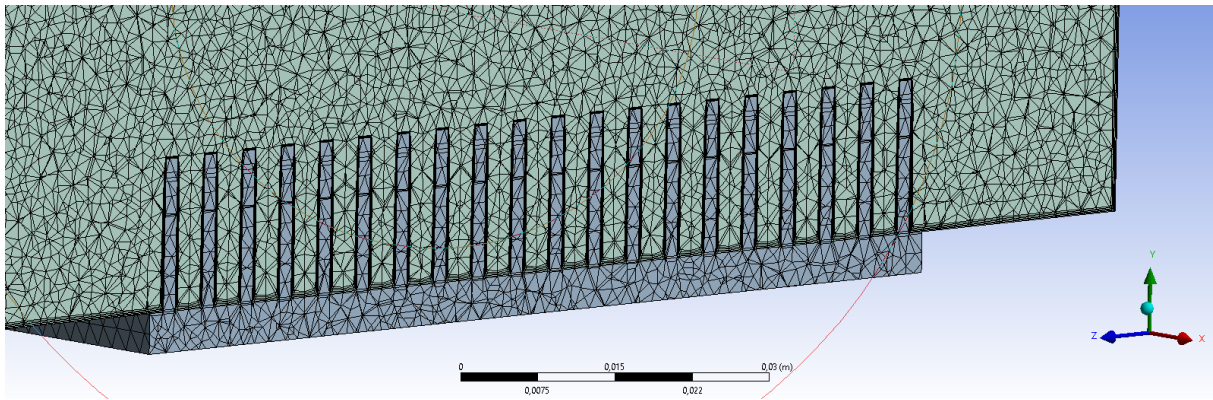
### Numerical Analysis and Boundary Conditions

Three-dimensional models were created with Ansys Design Modeler and meshed with Ansys Mesher. Ansys Fluent program is used to carry out numerical calculations. Conservation and turbulence equations were solved using second-order upwind scheme, velocity and pressure values were coupled with Coupled algorithm. Convergence criteria is set for energy equation as  $10^{-8}$ , for other equations as  $10^{-5}$ . Tetrahedral elements were used near the heat sink region, and hexahedral elements were chosen for the other regions to create mesh. For the wall surfaces, inflation layers were utilized in order to keep  $y^+$  values in the range of 1 and 5.

The mesh of the PFHS in the flow direction replacement and cross-sectional view of the mesh are shown in Figures 7a and 7b, respectively.



(a)



(b)

**Figure 7.** (a) Mesh of the PFHS in the flow direction replacement (b) cross-sectional view of the mesh

The boundaries for PFHS for both in the flow direction and perpendicular to flow replacements are presented in Figure 8. Velocity and temperature values are constant for the inlet boundary ( $u = V_{in}$  and  $T_{in} = 300 \text{ K}$ ). For the outlet boundary, pressure value is assigned to atmospheric pressure ( $P = P_{atm}$ ). Constant heat flux is applied in the base plate of heat sink ( $q'' = 5000 \text{ W / m}^2$ ). It is assumed that there is no heat transfer to the surroundings for the wall surfaces except heated base plate, so adiabatic boundary condition ( $q'' = 0 \text{ W / m}^2$ ) is used for these walls. The computational domain consists of solid and fluid zones. Conjugate heat transfer is modeled for the heat transfer where heat is transferred from base plate to heat sink conductively, and heat sink to air convectively.

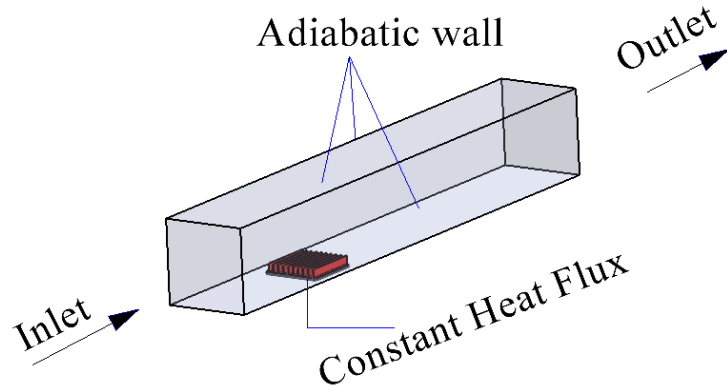


**Figure 8.** Boundaries for PFHS for both in the flow direction and perpendicular to flow replacements

### Mesh Independence Study

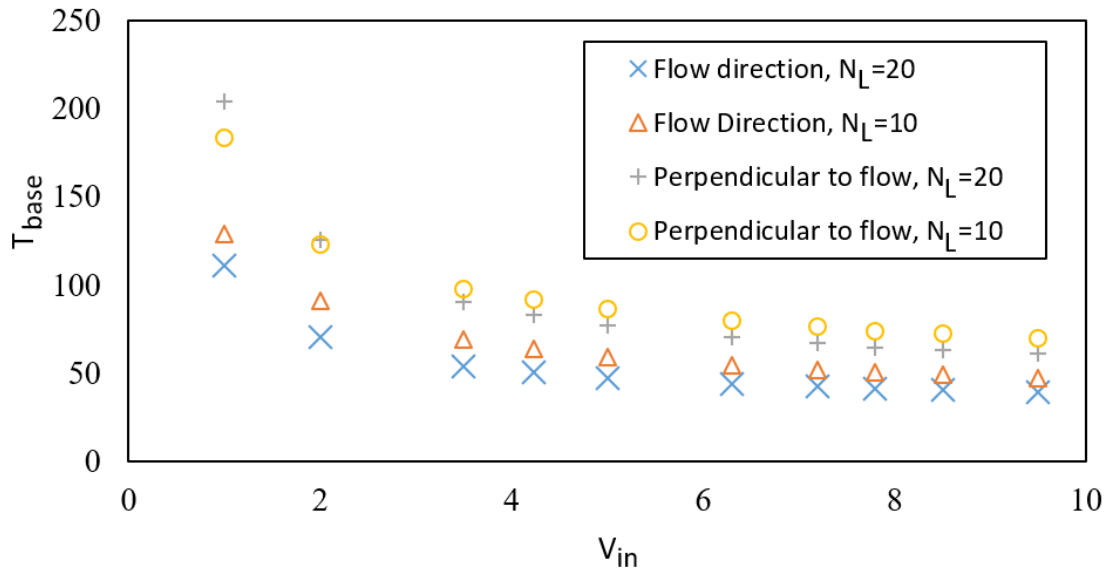
Numerical results reliability must be controlled for the results' validity. Moreover, it is important to choose sufficient element sizes due to computation time and compute resources considerations. Four different element size is chosen for the mesh independency study where  $V_{in} = 5 \text{ m/s}$  and PFHS is mounted in the flow direction. For the element sizes of third and fourth meshes are 5.215.209 and 8.115.309, differences for  $T_{base}$  is 1.39% and  $\Delta P$  is 1.52%, so the third mesh structure is used for the other calculations.

## 4.RESULTS AND CONCLUSIONS

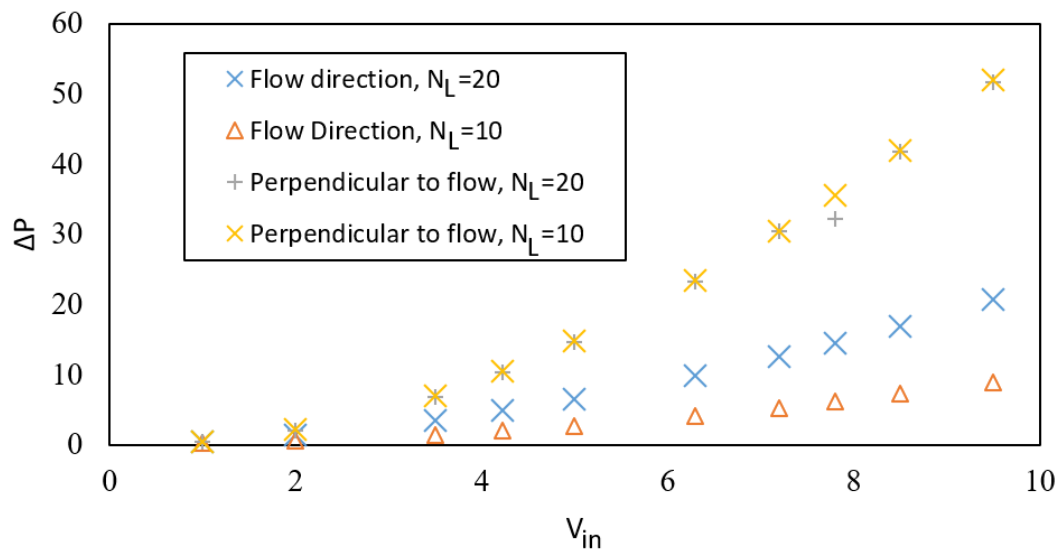
Numerical results of  $T_{base}$  vs.  $V_{in}$  and  $\Delta P$  vs.  $V_{in}$  are given in Figures 9a and 9b, respectively. As it is expected, increasing the inlet velocity decreases the base plate temperature and increases the pressure drop. For the studied cases, PFHS replacement in the flow direction has better performance as compared to perpendicular to flow replacement. Minimum  $T_{base}$  for  $N_L = 20$  in the flow direction and perpendicular to flow replacements are 39.59 and 61.31. Moreover, pressure drop values are 20.68 and 51.66. It can be inferred that perpendicular to flow replacement exhibit worse performances in terms of base plate temperature and pressure drop.

For the replacement in the flow direction, minimum  $T_{base}$  for  $N_L = 20$  and  $N_L = 10$  are 39.59 and 47.36, respectively. At this velocity, pressure drop values are 20.68 and 8.90. Decreasing the number of fins from 20 to 10 led to 19.63% increment in  $T_{base}$ , 56.96% decrement in  $\Delta P$ . For the replacement perpendicular to flow, minimum  $T_{base}$  for  $N_L = 20$  and  $N_L = 10$  are

61.31 and 69.87, respectively. Pressure drop values are nearly same (51.66 and 51.89). So, increasing the number of fins does not affect the pressure drop, only decrease  $T_{base}$ .



(a)



(b)

**Figure 9.** Variations of (a)  $T_{base}$  vs.  $V_{in}$  (b)  $\Delta P$  vs.  $V_{in}$

For  $N_L = 20$ , experimental studies were carried out for both replacements of in the flow direction and perpendicular to flow. Comparisons of these cases are given in Figure 10, numerically and experimentally. It is shown that experimental and numerical results show less difference.

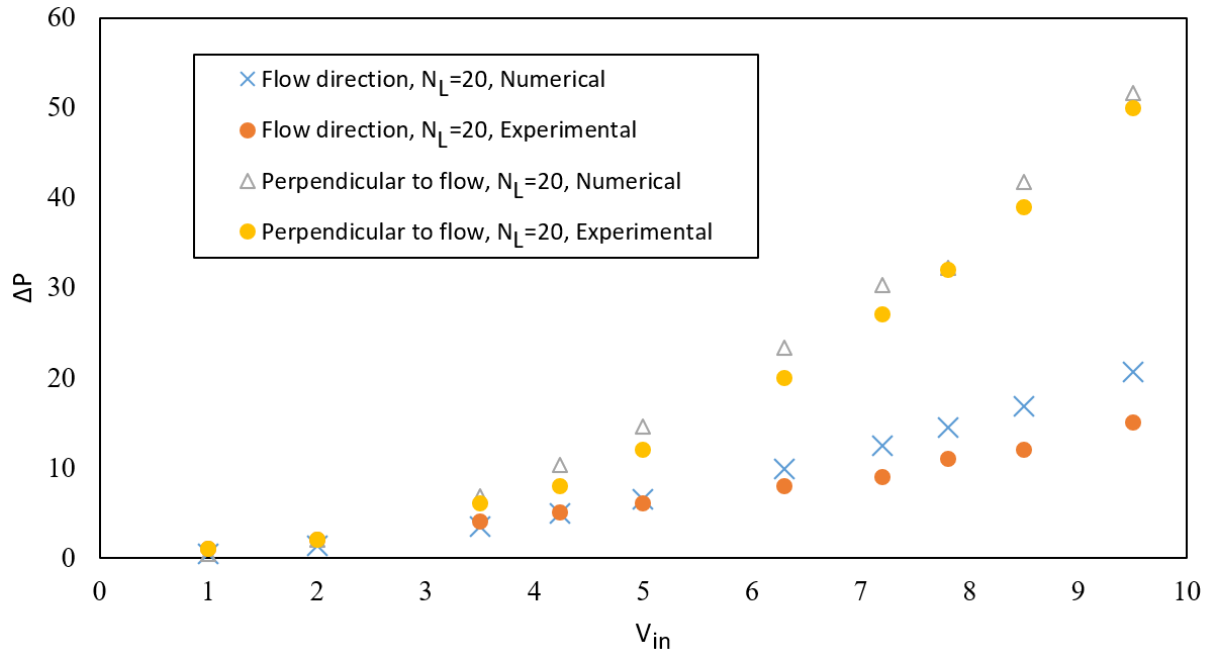
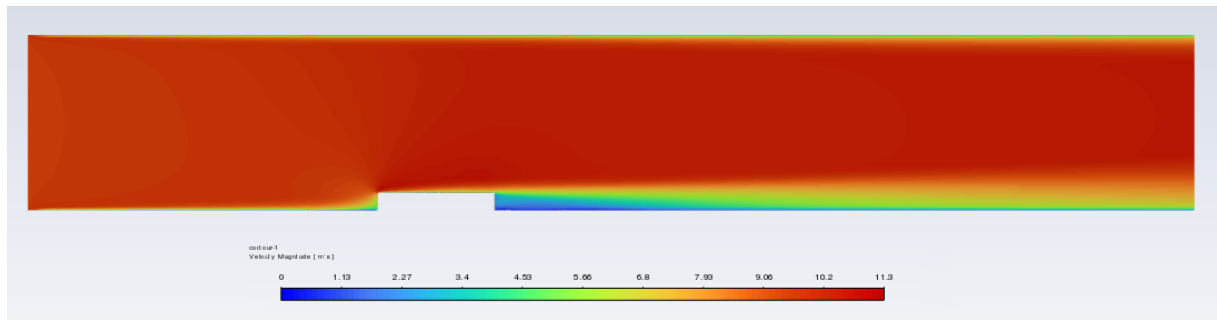


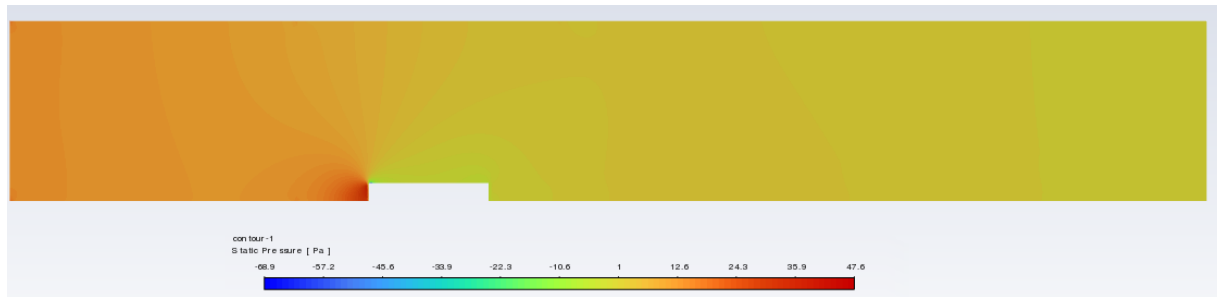
**Figure 10.** Comparison of numerical and experimental studies,  $\Delta P$  vs.  $V_{in}$

Contours of velocity, pressure and temperature for PFHS in the flow direction and perpendicular to flow replacements at  $V_{in} = 9.5 \text{ m/s}$  and  $z = 0.075 \text{ m}$  are shown in Figures 11 and 12. Perpendicular replacement obstructs the flow entrance between the plate fins, so heat is not extracted from the heated base plate which led to higher base plate temperature.

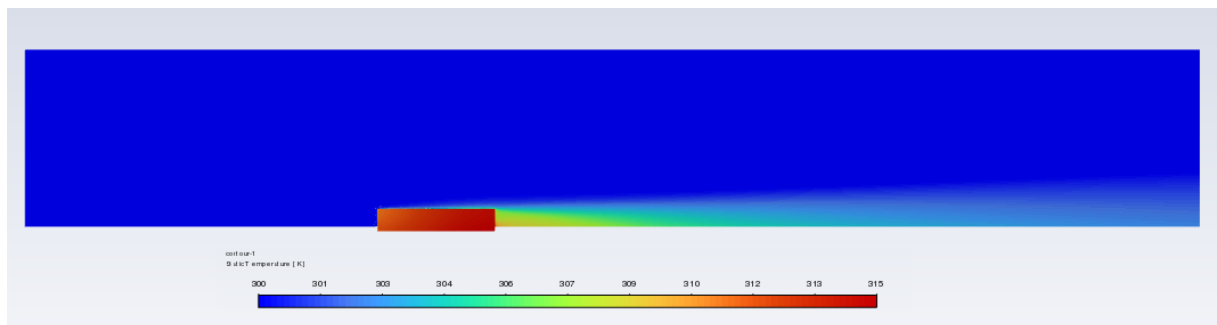




(a)

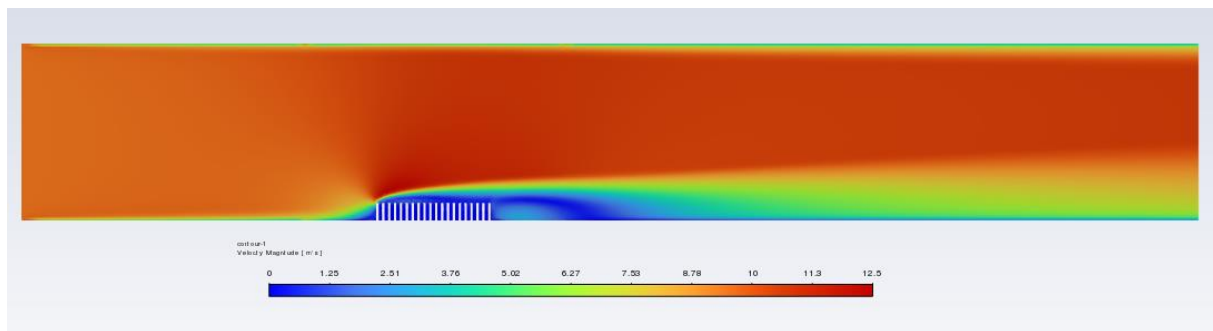


(b)

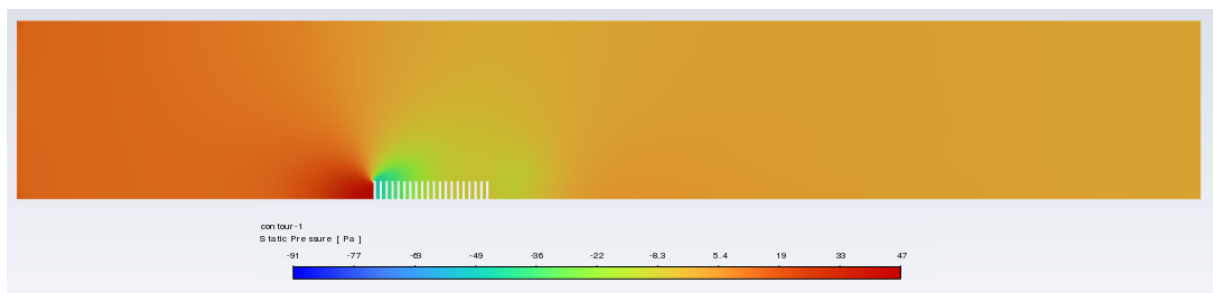


(c)

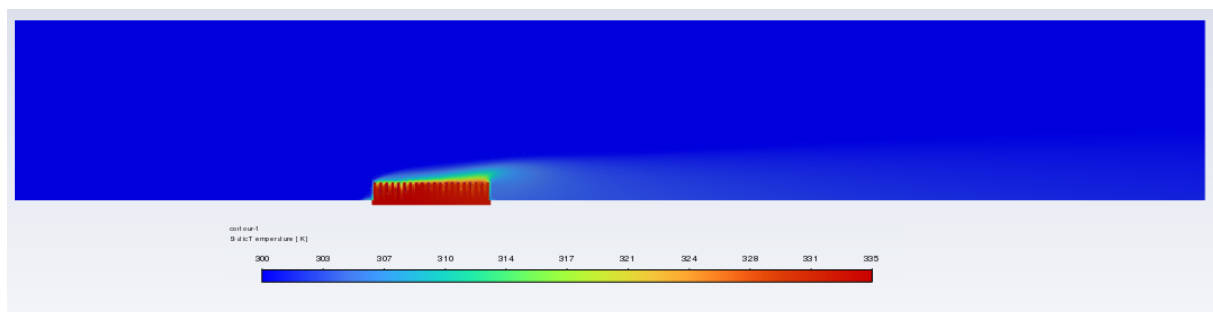
**Figure 11.** Contours of (a) velocity (b) pressure (c) temperature for PFHS in the flow direction replacement at  $V_{in} = 9.5 \text{ m/s}$  and  $z = 0.075 \text{ m}$



(a)



(b)



(c)

**Figure 12.** Contours of (a) velocity (b) pressure (c) temperature for PFHS perpendicular to flow replacement at  $V_{in} = 9.5 \text{ m/s}$  and  $z = 0.075 \text{ m}$

## REFERENCES

1. A.B. Inci, Ö. Bayer, Experimental and numerical study on heat transfer performance of square, cylindrical and plate heat sinks in external transition flow regime, J. Therm. Sci. Technol. 39, 151–161, 2019.
2. A. Gupta, M. Kumar, A.K. Patil, Enhanced heat transfer in plate fin heat sink with dimples and protrusions, Heat Mass Transf. 55, 2247–2260, 2019. <https://doi.org/10.1007/s00231-019-02561-w>.
3. E. Ayli, O. Bayer, S. Aradag, Experimental investigation and CFD analysis of rectangular profile FINS in a square channel for forced convection regimes, Int. J. Therm. Sci. 109,

- 279–290, 2016. <https://doi.org/10.1016/j.ijthermalsci.2016.06.021>.
4. W. Yuan, J. Zhao, C.P. Tso, T. Wu, W. Liu, T. Ming, Numerical simulation of the thermal hydraulic performance of a plate pin fin heat sink, *Appl. Therm. Eng.* 48, 81–88, 2012. <https://doi.org/10.1016/j.applthermaleng.2012.04.029>.
  5. F. Zhou, I. Catton, Numerical evaluation of flow and heat transfer in plate-pin fin heat sinks with various pin cross-sections, *Numer. Heat Transf. Part A Appl.* 60, B107–128, 2011. <https://doi.org/10.1080/10407782.2011.588574>.
  6. O.N Şara, Performance analysis of rectangular ducts with staggered square pin fins, *Energy Conv. and Management* 44, 11, 1787-1803, 2003.
  7. E.M. Sparrow, V.B. Grannis, Pressure drop characteristics of heat exchangers consisting of arrays of diamond-shaped pin fins, *Int. J. Heat Mass Transf.* 34, 589–600, 1991. [https://doi.org/10.1016/0017-9310\(91\)90108-Q](https://doi.org/10.1016/0017-9310(91)90108-Q).
  8. W. Jin, J. Wu, N. Jia, J. Lei, W. Ji, G. Xie, Effect of shape and distribution of pin-fins on the flow and heat transfer characteristics in the rectangular cooling channel, *Int. J. Therm. Sci.* 161, 106758, 2021. <https://doi.org/10.1016/j.ijthermalsci.2020.106758>.
  9. I. Kotcioglu, S. Caliskan, S. Baskaya, Experimental study on the heat transfer and pressure drop of a cross-flow heat exchanger with different pin-fin arrays, *Heat Mass Transf.* 47, 1133–1142, 2011. <https://doi.org/10.1007/s00231-011-0779-7>.
  10. H. Zhao, Z. Liu, C. Zhang, N. Guan, H. Zhao, Pressure drop and friction factor of a rectangular channel with staggered mini pin fins of different shapes, *Exp. Therm. Fluid Sci.* 71, 57–69, 2016. <https://doi.org/10.1016/j.expthermflusci.2015.10.010>.
  11. V. Choudhary, M. Kumar, A.K. Patil, Experimental investigation of enhanced performance of pin fin heat sink with wings, *Appl. Therm. Eng.* 155, 546–562, 2019. <https://doi.org/10.1016/j.applthermaleng.2019.03.139>.
  12. M. Nasif Kuru, M.T. Erdinc, A. Yilmaz, Optimization of Heat Transfer and Pressure Drop in Axially Finned Staggered Tube Banks, *Heat Transf. Eng.*, 42, 1–18, 2020. <https://doi.org/10.1080/01457632.2020.1785696>.
  13. C.K. Mangrulkar, A.S. Dhoble, J.D. Abraham, S. Chamoli, Experimental and numerical investigations for effect of longitudinal splitter plate configuration for thermal-hydraulic performance of staggered tube bank, *Int. J. Heat Mass Transf.*, 161, 2020. <https://doi.org/10.1016/j.ijheatmasstransfer.2020.120280>.
  14. Ansys Fluent User's Guide, ANSYS Inc., 2019.

# DEEP LEARNING BASED BRAIN TUMOR DETECTION

Kader Özen<sup>1</sup>, Anıl Utku<sup>2</sup>

<sup>1</sup>Department of Computational Sciences and Engineering, Munzur University, Tunceli, Turkey

<sup>2</sup>Department of Computer Engineering, Munzur University, Tunceli, Turkey

[kaderozen014@gmail.com](mailto:kaderozen014@gmail.com), [anilutku@munzur.edu.tr](mailto:anilutku@munzur.edu.tr)

## Abstract

Artificial intelligence is systems that allow machines to perform various tasks, learn from experience, and adapt to new inputs, similar to humans. Artificial intelligence is aimed at developing human competencies and contributing to them. Because artificial intelligence can identify meaningful relationships in raw data, it can support diagnosis, treatment, and predictions in many medical conditions. With the rapidly developing image processing and artificial intelligence technologies, many technologies are being developed for diagnosing and diagnosing diseases to be defined more automatically, faster, and more accurately. Artificial intelligence in medical diagnosis systems is being developed to provide many benefits to patients, healthcare professionals, and healthcare institutions, such as early disease diagnosis, treatment quality, and cost reduction. This study developed a diagnostic system for diagnosing brain tumors from MRI images using the DenseNet121 model. The dataset used consists of 7022 MRI images with glioma, meningioma, no tumor and pituitary labels. Experimental results showed that the developed DenseNet121 model has 94.51% accuracy in brain tumor detection.

**Keywords:** Artificial intelligence; Deep learning; Brain tumor; DenseNet121.

## 1.INTRODUCTION

Integrating artificial intelligence into the radiology workflow increases the speed and quality of the examination [1]. This way, speeding up the examination and improving image quality is possible. In addition, the abnormal findings and possible differential diagnoses that artificial intelligence will prepare for the radiologist before the report improves the quality of diagnosis [2]. These also lead to an increase in productivity. Radiology doctors visually evaluate radiology images and try to characterize the images by detecting abnormal findings. In this way, they diagnose diseases by reporting their findings [3]. The success of the radiologist depends on his/her training and long years of experience. While the weight and importance of imaging devices in diagnosing and treating diseases in the modern medical approach are increasing daily, the expectation of faster and more precise results is also increasing [4]. It is seen that the number of radiological examinations all over the world

continues to increase disproportionately when compared with the number of available radiologists.

Automated segmentation and classification of brain tumors is becoming a popular research area due to advances in medical imaging technologies, artificial intelligence, and deep learning [5]. While traditional approaches may work well for one dataset, they may need to be revised for another as the right features need to be extracted [6]. Convolution filters, available in deep learning architectures for every data format, eliminate the need for manual feature extraction [7].

Artificial intelligence models have been widely used in the literature for brain tumor diagnosis. Arı et al. [8] segmented MRI images in the preprocessing stage and classified the features obtained from these regions. They achieved a classification success of 83.39% in experimental studies. Bulut et al. [9] proposed a model based on the segmentation of MRI images for brain tumor detection. In experimental studies, they detected brain tumors with 87% accuracy with Markov random field method. Mohsen et al. [10] proposed a new method to classify brain tumors using deep learning methods and Discrete Wavelet Transform (DWT) model. They obtained 93.94% accuracy with this model in experimental studies.

In this study, a deep learning model was developed for brain tumor diagnosis. The developed DenseNet121 model was tested using 7022 MRI images belonging to 4 classes: glioma, meningioma, no-tumor, and pituitary. Experimental results showed that the developed DenseNet121 model has 94.51% accuracy in brain tumor detection.

## 2.MATERIAL AND METHOD

This study used a public dataset of MRI images with and without tumors [11]. The dataset consists of 7022 MRI images labeled glioma, meningioma, tumor-free, and pituitary. An example of the dataset is shown in Fig.1.

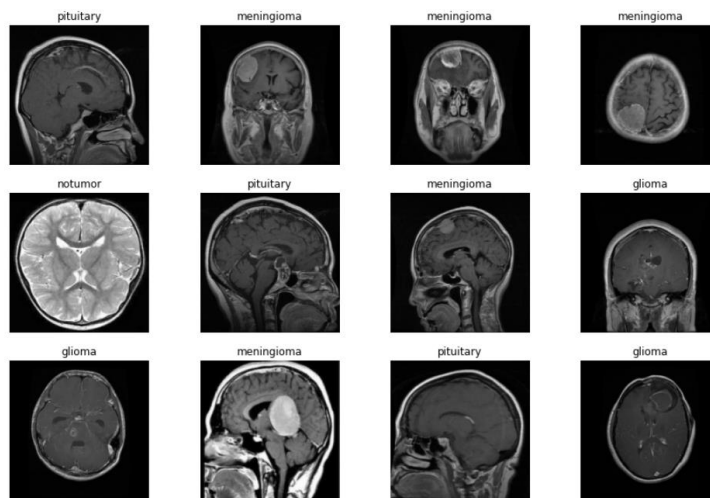


Figure 1. An example of the dataset

Fig. 2 shows the class distributions in the used dataset.

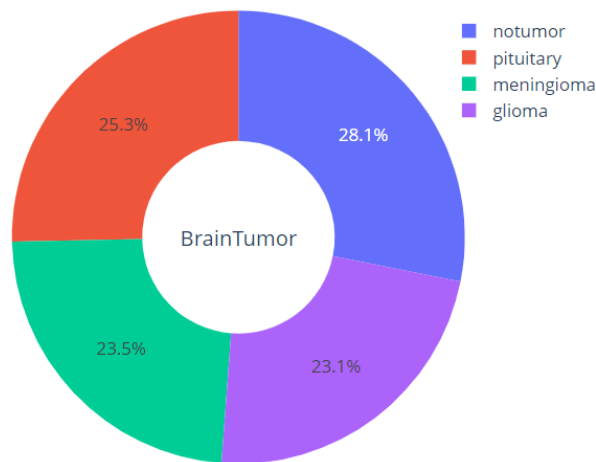


Figure 2. Class distributions in the dataset used

As seen in Fig. 2, 28.1% of the images in the used dataset belong to the non-tumor, 25.3% to pituitary, 23.5% to meningioma, and 23.1% to glioma classes.

The structure of the developed DenseNet121 model is shown in the Fig. 3.

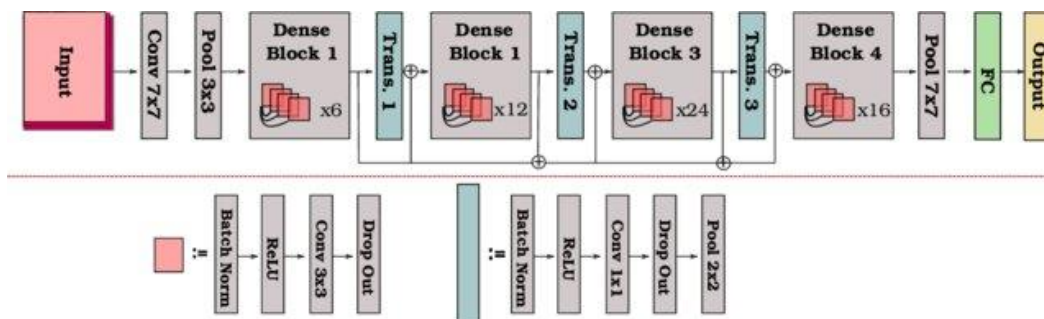


Figure 3. The structure of the developed DenseNet121 model

DenseNet architecture is an enhanced ResNet architecture in which each layer is heavily connected to the other layers [12]. The advantage of DenseNet121 is that each layer can receive feature maps from the layers preceding it. In this way, layers can pass on their feature maps to subsequent layers [13].

### 3. THE EXPERIMENTAL RESULTS

The dataset was split into 80% for train and 20% for test. The train data was split into 90%

for training and %10 for validation. The validation data were used in test runs to optimize the model parameters. Grid search was used for hyper parameter tuning. The train data consists of 5712 images and the test dataset consists of 1311 images.

The training dataset includes 1457 pituitary, 1595 no-tumor, 1339 meningioma and 1321 glioma images. The testing dataset includes 300 pituitary, 405 no-tumor, 306 meningioma and 300 glioma images. Table 1 shows the confusion matrix for the developed DenseNet121 model.

Table 1. Confusion matrix for the developed DenseNet121 model

Predicted values	Real values				
		Pituitary (0)	No-tumor (1)	Meningioma (2)	Glioma (3)
	Pituitary (0)	286	8	6	7
	No-tumor (1)	2	382	5	2
	Meningioma (2)	5	6	284	4
	Glioma (3)	7	9	11	287

Table 2 shows the experimental results for each class and overall results.

Table 2. The experimental results for each class and overall results

Classes	Accuracy	Precision	Recall	F-score
Pituitary	95.33%	93.15%	95.33%	94.22%
No-tumor	94.32%	97.69%	94.32%	95.97%
Meningioma	92.81%	94.98%	92.81%	93.88%
Glioma	95.66%	91.40%	95.66%	93.48%
Overall results	94.51%	94.30%	94.53%	94.38%

As seen in the table, the developed DenseNet121 model had 94.51% accuracy, 94.30% precision, 94.53% recall and 94.38% F-score in brain tumor detection.

The accuracy/loss graphs of the DenseNet121 model are shown in the Fig. 4.

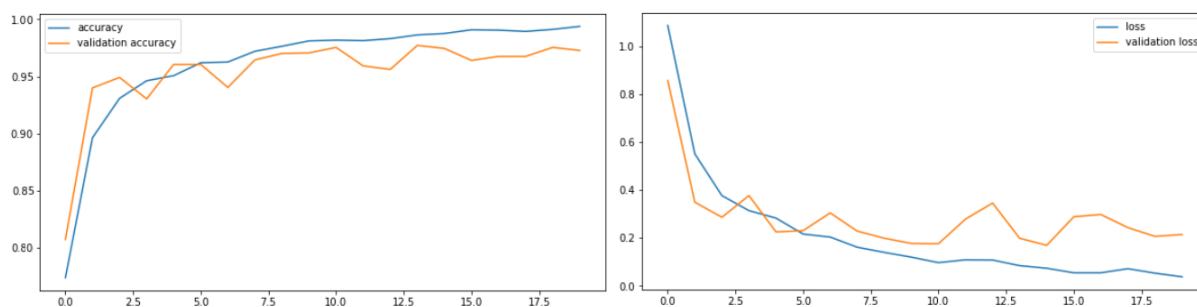


Figure 4. The accuracy/loss graphs of the DenseNet121 model

## 4.CONCLUSIONS

Artificial intelligence is a technology that directly affects areas such as social life, medicine, and economy. In recent years, artificial intelligence technologies have developed considerably thanks to the developments in the processing capacity of computers and the accumulation of extensive data. Medical studies based on imaging data in radiology, pathology, and dermatology have increased, and the application of artificial intelligence methods in these fields has an important place in treating and diagnosing diseases. By examining scan images and other medical data, AI systems can detect signs of illness. This way, doctors can identify the disease early and manage the treatment process more effectively. Artificial intelligence systems can identify symptoms in images using deep learning algorithms.

In this study, DenseNet121 deep learning model for brain tumor detection was developed. The experimental results of the developed model are evaluated using the performance evaluation metrics of precision, recall, accuracy, and F-score. The developed model correctly classified 1239 images out of 1311 images. The developed model misclassified 72 images. The overall accuracy of the developed model is 94.51%.

## REFERENCES

1. Kapoor, N., Lacson, R., Khorasani, R., Workflow applications of artificial intelligence in radiology and an overview of available tools, *Journal of the American College of Radiology*, Vol:17, No:11, 1363-1370, 2020.
2. Lecler, A., Duron, L., Soyer, P., Revolutionizing radiology with GPT-based models: Current applications, future possibilities and limitations of ChatGPT, *Diagnostic and Interventional Imaging*, Vol:104, No:6, 269-274, 2023.
3. Hosny, A., Parmar, C., Quackenbush, J., Schwartz, L. H., Aerts, H. J., Artificial intelligence in radiology, *Nature Reviews Cancer*, Vol:18, No:8, 500-510, 2018.
4. Pugh, D., Karabayas, M., Basu, N., Cid, M. C., Goel, R., Goodyear, C. S., Dhaun, N., Large-vessel vasculitis, *Nature Reviews Disease Primers*, Vol:7, No:1, 93, 2021.
5. Arabahmadi, M., Farahbakhsh, R., Rezazadeh, J., Deep learning for smart Healthcare-A survey on brain tumor detection from medical imaging, *Sensors*, Vol:22, No:5, 1960, 2022.
6. Behera, R. K., Jena, M., Rath, S. K., Misra, S. (2021). Co-LSTM: Convolutional LSTM model for sentiment analysis in social big data, *Information Processing & Management*, Vol:58, No:1, 2021.



7. Jadhav, P., Rajguru, G., Datta, D., Mukhopadhyay, S., Automatic sleep stage classification using time–frequency images of CWT and transfer learning using convolution neural network, *Biocybernetics and Biomedical Engineering*, Vol:40, No:1, 494-504, 2020.
8. Ari, A., Alpaslan, N., Hanbay, D., Computer-aided tumor detection system using brain MR images, 2015 Medical Technologies National Conference, 1–4, 2015.
9. Bulut, F., Kiliç, I., Ince, I. F., Beyin Tümörü Tespitinde Görüntü Bölütleme Yöntemlerine Ait Başarımların Karşılaştırılması ve Analizi, *Dokuz Eylül Üniversitesi Mühendislik Fakültesi Fen ve Mühendislik Dergisi*, Vol:20, No:58, 173–186, 2018.
10. Mohsen, H., El-Dahshan, E. S. A., El-Horbaty, E. S. M., Salem, A. B. M., Classification using deep learning neural networks for brain tumors, *Future Computing and Informatics Journal*, Vol:3, No:1, 68–71, 2018.
11. Brain Tumor MRI Images. (2022). Total Population by Country. Retrieved from <https://www.kaggle.com/datasets/adityakomaravolu/brain-tumor-mri-images>. Accessed April 27, 2023.
12. Lodhi, B., Kang, J., Multipath-DenseNet: A Supervised ensemble architecture of densely connected convolutional networks, *Information Sciences*, Vol:482, 63-72, 2019.
13. Huang, G., Liu, Z., Pleiss, G., Van Der Maaten, L., Weinberger, K. Q., Convolutional networks with dense connectivity, *IEEE transactions on pattern analysis and machine intelligence*, Vol:44, No:12, 8704-8716, 2019.

# A COMPARATIVE ANALYSIS BASED ON MACHINE LEARNING FOR SUICIDE AND DEPRESSION DETECTION

Fatoş Öztürk<sup>1</sup>, Umit Can<sup>2</sup>

<sup>1</sup> Department of Computational Sciences and Engineering of Munzur, Tunceli, Turkey

[ozturkfatos111@gmail.com](mailto:ozturkfatos111@gmail.com),

<sup>2</sup>Computer Engineering Department, Munzur University, 62000 Tunceli, Turkey.

[ucan@munzur.edu.tr](mailto:ucan@munzur.edu.tr)

## Abstract

People can feel hopeless, sad, and helpless at some point in their lives, and this normal situation can become quite dangerous over time. While many people show symptoms of depression in their daily lives and learn to live with them, the more critical issue of 'suicidal ideation' can take over. This is a very serious problem considering the worldwide suicide rate. Artificial intelligence methods are used in addition to traditional methods to detect and solve this problem. These methods can make inferences about people's psychological states by using the data they obtain from various internet media. Online social networks such as Twitter, Facebook, and Instagram, which have become very popular in recent years, provide very useful and large-scale information for the early detection and prevention of depression and suicidal thoughts. In this study, a machine learning-based text classifier was created to detect suicidal thoughts of depressed people and predict whether they will commit suicide or not. For this purpose, suicidal ideation prediction models were created using machine learning algorithms such as Naive Bayes (NB), Logistic Regression (LR), K-nearest Neighbors (kNN), Random Forest (RF), and Decision Tree (DT), and the results were compared using various metrics. According to the experimental results, the Logistic Regression method was the most successful model.

**Keywords:** Artificial intelligence; Suicide and depression prediction; Machine learning

## 1. INTRODUCTION

Suicidal ideation, anxiety and depression are some of the most common mental health disorders among adolescents and young adults, with just under 800,000 people dying by suicide each year [1,2]. Fortunately, in recent years there was growing recognition of this fact and a better understanding of the importance of ensuring that young people develop mental resilience from

an early stage. Communication is at the heart of society and currently written digital communication is one of the most popular forms of self-expression. Social networks are used to detail human activities or routines, describe their emotions, mental states and desires [3].

The expanding use of social media has the potential to strengthen the early detection of mental health disorders. Since data collected through social media is digital, it has the ability to further accelerate mental health analysis. While previous studies have shown that even short texts on Twitter can provide some insights into the relationship between language and mental health conditions, longer-form content is currently being explored to gain more insight [4].

Prevention and early detection of mental health illnesses with tools that complement traditional medical approaches have the ability to reduce the shortage of mental health facilities by improving different types of counseling or support to those in need, such as connecting a depressed person to resources or peer support when they need it most [5].

In online social networks, posts are shared from which we can obtain many clues about people's mental health. This data can be analyzed with natural language processing and machine learning methods to determine whether a person is depressed or suicidal. In this study, NB, LR, kNN, RF, and DT machine learning methods were used to detect suicide in online social networks. As a result of comparisons using various success metrics, the LR model achieved the highest success.

## **2. MATERIAL AND METHOD**

In this study, suicide detection was performed using machine learning methods using data obtained from Reddit, a social network platform.

### **2.1. CLASSIFICATION METHODS USED**

The machine learning methods used in this study are briefly described below.

*NB*: This effective classification method aims to determine the class of data presented to the system by a series of calculations defined according to probability principles. In NB classification, the system is presented with a certain amount of trained data. Of course, the more the number of trained data, the more precise it can be to determine the true category of the test data. NB classification method has many applications [6].

*LR*: This model is an important technique in the field of machine learning. It is a data analysis technique that uses mathematics to find relationships between two variables. Logistic regression then uses this relationship to predict the value of one of these factors based on the other. The prediction usually has a limited number of outcomes, such as yes or no. They can use this information for predictive analysis to reduce operational costs, improve efficiency and scale faster [7].

*RF*: It is a widely used machine learning algorithm that combines the output of a decision tree to arrive at a single conclusion. Its ease of use and flexibility has accelerated its adoption as it addresses both classification and regression problems. While decision trees are common

supervised learning algorithms, they can be prone to problems such as bias and overfitting. However, when multiple decision trees form an ensemble in a random forest algorithm, they predict more accurate results, especially when individual trees are uncorrelated [8].

*DT:* This efficient method is widely used in operations research, especially in decision analysis [9], to help identify a strategy that is most likely to achieve a goal, but it is also a popular tool in machine learning. A decision tree is a decision support hierarchical model that uses a tree-like decision model and its possible outcomes, including chance event outcomes, resource costs and utility. It is a way of visualizing an algorithm that contains only conditional control statements [10].

*k-NN:* This method is a non-parametric, supervised learning classifier that uses proximity to make classifications or predictions about the grouping of an individual data point. Although it can be used for both regression and classification problems, it is typically used as a classification algorithm that works on the assumption that similar points can be found close to each other [11].

## 2.2. DATASET

This dataset is a dataset that can be used to detect suicide and depression in a text. The dataset is a collection of posts from the "SuicideWatch" and "depression" subreddits of the Reddit platform. In order to detect suicidal ideation, a text classifier was created to determine whether a person would commit suicide or not. Our dataset consists of 232,074 rows of data in total. The dataset is divided into training and test dataset, with 40% as test dataset and the remaining 60% as training dataset. The dataset has two column numbers, 'text' and 'class'.

Unnamed: 0		text	class
0	2	Ex Wife Threatening SuicideRecently I left my ...	suicide
1	3	Am I weird I don't get affected by compliments...	non-suicide
2	4	Finally 2020 is almost over... So I can never ...	non-suicide
3	8	I need helpjust help me im crying so hard	suicide
4	9	I'm so lostHello, my name is Adam (16) and I've...	suicide

**Resim 1 :** 'text' ve 'class' iki sütun sayısı

## 2.3. APPLICATION STEPS OF SUICIDE DETECTION

This section describes the stages of the suicide detection model.

### 2.3.1. TEXT PRE-PREPROCESSING

Generally, unstructured data needs to be processed. In order to extract meaning from unstructured data, the following operations were performed to make the data processable.

- Tokenization: It is the process of dividing the text into arrays by fragmenting it in the desired way.
- Removing Stop Words: It is the process of removing words in the text that do not make any change in the meaning.
- Removing punctuation and digits: It includes the removal of punctuation marks and numbers in the text.
- Normalization: It is the process of eliminating the uppercase and lowercase distinction in the text.
- Stemming: It is the process of recording the word roots by discarding the affixes in the words in the text [12]

### 2.3.2. VECTORIZATION OF DATA

In this step, the features obtained after the text preprocessing step are expressed in vector form.

### 2.3.3. FEATURE SCALING

It is a method that enables to analyze the values of two different features/variables in the data set in the most accurate way.

## 2.4. EXPERIMENTAL RESULTS

In this study, DT, NB, LR, kNN, and RF models are compared practically using accuracy, precision, recall, and F-score metrics.

Table 1 shows the confusion matrix for DT.

Table 1. The confusion matrix of DT

		Actual values	
		Suicide	Non-Suicide
Predicted values	Suicide	2564	566
	Non-Suicide	530	2529

As shown in Table 1, DT correctly classified 5093 tweets and incorrectly classified 1096 tweets. For DT, TP is 2564, FP is 566, FN is 530 and TN is 2529.

Table 2 shows the confusion matrix for NB.

Table 2. The confusion matrix of NB

		Actual values	
		Suicide	Non-Suicide
Predicted values	Suicide	2893	202
	Non-Suicide	565	2529

As shown in Table 2, NB correctly classified 5422 tweets and incorrectly classified 767 tweets. For NB, TP is 2893, FP is 202, FN is 565 and TN is 2529.

Table 3 shows the confusion matrix for LR.

Table 3. The confusion matrix of LR

Predicted values	Actual values	
	Suicide	Non-Suicide
	Suicide	Non-Suicide
Suicide	2721	374
Non-Suicide	295	2799

As shown in Table 3, LR correctly classified 5520 tweets and incorrectly classified 669 tweets. For DT, TP is 2721, FP is 374, FN is 295, and TN is 2799.

Table 4 shows the confusion matrix for k-NN.

Table 4. The confusion matrix of kNN

Predicted values	Actual values	
	Suicide	Non-Suicide
	Suicide	Non-Suicide
Suicide	921	2174
Non-Suicide	564	2530

As shown in Table 4, kNN correctly classified 3451 tweets and incorrectly classified 2738 tweets. For DT, TP is 921, FP is 2174, FN is 564 and TN is 2530.

Table 5 presents the confusion matrix for RF.

Table 5. The confusion matrix of RF

Predicted values	Actual values	
	Suicide	Non-Suicide
	Suicide	Non-Suicide
Suicide	2747	348
Non-Suicide	361	2733

As shown in Table 5, RF correctly classified 5480 tweets and incorrectly classified 709 tweets. For RF, TP is 2747, FP is 348, FN is 361 and TN is 2733.

Table 6 shows the comparative results of all methods according to the metrics.

Table 6. Comparative results of the methods

Algorithm	Accuracy	Precision	Recall	F-Score
DT	0.83	0.82	0.83	0.82
NB	0.90	<b>0.93</b>	0.82	0.87
LR	<b>0.92</b>	0.88	<b>0.90</b>	<b>0.89</b>
kNN	0.56	0.54	0.82	0.65
RF	0.89	0.89	0.88	0.89

According to the results in Table 6, the LR method got the best result in Accuracy, Recall, and F-Score metrics. In the Precision metric, the NB method received the highest score.

### 3. CONCLUSIONS

Mental health problems are increasing worldwide. Psychological disorders, which have become a social health problem, have various consequences. As a result of depression, which is one of the most important of these disorders, people can commit suicide. Suicidal behavior, which is the voluntary ending of one's life, is a state of aggression directed against one's self - the turning of anger inward - a state of aggression. This phenomenon is seen as a symptom of a serious emotional and communicative problem. In addition to the traditional detection of suicidal tendencies, today, suicidal tendencies can be detected from the posts of people on social networks in advance and contribute to taking the necessary measures.

In this study, machine learning-based models were used to detect whether depressed people would commit suicide from their posts on social networks and these models were compared. As a result of the comparisons, the LR model was the most successful model.

### REFERENCES

1. World Health Organization Mental Health. [http://www.who.int/mental\\_health/en/](http://www.who.int/mental_health/en/). ,Accessed 10 Oct 2019.
2. Mental health atlas (2017). (Geneva: World Health Organization, 2018)
3. Calvo, R.A., Milne, D.N., Hussain, M.S., Christensen, H.: Natural language processing in mental health applications using non-clinical texts. *Nat. Lang. Eng.* 23(5), 649–685 2017.
4. A. Trifan, R. Antunes, S. Matos & J. L. Oliveira ,“Understanding Depression from Psycholinguistic Patterns in Social Media Texts”, Part of the Lecture Notes in Computer Science book series (LNISA,volume 12036),2020.
5. Coppersmith, G., Leary, R., Whyne, E., Wood, T.: Quantifying suicidal ideation via language usage on social media. In: Joint Statistics Meetings Proceedings, Statistical Computing Section, JSM 2015.

6. Reddy, E. M. K., Gurralla, A., Hasitha, V. B., & Kumar,” K. V. R. Introduction to Naive Bayes and a Review on Its Subtypes with Applications. Bayesian Reasoning and Gaussian Processes for Machine Learning Applications”, 1-14, 2022.
7. Bisong, E., & Bisong, E. “Logistic regression. Building machine learning and deep learning models on google cloud platform: A comprehensive guide for beginners”, 243-250, 2019.
8. Biau, G., & Scornet, “E. A random forest guided tour.” Test, 25, 197-227, 2016.
9. Charbuty, B., & Abdulazeez, “A. Classification based on decision tree algorithm for machine learning. Journal of Applied Science and Technology Trends”, 2(01), 20-28, 2021.
10. von Winterfeldt, Detlof; Edwards, Ward , "Decision trees". “Decision Analysis and Behavioral Research. Cambridge University Press”. pp. 63–89. ISBN 0-521-27304-8, 1986.
11. M. F. AKCA,” Metin Madenciliğinde Veri Ön İşleme”,2020
12. Abu Alfeilat, H. A., Hassanat, A. B., Lasassmeh, O., Tarawneh, A. S., Alhasanat, M. B., Eyal Salman, H. S., & Prasath, “V. S. Effects of distance measure choice on k-nearest neighbor classifier performance: a review. Big data”, 7(4), 221-248, 2019.



# FORMAL LANGUAGES AND PISOT NUMBERS

Arben Baushi<sup>1</sup>

<sup>1</sup>Department of Mathematics, University "Ismail Qemali" Vlora, ALBANIA

[arben.baushi@univlora.edu.al](mailto:arben.baushi@univlora.edu.al)

Kaçe Baushi<sup>2</sup>

<sup>2</sup>Department of Mathematics, University "Ismail Qemali" Vlora, ALBANIA

[kace.baushi@uniel.edu.al](mailto:kace.baushi@uniel.edu.al)

## Abstract

Around 1950 was developed the theory of automata and the theory of formal languages. These topics are closely related and form a distinct part of what is described as “computer science.” Studying these, the researchers had to use mathematical concepts, theorems, algebraic methods, verification supported in logic[3]. There are connections between Pisot numbers and formal languages. In this article we describe some of this connection. Finite automata are important for software and hardware[6]. The central concepts of Automata theory are the notions of an automaton and of a set recognized by an automaton. The sets in question are subsets of a free monoid  $\Sigma^*$  where  $\Sigma$  is a finite alphabet,  $\Sigma = \{0, 1, \dots, [\beta]\}$ , where  $\beta$  is a Pisot number. The number  $\beta > 1$  is called a Pisot number if all its algebraic conjugates satisfy  $|\beta'| < 1$ . Thus we shall be dealing with sets of words in a finite alphabet. Take the space of infinite or bi-infinite sequences of letters by alphabet,  $\Sigma$ , sequences (strings) find their applications in symbolic dynamics, linguistics data-transmissions and storage and computer science[10]. Some property of Pisot of degree four I am going to give at the end of this talk..

**Keywords:** Automata theory, Beta-integer, Alphabet, Pisot number, algebraic number.

## 1. INTRODUCTION

Around 1950 was developed the theory of Automata and the Theory of formal languages. These topics are closely related and form a distinct part of what is described as “computer science.” Studying these, the researchers had to use mathematical concepts, theorems, algebraic methods, verification supported in logic[3]. An automaton is an abstract model of a digital computer. An automaton has a mechanism to read input, which is a string over a given alphabet. The central concepts of Automata theory are the notions of an automaton and of a set recognized by an automaton. The sets in question are subsets of a free monoid  $\Sigma^*$  where  $\Sigma$  is a finite alphabet  $\Sigma = \{0, 1, \dots, b\}$  where  $b \in \mathbb{Z}^+$ [1]. In this talk we take  $\Sigma = \{0, 1, \dots, [\beta]\}$  where  $\beta$  be a Pisot number. Thus we shall be dealing with sets of words in a finite alphabet. Take the space of infinite or bi-infinite sequences of letters by alphabet, sequences (strings) find their applications in symbolic dynamics, linguistics data-transmissions and storage and computer science[11].  $\Sigma^*$  Denote the free monoid over alphabet  $\Sigma$ , the set of all finite strings of symbols chosen from  $\Sigma$  and operation of concatenation so  $\Sigma^* = \{\epsilon, 0, 1, \dots, 00, 01, 11, \dots, 001, \dots\}$  where  $\epsilon$  is empty string. A formal language is any subset of  $\Sigma^*$ . Take  $A, A_1, A_2$  languages. We take  $A_1 A_2 = \{u_1 u_2 | u_1 \in A_1, u_2 \in A_2\}$ ,  $A^0 = \{\epsilon\}$  and  $A^n = A A^{n-1}$  for  $n \geq 1$ .

Define the Kleene closure of a language[1]

$$A^* = \bigcup_{n \geq 0} A^n$$

A regular sentences over an alphabet  $\Sigma$  is a languages-a finite expression using the alphabet  $\Sigma$  together with  $+$  (to denote union),  $*$  (to denote Kleene closure),  $\epsilon$  (to denote the empty string),  $\Phi$  (to denote the empty set), and parentheses for grouping[10]. For example, the regular expression  $(\epsilon + 0)(1 + 02)^*$  denotes the set of all strings over alphabet take by us  $\Sigma = \{0, 1, \dots, [\beta]\}$ , containing no two consecutive 0's. If a language can be represented by a regular sentences, it is said to be regular.

## 2. SOME BASIC NOTATION

### 2.1. A deterministic finite automaton DFA

**Definition 1[4].** A deterministic finite accepter defined by the quintuple  $M = (Q, \Sigma, \delta, q_0, F)$

Where  $Q$  is a finite set of internal states,  $\Sigma$  is a finite set of symbols called the input alphabet,  $\delta: Q \times \Sigma \rightarrow Q$  is a total function called the transition function,  $q_0 \in Q$  is the initial state,  $F \subseteq Q$  is a set of final states.

A deterministic automata is one in which each move (transition from one state to another) is uniquely determined by the current configuration. If the internal state, input and contents of the storage are known, it is possible to predict the future behaviour of the automaton. This is said to be deterministic automata otherwise it is nondeterminist automata[7].

**Examples 1.** Draw a DFA for the language accepting strings ending with '012' over input alphabets  $\Sigma = \{0, 1, 2\}$

DFA is shown in Figure 1.

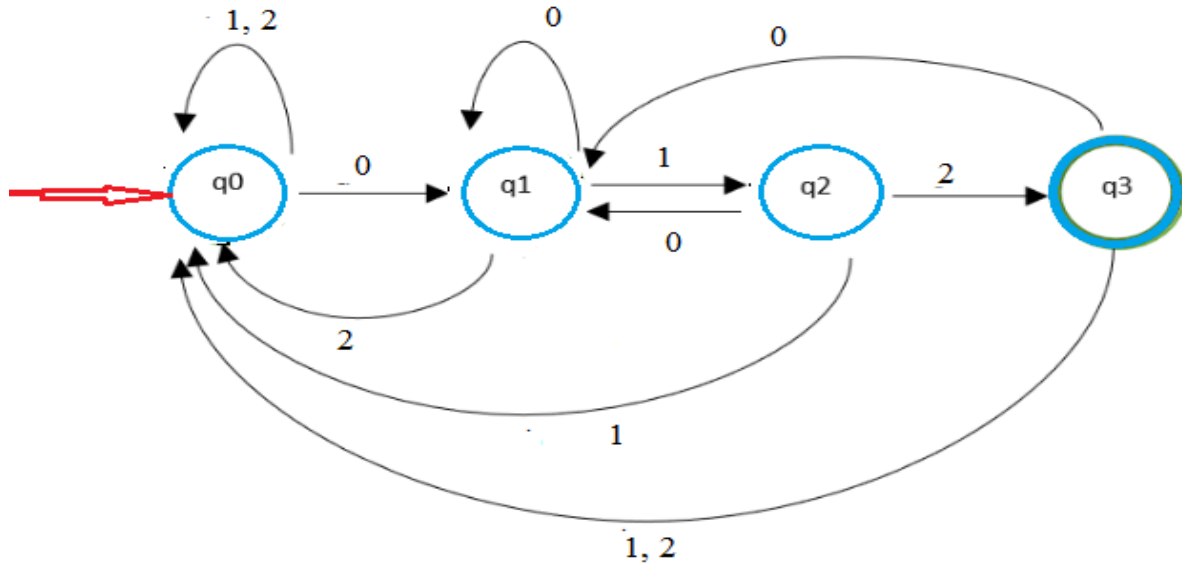


Figure 1. DFA over alphabet  $\Sigma = \{0, 1, 2\}$

Where  $q_0, q_1, q_2, q_3$  are the defined states. 0, 1, and 2 are valid symbols. Each state has a transition defined for 0, 1, and 2.  $q_3$  is the final state.

## 2.2 Non-Deterministic Finite Automata .

Non-Deterministic Finite Automata (N DFA / NFA) is an automata in which for some current state and input symbol, there exists more than one next output states[9].. It is also known as Non-Deterministic Finite Acceptor (NFA).

**Definition 2[10,11].** A nondeterministic finite automaton is a quintuple  $M = (Q, \Sigma, \delta, q_0, F)$ , where  $Q$  is a finite set of states,  $\Sigma$  is a finite set of symbols called alphabet,  $\delta: Q \times \Sigma \rightarrow \mathcal{P}(Q)$  is a total function called the transition function,  $q_0 \in Q$  is a distinguished state known as the start state,  $F \subseteq Q$  is a set of final states.

**Examples 2.** Transition Table for Non-Deterministic Finite Automata

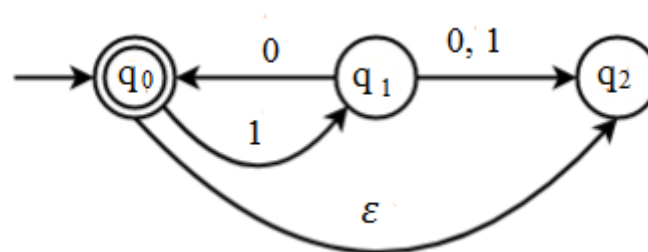


Figure 2 . NFA  $\Sigma = \{0, 1\}$

States\ alphabets	$\varepsilon$	0	1
$q_0$	$q_2$	-	$q_1$
$q_1$	-	$\{q_0, q_2\}$	$q_2$
$q_2$	-	-	-

**Definition 3 .** Two finite accepters,  $M_1$  and  $M_2$ , are said to be equivalent if that is, if they both accept the same language  $L(M_1) = L(M_2)$

When we compare different classes of automata, the question invariably arises whether one class is more powerful than the other. That mean that an automaton of one kind can achieve something that cannot be done by any automaton of the other kind [7].

**Examples 3.** Let  $L = \{0^*1^*0^*0 \mid \Sigma = \{0,1\}\}$  . N DFA that accepts  $L$ , DFA that accepts  $L$

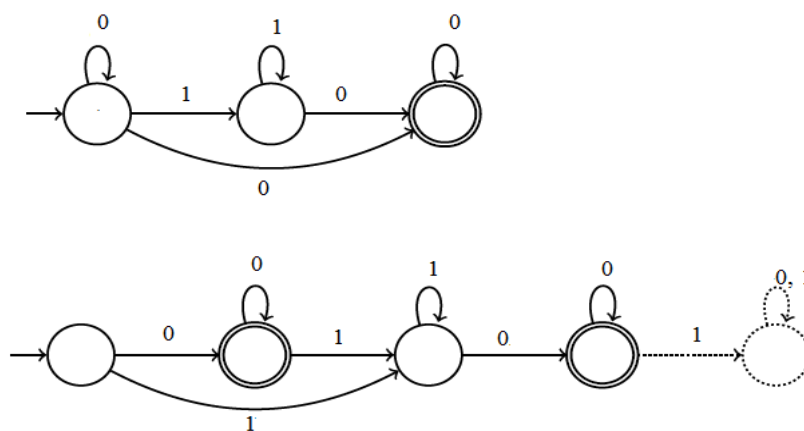


Figure 3. N DFA to DFA

**Theorem 1.** Every non deterministic finite automaton (N DFA) has an equivalent deterministic finite automaton (DFA).

We illustrated the thorem given the example 4 below.

**Examples 4.** Transform the following N DFA ; over  $\Sigma = \{0,1,2\}$  into an equivalent DFA. Figure 4.

Both DFA and N DFA are exactly same in power. For any regular language, both DFA and N DFA can be constructed. There exists an equivalent DFA corresponding to every N DFA. Every N DFA can be converted into its equivalent DFA. There exists no N DFA that can not be converted into its equivalent DFA[9]. Every DFA is a N DFA but every N DFA is not a DFA. The transitino function of a DFA as a function from  $Q \times \Sigma$  to singleton sets of alphabet elements, the family of DFAs may be considered to be a subset of the family of N DFAs.

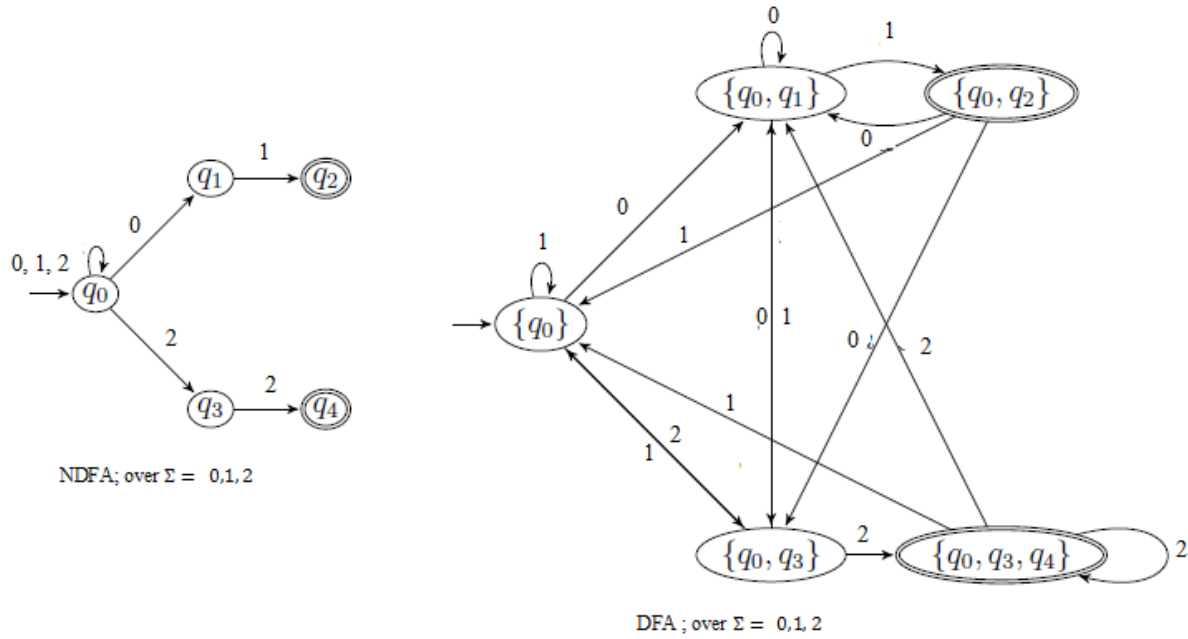


Figure 4. NFA to DFA

### 3. PISOT NUMBERS

**Definition 4**[5]. A number  $\alpha$  is an algebraic integer if it is the root of a monic integer polynomial. There is a unique monic integer polynomial  $p(x)$ , called the minimal polynomial, for which  $\alpha$  is a root and the degree of  $p(x)$  is minimal.

$$p(x) = a_n x^n + a_{n-1} x^{n-1} + \dots + a_1 x + a_0$$

$$a_0, a_1, \dots, a_{n-1}, a_n \in \mathbb{Z}, a_n = 1$$

$$\alpha = \frac{5+\sqrt{5}}{2}, \text{ root of polynomial, } p(x) = x^2 - 5x + 5$$

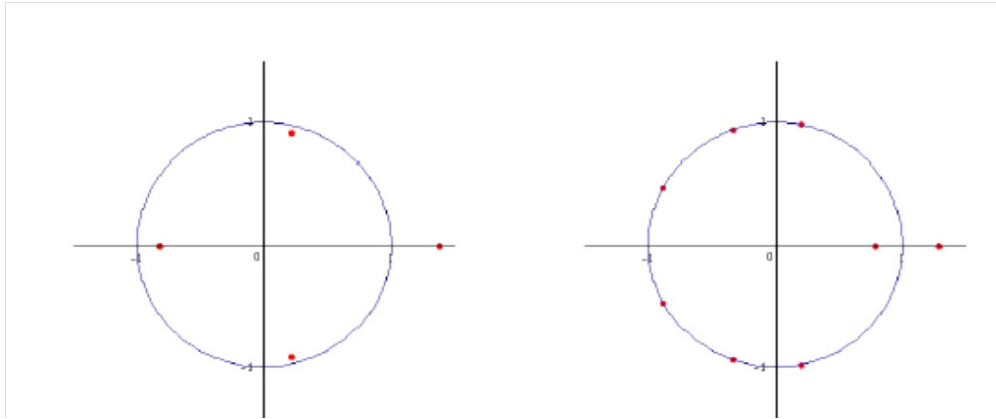
**Definition 5**[6,8]. If  $\alpha$  is an algebraic integer, and  $p(x)$  is its minimal polynomial, then we say that all of the other roots of  $p(x)$  are the conjugates of  $\alpha$ .

**Definition 6.** A Pisot number  $\beta$  satisfies the following conditions:

- $\beta$  is an algebraic integer
- $\beta > 1$
- all of  $\beta$ 's conjugates  $\beta_2, \beta_3, \dots, \beta_d$  (where  $d$  is the degree of the minimal polynomial of  $\beta$ ) are strictly less than 1 in modulus,  $|\beta_i| < 1, i = 2, 3, \dots, d$

**Definition 7.** A Salem number  $\tau$  is a real algebraic integer  $\tau > 1$  such that all of  $\tau$ 's conjugates are less than or equal to 1 in modulus, and at least one conjugate is equal to 1 in modulus.

## Examples 5.



The Pisot number 1.3803... and the other roots of  $x^4 - x^3 - 1$

The Salem number 1.2806..., and the other roots of  $x^8 - x^5 - x^4 - x^3 + 1$

$\mathbb{Q}(\beta)$  minimum field containing the rational numbers  $\mathbb{Q}$  and Pisot  $\beta$ . The properties of  $\beta$  – expansions are strongly related to symbolic dynamic. The closure of a set of infinite sequences, appearing as  $\beta$  – expansions is called a  $\beta$  – shift. It is a symbolic dynamical system that is closed shift-invariant subset of  $\mathcal{A}_\beta^{\mathbb{N}}$ .  $\beta$  – shift is finite iff  $T_\beta^n(1) = 0$  for some  $n$ , and it is sofic iff the orbit  $\{T_\beta^n(1)\}$  is finite.[4]

A greedy expansions in base  $\beta$  of a positive real number  $x$  is in form

$$x = \sum_{i=-k}^{\infty} a_{-i} \beta^{-i}$$

With  $a_{-i} \in \mathcal{A}_\beta = [0, \beta) \cap \mathbb{Z}$  and greedy condition

$$\left| x - \sum_{N_0 \leq k \leq N} a_k \beta^{-k} \right| < \beta^{-N}$$

For all  $N \geq N_0$

$.a_{-1}a_{-2}\dots$  is the fractional part of  $x$  denote by  $\{x\}$ . And  $a_k a_{k-1} \dots a_1 a_0$  is the integer part of  $x$  denote by  $[x]$ . The digit  $a_k$  obtained by greedy algorithm are integer from the set  $\mathcal{A}_\beta = \{0, \dots, \beta - 1\}$  if  $\beta$  is an integer or the set  $\mathcal{A}_\beta = \{0, \dots, [\beta]\}$  if  $\beta$  is not an integer[8,6]. This expansion for  $x \in [0, 1)$  is produced by iterating the beta transform :

$$T_\beta: x \rightarrow \beta x - [\beta x] \quad \text{where} \quad [\beta x] \in \mathcal{A}_\beta$$

Let  $1 = d_{-1} \beta^{-1} + d_{-2} \beta^{-2} + \dots$  be an expansion of 1 defined by the algorithm

$c_{-i} = \beta c_{-i+1} - [\beta c_{-i+1}]$ ,  $d_{-i} = [\beta c_{-i+1}]$ , with  $c_0 = 1$ , where  $[x]$  denoted the maximal integer not exceeding  $x$ . This expansion is achieved as a trajectory of  $e T_\beta^n(1)$  ( $n = 1, 2, \dots$ ).  $d_\beta(1) = d_{-1}, d_{-2}, \dots$  is called  $\beta$ -expansion of 1. Parry has shown that a sequence  $x = a_1, a_2, \dots$  of non negative integers give a  $\beta$ -expansion of pozitiv real number iff satisfies lexicographical condition:[8]

$$\forall p \geq 0, \quad \sigma^p(d) < \text{lex } d^*(1)$$

$$\text{with } d^*(1) = \begin{cases} d_\beta(1) & \text{if } d_\beta(1) \text{ is infinite} \\ (d_{-1}, d_{-2} \dots \dots d_{-n+1}, (d_{-n} - 1))^\omega & \text{if } d_\beta(1) = d_{-1}, \dots d_{-n} \end{cases}$$

where the string of simbols  $w$ ,  $w^\omega$  is a periodic expansions  $w$ ,  $w, \dots$  and  $\sigma$  is the shift defined by

$$\sigma((a_i)_{i \leq M}) = (a_{i-1})_{i \leq M} \text{ so the sequence } x = a_1, a_2, a_3 \dots \text{ is called admissible.}$$

Root of  $P(x) = x^4 - 3x^3 + x^2 - 2x - 1$ , is a pisot numbers of degree 4.  $\beta \approx 2,93132$ .

$$d_\beta(1) = 2, 2, 1, 3, 1 = 2, 2, 1, 2, 4, 2, 1, 3, 1 \dots$$

To get an expansion of  $x$  in base  $\beta$ , we need to compare that with expansion of 1. To check that this is corect we can use the thory of automaton. Studing finite automata as acceptors of infinite words goes to Büchi. The first question we address in this work is the one of the recognizability by a finite Büchi automaton of the set of infinite  $\beta$ -representations of 0 when  $\beta$  is a real number and the digits are integer. The set of infinite  $\beta$ -representations of 0 on the alphabet  $\{-l, \dots, l\}$ ,  $l \geq 1$  integer, is denoted  $\mathbb{Z}_{\beta, l} = \{a_1 a_2 \dots \mid \sum_{i \geq 1} a_i \beta^{-i}, a_i \in \{-l, \dots, l\}\}$ . In their work Ch. Frougny and J. Sakarovitch, [Number representation and finite automata, Chapter 2 in Combinatorics, Automata and Number Theory, C.U.P., 2010] we get this theorem.

**Theorem 2[9,10].** Let  $\beta > 1$ . The following conditions are equivalent:

1. the set  $\mathbb{Z}_{\beta, l}$  is recognizable by a finite Büchi automaton for every integer  $l$ ,
2. the set  $\mathbb{Z}_{\beta, l}$  is recognizable by a finite Büchi automaton for every integer  $l \geq [\beta]$ ,
3.  $\beta$  is a Pisot number.

#### 4.CONCLUSIONS

There is a lot of research on formal languages and number theory. their connection constitutes a new field of research that is growing to enrich both of these fields. Since number theory deals with the properties of integers, and formal language theory deals with the properties of strings[2]. At the intersection lies (a) the study of the properties of integers based on their representation for example, representation in base  $k$ ; and (b) the study of the properties of strings of digits based on the integers they represent.

## REFERENCES

1. Samuel Eilenberg, Automata, Language, And Machines : Volume: A, 12-29,1974
2. Jeffrey Shallit, Number theory and formal Language 1999, <https://cs.uwaterloo.ca/~shallit/Papers/ntfl.pdf>
3. Arben Baushi, Fractals and their topological properties, 2019 phd thesis [https://univlora.edu.al/wp-content/uploads/2019/09/Versioni-on-Line\\_Arben\\_baushi.pdf](https://univlora.edu.al/wp-content/uploads/2019/09/Versioni-on-Line_Arben_baushi.pdf)
4. Linz, Peter, An introduction to formal languages and automata, Fifth Edition 2012 by Jones & Bartlett Learning, LLC
5. Arben Baushi, Characteristic of tiling generated by root of polynomial  $P(x) = x^4 - 3x^3 + x^2 - 2x - 1$  <http://cmm2016.smm.com.mk/>
6. Xhevdet Spahiu, Arben Baushi: A Note On Beta Expansion And Numbers Badly Approximable , <https://www.jmest.org/vol-7-issue-8-august-2020/>
7. Thomas A. Sudkamp, An Introduction to the Theory of ComputerScience Second Edition , 1997 by Addison Wesley Longman, Inc.
8. Gjini, N. A Self-Similar Tiling Generated By The Pisot Number Which Is The Root Of The Equation  $x^3 - x^2 - 1 = 0$ , Osaka J. Math. 38 (2001), 303–319
9. Christiane Frougny, and Edita Pelantova, Two applications of the spectrum of numbers, arXiv:1512.04234v3 [math.NT] 18 Mar 2018
10. Ch. Frougny and J. Sakarovitch, [Number representation and finite automata, Chapter 2 in Combinatorics, Automata and Number Theory, C.U.P., 2010
11. Lecture Notes in Computer Science , Developments in Language Theory 22nd International Conference, DLT 2018 Tokyo, Japan, September 10–14, 2018 Proceedings



# A Limit-circle criterion for the Beta-Sturm-Liouville operator

Yüksel Yalçinkaya<sup>1</sup>

<sup>1</sup> Mathematics Teacher, Ministry of National Education, Isparta, Turkey

matyuksel@hotmail.com

## Abstract

Limit-point/Limit-circle theory, first developed by Herman Weyl in the early 1900s, has become increasingly important in solving various singular second-order Sturm-Liouville problems. In this study, the singular beta Sturm-Liouville operator defined as

$$\Omega(y) = -T_{\beta}(f(t)T_{\beta}y(t) + g(t)y(t) \text{ on } [0, \infty)$$

is considered where  $f(t)$  and  $g(t)$  real valued functions. In this context, first of all, the basic concepts of beta calculus are given. Later, a criterion will be obtained for Weyl's limit circle case of the Beta-Sturm-Liouville operators.

**Keywords:** Limit-circle case criterion, beta Sturm-Liouville operator.

## 1. INTRODUCTION

Fractional calculations, which emerged towards the end of the 17th century, have been the research subject since then. Particularly in the case of continuity, studies on fractional analysis gained more importance towards the end of the 19. century. Fractional differential equations, which is a sub-field of differential equations, has started to be used frequently in many fields today with the development of technology. Fractional differential equations are used in many applications such as viscoelasticity, electroanalytical chemistry, control theory and physics problems, engineering sciences in particular, genetics, medicine, biology, geology, economics, statistics, pharmacy, psychology, etc.

In 2014, Khalil et al. [1] gave a new definition of the conformable fractional derivative and conformable fractional integral. Abdeljawad [2] defined right and left conformable fractional derivatives, fractional chain rule and higher-order fractional integrals. Later, Atangana et al. beta derivative has been described ([3],[4]). Although these definitions are not exactly fractional derivatives, they have attracted the attention of researchers because they are an extension of ordinary derivatives. In [5], the authors examined the space-time generalized

nonlinear Schrödinger equation including the beta derivative. Fadhal et al. ([6]) examined the nonlinear Sasa-Satsuma equation with a beta derivative.

Limit-Point and Limit-Circle theory was first developed by Herman Weyl in 1910 [7]. Wely showed that the solution of the differential equation established with a second-order singular symmetric operator is square integrable. Thus, differential operators are divided into two groups those in the limit circle state and those in the limit point state. While all solutions of linearly independent solutions of differential operators in the limit circle case are quadratically integrable, only one of the linearly independent solutions for those in the limit point situation is quadratically integrable. After from Weyl, Titchmarsh studied some properties of m-functions known as Titchmarsh-Weyl functions [8]. Thus, with the help of the Titchmarsh-Weyl function, spectral function, boundary value operators, scattering function, and characteristic function can be established. Since then, such methods have become increasingly important thanks to their accurate estimates of the for of the potential in applications, which can easily provide basic information about solving a wide variety of singular quadratic Sturm-Liouville problems. Since then, such methods have become more important in solving singular second-order Sturm-Liouville problems, thanks to their accurate predictions. When the literature is examined, it is seen that there are studies on limit-point and limit-circle states of differential equations [9], [10], [11], [12], [13], [14] .

Allahverdiev et al. [15], in their study, examined the criteria in which the fractional conformable singular Sturm-Liouville equation is of the limit-circle case. In [16] Chen and Shi gave certain constrained conditions regarding the limit circle and limit point criteria of second-order linear difference equations. In [17] Anderson investigated the problem of determining sufficient conditions for  $L$  to be of the limit point type or the limit circle type for certain classes of  $L$  singular symmetric differential operators of order  $2n$ .

In this article, we give some criteria for the Beta-Sturm-Liouville operator in the limit-circle state, and we use the machinery and methods in [18, 19] to prove our results.

## 2. PRELIMINARIES

**Definition 1:** ([3],[5]) Let  $\beta$  be a positive number with  $0 < \beta < 1$  A function  $f: [0, \infty) \rightarrow \mathbb{R} := (-\infty, \infty)$  the  $\beta$  derivative of  $f(t)$  of order  $\beta$  is given by

$$T_{\beta}f(t) = \lim_{\varepsilon \rightarrow 0} \frac{f\left(t + \varepsilon\left(t + \frac{1}{\Gamma(\beta)}\right)^{1-\beta}\right) - f(t)}{\varepsilon} \quad (1)$$

and  $(T_\beta f)(t) = \frac{d^\beta f(t)}{dt^\beta}$ .

**Definition 2:** Let  $f: [a, \infty) \rightarrow \mathbb{R}$  is given function, then we propose that the beta-integral of  $f$  is:

$${}_a I_\beta(f(t)) = \int_a^t (x + \frac{1}{\Gamma(\beta)})^{\beta-1} f(x) dx \quad (2)$$

where  $0 < \beta \leq 1$  and  $({}^b T_\beta f)(t) = \lim_{t \rightarrow b^-} ({}^b T_\beta f)(t)$ .

**Theorem 3:** Let  $f, g$  be  $\beta$ -differentiable functions for  $t > 0$  and  $0 < \beta \leq 1$  Some properties are discussed as follows

- i.  $T_\beta(\lambda f(t) + \delta g(t)) = \lambda T_\beta f(t) + \delta T_\beta g(t)$  for all  $\lambda, \delta \in \mathbb{R}$
- ii.  $T_\beta(f(t)g(t)) = f(t)T_\beta g(t) + g(t)T_\beta f(t)$
- iii.  $T_\beta\left(\frac{f(t)}{g(t)}\right) = \frac{f(t)T_\beta g(t) - g(t)T_\beta f(t)}{g^2(t)}$
- iv.  $T_\beta f(t) = \left(t + \frac{1}{\Gamma(\beta)}\right)^{1-\beta} \frac{df(t)}{dt}$ .

**Theorem 4:** Let  $f, g: [0, b] \rightarrow \mathbb{R}$  be  $\beta$ -differentiable functions. Then, the following relation holds

$$\int_0^b f(t)T_\beta g(t) d_\beta t = f(t)g(t)|_0^b - \int_0^b g(t)T_\beta f(t) d_\beta t.$$

**Proof:** By Theorem 3, we obtain

$$\begin{aligned} & \int_0^b f(t)T_\beta g(t) d_\beta t + \int_0^b g(t)T_\beta f(t) d_\beta t \\ &= \int_0^b f(t) \left(t + \frac{1}{\Gamma(\beta)}\right)^{\beta-1} g'(t) d_\beta t \\ &+ \int_0^b g(t) \left(t + \frac{1}{\Gamma(\beta)}\right)^{\beta-1} f'(t) d_\beta t \\ &= f(t)g(t)|_0^b - \int_0^b g(t) \left(t + \frac{1}{\Gamma(\beta)}\right)^{\beta-1} f'(t) d_\beta t \\ &+ \int_0^b g(t) \left(t + \frac{1}{\Gamma(\beta)}\right)^{\beta-1} f'(t) d_\beta t \\ &= f(b)g(b) - f(0)g(0). \end{aligned}$$

Let

$$L_{\beta}^2(0, b) = \left\{ f: \left( \int_0^b |f(t)|^2 d_{\beta} t \right)^{1/2} < \infty \right\}$$

Then  $L_{\beta}^2(0, b)$  is a Hilbert space endowed with the inner product

$$\langle f, g \rangle = \int_0^b f(t) \overline{g(t)} d_{\beta} t, \quad f, g \in L_{\beta}^2(0, b).$$

**Theorem 5:** Assume that  $f: (-\infty, b] \rightarrow \mathbb{R}$  is continuous and  $0 < \beta \leq 1$ . Then for  $t < b$ , we have

$$T_{\beta}^{-b} I_{\beta} = f(t).$$

### 3. MAIN RESULTS

The fractional Beta-Sturm--Liouville equation is

$$\Omega(y) = -T_{\beta}(f(t)T_{\beta}y(t) + g(t)y(t)) \quad \text{on } \mathcal{J} \quad (3)$$

where  $\mathcal{J} := [0, b)$  and  $0 < b \leq \infty$   $b$  is the singular endpoint. The coefficients  $f(\cdot)$  and  $g(\cdot)$  are real-valued functions on  $\mathcal{J}$  and satisfy the conditions  $\frac{1}{f(\cdot)}, g(\cdot) \in L_{\beta, loc}^2(\mathcal{J})$ . Let

$$\mathcal{D} := \{y \in L_{\beta}^2(\mathcal{J}): y, T_{\beta}y \in AC_{\beta, loc}(\mathcal{J}), \Omega(y) \in L_{\beta}^2(\mathcal{J})\},$$

where  $AC_{\beta, loc}(\mathcal{J})$  denotes the class of complex-valued functions which are absolutely continuous on all compact sub-intervals of  $\mathcal{J}$ . For  $z_1, z_2 \in \mathcal{D}$  we have the following Green's formula

$$\int_0^{\infty} \Omega(z_1)(t) \overline{z_2(t)} d_{\beta} t - \int_0^{\infty} z_1(t) \overline{\Omega(z_2)(t)} d_{\beta} t = [z_1, z_2](\infty) - [z_1, z_2](0), \quad (4)$$

where  $[z_1, z_2](t) = f(t)\{z_1(t) \overline{T_{\beta}z_2(t)} - T_{\beta}z_1(t) \overline{z_2(t)}\}$ ,  $t \in \mathcal{J}$ .

**Remark 6:** It follows from (5) that  $\lim_{t \rightarrow b} [z_1, z_2](t)$  exists and is finite for all  $z_1, z_2 \in \mathcal{D}$

Furthermore, we know that  $\Omega$  is limit-point at  $b$  if and only if  $\lim_{t \rightarrow b} [z_1, z_2](t) = 0$  for all

$z_1, z_2 \in \mathcal{D}$  (see ([5])).

**Theorem 7:** Let the coefficients  $f$  and  $g$  satisfy the following conditions:

- i.  $g \in C_{\beta}(\mathcal{J}), T_{\beta}f, T_{\beta}g \in AC_{\beta, loc}(\mathcal{J})$  and  $T_{\beta}^2f, T_{\beta}^2g \in L_{\beta, loc}^2(\mathcal{J})$ ,
- ii.  $g(t) < 0$  and  $f(t) > 0$  for all  $t \in \mathcal{J}$ ,
- iii.  $(-fg)^{1/2} \in L_{\beta}^2(\mathcal{J})$ ,
- iv.  $T_{\beta}\{fT_{\beta}(fg)(-fg)^{1/2}\} \in L_{\beta}^2(\mathcal{J})$ , (5)

then  $\Omega$  is in the limit-circle case at  $b$ .

**Proof:** We shall produce one pair  $y, z$  of elements of  $\mathcal{D}$  such that

$$\lim_{t \rightarrow b} [y, z](t) \neq 0. \quad (6)$$

We take  $y = z$  and determine  $y$  by

$$y(t) = \{-f(t)g(t)\}^{\frac{1}{2}} \exp \left[ i \int_0^t \left\{ -\frac{g(\varepsilon)}{f(\varepsilon)} \right\}^{\frac{1}{2}} d_\beta \varepsilon \right], \quad (7)$$

where  $t \in \mathcal{J}$ . A calculation shows that

$$T_\beta y = \left[ \frac{i(-f)^{\frac{1}{2}}}{g^{\frac{1}{2}}} + \frac{1}{4} \frac{T_\beta(fg)}{(-fg)^{1/2}} \right] * \exp \left[ i \int_0^t \left\{ -\frac{g(\varepsilon)}{f(\varepsilon)} \right\}^{\frac{1}{2}} d_\beta \varepsilon \right]$$

and

$$T_\beta^2 y = \left[ -\frac{(-g)^{\frac{1}{2}}}{f^{\frac{1}{2}}} + \frac{i}{4} \frac{T_\beta(fg)}{f^{\frac{1}{2}}(-g)^{\frac{1}{2}}} - \frac{i}{4} \frac{T_\beta f}{(-fg)^{\frac{1}{2}}} - \frac{3i}{4} \frac{(-g)^{\frac{1}{2}} T_\beta f}{f^{\frac{1}{2}}} + \frac{1}{4} \frac{T_\beta^2(gf)}{(-fg)^{\frac{1}{2}}} + \frac{5}{16} \frac{\{T_\beta(fg)\}^2}{(-fg)^{\frac{1}{2}}} \right] \\ * \exp \left[ i \int_0^t \left\{ -\frac{g(\varepsilon)}{f(\varepsilon)} \right\}^{\frac{1}{2}} d_\beta \varepsilon \right].$$

Thus we get

$$[y, y](t) = -2i, \quad (8)$$

where  $t \in \mathcal{J}$  and, with details of the calculation omitted,

$$\Omega[y] = -f T_\beta^2 y - T_\beta f y + g y = \frac{1}{4} T_\beta \left\{ f T_\beta(fg) (-fg)^{\frac{1}{2}} \right\} \exp \left[ i \int_0^t \left\{ -\frac{g(\varepsilon)}{f(\varepsilon)} \right\}^{\frac{1}{2}} d_\beta \varepsilon \right]. \quad (9)$$

It follows from (7) and conditions (ii) and (iii) of the Theorem that  $y \in L_\beta^2(\mathcal{J})$ . From (7) and condition (i), we obtain  $T_\beta y \in AC_{\beta,loc}(\mathcal{J})$ . It follows from (9) and condition (iv) that  $\Omega[y] \in L_\beta^2(\mathcal{J})$ . In this way, we have  $y \in \mathcal{D}$ . From (6) and (8) it now follows that the differential expression  $\Omega[\cdot]$  is in the limit-circle case at  $b$ .

## REFERENCES

1. R. Khalil, M. Al Horani, A. Yousef and M. Sababheh, A new definition of fractional derivative, J. Comput. Appl. Math, Vol:264, 65-70, 2014.
2. T. Abdeljawad, On conformable fractional calculus, J. Comput Appl Math, Vol:279, 57-66, 2015.
3. A. Atangana and R. T. Alqahtani, Modelling the spread of river blindness disease via the Caputo fractional derivative and the beta-derivative, Entropy, Vol:18(2), 40, 2016,

4. A. Atangana, D. Baleanu and A. Alsaedi, Analysis of time-fractional Hunter--Saxton equation: a model of neumatic liquid crystal, *Open Phys.* Vol:14 (1), 145-149, 2016.
5. Y. P. Martinez, J. P. Gomez-Aguilar and D. Baleanu, Beta-derivative and sub-equation method applied to the optical solitons in medium with parabolic law nonlinearity and higher order dispersion. *Optik*, Vol:155, 357-365, 2018
6. E. Fadhal, A. Akbulut, M. Kaplan, M. Awadalla and K. Abuasbeh, Extraction of Exact Solutions of Higher Order Sasa-Satsuma Equation in the Sense of Beta Derivative. *Symmetry*, Vol:14(11), 2390, 2022, <https://doi.org/10.3390/sym14112390>
7. H. Weyl, Über gewöhnliche Differentialgleichungen mit Singularitäten und die zugehörigen Entwicklungen willkürlicher Functionen, *Math. Ann.* Vol:68, 222-269, 1910.
8. E. C. Titchmarsh, *Eigenfunction Expansions Associated with Second-Order Differential Equations. Part I.* Second Edition Clarendon Press, Oxford, 1962.
9. E. Bairamov and A. M. Krall, Dissipative operators generated by the Sturm-Liouville differential expression in the Weyl limit circle case, *J. Math. Anal. Appl.* Vol: 254, 178-190, 2001.
10. W. N. Everitt, I. W. Knowles and T. T. Read, Limit-point and limit-circle criteria for Sturm-Liouville equations with intermittently negative principal coefficients, *proceedings of the Royal Society of Edinburgh*, 103A, 215-228, 1986.
11. S. Huaqing and S. Yuming, Limit-point and limit-circle criteria for singular second-order linear difference equations with complex coefficients, *Comput. Math. Appl.*, Vol: 52 (3-4), 539-554, 2006.
12. B. P. Allahverdiev, Nonselfadjoint Sturm--Liouville operators in limit-circle case. *Taiwan. J. Math.* Vol:16(6), 2035-2052, 2012.
13. V. F. Bellino and G. Esposito, Revisited version of Weyl's limit-point limit-circle criterion for essential self-adjointness, *J. Phys. Commun.*, Vol: 3, 035017, 2019, <https://doi.org/10.1088/2399-6528/ab0e44>
14. C. T. Fulton, Parametrization of Titchmarsh's  $m(\lambda)$  -functions in the limit circle case, *Trans. Amer. Math. Soc.*, Vol:229, 51-63, 1977.
15. B. P. Allahverdiev, H. Tuna and Y. Yalçınkaya, Remarks on the Limit-Circle Classification of Conformable Fractional Sturm-Liouville Operators, *Lecture Notes on Data Engineering and Communications Technologies* 76, 10-14, 2020.
16. C. Jingnian and S. Yuming, The Limit Circle and Limit Point Criteria for Second-Order Linear Difference Equations, *Computers and Mathematics with Applications*, Vol:47,

- 967-976, 2004.
17. R. L. Anderson, Limit point and limit circle criteria for a class of singular symmetric differential operators, Can. J. Math., XXVIII, Vol:5, 905-914, 1976.
  18. W. N. Everitt, On the limit-circle classification of second order differential expressions, Quart. J. Math. (Oxford), Vol:23(2), 193-196, 1972,  
<https://doi.org/10.1093/qmath/23.2.193>
  19. W. N. Everitt, On the limit-point classification of second-order differential expressions, J. London Math. Soc., Vol:41, 531-534, 1966.

# ESTIMATIONS OF BOUNDS FOR PARAMETERIZED SIMPSON'S TYPE INEQUALITIES USING $(s, m)$ -DIFFERENTIABLE CONVEX FUNCTIONS VIA GENERALIZED FRACTIONAL INTEGRALS

Rozana Liko<sup>1</sup>, Artion Kashuri<sup>1</sup>

<sup>1</sup>Department of Mathematics, Faculty of Technical and Natural Sciences, University Ismail Qemali, 9400 Vlora, Albania

[rozana.liko@univlora.edu.al](mailto:rozana.liko@univlora.edu.al), [artion.kashuri@univlora.edu.al](mailto:artion.kashuri@univlora.edu.al)

## Abstract

In this paper, we obtain a new integral identity for differentiable functions with two parameters involving generalized fractional integral operators. By applying this as an auxiliary result, we deduce several new Simpson type inequalities for  $(s, m)$ -differentiable convex functions. For suitable choices of parameters, some special cases are given and some known results are recaptured as well. To validate the accuracy of our main results, we present some examples.

**Keywords:** Simpson's inequalities;  $(s, m)$ -convex functions; Generalized fractional integrals; Hölder's inequality; Power-mean inequality.

## 1. INTRODUCTION

Convex functions and their generalizations have various applications in the fields of pure and applied sciences.

**Definition 1.1.** A function  $f: I \subseteq \mathbb{R} \rightarrow \mathbb{R}$  is said to be convex on  $I$ , if

$$f(tx + (1 - t)y) \leq tf(x) + (1 - t)f(y) \quad (1)$$

holds for all  $x, y \in I$  and  $t \in [0, 1]$ .

In their paper [1], Hudzik and Maligranda considered, among others, the class of  $s$ -convex functions in the second sense. This class is defined in the following way:

**Definition 1.2.** A function  $f: [0, +\infty[ \rightarrow \mathbb{R}$  is said to be  $s$ -convex in the second sense, if

$$f(tx + (1 - t)y) \leq t^s f(x) + (1 - t)^s f(y) \quad (2)$$

holds for all  $x, y \in [0, +\infty[$ ,  $t \in [0, 1]$  and for some fixed  $s \in (0, 1]$ .



**Definition 1.3.** [2] A function  $f: [0, +\infty[ \rightarrow \mathbb{R}$  is said to be  $m$ -convex for  $m \in (0, 1]$ , if the following inequality holds

$$f(tx + (1 - t)y) \leq tf(x) + m(1 - t)f(y), \quad (3)$$

for all  $x, y \in [0, +\infty[, x < y$ .

By combining the last two definitions, then the following definition is obtained, see [3, 4, 5].

**Definition 1.4.** A function  $f: [0, +\infty[ \rightarrow \mathbb{R}$  is said to be  $(s, m)$ -convex in the second sense if  $f$  satisfies

$$f(tx + (1 - t)y) \leq t^s f(x) + m(1 - t)^s f(y), \quad (4)$$

for all  $x, y \in [0, +\infty[, t \in [0, 1]$  and for some fixed  $(s, m) \in (0, 1]^2$ .

**Definition 1.5.** The generalized left-side and right-side fractional integrals are given as follows:

$${}_{a_1^+}I_\varphi f(x) = \int_{a_1}^x \frac{\varphi(x - t)}{x - t} f(t) dt, \quad (x > a_1) \quad (5)$$

and

$${}_{a_2^-}I_\varphi f(x) = \int_x^{a_2} \frac{\varphi(t - x)}{t - x} f(t) dt, \quad (x < a_2), \quad (6)$$

where  $\varphi: [0, +\infty[ \rightarrow [0, +\infty[$  is a function constructed by Sarikaya *et al.*, see [6], that satisfies the following four conditions:

$$\begin{aligned} \int_0^1 \frac{\varphi(t)}{t} dt &< +\infty, \\ \frac{1}{A_1} &\leq \frac{\varphi(t_1)}{\varphi(t_2)} \leq A_1 \text{ for } \frac{1}{2} \leq \frac{t_1}{t_2} \leq 2, \\ \frac{\varphi(t_2)}{t_2^2} &\leq A_2 \leq \frac{\varphi(t_1)}{t_1^2} \text{ for } t_1 \leq t_2 \end{aligned} \quad (7)$$

and

$$\left| \frac{\varphi(t_2)}{t_2^2} - \frac{\varphi(t_1)}{t_1^2} \right| \leq A_3 |t_2 - t_1| \frac{\varphi(t_2)}{t_2^2} \text{ for } \frac{1}{2} \leq \frac{t_1}{t_2} \leq 2,$$

where  $A_1, A_2$  and  $A_3 > 0$  are independent from  $t_1, t_2 > 0$ .

The generalized fractional integrals given by Definition 1.5 may contain some types of fractional integrals such as the Riemann-Liouville and other fractional integrals for some special choices of function  $\varphi$ .

**Definition 1.6.** The left and right Riemann–Liouville fractional integrals (R-L) are given as follows:

$$J_{a+}^{\alpha} f(x) = \frac{1}{\Gamma(\alpha)} \int_a^x (x-t)^{\alpha-1} f(t) dt, \quad (x > a)$$

$$J_b^{-\alpha} f(x) = \frac{1}{\Gamma(\alpha)} \int_x^b (t-x)^{\alpha-1} f(t) dt, \quad (x < b).$$

Simpson's rules are well-known in the literature of numerical integration and numerical estimation of definite integrals. The following rules are given by Simpson:

1) Simpson's 1/3 rule:

$$\int_{x_1}^{x_2} f(x) dx \approx \frac{(x_2 - x_1)}{3} \left[ f(x_1) + 4f\left(\frac{x_1 + x_2}{2}\right) + f(x_2) \right], \quad (8)$$

where  $x_1 < x_2$ .

2) Simpson's 3/8 rule:

$$\int_{x_1}^{x_2} f(x) dx \approx \frac{(x_2 - x_1)}{8} \left[ f(x_1) + 3f\left(\frac{2x_1 + x_2}{3}\right) + f\left(\frac{x_1 + 2x_2}{3}\right) + f(x_2) \right]. \quad (9)$$

The following inequality is known in the literature as Simpson's inequality.

**Theorem 1.1.** Let  $f : [a, b] \rightarrow \mathbb{R}$  be a four times continuously differentiable function on  $(a, b)$  and  $\|f^{(4)}\|_{\infty} := \sup_{x \in (a, b)} |f^{(4)}(x)| < \infty$ . Then the following inequality holds:

$$\left| \frac{1}{3} \left[ \frac{f(a) + f(b)}{2} + 2f\left(\frac{a+b}{2}\right) \right] - \frac{1}{(b-a)} \int_a^b f(x) dx \right| \leq \frac{1}{2880} \|f^{(4)}\|_{\infty} (b-a)^4. \quad (10)$$

Later, many authors have focused on Simpson's type inequalities for various classes of convex functions, see [7, 8, 9, 10, 11, 12, 13].

Our final paper is organised as follows: In Section 2, we will obtain a new integral identity for differentiable functions with two parameters involving generalized fractional integral operators. Moreover, by applying this as an auxiliary result, we will deduce several new Simpson type inequalities for  $(s, m)$ -differentiable convex functions utilising the well-known Hölder and power-mean inequalities. In Section 3, for suitable choices of parameters, some special cases will be deduced and some known results will be recaptured. In Section 4, we offer some examples in order to validate the accuracy of our main results given in Section 2. The conclusions and recommendations for further study will be provided in Section 5.

## 2. MAIN RESULTS

Before we give our main results, let us denote by

$$\Delta_m(t) := \int_0^t \frac{\varphi((b-ma)u)}{u} du < +\infty, \quad \text{for all } m \in ]0, 1]. \quad (11)$$

**Lemma 2.1.** Let  $f: [a, b] \rightarrow \mathbb{R}$  be a differentiable function on  $(a, b)$ . If  $f'$  is continuous on  $(a, b)$ , then for  $\lambda, \mu \geq 0$ , we have

$$\begin{aligned} (b - ma) & \left[ \int_0^{1/2} (\Delta_m(t) - \Delta_m(1)\lambda) f'(tb + m(1-t)a) dt \right. \\ & \quad \left. + \int_{1/2}^1 (\Delta_m(t) - \Delta_m(1)\mu) f'(tb + m(1-t)a) dt \right] \\ & = \Delta_m(1)\lambda f(ma) + \Delta_m(1)(\mu - \lambda) f\left(\frac{ma+b}{2}\right) + \Delta_m(1)(1 - \mu) f(b) \\ & \quad - \left[ \left(\frac{ma+b}{2}\right)^+ I_\varphi f(b) + \left(\frac{ma+b}{2}\right)^- I_\varphi f(ma) \right]. \end{aligned} \quad (12)$$

**Proof.** Let denote by

$$I := (b - ma) \left[ \int_0^{1/2} (\Delta_m(t) - \Delta_m(1)\lambda) f'(tb + m(1-t)a) dt \right. \\ \left. + \int_{1/2}^1 (\Delta_m(t) - \Delta_m(1)\mu) f'(tb + m(1-t)a) dt \right] = (b - ma)[I_1 + I_2], \quad (13)$$

where

$$I_1 := \int_0^{1/2} (\Delta_m(t) - \Delta_m(1)\lambda) f'(tb + m(1-t)a) dt$$

and

$$I_2 := \int_{1/2}^1 (\Delta_m(t) - \Delta_m(1)\mu) f'(tb + m(1-t)a) dt.$$

Integrating by parts the first integral, we obtain

$$\begin{aligned} I_1 & = \frac{\Delta_m(t) - \Delta_m(1)\lambda}{b - ma} f(tb + m(1-t)a) \Big|_0^{1/2} \\ & \quad - \frac{1}{b - ma} \int_0^{1/2} \frac{\varphi((b - ma)t)}{t} f(tb + m(1-t)a) dt \\ & = \frac{\Delta_m\left(\frac{1}{2}\right) - \Delta_m(1)\lambda}{b - ma} f\left(\frac{ma+b}{2}\right) + \frac{\Delta_m(1)\lambda}{b - ma} f(ma) \\ & \quad - \frac{1}{b - ma} \int_0^{1/2} \frac{\varphi((b - ma)t)}{t} f(tb + m(1-t)a) dt. \end{aligned}$$

By changing the variable of integration in the last integral,  $w = t(b - ma) + ma$ , we get

$$I_1 = \frac{\Delta_m\left(\frac{1}{2}\right) - \Delta_m(1)\lambda}{b - ma} f\left(\frac{ma+b}{2}\right) + \frac{\Delta_m(1)\lambda}{b - ma} f(ma) - \frac{1}{b - ma} \left(\frac{ma+b}{2}\right)^- I_\varphi f(ma). \quad (14)$$

Similarly,

$$I_2 = \frac{\Delta_m(1)(1-\mu)}{b-ma} f(b) - \frac{\Delta_m\left(\frac{1}{2}\right) - \Delta_m(1)\mu}{b-ma} f\left(\frac{ma+b}{2}\right) - \frac{1}{b-ma} \left(\frac{ma+b}{2}\right)^+ I_\varphi f(b). \quad (15)$$

Substituting (14) and (15) in equation (13), we have

$$I = \Delta_m(1)\lambda f(ma) + \Delta_m(1)(\mu - \lambda) f\left(\frac{ma+b}{2}\right) + \Delta_m(1)(1-\mu) f(b) \\ - \left[ \left(\frac{ma+b}{2}\right)^+ I_\varphi f(b) + \left(\frac{ma+b}{2}\right)^- I_\varphi f(ma) \right].$$

The proof of Lemma 2.1 is completed. ■

**Remark 2.1.** Taking  $m = 1$  in Lemma 2.1, we get [14, Lemma 1].

**Remark 2.2.** Choosing  $\phi(t) = t$  in Lemma 2.1, we obtain [15, Lemma 2.1].

**Theorem 2.1.** Let  $|f'|$  be a  $(s, m)$ -convex function for  $(s, m) \in (0, 1]^2$ . Then for  $\lambda, \mu \in [0, 1]$ , the following inequality holds:

$$|I| \leq (b-ma) \left[ |f'(b)| \{Y_1^\varphi(\lambda, m, s) + Y_3^\varphi(\mu, m, s)\} + m |f'(a)| \{Y_2^\varphi(\lambda, m, s) + Y_4^\varphi(\mu, m, s)\} \right], \quad (16)$$

where

$$Y_1^\varphi(\lambda, m, s) := \int_0^{1/2} t^s |\Delta_m(t) - \Delta_m(1)\lambda| dt;$$

$$Y_2^\varphi(\lambda, m, s) := \int_0^{1/2} (1-t)^s |\Delta_m(t) - \Delta_m(1)\lambda| dt;$$

$$Y_3^\varphi(\mu, m, s) := \int_{1/2}^1 t^s |\Delta_m(t) - \Delta_m(1)\mu| dt$$

and

$$Y_4^\varphi(\mu, m, s) := \int_{1/2}^1 (1-t)^s |\Delta_m(t) - \Delta_m(1)\mu| dt.$$

**Proof.** From Lemma 2.1 and properties of the modulus, we have

$$|I| \leq (b-ma) \left[ \int_0^{1/2} |\Delta_m(t) - \Delta_m(1)\lambda| |f'(tb + m(1-t)a)| dt \right. \\ \left. + \int_{1/2}^1 |\Delta_m(t) - \Delta_m(1)\mu| |f'(tb + m(1-t)a)| dt \right]$$

Using  $(s, m)$ -convexity of  $|f'|$ , we get

$$\begin{aligned}
|I| &\leq (b - ma) \left[ \int_0^{\frac{1}{2}} |\Delta_m(t) - \Delta_m(1)\lambda| [t^s |f'(b)| + m(1-t)^s |f'(a)|] dt \right. \\
&\quad \left. + \int_{\frac{1}{2}}^1 |\Delta_m(t) - \Delta_m(1)\mu| [t^s |f'(b)| + m(1-t)^s |f'(a)|] dt \right] \\
&= (b - ma) \\
&\quad \cdot \left[ m|f'(a)| \left\{ \int_0^{\frac{1}{2}} (1-t)^s |\Delta_m(t) - \Delta_m(1)\lambda| dt \right. \right. \\
&\quad \left. \left. + \int_{\frac{1}{2}}^1 (1-t)^s |\Delta_m(t) - \Delta_m(1)\mu| dt \right\} \right. \\
&\quad \left. + |f'(b)| \left\{ \int_0^{\frac{1}{2}} t^s |\Delta_m(t) - \Delta_m(1)\lambda| dt + \int_{\frac{1}{2}}^1 t^s |\Delta_m(t) - \Delta_m(1)\mu| dt \right\} \right].
\end{aligned}$$

Hence,

$$\begin{aligned}
|I| &\leq (b - ma) [|f'(b)| \{Y_1^\varphi(\lambda, m, s) + Y_3^\varphi(\mu, m, s)\} \\
&\quad + m|f'(a)| \{Y_2^\varphi(\lambda, m, s) + Y_4^\varphi(\mu, m, s)\}].
\end{aligned}$$

■

**Corollary 2.1.** If we take  $s = m = 1$  in Theorem 2.1, we obtain [14, Theorem 3].

**Corollary 2.2.** If we choose  $\varphi(t) = t$  in Theorem 2.1, we get [15, Theorem 2.1].

**Corollary 2.3.** If we take  $\varphi(t) = \frac{t^\alpha}{\Gamma(\alpha)}$  in Theorem 2.1, we have

$$\begin{aligned}
&\left| \lambda f(ma) + (\mu - \lambda) f\left(\frac{ma+b}{2}\right) + (1 - \mu) f(b) \right. \\
&\quad \left. - \frac{\Gamma(\alpha + 1)}{(b - ma)^\alpha} \left\{ \mathcal{J}_{\left(\frac{ma+b}{2}\right)^+}^\alpha f(b) + \mathcal{J}_{\left(\frac{ma+b}{2}\right)^-}^\alpha f(ma) \right\} \right| \\
&\leq (b - ma) [|f'(b)| \{Y'_1 + Y'_3\} + m|f'(a)| \{Y'_2 + Y'_4\}],
\end{aligned} \tag{17}$$

where  $\mathcal{J}_x^\alpha f$ ,  $\mathcal{J}_x^\alpha f$  are the right and left R-L fractional integrals and

$$\begin{aligned}
Y'_1 &:= \frac{2\alpha}{(s+1)(s+\alpha+1)} \lambda^{\frac{s+\alpha+1}{\alpha}} - \frac{\lambda}{2^{s+1}(s+1)} + \frac{1}{2^{s+\alpha+1}(s+\alpha+1)}; \\
Y'_2 &:= \frac{\lambda}{s+1} + \frac{\lambda}{2^{s+1}(s+1)} - \frac{2\lambda \left(1 - \lambda^{\frac{1}{\alpha}}\right)^{s+1}}{s+1} - 2B_{\frac{1}{\lambda\alpha}}(\alpha+1, s+1) + B_{\frac{1}{2}}(\alpha+1, s+1); \\
Y'_3 &:= \frac{2\alpha}{(s+1)(s+\alpha+1)} \mu^{\frac{s+\alpha+1}{\alpha}} - \frac{\mu}{2^{s+1}(s+1)} - \frac{\mu}{s+1} + \frac{1}{2^{s+\alpha+1}(s+\alpha+1)} + \frac{1}{s+\alpha+1}; \\
Y'_4 &:= \frac{\mu}{2^{s+1}(s+1)} - \frac{2\mu \left(1 - \mu^{\frac{1}{\alpha}}\right)^{s+1}}{s+1} - 2B_{\frac{1}{\mu\alpha}}(\alpha+1, s+1) + B_{\frac{1}{2}}(\alpha+1, s+1) \\
&\quad + B(\alpha+1, s+1).
\end{aligned}$$

**Corollary 2.4.** If we choose  $s = m = 1$  and  $\varphi(t) = t$ , we obtain

$$\begin{aligned} & \left| \lambda f(a) + (\mu - \lambda) f\left(\frac{a+b}{2}\right) + (1 - \mu) f(b) - \frac{1}{b-a} \int_a^b f(t) dt \right| \\ & \leq (b-a) \left[ |f'(b)| \left\{ \frac{\lambda^3}{3} - \frac{\lambda}{8} + \frac{\mu^3}{3} - \frac{\mu}{2} + \frac{5}{12} \right\} \right. \\ & \quad \left. + |f'(a)| \left\{ \frac{(1-\lambda)^3}{3} - \frac{9}{16} (1-\lambda) + \frac{(1-\mu)^3}{3} - \frac{\mu}{16} + \frac{5}{12} \right\} \right]. \end{aligned} \quad (18)$$

**Theorem 2.2.** Let  $|f'|^r$  be a  $(s, m)$ -convex function for  $(s, m) \in (0, 1]^2$ . Then for  $\lambda, \mu \in [0, 1]$  and  $r \geq 1$ , the following inequality holds:

$$\begin{aligned} |I| & \leq (b-a) \cdot \left\{ \left( \int_0^{\frac{1}{2}} |\Delta_m(t) - \Delta_m(1)\lambda| dt \right)^{1-\frac{1}{r}} \right. \\ & \quad \cdot \left( Y_1^\varphi(\lambda, m, s) |f'(b)|^r + m Y_2^\varphi(\lambda, m, s) |f'(a)|^r \right)^{\frac{1}{r}} \\ & \quad + \left( \int_{\frac{1}{2}}^1 |\Delta_m(t) - \Delta_m(1)\mu| dt \right)^{1-\frac{1}{r}} \\ & \quad \cdot \left. \left( Y_3^\varphi(\lambda, m, s) |f'(b)|^r + m Y_4^\varphi(\lambda, m, s) |f'(a)|^r \right)^{\frac{1}{r}} \right\}, \end{aligned} \quad (19)$$

where  $Y_i^\varphi, i = \overline{1,4}$ , are defined as in Theorem 2.1.

**Proof.** From Lemma 2.1, power-mean inequality and properties of the modulus, we have

$$\begin{aligned} |I| & \leq (b-a) \left\{ \left( \int_0^{\frac{1}{2}} |\Delta_m(t) - \Delta_m(1)\lambda| dt \right)^{1-\frac{1}{r}} \right. \\ & \quad \cdot \left( \int_0^{\frac{1}{2}} |\Delta_m(t) - \Delta_m(1)\lambda| |f'(tb + m(1-t)a)|^r dt \right)^{\frac{1}{r}} \\ & \quad + \left( \int_{\frac{1}{2}}^1 |\Delta_m(t) - \Delta_m(1)\mu| dt \right)^{1-\frac{1}{r}} \\ & \quad \cdot \left. \left( \int_{\frac{1}{2}}^1 |\Delta_m(t) - \Delta_m(1)\mu| |f'(tb + m(1-t)a)|^r dt \right)^{\frac{1}{r}} \right\}. \end{aligned}$$

Using  $(s, m)$  – convexity of  $|f'|^r$ , we get

$$\begin{aligned}
& |I| \\
& \leq (b - ma) \\
& \quad \left( \int_0^{\frac{1}{2}} |\Delta_m(t) - \Delta_m(1)\lambda| dt \right)^{1-\frac{1}{r}} \cdot \left( \int_0^{\frac{1}{2}} |\Delta_m(t) - \Delta_m(1)\lambda| [t^s |f'(b)|^r + m(1-t)^s |f'(a)|^r] dt \right)^{\frac{1}{r}} + \\
& \quad \left( \int_{\frac{1}{2}}^1 |\Delta_m(t) - \Delta_m(1)\mu| dt \right)^{1-\frac{1}{r}} \cdot \left( \int_{\frac{1}{2}}^1 |\Delta_m(t) - \Delta_m(1)\mu| [t^s |f'(b)|^r + m(1-t)^s |f'(a)|^r] dt \right)^{\frac{1}{r}} \\
& = (b - ma) \\
& \quad \left( \int_0^{\frac{1}{2}} |\Delta_m(t) - \Delta_m(1)\lambda| dt \right)^{1-\frac{1}{r}} \cdot (Y_1^\varphi(\lambda, m, s) |f'(b)|^r + mY_2^\varphi(\lambda, m, s) |f'(a)|^r)^{\frac{1}{r}} \\
& \quad + \left( \int_{\frac{1}{2}}^1 |\Delta_m(t) - \Delta_m(1)\mu| dt \right)^{1-\frac{1}{r}} \cdot (Y_3^\varphi(\lambda, m, s) |f'(b)|^r + mY_4^\varphi(\lambda, m, s) |f'(a)|^r)^{\frac{1}{r}} \quad \blacksquare
\end{aligned}$$

**Corollary 2.5.** If we take  $s = m = 1$  in Theorem 2.2, we obtain [14, Theorem 4].

**Corollary 2.6.** If we choose  $\varphi(t) = t$  in Theorem 2.2, we have [15, Theorem 2.3].

**Corollary 2.7.** If we take  $\varphi(t) = \frac{t^\alpha}{\Gamma(\alpha)}$  in Theorem 2.2, we get

$$\begin{aligned}
& \left| \lambda f(ma) + (\mu - \lambda) f\left(\frac{ma+b}{2}\right) + (1 - \mu) f(b) \right. \\
& \quad \left. - \frac{\Gamma(\alpha + 1)}{(b - ma)^\alpha} \left\{ \mathcal{J}_{\left(\frac{ma+b}{2}\right)^+}^\alpha f(b) + \mathcal{J}_{\left(\frac{ma+b}{2}\right)^-}^\alpha f(ma) \right\} \right| \\
& \leq (b - ma) \left\{ \left( \frac{2\alpha}{\alpha + 1} \lambda^{\frac{\alpha+1}{\alpha}} - \lambda + \frac{1}{\alpha + 1} \right)^{1-\frac{1}{r}} (Y_1' |f'(b)|^r + mY_2' |f'(a)|^r)^{\frac{1}{r}} \right. \\
& \quad + \left( \frac{2\alpha}{\alpha + 1} \mu^{\frac{\alpha+1}{\alpha}} - \frac{3}{2} \mu + \frac{1}{2^{\alpha+1}(\alpha + 1)} + \frac{1}{\alpha + 1} \right)^{1-\frac{1}{r}} (Y_3' |f'(b)|^r \\
& \quad \left. + mY_4' |f'(a)|^r)^{\frac{1}{r}} \right\},
\end{aligned} \tag{20}$$

where  $Y_i'$ ,  $i = \overline{1,4}$ , are defined as in Corollary 2.3.

**Theorem 2.3.** Let  $|f'|^r$  be a  $(s, m)$  – convex function for  $(s, m) \in (0, 1]^2$ . Then for  $\lambda, \mu \in [0, 1]$ ,  $r > 1$  and  $\frac{1}{r} + \frac{1}{q} = 1$ , the following inequality holds:

$$\begin{aligned}
|I| \leq (b - ma) & \left\{ \left( \int_0^{\frac{1}{2}} |\Delta_m(t) - \Delta_m(1)\lambda|^q dt \right)^{\frac{1}{q}} \right. \\
& \cdot \left( \frac{1}{(s+1)2^{s+1}} |f'(b)|^r + m \frac{2^{s+1}-1}{(s+1)2^{s+1}} |f'(a)|^r \right)^{\frac{1}{r}} \\
& + \left( \int_{\frac{1}{2}}^1 |\Delta_m(t) - \Delta_m(1)\mu|^q dt \right)^{\frac{1}{q}} \\
& \cdot \left( \frac{2^{s+1}-1}{(s+1)2^{s+1}} |f'(b)|^r + m \frac{1}{(s+1)2^{s+1}} |f'(a)|^r \right)^{\frac{1}{r}} \Bigg\}.
\end{aligned} \tag{21}$$

**Proof.** From Lemma 2.1, Hölder's inequality,  $(s, m)$  – convexity of  $|f'|^r$  and properties of the modulus, we have

$$\begin{aligned}
|I| \leq (b - ma) & \left\{ \left( \int_0^{\frac{1}{2}} |\Delta_m(t) - \Delta_m(1)\lambda|^q dt \right)^{\frac{1}{q}} \cdot \left( \int_0^{\frac{1}{2}} |f'(tb + m(1-t)a)|^r dt \right)^{\frac{1}{r}} \right. \\
& + \left. \left( \int_{\frac{1}{2}}^1 |\Delta_m(t) - \Delta_m(1)\mu|^q dt \right)^{\frac{1}{q}} \cdot \left( \int_{\frac{1}{2}}^1 |f'(tb + m(1-t)a)|^r dt \right)^{\frac{1}{r}} \right\} \\
& \leq (b - ma) \left\{ \left( \int_0^{\frac{1}{2}} |\Delta_m(t) - \Delta_m(1)\lambda|^q dt \right)^{\frac{1}{q}} \right. \\
& \cdot \left( \int_0^{\frac{1}{2}} [t^s |f'(b)|^r + m(1-t)^s |f'(a)|^r] dt \right)^{\frac{1}{r}} + \left( \int_{\frac{1}{2}}^1 |\Delta_m(t) - \Delta_m(1)\mu|^q dt \right)^{\frac{1}{q}} \\
& \cdot \left. \left( \int_{\frac{1}{2}}^1 [t^s |f'(b)|^r + m(1-t)^s |f'(a)|^r] dt \right)^{\frac{1}{r}} \right\}.
\end{aligned}$$

Hence,

$$\begin{aligned}
|I| \leq (b - ma) & \left\{ \left( \int_0^{\frac{1}{2}} |\Delta_m(t) - \Delta_m(1)\lambda|^q dt \right)^{\frac{1}{q}} \cdot \left( \frac{1}{(s+1)2^{s+1}} |f'(b)|^r + m \frac{2^{s+1}-1}{(s+1)2^{s+1}} |f'(a)|^r \right)^{\frac{1}{r}} \right. \\
& + \left. \left( \int_{\frac{1}{2}}^1 |\Delta_m(t) - \Delta_m(1)\mu|^q dt \right)^{\frac{1}{q}} \cdot \left( \frac{2^{s+1}-1}{(s+1)2^{s+1}} |f'(b)|^r + m \frac{1}{(s+1)2^{s+1}} |f'(a)|^r \right)^{\frac{1}{r}} \right\}. \quad \blacksquare
\end{aligned}$$

**Corollary 2.8.** If we take  $s = m = 1$  in Theorem 2.3, we obtain [14, Theorem 5].

**Corollary 2.9.** If we choose  $\varphi(t) = t$  in Theorem 2.3, we get



$$\begin{aligned}
& \left| \lambda f(a) + (\mu - \lambda) f\left(\frac{a+b}{2}\right) + (1 - \mu) f(b) - \frac{1}{b-a} \int_a^b f(t) dt \right| \\
& \leq (b - ma) \left\{ \left( \int_0^{\frac{1}{2}} |t - \lambda|^q dt \right)^{\frac{1}{q}} \right. \\
& \quad \cdot \left( \frac{1}{(s+1)2^{s+1}} |f'(b)|^r + m \frac{2^{s+1} - 1}{(s+1)2^{s+1}} |f'(a)|^r \right)^{\frac{1}{r}} + \left( \int_{\frac{1}{2}}^1 |t - \mu|^q dt \right)^{\frac{1}{q}} \\
& \quad \cdot \left( \frac{2^{s+1} - 1}{(s+1)2^{s+1}} |f'(b)|^r + m \frac{1}{(s+1)2^{s+1}} |f'(a)|^r \right)^{\frac{1}{r}} \Bigg\}.
\end{aligned} \tag{22}$$

**Corollary 2.10.** If we take  $\varphi(t) = \frac{t^\alpha}{\Gamma(\alpha)}$  in Theorem 2.3, we have

$$\begin{aligned}
& \left| \lambda f(ma) + (\mu - \lambda) f\left(\frac{ma+b}{2}\right) + (1 - \mu) f(b) - \frac{\Gamma(\alpha+1)}{(b-ma)^\alpha} \left\{ \mathcal{J}_{\left(\frac{ma+b}{2}\right)^+}^\alpha f(b) + \mathcal{J}_{\left(\frac{ma+b}{2}\right)^-}^\alpha f(ma) \right\} \right| \\
& \leq (b - ma) \left\{ \left( \int_0^{\frac{1}{2}} |t^\alpha - \lambda|^q dt \right)^{\frac{1}{q}} \right. \\
& \quad \cdot \left( \frac{1}{(s+1)2^{s+1}} |f'(b)|^r + m \frac{2^{s+1} - 1}{(s+1)2^{s+1}} |f'(a)|^r \right)^{\frac{1}{r}} \\
& \quad \left. + \left( \int_{\frac{1}{2}}^1 |t^\alpha - \mu|^q dt \right)^{\frac{1}{q}} \cdot \left( \frac{2^{s+1} - 1}{(s+1)2^{s+1}} |f'(b)|^r + m \frac{1}{(s+1)2^{s+1}} |f'(a)|^r \right)^{\frac{1}{r}} \right\}.
\end{aligned} \tag{23}$$

**Corollary 2.11** If we choose  $s = 1$  in Corollary 2.10, we obtain

$$\begin{aligned}
& \left| \lambda f(ma) + (\mu - \lambda) f\left(\frac{ma+b}{2}\right) + (1 - \mu) f(b) - \frac{\Gamma(\alpha+1)}{(b-ma)^\alpha} \left\{ \mathcal{J}_{\left(\frac{ma+b}{2}\right)^+}^\alpha f(b) + \mathcal{J}_{\left(\frac{ma+b}{2}\right)^-}^\alpha f(ma) \right\} \right| \\
& \leq (b - ma) \left\{ \left( \int_0^{\frac{1}{2}} |t^\alpha - \lambda|^q dt \right)^{\frac{1}{q}} \cdot \left( \frac{1}{2^3} |f'(b)|^r + m \frac{3}{2^3} |f'(a)|^r \right)^{\frac{1}{r}} \right. \\
& \quad \left. + \left( \int_{\frac{1}{2}}^1 |t^\alpha - \mu|^q dt \right)^{\frac{1}{q}} \cdot \left( \frac{3}{2^3} |f'(b)|^r + m \frac{1}{2^3} |f'(a)|^r \right)^{\frac{1}{r}} \right\}.
\end{aligned} \tag{24}$$

### 3. SPECIAL CASES

**A.** If we take  $\lambda = \frac{1}{6}, \mu = \frac{5}{6}$  and  $m = 1$  in Corollary 2.3, we get

$$\left| \frac{1}{6}f(a) + \frac{4}{6}f\left(\frac{a+b}{2}\right) + \frac{1}{6}f(b) - \frac{\Gamma(\alpha+1)}{(b-a)^\alpha} \left\{ \mathcal{J}_{\left(\frac{a+b}{2}\right)^+}^\alpha f(b) + \mathcal{J}_{\left(\frac{a+b}{2}\right)^-}^\alpha f(a) \right\} \right|$$

$$\leq (b-a)[|f'(b)|\{\Omega_1 + \Omega_3\} + |f'(a)|\{\Omega_2 + \Omega_4\}],$$

where

$$\Omega_1 := \frac{2\alpha}{(s+1)(s+\alpha+1)6^{\frac{s+\alpha+1}{\alpha}}} - \frac{1}{6 \cdot 2^{s+1}(s+1)} + \frac{1}{2^{s+\alpha+1}(s+\alpha+1)};$$

$$\Omega_2 := \frac{1}{6(s+1)} + \frac{1}{6 \cdot 2^{s+1}(s+1)} - \frac{\left(1 - 6^{-\frac{1}{\alpha}}\right)^{s+1}}{3(s+1)} - 2B_{6^{-\frac{1}{\alpha}}}(\alpha+1, s+1) + B_{\frac{1}{2}}(\alpha+1, s+1);$$

$$\Omega_3 := \frac{2\alpha}{(s+1)(s+\alpha+1)}\left(\frac{5}{6}\right)^{\frac{s+\alpha+1}{\alpha}} - \frac{5(2^{s+1}+1)}{6 \cdot 2^{s+1}(s+1)} + \frac{1}{2^{s+\alpha+1}(s+\alpha+1)} + \frac{1}{s+\alpha+1};$$

$$\Omega_4 := \frac{5}{6 \cdot 2^{s+1}(s+1)} - \frac{5\left(1 - \left(\frac{5}{6}\right)^{\frac{1}{\alpha}}\right)^{s+1}}{3(s+1)} - 2B_{\left(\frac{5}{6}\right)^{\frac{1}{\alpha}}}(\alpha+1, s+1) + B_{\frac{1}{2}}(\alpha+1, s+1) + B(\alpha+1, s+1).$$

**B.** If we choose  $\lambda = \frac{1}{6}$ ,  $\mu = \frac{5}{6}$  and  $s = 1$  in Corollary 2.3, we obtain

$$\left| \frac{1}{6}f(ma) + \frac{4}{6}f\left(\frac{ma+b}{2}\right) + \frac{1}{6}f(b) - \frac{\Gamma(\alpha+1)}{(b-ma)^\alpha} \left\{ \mathcal{J}_{\left(\frac{ma+b}{2}\right)^+}^\alpha f(b) + \mathcal{J}_{\left(\frac{ma+b}{2}\right)^-}^\alpha f(a) \right\} \right|$$

$$\leq (b-ma)[|f'(b)|\{\Omega'_1 + \Omega'_3\} + |f'(ma)|\{\Omega'_2 + \Omega'_4\}],$$

where

$$\Omega'_1 := \frac{\alpha}{(2+\alpha)6^{\frac{2+\alpha}{\alpha}}} + \frac{1}{(2+\alpha)2^{2+\alpha}} - \frac{1}{48};$$

$$\Omega'_2 := \frac{5}{48} - \frac{1}{6}\left(1 - \frac{1}{6^{\frac{1}{\alpha}}}\right)^2 - 2\frac{1}{(\alpha+1)6^{\frac{\alpha+1}{\alpha}}} + 2\frac{1}{(\alpha+2)6^{\frac{\alpha+2}{\alpha}}} + \frac{\alpha+3}{(\alpha+1)(\alpha+2)2^{\alpha+2}};$$

$$\Omega'_3 := \frac{\alpha}{(2+\alpha)}\left(\frac{5}{6}\right)^{\frac{2+\alpha}{\alpha}} + \frac{1}{(2+\alpha)2^{2+\alpha}} + \frac{1}{2+\alpha} - \frac{100}{48};$$

$$\Omega'_4 := \frac{5}{48} - \frac{5}{6}\left(1 - \left(\frac{5}{6}\right)^{\frac{1}{\alpha}}\right)^2 - \frac{2}{\alpha+1}\left(\frac{5}{6}\right)^{\frac{\alpha+1}{\alpha}} + \frac{2}{\alpha+2}\left(\frac{5}{6}\right)^{\frac{\alpha+2}{\alpha}} + \frac{\alpha+3}{(\alpha+1)(\alpha+2)2^{\alpha+2}} + \frac{1}{(\alpha+1)(\alpha+2)}.$$

C. If we take  $\lambda = \frac{1}{2}$ ,  $\mu = \frac{1}{2}$  and  $m = 1$  in Corollary 2.3, we have

$$\left| \frac{1}{2}f(a) + \frac{1}{2}f(b) - \frac{\Gamma(\alpha+1)}{(b-a)^\alpha} \left\{ \mathcal{J}_{\left(\frac{a+b}{2}\right)^+}^\alpha f(b) + \mathcal{J}_{\left(\frac{a+b}{2}\right)^-}^\alpha f(a) \right\} \right| \\ \leq (b-a)[|f'(b)|\{\Omega_1^1 + \Omega_3^1\} + |f'(a)|\{\Omega_2^1 + \Omega_4^1\}],$$

where

$$\Omega_1^1 := \frac{2\alpha}{(s+1)(s+\alpha+1)} \frac{1}{2^{\frac{s+\alpha+1}{\alpha}}} - \frac{1}{2^{s+2}(s+1)} + \frac{1}{2^{s+\alpha+1}(s+\alpha+1)};$$

$$\Omega_2^1 := \frac{1}{2(s+1)} + \frac{1}{2^{s+2}(s+1)} - \frac{\left(1 - 2^{-\frac{1}{\alpha}}\right)^{s+1}}{s+1} - 2B_{\frac{1}{2} - \frac{1}{\alpha}}(\alpha+1, s+1) + B_{\frac{1}{2}}(\alpha+1, s+1);$$

$$\Omega_3^1 = \frac{2\alpha}{(s+1)(s+\alpha+1)} \frac{1}{2^{\frac{s+\alpha+1}{\alpha}}} - \frac{1}{2^{s+2}(s+1)} - \frac{1}{2(s+1)} + \frac{1}{2^{s+\alpha+1}(s+\alpha+1)} \\ + \frac{1}{s+\alpha+1};$$

$$\Omega_4^1 = \frac{1}{2^{s+2}(s+1)} - \frac{\left(1 - \frac{1}{2^{\frac{1}{\alpha}}}\right)^{s+1}}{s+1} - 2B_{\frac{1}{2} - \frac{1}{\alpha}}(\alpha+1, s+1) + B_{\frac{1}{2}}(\alpha+1, s+1) \\ + B(\alpha+1, s+1).$$

D. If we choose  $\lambda = \frac{1}{2}$  and  $\mu = \frac{1}{2}$  and  $s = 1$  in Corollary 2.3, we get

$$\left| \frac{1}{2}f(a) + \frac{1}{2}f(b) - \frac{\Gamma(\alpha+1)}{(b-a)^\alpha} \left\{ \mathcal{J}_{\left(\frac{a+b}{2}\right)^+}^\alpha f(b) + \mathcal{J}_{\left(\frac{a+b}{2}\right)^-}^\alpha f(a) \right\} \right| \\ \leq (b-ma)[|f'(b)|\{\Omega'_1 + \Omega'_3\} + |f'(ma)|\{\Omega'_2 + \Omega'_4\}].$$

E. If we take  $\lambda = 0$  and  $\mu = 1$  in Corollary 2.3, we obtain

$$\left| f\left(\frac{ma+b}{2}\right) - \frac{\Gamma(\alpha+1)}{(b-ma)^\alpha} \left\{ \mathcal{J}_{\left(\frac{ma+b}{2}\right)^+}^\alpha f(b) + \mathcal{J}_{\left(\frac{ma+b}{2}\right)^-}^\alpha f(a) \right\} \right| \\ \leq (b-ma) \left[ |f'(b)| \left\{ \frac{1}{2^{s+\alpha}(s+\alpha+1)} + \frac{\alpha}{(s+1)(s+\alpha+1)} - \frac{1}{2^{s+1}(s+1)} \right\} \right. \\ \left. + m|f'(ma)| \left\{ \frac{1}{2^{s+1}(s+1)} + 2B_{\frac{1}{2}}(\alpha+1, s+1) - B(\alpha+1, s+1) \right\} \right].$$

F. If we choose  $\lambda = \frac{1}{6}$ ,  $\mu = \frac{5}{6}$  and  $m = 1$  in Corollary 2.7, we have

$$\begin{aligned}
& \left| \frac{1}{6}f(a) + \frac{4}{6}f\left(\frac{a+b}{2}\right) + \frac{1}{6}f(b) - \frac{\Gamma(\alpha+1)}{(b-a)^\alpha} \left\{ \mathcal{J}_{\left(\frac{a+b}{2}\right)^+}^\alpha f(b) + \mathcal{J}_{\left(\frac{a+b}{2}\right)^-}^\alpha f(a) \right\} \right| \\
& \leq (b-a) \left( \frac{2\alpha}{\alpha+1} \frac{1}{6^{\frac{\alpha+1}{\alpha}}} - \frac{1}{6} + \frac{1}{\alpha+1} \right)^{1-\frac{1}{r}} \\
& \quad \cdot (\Omega_1 |f'(b)|^r + \Omega_2 |f'(a)|^r)^{\frac{1}{r}} \\
& \quad + \left( \frac{2\alpha}{\alpha+1} \left(\frac{5}{6}\right)^{\frac{\alpha+1}{\alpha}} - \frac{5}{4} + \frac{1}{2^{\alpha+1}(\alpha+1)} + \frac{1}{\alpha+1} \right)^{1-\frac{1}{r}} \\
& \quad \cdot (\Omega_3 |f'(b)|^r + \Omega_4 |f'(a)|^r)^{\frac{1}{r}} .
\end{aligned}$$

**G.** If we take  $\lambda = \frac{1}{2}$ ,  $\mu = \frac{1}{2}$  and  $m = 1$  in Corollary 2.7, we get

$$\begin{aligned}
& \left| \frac{1}{2}f(a) + \frac{1}{2}f(b) - \frac{\Gamma(\alpha+1)}{(b-a)^\alpha} \left\{ \mathcal{J}_{\left(\frac{a+b}{2}\right)^+}^\alpha f(b) + \mathcal{J}_{\left(\frac{a+b}{2}\right)^-}^\alpha f(a) \right\} \right| \\
& \leq (b-a) \left\{ \left( \frac{2\alpha}{\alpha+1} \frac{1}{2^{\frac{\alpha+1}{\alpha}}} - \frac{1}{2} + \frac{1}{\alpha+1} \right)^{1-\frac{1}{r}} \cdot (\Omega_1^1 |f'(b)|^r + \Omega_2^1 |f'(a)|^r)^{\frac{1}{r}} \right. \\
& \quad + \left( \frac{2\alpha}{\alpha+1} \frac{1}{2^{\frac{\alpha+1}{\alpha}}} - \frac{3}{4} + \frac{1}{2^{\alpha+1}(\alpha+1)} + \frac{1}{\alpha+1} \right)^{1-\frac{1}{r}} \\
& \quad \left. \cdot (\Omega_3^1 |f'(b)|^r + \Omega_4^1 |f'(a)|^r)^{\frac{1}{r}} \right\} .
\end{aligned}$$

**H.** If we choose  $\lambda = 0$  and  $\mu = 1$  in Corollary 2.7, we obtain

$$\begin{aligned}
& \left| f\left(\frac{ma+b}{2}\right) - \frac{\Gamma(\alpha+1)}{(b-ma)^\alpha} \left\{ \mathcal{J}_{\left(\frac{ma+b}{2}\right)^+}^\alpha f(b) + \mathcal{J}_{\left(\frac{ma+b}{2}\right)^-}^\alpha f(a) \right\} \right| \\
& \leq (b-ma) \\
& \quad \cdot \left\{ \left( \frac{1}{\alpha+1} \right)^{1-\frac{1}{r}} \cdot \left[ \frac{1}{2^{s+\alpha+1}(s+\alpha+1)} |f'(b)|^r + m B_{\frac{1}{2}}(\alpha+1, s+1) |f'(ma)|^r \right]^{\frac{1}{r}} \right. \\
& \quad + \left( \frac{3\alpha}{\alpha+1} - \frac{3}{2} + \frac{1}{2^{\alpha+1}(\alpha+1)} \right)^{1-\frac{1}{r}} \\
& \quad \cdot \left[ \left( \frac{\alpha}{(s+1)(s+\alpha+1)} - \frac{1}{2^{s+1}(s+1)} + \frac{1}{2^{s+\alpha+1}(s+\alpha+1)} \right) |f'(b)|^r \right. \\
& \quad \left. \left. + m \left( \frac{1}{2^{s+1}(s+1)} - B(\alpha+1, s+1) + B_{\frac{1}{2}}(\alpha+1, s+1) \right) |f'(ma)|^r \right]^{\frac{1}{r}} \right\} .
\end{aligned}$$

**I.** If we take  $\lambda = \frac{1}{6}$ ,  $\mu = \frac{5}{6}$  and  $m = 1$  in Corollary 2.10, we have

$$\begin{aligned}
& \left| \frac{1}{6}f(a) + \frac{4}{6}f\left(\frac{a+b}{2}\right) + \frac{1}{6}f(b) - \frac{\Gamma(\alpha+1)}{(b-a)^\alpha} \left\{ \mathcal{J}_{\left(\frac{a+b}{2}\right)^+}^\alpha f(b) + \mathcal{J}_{\left(\frac{a+b}{2}\right)^-}^\alpha f(a) \right\} \right| \\
& \leq (b-a) \\
& \quad \cdot \left\{ \left( \int_0^{\frac{1}{2}} \left| t^\alpha - \frac{1}{6} \right|^q dt \right)^{\frac{1}{q}} \left( \frac{1}{(s+1)2^{s+1}} |f'(b)|^r \right. \right. \\
& \quad \left. \left. + m \frac{2^{s+1}-1}{(s+1)2^{s+1}} |f'(a)|^r \right)^{\frac{1}{r}} + \left( \int_{\frac{1}{2}}^1 \left| t^\alpha - \frac{5}{6} \right|^q dt \right)^{\frac{1}{q}} \right. \\
& \quad \left. \cdot \left( \frac{2^{s+1}-1}{(s+1)2^{s+1}} |f'(b)|^r + m \frac{1}{(s+1)2^{s+1}} |f'(a)|^r \right)^{\frac{1}{r}} \right\}.
\end{aligned}$$

**J.** If we choose  $\lambda = \frac{1}{2}$ ,  $\mu = \frac{1}{2}$  and  $m = 1$  in Corollary 2.10, we get

$$\begin{aligned}
& \left| \frac{1}{2}f(a) + \frac{1}{2}f(b) - \frac{\Gamma(\alpha+1)}{(b-a)^\alpha} \left\{ \mathcal{J}_{\left(\frac{a+b}{2}\right)^+}^\alpha f(b) + \mathcal{J}_{\left(\frac{a+b}{2}\right)^-}^\alpha f(a) \right\} \right| \\
& \leq (b-a) \left\{ \left( \int_0^{\frac{1}{2}} \left| t^\alpha - \frac{1}{2} \right|^q dt \right)^{\frac{1}{q}} \right. \\
& \quad \cdot \left( \frac{1}{(s+1)2^{s+1}} |f'(b)|^r + \frac{2^{s+1}-1}{(s+1)2^{s+1}} |f'(a)|^r \right)^{\frac{1}{r}} \\
& \quad \left. + \left( \int_{\frac{1}{2}}^1 \left| t^\alpha - \frac{1}{2} \right|^q dt \right)^{\frac{1}{q}} \right. \\
& \quad \left. \cdot \left( \frac{2^{s+1}-1}{(s+1)2^{s+1}} |f'(b)|^r + \frac{1}{(s+1)2^{s+1}} |f'(a)|^r \right)^{\frac{1}{r}} \right\}.
\end{aligned}$$

**K.** If we take  $\lambda=0$  and  $\mu=1$  in Corollary 2.10, we obtain

$$\begin{aligned}
& \left| f\left(\frac{ma+b}{2}\right) - \frac{\Gamma(\alpha+1)}{(b-ma)^\alpha} \left\{ \mathcal{J}_{\left(\frac{ma+b}{2}\right)^+}^\alpha f(b) + \mathcal{J}_{\left(\frac{ma+b}{2}\right)^-}^\alpha f(a) \right\} \right| \\
& \leq (b-ma) \left\{ \left( \frac{1}{\alpha+q+1} \right)^{\frac{1}{q}} \right. \\
& \quad \cdot \left( \frac{1}{(s+1)2^{s+1}} |f'(b)|^r + m \frac{2^{s+1}-1}{(s+1)2^{s+1}} |f'(a)|^r \right)^{\frac{1}{r}} + \left( \int_{\frac{1}{2}}^1 |t^\alpha - 1|^q dt \right)^{\frac{1}{q}} \\
& \quad \cdot \left( \frac{2^{s+1}-1}{(s+1)2^{s+1}} |f'(b)|^r + m \frac{1}{(s+1)2^{s+1}} |f'(a)|^r \right)^{\frac{1}{r}} \Big\}.
\end{aligned}$$

#### 4. APPLICATIONS

Consider the following special means for different positive real numbers  $a < b$ :

- Arithmetic mean:  $A(a, b) := \frac{a+b}{2}$ ;
- The  $k$ -generalized log-mean:  $L_k(a, b) := \left[ \frac{b^{k+1} - a^{k+1}}{(k+1)(b-a)} \right]^{\frac{1}{k}}$ ,  $k \in \mathbb{R} \setminus \{-1, 0\}$ .

**Proposition 4.1.** Let  $0 < a < b$  and  $s \in (0, 1]$ , then

$$|2A(a^s, b^s) + 4A^s(a, b) - 6L_s^s(a, b)| \leq s(b-a)[a^{s-1}\mathcal{M} + b^{s-1}\aleph], \quad (25)$$

where

$$\mathcal{M} := \frac{30}{2^{s+1}(s+1)(s+2)} + \frac{s-4}{(s+1)(s+2)} + \frac{9 \cdot 5^{s+1} + 10s + 21}{3 \cdot 6^s(s+1)(s+2)}$$

and

$$\aleph := \frac{5^{s+2} + 1}{3 \cdot 6^s(s+1)(s+2)} + \frac{2^{s+1}(s-4) - 6}{2^{s+1}(s+1)(s+2)}.$$

**Proof.** Taking  $f(x) = x^s$  for  $x > 0$ ,  $s \in (0, 1]$ ,  $0 < a < b$  in Corollary 2.3 with  $\lambda = \frac{1}{6}$ ,  $\mu = \frac{5}{6}$ ,  $\alpha = 1$  and  $m = 1$ , we obtain the desired result.

**Proposition 4.2.** Let  $0 < a < b$ ,  $s \in (0, 1]$ , then

$$\begin{aligned} & |A(a^s, b^s) - L_s^s(a, b)| \\ & \leq s(b-a) \left[ a^{s-1} \left( \frac{1}{s+2} - \frac{1}{s+1} - \frac{s+2}{2^{s+1}(s+1)(s+2)} \right) \right. \\ & \quad \left. + b^{s-1} \left( \frac{2}{2^{s+1}(s+1)(s+2)} + \frac{s}{2(s+1)(s+2)} \right) \right]. \end{aligned} \quad (26)$$

**Proof.** Choosing  $f(x) = x^s$  for  $x > 0$ ,  $s \in (0, 1]$ ,  $0 < a < b$  in Corollary 2.3 with  $\lambda = \frac{1}{2}$ ,  $\mu = \frac{1}{2}$ ,  $\alpha = 1$  and  $m = 1$ , we deduce the desired result.

**Proposition 4.3.** Let  $0 < a < b$ ,  $s \in (0, 1]$ , then

$$\begin{aligned} & |A^s(a, b) - L_s^s(a, b)| \\ & \leq s(b-a) \left[ a^{s-1} \left( \frac{s+1}{2^{s+2}(s+1)(s+2)} \right) + b^{s-1} \left( \frac{2^{s+1} - 1}{2^{s+1}(s+1)(s+2)} \right) \right]. \end{aligned} \quad (27)$$

**Proof.** Taking  $f(x) = x^s$  for  $x > 0$ ,  $s \in (0, 1]$ ,  $0 < a < b$  in Corollary 2.3 with  $\lambda = 0$ ,  $\mu = 1$ ,  $\alpha = 1$  and  $m = 1$ , we get the desired result.

**Proposition 4.4.** Let  $0 < a < b$ ,  $s \in (0, 1]$  and  $r \geq 1$ , then

$$\begin{aligned}
& |2A(a^s, b^s) + 4A^s(a, b) - 6L_s^s(a, b)| \\
& \leq s(b-a) \\
& \cdot \left\{ \left( \frac{13}{6} \right)^{1-\frac{1}{r}} \left( \frac{1}{(s+1)(s+2)} \left[ \frac{2}{6^{s+1}} + \frac{2s+1}{2^{s+1}} \right] b^{(s-1)r} \right. \right. \\
& + \left[ \frac{s-4}{(s+1)(s+2)} - \frac{2s+7}{2^{s+1}(s+1)(s+2)} + \frac{2 \cdot 5^{s+2}}{(s+1)(s+2)6^{s+1}} \right] a^{(s-1)r} \Big)^{\frac{1}{r}} \\
& + \left( \frac{55}{12} \right)^{1-\frac{1}{r}} \left( \left[ \frac{2 \cdot 5^{s+2}}{6^{s+1}(s+1)(s+2)} - \frac{2s+7}{2^{s+1}(s+1)(s+2)} \right. \right. \\
& + \left. \left. \frac{s-4}{(s+1)(s+2)} \right] b^{(s-1)r} + \frac{1}{(s+1)(s+2)} \left[ \frac{2}{6^{s+1}} + \frac{2s+1}{2^{s+1}} \right] a^{(s-1)r} \right)^{\frac{1}{r}} \Big\}.
\end{aligned} \tag{28}$$

**Proof.** Choosing  $f(x) = x^s$  for  $x > 0$ ,  $s \in (0, 1]$ ,  $0 < a < b$  in Corollary 2.7 with  $\lambda = \frac{1}{6}$ ,  $\mu = \frac{5}{6}$ ,  $\alpha = 1$  and  $m = 1$ , we have the desired result.

**Proposition 4.5.** Let  $0 < a < b$ ,  $s \in (0, 1]$  and  $r \geq 1$ , then

$$\begin{aligned}
& |A(a^s, b^s) - L_s^s(a, b)| \\
& \leq s(b-a) \\
& \cdot \left\{ \left( \frac{1}{4} \right)^{1-\frac{1}{r}} \left( \frac{1}{2^{s+2}(s+1)(s+2)} b^{(s-1)r} + \frac{1+s2^{s+1}}{2^{s+2}(s+1)(s+2)} a^{(s-1)r} \right)^{\frac{1}{r}} \right. \\
& + \left. \left( \frac{1}{8} \right)^{1-\frac{1}{r}} \left( \frac{1+s2^{s+1}}{2^{s+2}(s+1)(s+2)} b^{(s-1)r} + \frac{1}{2^{s+2}(s+1)(s+2)} a^{(s-1)r} \right)^{\frac{1}{r}} \right\}.
\end{aligned} \tag{29}$$

**Proof.** Taking  $f(x) = x^s$  for  $x > 0$ ,  $s \in (0, 1]$ ,  $0 < a < b$  in Corollary 2.7 with  $\lambda = \frac{1}{2}$ ,  $\mu = \frac{1}{2}$ ,  $\alpha = 1$  and  $m = 1$ , we obtain the desired result.

**Proposition 4.6.** Let  $0 < a < b$ ,  $s \in (0, 1]$  and  $r \geq 1$ , then

$$\begin{aligned}
& |A^s(a, b) - L_s^s(a, b)| \\
& \leq s(b-a) \\
& \cdot \left\{ \left( \frac{1}{2} \right)^{1-\frac{1}{r}} \left( \frac{1}{2^{s+2}(s+2)} b^{(s-1)r} + \frac{2^{s+2} - s - 3}{2^{s+2}(s+1)(s+2)} a^{(s-1)r} \right)^{\frac{1}{r}} \right. \\
& + \left. \left( \frac{1}{8} \right)^{1-\frac{1}{r}} \left( \frac{2^{s+2} - s - 3}{2^{s+2}(s+1)(s+2)} b^{(s-1)r} + \frac{1}{2^{s+2}(s+2)} a^{(s-1)r} \right)^{\frac{1}{r}} \right\}.
\end{aligned} \tag{30}$$

**Proof.** Choosing  $f(x) = x^s$  for  $x > 0$ ,  $s \in (0, 1]$ ,  $0 < a < b$  in Corollary 2.7 with  $\lambda = 0$ ,  $\mu = 1$ ,  $\alpha = 1$  and  $m = 1$ , we get the desired result.

## 5. CONCLUSIONS

In this paper, we derived a new integral identity for differentiable functions with two parameters involving generalized fractional integral operators. Using this as an auxiliary result, we deduced several new Simpson type inequalities for  $(s, m)$ -differentiable convex functions and several special cases are found for suitable choices of uniformly convex functions, and many known results are recaptured. To validate the accuracy of our main results, we offer some nice examples using special means for positive real numbers. Our results can be extended and refined in quantum and post-quantum calculus, and can open many avenues for interested researchers working in this field. Moreover, they can discover further approximations and error quadrature formulas for different kinds of fractional integral operators and convex functions.

## REFERENCES

1. Hudzik, H., Maligranda, L. 1994. Some remarks on  $s$ -convex functions, *Aequ. Math.*, 48, 100-111.
2. Pavić, Z.; Ardic, M.A. 2017. The most important inequalities for  $m$ -convex functions. *Turk. J. Math.*, 41, 625–635.
3. Vivas-Cortez, M.J.; Kashuri, A.; Liko, R.; Hernández, J.E.H. 2019. Some Inequalities Using Generalized Convex Functions in Quantum Analysis. *Symmetry*, 11, 1402. <https://doi.org/10.3390/sym11111402>
4. Bakula, M.K.; Pečarić, J.; Ribarić, M. Companion Inequalities to Jensen's Inequality for  $m$ -convex and  $(s, m)$ -Convex Functions. *J. Ineq. Pure Appl. Math.* 2006, 7, 194.
5. Eftekhari, N. Some Remarks on  $(s, m)$ -convexity in the second sense. *J. Math. Ineq.* 2014, 8, 489–495.
6. Sarikaya, M. Z., Ertuğral, F. 2020. On the generalized Hermite-Hadamard inequalities, *Annals of the University of Craiova, Mathematics and Computer Science Series*, 47, 193-213.
7. Alomari, M., Darus, M. and Dragomir, S.S., 2009. New inequalities of Simpson's type for  $s$ -convex functions with applications. *Research report collection*, 12(4).
8. Alomari MO, Darus MA. On some inequalities of Simpson-type via quasi-convex functions and applications. *Transylvanian Journal of Mathematics and Mechanics*. 2010 Mar 9;2(1):15-24.
9. Kashuri A, Meftah B, Mohammed PO. Some weighted Simpson type inequalities for differentiable  $s$ -convex functions and their applications: Some weighted Simpson type inequalities. *Journal of Fractional Calculus and Nonlinear Systems*. 2020;1(1):75-94.
10. Tunç M, Göv E, Balgeçti S. Simpson type quantum integral inequalities for convex functions. *Miskolc Math. Notes*. 2018 Jan 1;19(1):649-64.



11. Budak, H., Erden, S. and Ali, M.A., 2021. Simpson and Newton type inequalities for convex functions via newly defined quantum integrals. *Mathematical Methods in the Applied Sciences*, 44(1), pp.378-390.
12. Matłoka, M., 2017. Weighted Simpson type inequalities for h-convex functions. *J. Nonlinear Sci. Appl*, 10(11), pp.5770-5780.
13. Hasan Kara, Hüseyin Budak, Muhammad Aamir Ali, Fatih Hezenci, On inequalities of Simpson's type for convex functions via generalized fractional integrals, *Communications*, Vol:71, No:3, 806-825, 2022.
14. Xuexiao You, Muhammad Aamir Ali, Hüseyin Budak, Hasan Kara, Dafang Zhao, Some parameterized Simpson's type inequalities for differentiable convex functions involving generalized fractional integrals, *Advances in Continuous and Discrete Models*, Vol:2022, No:22, 1–23, 2022.
15. Tingsong Du, Yujiao Li, Zhiqiao Yang, A generalization of Simpson's inequality via differentiable mapping using extended (s,m)-convex functions, *Applied Mathematics and Computation*, Vol:293, 359–369, 2017.

# SOME NEW TEMPERED FRACTIONAL HERMITE-HADAMARD TYPE INEQUALITIES VIA UNIFORMLY CONVEX FUNCTIONS

Artion Kashuri<sup>1</sup>, Rozana Liko<sup>1</sup>

<sup>1</sup> Department of Mathematics, Faculty of Technical and Natural Sciences,  
University Ismail Qemali, 9400 Vlora, Albania

[artion.kashuri@univlora.edu.al](mailto:artion.kashuri@univlora.edu.al), [rozana.liko@univlora.edu.al](mailto:rozana.liko@univlora.edu.al)

## Abstract

In this paper, we obtain some new tempered fractional Hermite-Hadamard type inequalities for uniformly convex functions. Moreover, using a new identity as an auxiliary result, we deduce several inequalities for uniformly convex functions pertaining to tempered fractional integrals, and some special cases are given as well. To validate the accuracy of our main results, we offer some nice examples.

**Keywords:** Hermite-Hadamard inequalities; Uniformly convex functions; Tempered fractional integral operators; Hölder's inequality; Power-mean inequality.

## 1. INTRODUCTION

One effective technique that is primarily utilised to address several challenges in both pure and applied research is the convexity of functions. There are several important properties of symmetric convex sets. The Hermite-Hadamard inequality (H-H), one of the most significant mathematical inequality linked to convex function, is what follows and is often utilised in many other branches of computer mathematics.

**Theorem 1.1.** [1]: Suppose that  $f: I \subseteq \mathbb{R} \rightarrow \mathbb{R}$  is a convex function and  $a, b \in I$  with  $a \neq b$ , then

$$f\left(\frac{a+b}{2}\right) \leq \frac{1}{b-a} \int_a^b f(t) dt \leq \frac{f(a) + f(b)}{2}.$$

Due to the significance of this inequality, over the past ten years, numerous types of convexity, such as harmonically convex, exponentially convex, co-ordinated convex functions, etc., have been explored in the literature along with versions of the H-H inequality. In addition, numerous authors have helped this subject advance by using the discovered kernels and identities, see [2-13] and the references therein.

The following definitions can be found in [14-16].

**Definition 1.1.** Let  $f: I \subseteq \mathbb{R} \rightarrow \mathbb{R}$  be a function. Then  $f$  is called uniformly convex with modulus  $\psi: [0, +\infty[ \rightarrow [0, +\infty[$  if  $\psi$  is increasing,  $\psi$  vanishes only at 0, and

$$f(tx + (1-t)y) + t(1-t)\psi(|x-y|) \leq tf(x) + (1-t)f(y), \quad (1.1)$$

for each  $x, y \in \mathbb{R}$  and  $t \in [0, 1]$ .

If we take  $\psi(t) \equiv 0$  in (1.1), then we get the well-known definition of convex function.

In the following we give a simple example of a uniformly convex function ([14], Corollary 2.14).

**Example 1.1.** The function  $f(t) = t^2$  is uniformly convex with modulus  $\psi(t) = t^2$  for all  $t \geq 0$ .

For further recently published papers about uniformly convexity property, see [17-20].

Fractional calculus has emerged as one of the most important interdisciplinary subjects. In recent past it experienced rapid development and consequently several new generalizations of classical concepts of fractional calculus have been obtained in the literature, see [15,21].

The classical Riemann-Liouville fractional integrals are defined as follows.

**Definition 1.2.** [15,21]: Let  $f \in L[a, b]$  (the set of all Lebesgue integrable functions on  $[a, b]$ ). Then the Riemann-Liouville integrals  $J_{a+}^{\alpha}f$  and  $J_{b-}^{\alpha}f$  of order  $\alpha > 0$  with  $a \geq 0$  are defined by

$$J_{a+}^{\alpha}f(x) := \frac{1}{\Gamma(\alpha)} \int_a^x (x-t)^{\alpha-1} f(t) dt, \quad x > a$$

and

$$J_{b-}^{\alpha}f(x) := \frac{1}{\Gamma(\alpha)} \int_x^b (t-x)^{\alpha-1} f(t) dt, \quad x < b,$$

where

$$\Gamma(x) := \int_0^{\infty} e^{-t} t^{x-1} dt,$$

is the well-known gamma function.

Fractional analogues of integral inequalities have a great many applications in numerical quadrature, transform theory, probability, statistical problems etc. Therefore, a significant and rapid development in this field has been noticed, see [22-27].

Fractional calculus is currently concerned with the study of so-called fractional order integral and derivative functions over real and complex domains, as well as its applications. The findings drawn from fractional mathematical models are more conclusive and accurate than those drawn from classical mathematical models because they are particular examples of fractional order mathematical models. To describe the specific transmission patterns of the

endemics and comprehend how infection impacts a new population, various mathematical models are applied, see [28-36]. In recent years, mathematicians have become more and more interested in using a variety of cutting-edge theories of fractional integral operators to demonstrate well-known inequalities.

Let's sum up by reviewing the definition of tempered fractional integral operators that will be utilised in the continuation.

**Definition 1.3.** [21]: Let  $f \in L[a, b]$ , where  $0 \leq a < b$ . Then for  $\lambda \geq 0$ , the tempered fractional integral operators  $I_{a+}^{\alpha, \lambda} f$  and  $I_{b-}^{\alpha, \lambda} f$  of order  $\alpha > 0$  are defined as

$$I_{a+}^{\alpha, \lambda} f(x) := \frac{1}{\Gamma(\alpha)} \int_a^x (x-t)^{\alpha-1} e^{-\lambda(x-t)} f(t) dt, \quad x > a$$

and

$$I_{b-}^{\alpha, \lambda} f(x) := \frac{1}{\Gamma(\alpha)} \int_x^b (t-x)^{\alpha-1} e^{-\lambda(t-x)} f(t) dt, \quad x < b,$$

respectively.

**Definition 1.4.** For any real number  $\alpha > 0$  and  $x, \lambda \geq 0$ , the  $\lambda$ -incomplete gamma function is defined as

$$\gamma_\lambda(\alpha, x) := \int_0^x t^{\alpha-1} e^{-\lambda t} dt.$$

From Definition 1.4, we obtain the following relation

$$\gamma_{\lambda(b-a)}(\alpha, 1) = \frac{\gamma_\lambda(\alpha, b-a)}{(b-a)^\alpha}.$$

Our final paper is organised as follows: For uniformly convex functions, we will find new tempered fractional integral H-H type inequalities and some known results will be recaptured as special cases of our result in Section 2. We will derive many inequalities for uniformly convex functions relevant to tempered fractional integrals in Section 3 utilising a new identity as an auxiliary result and the well-known Hölder and power-mean inequalities. In Section 4, we provide several nice examples for appropriate selections of uniformly convex functions to verify the veracity of our results. In Section 5, the conclusions and recommendations for further study will be provided.

## 2. MAIN RESULTS

The tempered fractional H-H type inequalities for uniformly convex functions are given as follows:

**Theorem 2.1.** Let  $f: I \subseteq \mathbb{R} \rightarrow [0, +\infty[$  be uniformly convex function with modulus  $\psi$ , where  $0 \leq a < b$ . Then for  $\alpha > 0$  and  $\lambda \geq 0$ , the following inequalities hold true:

$$f\left(\frac{a+b}{2}\right) + \frac{1}{2^{\alpha+2}\gamma_\lambda(\alpha, b-a)}\Theta(\alpha, \lambda; \psi) \leq \frac{\Gamma(\alpha)}{2\gamma_\lambda(\alpha, b-a)}[I_{a^+}^{\alpha, \lambda}f(b) + I_{b^-}^{\alpha, \lambda}f(a)]$$

$$\leq \frac{\gamma_\lambda(\alpha, b-a)}{(b-a)^\alpha} \left( \frac{f(a) + f(b)}{2} \right) + \left[ \frac{\gamma_\lambda(\alpha+2, b-a)}{(b-a)^{\alpha+2}} - \frac{\gamma_\lambda(\alpha+1, b-a)}{(b-a)^{\alpha+1}} \right] \psi(|a-b|), \quad (2.1)$$

where

$$\Theta(\alpha, \lambda; \psi) := \int_{a-b}^{b-a} (b-a-t)^{\alpha-1} e^{-\frac{\lambda}{2}(b-a-t)} \psi(|t|) dt.$$

**Proof.** Taking  $t = \frac{1}{2}$  in (1.1), we have

$$f\left(\frac{x+y}{2}\right) + \frac{1}{4}\psi(|x-y|) \leq \frac{f(x) + f(y)}{2}. \quad (2.2)$$

Now in (2.2), set  $x = ta + (1-t)b$  and  $y = (1-t)a + tb$ , we get

$$f\left(\frac{a+b}{2}\right) + \frac{1}{4}\psi(|(2t-1)(a-b)|) \leq \frac{f(ta + (1-t)b) + f((1-t)a + tb)}{2}. \quad (2.3)$$

Multiplying (2.3) on both sides with  $t^{\alpha-1}e^{-\lambda(b-a)t}$  and integrating on  $[0, 1]$  with respect to  $t$ , we obtain

$$f\left(\frac{a+b}{2}\right) \int_0^1 t^{\alpha-1} e^{-\lambda(b-a)t} dt + \frac{1}{4} \int_0^1 t^{\alpha-1} e^{-\lambda(b-a)t} \psi(|(2t-1)(a-b)|) dt$$

$$\leq \frac{1}{2} \left[ \int_0^1 t^{\alpha-1} e^{-\lambda(b-a)t} f(ta + (1-t)b) dt + \int_0^1 t^{\alpha-1} e^{-\lambda(b-a)t} f((1-t)a + tb) dt \right].$$

From easy calculations, we deduce

$$f\left(\frac{a+b}{2}\right) + \frac{1}{2^{\alpha+2}\gamma_\lambda(\alpha, b-a)}\Theta(\alpha, \lambda; \psi) \leq \frac{\Gamma(\alpha)}{2\gamma_\lambda(\alpha, b-a)}[I_{a^+}^{\alpha, \lambda}f(b) + I_{b^-}^{\alpha, \lambda}f(a)],$$

which is the left hand side of (2.1). In order to prove the right hand side of (2.1), since  $f$  be uniformly convex function with modulus  $\psi$ , we have

$$f(tx + (1-t)y) + t(1-t)\psi(|x-y|) \leq tf(x) + (1-t)f(y),$$

$$f(ty + (1-t)x) + t(1-t)\psi(|x-y|) \leq tf(y) + (1-t)f(x).$$

Adding above inequalities, we get

$$f(tx + (1-t)y) + f(ty + (1-t)x) + 2t(1-t)\psi(|x-y|) \leq f(x) + f(y). \quad (2.4)$$

Putting  $x = a$  and  $y = b$  in (2.4), we obtain

$$f(ta + (1-t)b) + f(tb + (1-t)a) + 2t(1-t)\psi(|a-b|) \leq f(a) + f(b). \quad (2.5)$$

Multiplying (2.5) on both sides with  $\frac{1}{2}t^{\alpha-1}e^{-\lambda(b-a)t}$  and integrating on  $[0, 1]$  with respect to  $t$ , we have

$$\begin{aligned} \frac{1}{2} \left[ \int_0^1 t^{\alpha-1} e^{-\lambda(b-a)t} f(ta + (1-t)b) dt + \int_0^1 t^{\alpha-1} e^{-\lambda(b-a)t} f(tb + (1-t)a) dt \right] \\ + \int_0^1 t^{\alpha-1} e^{-\lambda(b-a)t} t(1-t) \psi(|a-b|) dt \leq \left( \frac{f(a) + f(b)}{2} \right) \int_0^1 t^{\alpha-1} e^{-\lambda(b-a)t} dt. \end{aligned}$$

From easy calculations, we get

$$\begin{aligned} & \frac{\Gamma(\alpha)}{2\gamma_\lambda(\alpha, b-a)} [I_{a^+}^{\alpha, \lambda} f(b) + I_{b^-}^{\alpha, \lambda} f(a)] \\ & \leq \frac{\gamma_\lambda(\alpha, b-a)}{(b-a)^\alpha} \left( \frac{f(a) + f(b)}{2} \right) + \left[ \frac{\gamma_\lambda(\alpha+2, b-a)}{(b-a)^{\alpha+2}} - \frac{\gamma_\lambda(\alpha+1, b-a)}{(b-a)^{\alpha+1}} \right] \psi(|a-b|), \end{aligned}$$

which is the right hand side of (2.1). The proof of Theorem 2.1 is completed. ■

**Corollary 2.1.** Taking  $\alpha = 1$  and  $\lambda = 0$  in Theorem 2.1, we have

$$f\left(\frac{a+b}{2}\right) + \frac{1}{8(b-a)} \int_{a-b}^{b-a} \psi(|t|) dt \leq \frac{1}{b-a} \int_a^b f(t) dt \leq \frac{f(a) + f(b)}{2} - \frac{1}{6} \psi(|a-b|),$$

which is established by Barsam *et al.* in ([17], Theorem 2). ■

**Corollary 2.2.** Choosing  $\lambda = 0$  in Theorem 2.1, we get

$$\begin{aligned} f\left(\frac{a+b}{2}\right) + \frac{\Gamma(\alpha+1)}{2^{\alpha+2}(b-a)^\alpha} J_{(a-b)^+}^\alpha \psi(|a-b|) \leq \frac{\Gamma(\alpha+1)}{2(b-a)^\alpha} [J_{a^+}^\alpha f(b) + J_{b^-}^\alpha f(a)] \\ \leq \frac{f(a) + f(b)}{2} - \alpha\beta(\alpha+1, 2) \psi(|a-b|), \end{aligned}$$

which is obtained by Barsam *et al.* in ([17], Theorem 8). ■

### 3. FURTHER RESULTS

Before we start this section, we will prove the following lemma which will be used in the remaining paper.

**Lemma 3.1.** Let  $f: I \subseteq \mathbb{R} \rightarrow [0, +\infty[$  be a differentiable continuous function with  $0 \leq a < b$ . Then for  $\alpha > 0$  and  $\lambda \geq 0$ , the following tempered fractional integral equality holds true:

$$\frac{f(a) + f(b)}{2} - \frac{2^{\alpha-1}\Gamma(\alpha)}{\gamma_\lambda(\alpha, b-a)} \left[ I_{a^+}^{\alpha, 2\lambda} f\left(\frac{a+b}{2}\right) + I_{b^-}^{\alpha, 2\lambda} f\left(\frac{a+b}{2}\right) \right] = \frac{(b-a)^{\alpha+1}}{4\gamma_\lambda(\alpha, b-a)}$$

$$\times \int_0^1 \gamma_{\lambda(b-a)}(\alpha, t) \left[ f' \left( a + \frac{1+t}{2} (b-a) \right) - f' \left( a + \frac{1-t}{2} (b-a) \right) \right] dt. \quad (3.1)$$

**Proof.** Let us denote, respectively

$$I_1 := \int_0^1 \gamma_{\lambda(b-a)}(\alpha, t) f' \left( a + \frac{1+t}{2} (b-a) \right) dt,$$

$$I_2 := \int_0^1 \gamma_{\lambda(b-a)}(\alpha, t) f' \left( a + \frac{1-t}{2} (b-a) \right) dt.$$

Then, we have

$$\int_0^1 \gamma_{\lambda(b-a)}(\alpha, t) \left[ f' \left( a + \frac{1+t}{2} (b-a) \right) - f' \left( a + \frac{1-t}{2} (b-a) \right) \right] dt = I_1 - I_2. \quad (3.2)$$

Using integration by parts and changing the variable, we get

$$\begin{aligned} I_1 &= \frac{2}{b-a} \gamma_{\lambda(b-a)}(\alpha, t) f \left( a + \frac{1+t}{2} (b-a) \right) \Big|_0^1 \\ &\quad - \frac{2}{b-a} \int_0^1 t^{\alpha-1} e^{-\lambda(b-a)t} f \left( a + \frac{1+t}{2} (b-a) \right) dt \\ &= \frac{2}{b-a} \gamma_{\lambda(b-a)}(\alpha, 1) f(b) - \left( \frac{2}{b-a} \right)^{\alpha+1} \int_{\frac{a+b}{2}}^b \left( t - \frac{a+b}{2} \right)^{\alpha-1} e^{-2\lambda \left( t - \frac{a+b}{2} \right)} f(t) dt \\ &= \frac{2}{b-a} \gamma_{\lambda(b-a)}(\alpha, 1) f(b) - \left( \frac{2}{b-a} \right)^{\alpha+1} \Gamma(\alpha) I_{b^-}^{\alpha, 2\lambda} f \left( \frac{a+b}{2} \right). \end{aligned}$$

Similarly,

$$I_2 = -\frac{2}{b-a} \gamma_{\lambda(b-a)}(\alpha, 1) f(a) + \left( \frac{2}{b-a} \right)^{\alpha+1} \Gamma(\alpha) I_{a^+}^{\alpha, 2\lambda} f \left( \frac{a+b}{2} \right).$$

Using the following relation

$$\gamma_{\lambda(b-a)}(\alpha, 1) = \frac{\gamma_{\lambda}(\alpha, b-a)}{(b-a)^{\alpha}},$$

and multiplying both sides of (3.2) with  $\frac{(b-a)^{\alpha+1}}{4\gamma_{\lambda}(\alpha, b-a)}$ , we obtain the desired result (3.1). ■

**Theorem 3.1.** Let  $f: I \subseteq \mathbb{R} \rightarrow [0, +\infty[$  be a differentiable continuous function. If  $|f'|^q$  is uniformly convex function with modulus  $\psi$ , where  $0 \leq a < b$  with  $p > 1$  and  $\frac{1}{p} + \frac{1}{q} = 1$ , then for  $\alpha > 0$  and  $\lambda \geq 0$ , the following tempered fractional integral inequality holds true:

$$\left| \frac{f(a) + f(b)}{2} - \frac{2^{\alpha-1}\Gamma(\alpha)}{\gamma_\lambda(\alpha, b-a)} \left[ I_{a^+}^{\alpha, 2\lambda} f\left(\frac{a+b}{2}\right) + I_{b^-}^{\alpha, 2\lambda} f\left(\frac{a+b}{2}\right) \right] \right| \leq \frac{(b-a)^{\alpha+1}}{4\gamma_\lambda(\alpha, b-a)} C^{\frac{1}{p}}(\gamma, p) \quad (3.3)$$

$$\times \left\{ \left[ \frac{1}{4} |f'(a)|^q + \frac{3}{4} |f'(b)|^q - \frac{1}{6} \psi(|a-b|) \right]^{\frac{1}{q}} + \left[ \frac{3}{4} |f'(a)|^q + \frac{1}{4} |f'(b)|^q - \frac{1}{6} \psi(|a-b|) \right]^{\frac{1}{q}} \right\},$$

where

$$C(\gamma, p) := \int_0^1 [\gamma_{\lambda(b-a)}(\alpha, t)]^p dt.$$

**Proof.** By using Lemma 3.1, Hölder's inequality, uniformly convexity of  $|f'|^q$  and properties of modulus, we have

$$\begin{aligned} & \left| \frac{f(a) + f(b)}{2} - \frac{2^{\alpha-1}\Gamma(\alpha)}{\gamma_\lambda(\alpha, b-a)} \left[ I_{a^+}^{\alpha, 2\lambda} f\left(\frac{a+b}{2}\right) + I_{b^-}^{\alpha, 2\lambda} f\left(\frac{a+b}{2}\right) \right] \right| \leq \frac{(b-a)^{\alpha+1}}{4\gamma_\lambda(\alpha, b-a)} \\ & \times \int_0^1 |\gamma_{\lambda(b-a)}(\alpha, t)| \left[ \left| f'\left(a + \frac{1+t}{2}(b-a)\right) \right| + \left| f'\left(a + \frac{1-t}{2}(b-a)\right) \right| \right] dt \\ & \leq \frac{(b-a)^{\alpha+1}}{4\gamma_\lambda(\alpha, b-a)} \left( \int_0^1 [\gamma_{\lambda(b-a)}(\alpha, t)]^p dt \right)^{\frac{1}{p}} \\ & \times \left( \int_0^1 \left| f'\left(a + \frac{1+t}{2}(b-a)\right) \right|^q dt \right)^{\frac{1}{q}} + \left( \int_0^1 \left| f'\left(a + \frac{1-t}{2}(b-a)\right) \right|^q dt \right)^{\frac{1}{q}} \\ & \leq \frac{(b-a)^{\alpha+1}}{4\gamma_\lambda(\alpha, b-a)} C^{\frac{1}{p}}(\gamma, p) \\ & \times \left[ \int_0^1 \left( \left( \frac{1-t}{2} \right) |f'(a)|^q + \left( \frac{1+t}{2} \right) |f'(b)|^q - \frac{1}{4} (1-t^2) \psi(|a-b|) \right) dt \right]^{\frac{1}{q}} \\ & + \left[ \int_0^1 \left( \left( \frac{1+t}{2} \right) |f'(a)|^q + \left( \frac{1-t}{2} \right) |f'(b)|^q - \frac{1}{4} (1-t^2) \psi(|a-b|) \right) dt \right]^{\frac{1}{q}} \end{aligned}$$



$$= \frac{(b-a)^{\alpha+1}}{4\gamma_\lambda(\alpha, b-a)} C^{\frac{1}{p}}(\gamma, p) \\ \times \left\{ \left[ \frac{1}{4} |f'(a)|^q + \frac{3}{4} |f'(b)|^q - \frac{1}{6} \psi(|a-b|) \right]^{\frac{1}{q}} + \left[ \frac{3}{4} |f'(a)|^q + \frac{1}{4} |f'(b)|^q - \frac{1}{6} \psi(|a-b|) \right]^{\frac{1}{q}} \right\}.$$

The proof of Theorem 3.1 is completed. ■

**Corollary 3.1.** Taking  $|f'| \leq K$  in Theorem 3.1, we have

$$\left| \frac{f(a) + f(b)}{2} - \frac{2^{\alpha-1}\Gamma(\alpha)}{\gamma_\lambda(\alpha, b-a)} \left[ I_{a^+}^{\alpha, 2\lambda} f\left(\frac{a+b}{2}\right) + I_{b^-}^{\alpha, 2\lambda} f\left(\frac{a+b}{2}\right) \right] \right| \\ \leq \frac{(b-a)^{\alpha+1}}{2\gamma_\lambda(\alpha, b-a)} C^{\frac{1}{p}}(\gamma, p) \left[ K^q - \frac{1}{6} \psi(|a-b|) \right]^{\frac{1}{q}}. \quad \blacksquare$$

**Theorem 3.2.** Let  $f: I \subseteq \mathbb{R} \rightarrow [0, +\infty[$  be a differentiable continuous function. If  $|f'|^q$  is uniformly convex function with modulus  $\psi$ , where  $0 \leq a < b$  with  $q \geq 1$ , then for  $\alpha > 0$  and  $\lambda \geq 0$ , the following tempered fractional integral inequality holds true:

$$\left| \frac{f(a) + f(b)}{2} - \frac{2^{\alpha-1}\Gamma(\alpha)}{\gamma_\lambda(\alpha, b-a)} \left[ I_{a^+}^{\alpha, 2\lambda} f\left(\frac{a+b}{2}\right) + I_{b^-}^{\alpha, 2\lambda} f\left(\frac{a+b}{2}\right) \right] \right| \leq \frac{(b-a)^{\alpha+1}}{4\gamma_\lambda(\alpha, b-a)} C^{1-\frac{1}{q}}(\gamma) \quad (3.4) \\ \times \left[ \frac{1}{2} (C(\gamma) - D(\gamma)) |f'(a)|^q + \frac{1}{2} |f'(b)|^q (C(\gamma) + D(\gamma)) - \frac{1}{4} (C(\gamma) - E(\gamma)) \psi(|a-b|) \right]^{\frac{1}{q}} \\ \left( + \left[ \frac{1}{2} (C(\gamma) + D(\gamma)) |f'(a)|^q + \frac{1}{2} |f'(b)|^q (C(\gamma) - D(\gamma)) - \frac{1}{4} (C(\gamma) - E(\gamma)) \psi(|a-b|) \right]^{\frac{1}{q}} \right),$$

where

$$C(\gamma) := \int_0^1 \gamma_{\lambda(b-a)}(\alpha, t) dt = \frac{\gamma_\lambda(\alpha, b-a)}{(b-a)^\alpha} - \frac{\gamma_\lambda(\alpha+1, b-a)}{(b-a)^{\alpha+1}}$$

and

$$D(\gamma) := \int_0^1 t \gamma_{\lambda(b-a)}(\alpha, t) dt, \quad E(\gamma) := \int_0^1 t^2 \gamma_{\lambda(b-a)}(\alpha, t) dt.$$

**Proof.** By using Lemma 3.1, power-mean inequality, uniformly convexity of  $|f'|^q$  and properties of modulus, we have

$$\left| \frac{f(a) + f(b)}{2} - \frac{2^{\alpha-1}\Gamma(\alpha)}{\gamma_\lambda(\alpha, b-a)} \left[ I_{a^+}^{\alpha, 2\lambda} f\left(\frac{a+b}{2}\right) + I_{b^-}^{\alpha, 2\lambda} f\left(\frac{a+b}{2}\right) \right] \right| \leq \frac{(b-a)^{\alpha+1}}{4\gamma_\lambda(\alpha, b-a)}$$

$$\begin{aligned}
& \times \int_0^1 |\gamma_{\lambda(b-a)}(\alpha, t)| \left[ \left| f' \left( a + \frac{1+t}{2}(b-a) \right) \right| + \left| f' \left( a + \frac{1-t}{2}(b-a) \right) \right| \right] dt \\
& \leq \frac{(b-a)^{\alpha+1}}{4\gamma_{\lambda}(\alpha, b-a)} \left( \int_0^1 \gamma_{\lambda(b-a)}(\alpha, t) dt \right)^{1-\frac{1}{q}} \\
& \quad \times \left( \int_0^1 \gamma_{\lambda(b-a)}(\alpha, t) \left| f' \left( a + \frac{1+t}{2}(b-a) \right) \right|^q dt \right)^{\frac{1}{q}} \\
& \quad \left( + \int_0^1 \gamma_{\lambda(b-a)}(\alpha, t) \left| f' \left( a + \frac{1-t}{2}(b-a) \right) \right|^q dt \right)^{\frac{1}{q}} \Bigg] \\
& \leq \frac{(b-a)^{\alpha+1}}{4\gamma_{\lambda}(\alpha, b-a)} C^{1-\frac{1}{q}}(\gamma) \\
& \quad \times \left[ \int_0^1 \gamma_{\lambda(b-a)}(\alpha, t) \left( \left( \frac{1-t}{2} \right) |f'(a)|^q + \left( \frac{1+t}{2} \right) |f'(b)|^q - \frac{1}{4}(1-t^2)\psi(|a-b|) \right) dt \right]^{\frac{1}{q}} \\
& \quad \left( + \int_0^1 \gamma_{\lambda(b-a)}(\alpha, t) \left( \left( \frac{1+t}{2} \right) |f'(a)|^q + \left( \frac{1-t}{2} \right) |f'(b)|^q - \frac{1}{4}(1-t^2)\psi(|a-b|) \right) dt \right)^{\frac{1}{q}} \Bigg] \\
& = \frac{(b-a)^{\alpha+1}}{4\gamma_{\lambda}(\alpha, b-a)} C^{1-\frac{1}{q}}(\gamma) \\
& \quad \times \left[ \frac{1}{2}(C(\gamma) - D(\gamma))|f'(a)|^q + \frac{1}{2}|f'(b)|^q(C(\gamma) + D(\gamma)) - \frac{1}{4}(C(\gamma) - E(\gamma))\psi(|a-b|) \right]^{\frac{1}{q}} \\
& \quad \left( + \left[ \frac{1}{2}(C(\gamma) + D(\gamma))|f'(a)|^q + \frac{1}{2}|f'(b)|^q(C(\gamma) - D(\gamma)) - \frac{1}{4}(C(\gamma) - E(\gamma))\psi(|a-b|) \right]^{\frac{1}{q}} \right)
\end{aligned}$$

which completes the proof of Theorem 3.2.  $\blacksquare$

**Corollary 3.2.** Choosing  $|f'| \leq K$  in Theorem 3.2, we get

$$\begin{aligned}
& \left| \frac{f(a) + f(b)}{2} - \frac{2^{\alpha-1}\Gamma(\alpha)}{\gamma_{\lambda}(\alpha, b-a)} \left[ I_{a^+}^{\alpha, 2\lambda} f \left( \frac{a+b}{2} \right) + I_{b^-}^{\alpha, 2\lambda} f \left( \frac{a+b}{2} \right) \right] \right| \\
& \leq \frac{(b-a)^{\alpha+1}}{2\gamma_{\lambda}(\alpha, b-a)} C^{1-\frac{1}{q}}(\gamma) \left[ K^q C(\gamma) - \frac{1}{4}(C(\gamma) - E(\gamma))\psi(|a-b|) \right]^{\frac{1}{q}}. \quad \blacksquare
\end{aligned}$$

#### 4. APPLICATIONS TO SPECIAL MEANS

Consider the following arithmetic mean for two real numbers  $a, b$  with  $0 \leq a < b$ :

$$A = A(a, b) := \frac{a + b}{2}.$$

**Example 4.1.** Let  $a, b \in \mathbb{R}$  with  $0 \leq a < b$ , then for  $\alpha > 0$  and  $\lambda \geq 0$ , the following inequalities hold true:

$$\begin{aligned} A^2(a, b) + \frac{1}{2^{\alpha+2}\gamma_\lambda(\alpha, b-a)}\Theta(\alpha, \lambda) &\leq \frac{\Gamma(\alpha)}{2\gamma_\lambda(\alpha, b-a)}[I_{a^+}^{\alpha, \lambda} b^2 + I_{b^-}^{\alpha, \lambda} a^2] \\ &\leq \frac{\gamma_\lambda(\alpha, b-a)}{(b-a)^\alpha} A(a^2, b^2) + \left[ \frac{\gamma_\lambda(\alpha+2, b-a)}{(b-a)^{\alpha+2}} - \frac{\gamma_\lambda(\alpha+1, b-a)}{(b-a)^{\alpha+1}} \right] |a-b|^2, \end{aligned} \quad (4.1)$$

where

$$\Theta(\alpha, \lambda) := \int_{a-b}^{b-a} |t|^2 (b-a-t)^{\alpha-1} e^{-\frac{\lambda}{2}(b-a-t)} dt.$$

**Proof.** From example 1.1 and applying Theorem 2.1, we have the desired result (4.1).

**Example 4.2.** Let  $a, b \in \mathbb{R}$  with  $0 \leq a < b$ , then for  $\alpha > 0$  and  $\lambda \geq 0$ , with  $p > 1$  and  $\frac{1}{p} + \frac{1}{q} = 1$ , the following inequality holds true:

$$\begin{aligned} \left| A(a^3, b^3) - \frac{2^{\alpha-1}\Gamma(\alpha)}{\gamma_\lambda(\alpha, b-a)} [I_{a^+}^{\alpha, 2\lambda} A^3(a, b) + I_{b^-}^{\alpha, 2\lambda} A^3(a, b)] \right| &\leq \frac{3(b-a)^{\alpha+1}}{4\gamma_\lambda(\alpha, b-a)} \left( \frac{1}{2} \right)^{\frac{1}{q}} C^{\frac{1}{p}}(\gamma, p) \\ &\times \left\{ \left[ A(a^{2q}, 3b^{2q}) - \frac{1}{3}|a-b|^2 \right]^{\frac{1}{q}} + \left[ A(3a^{2q}, b^{2q}) - \frac{1}{3}|a-b|^2 \right]^{\frac{1}{q}} \right\}. \end{aligned} \quad (4.2)$$

**Proof.** By example 1.1 and applying Theorem 3.1, we get the desired result (4.2).

**Example 4.3.** Let  $a, b \in \mathbb{R}$  with  $0 \leq a < b$ , then for  $\alpha > 0$  and  $\lambda \geq 0$  with  $q \geq 1$ , the following inequality holds true:

$$\begin{aligned} \left| A(a^3, b^3) - \frac{2^{\alpha-1}\Gamma(\alpha)}{\gamma_\lambda(\alpha, b-a)} [I_{a^+}^{\alpha, 2\lambda} A^3(a, b) + I_{b^-}^{\alpha, 2\lambda} A^3(a, b)] \right| &\leq \frac{3(b-a)^{\alpha+1}}{4\gamma_\lambda(\alpha, b-a)} C^{1-\frac{1}{q}}(\gamma) \\ &\times \left\{ \left[ \frac{a^{2q}}{2} (C(\gamma) - D(\gamma)) + \frac{b^{2q}}{2} (C(\gamma) + D(\gamma)) - \frac{1}{4} (C(\gamma) - E(\gamma)) |a-b|^2 \right]^{\frac{1}{q}} \right. \\ &\left. + \left[ \frac{a^{2q}}{2} (C(\gamma) + D(\gamma)) + \frac{b^{2q}}{2} (C(\gamma) - D(\gamma)) - \frac{1}{4} (C(\gamma) - E(\gamma)) |a-b|^2 \right]^{\frac{1}{q}} \right\}. \end{aligned} \quad (4.3)$$

**Proof.** Using example 1.1 and applying Theorem 3.2, we obtain the desired result (4.3).

## 5. CONCLUSIONS

In this paper, we derived some new tempered fractional Hermite-Hadamard type inequalities for uniformly convex functions. Moreover, using a new identity as an auxiliary result, we deduced several inequalities for uniformly convex functions via tempered fractional integrals, and several special cases are found for suitable choices of uniformly convex functions, and many known results are recaptured. To validate the accuracy of our main results, we presented some examples using arithmetic mean for nonnegative real numbers. Some future aspects of this concept could be defining uniformly convex functions on the coordinates and interval-valued uniformly convex functions, and establishing new kinds of tempered fractional integral inequalities of this types. We believe that these novel concepts can also be generalized via quantum and post-quantum calculus. Our results can open many avenues for interested researchers working in this field and they can discover further approximations for different kinds of fractional integral operators and functions as well.

## REFERENCES

1. J. Hadamard, Étude sur les propriétés des fonctions entières en particulier d'une fonction considérée par Riemann, *J. Math Pures. Appl.*, Vol:58, 171-215, 1893.
2. T. S. Du, M. U. Awan, A. Kashuri, S. S. Zhao, Some  $k$ -fractional extensions of the trapezium inequalities through generalized relative semi- $(m, h)$ -preinvexity, *Appl. Anal.*, Vol:100, 642-662, 2021.
3. D. S. Marinescu, M. Monea, A very short proof of the Hermite-Hadamard inequalities, *Am. Math. Month.*, Vol:127, 850-851, 2020.
4. S. Abramovich, L. E. Persson, Fejér and Hermite-Hadamard type inequalities for  $N$ -quasiconvex functions, *Math. Notes*, Vol:102, 599-609, 2017.
5. B. Ahmad, A. Alsaedi, M. Kirane, B. T. Torebek, Hermite-Hadamard, Hermite-Hadamard-Fejér, Dragomir-Agarwal and Pachpatte type inequalities for convex functions via new fractional integrals, *J. Comput. Appl. Math.*, Vol:353, 120-129, 2019.
6. F. X. Chen, Extensions of the Hermite-Hadamard inequality for harmonically convex functions via fractional integrals, *Appl. Math. Comput.*, Vol: 268, 121-128, 2015.
7. M. R. Delavar, M. D. L. Sen, A mapping associated to  $h$ -convex version of the Hermite-Hadamard inequality with applications, *J. Math. Inequal.*, Vol:14, 329-335, 2020.
8. S. S. Dragomir, Hermite-Hadamard type inequalities for generalized Riemann-Liouville fractional integrals of  $h$ -convex functions, *Math. Methods Appl. Sci.*, Vol:44, 2364-2380, 2021.
9. S. K. Sahoo, M. A. Latif, O. M. Alsalami, S. Treanță, W. Sudsutad, J. Kongson, Hermite-Hadamard, Fejér and Pachpatte-type integral inequalities for center-radius order interval-valued preinvex functions, *Fractal Fract.*, Vol:6, No:506, 2022.
10. H. M. Srivastava, S. K. Sahoo, P. O. Mohammed, D. Baleanu, B. Kodamasingh, Hermite-Hadamard type inequalities for interval-valued preinvex functions via fractional integral operators, *Internat. J. Comput. Intel. Syst.*, Vol:15, No:8, 2022.
11. T. S. Du, H. Wang, M. A. Khan, Y. Zhang, Certain integral inequalities considering generalized  $m$ -convexity on fractal sets and their applications, *Fractals*, Vol:27, 1-17, 2019.
12. T. Abdeljawad, P. O. Mohammed, A. Kashuri, New modified conformable fractional integral inequalities of Hermite-Hadamard type with applications, *J. Funct. Spaces*, Article ID 4352357, 2020.

13. S. K. Sahoo, B. Kodamasingh, A. Kashuri, H. Aydi, E. Ameer, Ostrowski type inequalities pertaining to Atangana-Baleanu fractional operators and applications containing special functions, *J. Inequal. Appl.*, Vol:2022, No:162, 2022.
14. H. H. Bauschke, P. L. Combettes, *Convex analysis and monotone operator theory in Hilbert spaces*, Springer-Verlag, 2011, pp. 468, doi: <https://doi.org/10.1007/978-1-4419-9467-7>.
15. M. Z. Sarikaya, E. Set, H. Yaldiz, N. Başak, Hermite-Hadamard's inequalities for fractional integrals and related fractional inequalities, *Mathematical and Computer Modelling*, Vol:57, No:9-10, 2403-2407, 2013.
16. T. Ali, M. A. Khan, Y. Khurshidi, Hermite-Hadamard inequality for fractional integrals via  $\eta$ -convex functions, *Acta Mathematica Universitatis Comenianae*, Vol:86, No:1, 153-164, 2017.
17. H. Barsam, A. R. Sattarzadeh, Hermite-Hadamard inequalities for uniformly convex functions and its applications in means, *Miskolc Mathematical Notes*, Vol:21, No:2, 621–630, 2020.
18. M. Niezgodą, An extension of Levin-Stečkin's theorem to uniformly convex and superquadratic functions, *Aequationes Mathematicae*, Vol:94, No:4, 303–321, 2020.
19. H. Barsam, Y. Sayyari, On some inequalities of differentiable uniformly convex mapping with applications, *Numerical Functional Analysis and Optimization*, Vol:44, No:4, 2023.
20. C. Zălinescu, On uniformly convex functions, *Journal of Mathematical Analysis and Applications*, Vol:95, No:2, 344–374, 1983.
21. P. O. Mohammed, M. Z. Sarikaya, D. Baleanu, D. On the generalized Hermite-Hadamard inequalities via the tempered fractional integrals, *Symmetry*, Vol:12, No:595, 2020.
22. A. Akkurt, Z. Kaçar, H. Yildirim, Generalized fractional integral inequalities for continuous random variables, *J. Probab. Stat.*, Vol:2015, 1-7, 2015.
23. A. A. Kilbas, H. M. Srivastava, J. J. Trujillo, *Theory and applications of fractional differential equations*. In: North-Holland Mathematics Studies, Vol:204. Elsevier, 2006.
24. G. A. Anastassiou, Riemann-Liouville fractional fundamental theorem of calculus and Riemann-Liouville fractional Polya type integral inequality and its extension to Choquet integral setting, *Bull. Korean Math. Soc.*, Vol:56, 1423-1433, 2019.
25. H. Chen, U. N. Katugampola, Hermite-Hadamard and Hermite-Hadamard-Fejér type inequalities for generalized fractional integrals, *J. Math. Anal. Appl.*, Vol:446, 1274-1291, 2017.
26. S. K. Sahoo, P. O. Mohammed, B. Kodamasingh, M. Tariq, Y. S. Hamed, New fractional integral inequalities for convex functions pertaining to Caputo-Fabrizio operator, *Fractal Fract.*, Vol:6, No:171, 2022.
27. T. Botmart, S. K. Sahoo, B. Kodamasingh, M. A. Latif, F. Jarad, A. Kashuri, Certain midpoint-type Fejér and Hermite-Hadamard inclusions involving fractional integrals with an exponential function in kernel, *AIMS Math.*, Vol:8, 5616-5638, 2023.
28. I. Ullah, S. Ahmad, Q. M. Al-Mdallal, Z. A. Khan, H. Khan, A. Khan, A. Stability analysis of a dynamical model of tuberculosis with incomplete treatment, *Adv. Differ. Equ.*, Vol:2020, 1-14, 2020.

29. K. Khan, R. Zarin, A. Khan, A. Yusuf, M. Al-Shomrani, A. Ullah, Stability analysis of five-grade Leishmania epidemic model with harmonic mean-type incidence rate, *Adv. Differ. Equ.*, Vol:2021, 1-27, 2021.
30. Z. A. Khan, A. Khan, T. Abdeljawad, H. Khan, Computational analysis of fractional order imperfect testing infection disease model, *Fractals*, Vol:30, 2022.
31. K. Shah, Z. A. Khan, A. Ali, R. Amin, H. Khan, A. Khan, Haar wavelet collocation approach for the solution of fractional order COVID-19 model using Caputo derivative, *Alex. Eng. J.*, Vol:59, 3221-3231, 2020.
32. A. Khan, H. M. Alshehri, T. Abdeljawad, Q. M. Al-Mdallal, H. Khan, Stability analysis of fractional nabla difference COVID-19 model, *Results Phys.*, Vol:22, Article ID103888, 2021.
33. H. Khan, C. Tunc, A. Khan, Green function's properties and existence theorems for nonlinear singular delay-fractional differential equations, *Disc. Cont. Dyn. Syst. –S*, Vol:13, Article ID 2475, 2022
34. A. Alkhazzan, P. Jiang, D. Baleanu, H. Khan, A. Khan, Stability and existence results for a class of nonlinear fractional differential equations with singularity, *Math. Meth. Appl. Sci.*, Vol:41, 9321-9334, 2018.
35. A. Khan, Z. A. Khan, T. Abdeljawad, H. Khan, Analytical analysis of fractional-order sequential hybrid system with numerical application, *Adv. Cont. Dis. Mod.*, Vol:2022, 1-19, 2022.
36. A. Kashuri, R. Liko, Some new Hermite-Hadamard type inequalities and their applications, *Studia Scientiarum Mathematicarum Hungarica*, Vol:56, No:1, 103-142, 2019.

# ON THE DARBOUX FRAME OF THE POLE INDICATRIX CURVE OF THE SPACELIKE SALKOWSKI CURVE WITH SPACELIKE BINORMAL IN LORENTZIAN 3-SPACE

Birkan AKSAN<sup>1</sup>, Sümeyye GÜR MAZLUM<sup>2</sup>

<sup>1</sup> Department of Mathematical Engineering, Gümüşhane University, Gümüşhane, Türkiye  
[birkan.0605@hotmail.com](mailto:birkan.0605@hotmail.com)

<sup>2</sup> Department of Computer Technology, Gümüşhane University, Gümüşhane, Türkiye  
[sumeyyegur@gumushane.edu.tr](mailto:sumeyyegur@gumushane.edu.tr)

## Abstract

In this study, Darboux frame, normal and geodesic curvatures, geodesic torsion, Darboux frame equations and Darboux vector belong to Darboux frame of the spacelike pole indicatrix curve on the Lorentzian sphere  $S_1^2$  of the spacelike Salkowski curve with spacelike binormal in Lorentzian 3-space  $E_1^3$  are obtained. Also, the relationships between Frenet and Darboux frames and Darboux vectors belong to these frames are given.

**Keywords:** Salkowski curve; Darboux frame; geodesic curvatures; pole curve

## 1. INTRODUCTION

Some studies on curves and surfaces in the Lorentzian space can be found in sources [6-8, 10, 13, 15, 19, 21, 22, 26, 29, 30, 34, 35]. While studying the geometry of a curve, any frame can be created at any point on the curve. One of these frames that consists of the tangent, normal, and binormal vectors of the curve is Frenet frame, [16, 24, 36]. This frame is a useful tool for examining the geometric properties of the curve. Through the elements of this frame the curvature and torsion of the curve is achieved. The curvature and torsion ratio of a general helix is constant. Slant helices make a fixed angle with a fixed direction. The studies on general and slant helices are available in related sources, [3, 4, 9]. One of the best examples of these helices is the Salkowski curve, [23]. Since those years, the various studies have been carried out on these curves both in Euclidean and Lorentzian 3-space, [1, 2, 12, 14, 20, 27, 28]. Besides, Frenet frame is thought to rotate around a fixed axis at every moment  $t$ . This axis is called Darboux axis and unit vector in the direction of this axis is called pole vector, [11]. The pole vector along a regular curve generate a spherical curve on the unit sphere. The spherical curve  $(\vec{C})$  is called pole indicatrix curve of  $(\vec{\alpha})$ . Let  $t_c$  be the parameter of  $(\vec{C})$ .

The parametric equation for this curve is  $(\vec{C}) = \vec{\alpha}_C(t_C) = \vec{C}(t)$ , [12]. On the other hand, if a curve is on a surface, another frame that can be installed on the curve besides Frenet frame is Darboux frame. The Darboux frame also helps us to examine the geometric properties of any curve on the surface. By means of the elements of this frame, geodesic and normal curvature and geodesic torsion of the curve are obtained. Some studies on this frame are [5, 17, 18, 25, 30-33]. In our study, we studied on the Frenet elements of the pole indicatrix curve of spacelike Salkowski curve with spacelike binormal in Lorentzian 3-space, [1]. In this study, we obtained Darboux frame, normal and geodesic curvatures, geodesic torsion, Darboux frame equations and Darboux vector belong to Darboux frame of the spacelike pole indicatrix curve on the Lorentzian sphere  $S_1^2$  of the spacelike Salkowski curve with spacelike binormal in Lorentzian 3-space  $E_1^3$ . Also, we give the relationships between Frenet and Darboux frames and Darboux vectors belong to these frames.

## 2. PRELIMINARIES

For the vectors  $\vec{\xi} = (\xi_1, \xi_2, \xi_3)$  and  $\vec{\zeta} = (\zeta_1, \zeta_2, \zeta_3) \in E_1^3$ , let the inner product function be defined as

$$\langle \cdot, \cdot \rangle : E_1^3 \times E_1^3 \rightarrow R, \quad \langle \vec{\xi}, \vec{\zeta} \rangle = \xi_1 \zeta_1 + \xi_2 \zeta_2 - \xi_3 \zeta_3, \quad (1)$$

and the vector product function as

$$\wedge : E_1^3 \times E_1^3 \rightarrow E_1^3, \quad \vec{M} \wedge \vec{R} = (\xi_3 \zeta_2 - \xi_2 \zeta_3, \xi_1 \zeta_3 - \xi_3 \zeta_1, \xi_1 \zeta_2 - \xi_2 \zeta_1). \quad (2)$$

Here, the function  $\langle \cdot, \cdot \rangle$  is called as Lorentzian metric. The space  $E^3$  with the Lorentzian metric is called Lorentzian 3-space and is showed by  $E_1^3$ . For  $\vec{\xi} \in E_1^3$ ,  $\vec{\xi}$  is spacelike (sl) vector, if  $\langle \vec{\xi}, \vec{\xi} \rangle > 0$  or  $\vec{\xi} = 0$ ,  $\vec{\xi}$  is timelike (tl) vector, if  $\langle \vec{\xi}, \vec{\xi} \rangle < 0$ ,  $\vec{\xi}$  is lightlike or null vector, if  $\langle \vec{\xi}, \vec{\xi} \rangle = 0$  and  $\vec{\xi} \neq 0$ . Besides,  $\vec{\xi}$  is future pointing (fp) timelike vector, if  $\langle \vec{\xi}, \vec{E} \rangle < 0$  or  $\vec{\xi}$  is past pointing (pp) timelike vector, if  $\langle \vec{\xi}, \vec{E} \rangle > 0$ , where  $\vec{E} = (0, 0, 1)$ . The vectors  $\vec{\xi}$  and  $\vec{\zeta}$  in  $E_1^3$  are Lorentz orthogonal vectors, if  $\langle \vec{\xi}, \vec{\zeta} \rangle = 0$ . Let  $\vec{\xi}$  and  $\vec{\zeta}$  be nonzero Lorentz orthogonal vectors in  $E_1^3$ , if  $\vec{\xi}$  is timelike, then  $\vec{\zeta}$  is spacelike, [22].

$\|\vec{\xi}\| = \sqrt{|\langle \vec{\xi}, \vec{\xi} \rangle|}$  is the norm of the vector  $\vec{\xi} \in E_1^3$ .  $\vec{\xi}$  is a unit vector, if  $\|\vec{\xi}\| = 1$ . The sets  $S_1^2 = \{\vec{\xi} \in E_1^3 \mid \vec{\xi} \text{ is spacelike}\}$  and  $H_0^2 = \{\vec{\xi} \in E_1^3 \mid \vec{\xi} \text{ is timelike}\}$  are unit Lorentzian and unit hyperbolic spheres, respectively. An curve  $(\vec{\alpha})$  in  $E_1^3$  is spacelike, timelike or lightlike curve, if all of the velocity vector of the curve are the spacelike, timelike or lightlike, respectively. When plotting a spacelike curve  $(\vec{\alpha})$  in  $E_1^3$ , the endpoints of the spacelike pole vector  $\vec{C}$  of the curve  $(\vec{\alpha})$  draw a spacelike curve  $(\vec{C})$  on the Lorentz unit sphere  $S_1^2$ , [30], Figure 1.



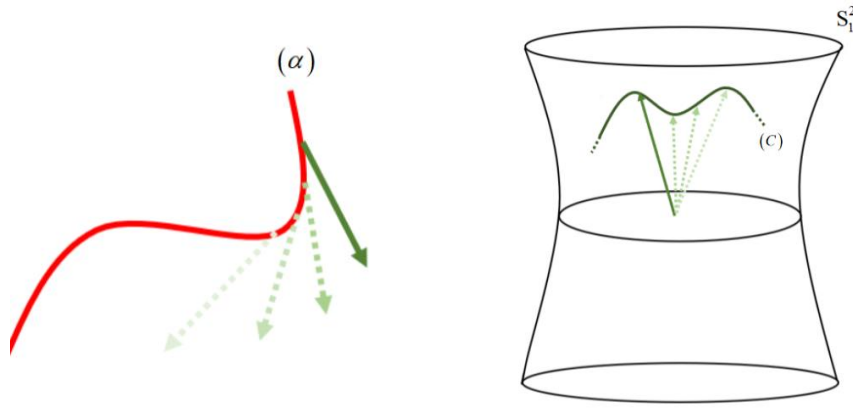


**Figure 1.** The spacelike indicatrix curve  $(\bar{C})$  on  $S_1^2$  of the curve  $(\bar{\alpha})$

A surface in  $E_1^3$  is a spacelike (timelike), if the normal vector field of the surface at every points is timelike (spacelike). Let's assume that the regular spacelike curve  $(\bar{\alpha}) = \bar{\alpha}(t)$  is on a timelike surface. Let  $\{\bar{T}(t), \bar{g}(t), \bar{n}(t)\}$  be the Darboux trihedron of this curve, where  $\bar{n}(t)$  is the spacelike normal vector of the timelike surface and  $\bar{g}(t) = \bar{n}(t) \wedge \bar{T}(t)$  is timelike, [30]. The normal curvature, geodesic curvature and geodesic torsion of this curve are  $\kappa_n(t) = \frac{1}{v^2(t)} \langle \bar{\alpha}''(t), \bar{n}(t) \rangle$ ,  $\kappa_g(t) = \frac{1}{v^2(t)} \langle \bar{\alpha}''(t), \bar{g}(t) \rangle$  and  $\tau_g(t) = -\frac{1}{v^2(t)} \langle \bar{n}'(t), \bar{g}(t) \rangle$ , respectively, where  $v(t) = \|\bar{\alpha}'(t)\|$ .  $(\bar{\alpha})$  is a asymptotic curve, if  $\kappa_n(t) = 0$ ,  $(\bar{\alpha})$  is a geodesic curve, if  $\kappa_g(t) = 0$  and  $(\bar{\alpha})$  is a curvature line, if  $\tau_g(t) = 0$ , [36].

**Definition 2.1.** Spacelike Salkowski curve with the spacelike binormal in  $E_1^3$  is as follows:

$$\begin{aligned} \bar{\gamma}_m(t) = & \left( 2 \sin t - \frac{1+n}{1-2n} \sin[(1-2n)t] - \frac{1-n}{1+2n} \sin[(1+2n)t], \right. \\ & \left. 2 \cos t - \frac{1+n}{1-2n} \cos[(1-2n)t] - \frac{1-n}{1+2n} \cos[(1+2n)t], \frac{1}{m} \cos(2nt) \right), \end{aligned}$$

for  $m \in \mathbb{R}$ ,  $m > 1$  or  $m < -1$ ,  $n = \frac{m}{\sqrt{m^2-1}}$  and  $\|\bar{\gamma}_m'(t)\| = v(t) = \frac{\sin(nt)}{\sqrt{m^2-1}}$ , [2], Figure 2.

The Frenet vectors of  $\bar{\gamma}_m(t)$  are

$$\begin{cases} \bar{T}(t) = \left( \cos t \sin(nt) - n \sin t \cos(nt), -\sin t \sin(nt) - n \cos t \cos(nt), -\frac{n}{m} \cos(nt) \right) \text{ sl}, \\ \bar{N}(t) = \frac{n}{m} (\sin t, \cos t, m) \text{ tl}, \\ \bar{B}(t) = \left( -\cos t \cos(nt) - n \sin t \sin(nt), \sin t \cos(nt) - n \cos t \sin(nt), -\frac{n}{m} \sin(nt) \right) \text{ sl}. \end{cases} \quad (3)$$

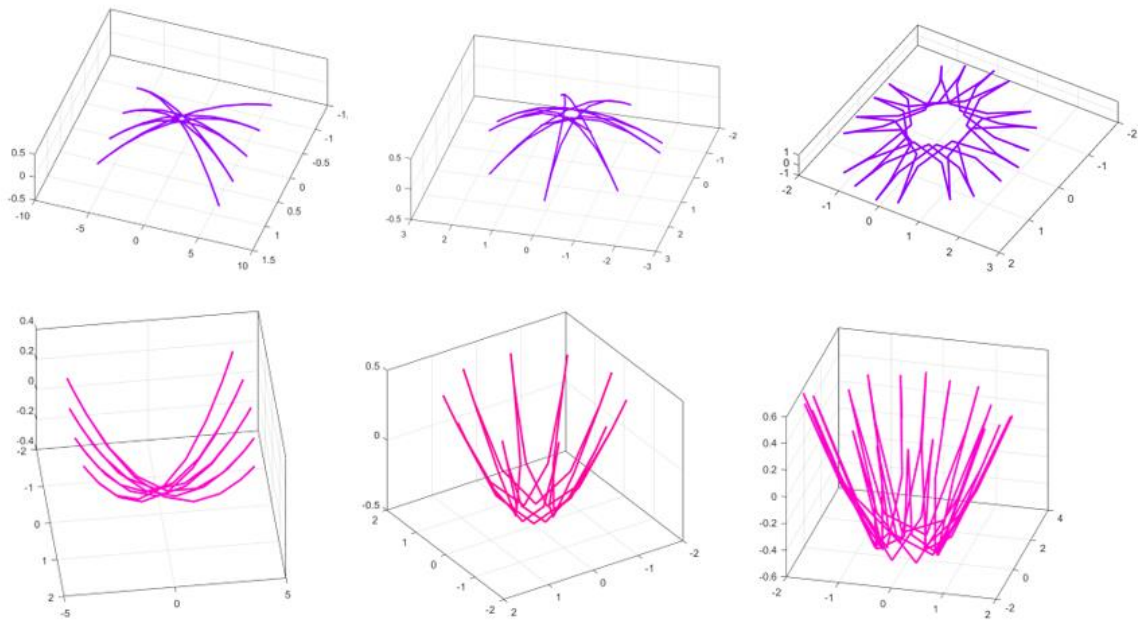


**Figure 2.** The curve  $\overrightarrow{\gamma}_m(t)$  for  $m = -6, -2, -\frac{10}{9}, 4, \frac{5}{4}, \frac{10}{9}$  resp.

In addition, the unit pole vector  $\overrightarrow{C}(t)$  of  $\overrightarrow{\gamma}_m(t)$  is as follows [1]:

$$\overrightarrow{C}(t) = \left( -n \sin t, -n \cos t, -\frac{n}{m} \right) \quad \text{s.t.} \quad (4)$$

The spacelike pole indicatrix curve  $(\overrightarrow{C})$  on  $S_1^2$  of  $\overrightarrow{\gamma}_m(t)$  is a planar circle of radius  $n$  on  $S_1^2$ , [1], Figure 3, also

$$v_C(t) = \|\overrightarrow{C}'(t)\| = n. \quad (5)$$

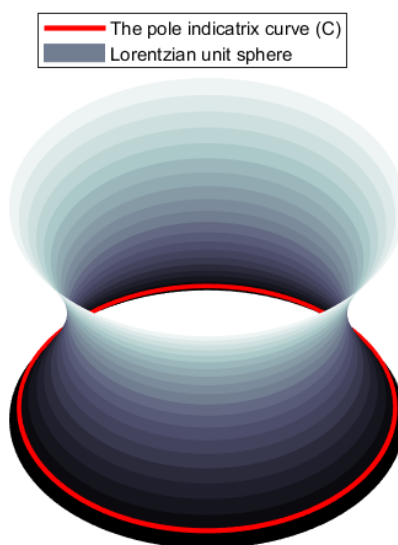


**Figure 3.** The spacelike pole indicatrix curve  $(\overrightarrow{C})$  on  $S_1^2$  of  $\overrightarrow{\gamma}_m(t)$

The Frenet frame  $\{\overrightarrow{T}_C(t), \overrightarrow{N}_C(t), \overrightarrow{B}_C(t)\}$  of spacelike pole indicatrix curve  $(\overrightarrow{C})$  of  $\overrightarrow{\gamma}_m(t)$  is

$$\begin{cases} \overrightarrow{T}_C(t) = (-\cos t, \sin t, 0) & \text{sl,} \\ \overrightarrow{N}_C(t) = (\sin t, \cos t, 0) & \text{sl,} \\ \overrightarrow{B}_C(t) = (0, 0, -1) & \text{tl,} \end{cases} \quad (6)$$

[1]. The curvature and torsion of the spacelike pole indicatrix curve  $(\overrightarrow{C})$  of  $\overrightarrow{\gamma}_m(t)$  are as follows:

$$\kappa_C(t) = \frac{1}{n} \quad \text{and} \quad \tau_C(t) = 0, \quad (7)$$

respectively, [1].

### 3. ON THE DARBOUX FRAME OF THE POLE INDICATRIX CURVE OF THE SPACELIKE SALKOWSKI CURVE WITH SPACELIKE BINORMAL IN LORENTZIAN 3-SPACE

**Theorem 3.1.** The Darboux frame  $\{\overrightarrow{T}_C(t), \overrightarrow{g}_C(t), \overrightarrow{n}_C(t)\}$  of the spacelike pole indicatrix curve  $(\overrightarrow{C})$  on  $S_1^2$  of  $\overrightarrow{\gamma}_m(t)$  is as follows:

$$\begin{cases} \overrightarrow{T}_C(t) = (-\cos t, \sin t, 0) & \text{sl,} \\ \overrightarrow{g}_C(t) = \left( -\frac{n}{m} \sin t, -\frac{n}{m} \cos t, -n \right) & \text{tl,} \\ \overrightarrow{n}_C(t) = \left( -n \sin t, -n \cos t, -\frac{n}{m} \right) & \text{sl.} \end{cases} \quad (8)$$

**Proof:** Since the vectors  $\overrightarrow{T}_C(t)$  and  $\overrightarrow{C}(t)$  are spacelike,  $\overrightarrow{g}_C(t) = \overrightarrow{C}(t) \wedge \overrightarrow{T}_C(t)$ . From (4) and (6), we get

$$\overrightarrow{g}_C(t) = \overrightarrow{C}(t) \wedge \overrightarrow{T}_C(t) = \left( -\frac{n}{m} \sin t, -\frac{n}{m} \cos t, -n \right).$$

Besides, for the pole indicatrix curve  $(\overrightarrow{C})$  on the sphere  $S_1^2$ , the pole vector  $\overrightarrow{C}(t)$  can be taken as the normal vector of the surface, that is  $\overrightarrow{n}_C(t) = \overrightarrow{C}(t)$  as in (4). Thus, the Darboux frame  $\{\overrightarrow{T}_C(t), \overrightarrow{g}_C(t), \overrightarrow{n}_C(t)\} = \{\overrightarrow{T}_C(t), \overrightarrow{C}(t) \wedge \overrightarrow{T}_C(t), \overrightarrow{C}(t)\}$  is obtained as in (8).

**Theorem 3.2.** The normal curvature  $(\kappa_n)_C(t)$  of the spacelike pole indicatrix curve  $(\overrightarrow{C})$  on  $S_1^2$  of  $\overrightarrow{\gamma}_m(t)$  is as follows:

$$(\kappa_n)_C(t) = -1. \quad (9)$$

**Proof:** The normal curvature  $(\kappa_n)_C(t)$  of  $(\overrightarrow{C})$  is calculated by

$$(\kappa_n)_C(t) = \frac{1}{v_C^2(t)} \langle \overrightarrow{C''}(t), \overrightarrow{n_C}(t) \rangle. \quad (10)$$

From (4), we get

$$\overrightarrow{C''}(t) = (n \sin t, n \cos t, 0). \quad (11)$$

From (8) and (11), we have

$$\langle \overrightarrow{C''}(t), \overrightarrow{n_C}(t) \rangle = -n^2. \quad (12)$$

If we substitute (5) and (12) in (10), we obtain the normal curvature of  $(\overrightarrow{C})$  as in (9).

**Theorem 3.3.** The geodesic curvature  $(\kappa_g)_C(t)$  of the spacelike pole indicatrix curve  $(\overrightarrow{C})$  on  $S_1^2$  of  $\overrightarrow{\gamma_m}(t)$  is as follows:

$$(\kappa_g)_C(t) = -\frac{1}{m}. \quad (13)$$

**Proof:** The geodesic curvature  $(\kappa_g)_C(t)$  of  $(\overrightarrow{C})$  is calculated by

$$(\kappa_g)_C(t) = \frac{1}{v_C^2(t)} \langle \overrightarrow{C''}(t), \overrightarrow{g_C}(t) \rangle. \quad (14)$$

From (8) and (11), we have

$$\langle \overrightarrow{C''}(t), \overrightarrow{g_C}(t) \rangle = -\frac{n^2}{m}. \quad (15)$$

If we substitute (5) and (15) in (14), we obtain the geodesic curvature of  $(\overrightarrow{C})$  as in (13).

**Theorem 3.4.** The geodesic torsion  $(\tau_g)_C(t)$  of the spacelike pole indicatrix curve  $(\overrightarrow{C})$  on  $S_1^2$  of  $\overrightarrow{\gamma_m}(t)$  is as follows:

$$(\tau_g)_C(t) = 0. \quad (16)$$

**Proof:** The geodesic torsion  $(\tau_g)_C(t)$  of  $(\overrightarrow{C})$  is calculated by

$$(\tau_g)_C(t) = -\frac{1}{v_C^2(t)} \langle \overrightarrow{n_C'}(t), \overrightarrow{g_C}(t) \rangle. \quad (17)$$

From (8), we have

$$\overrightarrow{n_C'}(t) = (-n \cos t, n \sin t, 0). \quad (18)$$

So, from (8) and (18), we get

$$\langle \overrightarrow{n_C'}(t), \overrightarrow{g_C}(t) \rangle = 0. \quad (19)$$

If we substitute (5) and (19) in (17), we obtain the geodesic torsion of  $(\overrightarrow{C})$  as in (16).

**Corollary 3.5.** The spacelike pole indicatrix curve  $(\overrightarrow{C})$  on  $S_1^2$  of  $\overrightarrow{\gamma_m}(t)$  is a curvature line.

**Theorem 3.6.** Let  $\{\overrightarrow{T_C}(t), \overrightarrow{g_C}(t), \overrightarrow{n_C}(t)\}$  be the Darboux frame of the spacelike pole indicatrix curve  $(\overrightarrow{C})$  on  $S_1^2$  of  $\overrightarrow{\gamma_m}(t)$ . The Darboux frame equations of  $(\overrightarrow{C})$  are as follows:

$$\begin{bmatrix} \overrightarrow{T'_C}(t) \\ \overrightarrow{g'_C}(t) \\ \overrightarrow{n'_C}(t) \end{bmatrix} = \begin{bmatrix} 0 & \frac{n}{m} & -n \\ \frac{n}{m} & 0 & 0 \\ n & 0 & 0 \end{bmatrix} \begin{bmatrix} \overrightarrow{T_C}(t) \\ \overrightarrow{g_C}(t) \\ \overrightarrow{n_C}(t) \end{bmatrix}. \quad (20)$$

**Proof:** We can construct the following matrix equation between Darboux vectors and their derivatives:

$$\begin{bmatrix} \overrightarrow{T'_C}(t) \\ \overrightarrow{g'_C}(t) \\ \overrightarrow{n'_C}(t) \end{bmatrix} = \begin{bmatrix} a_1 & b_1 & c_1 \\ d_1 & e_1 & f_1 \\ k_1 & l_1 & m_1 \end{bmatrix} \begin{bmatrix} \overrightarrow{T_C}(t) \\ \overrightarrow{g_C}(t) \\ \overrightarrow{n_C}(t) \end{bmatrix}, \quad (21)$$

where  $a_1, b_1, c_1, d_1, e_1, f_1, k_1, l_1, m_1$  are arbitrary functions of  $t$ . Now let's find these coefficients in order. From (21), we write the equation below:

$$\overrightarrow{T'_C}(t) = a_1 \overrightarrow{T_C}(t) + b_1 \overrightarrow{g_C}(t) + c_1 \overrightarrow{n_C}(t). \quad (22)$$

Let's apply the inner product of the vectors  $\overrightarrow{T_C}(t)$ ,  $\overrightarrow{g_C}(t)$  and  $\overrightarrow{n_C}(t)$  to both sides of (22), respectively. So, we have

$$a_1 = \langle \overrightarrow{T_C}(t), \overrightarrow{T'_C}(t) \rangle, \quad b_1 = -\langle \overrightarrow{g_C}(t), \overrightarrow{T'_C}(t) \rangle, \quad c_1 = \langle \overrightarrow{n_C}(t), \overrightarrow{T'_C}(t) \rangle. \quad (23)$$

From (8), we get

$$\overrightarrow{T'_C}(t) = (\sin t, \cos t, 0). \quad (24)$$

From (8), (23) and (24), we have

$$a_1 = 0, \quad b_1 = \frac{n}{m}, \quad c_1 = -n. \quad (25)$$

From (21), we write the equation below:

$$\overrightarrow{g'_C}(t) = d_1 \overrightarrow{T_C}(t) + e_1 \overrightarrow{g_C}(t) + f_1 \overrightarrow{n_C}(t). \quad (26)$$

Let's apply the inner product of the vectors  $\overrightarrow{T_C}(t)$ ,  $\overrightarrow{g_C}(t)$  and  $\overrightarrow{n_C}(t)$  to both sides of (26), respectively. So, we have

$$d_1 = \langle \overrightarrow{T_C}(t), \overrightarrow{g'_C}(t) \rangle, \quad e_1 = \langle \overrightarrow{g_C}(t), \overrightarrow{g'_C}(t) \rangle, \quad f_1 = \langle \overrightarrow{n_C}(t), \overrightarrow{g'_C}(t) \rangle. \quad (27)$$

From (8), we get

$$\overrightarrow{g'_C}(t) = \left( -\frac{n}{m} \cos t, \frac{n}{m} \sin t, 0 \right). \quad (28)$$

From (8), (23) and (28), we have

$$d_1 = \frac{n}{m}, \quad e_1 = 0, \quad f_1 = 0. \quad (29)$$

From (21), we write the equation below:

$$\overrightarrow{n_c'}(t) = k_1 \overrightarrow{T_c}(t) + l_1 \overrightarrow{g_c}(t) + m_1 \overrightarrow{n_c}(t). \quad (30)$$

Let's apply the inner product of the vectors  $\overrightarrow{T_c}(t)$ ,  $\overrightarrow{g_c}(t)$  and  $\overrightarrow{n_c}(t)$  to both sides of (30), respectively. So, we have

$$k_1 = \langle \overrightarrow{T_c}(t), \overrightarrow{n_c'}(t) \rangle, \quad l_1 = \langle \overrightarrow{g_c}(t), \overrightarrow{n_c'}(t) \rangle, \quad m_1 = \langle \overrightarrow{n_c}(t), \overrightarrow{n_c'}(t) \rangle. \quad (31)$$

From (8), (18), (23) and (31), we have

$$k_1 = n, \quad l_1 = 0, \quad m_1 = 0. \quad (32)$$

If we substitute (25), (28) and (32) in (21), we get the expression (20).

**Theorem 3.7.** Let  $\{\overrightarrow{T_c}(t), \overrightarrow{N_c}(t), \overrightarrow{B_c}(t)\}$  and  $\{\overrightarrow{T_c}(t), \overrightarrow{g_c}(t), \overrightarrow{n_c}(t)\}$  be the Frenet and Darboux frames of the spacelike pole indicatrix curve  $(\overrightarrow{C})$  on  $S_1^2$  of  $\overrightarrow{\gamma_m}(t)$ , respectively. The hyperbolic angle  $\theta_c(t)$  between the spacelike vector  $\overrightarrow{N_c}(t)$  and the timelike vector  $\overrightarrow{g_c}(t)$  is as follows:

$$\theta_c(t) = \text{arc tanh} \left( \frac{1}{m} \right). \quad (33)$$

**Proof:** For the hyperbolic angle  $\theta_c(t)$  between the spacelike vector  $\overrightarrow{N_c}(t)$  and timelike vector  $\overrightarrow{g_c}(t)$ , Figure 4, we write [22]

$$\langle \overrightarrow{g_c}(t), \overrightarrow{N_c}(t) \rangle = \|\overrightarrow{g_c}(t)\| \|\overrightarrow{N_c}(t)\| \sinh \theta_c(t). \quad (34)$$

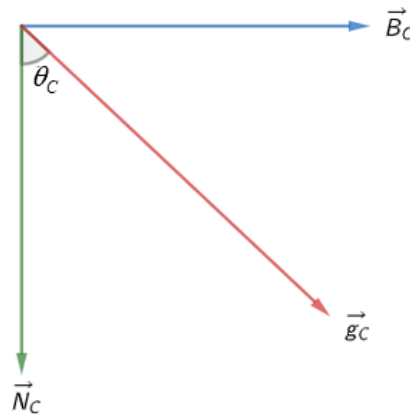


**Figure 4.** The hyperbolic angle  $\theta_c(t)$  between the vectors  $\overrightarrow{N_c}(t)$  and  $\overrightarrow{g_c}(t)$

Since the vectors  $\overrightarrow{N_c}(t)$  and  $\overrightarrow{g_c}(t)$  are unit vectors and using (6) and (8), from the inner product of the vectors  $\overrightarrow{N_c}(t)$  and  $\overrightarrow{g_c}(t)$  in (34), we get

$$\langle \overrightarrow{g_c}(t), \overrightarrow{N_c}(t) \rangle = \sinh \theta_c(t) = -\frac{n}{m}. \quad (35)$$

Similarly, for the past pointing timelike vectors  $\overrightarrow{B_c}(t)$  and  $\overrightarrow{g_c}(t)$ , we write

$$\langle \overrightarrow{g_c}(t), \overrightarrow{B_c}(t) \rangle = \|\overrightarrow{g_c}(t)\| \|\overrightarrow{B_c}(t)\| \cosh \theta_c(t),$$

[22]. Since the vectors  $\overrightarrow{B_C}(t)$  and  $\overrightarrow{g_C}(t)$  are unit vectors and using (6) and (8), from the inner product of the vectors  $\overrightarrow{B_C}(t)$  and  $\overrightarrow{g_C}(t)$ , we get

$$\langle \overrightarrow{g_C}(t), \overrightarrow{B_C}(t) \rangle = \cosh \theta_C(t) = -n. \quad (36)$$

From (35) and (36), we obtain the expression (33).

**Theorem 3.8.** The Darboux vector  $\overrightarrow{W_C}(t)$  belong to the Darboux frame of the spacelike pole indicatrix curve  $(\overrightarrow{C})$  on  $S_1^2$  of  $\overrightarrow{\gamma_m}(t)$  is as follows:

$$\overrightarrow{W_C}(t) = (0, 0, 1) \quad \text{tl.} \quad (37)$$

**Proof:** For the Darboux vector  $\overrightarrow{W_C}(t)$  belong to the Darboux frame, we know the equation

$$\overrightarrow{T_C}'(t) = \overrightarrow{W_C}(t) \wedge \overrightarrow{T_C}(t), \quad \overrightarrow{g_C}'(t) = \overrightarrow{W_C}(t) \wedge \overrightarrow{g_C}(t), \quad \overrightarrow{n_C}'(t) = \overrightarrow{W_C}(t) \wedge \overrightarrow{n_C}(t), \quad (38)$$

[30]. From (38), using (8) and (18), we get the expression (37).

**Corollary 3.9.** The Darboux vector  $\overrightarrow{W_C}(t)$  belong to the Darboux frame of the spacelike pole indicatrix curve  $(\overrightarrow{C})$  on  $S_1^2$  of  $\overrightarrow{\gamma_m}(t)$  is as follows:

$$\overrightarrow{W_C}(t) = -n\overrightarrow{g_C}(t) + \frac{n}{m}\overrightarrow{n_C}(t). \quad (39)$$

**Proof:** We write the vector  $\overrightarrow{W_C}(t)$  as a linear combination of the Darboux frame's vectors as follows:

$$\overrightarrow{W_C}(t) = x\overrightarrow{T_C}(t) + y\overrightarrow{g_C}(t) + z\overrightarrow{n_C}(t), \quad (40)$$

where  $x, y, z$  are arbitrary functions of  $t$ . For (33) and (38) to be satisfied simultaneously, we have

$$x = -\nu_C(t)(\tau_g)_C(t), \quad y = \nu_C(t)(\kappa_n)_C(t), \quad z = -\nu_C(t)(\kappa_g)_C(t)$$

in (40). If we substitute these values in (40), we obtain

$$\overrightarrow{W_C}(t) = \nu_C(t) \left[ -(\tau_g)_C(t)\overrightarrow{T_C}(t) + (\kappa_n)_C(t)\overrightarrow{g_C}(t) - (\kappa_g)_C(t)\overrightarrow{n_C}(t) \right], \quad (41)$$

[30]. If we substitute (5), (9), (13) and (16) in (41), we get (39). Moreover, if we substitute (8) in (39) also, it is clear that we get the expression (37), Figure 5.

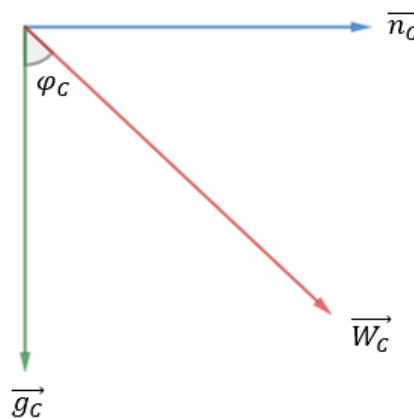


**Figure 5.** The Darboux vector  $\overrightarrow{W_C}(t)$  belong to the Darboux frame

**Theorem 3.10.** There are the following relationships between the normal curvature  $(\kappa_n)_C(t)$ , the geodesic curvatures  $(\kappa_g)_C(t)$ , the geodesic torsion  $(\tau_g)_C(t)$  and the curvature  $\kappa_C(t)$ , the torsion  $\tau_C(t)$  of the spacelike pole indicatrix curve  $(\bar{C})$  on  $S_1^2$  of  $\bar{\gamma}_m(t)$ :

$$\begin{cases} (\kappa_n)_C(t) = -n\kappa_C(t), \\ (\kappa_g)_C(t) = -\frac{n}{m}\kappa_C(t), \\ (\tau_g)_C(t) = -\tau_C(t). \end{cases} \quad (42)$$

**Proof:** For the Darboux vector  $\bar{F}_C(t)$  belong to the Frenet frame of  $(\bar{C})$ , we write

$$\bar{T}_C'(t) = \bar{F}_C(t) \wedge \bar{T}_C(t), \quad (43)$$

[30]. From the equality of (38) and (43), we have

$$(\bar{F}_C(t) - \bar{W}_C(t)) \wedge \bar{T}_C(t) = \vec{0}, \quad (44)$$

where

$$\bar{F}_C(t) = \nu_C(t) (\tau_C(t) \bar{T}_C(t) - \kappa_C(t) \bar{B}_C(t)) = (0, 0, 1), \quad (45)$$

[1]. If we substitute (41) and (45) in (44), we get

$$\kappa_C(t) \bar{N}_C(t) = (\kappa_n)_C(t) \bar{n}_C(t) - (\kappa_g)_C(t) \bar{g}_C(t). \quad (46)$$

If we apply the inner product with  $\bar{n}_C(t)$  and  $\bar{g}_C(t)$  on both sides of (46), respectively, we get

$$\begin{cases} (\kappa_n)_C(t) = \kappa_C(t) \langle \bar{N}_C(t), \bar{n}_C(t) \rangle + (\kappa_g)_C(t) \langle \bar{g}_C(t), \bar{n}_C(t) \rangle, \\ (\kappa_g)_C(t) = \kappa_C(t) \langle \bar{N}_C(t), \bar{g}_C(t) \rangle - (\kappa_n)_C(t) \langle \bar{g}_C(t), \bar{n}_C(t) \rangle. \end{cases} \quad (47)$$

From (6) and (8), we get

$$\langle \bar{N}_C(t), \bar{n}_C(t) \rangle = -n. \quad (48)$$

If we substitute (35) and (48) in (47), we have

$$(\kappa_n)_C(t) = -n\kappa_C(t), \quad (\kappa_g)_C(t) = -\frac{n}{m}\kappa_C(t). \quad (49)$$

Besides, if we take the derivative of both sides of the equation  $\langle \bar{g}_C(t), \bar{N}_C(t) \rangle = \sinh \theta_C(t)$  in (35), we get

$$\langle \bar{g}_C'(t), \bar{N}_C(t) \rangle + \langle \bar{g}_C(t), \bar{N}_C'(t) \rangle = \frac{d\theta_C(t)}{dt} \cosh \theta_C(t). \quad (50)$$

If we substitute (33) in (50), we have

$$\nu_C(t) (\tau_g)_C(t) \langle \bar{n}_C(t), \bar{N}_C(t) \rangle + \nu_C(t) \tau_C(t) \langle \bar{B}_C(t), \bar{g}_C(t) \rangle = \frac{d\theta_C(t)}{dt} \cosh \theta_C(t). \quad (51)$$

If we substitute (36) and (48) in (51), we get

$$\nu_C(t) (\tau_g)_C(t) = -\nu_C(t) \tau_C(t) + \frac{d\theta_C(t)}{dt}. \quad (52)$$



Also, from (34), we have

$$\frac{d\theta_c(t)}{dt} = 0. \quad (53)$$

So, if we substitute (53) in (52), we obtain

$$(\tau_g)_c(t) = -\tau_c(t). \quad (54)$$

From (49) and (54), we obtain (42).

**Theorem 3.11.** Let  $\{\overrightarrow{T}_c(t), \overrightarrow{N}_c(t), \overrightarrow{B}_c(t)\}$  and  $\{\overrightarrow{T}_c(t), \overrightarrow{g}_c(t), \overrightarrow{n}_c(t)\}$  be the Frenet and Darboux frames of the spacelike pole indicatrix curve  $(\overrightarrow{C})$  on  $S_1^2$  of  $\overrightarrow{\gamma}_m(t)$ , respectively.

There is the following relationship between these frames:

$$\begin{bmatrix} \overrightarrow{T}_c(t) \\ \overrightarrow{N}_c(t) \\ \overrightarrow{B}_c(t) \end{bmatrix} = \begin{bmatrix} 1 & 0 & 0 \\ 0 & \frac{n}{m} & -n \\ 0 & n & -\frac{n}{m} \end{bmatrix} \begin{bmatrix} \overrightarrow{T}_c(t) \\ \overrightarrow{g}_c(t) \\ \overrightarrow{n}_c(t) \end{bmatrix}. \quad (55)$$

**Proof:** We can construct the following matrix equation between the vectors of the Frenet and Darboux frames:

$$\begin{bmatrix} \overrightarrow{T}_c(t) \\ \overrightarrow{N}_c(t) \\ \overrightarrow{B}_c(t) \end{bmatrix} = \begin{bmatrix} a_2 & b_2 & c_2 \\ d_2 & e_2 & f_2 \\ k_2 & l_2 & m_2 \end{bmatrix} \begin{bmatrix} \overrightarrow{T}_c(t) \\ \overrightarrow{g}_c(t) \\ \overrightarrow{n}_c(t) \end{bmatrix}, \quad (56)$$

where  $a_2, b_2, c_2, d_2, e_2, f_2, k_2, l_2, m_2$  are arbitrary functions of  $t$ . Now let's find these coefficients in order. From (56), we write the equation below:

$$\overrightarrow{T}_c(t) = a_2 \overrightarrow{T}_c(t) + b_2 \overrightarrow{g}_c(t) + c_2 \overrightarrow{n}_c(t). \quad (57)$$

Let's apply the inner product of the vectors  $\overrightarrow{T}_c(t)$ ,  $\overrightarrow{g}_c(t)$  and  $\overrightarrow{n}_c(t)$  to both sides of (57), respectively. So, it is clear that

$$a_2 = 1, \quad b_2 = 0, \quad c_2 = 0. \quad (58)$$

Similarly, from (56), we write

$$\overrightarrow{N}_c(t) = d_2 \overrightarrow{T}_c(t) + e_2 \overrightarrow{g}_c(t) + f_2 \overrightarrow{n}_c(t). \quad (59)$$

Let's apply the inner product of the vectors  $\overrightarrow{T}_c(t)$ ,  $\overrightarrow{g}_c(t)$  and  $\overrightarrow{n}_c(t)$  to both sides of (59), respectively. From (35) and (48), we get

$$d_2 = 0, \quad e_2 = \frac{n}{m}, \quad f_2 = -n \quad (60)$$

Similarly, from (56), we write

$$\overrightarrow{B}_c(t) = k_2 \overrightarrow{T}_c(t) + l_2 \overrightarrow{g}_c(t) + m_2 \overrightarrow{n}_c(t). \quad (61)$$

Let's apply the inner product of the vectors  $\overrightarrow{T}_c(t)$ ,  $\overrightarrow{g}_c(t)$  and  $\overrightarrow{n}_c(t)$  to both sides of (61), respectively. From (6) and (8), we get

$$\langle \overrightarrow{B_C}(t), \overrightarrow{n_C}(t) \rangle = \langle \overrightarrow{B_C}(t), \overrightarrow{g_C}(t) \wedge \overrightarrow{T_C}(t) \rangle = \langle \overrightarrow{N_C}(t), \overrightarrow{g_C}(t) \rangle = -\frac{n}{m}. \quad (62)$$

From (36) and (62), we have

$$k_2 = 0, \quad l_2 = n, \quad m_2 = -\frac{n}{m}. \quad (63)$$

If we substitute (58), (60) and (63) in (56), we obtain the expression (55).

**Theorem 3.12.** Let  $\{\overrightarrow{T_C}(t), \overrightarrow{g_C}(t), \overrightarrow{n_C}(t)\}$  be the Darboux frame of the spacelike pole indicatrix curve  $(\overrightarrow{C})$  on  $S_1^2$  of  $\overrightarrow{\gamma_m}(t)$ . There is the following relationship between the Darboux vectors  $\overrightarrow{F_C}(t)$  and  $\overrightarrow{W_C}(t)$  belong to the Frenet and Darboux frames, respectively:

$$\overrightarrow{W_C}(t) = \overrightarrow{F_C}(t). \quad (64)$$

**Proof:** It is clear that (37) and (45).

**Theorem 3.13.** The hyperbolic angle  $\varphi_C(t)$  between the vectors  $\overrightarrow{W_C}(t)$  and  $\overrightarrow{g_C}(t)$  of the spacelike pole indicatrix curve  $(\overrightarrow{C})$  on  $S_1^2$  of  $\overrightarrow{\gamma_m}(t)$  is as follows:

$$\varphi_C(t) = \operatorname{arc} \tanh \left( \frac{1}{m} \right). \quad (65)$$

**Proof:** If the hyperbolic angle  $\varphi_C(t)$  between the vectors  $\overrightarrow{W_C}(t)$  and  $\overrightarrow{g_C}(t)$ , since  $\overrightarrow{W_C}(t)$  and  $\overrightarrow{g_C}(t)$  are unit past pointing timelike vectors, we write

$$\langle \overrightarrow{g_C}(t), \overrightarrow{W_C}(t) \rangle = \|\overrightarrow{g_C}(t)\| \|\overrightarrow{W_C}(t)\| \cosh \varphi_C(t) = \cosh \varphi_C(t). \quad (66)$$

Besides from Figure 5, we have

$$\langle \overrightarrow{n_C}(t), \overrightarrow{W_C}(t) \rangle = \|\overrightarrow{n_C}(t)\| \|\overrightarrow{W_C}(t)\| \sinh \varphi_C(t) = \sinh \varphi_C(t). \quad (67)$$

On the other hand, from (8) and (37), we get

$$\langle \overrightarrow{g_C}(t), \overrightarrow{W_C}(t) \rangle = n, \quad \langle \overrightarrow{n_C}(t), \overrightarrow{W_C}(t) \rangle = \frac{n}{m}. \quad (68)$$

From (66), (67) and (68), we obtain

$$\cosh \varphi_C(t) = n \quad \text{and} \quad \sinh \varphi_C(t) = \frac{n}{m}. \quad (69)$$

From (69), we obtain the expression (65).

## 4.CONCLUSIONS

In this study, the elements obtained for the spacelike pole indicatrix curve  $(\overrightarrow{C})$  on the Lorentzian sphere  $S_1^2$  of spacelike Salkowski curve with spacelike binormal in Lorentzian 3-space  $E_1^3$  can also be obtained on the other indicatrix curves (tangent, principal normal and binormal indicatrix curves) of the curve. Besides, similar studies can also be done on other types of Salkowski and anti-Salkowski curves in Lorentzian 3-space or other special curves.

## REFERENCES

1. Aksan, B., Gür Mazlum, S., On the pole indicatrix curve of the spacelike Salkowski curve with timelike principal normal in Lorentzian 3-space, *Gümüşhane Üniversitesi Fen Bilimleri Dergisi*, 12(4), 1168–1179, 2022.
2. Ali, A. T., Spacelike Salkowski and anti-Salkowski curves with timelike principal normal in Minkowski 3-space. *Mathematica Aeterna*, 1(4), 201–210, 2011.
3. Ali, A. T., Position vectors of slant helices in Euclidean 3-space, *Journal of the Egyptian Mathematical Society*, 20, 1–6, 2012.
4. Ali, A.T., Lopez, R., Slant helices in Minkowski space, *J. Korean Math. Soc.* 48(1), 159–167, 2011.
5. Aydınalp, M., Kazaz, M., Uğurlu, H. H., The Forward Kinematics of Rolling Contact of Timelike Surfaces With Spacelike Trajectory Curves, *Journal of Informatics & Mathematical Sciences*, 11(2), 133–146, 2019.
6. Beem, J. K., Paul, E. E., Kevin, L. E., *Global lorentzian geometry*. Routledge, 2017.
7. Bilici, M., Çalışkan, M., Some new results on the curvatures of the spherical indicatrices of the involutes of a spacelike curve with a spacelike binormal in Minkowski 3-space, *MathLAB Journal*, 2(1), 110–119, 2019.
8. Birman, G. S., Nomizu, K., Trigonometry in Lorentzian geometry. *Ann. Math. Mont.* 91, 534–549, 1984.
9. Bulut, F., Bektaş, M., Special helices on equiform differential geometry of spacelike curves in Minkowski space-time. *Communications Faculty of Sciences University of Ankara Series A1 Mathematics and Statistics*, 69, 1045–1056, 2020.
10. Bükcü, B., Karacan, M. K., On the involute and evolute curves of the spacelike curve with a spacelike binormal in Minkowski 3-space. *Int. J. Contemp. Math. Sciences*, 2(5), 221–232, 2007.
11. Fenchel, W., On the Differential Geometry of Closed Space Curves, *Bull. Am. Math. Soc.*, 57, 44–54, 1951.
12. Gür, S., Şenyurt, S., Frenet vectors and geodesic curvatures of spheric indicators of Salkowski curve in  $E^3$ , *Hadronic Journal*, 33(5), 485–512, 2010.
13. Gür, S., Şenyurt, S., Spacelike–timelike involute–evolute curve couple on dual Lorentzian space. *J. Math. Comput. Sci.*, 3(4), 1054–1075, 2013.
14. Gür Mazlum, S., Şenyurt, S., Bektaş, M., Salkowski Curves and Their Modified Orthogonal Frames in  $E^3$ , *Journal of New Theory*, 40(2022), 12–26, 2022.
15. Gür Mazlum, S., Geometric properties of timelike surfaces in Lorentz-Minkowski 3-space, *Filomat*, 37(17), 5735–5749, 2023.
16. Hacısalihoğlu, H. H., *Differential geometry*. İnönü University, Publication of Faculty of Sciences and Arts: Malatya, Türkiye, 1983.
17. Kızıltuğ, S., Çakmak, A., Developable ruled surfaces with Darboux Frame in Minkowski 3-space, *Life Science Journal*, 10(4), 1906–1914, 2013.
18. Li, Y., Gür Mazlum, S., Şenyurt, S., The Darboux trihedrons of timelike surfaces in the Lorentzian 3-space, *International Journal of Geometric Methods in Modern Physics*, 20(2), 2350030–82, 2023.

19. Lopez, R., Differential geometry of curves and surfaces in Lorentz-Minkowski space, *International Electronic Journal of Geometry*, 7, 44–107, 2014.
20. Monterde, J., Salkowski curves revisited: A family of curves with constant curvature and non-constant torsion, *Computer Aided Geometric Design*, 26(3), 271–278, 2009.
21. O'Neill, B., *Semi-Riemannian geometry with applications to relativity*. Academic Press: London, England, 1983.
22. Ratcliffe, J. G., *Foundations of hyperbolic manifolds*. Springer-Verlag: Tokyo, Japanese, 1994.
23. Salkowski, E., Zur transformation von raumkurven. *Mathematische Annalen*, 66(4), 517–557, 1909.
24. Şenatalar, M., *Differential geometry (curves and surfaces theory)*, Istanbul State Engineering and Architecture Academy Publications: İstanbul, Türkiye, 1978.
25. Şentürk, G. Y., Yüce, S., Characteristic properties of the ruled surface with Darboux frame in E3, *Kuwait Journal of Science*, 42(2), 14–33, 2015.
26. Şenyurt, S., Gür, S., Spacelike surface geometry. *International Journal of Geometric Methods in Modern Physics*, 14, 689–700, 2017.
27. Şenyurt, S., Gür, S., Özyılmaz, E., The Frenet vectors and the geodesic curvatures of spherical indicatrix of the timelike Salkowski curve in Minkowski 3-space. *Journal of Advanced Research in Dynamical and Control Systems*. 7(4), 20–42, 2015.
28. Şenyurt, S., Kemal, E., Smarandache curves of spacelike anti-Salkowski curve with a spacelike principal normal according to Frenet frame. *Gümüşhane University, Journal of Science and Technology*, 10, 251–260, 2020.
29. Uğurlu, H. H., On the geometry of time-like surfaces, *Communications, Faculty of Sciences, University of Ankara, A1 Series*, 46, 211–223, 1997.
30. Uğurlu, H. H., Çalışkan, A., *Darboux ani dönme vektörleri ile spacelike ve timelike yüzeyler geometrisi*, Celal Bayar University Press: Manisa, Türkiye, 2012.
31. Uğurlu, H. H., Çalışkan, A., Frenet and Darboux vectors of a timelike curve on timelike ruled surface, I. *The Convention of Sciences, Manisa, Türkiye*, 1995.
32. Uğurlu, H. H., Topal, A., Relation between Darboux instantaneous rotation vectors of curves on time-like surface, *Mathematical and Computational Appl.*, 1, 149–157, 1996.
33. Uğurlu, H. H., Kocayiğit, H., The Frenet and Darboux instantaneous rotation vectors of curves on time-like surface. *Mathematical and Computational Appl.*, 1(2), 133–141, 1996.
34. Walrave, J., *Curves and surfaces in Minkowski space*, Ph.D. Thesis, Katholieke Universiteit, Leuven, Belgium, 1995.
35. Woestijne, I. V., Minimal surfaces of the 3-dimensional Minkowski space, *Geometry and Topology of Submanifolds: II*, Word Scientific, Singapore, 344–369, 1990.
36. Yüce S. (2017) *Öklid uzayında diferansiyel geometri*, Pegem Akademi, Ankara, Türkiye.

# ON TOPOLOGICAL PROPERTIES SOME NEW MODULAR SEQUENCE SPACES

Gülcan Atıcı Turan<sup>1</sup>

<sup>1</sup> Munzur University, Vocational School of Tunceli, Tunceli, Turkey

gatici23@hotmail.com,

## Abstract

In this paper, we introduce some new classes of sequence spaces using Modular sequence spaces. We study some of their properties, like linear space, total paranorm, solidity, symmetricity etc. We obtain some relations between these spaces.

**Keywords:** Sequence spaces; Orlicz function; solid space; symmetric space.

## 1. INTRODUCTION

Let  $w$  denote the set of all sequences  $x = (x_k)$ , and  $\ell_\infty$ ,  $c$  and  $c_0$  be the linear spaces of bounded, convergent and null sequences with real terms, respectively, normed by  $\|x\|_\infty = \sup_k |x_k|$ .

An Orlicz function is a function  $M : [0, \infty) \rightarrow [0, \infty)$  which is continuous, non-decreasing and convex with  $M(0) = 0$ ,  $M(x) > 0$  for  $x > 0$  and  $M(x) \rightarrow \infty$  as  $x \rightarrow \infty$ .

It is well known that if  $M$  is a convex function and  $M(0) = 0$ , then  $M(\lambda x) \leq \lambda M(x)$  for all  $\lambda$  with  $0 < \lambda < 1$ .

Lindenstrauss and Tzafriri [2] used the idea of Orlicz function to define what is called an Orlicz sequence space

$$\ell_M = \left\{ x \in w : \sum_{k=1}^{\infty} \left( M \left( \frac{|x_k|}{\rho} \right) \right) < \infty, \text{ for some } \rho > 0 \right\}$$

which is a Banach space with the norm

$$\|x\| = \inf \left\{ \rho > 0 : \sum_{k=1}^{\infty} \left( M \left( \frac{|x_k|}{\rho} \right) \right) \leq 1 \right\}.$$

The concept of paranorm is closely related to linear metric spaces. It is a generalization of that of absolute value. Let  $X$  be a linear space. A function  $g : X \rightarrow \mathbb{R}$  is called paranorm, if

[P1]  $g(x) \geq 0$ , for all  $x \in X$ ,

[P2]  $g(-x) = g(x)$ , for all  $x \in X$ ,

[P3]  $g(x + y) \leq g(x) + g(y)$ , for all  $x, y \in X$ ,

**[P4]** If  $(\lambda_n)$  is a sequence of scalars with  $\lambda_n \rightarrow \lambda$  ( $n \rightarrow \infty$ ) and  $(x_n)$  is a sequence of vectors with  $(x_n - x) \rightarrow 0$  ( $n \rightarrow \infty$ ), then  $g(\lambda_n x_n - \lambda x) \rightarrow 0$  ( $n \rightarrow \infty$ ).

A paranorm  $g$  for which  $g(x) = 0$  implies  $x = 0$  is called a total paranorm on  $X$ , and the pair  $(X, g)$  is called a totally paranormed space. It is well known that the metric of any linear metric space is given by some total paranorm [5].

**Definition 1.1.** Let  $X$  be a sequence space. Then  $X$  is called

- (i) Solid (or normal), if  $(\alpha_k x_k) \in X$  whenever  $(x_k) \in X$  for all sequences  $(\alpha_k)$  of scalars with  $|\alpha_k| \leq 1$ .
- (ii) Monotone provides  $X$  contains the canonical preimages of all its stepspace.
- (iii) Symmetric if  $(x_k) \in X$  implies  $(x_{\pi(k)}) \in X$ , where  $\pi(k)$  is a permutation of  $\mathbb{N}$ .
- (iv) A sequence algebra if  $(x_k), (y_k) \in X$  implies  $(x_k y_k) \in X$ .
- (v) Convergence free if  $(y_k) \in X$  whenever  $(x_k) \in X$  and  $y_k = \theta$  whenever  $x_k = \theta$  [1].

Parashar and Choudhary [6] introduced and examined some properties of four sequence spaces defined using an Orlicz function  $M$ , which generalized the well-known Orlicz sequence space  $\ell_M$  and strongly summable sequence spaces  $[C, 1, p]$ ,  $[C, 1, p]_0$  and  $[C, 1, p]_\infty$ . It may be noted that the spaces of strongly summable sequences were discussed by Maddox [7]. Mursaleen et al. [8] and Savaş [11], Raj et al. [10] also used an Orlicz function to obtain some sequence spaces.

Let  $u = (u_k)$  be a sequence such that  $u_k \neq 0$  for all  $k \in \mathbb{N}$  and  $t = (t_k)$  be a strictly increasing sequence of positive real numbers. The new generalized difference triangle matrix  $T = (t_{nk}^u)$  constituted by using sequence  $(t_n)$  and non-zero sequence  $(u_n)$  defined by (see [3])

$$t_{nk}^u = \begin{cases} \frac{t_n - t_{n-1}}{t_n} u_n & \text{if } k = n; \\ \frac{t_{n-2} - t_{n-1}}{t_n} u_{n-1} & \text{if } k = n - 1 \\ 0 & \text{if } 0 \leq k < n - 1 \text{ or } k > n \end{cases}$$

where  $k, n \in \mathbb{N}$ . Throughout the paper, we shall denote  $T$ -transforms of a sequence  $x = (x_k)$  denoted by

$$T_k(x) = \frac{t_k - t_{k-1}}{t_k} u_k x_k - \frac{t_{k-1} - t_{k-2}}{t_k} u_{k-1} x_{k-1} \quad [4].$$

Let  $V$  be the set of all sequences  $v$  such that  $v_i \neq 0$  for all  $i \in \mathbb{N}$ .

The following inequality is be used throughout the article. Let  $p = (p_k)$  be a positive sequence of real numbers with  $0 < p_k \leq \sup p_k = H$ ,  $D = \max(1, 2^{H-1})$ . Then for all  $a_k, b_k \in \mathbb{C}$  for all  $k \in \mathbb{N}$ , we have

$$|a_k + b_k|^{p_k} \leq D\{|a_k|^{p_k} + |b_k|^{p_k}\}.$$

## 2. Main Results

**Definition 2.1.** Let  $\mathcal{M} = (M_k)$  be a sequence of Orlicz functions and  $p = (p_k)$  be any sequence of strictly positive real numbers. Then we define the following sequence spaces:

$$\begin{aligned} S_0[\mathcal{M}, T_u, p, v] &= \left\{ x = (x_k) : \lim_n \frac{1}{n} \sum_{k=1}^n v_k \left[ M_k \left( \frac{|T_k(x)|}{\rho} \right) \right]^{p_k} = 0 \right\} \\ S[\mathcal{M}, T_u, p, v] &= \left\{ x = (x_k) : \lim_n \frac{1}{n} \sum_{k=1}^n v_k \left[ M_k \left( \frac{|T_k(x) - l|}{\rho} \right) \right]^{p_k} = 0 \right\} \\ S_\infty[\mathcal{M}, T_u, p, v] &= \left\{ x = (x_k) : \sup_n \frac{1}{n} \sum_{k=1}^n v_k \left[ M_k \left( \frac{|T_k(x)|}{\rho} \right) \right]^{p_k} < \infty \right\} \end{aligned}$$

where for some  $l$  and  $\rho > 0$ .

Some well-known spaces are obtained by specializing  $p$  and  $v$ .

If  $p_k = 1$  for all  $k \in \mathbb{N}$ , then  $S_0[\mathcal{M}, T_u, p, v]$ ,  $S[\mathcal{M}, T_u, p, v]$  and  $S_\infty[\mathcal{M}, T_u, p, v]$  reduce to  $S_0[\mathcal{M}, T_u, v]$ ,  $S[\mathcal{M}, T_u, v]$  and  $S_\infty[\mathcal{M}, T_u, v]$ , respectively as follows:

$$\begin{aligned} S_0[\mathcal{M}, T_u, v] &= \left\{ x = (x_k) : \lim_n \frac{1}{n} \sum_{k=1}^n v_k M_k \left( \frac{|T_k(x)|}{\rho} \right) = 0 \right\} \\ S[\mathcal{M}, T_u, v] &= \left\{ x = (x_k) : \lim_n \frac{1}{n} \sum_{k=1}^n v_k M_k \left( \frac{|T_k(x)|}{\rho} \right) = 0 \right\} \\ S_\infty[\mathcal{M}, T_u, v] &= \left\{ x = (x_k) : \sup_n \frac{1}{n} \sum_{k=1}^n v_k M_k \left( \frac{|T_k(x)|}{\rho} \right) < \infty \right\} \end{aligned}$$

where for some  $l$  and  $\rho > 0$ .

If  $v_k = 1$  for all  $k \in \mathbb{N}$ , then  $S_0[\mathcal{M}, T_u, p, v]$ ,  $S[\mathcal{M}, T_u, p, v]$  and  $S_\infty[\mathcal{M}, T_u, p, v]$  reduce to  $S_0[\mathcal{M}, T_u, p]$ ,  $S[\mathcal{M}, T_u, p]$  and  $S_\infty[\mathcal{M}, T_u, p]$ , respectively as follows:

$$S_0[\mathcal{M}, T_u, p] = \left\{ x = (x_k) : \lim_n \frac{1}{n} \sum_{k=1}^n \left[ M_k \left( \frac{|T_k(x)|}{\rho} \right) \right]^{p_k} = 0 \right\}$$

$$S[\mathcal{M}, T_u, p] = \left\{ x = (x_k) : \lim_n \frac{1}{n} \sum_{k=1}^n \left[ M_k \left( \frac{|T_k(x) - l|}{\rho} \right) \right]^{p_k} = 0 \right\}$$

$$S_\infty[\mathcal{M}, T_u, p] = \left\{ x = (x_k) : \sup_n \frac{1}{n} \sum_{k=1}^n \left[ M_k \left( \frac{|T_k(x)|}{\rho} \right) \right]^{p_k} < \infty \right\}$$

where for some  $l$  and  $\rho > 0$ .

**Theorem 2.2.** Let  $\mathcal{M} = (M_k)$  be a sequence of Orlicz functions and  $p = (p_k)$  be a bounded sequence of strictly positive real numbers, then  $S_0[\mathcal{M}, T_u, p, v]$ ,  $S[\mathcal{M}, T_u, p, v]$  and  $S_\infty[\mathcal{M}, T_u, p, v]$  are linear spaces over the field of complex numbers.

**Proof.** We shall prove only for  $S_0[\mathcal{M}, T_u, p, v]$ . The other cases can be proved similarly. Let  $x, y \in S_0[\mathcal{M}, T_u, p, v]$  and  $a, b \in \mathbb{C}$ . Then there exist positive numbers  $\rho_1$  and  $\rho_2$  such that

$$\lim_n \frac{1}{n} \sum_{k=1}^n v_k \left[ M_k \left( \frac{|T_k(x)|}{\rho_1} \right) \right]^{p_k} = 0,$$

and

$$\lim_n \frac{1}{n} \sum_{k=1}^n v_k \left[ M_k \left( \frac{|T_k(y)|}{\rho_2} \right) \right]^{p_k} = 0,$$

uniformly in  $n$ .

Define  $\rho_3 = \max(2|a|\rho_1, 2|b|\rho_2)$ . Since  $M_k$  are non-decreasing and convex

$$\begin{aligned} \sum_{k=1}^n v_k \left[ M_k \left( \frac{|T_k(ax + by)|}{\rho_3} \right) \right]^{p_k} &\leq \sum_{k=1}^n v_k \left[ M_k \left( \frac{|aT_k(x)|}{\rho_3} + \frac{|bT_k(y)|}{\rho_3} \right) \right]^{p_k} \\ &< \sum_{k=1}^n \frac{1}{2^{p_k}} v_k \left[ M_k \left( \frac{|T_k(x)|}{\rho_1} + \frac{|T_k(y)|}{\rho_2} \right) \right]^{p_k} \\ &< \sum_{k=1}^n v_k \left[ M_k \left( \frac{|T_k(x)|}{\rho_1} + \frac{|T_k(y)|}{\rho_2} \right) \right]^{p_k} \\ &< D \sum_{k=1}^n v_k \left[ M_k \left( \frac{|T_k(x)|}{\rho_1} \right) \right]^{p_k} \\ &\quad + D \sum_{k=1}^n v_k \left[ M_k \left( \frac{|T_k(y)|}{\rho_2} \right) \right]^{p_k} \rightarrow 0 \end{aligned}$$



where  $D = \max(1, 2^{H-1})$ ,  $H = \sup p_k$ . This proves that  $S_0[\mathcal{M}, T_u, p, v]$  is a linear space.

**Theorem 2.3.** Let  $\mathcal{M} = (M_k)$  be a sequence of Orlicz functions and  $p = (p_k)$  be a bounded sequence of strictly positive real numbers. Then  $S_0[\mathcal{M}, T_u, p, v]$  is a topological linear space, total paranormed by

$$g_T(x) = \inf \left\{ \rho^{\frac{pn}{H}} : \left( \frac{1}{n} \sum_{k=1}^n v_k \left[ M_k \left( \frac{|T_k(x)|}{\rho} \right) \right]^{p_k} \right)^{1/H} \leq 1, \quad n = 1, 2, \dots \right\}$$

where  $H = \max(1, \sup p_k)$ .

**Proof.** It is easy to prove that  $g_T(\theta) = 0$  and  $g_T(x) = g_T(-x)$ . When  $a = b = 1$  is taken in the proof of Theorem 1, we write  $g_T(x + y) \leq g_T(x) + g_T(y)$ . Since  $M_k(0) = 0$  for all  $k \in \mathbb{N}$ , we have  $\inf \left\{ \rho^{\frac{pn}{H}} \right\} = 0$  for  $x = 0$ . Conversely, suppose  $g_T(x) = 0$ , then

$$\inf \left\{ \rho^{\frac{pn}{H}} : \left( \frac{1}{n} \sum_{k=1}^n v_k \left[ M_k \left( \frac{|T_k(x)|}{\rho} \right) \right]^{p_k} \right)^{1/H} \leq 1, \quad n = 1, 2, \dots \right\}.$$

This implies that for given  $\epsilon > 0$ , there are some  $\rho_\epsilon (0 < \rho_\epsilon < \epsilon)$  such that

$$\left( \frac{1}{n} \sum_{k=1}^n v_k \left[ M_k \left( \frac{|T_k(x)|}{\rho_\epsilon} \right) \right]^{p_k} \right)^{1/H} \leq 1$$

for each  $n$ . Therefore,

$$\left( \frac{1}{n} \sum_{k=1}^n v_k \left[ M_k \left( \frac{|T_k(x)|}{\epsilon} \right) \right]^{p_k} \right)^{1/H} \leq \left( \frac{1}{n} \sum_{k=1}^n v_k \left[ M_k \left( \frac{|T_k(x)|}{\rho_\epsilon} \right) \right]^{p_k} \right)^{1/H} \leq 1$$

for each  $n \in \mathbb{N}$ . Suppose that  $x_m \neq 0$  for some  $m \in \mathbb{N}$ . Let  $\epsilon \rightarrow 0$ , then  $(\frac{|x_m|}{\epsilon}) \rightarrow \infty$ . It follows

that Suppose that  $x_m \neq 0$  for some  $m \in \mathbb{N}$ . Let  $\epsilon \rightarrow 0$ , then  $(\frac{|x_m|}{\epsilon}) \rightarrow \infty$ . It follows that

$$\left( \frac{1}{m} \sum_{k=1}^m v_k \left[ M_k \left( \frac{|T_k(x)|}{\epsilon} \right) \right]^{p_k} \right)^{1/H} \rightarrow \infty$$

which is a contradiction. Hence  $x_m = 0$  for each  $m$ . Finally, we prove that scalar multiplication is continuous. Let  $\lambda$  be any complex number. By definition,

$$\begin{aligned} g_T(\lambda x^{(m)}) &= \inf \left\{ \rho^{\frac{pn}{H}} : \left( \frac{1}{n} \sum_{k=1}^n v_k \left[ M_k \left( \frac{|T_k(\lambda x^{(m)})|}{\rho} \right) \right]^{p_k} \right)^{1/H} \leq 1, \quad n = 1, 2, \dots \right\} \\ &= \inf \left\{ (|\lambda|s)^{\frac{pn}{H}} : \left( \frac{1}{n} \sum_{k=1}^n v_k \left[ M_k \left( \frac{|T_k(x^{(m)})|}{s} \right) \right]^{p_k} \right)^{1/H} \leq 1, \quad n = 1, 2, \dots \right\} \end{aligned}$$

where  $s = \left(\frac{\rho}{|\lambda|}\right)$ . Since  $|\lambda|^{p_n} \leq \max\{1, |\lambda|^H\}$ , then  $|\lambda|^{p_n/H} \leq (\max\{1, |\lambda|^H\})^{1/H}$ . We have

$$g_T(\lambda x^{(m)}) \leq (\max\{1, |\lambda|^H\})^{1/H} \inf \left\{ s^{\frac{p_n}{H}} : \left( \frac{1}{n} \sum_{k=1}^n v_k \left[ M_k \left( \frac{|T_k(x^{(m)})|}{s} \right) \right]^{p_k} \right)^{1/H} \leq 1 \right\}$$

$$= (\max\{1, |\lambda|^H\})^{1/H} g_T(x^{(m)})$$

which converges to 0 as  $g_T(x^{(m)})$  converges to 0 in  $S_0[\mathcal{M}, T_u, p, v]$ .

Now, suppose that  $\lambda_m \rightarrow 0$  and  $x$  is in  $S_0[\mathcal{M}, T_u, p, v]$ . For arbitrary  $\epsilon > 0$ , let  $N$  be a positive integer such that

$$\frac{1}{n} \sum_{k=1}^n v_k \left[ M_k \left( \frac{|T_k(x)|}{\epsilon} \right) \right]^{p_k} < (\epsilon/2)^H$$

for some  $\rho > 0$  and for all  $n > N$ . This implies that

$$\left( \frac{1}{n} \sum_{k=1}^n v_k \left[ M_k \left( \frac{|T_k(x)|}{\epsilon} \right) \right]^{p_k} \right)^{1/H} < \epsilon/2$$

for some  $\rho > 0$  and for all  $n > N$ . Let  $0 < |\lambda| < 1$ . Using convexities of  $M_k$ , for  $n > N$ , we have

$$\frac{1}{n} \sum_{k=1}^n v_k \left[ M_k \left( \frac{|\lambda T_k(x)|}{\rho} \right) \right]^{p_k} \leq \frac{1}{n} \sum_{k=1}^n v_k \left[ |\lambda| M_k \left( \frac{|T_k(x)|}{\rho} \right) \right]^{p_k} < \left( \frac{\epsilon}{2} \right)^H. \quad (1)$$

Since  $M_k$  are continuous everywhere in  $[0, \infty)$ , for  $n \leq N$ , we get

$$f(t) = \frac{1}{n} \sum_{k=1}^n v_k \left[ M_k \left( \frac{|t T_k(x)|}{\rho} \right) \right]^{p_k}$$

is continuous at 0. Therefore, there exists  $0 < \delta < 1$  such that  $|f(t)| < (\epsilon/2)^H$  for  $0 < t < \delta$ .

Since  $\lambda_m \rightarrow 0$ ,  $\exists K$  such that  $|\lambda_m| < \delta$  for  $m > K$ . Then for  $m > K$  and  $n \leq N$ ,

$$\frac{1}{n} \sum_{k=1}^n v_k \left[ M_k \left( \frac{|\lambda_m T_k(x)|}{\rho} \right) \right]^{p_k} < (\epsilon/2)^H. \quad (2)$$

From the Eqs. (1) and (2), we have

$$\frac{1}{n} \sum_{k=1}^n v_k \left[ M_k \left( \frac{|\lambda_m T_k(x)|}{\rho} \right) \right]^{p_k} < (\epsilon/2)^H$$

and so  $g(\lambda_m x) \rightarrow 0$  as  $m \rightarrow \infty$ .

**Theorem 2.4.** Let  $0 < q_k \leq p_k < \infty$  for each  $k$ . Then  $S_0[\mathcal{M}, T_u, q, v] \subseteq S_0[\mathcal{M}, T_u, p, v]$  and  $S[\mathcal{M}, T_u, q, v] \subseteq S[\mathcal{M}, T_u, p, v]$ .

**Proof.** Let  $x \in S_0[\mathcal{M}, T_u, q, v]$ . Then there is  $\exists \rho > 0$  such that

$$\frac{1}{n} \sum_{k=1}^n v_k \left[ M_k \left( \frac{|T_k(x)|}{\rho} \right) \right]^{q_k}$$

as  $n \rightarrow \infty$ . Since  $q_k \leq p_k$  and for sufficiently large  $n$ ,

$$\frac{1}{n} \sum_{k=1}^n v_k \left[ M_k \left( \frac{|T_k(x)|}{\rho} \right) \right]^{p_k} \leq \frac{1}{n} \sum_{k=1}^n v_k \left[ M_k \left( \frac{|T_k(x)|}{\rho} \right) \right]^{q_k}.$$

Hence  $x \in S_0[\mathcal{M}, T_u, p, v]$ . Similarly, we can prove another result.

**Corollary 2.5.** (i) If  $0 < \inf p_k \leq p_k \leq 1$  for all  $k$ , then  $S_0[\mathcal{M}, T_u, p, v] \subseteq S_0[\mathcal{M}, T_u, v]$  and  $S[\mathcal{M}, T_u, p, v] \subseteq S[\mathcal{M}, T_u, v]$ ,

(ii)  $1 < p_k \leq \sup p_k < \infty$  for all  $k$ , then  $S_0[\mathcal{M}, T_u, v] \subseteq S_0[\mathcal{M}, T_u, p, v]$  and  $S[\mathcal{M}, T_u, v] \subseteq S[\mathcal{M}, T_u, p, v]$ .

**Theorem 2.6.** Let  $0 < p_k \leq q_k < \infty$  for each  $k$  and  $(q_k/p_k)$  be bounded, then  $S_0[\mathcal{M}, T_u, q, v] \subseteq S_0[\mathcal{M}, T_u, p, v]$  and  $S[\mathcal{M}, T_u, q, v] \subseteq S[\mathcal{M}, T_u, p, v]$ .

**Proof.** Let  $x \in S[\mathcal{M}, T_u, q, v]$ . Write

$$z_k = \left[ M_k \left( \frac{|T_k(x) - l|}{\rho} \right) \right]^{q_k} \quad \text{and} \quad \lambda_k = \frac{p_k}{q_k},$$

so that  $p_k \leq q_k$ ,  $0 < \lambda_k \leq 1$ . Take  $0 < \lambda < \lambda_k$ . We define the sequences  $(w_k)$  and  $(\mu_k)$  as follows:

$$w_k = \begin{cases} z_k & \text{if } z_k < 1 \\ 0 & \text{if } z_k \geq 1 \end{cases}$$

and

$$\mu_k = \begin{cases} 0 & \text{if } z_k < 1 \\ z_k & \text{if } z_k \geq 1 \end{cases}.$$

Then it is clear that for all  $k \in \mathbb{N}$ , we have

$$z_k = w_k + \mu_k, \quad z_k^{\lambda_k} = w_k^{\lambda_k} + \mu_k^{\lambda_k}.$$

Now it follows that

$$\mu_k^{\lambda_k} \leq \mu_k < z_k \quad \text{and} \quad w_k^{\lambda_k} \leq w_k^{\lambda}.$$

Therefore,

$$\frac{1}{n} \sum_{k=1}^n v_k z_k^{\lambda_k} \leq \frac{1}{n} \sum_{k=1}^n v_k z_k + \left[ \frac{1}{n} \sum_{k=1}^n v_k w_k \right]^{\lambda}.$$

Hence,  $x \in S[\mathcal{M}, T_u, p, v]$ .

**Theorem 2.7.** For any two sequences  $p = (p_k)$  and  $q = (q_k)$  are of strictly positive real numbers. Then

- (i)  $S_0[\mathcal{M}, T_u, p, v] \cap S_0[\mathcal{M}, T_u, q, v] \neq \emptyset$ ,
- (ii)  $S[\mathcal{M}, T_u, p, v] \cap S[\mathcal{M}, T_u, q, v] \neq \emptyset$ ,
- (iii)  $S_\infty[\mathcal{M}, T_u, p, v] \cap S_\infty[\mathcal{M}, T_u, q, v] \neq \emptyset$ .

**Theorem 2.8.** Let  $\mathcal{M} = (M_k)$  and  $\mathcal{Y} = (Y_k)$  are two sequences of Orlicz functions. Then

- (i)  $S_0[\mathcal{M}, T_u, p, v] \cap S_0[\mathcal{Y}, T_u, p, v] \subseteq S_0[\mathcal{M} + \mathcal{Y}, T_u, p, v]$ ,
- (ii)  $S[\mathcal{M}, T_u, p, v] \cap S[\mathcal{Y}, T_u, p, v] \subseteq S[\mathcal{M} + \mathcal{Y}, T_u, p, v]$ ,
- (iii)  $S_\infty[\mathcal{M}, T_u, p, v] \cap S_\infty[\mathcal{Y}, T_u, p, v] \subseteq S_\infty[\mathcal{M} + \mathcal{Y}, T_u, p, v]$ .

**Proof.** Let  $x \in S_0[\mathcal{M}, T_u, p, v] \cap S_0[\mathcal{Y}, T_u, p, v]$ . Then, there are positive numbers  $\rho_1$  and  $\rho_2$  such that

$$\frac{1}{n} \sum_{k=1}^n v_k \left[ M_k \left( \frac{|T_k(x)|}{\rho_1} \right) \right]^{p_k} \rightarrow 0$$

as  $n \rightarrow \infty$  and

$$\frac{1}{n} \sum_{k=1}^n v_k \left[ Y_k \left( \frac{|T_k(x)|}{\rho_2} \right) \right]^{p_k} \rightarrow 0$$

as  $n \rightarrow \infty$ . Now,

$$\begin{aligned} & \frac{1}{n} \sum_{k=1}^n v_k \left[ (M_k + Y_k) \left( \frac{|T_k(x)|}{\rho_1 + \rho_2} \right) \right]^{p_k} \\ & \leq D \frac{1}{n} \sum_{k=1}^n v_k \left[ \frac{\rho_1}{\rho_1 + \rho_2} M_k \left( \frac{|T_k(x)|}{\rho_1} \right) \right]^{p_k} + D \frac{1}{n} \sum_{k=1}^n v_k \left[ \frac{\rho_2}{\rho_1 + \rho_2} Y_k \left( \frac{|T_k(x)|}{\rho_2} \right) \right]^{p_k} \end{aligned}$$

where  $D = \max(1, 2^{\sup p_k - 1})$ . Thus,  $x \in S_0[\mathcal{M} + \mathcal{Y}, T_u, p, v]$ .

**Theorem 2.9.** The sequence spaces  $S_0[\mathcal{M}, T_u, p, v]$ ,  $S[\mathcal{M}, T_u, p, v]$  and  $S_\infty[\mathcal{M}, T_u, p, v]$  are not convergence free in general.

**Proof.** Let  $p_k = 1$ ,  $v_k = 1$ ,  $t_k = k^2$ ,  $u_k = \frac{1}{t_k - t_{k-1}}$ ,  $x_k = k$ ,  $y_k = (-1)^k k^3$  and  $M_k(x) = x$   $\forall k \in [0, \infty) \forall k \in \mathbb{N}$ . Then  $x = (x_k) \in S_0[\mathcal{M}, T_u, p, v]$ , but  $y = (y_k) \notin S_0[\mathcal{M}, T_u, p, v]$ .

**Theorem 2.10.** The sequence spaces  $S_0[\mathcal{M}, T_u, p, v]$ ,  $S[\mathcal{M}, T_u, p, v]$  and  $S_\infty[\mathcal{M}, T_u, p, v]$  are not symmetric in general.

**Proof.** Let  $t_k = k$ ,  $v_k = 1$ ,  $p_k = 1$ ,  $M_k(x) = x \quad \forall k \in [0, \infty)$ ,

$$u_k = \begin{cases} k & \text{if } k \text{ is odd} \\ 0 & \text{if } k \text{ is even} \end{cases} \quad \text{and} \quad x_k = \begin{cases} 0 & \text{if } k \text{ is odd} \\ k & \text{if } k \text{ is even} \end{cases}$$

$\forall k \in \mathbb{N}$ . Consider the arrangement  $(y_k)$  of  $(x_k)$  defined by  $(y_k) = (2, 0, 4, 0, 6, 0, \dots)$ . Then, we have

$$\frac{1}{n} \sum_{k=1}^n \left[ M_k \left( \frac{|T_k(y)|}{\rho} \right) \right]^{p_k} \rightarrow \infty$$

as  $n \rightarrow \infty$ . Thus,  $(y_k) \notin S_0[\mathcal{M}, T_u, p, v]$ . Hence, the space  $S_0[\mathcal{M}, T_u, p, v]$  is not symmetric.

**Theorem 2.11.** The sequence spaces  $S_0[\mathcal{M}, T_u, p, v]$ ,  $S[\mathcal{M}, T_u, p, v]$  and  $S_\infty[\mathcal{M}, T_u, p, v]$  are not monotone in general.

**Proof.** Let  $p_k = 1$ ,  $v_k = 1$ ,  $t_k = \sqrt{k}$ ,  $u_k = \frac{1}{t_k - t_{k-1}}$  and  $M_k(x) = x \quad \forall k \in [0, \infty) \quad \forall k \in \mathbb{N}$ .

Consider  $K$ th step space of a sequence space  $E$  defined by  $(x_k), (y_k) \in E^K$  implies that  $y_k = x_k$  for  $k$  is odd and  $y_k = 0$  for  $k$  is even. Now, take  $x_k = k$  for all  $k \in \mathbb{N}$ . Then  $x = (x_k) \in S_0[\mathcal{M}, T_u, p, v]$ , but  $y = (y_k) \notin S_0[\mathcal{M}, T_u, p, v]$ . Hence its  $K$ th canonical preimage  $y = (y_k) \notin S_0[\mathcal{M}, T_u, p, v]$ . Therefore, the space  $S_0[\mathcal{M}, T_u, p, v]$  is not monotone.

**Lemma 2.12.** If a sequence space  $X$  is solid, then  $X$  is monotone.

**Corollary 2.13.** The spaces  $S_0[\mathcal{M}, T_u, p, v]$ ,  $S[\mathcal{M}, T_u, p, v]$  and  $S_\infty[\mathcal{M}, T_u, p, v]$  are not solid in general.

**Theorem 2.14.** The sequence spaces  $S_0[\mathcal{M}, T_u, p, v]$ ,  $S[\mathcal{M}, T_u, p, v]$  and  $S_\infty[\mathcal{M}, T_u, p, v]$  are not sequence algebra in general.

**Proof.** Let  $p_k = 1$ ,  $v_k = 1$ ,  $t_k = \sqrt{k}$ ,  $u_k = \frac{1}{t_k - t_{k-1}}$ ,  $x_k = y_k$  and  $M_k(x) = x \quad \forall k \in [0, \infty)$ . Then  $x = (x_k), y = (y_k) \in S_0[\mathcal{M}, T_u, p, v]$ , but  $xy = (x_k y_k) = (k^2) \notin S_0[\mathcal{M}, T_u, p, v]$ . Therefore, the space  $S_0[\mathcal{M}, T_u, p, v]$  is not sequence algebra.

## REFERENCES

1. Kamthan P. K. and Gupta M. Sequence spaces and series, Marcel D. Inc. New York, 1981.
2. Lindenstrauss J. and Tzafriri L. On Orlicz sequence spaces., Israel J. Math, 10, 379-390, 1971.
3. Shanmugavel S. and Pandiarani A. Some new classes of sequence spaces of non-absolute type, International Journal of Pure and Applied Mathematics. 113(10), 119-128 2017.
4. Shanmugavel S. and Pandiarani A. New classes of sequence spaces defined by Orlicz function, The Journal of Analysis, <https://doi.org/10.1007/s41478-018-0149-7>, 2018 .
5. Wilansky A.. Summability Through Functional Analysis, North-Holland Mathematical Studies, 85, 1984.
6. Parashar S.D. and B. Choudhary. Sequence spaces defined by Orlicz functions, Indian Journal of Pure and Applied Mathematics, 25(14), 419–428, 1994.
7. Maddox I.J. Spaces of strongly summable sequences, Quarterly Journal of Mathematics Oxford Series,18, 345–355, 1967.
8. Mursaleen Mushir M. Qamaruddin. Some difference sequence spaces defined by Orlicz functions, Matimyas Mathematica, 24, 42-47, 2001.
9. Musielak J. Orlicz spaces and modular spaces, Lecture Notes in Mathematics, 1034, 1983.
10. Raj K. and Sharma S.K. A new sequence space defined by a sequence of Orlicz functions over n-normed spaces, Acta Univ. Palacki. Olomuc. Fac. rer. nat., Mathematica, 51(1), 89–100, 2012.
11. Savaş E. and Rhoades B.E. On some new sequence spaces of invariant means defined by Orlicz functions. Mathematical Inequalities and Applications, 5(2), 271–281, 2002.
12. Atici Turan G. On Some Topological Properties of Generalized Difference Sequence Spaces Defined, International Journal of Applied Mathematics, 3, 151-161, 2017.
13. Bektaş Ç. A., Atici G. On some new modular sequence spaces, Bol. Soc. Paran. Mat., 31, 55-65, 2013.

# A NUMERICAL COMPARISON ON OPTIMAL CONTROL OF AN ANOMALOUS DIFFUSION PROCESS

Derya AVCI<sup>1</sup>

<sup>1</sup>Department of Mathematics, Faculty of Arts and Sciences, Balıkesir University, Balıkesir, Turkey

<sup>1</sup>[dkaradeniz@balikesir.edu.tr](mailto:dkaradeniz@balikesir.edu.tr),

## Abstract

This study focuses on a numerical comparison of optimal control problem for a one - dimensional anomalous diffusion process modeled via fractional Laplacian and Caputo fractional operators. The anomalous concentration of the process is considered as the state function and the external force effect on the process denotes the control function. In the preliminary study of the present work, the model was reduced to a system of ordinary differential equations depending on state and control functions by applying the separation of variables method. In that study, the problem was solved by the Grünwald-Letnikov method. The present study reveals numerical solutions to the problem by Diethelm's Predictor Corrector method. Comparative results for the Grünwald-Letnikov and Predictor-Corrector methods are illustrated by various Matlab simulations.

**Keywords:** Anomalous diffusion; Space-time fractional diffusion; Optimal control; Predictor-Corrector method.

## 1. INTRODUCTION

The diffusion phenomenon is the movement of particles in nature from a higher concentration to a lower concentration. This natural phenomenon is frequently studied by physicists and biologists because of the physical behavior and molecular structure of molecules, by medical researchers because it occurs at the cellular level in living tissues, and by mathematicians since it needs mathematical modeling [1]. Adolf Fick is accepted the father of the diffusion law. Hence, classical diffusion process is also known as Fickian diffusion. Fick proposed a physical relation between flux of a matter and the gradient of its concentration. The solution of the classical diffusion equation arising from Fick's law corresponds to a probability density function. From the viewpoint of probability theory, Fickian particles show a normal distribution. Fick's works primarily was based on diffusion of fluids. However, over time, it has been observed that the diffusion of many substances does not comply with this law [2]. For example, diffusion occurring in heterogeneous porous medium does not obey Fick's law and is therefore called non-Fickian diffusion. Particles acting non-Fickian can diffuse slower or faster than normal due to the heterogeneity of the medium. The diffusion equations modeling their behavior naturally differ as well. The basic tools of fractional calculus are often quite successful compared to the classical derivative and

integral definitions to provide realistic models for anomalous diffusion processes [3]-[6]. Because time-dependent fractional derivatives are able to represent memory and heritability properties in diffusive transports, spatial fractional derivatives are also capable to represent random jumps (long/short) of diffused particles.

Optimal control of the anomaly in the diffusion process is just as important as the physical interpretation of the behavior. The aim is to keep the diffusion process under control with a force function acting from the environment. In terms of the basic concepts of optimal control theory, the substance concentration in the diffusion process is called the state function, and the external force acting on the process as desired is called the control function. Agrawal [7] was the first to reveal the necessary conditions of optimal control for fractional order systems in sense of Riemann-Liouville definition. Subsequently, he extended this work to multi-dimensional systems with Baleanu [8]. In addition, Agrawal revealed the optimality conditions for fractional-order systems in the Caputo sense [9]. The eigenfunction expansion approach to solve the optimal control of partial fractional order systems was also first introduced by Agrawal [10]. This approach was successfully applied to the problems in different curvilinear coordinate systems [11]-[16]. The basic methodology in [7] has been a classical technique used to obtain optimality conditions for systems with other fractional derivatives [17], [18].

In the present work, comparative results are detailed for Grünwald-Letnikov and Diethelm's Predictor-Corrector methods on a space-time fractional anomalous diffusion model. Numerical results are graphed comparatively. This study is not intended to emphasize the superiority or weakness of numerical methods. On the contrary, it reveals important differences between the two numerical methods in practice.

## 2. PROBLEM FORMULATION

The discussed model in the present work is described in a line segment [15]:

$${}_0^C D_t^\alpha c(x, t) = -\kappa_\beta (-\Delta)^{\beta/2} c(x, t) + f(x, t), \quad x \in [0, 1], \quad (1.1)$$

where  $c(x, t)$  denotes the anomalous concentration, namely state function,  $f(x, t)$  is the external force considered as a control function,  ${}_0^C D_t^\alpha$  and  $(-\Delta)^{\beta/2}$  represent the Caputo and fractional Laplacian operators. Initial and boundary conditions are respectively given by

$$\begin{aligned} c(x, 0) &= c_0(x), \\ c(0, t) &= c(L, t) = 0. \end{aligned} \quad (1.2)$$

The main goal is to minimize the following performance index function subject to the dynamical constraint(1.1):



$$J(u) = \frac{1}{2} \int_0^1 \int_0^L [\omega_1 c^2(x, t) + \omega_2 f^2(x, t)] dx dt, \quad (1.3)$$

where  $\omega_1$  and  $\omega_2$  are the positive weight coefficients which balance the cost of external force  $f$ . It belongs to the admissible set of control functions:

$$U_{ad} = \{f(x, t) : f \text{ is measurable and } 0 \leq f \leq 1\}. \quad (1.4)$$

This is a type of fixed final state and free final time optimal control problem. Before determining the optimality conditions of the problem, the dynamical constraint is reduced to a system of ordinary fractional differential equations. For this purpose, the eigenfunction approach was used in the study (1), which is the pioneering work of the current study. The invariant property of the fractional Laplacian operator allows us to obtain separable solutions with this approach. In that work, the eigenfunction series corresponding to the state and control functions are as follows:

$$\begin{aligned} c(x, t) &= \sum_{k=1}^m c_k(t) \sin\left(\frac{k\pi x}{L}\right), \\ f(x, t) &= \sum_{k=1}^m f_k(t) \sin\left(\frac{k\pi x}{L}\right). \end{aligned} \quad (1.5)$$

Similarly, fractional Laplacian of state function can be represented by the following eigenfunction series expansion:

$$(-\Delta)^{\beta/2} c(x, t) = \sum_{k=1}^m c_k(t) \left(\frac{k\pi}{L}\right)^\beta \sin\left(\frac{k\pi x}{L}\right). \quad (1.6)$$

Note that the upper limit of the series (1.5) and (1.6) theoretically is infinite. However as expected, in numerical calculations, the finite upper limit value  $m$  is assumed by considering the prescribed error tolerance value. That is, the solution series is truncated with an admissible upper bound. Substitution the series (1.5) and (1.6) into the dynamical constraint (1.1) gives

$${}_0^C D_t^\alpha c_k(t) = -\kappa_\beta \left(\frac{n\pi}{L}\right)^\beta c_k(t) + f_k(t), \quad k = 1, 2, \dots, m. \quad (1.7)$$

If the same procedure is applied to the performance index, we obtain

$$J(u) = \int_0^1 \mathcal{L}(c_k, f_k, t) dt, \quad (1.8)$$

where the integrand known as Lagrangian function is

$$\mathcal{L}(c_k, f_k, t) = \frac{L}{4} [\omega_1 c_k^2(t) + \omega_2 f_k^2(t)].$$

Also, the initial condition  $c_0(x)$  can be calculated by taking  $t = 0$  in the series (1.5) and using the orthogonality property for the family  $\left\{ \sin\left(\frac{k\pi x}{L}\right) \right\}_{k=1}^{\infty}$  in the following

$$c_k(0) = \frac{2}{L} \int_0^L c_0(\zeta) \sin\left(\frac{n\pi\zeta}{L}\right) d\zeta. \quad (1.9)$$

Let us denote the right-hand side of Eq.(1.7) by

$$G(c_k, f_k, t) = -\kappa_\beta \left(\frac{k\pi}{L}\right)^\beta c_k(t) + f_k(t). \quad (1.10)$$

The optimality system for the fractional optimal control problem firstly proposed by Agrawal is defined as

$$\begin{aligned} {}^C_0 D_t^\alpha c_k(t) &= G(c_k, f_k, t) && \text{(State condition),} \\ {}^C_t D_1^\alpha \lambda_k(t) &= \frac{\partial \mathcal{L}}{\partial c_k} + \lambda_k(t) \frac{\partial G}{\partial c_k} && \text{(Co-state condition),} \\ \frac{\partial \mathcal{L}}{\partial f_k} + \lambda_k(t) \frac{\partial G}{\partial f_k} &= 0 && \text{(Control condition),} \end{aligned} \quad (1.11)$$

where  $\lambda_k$  represents the Lagrange multiplier (co-state) function. It is a mathematical tool that relates the performance index and the dynamical constraint to each other. It does not make real sense like state and control functions. State condition corresponds to the reduced dynamical constraint (1.7). Co-state condition can be easily determined using  $\mathcal{L}$  and  $G$  functions as follows:

$${}^C_t D_1^\alpha \lambda_k(t) = -\kappa_\beta \left(\frac{k\pi}{L}\right)^\beta \lambda_k(t) + \omega_1 \frac{L}{2} c_k(t). \quad (1.12)$$

such that initial condition for state component and final control component are respectively given by

$$\begin{aligned} c_k(0) &= c_{k0}, \\ \lambda_k(1) &= 0. \end{aligned} \quad (1.13)$$

By calculating the co-state function in terms of control component  $f_k(t)$  from the 3<sup>rd</sup> optimality condition and substituting this into Eq.(1.12) leads to

$${}^C_t D_1^\alpha f_k(t) = \frac{\omega_1}{\omega_2} c_k(t) - \kappa_\beta \left(\frac{k\pi}{L}\right)^\beta f_k(t). \quad (1.14)$$

As a result, fractional optimal system consists of Eq.(1.7) and Eq.(1.14). This system was solved applying Grünwald-Letnikov method in [14]. In the present work, we aim to propose numerical results by Diethelm's Predictor-Corrector (DPC) algorithm and also to compare both results in sense of their differences and similarities. To remind the DPC algorithm, let us consider the following fractional initial-value problem in the Caputo sense:

$$\begin{aligned} {}^C D^\alpha y(t) &= g(t, y(t)), \\ y^{(k)}(0) &= y_0^k, \quad (k = 0, 1, \dots, m = \lceil \alpha \rceil - 1). \end{aligned} \quad (1.15)$$

Integrating both sides reduces the problem to Volterra integral equation as below:

$$y(t) = \sum_{k=0}^{m-1} y_0^{(k)} \frac{t^k}{k!} + \frac{1}{\Gamma(\alpha)} \int_0^t (t-\tau)^{\alpha-1} g(\tau, y(\tau)) d\tau. \quad (1.16)$$

In the classical case, for  $\alpha = 1$ , the problem reduces to

$$\begin{aligned} Dy(t) &= g(t, y(t)), \\ y(0) &= y_0. \end{aligned} \quad (1.17)$$

For this case, the algorithm works in the following steps:

- i. Time length  $T$  is divided into the  $N$  subintervals with the step size  $h = \frac{T}{N}$  such that the set of time nodes is as below:

$$\{t_n = nh : n = 0, 1, \dots, N\}.$$

- ii. The basic idea is to calculate the value  $y_h(t_j) \approx y(t_j)$ , ( $j = 1, 2, \dots, n$ ). Hence, the discretized form of the Volterra equation (1.16) is written as

$$y(t_{n+1}) = y(t_n) + \int_{t_n}^{t_{n+1}} g(\tau, y(\tau)) d\tau. \quad (1.18)$$

- iii. Integration in the right hand side of Eq.(1.18) can be evaluated with trapezoidal rule with two points:

$$\int_a^b g(\tau) d\tau = \frac{b-a}{2} [g(a) + g(b)]. \quad (1.19)$$

Using the relation (1.19), Eq.(1.18) can be rearranged as follows:

$$y(t_{n+1}) = y(t_n) + \frac{h}{2} [f(t_n, y(t_n)) + f(t_{n+1}, y(t_{n+1}))] \quad (1.20)$$

By replacing  $y(t_n)$  with  $y_h(t_n)$ , Eq.(1.20) can be rewritten as

$$y_h(t_{n+1}) = y_h(t_n) + \frac{h}{2} [f(t_n, y_h(t_n)) + f(t_{n+1}, y_h(t_{n+1}))]. \quad (1.21)$$

Notice that the term  $y_h(t_{n+1})$  is stated in the both hand side of Eq.(1.21) and hence it cannot be calculated directly due to the nonlinear function  $f$ . Therefore, a numerical method should be constructed. For this purpose, a predictor term represented by  $y_h^p(t_{n+1})$  is considered and calculated similar to  $y_h(t_{n+1})$  in Eq.(1.20). This term is calculated in each step of algorithm. By considering an error tolerance value for recursive values of solution, algorithm proceeds to run. Because of this procedure, the method is also called as “Adams predictor-corrector algorithm”.

For  $\alpha \neq 1$ , Diethelm et al. [19] improved the algorithm for initial-value problem (1.15). In that work, the integration range is taken as  $[0, t_n]$  different from the integral in Eq.(1.18). Similar to the classical case, the following integration is used in the algorithm:

$$\int_0^{t_{n+1}} (t_{n+1} - \tau)^{\alpha-1} g(\tau) d\tau \approx \int_0^{t_{n+1}} (t_{n+1} - \tau)^{\alpha-1} \bar{g}_{n+1}(\tau) d\tau, \quad (1.22)$$

in where  $\bar{g}_{n+1}$  is a piecewise linear interpolation function at the time nodes  $t_j$  ( $j = 0, 1, \dots, n+1$ ). By some computational techniques of quadrature theory, the integral in (1.22) can be calculated as follows:

$$\int_0^{t_{n+1}} (t_{n+1} - \tau)^{\alpha-1} g(\tau) d\tau \approx \frac{h^\alpha}{\alpha(\alpha+1)} \sum_{j=0}^{n+1} a_{j,n+1} g(t_j), \quad (1.23)$$

where

$$a_{j,n+1} = \begin{cases} n^{\alpha+1} - (n-\alpha)(n+1)^\alpha, & j=0, \\ (n-j+2)^{\alpha+1} + (n-j)^{\alpha+1} - 2(n-j+1)^{\alpha+1}, & 1 \leq j \leq n, \\ 1, & j=n+1. \end{cases} \quad (1.24)$$

Using this result, the integral equation in Eq.(1.16) was approximated [19] as follows:

$$y_h(t_{n+1}) = \sum_{k=0}^{m-1} y_0^{(k)} \frac{t_{n+1}^k}{k!} + \frac{h^\alpha}{\Gamma(\alpha+2)} \left[ f(t_{n+1}, y_h^p(t_{n+1})) + \sum_{j=0}^n a_{j,n+1} f(t_j, y_h(t_j)) \right]. \quad (1.25)$$

Notice that this iteration is valid for left-sided Caputo fractional derivative. However, both of left- and right-sided fractional derivatives naturally arise in the formulation of fractional optimal control problems. Hence, the approximation for right-sided operators is needed for such problems. By noticing this detail, Agrawal firstly [9] improved the Diethelm’s algorithm

to use for fractional optimal control problems. Let us consider the optimal system given by Eqs.(1.7) and (1.14). We use the following abbreviations:

$$k_1 = k_4 = \kappa_\beta \left( \frac{n\pi}{L} \right)^\beta, k_2 = 1, k_3 = \frac{\omega_1}{\omega_2}. \quad (1.26)$$

and hence rewrite the system as follows:

$$\begin{aligned} {}^C_0 D_t^\alpha c_k(t) &= -k_1 c_k(t) + k_2 f_k(t), \\ {}^C_t D_1^\alpha f_k(t) &= -k_3 c_k(t) - k_4 f_k(t). \end{aligned} \quad (1.27)$$

This system can be converted to Volterra integral equation system:

$$\begin{aligned} c(t) &= c(0) + \frac{1}{\Gamma(\alpha)} \int_0^t (t-\tau)^{\alpha-1} (k_2 f(\tau) - k_1 c(\tau)) d\tau, \\ f(t) &= f(1) - \frac{1}{\Gamma(\alpha)} \int_t^1 (\tau-t)^{\alpha-1} (k_4 f(\tau) + k_3 c(\tau)) d\tau, \end{aligned} \quad (1.28)$$

where  $c(0)$  is the initial state and  $f(1)$  is the final control components. The discretized form of  $c(t)$  is as follows:

$$c(t_i) = c(0) + \sum_{j=0}^i a_{ij} [k_2 f(t_j) - k_1 c(t_j)], i = 1, 2, \dots, N. \quad (1.29)$$

or

$$c(t_i) = \frac{1}{1 + k_1 a_{ii}} \left\{ c(0) - k_1 \sum_{j=0}^{i-1} a_{ij} c(t_j) + k_2 \sum_{j=0}^i a_{ij} f(t_j) + k_2 a_{ii} f(t_i) \right\}, i = 1, 2, \dots, N. \quad (1.30)$$

Similarly, discretized form of control component  $f(t)$  is written as

$$f(t_i) = f(1) - \sum_{j=i}^N b_{ij} [k_3 c(t_j) + k_4 f(t_j)], i = N-1, N-2, \dots, 0, \quad (1.31)$$

where  $b_{ij}$  coefficients are given by

$$b_{ij} = \frac{h^\alpha}{\Gamma(\alpha+2)} \begin{cases} 1, & j = i \\ (j-i+1)^{\alpha+1} + (j-i-1)^{\alpha+1} - 2(j-i)^{\alpha+1}, & i+1 \leq j \leq N-1, \\ (N-i-1)^{\alpha+1} - (N-i)^{\alpha+1} + (\alpha+1)(N-i)^\alpha, & j = N. \end{cases} \quad (1.32)$$

Eq.(1.31) can be easily rewritten similar to Eq.(1.30). Eqs.(1.30) and (1.31) are used to construct the algorithm in Matlab.

Let  $k$  denotes the iteration number. Therefore, the prescribed error values for state and control components are described as follows:

$$\varepsilon_c = \max |c_{hj}^{k+1} - c_{hj}^k|, \quad \varepsilon_f = \max |f_{hj}^{k+1} - f_{hj}^k| \quad (1.33)$$

In this approximation, the variation of iteration number  $k$  changes the prescribed error values. For example, for  $k=6$  iteration, both of the error values are 0.01. On the other hand, for  $k=14$  iteration, the error values change as 0.001 as expected. This is a natural result for iterative approximations.

The table below shows the main differences between GL approximation and Diethelm's method:

Grünwald-Letnikov (GL) approximation [14], [15]	Diethelm's predictor-corrector algorithm [9], [19]
The method is directly applied to the fractional differential equation system.	The method is applied after the fractional differential equation system is converted to the Volterra integral equation system.
The definition of GL derivative, and the relations to RL and Caputo derivatives are used to get the numerical solutions.	It is an iterative approach used in the numerical calculation of integrals.
While creating the algorithm, the initial state and the final control values should be known.	In this approach, the initial value of the control should also be known. For this, an estimation is made by considering a tolerance value.
Since it only depends on time discretization, the convergence of the solution is guaranteed by reducing the sub-interval time lengths ( $h$ ) instead of defining specific error parameters for the state and control functions and testing them at each step.	In the algorithm of this approach, error parameters are defined for state and control functions.
Since the analytical and numerical solutions almost overlap after a specific $h$ value, there is no need to use a very small $h$ value when reaching numerical solutions. This allows the GL algorithm to run faster than the iterative approach.	As the value of the estimated errors for the state and control functions decreases, the numerical solutions converge to the analytical solutions. However, unfortunately, the number of iterations also increases, which extends the running time of the algorithm.
The difference between the two approaches is not significant for $\alpha$ and $\beta$ variations.	The difference between the two approaches is not significant for $\alpha$ and $\beta$ variations.

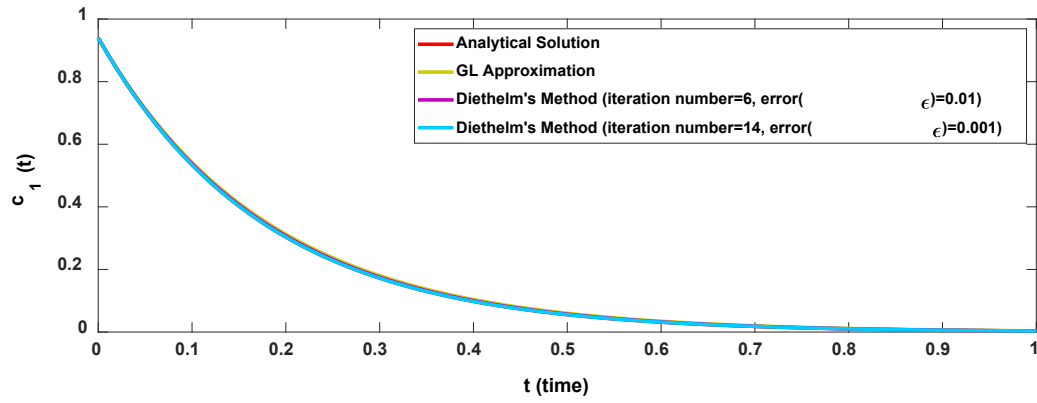


Figure 1. A comparison for state component function:  $\alpha = 1, \beta = 1.75, N = 100$  [15].

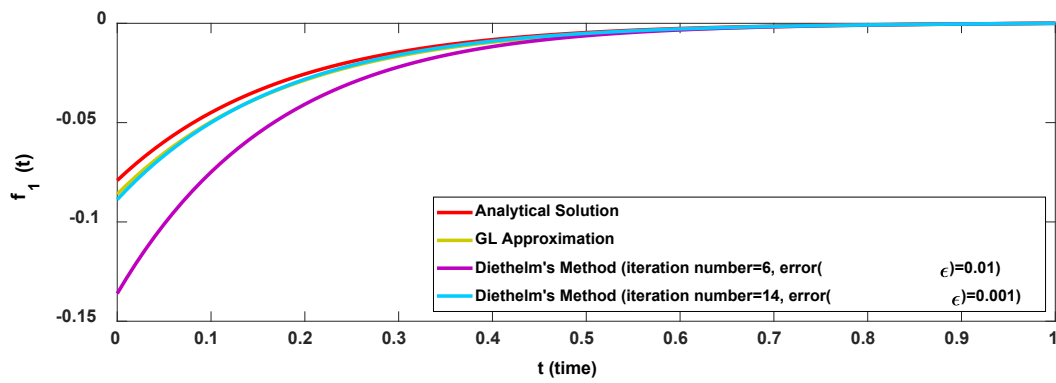


Figure 2. A comparison for control component function:  $\alpha = 1, \beta = 1.75, N = 100$  [15].

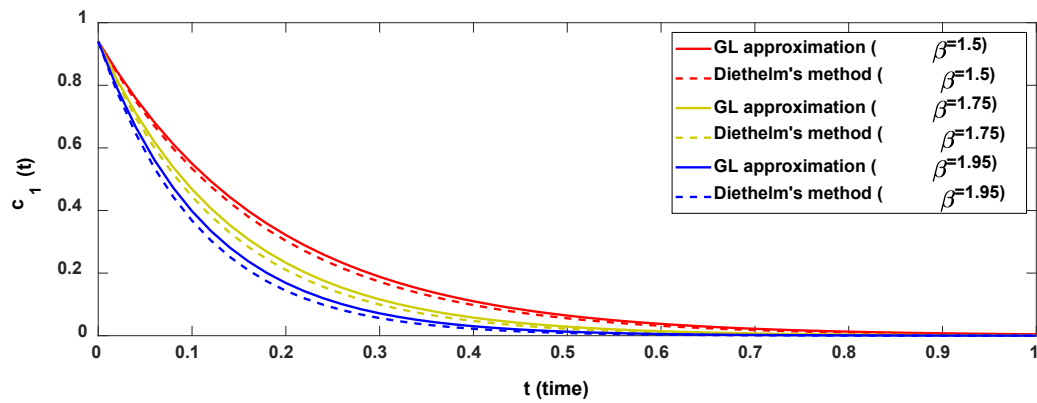


Figure 3. Dependence of state component function on  $\beta$  parameter:  $\alpha = 1, N = 50$  [15].

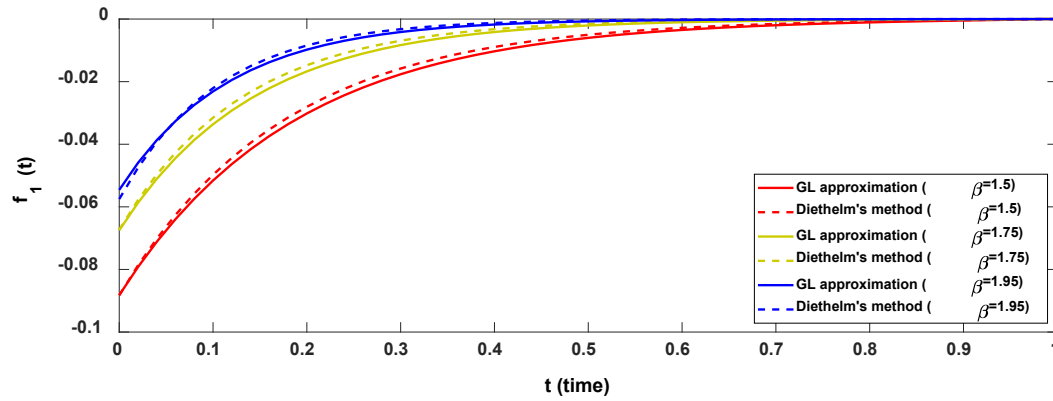


Figure 4. Dependence of control component function on  $\beta$  parameter:  $\alpha=1, N=50$  [15].

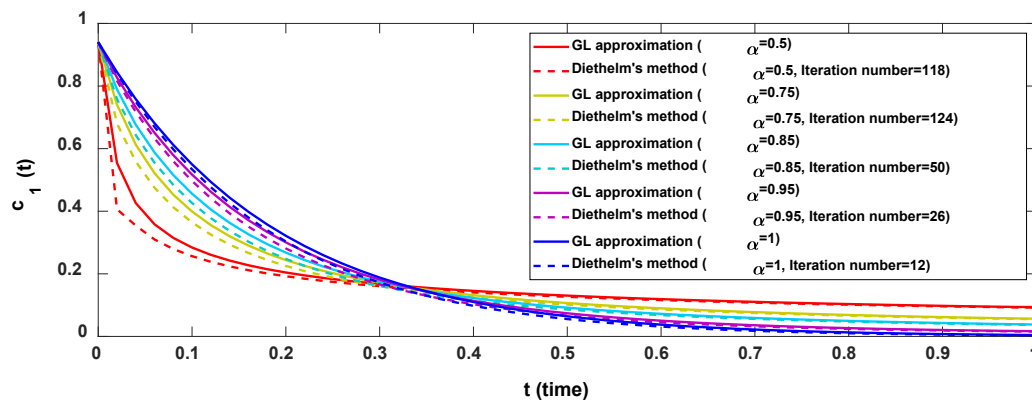


Figure 5. The behavior of state component function for the variations of  $\alpha$  and iteration number [15].

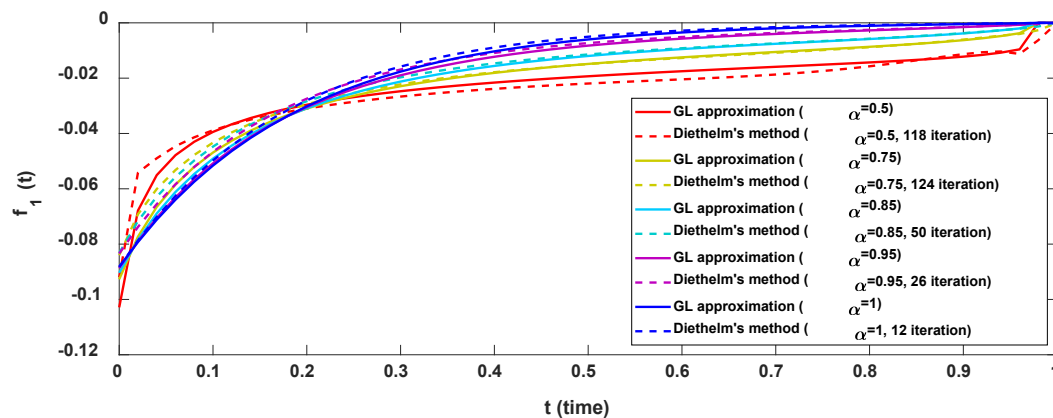


Figure 6. The behavior of control component function for the variations of  $\alpha$  and iteration number [15].

### 3. CONCLUSIONS

This study has focused on comparing the Grünwald-Letnikov and Diethelm's Predictor-Corrector methods for a space-time fractional diffusion model. The differences in the application of both numerical methods have been presented. The dependence of numerical



solutions on various parameters has been demonstrated with graphics. Orthogonal polynomial families have also been widely used for solving fractional optimal control problems, especially in recent years. However, the number of numerical methods that can be applied in solving fractional optimal control problems is still limited.

## REFERENCES

- [1] Crank, John, The mathematics of diffusion, Oxford university press, 1979.
- [2] Deng, Weihua, Hou, Ru, Wang, Wanli, Xu, Pengbo, Modeling anomalous diffusion: from statistics to mathematics, World Scientific, 2020.
- [3] Metzler, Ralf, Klafter, Joseph, The random walk's guide to anomalous diffusion: a fractional dynamics approach, Physics Reports, Vol:339, No:1, 1–77, 2000.
- [4] Mainardi, Francesco, Luchko, Yuri, Pagnini, Gianni, The fundamental solution of the space-time fractional diffusion equation, Fractional Calculus and Applied Analysis, Vol:4, No:2, 153-192, 2001.
- [5] Povstenko, Yuriy, Linear fractional diffusion-wave equation for scientists and engineers, Switzerland: Springer International Publishing, 2015.
- [6] Evangelista, Luiz R., Kaminski Lenzi, Ervin, Fractional diffusion equations and anomalous diffusion, Cambridge University Press, 2018.
- [7] Agrawal, Om P., A General Formulation and Solution Scheme For Fractional Optimal Control Problems, Nonlinear Dynamics, Vol:38, 323-337, 2004.
- [8] Agrawal, Om P., Baleanu, Dumitru, A Hamiltonian Formulation and A Direct Numerical Scheme For Fractional Optimal Control Problems, Journal of Vibration and Control, Vol:13, 1269-1281, 2007.
- [9] Agrawal, Om P., A Formulation and Numerical Scheme for Fractional Optimal Control Problems, Journal of Vibration and Control, Vol: 14, 1291-1299, 2008.
- [10] Agrawal, Om P., Fractional Optimal Control of A Distributed System Using Eigenfunctions, Journal of Computational and Nonlinear Dynamics, Vol:3 No:2, 021204 (6 pages), 2008.
- [11] Özdemir, Necati, Agrawal, Om P., İskender, Beyza B., Karadeniz, Derya, Fractional Optimal Control of A 2-Dimensional Distributed System Using Eigenfunctions, Nonlinear Dynamics, Vol:55, No:3, 251-260, 2009.

- [12] Özdemir, Necati, Agrawal, Om P., Karadeniz, Derya, İskender, Beyza B., Fractional Optimal Control of An Axis-Symmetric Diffusion-Wave Propagation, *Physica Scripta*, Vol: 2009, No:T134, 014024, 2009.
- [13] Özdemir, Necati, Karadeniz, Derya, İskender, Beyza B., Fractional Optimal Control Problem of A Distributed System in Cylindrical Coordinates, *Physics Letters A*, Vol:373, No:2, 221-226, 2009.
- [14] Özdemir, Necati, Avcı, Derya, Optimal control of a linear time-invariant space-time fractional diffusion process, *Journal of Vibration and Control*, Vol:20, No:3, 370-380, 2012.
- [15] Avcı, Derya, Uzay-zaman kesirli difüzyon sistemlerinin optimal kontrolü, PhD Dissertation, No: 324659, 129 pages, 2013.
- [16] Avcı, Derya, Özdemir, Necati, Yavuz, Mehmet, Fractional optimal control of diffusive transport acting on a spherical region, *Methods of Mathematical Modelling: Fractional Differential Equations*, Vol:1, 63-82, 2019.
- [17] Baleanu, Dumitru, Jajarmi, Amin, Hajipour, Mojtaba, A new formulation of the fractional optimal control problems involving Mittag–Leffler nonsingular kernel, *Journal of Optimization Theory and Applications*, No:175, 718-737, 2017.
- [18] Akman Yıldız, Tuğba, Jajarmi, Amin, Yıldız, Burak, Baleanu, Dumitru, New aspects of time fractional optimal control problems within operators with nonsingular kernel, *Discrete & Continuous Dynamical Systems-S*, Vol:13, No:3, 407-428, 2020.
- [19] Diethelm, Kai, Ford, Neville J., Freed, Alan D., A Predictor-Corrector Approach for the Numerical Solution of Fractional Differential Equations, *Nonlinear Dynamics*, Vol:29, No:1-4, 3-22, 2002.

# LINEAR VIBRATION OF NANOBEAM IN THERMAL ENVIRONMENT USING MODIFIED COUPLE STRESS THEORY

Redwan Mohammed Mamu<sup>1</sup>, Necla Togun<sup>1,\*</sup>

<sup>1</sup> Department of Mechanical Engineering, Gaziantep University, 27310 Gaziantep, Turkey

[nkara@gantep.edu.tr](mailto:nkara@gantep.edu.tr)

## Abstract

Nanostructures are used widely in nanotechnology and nano-device in recent years and this paper presents the implementation of perturbation method for the vibration analysis of simple and fixed supported Euler-Bernoulli nanobeam in thermal environment. Considering the thermal loading, the equations of motion of the Euler-Bernoulli nanobeam are obtained using modified couple stress theory. The effect of thermal loadings on the linear vibration of the Euler-Bernoulli nanobeam is presented. Hamilton's principle is employed for obtaining differential equation of motion of nanobeam in cooperation with suitable boundary conditions. An approximate solution of the presented system is developed considering the method of multiple scales, which is one of the perturbation techniques. The effects of temperature ( $\Delta T$ ) and the effect of the material length scale parameter ( $h/l$ ), as well as effects of the simple-simple and clamped-clamped boundary conditions on the vibrations are determined and presented numerically and graphically.

**Keywords:** Vibration; Nanobeam; Modified couple stress theory; Temperature effect

## 1. INTRODUCTION

In recent years, advancement of modern technologies, micro electro-mechanical and nano-electromechanical systems (MEMS/NEMS) consisting of features such as lightweight, small size, high sensitivity, fast response, low energy dissipation, and increasing durability have been found to have wide range of applications [1]. This technological advancement in many engineering fields has facilitated the application of nanostructures because of their extraordinary electrical, thermal and mechanical properties. Nanostructures with temperature dependent properties have been used in nano-electromechanical systems (NEMS). Thus, introducing an accurate mathematical model of nanobeams with temperature-dependent properties is a major and important topic for the design of NEMS. This observation is very important in the industry, especially in the design of precision devices and machines. Nanostructures are capable of making significant difference in people's lives and study on nanobeams, which are an important element of nanostructures, are necessary. Due to widespread utilization of this peerless category of materials at micro and nano scales, during past few years, many experimental tests have been done and a lot of experimental papers have been published on this topic to get the most compatible theory to analyze their behavior [2-11].

The performance of such systems largely depends on a characteristic, termed as the quality factor. The quality factor is defined as the ratio of stored energy in the system and dissipated energy by the system per cycle of vibration. A high quality factor indicates a lower rate of energy dissipation in the vibrating systems. This implies that we need to design systems with high quality factor so that the systems can vibrate for a longer time [1].

The static and dynamic behavior of nanobeam has received considerable attention. Classical elasticity and plasticity cannot be used to interpret the size effect observed in numerous tests at micron and nanometer scales because of their lack in an internal material length scale parameter. However, higher-order (non-local) continuum theories contain material length scale parameters and are capable of explaining microstructure related size (and other) effects. Couple stress theories represent one class of such higher-order theories [3].

The classical couple stress elasticity theory contains four material constants (two classical and two additional) for isotropic elastic materials. The two additional constants are related to the underlying microstructure of the material and are inherently difficult to determine, opening a door for a development of higher order theories like modified couple stress theory. Compared to the classical theory, the modified theory has two advantages: the couple stress tensor being symmetric, and only one internal length scale parameter involved. These features make the modified couple stress theory easier to use.

## 2. MODIFIED COUPLE STRESS THEORY

### 2.1 Description

According to the modified couple stress theory of Yang et al [12], the strain energy is a function of both strain (conjugated with stress) and curvature (conjugated with couple stress). It then follows that the strain energy  $U$  in a deformed isotropic linear elastic material occupying region  $\Omega$  is given by

$$U = \frac{1}{2} \iiint_{\Omega} (\sigma : \varepsilon + m : \chi) dv \quad (1)$$

$$\varepsilon = \frac{1}{2} ((\nabla u) + (\nabla u)^T) = \frac{1}{2} (u_{i,j} + u_{j,i}) \quad (2)$$

$$\chi = \frac{1}{2} ((\nabla \theta) + (\nabla \theta)^T) = \frac{1}{2} (\theta_{i,j} + \theta_{j,i}) \quad (3)$$

$$\sigma = \lambda \text{tr}(\varepsilon) I + 2\mu \varepsilon \quad (4)$$

$$m = 2l^2 \mu \chi \quad (5)$$

where  $\sigma$  (stress tensor),  $\varepsilon$  (strain tensor),  $m$  (deviatoric part of the couple stress tensor),  $\chi$  (symmetric curvature tensor),  $\lambda$  and  $\mu$  being Lamé's constants,  $l$  is a material length scale parameter,  $u$  is a displacement vector, and  $\theta$  is the rotation vector.

## 2.2 Equation of Motion and Boundary Conditions

In this study, vibration of nanobeam in thermal environment is carried out. The two types of boundary conditions that are considered in this study are simple-simple and clamped-clamped boundary conditions. Hamilton's principle and the modified couple stress theory are used to derive the governing equations of motion and boundary condition of Euler-Bernoulli beam model nanobeam.

$$\begin{aligned} \mathcal{E} = & \frac{1}{2} \int_0^L \rho A \left( \frac{\partial y^*}{\partial t^*} \right)^2 dx^* - \frac{1}{2} \int_0^L EI \left( \frac{\partial^2 y^*}{\partial x^{*2}} \right)^2 dx^* - \frac{1}{2} \frac{E}{2(1+\nu)} A l^2 \int_0^L \left( \frac{\partial^2 y^*}{\partial x^{*2}} \right)^2 dx^* + \\ & \frac{1}{2} \int_0^L \bar{N}_t^* \left( \frac{\partial y^*}{\partial x^*} \right)^2 dx^* - \frac{1}{2} \int_0^L N^* \left( \frac{\partial y^*}{\partial x^*} \right)^2 dx^* \end{aligned} \quad (6)$$

where  $y^*$  denotes the transverse displacement of the beam section between supports,  $L$  is the length of the beam,  $t^*$  is the time,  $\rho A$  is the mass per unit length,  $N^*$  is the axial force,  $EA$  is longitudinal rigidity and  $EI$  is flexural rigidity.

Hamilton's principle is one of the most fundamental principles in vibration analysis. It leads to the basic equations of dynamics and elasticity. It is based on the assumption that when a system moves from a state at a time  $t_1$  to a new state at the time  $t_2$ , in a Newtonian route, then the actual route out of all the possible ones obeys stationarity. Hamilton's Principle is given as

$$\delta \int_{t_1}^{t_2} L dt = 0 \quad (7)$$

$$\int_{t_1}^{t_2} (\delta T - (\delta U - \delta W^{\text{ext}})) dt^* = 0 \quad (8)$$

By applying integration by part the following result is obtained.

$$\left( EI + \frac{E}{2(1+\nu)} A l^2 \right) \frac{\partial^4 y^*}{\partial x^{*4}} + \rho A \frac{\partial^2 y^*}{\partial t^{*2}} + \frac{E \alpha A (\Delta T)}{(1-2\nu)} \frac{\partial^2 y^*}{\partial x^{*2}} = \frac{EA}{2L} \left[ \int_0^L \left( \frac{\partial y^*}{\partial x^*} \right)^2 dx^* \right] \frac{\partial^2 y^*}{\partial x^{*2}} \quad (9)$$

The following parameters are then used to convert the above equation into dimensionless form

$$x = \frac{x^*}{L}, \quad y = \frac{y^*}{L}, \quad \xi = \frac{h}{l}, \quad t = \frac{t^*}{L^2} \sqrt{\frac{EI}{\rho A}}, \quad \eta = \frac{6}{(1+\nu)\xi^2}, \quad N_t = \frac{\alpha A (\Delta T) L^2}{I(1-2\nu)} \quad (10)$$

The dimensionless equation then becomes

$$(1 + \eta) \frac{\partial^4 y}{\partial x^4} + \frac{\partial^2 y}{\partial t^2} + N_t \frac{\partial^2 y}{\partial x^2} = \frac{1}{2} \int_0^L \left[ \left( \frac{\partial y}{\partial x} \right)^2 dx \right] \frac{\partial^2 y}{\partial x^2} \quad (11)$$

The boundary conditions are given in Table 1

Table 1 Boundary conditions

S-S case	C-C case
$y(0) = 0$ $y(1) = 0$	$y(0) = 0$ $y(1) = 0$
$y''(0) = 0$ $y''(1) = 0$	$y'(0) = 0$ $y'(1) = 0$

### 3. PERTURBATION ANALYSIS

Analytical solution will be obtained approximately with the help of the multiple scale method, which is one of a perturbation technique Nayfeh [13,14]. According to the following expansion;

$$y(x, t; \epsilon) = y_0(x, T_0, T_1) + \epsilon y_1(x, T_0, T_1) \quad (12)$$

where  $T_n$ , are defined

$$\begin{aligned} T_0 &= t; \quad T_1 = \epsilon t \\ \frac{\partial}{\partial t} &= \epsilon^0 D_0 + \epsilon^1 D_1 \\ \frac{\partial^2}{\partial t^2} &= \epsilon^0 D_0^2 + 2\epsilon D_0 D_1 \end{aligned} \quad (13)$$

where  $\epsilon$  is a small dimensionless parameter and  $D_n$  is the new differential operator, which is defined as:

$$D_n = \frac{\partial}{\partial T_n}, \quad n = 0, 1, 2, 3, \dots \quad (14)$$

Substituting the above equations into our equation of motion and categorizing them according to their respective order

Order (1):

$$(1 + \eta)y_0^{iv} + D_0^2 y_0 + N_t y_0'' = 0 \quad (15)$$

Order ( $\epsilon$ ):

$$\begin{aligned} (1 + \eta)y_1^{iv} + D_0^2 y_1 + N_t y_1'' \\ = -2D_0 D_1 y_0 + \frac{1}{2} \int_0^L [y_0']^2 dx y_0'' + F \cos \Omega t - 2\mu D_0 y_0 \end{aligned} \quad (16)$$

#### 3.1. Linear Problem

In this section, solutions of first-order equations are performed to obtain fundamental linear frequencies and mode shapes. The first order of perturbation, which is linear, the solution is represented by

$$y_0(x, T_0, T_1) = [A(T_1)e^{i\omega T_0} + cc]Y(x) \quad (17)$$

where  $cc$ ,  $\omega$ ,  $A(T_1)$  represent to the complex conjugate, natural frequency, complex amplitude respectively. By substituting the above equation into order (1) results in

$$(1 + \eta)Y^{iv}(x) + (N_t)Y''(x) - \omega^2 Y(x) = 0 \quad (18)$$

The following shape function for any beam segment is considered for solution of the equation

$$Y(x) = c_1 e^{i\beta_1 x} + c_2 e^{i\beta_2 x} + c_3 e^{i\beta_3 x} + c_4 e^{i\beta_4 x} \quad (19)$$

#### 4. NUMERICAL SOLUTIONS

The numerical applications of multiple scale method developed for the linear vibration analysis of nanobeams under temperature effect are presented in this section. The material and geometric properties are selected as follows: height and thickness of rectangular cross-section are  $h=1$  nm and  $b=2h$ , length of nanobeam is  $L=20$  nm. Modulus of elasticity, Poisson's ratio and mass of unit volume are  $E=30$ Gpa,  $\nu=0.3$  and  $\rho=1$  kg/m<sup>3</sup>, respectively. At temperature equal to or lower than room temperature,  $\alpha=-1.6\times 10^{-6}$ , the values of temperature change considered are  $T=0K$ ,  $T=100K$  and  $T=200K$ . At temperature higher than room temperature,  $\alpha=1.1\times 10^{-6}$ , the values of temperature change considered are  $T=400K$ ,  $T=600K$  [15].

Table 1. First three non-dimensional frequencies for Simple-Simple and Clamped-Clamped

		Boundary Conditions					
		S-S			C-C		
h/l	$\Delta T(K)$	Mode 1	Mode 2	Mode 3	Mode 1	Mode 2	Mode 3
Temperature $\Delta T$ is low and room							
1	0	23.3878	93.5512	210.49	53.0175	146.145	286.502
	50	23.5895	93.7536	210.693	53.1288	146.296	286.668
	100	23.7895	93.9555	210.895	53.2398	146.447	286.834
	200	24.1845	94.358	211.299	53.461	146.749	287.164
2	0	14.4846	57.9385	130.362	32.835	90.511	177.438
	50	14.8081	58.2646	130.688	33.0143	90.7548	177.705
	100	15.1246	58.589	131.014	33.1926	90.998	177.972
	200	15.7386	59.2323	131.663	33.5459	91.4822	178.505
3	0	12.1393	48.5572	109.254	27.5184	75.8556	148.707
	50	12.5235	48.9459	109.643	27.7321	76.1464	149.026
	100	12.8962	49.3315	110.031	27.944	76.436	149.344
	200	13.6111	50.0939	110.804	28.3625	77.0117	149.979
4	0	11.203	44.8121	100.827	25.396	70.0051	137.238
	50	11.6182	45.233	101.249	25.6274	70.3201	137.583
	100	12.019	45.65	101.669	25.8565	70.6336	137.928
	200	12.7831	46.4728	102.505	26.3081	71.2561	138.615
5	0	10.7421	42.9683	96.6787	24.3511	67.1247	131.591
	50	11.1744	43.4071	97.1187	24.5923	67.4532	131.952
	100	11.5906	43.8415	97.5568	24.8309	67.7799	132.311
	200	12.3811	44.6976	98.427	25.3007	68.4283	133.026
Temperature $\Delta T$ is high							
1	0	23.3878	93.5512	210.49	53.0175	146.145	286.502
	200	22.824	92.9925	209.932	52.7103	145.728	286.046
	400	22.2459	92.4304	209.373	52.401	145.31	285.59
	600	21.6523	91.8649	208.812	52.0897	144.891	285.132
2	0	14.4846	57.9385	130.362	32.835	90.511	177.438
	200	13.5554	57.032	129.459	32.3363	89.8367	176.7
	400	12.5576	56.1108	128.55	31.8289	89.1569	175.96
	600	11.4733	55.1743	127.635	31.3126	88.4716	175.216
3	0	12.1393	48.5572	109.254	27.5184	75.8556	148.707
	200	11.0139	47.4718	108.175	26.9212	75.0497	147.827
	400	9.75966	46.3611	107.086	26.309	74.2343	146.941
	600	8.31837	45.2231	105.985	25.6808	73.4093	146.049
4	0	11.203	44.8121	100.827	25.396	70.0051	137.238
	200	9.97257	43.6337	99.6576	24.7475	69.1309	136.283
	400	8.56717	42.4226	98.474	24.0797	68.2448	135.322
	600	6.88045	41.1759	97.2761	23.3911	67.3461	134.353
5	0	10.7421	42.9683	96.6787	24.3511	67.1247	131.591
	200	9.4518	41.7379	95.4582	23.6739	66.2125	130.595
	400	7.95492	40.4701	94.2219	22.9747	65.2866	129.592
	600	6.10123	39.1613	92.9692	22.2514	64.3465	128.58

The first three nondimensional vibration frequency values of a nanobeam in thermal environment are tabulated in Table 2 for different values of height-to-height ratio ( $h/l$ ), and temperature change ( $\Delta T(K)$ ). On this study, Table 2 is constructed by taking the values of  $h/l = 1, 2, 3, 4$  and  $5$  values and  $\Delta T = 0, 50, 100, 200$  K for room and low temperature and  $\Delta T = 0, 200, 400$  and  $600$  K for high temperature. In this table, S-S and C-C are considered as boundary condition types of nanobeam. The results of Table 2 indicated that the high temperatures decrease the fundamental frequencies, and low temperatures increase the fundamental frequencies. It is because that nanobeam stiffness rises at a low temperature and decreases at a high temperature. And also it is seen that the thermal effect has a significant effect on the vibration analysis of nanobeam. This holds true for both kinds of boundary conditions. Mode shapes of linear first three frequencies of S-S and C-C are plotted in Fig. 2 for  $h/l=1$  and  $\Delta T=100$  K values, respectively.

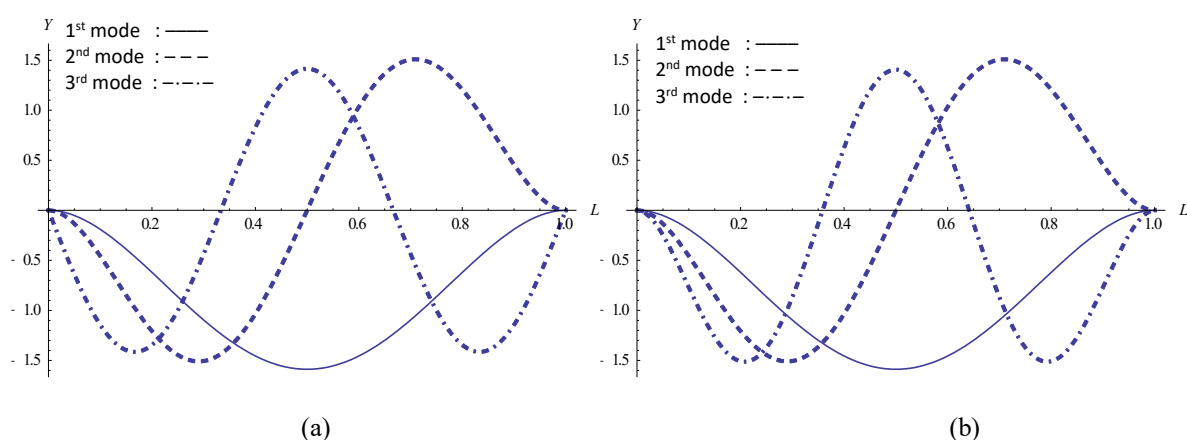


Fig.1. First three vibration modes shape for  $\Delta T=100K$  and  $h/l=1$  a) Simply supported b) Clamped-clamped supported

## 5.CONCLUSIONS

In this study, vibration analysis of nanobeam in thermal environment has been investigated. Euler-Bernoulli beam theory is used to model it and modified couple stress theory is used to describe the problem. The equation of motion of the system is obtained using the Hamilton's principle. These equations are then solved by using one of the perturbation techniques, which is a multiple scale method. The frequency values for simple-simple and clamped-clamped boundary conditions are obtained using height-to-height ratio ( $h/l$ ), and temperature change ( $\Delta T(K)$ ) into consideration. The low temperature increases the fundamental frequency value of the SS and CC nanobeams and the high temperature decreases the fundamental frequency values both type of boundary conditions. It is because of a reduction in the stiffness, and the induced damping effect by the temperature. Any parameter acting on the nanobeam influences the fundamental frequency values.

## Acknowledgments

The authors are grateful to the Gaziantep University Scientific Research Projects (BAPYB) for supporting this work.



## REFERENCES

1. Kumar H, Mukhopadhyay S, Response of deflection and thermal moment of Timoshenko microbeams considering modified couple stress theory and dual-phase-lag heat conduction model, *Composite Structures*, 263, 113620, 2021.
2. Park SK, Gao XL, Bernoulli–Euler beam model based on a modified couple stress theory, *Journal of Micromechanics and Microengineering*, 16(11), 2355, 2006.
3. Park SK, Gao XL, Variational formulation of a modified couple stress theory and its application to a simple shear problem. *Zeitschrift für angewandte Mathematik und Physik*, 59, 904-917, 2008.
4. Mohandes M, Ghasemi AR, Modified couple stress theory and finite strain assumption for nonlinear free vibration and bending of micro/nanolaminated composite Euler-Bernoulli beam under thermal loading, *Proceedings of the Institution of Mechanical Engineers, Part C: Journal of Mechanical Engineering Science*, 231(21), 4044-4056, 2017.
5. Abouelregal AE, Marin M, The Response of nanobeams with temperature-dependent properties using state-space method via modified couple stress theory, *Symmetry*, 12(8), 1276, 2020.
6. Majid G, Navvab S, Vibration analysis of rotating functionally graded Timoshenko microbeam based on modified couple stress theory under different temperature distributions, *Acta Astronautica*, 121, 221-240, 2016.
7. Rahmani A, Faroughi S, Sari M, Abdelkefi A, Selection of size dependency theory effects on the wave's dispersions of magneto-electro-thermo-elastic nano-beam resting on visco-elastic foundation, *European Journal of Mechanics - A/Solids*, 95, 104620, 2022.
8. Ragb O, Mohamed M, Matbuly MS, Free vibration of a piezoelectric nanobeam resting on nonlinear Winkler-Pasternak foundation by quadrature methods, *Heliyon*, 5(6), e01856, 2019.
9. Rahmani A, Safaei B, Qin Z, On wave propagation of rotating viscoelastic nanobeams with temperature effects by using modified couple stress-based nonlocal Eringen's theory. *Engineering with Computers*, 38 (Suppl 4), 2681-2701, 2022.
10. Abouelregal, AE, Mohammed WW, Effects of nonlocal thermoelasticity on nanoscale beams based on couple stress theory, *Mathematical Methods in the Applied Sciences*, 2020.
11. Qi Z, Peng W, He T, Investigation on the thermoelastic response of a nanobeam in modified couple stress theory considering size-dependent and memory-dependent effects, *Journal of Thermal Stresses*, 45(10), 773-792, 2022.
12. Yang, FACM, Chong ACM, Lam DCC, Tong P, Couple stress-based strain gradient theory for elasticity, *International Journal of Solids and Structures*, 39(10), 2731–2743, 2002.
13. Nayfeh AH, *Introduction to perturbation techniques*. John Wiley & Sons, 2011.
14. Nayfeh AH, Mook DT, *Nonlinear Oscillations*, John Wiley, New York, 1979.
15. Yao X, Han Q, Buckling analysis of multiwalled carbon nanotubes under torsional load coupling with temperature change, *Journal of Engineering Materials and Technology*, 128(3), 419-428, 2006.

# LINEAR VIBRATION OF NANOBEAM IN THERMAL ENVIRONMENT USING NONLOCAL ELASTICITY THEORY

Redwan Mohammed Mamu<sup>1</sup>, Necla Togun<sup>1,\*</sup>

<sup>1</sup> Department of Mechanical Engineering, Gaziantep University, 27310 Gaziantep, Turkey

[nkara@gantep.edu.tr](mailto:nkara@gantep.edu.tr)

## Abstract

The linear vibrations of a Euler-Bernoulli nanobeam under the thermal effect are investigated based on nonlocal elasticity theory. The governing equation is proposed by Hamilton's principle considering geometric nonlinearity due to stretching effect. The method of multiple scales is applied to the governing equation to evaluate the linear fundamental frequencies and mode shapes. In the analyses, simple-simple (S-S) and clamped-clamped (C-C) are considered as boundary condition types of nanobeam. The influence of the small scale parameter ( $\gamma$ ) and temperature change parameter ( $\Delta T$ ) as well as effects of different boundary conditions on vibrational frequency are investigated numerically and presented graphically.

**Keywords:** Vibration; Nanobeam; Nonlocal elasticity theory; Thermal environment

## 1. INTRODUCTION

Nanotechnology is an evolving technology, and we can see more applications in nanotechnology. Nowadays, it is clear that it will spread much wider in the future. Nanotechnology can be said to be a golden key for technology, as technology developments continue and human needs is now being ensured by smaller materials and tools [1]. Nanomaterials attracted great concentration due to numerous applications in science and engineering areas such as mechanical, automobile, aviation and space research, defense sector, environment and energy, wireless networks (communication), biomedical sectors electronics (nanorods), material and manufacturing industry, optics, several engineering structures and etc. Hence, detailed investigation of the mechanical behavior of nanostructures including bending, buckling and vibration are necessary to increase their reliability and obtain the proper design of small-scale systems.

In the 1970s and later, Eringen [2,3] proposed the nonlocal elasticity theory to model materials with nonlocal stress not only dependent on the classical local stress at a particular point but also dependent on a spatial integral which represents weighted averages of the contributions of local stress of all points in the domain. The application of nonlocal elasticity theory to micro and nano structures, the version proposed by Peddieson et al.[4], has received much attention in the nanotechnology community, because of the simple constitutive equations that incorporate the small scale parameter. Deformation of nanobeams based on Euler-Bernoulli, Timoshenko or

the shell model was investigated to understand the contribution of the nonlocal effect [4-9]. Lim and Wang [10] used a high-order strain gradient nonlocal stress model to derive bending solutions of a nanobeam at different boundary conditions.

The nonlocal elasticity theory of beams and bars and their static and dynamic analysis led to an understanding of the mechanical behavior of structures at the atomic scale. Numanoglu et al. [11] investigated thermo-mechanical vibrational response of Timoshenko nanobeams by using nonlocal elasticity theory. Abdullah et al. [12] studied nonlinear vibration of nanobeams embedded in the linear and nonlinear elastic materials under magnetic and temperature effects. Demir and Civalek [13] presented vibration analysis of nanobeams embedded in nonlinear elastic medium under thermal and magnetic effects. Magneto-electro-mechanical size dependent nonlinear vibration of a nanobeam embedded in multilayer foundation is studied by using nonlocal elasticity theory [14]. Sari [15] investigated the second and third order superharmonic resonances of a simply supported nonlocal nano Euler-Bernoulli beam which is resting on elastic foundation and subjecting thermal and magnetic axial loads as well as uniform transverse harmonic excitation. Karličić et al. [16] developed a model to describe the free vibration behavior of a cracked nanobeam embedded in an elastic medium by considering the effects of longitudinal magnetic field and temperature change. Lal and Dangi [17] analyzed the vibrational characteristics of a functionally graded non-uniform Timoshenko nanobeam under linear and nonlinear temperature profiles on the base of nonlocal elasticity theory.

In view of above literature survey, in this research is develop numerical methods that best suits to solve the vibration analysis of nanobeam in thermal environment. In this article presents vibration analysis of Euler-Bernoulli nanobeam considering a thermal effect. Size dependency of the nanobeam is described via nonlocal elasticity theory. The governing equations are obtained by Hamilton principle and solved by using multiple scale perturbation method.

## 2. THEORY

### 2.1 Nonlocal elasticity theory

According to the Eringen's nonlocal elasticity theory [3,18,19], the nonlocal stress tensor  $\sigma_{ij}$  at point  $x$  of a homogenous and isotropic nanobeam relates to the local stress-tensor ( $t_{ij}$ ) can be written as:

$$[1 - (e_0 a)^2 \nabla^2] \sigma_{ij} = [1 - (\tau l)^2 \nabla^2] \sigma_{ij} = E \varepsilon(x) = t_{ij} \quad (1)$$

$$\sigma_{xx} - (e_0 a)^2 \frac{\partial^2 \sigma_{xx}}{\partial x^2} = E \varepsilon_{xx} = t_{xx} \quad (2)$$

where  $t_{xx}$  and  $\sigma_{xx}$  are the local and nonlocal normal stresses respectively. Here  $(e_0 a)^2$ ,  $\varepsilon_{xx}$  and  $E$  are the nonlocal parameter, local strain and elastic modulus, respectively. Also,  $e_0$  is a constant appropriate to each material,  $a$  is an internal characteristic length (e.g, lattice parameter, granular distance) and  $L$  is an external characteristic length (e.g, crack length, wavelength). Generally, a conservative estimate of the nonlocal parameter is  $0 \leq e_0 a \leq 2$  nm for SWCNTs is proposed by Wang [20].

## 2.2 Nonlocal Euler Bernoulli beam equation and boundary conditions

Consider a nanobeam in thermal environment as shown in Figure 1. The nanobeam is subjected to stretching effects in a thermal environment as depicted in the figure. Applying the Hamilton's principle and nonlocal theory presented by Eringen [3,18,19] and considering Euler-Bernoulli beam model, the following governing equation is developed

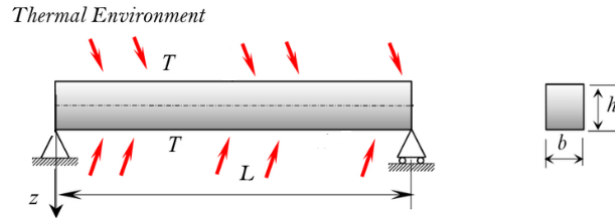


Fig.1. Nanobeam in thermal environment

$$EI \frac{\partial^4 \bar{w}}{\partial \bar{x}^4} + \rho A \frac{\partial^2}{\partial \bar{t}^2} \left[ \bar{w} - (e_0 a)^2 \frac{\partial^2 \bar{w}}{\partial \bar{x}^2} \right] + \frac{EA \alpha \Delta T}{1-2\nu} \frac{\partial^2}{\partial \bar{x}^2} \left[ \bar{w} - (e_0 a)^2 \frac{\partial^2 \bar{w}}{\partial \bar{x}^2} \right] = \frac{EA}{2L} \left[ \int_0^L \left( \frac{\partial \bar{w}}{\partial \bar{x}} \right)^2 d\bar{x} \right] \left[ \frac{\partial^2 \bar{w}}{\partial \bar{x}^2} - (e_0 a)^2 \frac{\partial^4 \bar{w}}{\partial \bar{x}^4} \right] \quad (3)$$

where  $\bar{w}$  is the transverse deflection,  $\bar{t}$  is the time,  $L$  is the length of the beam,  $A$  and  $I$  are area of beam and moment of inertia of the cross section, respectively. Additionally,  $\rho$  is mass density of nanobeam,  $E$  is the Young's modulus of Elasticity,  $\alpha$  is the thermal expansion coefficient,  $\Delta T$  is the temperature change. In Eq. 1, the third term on the left hand side represents the thermal load and the right hand side term represents the stretching load.

The following boundary conditions for the nanobeam are considered in this work.

For simply supported (S-S) nanobeam

$$\begin{aligned} \bar{w}(0, \bar{t}) &= 0, \quad \bar{w}(L, \bar{t}) = 0 \\ \bar{w}''(0, \bar{t}) &= 0, \quad \bar{w}''(L, \bar{t}) = 0 \end{aligned}$$

For clamped-clamped supported (C-C) nanobeam (4)

$$\begin{aligned} \bar{w}(0, \bar{t}) &= 0, \quad \bar{w}(L, \bar{t}) = 0 \\ \bar{w}'(0, \bar{t}) &= 0, \quad \bar{w}'(L, \bar{t}) = 0 \end{aligned}$$

Using the following nondimensional constants and variables

$$w = \frac{\bar{w}}{L}; \quad x = \frac{\bar{x}}{L}; \quad t = \frac{\bar{t}}{L^2} \sqrt{\frac{EI}{\rho A}}; \quad \gamma = \frac{e_0 a}{L}; \quad N_{Temp} = \frac{A \alpha \Delta T L^2}{I(1-2\nu)} \quad (5)$$

The nondimensional form of the governing equation of motion for the nanobeam is given as

$$\begin{aligned} \frac{\partial^4 w}{\partial x^4} + \frac{\partial^2 w}{\partial t^2} - \gamma^2 \frac{\partial^4 w}{\partial x^2 \partial t^2} + N_{Temp} \frac{\partial^2 w}{\partial x^2} - N_{Temp} \gamma^2 \frac{\partial^4 w}{\partial x^4} \\ = \frac{1}{2} \left[ \int_0^1 \left( \frac{\partial w}{\partial x} \right)^2 dx \right] \left[ \frac{\partial^2 w}{\partial x^2} - \gamma^2 \frac{\partial^4 w}{\partial x^4} \right] \end{aligned} \quad (6)$$

and the nondimensional boundary conditions become,

For simply supported (S-S) nanobeam

$$\begin{aligned} w(0, t) &= 0, \quad w(1, t) = 0 \\ w''(0, t) &= 0, \quad w''(1, t) = 0 \end{aligned}$$

$$\begin{aligned} \text{For clamped-clamped supported (C-C) nanobeam} \\ w(0, t) = 0, \quad w(1, t) = 0 \\ w'(0, t) = 0, \quad w'(1, t) = 0 \end{aligned} \quad (7)$$

### 3. METHOD OF SOLUTION

Analytical solution will be obtained approximately with the help of the multiple scale method [21,22], which is one of a perturbation technique Nayfeh [21]. According to a set of first order approximations are sought in the the following expansion;

$$w(x, t; \epsilon) = w_0(x, T_0, T_1) + \epsilon w_1(x, T_0, T_1) \quad (8)$$

where  $\epsilon$  is a small book-keeping parameter representing that the deflections are small.  $T_0 = t$  is the fast time scale characterizing the motions corresponding to the unperturbed linear system, and  $T_1 = \epsilon t$  is the slow time scale characterizing the modulation of the amplitudes and phases due to nonlinearity. The time derivatives are expressed in terms of the new time variables as follows

$$\begin{aligned} \frac{\partial}{\partial t} &= \frac{\partial}{\partial T_0} + \epsilon \frac{\partial}{\partial T_1} \\ \frac{\partial^2}{\partial t^2} &= \frac{\partial^2}{\partial T_0^2} + 2\epsilon \frac{\partial^2}{\partial T_0 \partial T_1} \end{aligned} \quad (9)$$

Substituting the above equations into our equation of motion and categorizing them according to their respective order

Order (1):

$$w_0^{iv} + D_0^2 w_0 - \gamma^2 D_0^2 w_0'' + N_{Temp} w_0'' - N_{Temp} \gamma^2 w_0'^v = 0 \quad (10)$$

Order ( $\epsilon$ ):

$$\begin{aligned} w_1^{iv} + D_0^2 w_1 - \gamma^2 D_0^2 w_1'' + N_{Temp} w_1'' - N_{Temp} \gamma^2 w_1'^v \\ = -2D_0 D_1 w_0 + 2\gamma^2 D_0 D_1 w_0'' + \frac{1}{2} \int_0^1 [w_0'^2 dx] [w_0'' - \gamma^2 w_0'^v] + F \cos \Omega t - 2\mu D_0 w_0 \end{aligned} \quad (11)$$

#### 3.1. Linear Problem

In this section, solutions of first-order equations are performed to obtain fundamental linear frequencies and mode shapes. The first order of perturbation, which is linear, the solution is represented by:

$$w_0(x, T_0, T_1) = [A(T_1)e^{i\omega T_0} + cc]Y(x) \quad (12)$$

where  $cc$ ,  $\omega$ ,  $A(T_1)$  represent to the complex conjugate, natural frequency, complex amplitude, respectively. By substituting the above equation into order (1), the dispersion relation can be found as

$$(1 - N_{Temp} \gamma^2)Y^{iv}(x) + (\gamma^2 \omega^2 + N_{Temp})Y''(x) - \omega^2 Y(x) = 0 \quad (13)$$

The following shape function for any beam segment is considered for solution of the equation

$$Y(x) = c_1 e^{i\beta_1 x} + c_2 e^{i\beta_2 x} + c_3 e^{i\beta_3 x} + c_4 e^{i\beta_4 x} \quad (14)$$

#### 4. NUMERICAL EXAMPLES

In this section, the linear vibration characteristics of the nanobeam under temperature effect are studied. The material constants used in the calculation are Young's modulus  $E=30\text{GPa}$ , the mass density  $\rho=1\text{ kg/m}^3$  and Poisson's ratio  $\nu=0.3$ . The geometrical properties used in the calculation are height and thickness of rectangular cross-section are  $h=1\text{ nm}$  and  $b=2h$ , length of nanobeam is  $L=20\text{ nm}$ .

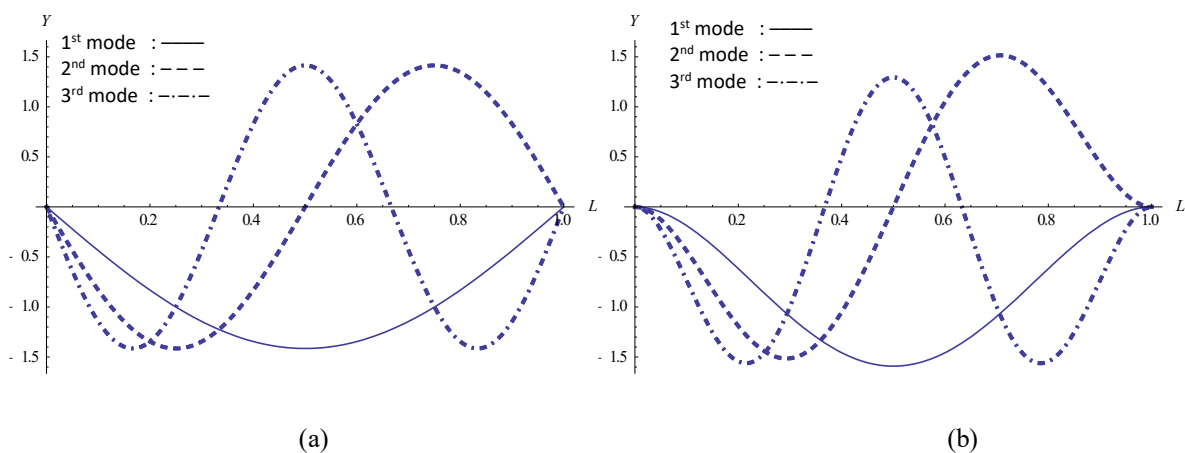


Fig.2. First three vibration modes shape for  $\Delta T=100\text{K}$  and  $e_0a/L=0.1$  a) Simply supported b) Clamped-clamped supported

It should be noted that according to the previous discussions about the values of  $e_0$  and  $a$  in detail,  $e_0a$  is usually considered as the single scale coefficient which is smaller than  $2.0\text{ nm}$  for the nano structures. At temperature equal to or lower than room temperature, thermal expansion coefficient,  $\alpha=-1.6\times 10^{-6}$ , the values of temperature change considered are  $T=0\text{K}$ ,  $T=100\text{K}$  and  $T=200\text{K}$ . At temperature higher than room temperature, thermal expansion coefficient,  $\alpha=1.1\times 10^{-6}$ , the values of temperature change considered are  $T=400\text{K}$ ,  $T=600\text{K}$  [23]. In the analyses, simple-simple (S-S) and clamped-clamped (C-C) are considered as boundary condition types of nanobeam.

In order to show the usability and validity of developed formulation, nondimensional fundamental frequencies of S-S and C-C nanobeams at the room, low and high temperatures are given in Table 1 for different values of small scale parameter,  $\gamma$ , and temperature change ( $\Delta T(\text{K})$ ). The first three modes analytical nondimensional frequencies are also calculated. Table 1 is constructed by taking the small scale parameters as  $\gamma = \frac{e_0a}{L} = 0, 0.1, 0.2, 0.3, 0.4$  and  $0.5$ . and  $\Delta T = 0, 50, 100, 200\text{ K}$  for room and low temperature and  $\Delta T = 0, 200, 400$  and  $600\text{ K}$  for high temperature. According to Table 1, at the temperature  $\Delta T$  is high, we observe that fundamental frequencies decrease by increasing temperature change, while at the temperature  $\Delta T$  is low and room, the fundamental frequencies increases by increasing temperature change. This phenomenon is more visible for lower modes. It is because that nanobeam stiffness rises

at a low temperature and decreases at a high temperature. Also, it is seen from Table1 that an increase in the nondimensional nonlocal parameter gives rise to a decrement in the frequencies. Additionally, it is seen that the thermal effect has a significant effect on the vibration analysis of nanobeam. This holds true for both kinds of boundary conditions. Mode shapes of linear first three frequencies of S-S and C-C are plotted in Fig. 2 for  $\gamma=0.1$  and  $\Delta T=100K$  values, respectively.

Table 1. First three non-dimensional frequencies for Simple-Simple and Clamped-Clamped

		Boundary Conditions					
		S-S			C-C		
$c_0a/L$	$\Delta T(K)$	Mode 1	Mode 2	Mode 3	Mode 1	Mode 2	Mode 3
Temperature $\Delta T$ is low and room							
0	0	9.8696	39.4784	88.8264	22.3733	61.6728	120.903
	50	10.3385	39.9555	89.3051	22.6355	62.0301	121.295
	100	10.787	40.427	89.7813	22.8945	62.3852	121.686
	200	11.6322	41.3539	90.7261	23.4029	63.089	122.464
0.1	0	9.41588	33.4277	64.6414	21.109	50.9832	85.7164
	50	9.90624	33.9898	65.2977	21.4577	51.5244	86.403
	100	10.3734	34.5428	65.9474	21.8006	52.0599	87.0842
	200	11.2498	35.6231	67.228	22.47	53.1146	88.4309
0.2	0	8.35692	24.5823	41.6285	18.2894	36.4239	54.524
	50	8.90578	25.3414	42.6404	18.8509	37.327	55.7304
	100	9.42273	26.0785	43.6289	19.3961	38.2102	56.9113
	200	10.3797	27.4934	45.5415	20.4425	39.9165	59.2025
0.3	0	7.18238	18.5016	29.6181	15.3536	27.0017	38.834
	50	7.81418	19.4989	31.0242	16.1798	28.2973	40.5926
	100	8.39858	20.4476	32.3694	16.9658	29.5362	42.2781
	200	9.4597	22.224	34.9045	18.4373	31.8698	45.4621
0.4	0	6.14558	14.5951	22.7743	12.9047	21.1398	29.9624
	50	6.87335	15.8403	24.5753	14.0051	22.822	32.2671
	100	7.53112	16.9946	26.2529	15.0251	24.3885	34.4178
	200	8.6987	19.0949	29.3217	16.8812	27.2525	38.3592
0.5	0	5.30027	11.9744	18.439	10.9914	17.273	24.3324
	50	6.12925	13.4642	20.622	12.3586	19.3263	27.1622
	100	6.85875	14.8049	22.5952	13.589	21.1815	29.7238
	200	8.12355	17.1751	26.0977	15.7642	24.4736	34.2774
Temperature $\Delta T$ is high							
0	0	9.8696	39.4784	88.8264	22.3733	61.6728	120.903
	200	8.44709	38.1356	87.4965	21.634	60.6786	119.819
	400	6.73035	36.7437	86.146	20.866	59.6667	118.724
	600	4.38655	35.297	84.774	20.0657	58.636	117.618
0.1	0	9.41588	33.4277	64.6414	21.109	50.9832	85.7164
	200	7.91221	31.8306	62.8014	20.1177	49.4639	83.7995
	400	6.04544	30.149	60.9057	19.0725	47.8958	81.838
	600	3.23907	28.368	58.9492	17.9638	46.2739	79.8285
0.2	0	8.35692	24.5823	41.6285	18.2894	36.4239	54.524
	200	6.61682	22.3622	38.7096	16.6471	33.814	51.0597
	400	4.2103	19.8958	35.5518	14.822	30.9848	47.343
	600	3.09032	17.0769	32.0847	12.7346	27.8694	43.3093
0.3	0	7.18238	18.5016	29.6181	15.3536	27.0017	38.834
	200	5.0528	15.43	25.3521	12.8092	23.0662	33.5256
	400	3.49807	11.5698	20.2046	9.61139	18.3033	27.2007
	600	1.99987	5.44411	13.1804	4.53143	11.7453	18.8654
0.4	0	6.14558	14.5951	22.7743	12.9047	21.1398	29.9624
	200	3.42233	10.4304	16.8573	9.22467	15.6052	22.4354
	400	2.13787	7.04748	10.7518	6.33634	13.7989	20.4792
	600	1.25251	5.26593	8.06968	5.85428	11.6548	18.4978
0.5	0	5.30027	11.9744	18.439	10.9914	17.273	24.3324
	200	2.92726	6.25801	10.271	9.57549	13.8326	21.4315
	400	1.85002	5.87965	8.74501	7.34802	11.0257	18.8647
	600	1.03836	5.21252	7.82977	5.00532	9.7852	16.5814



## 5.CONCLUSIONS

The linear vibration characteristics of Euler-Bernoulli nanobeams under thermal effects are investigated by employing nonlocal elasticity theory. The governing equation is derived using the Hamilton's principle. The method of multiple scales is applied to the governing equation to evaluate the linear fundamental frequencies and mode shapes. In the analyses, simple-simple (S-S) and clamped-clamped (C-C) are considered as boundary condition types of nanobeam. Numerical examples show that fundamental frequencies decrease with increasing nonlocal parameter. Fundamental frequencies decrease with rising temperature change for the S-S and C-C end conditions when the temperature  $\Delta T$  is high. And fundamental frequencies increase with rising temperature change for the S-S and C-C end conditions when the temperature  $\Delta T$  is low and room. It is because of a reduction in the stiffness, and the induced damping effect by the temperature. Moreover, the nonlocal parameter is more effective in case of temperature rises.

## Acknowledgments

The authors are grateful to the Gaziantep University Scientific Research Projects (BAPYB) for supporting this work.

## REFERENCES

1. Yaylı MÖ, Küpeli T, Çavuş Y, Weighted residual approach for bending analysis of nanobeam using by modified couple stress theory. *International Journal of Engineering and Applied Sciences*, 13(2), 43-55, 2021.
2. Eringen AC, *Nonlocal Polar Field Models*, Academic Press, New York, 1976.
3. Eringen AC, On differential equations of nonlocal elasticity and solutions of screw dislocation and surface waves, *Journal of Applied Physics*, 54(9), 4703-4710, 1983.
4. Peddieson J, Buchanan GR, McNitt RP, Application of nonlocal continuum models to nanotechnology, *International Journal of Engineering Science*, 41(3), 305-312, 2003.
5. Sudak LJ, Column buckling of multiwalled carbon nanotubes using nonlocal continuum mechanics, *Journal of Applied Physics*, 94(11), 7281-7287, 2003.
6. Zhang YQ, Liu GR, Wang JS, Small-scale effects on buckling of multiwalled carbon nanotubes under axial compression, *Physical Review B*, 70(20), 205430, 2004.
7. Wang Y, Ru CQ, Mioduchowski A, Free vibration of multiwall carbon nanotubes, *Journal of Applied Physics*, 97(11), 114323, 2005.
8. Wang LF, Hu HY, Flexural wave propagation in single-walled carbon nanotubes, *Physical Review B*, 71, 195412, 2005.
9. Wang Q, Liew KM, Application of nonlocal continuum mechanics to static analysis of micro- and nano-structures, *Physical Letters A*, 363(3), 236-242, 2007.
10. Lim CW, Wang CM, Exact variational nonlocal stress modeling with asymptotic higher-order strain gradients for nanobeams, *Journal of Applied Physics*, 101(5), 054312, 2007.
11. Numanoğlu HM, Ersoy H, Akgöz B, Civalek Ö, A new eigenvalue problem solver for thermo-mechanical vibration of Timoshenko nanobeams by an innovative nonlocal finite element method, *Mathematical Methods in the Applied Sciences*, 45(5), 2592-2614, 2022.
12. Abdullah SS, Hosseini-Hashemi S, Hussein NA, Nazemnezhad R, Thermal stress and magnetic effects on nonlinear vibration of nanobeams embedded in nonlinear elastic medium, *Journal of Thermal Stresses*, 43(10), 1316-1332, 2020.



13. Demir Ç, Civalek Ö, A new nonlocal FEM via Hermitian cubic shape functions for thermal vibration of nano beams surrounded by an elastic matrix, *Composite Structures*, 168, 872-884, 2017.
14. Sobamowo GM, Size-dependent nonlinear vibration analysis of nanobeam embedded in multi-layer elastic media and subjected to electromechanical and thermomagnetic loadings, *Curved and Layered Structures*, 9(1), 403-424, 2022.
15. Sari MES, Superharmonic resonance analysis of nonlocal nano beam subjected to axial thermal and magnetic forces and resting on a nonlinear elastic foundation, *Microsystem Technologies*, 23, 3319-3330, 2017.
16. Karličić D, Jovanović D, Kozić P, Cajić M, Thermal and magnetic effects on the vibration of a cracked nanobeam embedded in an elastic medium. *Journal of Mechanics of Materials and Structures*, 10(1), 43-62, 2015.
17. Lal R, Dangi C, Thermal vibrations of temperature-dependent functionally graded non-uniform Timoshenko nanobeam using nonlocal elasticity theory, *Materials Research Express*, 6(7), 075016, 2019.
18. Eringen AC, Nonlocal polar elastic continua, *International Journal of Engineering Science*, 10(1), 1–16, 1972.
19. Eringen AC, Edelen D, On nonlocal elasticity, *International Journal of Engineering Science*, 10(3), 233–248, 1972.
20. Wang Q, Wave propagation in carbon nanotubes via nonlocal continuum mechanics, *Journal of Applied Physics*, 98(12), 124301, 2005.
21. Nayfeh AH, *Introduction to Perturbation Techniques*, John Wiley, New York, 1981.
22. Nayfeh AH, Mook DT, *Nonlinear Oscillations*, John Wiley, New York, 1979.
23. Yao X, Han Q, Buckling analysis of multiwalled carbon nanotubes under torsional load coupling with temperature change, *Journal of Engineering Materials and Technology*, 128(3), 419-428, 2006.

**7<sup>th</sup> INTERNATIONAL CONFERENCE ON  
COMPUTATIONAL MATHEMATICS AND  
ENGINEERING SCIENCES**

[www.cmescongress.org](http://www.cmescongress.org)

